Sivashankar Krishnamoorthy
Krzysztof (Kris) Iniewski *Editors*

Advances in Fabrication and Investigation of Nanomaterials for Industrial Applications

Springer

Advances in Fabrication and Investigation of Nanomaterials for Industrial Applications

Sivashankar Krishnamoorthy • Krzysztof (Kris) Iniewski
Editors

Advances in Fabrication and Investigation of Nanomaterials for Industrial Applications

Springer

Editors
Sivashankar Krishnamoorthy
Luxembourg Institute of Science and Technology
Belvaux, Luxembourg

Krzysztof (Kris) Iniewski
Redlen Technologies
Port Moody, BC, Canada

ISBN 978-3-031-42699-5 ISBN 978-3-031-42700-8 (eBook)
https://doi.org/10.1007/978-3-031-42700-8

© The Editor(s) (if applicable) and The Author(s), under exclusive license to Springer Nature Switzerland AG 2024
This work is subject to copyright. All rights are solely and exclusively licensed by the Publisher, whether the whole or part of the material is concerned, specifically the rights of translation, reprinting, reuse of illustrations, recitation, broadcasting, reproduction on microfilms or in any other physical way, and transmission or information storage and retrieval, electronic adaptation, computer software, or by similar or dissimilar methodology now known or hereafter developed.
The use of general descriptive names, registered names, trademarks, service marks, etc. in this publication does not imply, even in the absence of a specific statement, that such names are exempt from the relevant protective laws and regulations and therefore free for general use.
The publisher, the authors, and the editors are safe to assume that the advice and information in this book are believed to be true and accurate at the date of publication. Neither the publisher nor the authors or the editors give a warranty, expressed or implied, with respect to the material contained herein or for any errors or omissions that may have been made. The publisher remains neutral with regard to jurisdictional claims in published maps and institutional affiliations.

This Springer imprint is published by the registered company Springer Nature Switzerland AG
The registered company address is: Gewerbestrasse 11, 6330 Cham, Switzerland

Paper in this product is recyclable.

Contents

Supersonic Cluster Beam Deposition for the Integration of Functional Nanostructured Films in Devices 1
E. Barborini and S. Vinati

Advances in Colloidal Synthesis of "Giant" Core/Thick-Shell Quantum Dots 29
Tory A. Welsch, Jill M. Cleveland, D. Bruce Chase, and Matthew F. Doty

Emerging Trends in Nanotechnology for Forensic Science 51
Alexandro Mangueira Lima de Assis, Gerard de Oliveira Deokaran, and Adriana Santos Ribeiro

Nanoparticles-Induced Alignment of Nematic Liquid Crystals for Tunable Electro-Optical Devices 71
Ajay Kumar and Gautam Singh

Photoelectrochemical Immunosensor for Carcinoembryonic Antigen Detection: An Attempt for Early Cancer Screening 91
Longshan Zhao and Chunling Mao

Scanning Photodielectric Spectroscopy of CdZnTe Crystals 111
Oleg Chugai, Oleksii Poluboiarov, Serhii Oliinyk, and Sergei Sulima

Photoinduced Electron Transfer Dynamics in Hybrid Quantum Dot/Molecular Catalyst Systems for Artificial Photosynthesis 133
Thomas Michael Khazanov, Niharika Krishna Botcha, and Anusree Mukherjee

Interparticle Charge Transport Enhances Electrochemiluminescence of Quantum Dots 149
Xuwen Gao and Bin Cai

Optical Structural and Phonon Characteristics of Epitaxially Grown II –VI/III –V Films and Superlattices 169
Devki N. Talwar

Defect Engineering in Epitaxially Grown Cd(Zn)Te Thin Films on Lattice-Mismatch Substrates 205
Wenwu Pan, Lorenzo Faraone, and Wen Lei

Defect-Influenced Modeling of Photophysics in Lead-Based Hybrid and All-Inorganic Perovskites 223
Irina Gushchina and Masaru Kuno

Charge Carrier Dynamics of Halide Perovskite Nanocrystals: Application Toward X-Ray/Gamma-Ray Radiation Detection 239
Zheng Zhang

Development of Thallium-Based Semiconductors and Scintillators for High Energy Radiation Detection 257
Ge Yang, Doup Kim, and Ibrahim Hany

Printable Organic and Hybrid Semiconductors: A New Frontier for Detecting Ionizing Radiation 275
Jessie A. Posar and Matthew J. Griffith

Halide Perovskite Thin Films for Neutron and X-Ray Detection 293
Leunam Fernandez-Izquierdo, Martin G. Reyes-Banda, Mahsa Shekarnoush, Zeshaan H. Shamsi, Jesus A. Caraveo-Frescas, and Manuel Quevedo-Lopez

Metal Halide Perovskite Solar Modules: Manufacturing and Performance 309
Angelique Montgomery and Joshua Stein

Naturally Inspired Heme-Like Chemistries for the Oxygen Reduction Reaction: Going Beyond Platinum Group Metals in Proton Exchange Membrane Fuel Cell Catalysis 325
Robin J. White

Integration of Electrical Energy Storage Devices with Photovoltaic Solar Cells in One Hybrid System 353
Shikhamir Eminov, Arif Hashimov, Alovsat Rajabli, Jafar Guliev, Gultekin Mammadova, Samira Abdulayeva, and Aysel Karimova

Design and Optimization of CdTe QDs Luminescent Solar Concentrators Based on Analytic and Simulation Models 373
Alvaro Flores-Pacheco, Rosendo López-Delgado, Arturo A. Ayón, and Mario Enrique Álvarez-Ramos

Index 393

Supersonic Cluster Beam Deposition for the Integration of Functional Nanostructured Films in Devices



E. Barborini and S. Vinati

Acronyms

AFM	Atomic Force Microscopy
AI	Artificial Intelligence
CSC	Charge Storage Capacity
CTC	Circulating Tumor Cell
ECM	Extracellular Matrix
ECoG	Electrocorticography
FISH	Fluorescence In Situ Hybridization
IDE	Interdigitated Electrodes
IONM	Intraoperative Neurophysiological Monitoring
IoT	Internet of Things
MALDI-MS	Matrix-Assisted Laser Desorption/Ionization Mass Spectrometry
MSI	Mass Spectrometry Imaging
NOX	Nitrogen Oxides
PDMS	Polydimethylsiloxane
PMCS	Pulsed Microplasma Cluster Source
PMMA	Polymethyl Methacrylate
SCBD	Supersonic Cluster Beam Deposition
SEM	Scanning Electron Microscopy
TEM	Transmission Electron Microscopy
UHV	Ultrahigh Vacuum
VOC	Volatile Organic Compounds
XPS	X-Ray Photoelectron Spectroscopy

E. Barborini (✉)
Materials Research and Technology (MRT) Department, Luxembourg Institute of Science and Technology (LIST), Belvaux, Luxembourg
e-mail: emanuele.barborini@list.lu

S. Vinati
ParteQ GmbH, Malsch, Germany

© The Author(s), under exclusive license to Springer Nature Switzerland AG 2024

S. Krishnamoorthy, K. (Kris) Iniewski (eds.), *Advances in Fabrication and Investigation of Nanomaterials for Industrial Applications*,
https://doi.org/10.1007/978-3-031-42700-8_1

1 Introduction

Supersonic cluster beam deposition (SCBD) is nowadays a consolidated technology for the production of nanostructured layers by soft assembling of atomic clusters. The strength of the method relies, on one hand, on the capability of directly depositing nanostructured films onto any kind of substrate/device, in clean conditions at room temperature, and, on the other hand, on the peculiar properties of the cluster-assembled films, in which the characteristics of the nanoscale building blocks are preserved and exposed to the external environment, thanks to film's nanoporous structure. The weakness regards the relatively poor adhesion of the films in respect to mechanical scratch and friction. SCBD supports basic and applied research in several universities and research centers worldwide, including CIMaINA (Italy), University of Swansea (UK), I-LAMP (Italy), TASC (Italy), University of Catania (Italy), LIST (Luxembourg), PolyU (Hong-Kong), and NITech (Japan). Also, hi-tech companies, operating in the field of biomedical devices for cancer early detection and neurorecording/stimulation, do exist taking advantage of SCBD in their products, namely, Tethis (tethis-lab.com, Milan, Italy) and Wise (wiseneuro.com, Milan, Italy).

The aim of this chapter is (i) to provide the concept and some essential technical details about the deposition method; (ii) to present an overall description of the main properties of the nanostructured films obtained by SCBD – particularly those general aspects irrespective of a specific material; and (iii) eventually to report about noticeable examples of devices having nanostructured films by SCBD as core functional element, some of them closely approaching the market. Considering the multidisciplinary of the topic, efforts have been done in order to present the content of the chapter in a clear and understandable way for nonspecialist reader, trying to emphasize the rationale background and the logic traits behind exposed concepts.

Given the large scientific literature produced in the last two decades on nanostructured films by SCBD, a careful selection of the matter to be presented was carried out to avoid showing results not yet fully consolidated or too specific. The number of quoted references has been kept rather limited, and the most recent publications have been preferred, whenever possible. The reader who is interested in deepening a specific subject is encouraged to browse the literature mentioned in the most recent publications quoted.

In addition to this Introduction, the chapter has six main sections: Supersonic Cluster Beam Deposition, Main Properties of Cluster-Assembled Nanostructured Films, Chemoresistive Gas Microsensors, Surfaces for Cell Capture in Oncological Research and Diagnostics, Electrodes for Neurorecording and Neuromodulation, and Plates for Sample Processing by MALDI-MS in Proteomic Clinical Research. The short final section Perspectives is dedicated to a couple of very recent developments involving nanostructured materials by SCBD: neuromorphic devices and heterogeneous catalysis. Clearly, this chapter covers only in part the landscape of knowledge areas in which SCBD is feeding new discoveries and new applicative opportunities, and the reader is proposed to keep an eye on what is going on and coming next.

2 Supersonic Cluster Beam Deposition

2.1 Structure of an SCBD Apparatus

Supersonic cluster beam deposition is a vacuum-based physical method for the deposition of nanostructured thin films. Although several customizations are possible, addressing specific needs, the general structure of an SCBD apparatus consists of a deposition chamber operating in high-vacuum regime (base pressure 1×10^{-7}–1×10^{-5} mbar), to which another chamber – hosting the cluster source – is faced. This last is named expansion chamber as the supersonic gas expansion from the cluster source, forming the cluster beam, takes place within it. The two chambers are separated by a small-area orifice, with a peculiar conical shape ("skimmer"), that ensures differential vacuum conditions. During cluster source operation, the gas load in the expansion chamber is particularly high, and an adequate pumping setup dedicated to the expansion chamber only is required (typically a turbomolecular or diffusion pump with 1000–2000 l/s speed, backed with a primary pump with 30–40 m^3/h speed). Thanks to the differential vacuum conditions ensured by the orifice, however, the gas load into the deposition chamber is much lower, and the dedicated pumping setup can be less demanding: a turbomolecular pump with 300–500 l/s speed backed with a primary one with <10 m^3/h can perform well. Figure 1 shows the scheme of an SCBD apparatus, according to this description.

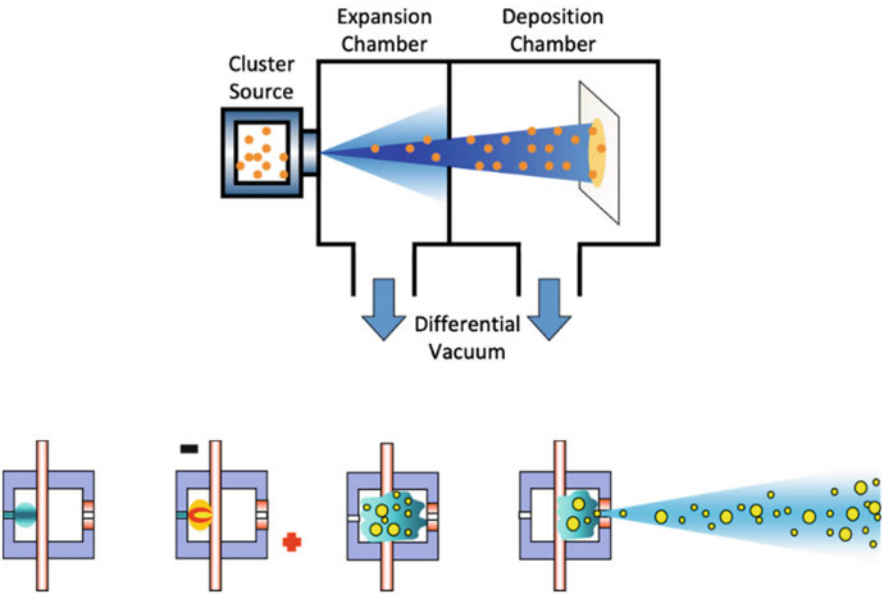


Fig. 1 *Top*: apparatus scheme for supersonic cluster beam deposition: a supersonic gas expansion takes place from the "high-pressure" region – inside the cluster source – toward a vacuum chamber (expansion chamber); the central part of the beam is allowed to proceed to the deposition chamber, where the substrate for film growth is exposed to the cluster beam. *Bottom*: principle of operation of the pulsed microplasma cluster source (see text for details). (Reprinted from Ref. [1])

A simplified scheme has been recently introduced, where a unique chamber equipped with a high-performing pumping setup plays both roles of expansion and deposition chamber. In such scheme, the cluster source is directly facing the deposition chamber. In general, the simplified scheme is preferred for industrial applications, while the scheme based on differential vacuum is preferred in fundamental materials science studies. In respect to these last, the number of stages of differential vacuum can be increased beyond two in the cases where deposition has to take place in ultrahigh-vacuum (UHV) conditions, to meet the requirements of surface-sensitive characterization facilities, e.g., X-ray photoelectron spectroscopies (XPS). Clearly, the length extension of the deposition system – from the cluster source to the deposition chamber – has an impact on the intensity of the cluster beam reaching the deposition substrate. However, as discussed in the following, one of the peculiarities of the beam generated by a supersonic gas expansion is its collimation, meaning that the main fraction of particles is concentrated along the beam axis and – upon proper alignment can reach the deposition substrate even if positioned remarkably away from the cluster source.

2.2 Supersonic Cluster Beam Sources

A supersonic cluster beam source exploits the expansion of a gas from a relatively high-pressure region inside the source body (where the thermodynamic state of the gas is named "stagnation state") to a low-pressure region (the expansion chamber), separated by a nozzle. During the expansion process, the enthalpy of the stagnation state is converted into ordered kinetic energy of the gas molecules/atoms, whose velocity vectors get aligned with the nozzle axis. The divergence of the beam can reach values as low as 1 degree. In the limit, ideal condition where the enthalpy is fully converted into kinetic energy, beam velocity can be estimated as

$$v_\infty = \sqrt{\frac{2k}{m}\left(\frac{\gamma}{\gamma - 1}\right) T_0} \tag{1}$$

where k is the Boltzmann constant, m is the mass of the expanding gas, γ is the adiabatic index, and T_0 is the stagnation temperature in K [2]. Velocities of the order of 1000 m/s can be easily obtained with low-mass gases, e.g., He and Ne. If the gas in the stagnation state is properly "populated" with particles, they will be carried by the expanding gas and accelerated close to the gas velocity, forming a supersonic beam of particles. To the purposes of this chapter, such particles are atomic clusters. But how the stagnation state can be populated with atomic clusters?

To this purpose, in the last decades, several kinds of cluster beam sources have been developed, including laser vaporization cluster sources, gas aggregation cluster sources based on magnetron sputtering, pulsed microplasma cluster sources, matrix assembly cluster sources, as well as solutions based on flame pyrolysis [3–5].

Although their principles of operation are very different, a common ground does exist: the vaporization of a tiny amount of a solid target (e.g., by a high-power laser pulse or high-power electrical discharge) followed by the thermalization of the vaporized atoms into an inert gas atmosphere acting as "thermal bath," which promotes atom aggregation into clusters, by homogeneous nucleation. Eventually, clusters are dragged out from the cluster source by gas expansion that forms the supersonic cluster beam.

Among the abovementioned cluster beam sources, in the mid-2000s, the pulsed microplasma cluster source (PMCS) underwent massive design optimization and process engineering enabling it to extend its usage possibilities from solid-state physics studies, where source intensity and related deposition rate is not a bottleneck, up to high-tech industrial applications, where adequate and stable deposition rates are required. In this chapter, we will consider the PMCS as the reference cluster source in respect to the examples provided of integration of nanostructured films in devices. As shown in Fig. 1, the PMCS operates according to the following steps: (i) injection of a pulse of inert gas into the source body by a solenoid valve; (ii) application of a high-voltage pulse to a pair of electrodes, where the cathode is a rod made of the material of interest, in order to ignite an intense electrical discharge; (iii) ion-sputtering of cathode, with atom removal and subsequent thermalization and aggregation to form atomic clusters, into the inert gas; and (iv) gas expansion dragging the atomic aggregates out of the source within a supersonic molecular beam. The PMCS's nozzle can be equipped with a set of aerodynamic lenses [6] ensuring the optimal focusing of the cluster beam and – at the same time – the removal of micrometric particulates that might form inside the source body and randomly released. Typical PMCS operational parameters are nominal gas pulse of 200 μs delivered by a solenoid valve backed with 40–50 bars of inert gas, discharge voltage of 500–800 V, discharge duration of 50 μs, and repetition rate of 4 Hz.

2.3 Sample Manipulation

A first consequence of the collimation of the supersonic cluster beam is the limited dimension of the deposition spot, which has a diameter <20 mm at a distance of 0.5 m from the nozzle source, in typical working conditions. To achieve larger coverage, rastering protocols have to be implemented through motorized sample holders. A Cartesian configuration constituted by a vertical and a horizontal axis represents the simplest solution. Although a theoretical limit to the extension of axes stroke, and in turn to the coverage area, does not exist, the deposition chamber has to accommodate sample holder movements; therefore, adequate dimensions are required. Vacuum-compatible linear actuators are available on the market (e.g., Physik Instruments, Newport, Thorlabs), enabling the design of in-vacuum, motorized sample holders. Alternatively, a more standard approach can be followed, where Cartesian movements of the sample holder are obtained through in-air, motorized translators acting on large-diameter bellows.

As the price of bellow-based solutions scales with bellow's dimensions, for strokes up to about 20 cm on both X and Y directions (from −10 cm to +10 cm relative horizontal displacement of bellow's flanges, from totally compressed to totally extended bellow in vertical direction), bellow-based solution is convenient, while for larger strokes in-vacuum linear actuators might be preferred. A low-cost, clever solution, where a small-size bellow only dedicated to vertical movement hosts a rotating shaft connected in vacuum with a gear rack couple driving the horizontal movement, has been recently introduced on an SCBD system by the prototype team of Luxembourg Institute of Science and Technology (LIST).

If much bigger areas have to be handled, e.g., for batch functionalization of devices, motorized sample holders with cylindrical symmetry (vertical translation and horizontal rotation) represent the only practical solution. Here, a carousel-like sample holder is rotated by an externally driven shaft and translated in the vertical direction through a bellow-based translator. Carousel-like sample holders with diameter and height of about 50 cm, leading to an accessible area of almost 1 m^2, have been developed and implemented, especially for high-tech industrial uses of SCBD (see Sects. 5, 6, and 7).

The design of a rastering protocol is not a trivial exercise, as it has to take into account the intensity profile of the beam in order to set the spacing of rastering lines in a way that the progressive overlap of deposition lines piles up, generating a thickness profile as flat as possible. To average over deposition rate drift, it is preferred to reach the target thickness with several rapid sweeps over the deposition area instead of a single slow sweep. Clearly, limitations do exist on the maximum speed allowed by the motorized translators.

A remarkable advantage over other thin film deposition systems, offered by the use of a rastering protocol, is the possibility to include a thickness monitoring system (e.g., a quartz crystal microbalance) in the deposition area, enabling to monitor in real time the growth of the film and stop the deposition process once the target thickness is reached.

2.4 Hard-Mask Patterning

A second consequence of the collimation of the supersonic cluster beam is the possibility to pattern the deposition through noncontact, hard-mask approach with micrometric lateral resolution. Following the demonstration and consolidation of the method at the University on Milan, where a lateral resolution of about 500 nm on nanostructured carbon films was obtained with a sharp-edge mask placed at about 0.3 mm from substrate surface [7], hard-mask patterning of cluster beam deposition has been applied to devices in a variety of contexts, from gas sensing to biomedical devices, as described in the following sections. Patterned deposition of nanostructured tungsten in the form of square shape dots having side as small as 5 μm has been demonstrated, as shown in Fig. 2 [8]. In the same work, the use of

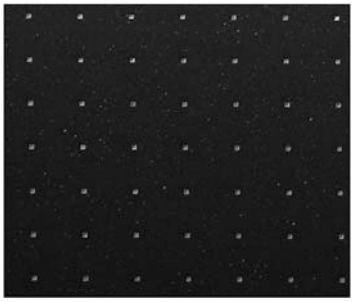


Fig. 2 Scanning electron microscopy (SEM) image of nanostructured tungsten pattern obtained with micromachined silicon mask coupled to SCBD; the side of square dots is 5 μm. (Reprinted from Ref. [8])

micromachined masks with suitable trapezoidal section allowing auto-alignment to a wafer containing 100 of micromachined devices has been also reported.

Although the performances of contactless hard-mask patterning in terms of lateral resolution are not at all comparable with the ones achieved by photolithography methods, a clear advantage of the former on the latter is to avoid the use of photoresist and related chemicals, which can be critical in respect to nanostructured film contamination, especially for the nanoporous nature of cluster-assembled materials.

3 Main Properties of Cluster-Assembled Nanostructured Films

3.1 Size Distribution

To date, several materials have been deposited in the form of nanostructured films by SCBD: limiting to the mostly studied ones, C, Ti, Zr, Au, Ag, Ni [1, 9–13], and bimetallic system Ti/Ag [14]. In all cases, the material of interest is obtained from a 2-mm-diameter rod, acting as cathode into the PMCS discharge circuit. The process gas is typically argon, whose relatively large mass (with respect to other common noble gases He and Ne) is particularly efficient in (i) cathode sputtering, (ii) thermalization of the sputtered atoms and promotion of their aggregation in atomic clusters by two- and three-body collisions, and (iii) cluster extraction from the source body to form the supersonic cluster beam. It is worth noting that PMCS approach to the vaporization of cathode material – based on a pulsed high-voltage, high-current electrical discharge – has demonstrated its efficiency also in the case of high melting point, refractory elements, as tungsten, molybdenum, and carbon.

For some of the materials listed above, namely, carbon, titanium, zirconium, gold, and nickel, a systematic characterization of cluster size distribution has been carried out, mainly by atomic force microscopy (AFM) and by transmission electron microscopy (TEM). To this purpose, sub-monolayer coverage was required to spot and analyze isolated clusters. Substrates cut from polished silicon wafer and

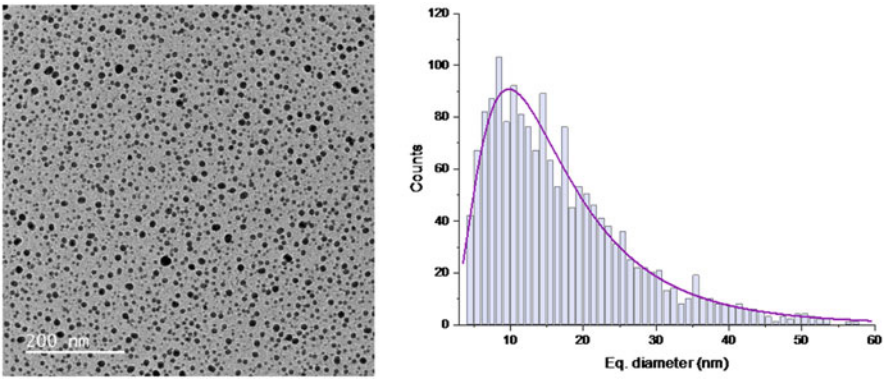


Fig. 3 *Left*: TEM image of low-coverage tin cluster sample deposited by SCBD. *Right*: size distribution of tin clusters including lognormal fitting (purple curve). (Courtesy of J.E. Martinez Medina and A.M. Philippe, Luxembourg Institute of Science and Technology (LIST))

properly treated were used for AFM characterizations while carbon-coated copper grids for TEM. In both cases, the preparation of the samples is straightforward, consisting in the exposure of the substrates to the cluster beam for a time of the order of 10 s. Due to tip radius convolution affecting in-plane measurements of objects' dimension in AFM, in these studies, height measurements were preferred.

Overall, the dimensions of the atomic clusters produced by PMCS and deposited by SCBD are mostly included in the range 1–20 nm, although within this range slight differences can be observed among the different materials. The size distributions have a lognormal shape, meaning that the logarithm of the particles' dimension has a Gaussian distribution. Figure 3 shows, as an example, a TEM image of tin clusters and the related size distribution.

Lognormal size distribution is typically shown by particles that form through gas-phase aggregation processes [3, 15–17]. In fact, as explained in Sect. 2.2, the sputtering of the cathode material produces a hot atomic vapor that thermalizes by collisions with the inert gas into PMCS body and aggregates in atomic clusters by homogeneous nucleation (Fig. 1). Growth proceeds until clusters are dragged out from the source by the expanding inert gas flow. Cluster growth definitively ceases due to the occurrence of the collisionless molecular regime, following the supersonic expansion.

3.2 Soft Assembling and Surface Morphology

As described in Sect. 2.2, atomic clusters are accelerated by the expanding inert gas up to a velocity having an upper limit expressed by the formula (1). Considering cluster dimensions reported in the previous section, it is straightforward to estimate the maximum kinetic energy per atom of a given material. As this value is generally

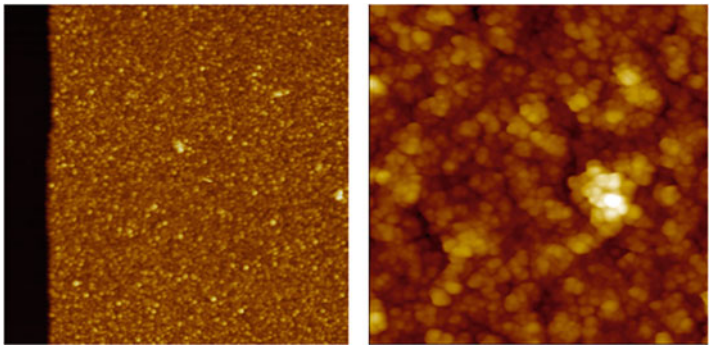


Fig. 4 *Left*: example of AFM image of cluster-assembled zirconium film showing film border obtained by hard-mask approach, where thickness can be measured (image side is 15 μm). *Right*: AFM image at higher magnification showing surface morphology, where roughness can be evaluated (image side is 1 μm). (Courtesy of J.E. Martinez Medina and P. Grysan, Luxembourg Institute of Science and Technology (LIST))

smaller than the binding energy per atom into the cluster, the last does not break apart at the impact with the substrate, maintaining its original structure. This is a fundamental property of cluster-assembled nanostructured films by SCBD: the "building blocks" of the film are atomic clusters that generally preserve – into the film – their individuality, a phenomenon often called "memory effect" that discloses the possibility to transfer to a "macroscopic system," as a film, the peculiar properties of the matter at the nanoscales.

Studies of surface texture unveiled that the morphology of cluster-assembled nanostructured films has self-affine character. In particular, surface roughness obeys scaling laws, where the most important one is represented by a power-law relationship between surface roughness w and thickness t:

$$w \approx t^{\beta} \tag{2}$$

By plotting the former versus the latter in a bi-logarithmic plot, experimental points distribute along straight lines whose slope is the exponent of the power law β, which carries information about the growth mechanism of the film. It is now widely demonstrated that growth mechanism of cluster-assembled films by SCBD can be ascribed to the ballistic model, whose main aspect is the sticking of particles at the point of contact with the growing film, with a substantial absence of rearrangement. This has the important consequence of giving the film a hierarchically structured nanoporous character, with open voids at different scales of dimension, which grant access to the inner part of the film. Figure 4 shows an example of AFM image of the surface of cluster-assembled nanostructured film of zirconium. Interestingly, the morphological features of the film in Fig. 4 are basically the same of the films made of almost any other material deposited by SCBD.- Exceptions are low melting point materials, e.g., tin, and metals non-prone to oxidation, i.e., gold.

3.3 Electrical Conduction

The granular nature of cluster-assembled nanostructured films constitutes a substantial difference with respect to atom-assembled polycrystalline films [18]. As explained in the previous section, in SCBD, clusters maintain their individuality in the film, and electrical transport takes place through the network of "point of contacts" among them, which in turn strongly depends on the growth mechanism of the film. Studies of electrical conduction in cluster-assembled metallic films carried out in situ during growth unveiled different regimes as a function of the thickness, where percolation phenomena dominate the observed trends.

At very low coverage, clusters do not form any percolation path and no conduction is observed. At a critical coverage, percolation threshold is reached, and electrical conduction can start; from here on, an increase of several orders of magnitude in conductance is observed, due to the development of the percolation network. Finally, this terrific increase of conductance slows down, as 2D percolation paths get saturated, and film starts a 3D growth. Interestingly, it has been observed that the resistivity of the cluster-assembled films in this 3D growth phase follows an increasing trend as a function of the thickness, as shown in Fig. 5 [19]. It is supposed that this behavior is strictly related to the ballistic growth mechanism for which in the topmost layers of the film clusters are always less connected than in bottom ones, as film growth proceeds. Films of several different materials (namely, Fe, Pd, Nb, W, and Mo) show the same trend, suggesting this being a peculiar trait of cluster-assembled nanostructured films obtained by SCBD. It is worth noting that the resistivity vs. thickness relationship follows a power law, as roughness vs. thickness does, which suggests an intimate connection between electrical transport properties and film morphology.

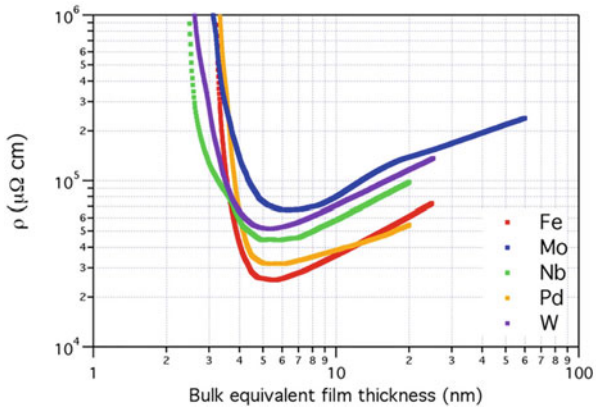


Fig. 5 In situ resistivity vs. thickness of metallic cluster-assembled films, where non-monotonic behavior is supposed to be related to topological evolution of the film during growth. The linear asymptotic trend at large thicknesses in the log-log plot indicates a power law. (Reprinted from Ref. [19])

Electrical transport in nanostructured films includes various other very interesting phenomena, the description of which however goes beyond the purposes of this chapter. These include, for example, resistance switching, quantized conductance, percolative tunneling phenomena, and IV curve hysteresis. The interested reader can find their description in [20–23] and references therein. The final section Perspectives returns briefly on these points introducing the idea of using nanostructured films by SCBD in devices for neuromorphic computing.

4 Chemoresistive Gas Microsensors

4.1 Metal Oxide Gas Sensors

Chemoresistive gas sensors are devices based on a metal oxide sensing layer, whose electrical resistance is affected by the presence of reactive compounds in the atmosphere which the sensing layer is exposed to. The sensing mechanism is based on a complex set of chemical reactions taking place at high temperature on the surface of the sensing layer, which involves the metal oxide layer, the atmospheric oxygen molecules, and the reactive gas molecules. At temperatures of the order of 300–400 °C, atmospheric oxygen molecules react at the surface of the metal oxide layer and get chemisorbed, decreasing the density of electrons at the surface of the metal oxide (depletion region, assuming the most common n-type semiconductor behavior of the metal oxide). If a reactive gas, for example, a volatile organic compound (VOC), is present in air, then it can react with the chemisorbed oxygen species and remove them from the surface, therefore acting as a reducing specie for the metal oxide. The reaction releases then some of the electrons engaged with the chemisorbed oxygen, narrowing the depletion region and favoring the electrical transport into the metal oxide layer, which in turn results globally in the decreasing of the electrical resistance of the metal oxide layer. The opposite process can also happen: a reactive specie prone to release oxygen, for example, nitrogen oxides (NOX), will increase the number of chemisorbed oxygen, which will further extend the depletion region that in turn result globally in an increase of the electrical resistance of the metal oxide layer.

Since the discovery of the chemoresistive phenomenon in the early 1960s on zinc oxide (ZnO), a massive development in the field took place, where a milestone is represented by the Taguchi device based on tin oxide (SnO_2), which – from that moment on – became the mostly adopted metal oxide in commercial chemoresistive gas sensors [24]. In the last decades, the advantages provided by nanoscale structures, including combinations of different metal oxide in heterostructures, in gas-sensing area have been widely demonstrated [25]. In general, a nanoporous nature of the sensing layer favors the interaction with the atmosphere, and, in this respect, nanostructured films produced by SCBD have been considered on purpose. SCBD in gas sensing has the additional advantage of allowing an easy

integration of the functional material (the nanoporous metal oxide sensing layer, in this case) onto the sensing platforms. Moreover, as described in the following section, the possibility to pattern the deposition by hard-mask approach enables in-batch functionalization of hundreds of devices avoiding photolithography steps, which might result in the contamination of the nanoporous sensing layer.

4.2 Nanostructured Film Integration on Microhotplates

According to the principle of operation of metal oxide gas sensors, where resistance changes of the sensing layer – kept at high temperature – represent the sensing signal, the platform hosting the sensing layer has to provide a couple of interdigitated electrodes (IDE) for resistance readout and an integrated heater to control device's temperature. The design of sensing platforms was originally based on ceramic plates with dimension of the order of 10 mm^2, having on front side the IDE pair and on back side the integrated heater, typically with meander shape. To operate the device at 300–400 °C, a heating power of the order of few watts was required. Exploiting micromachining capabilities, the design of the gas-sensing platform was afterward implemented in a miniaturized version named microhotplate, whose dimensions and heating power consumptions are of the order of 1 mm^2 and in the 1–10-mW range, respectively. Starting from the work by S. Semancik team, several versions of microhotplate design were developed; nevertheless, the concept and the functional elements (IDE and heater) remained the same no matter the different geometries [26].

SCBD has been successfully demonstrated as a viable technique to integrate nanoporous oxide films onto gas-sensing platforms, including microhotplate batches [8, 27–29]. Exploiting an auto-aligning micromachined hard mask, deposition of nanostructured tungsten oxide (WO_3) was performed on a 10 × 10 microhotplate array. Micrometric lateral resolution was by far adequate to pattern the deposition onto the microhotplate area containing IDE, having dimensions of 1.8 × 0.8 mm^2 (Fig. 6). As revealed by transmission electron microscopy (TEM), the sensing layer was constituted by atomic clusters having dimensions around 10 nm, assembled in a porous structure where single clusters clearly preserved their individuality. As-deposited clusters showed an amorphous structure, which progressively turned to crystalline upon annealing up to 400 °C. Annealing was intended to stabilize the structure of the sensing layer at a temperature larger than the operational one, to prevent material modifications during sensing measurements. The devices were then characterized for sensing performances with respect to both a reducing specie and an oxidizing one, i.e., ethanol and nitrogen oxide (NOX). An operating temperature of 300 °C was adopted in ethanol sensing measurements while of 200 °C in NOX ones, with heating power of 24 and 13 mW, respectively. Responses to concentrations in the ppm range were clearly observed, whose magnitude suggest for a limit of detection well below 1 ppm for both species.

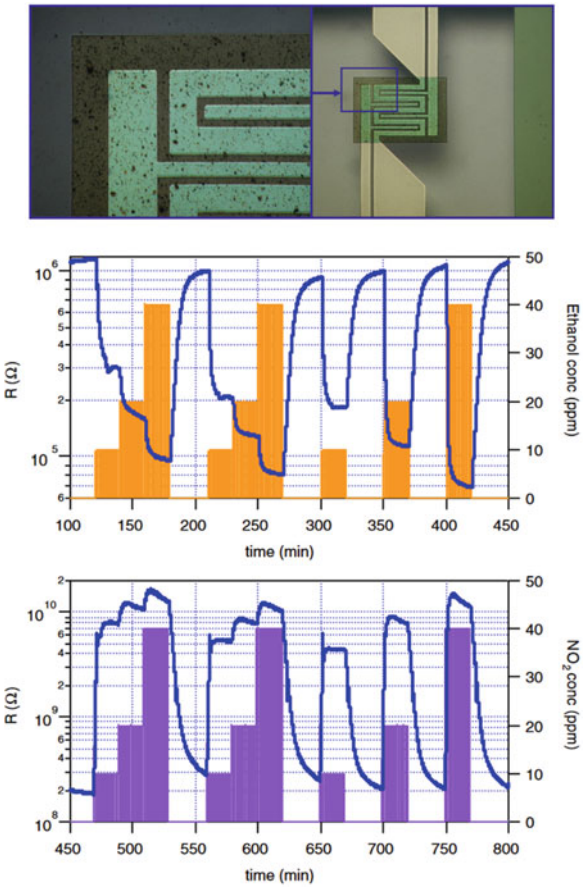


Fig. 6 *Top*: optical images of the sensing layer, made of nanostructured WO_3, deposited onto the microhotplate region hosting the interdigitated electrodes and the integrated heater. *Center* and *bottom*: sensing responses with respect to ethanol and NO_2, respectively; bar-like solid curves indicate the nominal concentration of the test gases (right axis), while the blue lines represent the electrical resistance of the sensing film (left axis, in log scale). (Reprinted from Ref. [8])

4.3 Outdoor Environmental Testing

The technology of ultraminiaturized, low-power consumption gas sensors is expected to become soon a game changer in the way air monitoring is performed in several indoor and outdoor scenarios, for example, smart buildings, industrial food production, pollution monitoring, and preservation of the cultural heritage. Taking advantage of the Internet of Things (IoT) infrastructures, pervasive wireless gas sensor networks will enable air quality mapping with unprecedented spatial resolution. Within this perspective, following the same approach described above, SCBD has been exploited to integrate nanoporous films onto multiparametric

micromachined sensing platforms, equipped with a first microhotplate dedicated to gas sensing, a second microhotplate dedicated to anemometric measurements, and an integrated thermometer, having an overall dimension of 3×5 mm^2 [30, 31]. Noncontact hard-mask method was successfully adopted in order to deposit the nanostructured film exclusively onto the microhotplate looking after the chemoresistive gas sensing. Iron oxide (FeOx) and tungsten oxide (WO_3) were selected as materials for gas-sensing layer, and two groups of devices were prepared accordingly. Sensing units for outdoor testing were assembled, hosting two of the mutiparametric devices described above (one with FeOx and one with WO_3 as gas-sensing layers) and a commercial miniaturized thermo-hygrometer (Sensirion SHT71). The use of different sensing materials aimed at spotting qualitative differences in the sensing signals generated by the exposure to the same complex outdoor atmosphere, in the perspective of sensing array approach. Analogic front-end for sensor readout, CPU, and wireless communication system (6LoWPAN Sensinode Nanomodule N100, based on Radiocrafts RC2300) completed the structure of the sensing unit.

In collaboration with ARPA Lombardia, Italy (the regional agency in charge of air quality measurements), the wireless sensing unit was installed on the roof of one of the ARPA stations located downtown Milan (Italy), close to the inlet of the pipe reaching standard gas chromatography instrumentations, in order to enable direct data comparison. Data collection took place over a period of several months of outdoor operation, during which gas sensors based on nanostructured FeOx and WO_3 generated a rich as well as complex dataset, where many interesting structures in the sensing signals could be highlighted. The comparison with gas chromatography data regarding NO, NO_2, CO, benzene, toluene, and xylene, suggested that nanostructured metal oxide gas sensors can detect events that are not visible by the standard instrumentation. Array approach and onboard Artificial Intelligence (AI) algorithms (e.g., neural networks, principal component analysis) for delocalized preprocessing of data, are the forthcoming steps that may promote further major advancements in the field, beside intensive validation of the technology in real-world contexts.

5 Surfaces for Cell Capture in Oncological Research and Diagnostics

5.1 Cell Adhesion on Nanostructured Surfaces

Within the broad concept of the biotic/abiotic interface, cell adhesion onto inorganic surfaces represents the first pivotal phase toward subsequent phases of proliferation and possibly differentiation. Cell adhesion in itself is the result of a complex sequence of steps in which cells "sense" and react to external stimuli provided by the microenvironment they are exposed to [32]. In this respect, nanoscale topological

features of extracellular matrix (ECM) are perceived by the cell, which initiates a cascade of biochemical processes leading to the modulation of cytoskeleton structure, nuclear rearrangements, and generally cell response: a capability known as mechanotransduction [33, 34]. In mechanotransduction, a primary role is played by integrin adhesion complexes (IACs), a transmembrane protein system mediating through ECM and the actin cytoskeleton.

In the last decade, the interest toward the use of nanostructured films obtained by SCBD in biomedical contexts triggered several studies dedicated to protein adsorption and cell adhesion in particular. These studies highlighted that properties such as nanoscale porosity, wettability, and isoelectric point [35] can be tuned to favor protein adsorption [36–38] and ultimately cell adhesion, proliferation, and differentiation [39–43], which has been demonstrated in respect to various cell lines including mouse embryo fibroblasts, human osteosarcoma, human fibroblasts, primary human melanocytes, and primary hippocampal neurons. Of particular interest is the observation that nanostructured films feature nanoscale roughness with hierarchical structure that mimic the morphological characteristics of physiological ECM and can trigger mechanotransductive phenomena accordingly.

Cell adhesion capabilities of nanostructured films, particularly TiO_2, have been exploited for the development of devices and "smart slides" for early diagnosis purposes in onco-hematology and mitigation of metastasis risk by early detection of circulating tumor cells (CTCs), as described in the following sections.

5.2 Microfluidic Devices for Fluorescence In Situ Hybridization (FISH) in Onco-hematology

Fluorescence in situ hybridization (FISH) is a conceptually simple analytical assay based on fluorescence readout, aiming to spot genetic rearrangements with very high specificity [44, 45]. FISH takes advantage of the so-called FISH probes, which are chemical complexes formed by a fluorophore bonded to a well-defined DNA sequence. During the hybridization process of cytological samples, carried out on cellular nuclei fixed onto microscopy slides, the FISH probe reaches the corresponding DNA sequence in cell's DNA and bonds to it. Afterward, high-magnification fluorescence microscopy is performed onto each single cell composing the cytological sample, and "fluorescent dots" are counted: if two dots are spotted, then the DNA sequence of the FISH probe is correctly present in the related pair of chromosomes, while if the number of counted dots is different from two, a genetic defect is unveiled. Exploiting fluorophores with different colors bonded to difference sequences, several genetic defects can be targeted within the same analysis. Provided the correlation between a given rearrangement and the cancerous nature of a cell is defined, such as in the case of the 9/22 translocation in chronic myeloid leukemia [46], FISH represents a powerful tool for cancer diagnosis and prognosis.

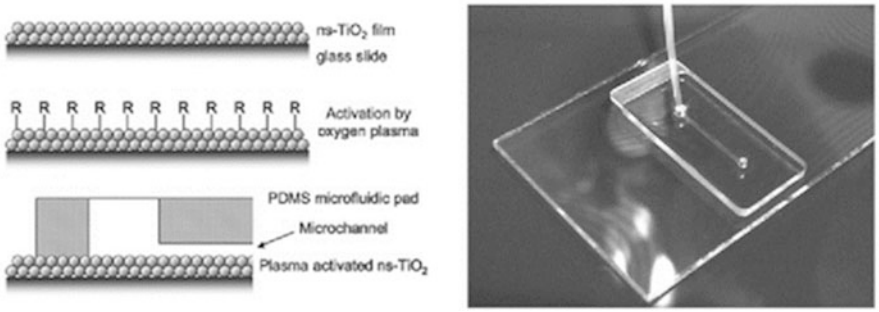


Fig. 7 *Left*: cross section of the microfluidic device for miniaturized FISH, schematically showing the bottom nanostructured surface activated by oxygen plasma (chemisorbed oxygen radicals are indicated as R). *Right*: picture of the device, where a 10-μL tip used for sample loading is visible (Reprinted from Ref. [48])

Although the strong diagnostic potential of FISH assay, widespread use is hampered by the high cost of the FISH probes. For this reason, in many clinical labs, FISH is only adopted as a confirmation second step on a restricted number of cases, following classical cytogenetic screening. In addition, applicability of FISH can be difficult in case of samples having poor cell content. A way to tackle both these limitations is through microfluidic devices, which however – in the case they implement assays where cells must be kept adhering to a surface – apply severe solicitation to the sample, due to shear stress of liquids moving in the microchannels. If cell-surface adhesion is not strong enough, this results in the loosing of the cytological sample [47]. Miniaturization of FISH through microfluidics could be a promising solution only if cell immobilization inside the microchannels is granted.

As described in Sect. 5.1, nanostructured TiO_2 films provide rapid and efficient immobilization of living cells. Interestingly, this property holds also for hematopoietic cells, which are circulating, nonadhering cells, even in the presence of intense shear stress. The startup company Tethis (tethis-lab.com, Milan, Italy) developed microfluidic devices aiming at the miniaturization of FISH assay by combining a microscopy glass slide (to enable fluorescence imaging) coated with a thin film of nanostructured TiO_2, with a polymeric pad hosting a microfluidic channel with dimensions of $10 \times 0.3 \times 0.05$ mm; two ports connect the microchannel with the upper surface of the pad, for reagent loading and removal, as shown in Fig. 7 [48]. The bottom area of the microchannel is constituted by the surface of the slide coated with nanostructured TiO_2; it has a dimension of 3 mm^2 and can accommodate a statistically meaningful number of cells for the FISH assay ($\geq$1000). Comparative experiments with standard FISH protocol show that microfluidic FISH has the same accuracy, quality, and reproducibility, with 10- to 30-fold less use of FISH probes.

5.3 *Platforms for the Capture of Circulating Tumor Cells (CTCs)*

It is now accepted that metastasis is triggered by the spreading through blood flow of tumor cells originating from solid primary or metastatic cancerous lesions, named circulating tumor cells (CTCs) [49]. Since early identification of CTCs in the blood stream of patients with cancer can help the monitoring of the disease progression and timely taking mitigation actions, great efforts are ongoing to develop technological solutions and devices to this purpose. In the specific case of breast cancer, CTCs have been observed as single cells as well as multicellular aggregates, which are considered more effective in determining metastases. Since multicellular aggregates are observed only in patients with advanced disease stages, one can ask whether they can be released in the blood flow also at early stages. If this is the case, the capability to capture and identify them at early disease stages would represent a big advancement in breast cancer research and treatment.

Nanostructured TiO_2 by SCBD has been exploited in special microscopy slides dedicated to CTC capture (Smart BioSurface Slides (SBS) by Tethis), taking advantage of the capabilities of such material to immobilize cells spontaneously and efficiently thanks to the formation of integrin-based focal adhesion points [38, 39]. In practice, the use of microscopy slides coated with a thin film of nanostructured TiO_2 enables to transform a liquid biopsy, i.e., a cytological samples in liquid solution, into a "two-dimensional tissue" made of all the cells composing the liquid biopsy uniformly distributed on the slide, with preserved morphological features (phenotype) and ready to subsequent nondisruptive optical analysis (Fig. 8).

This approach allowed to detect multicellular aggregates of CTCs in peripheral blood of patients affected by breast cancer at early stage, without clues of metastasis. The early identification of patients with CTC aggregates in the peripheral circulation might help in spotting high-risk individuals and to render them eligible for CTC anti-clustering treatments, in order to reduce the risk of metastasis progression [50].

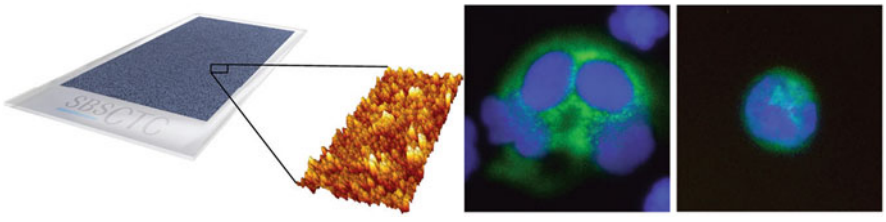


Fig. 8 *Left*: nanostructured TiO_2-coated microscopy slide for CTC immobilization (Smart BioSurface Slide by Tethis), including AFM image of nanoscale morphology of the film (short-side dimension of AFM image is 1 μm). *Right*: immunofluorescence images of a CTC aggregate and single CTCs captured on Smart BioSurface Slide, where DAPI-stained blue regions highlight genetic material (cell nuclei) while green regions regard pan-cytokeratin (CK) staining (Reprinted from Ref. [50])

6 Electrodes for Neurorecording and Neuromodulation

6.1 Supersonic Cluster Beam Implantation

Section 2.2 describes the formation of atomic clusters into PMCS and their acceleration by expansion of the process gas, whose velocity has an upper limit defined by formula (1). Even if the kinetic energy per atom is not enough to break apart clusters at the impact with the substrate, as commented in Sect. 3.2, in the case of the use of elastomeric substrates, clusters in supersonic beam have enough energy to penetrate the material, a phenomenon named supersonic cluster beam implantation. Discovered in 2009, during in situ electrical conduction experiments dedicated to SCBD of palladium clusters on polymethyl methacrylate (PMMA), supersonic cluster beam implantation has been afterward investigated in particular with gold clusters and polydimethylsiloxane (PDMS) substrates [51, 52]. Several studies then followed regarding Au cluster implantation in polystyrene, Ag clusters in PDMS, as well as the use of electro-active polymers [53–56].

It is important highlighting that – different from ion implantation in semiconductor industry – supersonic cluster beam implantation involves neutral clusters, not subjected to any external accelerating electrical field. Penetration occurs up to tens of nanometers and forms a nanocomposite layer on the elastomer surface, providing charge transport properties (Fig. 9). Limitations typical of standard metallization

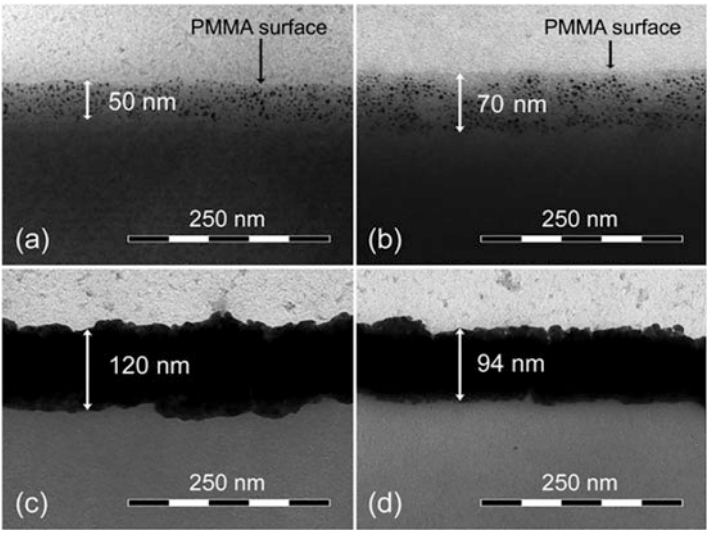


Fig. 9 TEM micrographs (cross-section cut by ultra-microtomy: thickness 60 nm) of Pd nanoparticles deposited on PMMA for different nominal thicknesses and substrate temperatures: (**a**) nominal thickness below 1 nm at room temperature, (**b**) nominal thickness below 1 nm at 95 °C, (**c**) 60-nm nominal thickness at room temperature, (**d**) 50-nm nominal thickness at 95 °C. (Reprinted with permission from Ref. [51])

approaches, in terms of performances (e.g., delamination) and processing (e.g., electrostatic charging, overheating and carbonization, use of solvents, use of adhesion layers), are totally avoided. Penetration depth can be tuned acting on the temperature at which deposition is performed.

If on one hand elastomers become electrically conductive upon implantation with metallic clusters, on the other hand, they preserve the capability of undergoing large mechanical deformation. Electrical conduction measurements carried out during mechanical strains showed the capability of Au-implanted PDMS to withstand more than 1×10^5 cycles of uniaxial stretching at 40% strain while preserving finite and reproducible electrical resistance [52]. Conductive nanocomposite layers obtained at the surface of elastomers by supersonic cluster beam implantation can find several applications in the areas of electrostimulation (as discussed in the following sections), sensing, actuators, and soft robotics in general.

6.2 Flexible and Conformal Electrodes

Taking advantage of supersonic cluster beam implantation, in the last decade, a vigorous effort toward the development of flexible, conformal, biocompatible, and implantable electrodes for rehabilitation and diagnostic purposes of central and peripheral nervous system has been made by the startup Wise (wiseneuro.com, Milan, Italy). Wise electrodes aim at mitigating the critical issue of fractures or displacements that affects current intracranial devices, upon mechanical solicitations by providing high mechanical adaptability to displacement and movement. As described by Gnatkovsky et al. [57], devices dedicated to cortical signal recording were produced exploiting a two-step supersonic cluster beam implantation for the deposition of platinum pads, to be exposed in vivo to the recording site, and gold interconnections, dedicated to wiring Pt pads, onto a thin silicone substrate. In both cases, stainless steel stencil masks with proper design for deposition patterning were adopted, as described in Sect. 2.4. This avoids the use of photolithography, which is known to be problematic on soft polymers. At the same time, devices that are themselves – or have their recording structures – highly miniaturized are not required in most of the applications currently known for neurorecording and neuromodulation, making hard-mask patterning well suitable for the purpose. After cluster implantation, a passivation silicone layer is selectively applied onto the gold interconnections. Figure 10 shows the scheme of the device, details in [57].

Cyclic voltammetry characterizations of the Pt nanostructured film, composing device's recording pads, have been carried out in comparison with standard Pt foil electrode, unveiling a larger capacitive component of the former in respect to the latter, which can be attributed to the difference in specific surface area. The charge storage capacity (CSC), calculated from the time integral of the cathodic current in a slow-sweep-rate cyclic voltammogram, gave 38 mC/cm^2 for the nanostructured film and 0.55 mC/cm^2 for the foil, corresponding to a factor 70 of increase

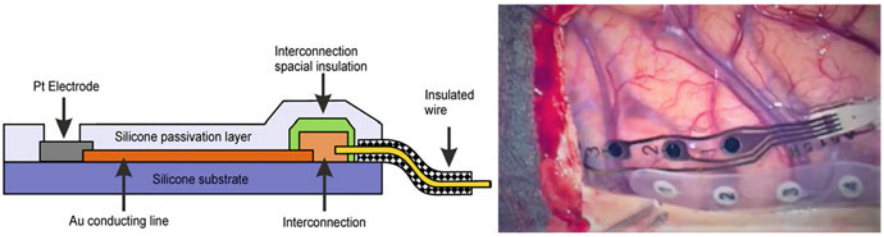


Fig. 10 *Left*: schematic view of the device for neurorecording. Platinum recording pad (gray) and gold interconnecting wires (orange) are deposited on the silicone substrate (purple) by supersonic cluster beam implantation (Reprinted from Ref. [57]). *Right*: strip electrodes in the surgical field, where the device based on nanostructured Pt pads (WISE Cortical Strip WCS®, visible as black circles and gray wirings) is tested in respect to a state-of-the-art comparator device (CD), visible at the bottom as numbered white circles. (Reprinted from Ref. [59])

ascribable to specific surface area. It is worth emphasizing that such improvement is obtained natively, without any postdeposition or post-processing step, as usually done in electrodes by standard technologies [58]. The large surface area favors efficient exchange of charge at the interface between the nanostructured surface and the surrounding fluids, granting low impedance to the electrode, beside high capacitance.

6.3 Clinical Validation in Somatosensory Monitoring

A version of the device described above underwent clinical validation in the context of intraoperative neurophysiological monitoring (IONM), an important diagnostic tool that helps surgeon during neurosurgical interventions in cranial neurosurgery, as shown in Fig. 10 [59]. In IONM, the signals from suitable electrodes placed directly in contact with the brain surface are collected (electrocorticography (ECoG)); therefore, optimal conformality properties, stability of the positioning, and low electrical impedance are required. Regarding the last, for example, low-impedance electrodes enable the recording of small-amplitude, high-frequency signals indicating epileptogenic tissues [60, 61].

The device is a silicone strip having length of 62 mm and thickness of 0.25 mm and hosting four nanostructured Pt electrodes of 2.3 mm diam. and center-to-center distance of 10 mm (Fig. 10). Its intended use is intraoperative recording of electrical signals and stimulation on the surface of the brain in patients affected by brain tumors or epilepsy [59]. This device received FDA clearance in December 2022, 510(k) number K221123, upon validation in a multicentric pre-market clinical study in Europe (WIN study, NCT03731455, whose results are summarized in [59]), that demonstrated safety, performance, and usability of the product.

7 Plates for Sample Processing by MALDI-MS in Proteomic Clinical Research

7.1 Wettability-Controlled Solid-State Wells

Matrix-assisted laser desorption/ionization mass spectrometry (MALDI-MS) is an analytical tool of paramount importance in research and clinical diagnostics for its capability to deal with biomolecules of any kind (peptides, proteins, nucleic acids, carbohydrates), as well as cells, viruses, bacteria, fungi, and whole histological sections [62–65]. The working principle of MALDI-MS (Nobel Prize for Chemistry in 2002) is based on laser-induced charge transfer from a "matrix" (typically an organic acid) to the macromolecules under investigation, which are mixed and pipetted on a suitable plate (MALDI plate). The efficiency of MALDI-MS analysis however critically depends on two main factors: the quality of sample preparation and the quality of the matrix-analyte mixture, particularly the way the mixture crystalizes onto the MALDI plate. Regarding the former, for example, protein sample preparation before MALDI-MS analysis requires a long workflow: protein extraction, denaturation, reduction, alkylation, cleaning, and enzymatic cleavage. Being carried out in test tubes, sample preparation often results in the loss of relevant fractions of peptides by capture on vial plastic/glass walls, altering peptide coverage and analysis outcomes.

With the purpose of allowing sample preparation to be fully carried out on the MALDI-MS plate, avoiding any passage in test tubes and potential sample alteration, nanostructured titanium dioxide (TiO_2) patterns in the form of circular areas of 2 mm diam. were deposited by SCBD onto hydrophobic polymeric plates [66]. Exploiting the phenomenon of UV photoinduced super-hydrophilicity occurring in Group IV metal oxides [67], as indeed TiO_2, a remarkable discontinuity in wettability surface properties, can be induced at the border of the nanostructured TiO_2 circles, which then acts as containment structure for water-based droplets of samples/reagents, as a sort of "solid-state well" (Fig. 11). UV photoinduced super-hydrophilic state in TiO_2 is obtained through a complex surface phenomenon in which photo-generated hydroxyl (OH) groups from ambient water induce nanoscale structural changes on TiO_2 nanoparticle surface, which in turn favor the spreading of water, as a kind of two-dimensional capillary effect [67, 68]. Water spreading is then abruptly stopped, and containment is provided, by the hydrophobic polymer surface surrounding nanostructured TiO_2 circles.

It has been observed that the super-hydrophilic state in nanostructured TiO_2 is stable for several days, a duration much longer than what observed in microcrystalline TiO_2, where the restoring of a more hydrophobic state occurs in few hours [68]. This might be a direct consequence of the cluster-assembled film nature, whose nanoscale granular structure is expected to effectively accommodate the mechanical stresses due to structural modification induced in the material by UV irradiation, and that are supposed to be the reason for spontaneous recovery from the metastable super-hydrophilic state to a more hydrophobic state.

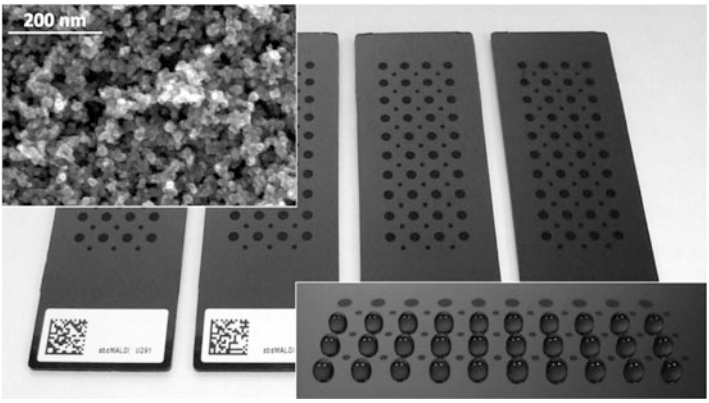


Fig. 11 Patterned deposition of nanostructured TiO_2 (appearing as black circles in the picture) onto polymeric MALDI plates. Top-left inset shows a scanning electron microscopy (SEM) image of the nanostructured TiO_2 surface. Bottom-right inset shows the confinement of water droplets due to the hydrophilic-hydrophobic barrier at the border of nanostructured TiO_2 circles, acting as a "solid-state well" and enabling on-plate sample processing. (Reprinted from Ref. [66])

7.2 Matrix-Sample Mixture Crystallization on Nanostructured Surfaces

In addition to the above, the introduction of cluster-assembled nanostructured layers onto MALDI plates has an interesting impact also on matrix-sample mixture crystallization. As mentioned at the beginning of the previous section, the way the matrix-analyte mixture crystallizes onto the MALDI plate is a critical factor affecting analysis outcomes. An irregular distribution of big clumps of crystals across the area subjected to laser shooting represents an unfavorable condition to get reliable mass spectrometry datasets, while finely grained, uniformly distributed crystals represent the ideal situation. In this respect, nanostructured films are capable to drive the crystallization of matrix-analyte mixture toward the preferred scenario by favoring the formation of smaller, homogeneous in size, and uniformly distributed crystals with respect to non-nanostructured surfaces [66]. It has been proposed that this might be related to nanoscale surface roughness (see Sect. 3.2), which provides abundance of "point-like defects" where crystal nucleation can begin.

7.3 On-Plate Sample Processing for 2D-MALDI

"2D-MALDI" is a recently introduced expression in proteomics meaning the capability to collect information by MALDI-MS applied to an intact protein sample and to the peptide ensemble generated by the enzymatic cleavage of exactly the

same sample. By extension, "multidimensional MALDI" indicates the process that moves forward beyond 2D-MALDI, for example, the study of a peptide fragment pattern, firstly with non-cleaved disulfide bonds and secondly upon releasing of disulfide bonds from exactly the same peptide sample. The mandatory requisite for 2D-MALDI (and multidimensional MALDI) is the capability of washing out from the MALDI plate the matrix used for the analysis of the protein sample while at the same time preserving the protein sample adsorbed onto the MALDI plate in view of the following step of enzymatic cleavage. Matrix removal must achieve the condition in which its acidic residuals would not alter the basicity of the subsequent enzyme buffer.

As discussed in Sect. 3.2, the ballistic model at the base of the growth mechanism of nanostructured films by SCBD foresees a hierarchically structured nanoporous nature of the films. In the case of TiO_2, it has been demonstrated that such nanoporosity, combined with the well-known affinity of the material in respect to biomolecules [36, 69, 70], can be exploited for the effective capture of the protein sample at the level expected to survive matrix washing and proceed for enzymatic cleavage. Thanks to droplet confinement by hydrophilic-hydrophobic barrier, the entire protocol sequence of 2D-MALDI (including the removal of the matrix for protein analysis, the incubation of trypsin for enzymatic cleavage, and the adding of the matrix for peptide analysis) can be performed onto the MALDI plate, on the exact same sample. After validation on bovine serum albumin (BSA), the method has been applied to a study with clinical relevance about hereditary gelsolin amyloidosis, where pathologic significance is attributed to the formation of oligomeric aggregates of a protein fragment of gelsolin during the amyloidogenesis. A peptide with specific mutation related to the pathology has been clearly identified through on-plate processing, while the same was totally missing in the control sample processed into test tube [66].

7.4 Nanostructured Surfaces for MALDI Imaging and Beyond

MALDI (mass spectrometry imaging (MSI)) takes advantage of modern, high-repetition rate lasers to perform a Cartesian scanning of histological samples and collect mass spectrometry data pixel by pixel, aiming at generating the image of the distribution of a given mass across the histological section. The mass of interest represents the molecule whose distribution has to be characterized, e.g., a protein, a peptide, and a drug. Clearly, the fundamental point here is the preservation of the original location of the molecule of interest, meaning that the diffusion onto the surface of the MALDI plate must be limited as much as possible. This is the technological challenge to be tackled by MALDI plates for MSI.

Nanoscale porosity and affinity to biomolecules of nanostructured TiO_2 might be of interest also for MSI, as local capture of biomolecules and homogeneous matrix distribution are expected to ensure optimal lateral resolution in imaging. In addition, improved tissue adhesion onto nanostructured TiO_2 film prevents

detachment, tearing, shrinking, and deformation in general during tissue processing. The adhesion of the histological section is of particular interest in pharmacokinetic studies by MSI, where any tissue treatment is excluded as it would cause the loss of drug localization [71].

8 Perspectives

Topics presented above have been selected with the aim to show examples of high-TRL (technology readiness level) applications exploiting nanostructured functional films by SCBD, of which the more advanced one is represented by cortical electrodes by Wise, recently receiving pre-market clearance by FDA. Several other researches are ongoing, where nanostructured films by SCBD are at the core of novel fundamental and technological developments. Although not exhaustive at all, this final section reports about a couple of them, in the areas of neuromorphic devices and of heterogeneous catalysis. Neuromorphic devices – or artificial neurons – are solid-state systems that implement computational functions mimicking the actions of biological neurons and their arrangement within the architecture of the nervous system. Interest on neuromorphic computing is motivated by the possibility to overcome the limitations of computing based on von Neumann architecture. It has been suggested that neuromorphic hardware can be obtained assembling probabilistic spiking units, in order to reproduce the stochastic behavior of spiking present in biological neuronal networks. Nanostructured films obtained by SCBD of gold clusters having a thickness substantially larger than the one of electrical percolation threshold show non-ohmic conduction behavior and resistive switching, characterized by groups of stochastic current spikes, which are indeed under investigation in the context of neuromorphic computing [22, 23]. It has been recently proposed that nanostructured gold films can be modeled as complex networks of metallic nanojunctions where thermal effects at the nanoscale induced by electrical current are at the base of sudden rearrangement of regions with different electrical resistance, causing the aimed stochastic spiking behavior [72].

Within the incredibly vast subject of heterogeneous catalysis, nanostructured films by SCBD are under investigation in areas of pivotal interest for environmental concerns and green energy transition. CO_2 conversion to syngas represents a clever way to tackle CO_2-related greenhouse effect issue and – at the same time – to storage carbon into chemicals of industrial interest, reducing the dependency on fossil fuels. Copper-based catalysts, properly supported by nanostructured oxides, are of particular interest for CO_2 conversion process and for the role of the supporting oxide, which can tune the selectivity of the catalyst support system. In this context, for example, nanostructured zirconia has been deposited by SCBD as support for sub-nanometer copper clusters within a study about the performances of the Cu-ZrO_2 system – and particularly the role of the nanostructured oxide support – in CO_2 conversion to methane [73].

Within hydrogen economy perspective, oxygen evolution reaction (OER) is one of the two half reactions at the base of electrochemical water splitting, one of the main methods proposed for green hydrogen production. As OER requires proper catalysts to happen and the most efficient ones belong to the expensive and low-sustainable platinum-group metals (PGM), namely, iridium and ruthenium, efforts are ongoing on one hand to decrease their usage through nanostructuring while on the other hand to find potential alternatives non-PGM. In this respect, for example, ruthenium, cobalt, and nickel-iron clusters by SCBD have been investigated for OER, the former showing interesting electrocatalytic performance in comparison to standard carbon-supported Ru and RuO_2 nanoparticle catalysts, while the two latter proposing potential alternatives to PMG materials [74, 75].

Conflict of Interest EB is employees of the Luxembourg Institute of Science and Technology (LIST), while SV is employee of ParteQ GmbH; both have not conflict of interest to disclose in respect to the presented matter, particularly in what regards the mentioned companies, namely, Tethis and Wise. The content of the chapter is supported by published information; unpublished data reported are in the full availability of the authors.

References

1. J.E. Martinez Medina et al., Vacuum 2023, 211, 111930. https://doi.org/10.1016/j.vacuum.2023.111930
2. G. Scoles (Ed.), Atomic and Molecular Beam Methods, Oxford University Press, New York (1998). ISBN 0-10-504280-8.
3. P. Milani and S. Iannotta, Cluster Beam Synthesis of Nanostructured Materials, Springer, Berlin, 1999.
4. K. Wegner et al., Nanotechnology 2012, 23, 185603. https://doi.org/10.1088/0957-4484/23/18/185603
5. R.E. Palmer et al., Review of Scientific Instruments 2016, 87, 046103. https://doi.org/10.1063/1.4947229
6. H. Vahedi Tafreshi et al., Journal of Nanoparticle Research 2002, 4, 511–524. https://doi.org/10.1023/A:1022845401781
7. E. Barborini et al., Applied Physics Letters 2000, 77, 1059. https://doi.org/10.1063/1.1289040
8. E. Barborini et al., Journal of Micromechanics and Microengineering 2008, 18, 5. https://doi.org/10.1088/0960-1317/18/5/055015
9. F. Borghi et al., Applied Surface Science 2019, 479, 395–402. https://doi.org/10.1016/j.apsusc.2019.02.066
10. A. Podestà et al., J. Appl. Phys. 2015, 118, 234309. https://doi.org/10.1063/1.4937549
11. F. Borghi et al., Physical Review Applied 2018, 9, 4, 044016. https://doi.org/10.1103/physrevapplied.9.044016
12. F. Bisio et al., Physical Review B: Condensed Matter and Materials Physics 2009, 80, 20, 205428/1-205428/8. https://doi.org/10.1103/physrevb.80.205428
13. G. Benetti et al., Nanomaterials 2021, 11, 11, 3116. https://doi.org/10.3390/nano11113116
14. E. Cavaliere et al., Nanomaterials 2017, 7, 12, 442. https://doi.org/10.3390/nano7120442
15. J. Söderlund et al., Physical Review Letters 1998, 80, 2386. https://doi.org/10.1103/PhysRevLett.80.2386
16. F. Siviero et al., Surface Science 2002, 513, 2, 381–388. https://doi.org/10.1016/S0039-6028(02)01786-7

17. Y. Huttel (Ed.), Gas-Phase Synthesis of Nanoparticles, John Wiley and Sons, 2017. ISBN: 978-3-527-34060-6
18. M. Mirigliano et al., Advances in Physics: X 2021, 6, 1, 1908847. https://doi.org/10.1080/23746149.2021.1908847
19. E. Barborini et al., New Journal of Physics 2010, 12, 073001. https://doi.org/10.1088/1367-2630/12/7/073001
20. J.B. Mallinson et al., Science Advances 2019, 5, 1. https://doi.org/10.1126/sciadv.aaw8438
21. M. Mirigliano et al., Nanoscale Advances 2019, 1, 8, 3119. https://doi.org/10.1039/C9NA00256A
22. M. Mirigliano et al., Scientific Reports 2020a, 10, 1, 1. https://doi.org/10.1038/s41598-020-76632-y
23. M. Mirigliano et al., Nanotechnology 2020b, 31, 234001. https://doi.org/10.1088/1361-6528/ab76ec
24. G. Neri, Chemosensors 2015, 3, 1–20. https://doi.org/10.3390/chemosensors3010001
25. R. Leturcq et al., Advances in Physics: X 2022, 7, 1. https://doi.org/10.1080/23746149.2022.2044904
26. K.D. Benkstein et al., Journal of Nanoparticles Research 2006, 8, 809–22. https://doi.org/10.1007/s11051-005-9019-8
27. T. Mazza et al., Applied Physics Letters 2005, 87, 103108. https://doi.org/10.1063/1.2035874
28. M. Decarli et al., Microelectronic Engineering 2009, 86, 4–6, 1247–1249. https://doi.org/10.1016/j.mee.2008.11.036
29. E. Barborini et al., Japanese Journal of Applied Physics 2011, 50, 01AK01. https://doi.org/10.1143/JJAP.50.01AK01
30. M. Leccardi et al., Sensors 2012, 12, 6, 8176–8192. https://doi.org/10.3390/s120608176
31. E. Barborini (2013). Microhotplates and Integration with Metal-Oxide Nanomaterials. In: Carpenter, M., Mathur, S., Kolmakov, A. (eds) Metal Oxide Nanomaterials for Chemical Sensors. Integrated Analytical Systems. Springer, New York, NY. https://doi.org/10.1007/978-1-4614-5395-6_16
32. J.Z. Gasiorowski et al., Annual Review of Biomedical Engineering 2013, 15, 155−176. https://doi.org/10.1146/annurev-bioeng-071811-150021
33. N. Wang et al., Nature Reviews Molecular Cell Biology 2009, 10, 75−82. https://doi.org/10.1038/nrm2594
34. J.D. Humphries et al., Trends in Cell Biology 2015, 25, 388−397. https://doi.org/10.1016/j.tcb.2015.02.008
35. F. Borghi et al., PLoS One 2013, 8, e68655. https://doi.org/10.1371/journal.pone.0068655
36. R. Carbone et al., Analytical Biochemistry 2009, 394, 7−12. https://doi.org/10.1016/j.ab.2009.07.005
37. P.E. Scopelliti et al., PLoS One 2010, 5, e11862. https://doi.org/10.1371/journal.pone.0011862
38. C. Schulte et al., Accounts of Chemical Research 2017, 50, 231–239. https://doi.org/10.1021/acs.accounts.6b00433
39. R. Carbone et al., Biomaterials 2006, 27, 3221−3229. https://doi.org/10.1016/j.biomaterials.2006.01.056
40. A.V. Singh et al., Nanotechnology 2012, 23, 475101. https://doi.org/10.1088/0957-4484/23/47/475101
41. M. Tamplenizza et al., Journal of Nanobiotechnology 2013, 11, 35. https://doi.org/10.1186/1477-3155-11-35
42. C. Schulte et al., Journal of Nanobiotechnology 2016a, 14, 18. https://doi.org/10.1186/s12951-016-0171-3
43. C. Schulte et al., Frontiers in Cellular Neuroscience 2016b, 10, 267. https://doi.org/10.3389/fncel.2016.00267
44. E.V. Volpi et al., FISH glossary: an overview of the fluorescence in situ hybridization technique. BioTechniques 2008, 45, 4, 385–386. https://doi.org/10.2144/000112811
45. M.G. Tibiletti et al., Cytogenetic and Genome Research 2007, 118, 229–236. https://doi.org/10.1159/000108305

46. L. Kearney et al., British Journal of Haematology 1999, 104, 648–658. https://doi.org/10.1046/j.1365-2141.1999.01181.x
47. L.S. Cheung et al., Lab on a Chip 2009, 9, 1721–1731. https://doi.org/10.1039/B822172C
48. A. Zanardi et al., Biotechniques 2010, 49, 1. https://doi.org/10.2144/000113445
49. M. Mohme et al., Nature Reviews Clinical Oncology 2017, 14, 155–167. https://doi.org/10.1038/nrclinonc.2016.144
50. I. Krol et al., British Journal of Cancer 2021, 125, 23–27. https://doi.org/10.1038/s41416-021-01327-8
51. L. Ravagnan et al., J. Phys. D: Appl. Phys. 2009, 42, 082002. https://doi.org/10.1088/0022-3727/42/8/082002
52. G. Corbelli et al., Adv. Mat. 2011, 23, 39, 4504–4508. https://doi.org/10.1002/adma.201102463
53. C. Ghisleri et al., J. Phys. D: Appl. Phys. 2014, 47, 015301. https://doi.org/10.1088/0022-3727/47/1/015301
54. F. Greco et al., ACS Applied Materials & Interfaces 2015, 7, 13, 7060–7065. https://doi.org/10.1021/acsami.5b00825
55. M. Potenza et al., Rev. Sci. Instrum. 2017, 88, 11, 113105. https://doi.org/10.1063/1.5009180
56. S. Taccola et al., J. Appl. Phys. 2018, 124, 6, 064901/1-064901/7. https://doi.org/10.1063/1.5038659
57. A. Gnatkovsky et al., Int J Nanomedicine 2019, 14, 10079–10089. https://doi.org/10.2147/IJN.S224243
58. C. Boehler et al., Biomaterials 2015, 67, 346–353. https://doi.org/10.1016/j.biomaterials.2015.07.036
59. J. Sarnthein et al., Clinical Neurophysiology 2022, 142, 44–51. https://doi.org/10.1016/j.clinph.2022.07.497
60. S. Burnos et al., Neuroimage Clin. 2016, 10, 318–25. https://doi.org/10.1016/j.nicl.2015.11.018.
61. T. Fedele et al., Clinical Neurophysiology 2017, 128, 1220–6. https://doi.org/10.1016/j.clinph.2017.03.038.
62. V. Greco et al., Exp. Rev. Prot. 2018, 15, 683–696. https://doi.org/10.1080/14789450.2018.1505510
63. M. Preianò et al., Bio.Chem 2021, 1, 250–278. https://doi.org/10.3390/biochem1030018
64. M.Z. Israr et al., Clin. Chem. Lab. Med. 2020, 58, 883–896. https://doi.org/10.1515/cclm-2019-0868
65. M. Muthu et al., J. Mass Spectrom. 2018, 53, 525–540. https://doi.org/10.1002/jms.4083
66. E. Barborini et al., Molecules 2022, 27, 4237. https://doi.org/10.3390/molecules27134237
67. R. Wang et al., Nature 1997, 388, 431–432. https://doi.org/10.1038/41233
68. K. Hashimoto et al., Japanese Journal of Applied Physics 2005, 44, 8269–8285. https://doi.org/10.1143/JJAP.44.8269
69. G.P. Rockwell et al., Colloids Surf. B 2012, 91, 90–96. https://doi.org/10.1016/j.colsurfb.2011.10.045
70. L. Gailite et al., Langmuir 2014, 30, 5973–5981. https://doi.org/10.1021/la500738u
71. G. Calza et al., Front. Pharmac. 2018, 9. https://www.frontiersin.org/articles/10.3389/fphar.2018.00141
72. F. Mambretti et al., Scientific Reports 2022, 12, 12234. https://doi.org/10.1038/s41598-022-15996-9
73. A. Halder et al., ACS Catalysis 2021, 11, 10, 6210–6224. https://doi.org/10.1021/acscatal.0c05029
74. J. Xu et al., ACS Applied Energy Materials 2018, 1, 7, 3013–3018. https://doi.org/10.1021/acsaem.8b00111
75. L. Ciambriello et al., Journal of Physical Chemistry C 2022, 126, 51, 21759–21770. https://doi.org/10.1021/acs.jpcc.2c06669

Advances in Colloidal Synthesis of "Giant" Core/Thick-Shell Quantum Dots



Tory A. Welsch, Jill M. Cleveland, D. Bruce Chase, and Matthew F. Doty

1 Introduction

Semiconducting colloidal quantum dots (QDs) are versatile building blocks for a broad range of photonic, photovoltaic, optoelectronic, and biomedical device applications due to their excellent size- and composition-dependent optoelectronic properties [1–5]. The overcoating of core QDs with a thin (few monolayer) shell enables further tunability of optical properties depending on the relative band alignments of the core/shell materials while generally improving the photoluminescence quantum yield (PLQY) due to passivation of surface states [6]. Of particular interest, so-called giant core/thick-shell QDs exhibit enhanced chemical stability, photostability, and unique optical properties such as suppression of blinking, photobleaching, and Auger recombination [7]. These distinctive characteristics have been studied for giant core/thick-shell CdSe/CdS [8–10], CdSe/ZnSe [11], PbSe/CdSe [12], $CuInS_2$/ZnS [13], and PbS/CdS [14] QDs, among others. While giant core/thick-shell QDs typically form a quasi-type II band structure, those able to form a true type II band structure (e.g., InP/CdSe [15], ZnSe/CdS [11], and CdTe/CdS [16]) are particularly desired to enable complete spatial separation of charge carriers, which serves as an important foundation to more complex dual-emitting and upconversion structures [15, 17–24].

Steady advances in colloidal chemistry techniques have enabled the synthesis of increasingly complex core/shell QDs tailored to achieve sophisticated optical functions. However, choosing the reaction conditions necessary to grow high-quality spherical shells presents a particular challenge for giant core/thick-shell QDs. In particular, desirable optical properties that originate in the addition of

T. A. Welsch (✉) · J. M. Cleveland · D. B. Chase · M. F. Doty
Department of Materials Science and Engineering, University of Delaware, Newark, DE, USA
e-mail: twelsch@udel.edu

© The Author(s), under exclusive license to Springer Nature Switzerland AG 2024

S. Krishnamoorthy, K. (Kris) Iniewski (eds.), *Advances in Fabrication and Investigation of Nanomaterials for Industrial Applications*,
https://doi.org/10.1007/978-3-031-42700-8_2

a thick shell, such as suppressed blinking, are highly dependent on the precise synthesis method employed. There have been numerous efforts to elucidate the complex network of competing reactions involved in the nanocrystal growth process [25–34]. However, the effects of synthesis variables on the growth mechanism are most commonly studied only for single-component QDs and thin-shelled structures. The findings of such studies cannot always be extended to different material types or morphologies where additional factors complicate the nanocrystal growth mechanism, which is the case for thick-shell growth [16, 27, 28, 34]. Furthermore, reaction parameters that are effective for thin-shell systems can have differing effects and become nonorthogonal when applied to thick-shell QDs that require different reagent and volume ratios [16, 35]. The multi-dimensional parameter space of reaction conditions for thick-shelled QDs must be comprehensively examined to reach a level of synthetic control comparable to that achieved for single component and thin-shelled systems.

In this chapter we discuss current progress toward the goal of developing rational and reliable colloidal synthesis methods for giant core/thick-shell QDs. We first briefly review systematic studies using the Successive Ionic Layer Adsorption and Reaction (SILAR) method to gain insights into thick-shell growth. We then discuss our investigation of reaction parameters to synthesize core/thick-shell CdTe/CdS using a hot-injection technique. From the results we generate experiment design criteria that can be used to guide the development of reliable synthesis methods for high-quality thick-shelled giant QDs.

2 Understanding Thick-Shell Growth via SILAR

Shelling reactions are commonly performed by a slow, monolayer-by-monolayer growth method known as the Successive Ionic Layer Adsorption and Reaction (SILAR) technique [9, 11, 12, 14, 15, 36–38]. In a typical SILAR method, monolayer equivalents of shell precursors are added sequentially to core QDs suspended in various coordinating ligands and solvents, where each monolayer is allowed to form over a specified growth time before precursors calculated for the subsequent monolayer are added. This approach allows for the formation of homogeneous shells with well-defined thicknesses, making SILAR a popular choice for synthesizing thick-shelled structures where a high degree of control over the growth process is necessary. However, the creation of thicker shells by SILAR is complicated by numerous reaction parameters that can lead to unwanted variations in optical and structural properties of the reaction product. There have been significant efforts elucidating the roles of such parameters, such as anneal times, ligand choices, and reactant ratios, in SILAR experiments specifically targeting thick shells. In particular, Jennifer Hollingsworth and co-workers have made substantial contributions toward understanding the complexities of thick-shell growth using SILAR techniques; we summarize two important results from her group below.

Ghosh et al. showed how multiple shelling reaction parameters in the synthesis of giant CdSe/CdS QDs determine the resulting QD morphology and optical performance [9]. These synthesis parameters may not play an obvious role for the growth of thin shells but can dramatically affect the growth of thick shells. We highlight four key insights reported in this work:

1. PLQY is enhanced with thin shell growth regardless of the anneal time between monolayer injections. In contrast, the anneal time has a significant effect on PLQY for thick shells. Ghosh et al. determined that thick shells grown for longer anneal times (3 hr per monolayer) resulted in QDs with nearly 2x the PLQY of those grown over shorter anneal times (20 min per monolayer), suggesting that longer anneal times are generally required for the SILAR growth of giant QDs.
2. Precipitation of the reaction solution after each addition of cadmium oleate precursor occurs after 7 monolayers of shell are added. Maintaining a homogeneous reaction solution is important to minimize batch-to-batch variability in structural and optical properties, meaning that such turbidity cycling could have a particularly negative impact on thick shell growth. Ghosh et al. found that variations in turbidity throughout the reaction could be reduced by replacing 1-octadecene (ODE) with octadecane (OD). However, they also found that extreme dilution of the CdSe core solution with OD resulted in non-spherical particles exhibiting low PLQY.
3. Through a study of SILAR reaction stoichiometry, i.e., the amounts of CdS shell precursors in the reaction as compared to the CdSe cores, Ghosh et al. found that non-stoichiometric reactions with an excess of shell precursors resulted in misshapen or rod-like structures with low PLQY. The products of these excess shell precursor reactions were improved by adding excess oleic acid, which likely aided shell growth by helping solubilize the excess precursor. This approach resulted in QDs with symmetric morphologies reaching PLQYs as high as 50%. Another non-stoichiometric method was attempted by starting with sufficient sulfur precursor for 13 monolayers in the reaction solution and injecting only cadmium aliquots throughout the SILAR process. There was less variability in the turbidity of the reaction solution throughout the experiment, but this method resulted in rod-like structures of predominantly zinc blende (*zb*) crystal type. This result was likely due to the excess sulfur being present from the beginning of the reaction pushing the growth process toward the kinetic product rather than the more stable wurtzite (*wz*) product.
4. A study of the effects of coordinating ligands on the thick shell growth revealed that the extent to which oleylamine serves as a coordinating ligand depends on the amount of oleic acid (OA) in the reaction solution. A Cd:OA ratio of 1:10 resulted in oleate ligand coverage of the resulting particles, whereas a ratio of 1:4 resulted in amine capped particles as determined by FTIR. While both ratios resulted in *wz*-CdS shells, the oleate coated particles were more faceted in appearance. The primary amine (oleylamine) was also replaced with a secondary amine (dioctylamine), which was found to result in octahedral-shaped particles that were essentially non-emissive. These structures were almost exclusively

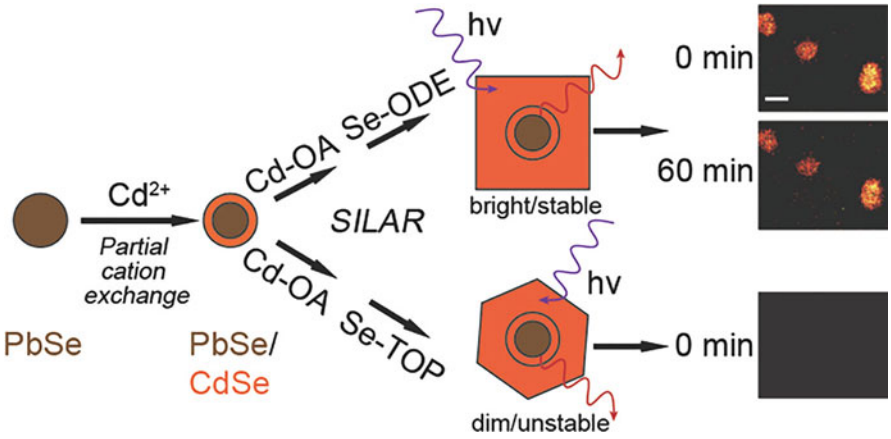


Fig. 1 Summary of giant PbSe/CdSe/CdSe synthesis methods and ligand-dependent results. Reproduced from Ref. [12]

oleate capped regardless of the OA:Cd ratio, likely due to steric hindrance of the branched amine. This steric effect was shown to be more substantial for thick-shell QDs, as thin-shelled QDs extracted throughout the reaction showed FTIR evidence of capping by the secondary amine. Such steric effects are generally enhanced for thicker shells due to the QD surface "flattening" effect with increasing particle size, which causes more ligand end-group crowding as the QD surface curvature decreases.

Hanson et al. also investigated the effects of coordinating ligands on thick-shell growth. In this case, the presence of trioctylphosphine (TOP) in the synthesis of PbSe/CdSe/CdSe giant QDs was studied, as summarized in Fig. 1 [12]. In this study a thick CdSe shell was added to PbSe cores through partial cation exchange followed by SILAR, rendering the otherwise highly unstable quantum emitters ultraphotostable. There are three key insights from this work:

1. Partial cation exchange of PbSe with Cd forms a thin *zb*-CdSe shell. Hanson et al. found that further cubic or hexagonal CdSe shell growth via SILAR determines the resulting PL efficiency and can be synthetically directed through ligand choice. The CdSe shelling can yield either *zb*- or *wz*-CdSe depending on the selenium precursor, where Se-ODE yields *zb* shell growth and Se-TOP yields *wz* shell growth. They postulated that the presence of TOP as an additional coordinating solvent grows a hexagonal shell by modulating Se reaction rates and passivating QD surface sites to reduce their reactivity toward Cd. In addition, TOP may lower the surface energy of the *wz* facets in comparison to the *zb* facets and cause the Cd-Se bond to be reversible, a combination of factors that favor the thermodynamic *wz* product. In the absence of TOP, growth directed by the crystal lattice of the core QD, i.e., faster kinetic growth, is favored.

2. While the PL peak position was unchanged between the products of the two Se precursor systems (Se-ODE vs. Se-TOP), the difference between these SILAR conditions strongly impact the PL efficiency and stability. The *zb*-CdSe shelled structures synthesized with Se-ODE had 3–10x higher PLQY than the *wz*-CdSe shelled structures synthesized with Se-TOP, which were likely inhibited by crystal strain at the *zb* core/*wz* shell interface. The *zb*-CdSe shelled structures also showed enhanced PL stability as a function of shell thickness, with nearly completely suppressed photobleaching over 1 hr for the thickest shelled giant structures (8.6 monolayers). In contrast, the *wz*-shelled structures were insufficiently emissive or stable, possibly due to asymmetric strained shelling resulting in thinner shelled regions. The *zb*-CdSe structures also showed a positive correlation between shell thickness and longer PL lifetime. This correlation suggests that emission stability is induced by thick shells passivating trap states for carriers both at the surface and at the core, reducing rapid non-radiative processes and increasing the overall PL lifetime.
3. The resulting particle shape after SILAR could be modulated by the thickness of the initial *zb*-CdSe shell formed by cation exchange. A thicker shell formed by a longer cation exchange reaction resulted in branched arm growth of CdSe by SILAR. Hanson et al. observed that a shape-directing effect from large seed facets combined with a sidewall-binding ligand (TOP) lead to anisotropic *wz* growth along the *c*-axis and the resulting tetrapoidal shapes. These tetrapoidal structures were determined to be essentially non-emissive, likely due to surface trapping states in the CdSe arms preventing carrier relaxation to the PbSe core.

In summary, the work by Hollingsworth and co-workers described in this section reveals important insights into the roles of key SILAR parameters on the synthesis of giant shelled QDs. In particular, choices of anneal times, solvents, and ligands may differently impact the resulting structure for thick-shell as opposed to thin-shell growth. These systematic studies demonstrate the importance of understanding the effects of reaction variables for the specific case of thick-shell growth.

3 Separating the Effects of Nonorthogonal Variables in the Hot-Injection Synthesis of Giant CdTe/CdS

While SILAR methods have been shown to achieve fine control over resulting thick-shelled QDs, hot-injection shelling reactions offer substantial advantages over SILAR in both reaction time and scalability, especially for thick-shelled or multi-shelled structures [16, 27]. In a hot-injection shelling reaction, all shell precursors for the total desired shell thickness are injected into the QD core solution, allowing for shorter reaction times at elevated temperatures. For example, we have adapted a "flash" shelling method developed for CdSe/CdS [39] to grow thick CdS shells on CdTe cores [16]. In short, CdTe core QDs and a sulfur-TOP precursor are rapidly injected into a cadmium oleate precursor and allowed to react at 350°C.

CdS shells of different thicknesses can be synthesized by adjusting the amounts of Cd-S precursors, oleic acid (OA) content, and reaction time. We found that while this simple adaptation of CdSe/CdS reaction conditions does allow for growth of increasingly thick CdS shells on CdTe cores, evidence from both TEM and optical measurements indicate that the resulting particle quality suffers as the shell thickness increases [16]. For example, the largest CdTe/CdS particles grown in a preliminary study (~20–30 nm in diameter) exhibit numerous visible crystal defects, including evidence of discontinuous shelling and particle agglomeration. This low crystal quality is likely due to non-ideal reaction kinetics leading to non-uniform shelling, ripening, and independent nucleation. We believed this to be the consequence of several synthetic factors that change as the target shell thickness increases, particularly impacting the particle concentration and optimal OA ratio.

In this section we discuss our systematic analysis of three key reaction parameters (particle concentration, OA:Cd ratio, and target shell thickness) to elucidate their separate and intersecting impacts on thick-shell growth [16]. Importantly, we designed these studies to isolate the effects of nonorthogonal variables by, for example, adjusting reagents to hold the particle concentration and target shell thickness constant despite an intentionally changing volume of OA. The synthesis methods and experimental design are described in full in Ref. [16]. We characterize the resulting giant CdTe/CdS structures through transmission electron microscopy (TEM), PL, and PLQY measurements to analyze the NP size and shell quality. We find that the particle concentration has a powerful impact on the quality of the resulting thick-shelled particles and identify a concentration threshold required for ideal shell growth. We also reveal that the effect of the OA:Cd ratio depends on whether the reaction is above or below the particle concentration threshold. Furthermore, we examine a shift in the range of optimal conditions needed to suppress homogeneous nucleation and ripening when targeting increasingly thick shells. We analyze these results to provide a mechanistic description of how the balance between competing reaction processes changes as a function of reaction parameters. Lastly, we suggest experimental design criteria to aid in the development of new thick-shelling reaction methods.

3.1 Systematic Study of Reaction [NP]

In giant shelling reactions, the total reaction volume and resulting reagent concentrations are particularly difficult to control [16]. A larger reaction volume is typically required because greater amounts of precursor materials are needed to grow a thick shell. The number of seed cores may also need to be reduced to compensate for the increased amounts of reagents consumed per reaction. For instance, reports of a hot-injection method for CdS shelling used a 100–200 nmol input of CdSe cores, which would not be feasible for much thicker shells without substantial variation of reagent volumes to account for solubility limits [39]. As a result, the concentration of nanoparticles in the reaction solution for thick shelling

reactions is typically extremely low in comparison to the concentrations used in thin-shell reactions. We hypothesized that low particle concentration could have an adverse effect on the reaction product. In fact, previous reports have observed that product size dispersion and quality is generally improved when syntheses are performed at a larger scale at higher seed concentrations [39]. A study of a heat-up method used to synthesize metal sulfide nanoparticles also showed that a higher concentration reaction condition is needed to reduce nanoparticle (NP) agglomeration [40]. This study found that the high viscosity of the reaction solution at higher concentrations leads to less agglomeration-type collisions between the NPs despite a higher availability of particles in solution. It is also known that ligands such as oleate are bound more weakly and with lower surface density to large NPs, which may contribute to increased particle dissolution and ripening of giant QDs [41]. A higher concentration reaction solution could offset this effect by stabilizing the NPs and reducing the energetic forces driving agglomeration. We determined that a systematic analysis was needed to understand the effects of particle concentration on the reaction product in hot-injection reactions, particularly in the case of thick-shell growth.

We investigated the effect of particle concentration on the thick CdS shelling reaction by varying the CdTe core input [16]. The amounts of Cd-S precursors were adjusted proportionally to hold the Cd-S:CdTe core ratio constant for a calculated shell thickness of 6 nm. Without this adjustment, increasing the core input would result in thinner shells rather than isolating the effects of the reaction concentration on otherwise equivalent thick-shelled products. The amount of oleic acid was also adjusted for a 4.5:1 OA:Cd ratio, while the same volumes of TOPO and TOP coordinating solvents were used for all reactions. This controlled modulation resulted in various overall reaction concentrations that are quantified and reported as the concentration of nanoparticles in the reaction, [NP]. For example, increasing the CdTe core input from 10 to 100 nmol requires 10x more CdO, S, and OA. Since the remainder of the reaction volume from TOPO and TOP remains the same, this 10x increase in the number of CdTe cores yields a 6x increase in [NP].

We found that the [NP] has a profound influence on the thick CdS shelling reaction product [16]. In comparing the TEM images in Fig. 2a, we observed that the lowest [NP] of 1.0 nmol/mL yields small, thin, triangular particles indicative of poorly controlled, non-spherical growth. Upon increasing [NP] to 3.8 nmol/mL, thick CdS shelling proceeds. This indicates that there is a minimum concentration necessary to facilitate spherical shelling and that this minimum concentration lies between 1.0 and 3.8 nmol/mL. The average particle size of the 3.8 nmol/mL samples is 19.0 $\pm$ 4.7 nm. This diameter corresponds to a 7.6 $\pm$ 2.3 nm CdS shell, which is larger than the target shell thickness of 6 nm, likely due to non-uniform shelling and particle agglomeration. We measure a decrease in average particle size upon further increasing the [NP] to 4.8 and 6.0 nmol/mL. The average particle diameter for samples at 6.0 nmol/mL is 15.5 $\pm$ 3.9 nm, corresponding to a 5.8 $\pm$ 1.9 nm CdS shell. While the size measurements of the samples at higher [NP] agree with the calculated shell thickness, it is important to note that particle sizing alone does not quantify the [NP] threshold for a high-quality shell. As shown in the TEM images,

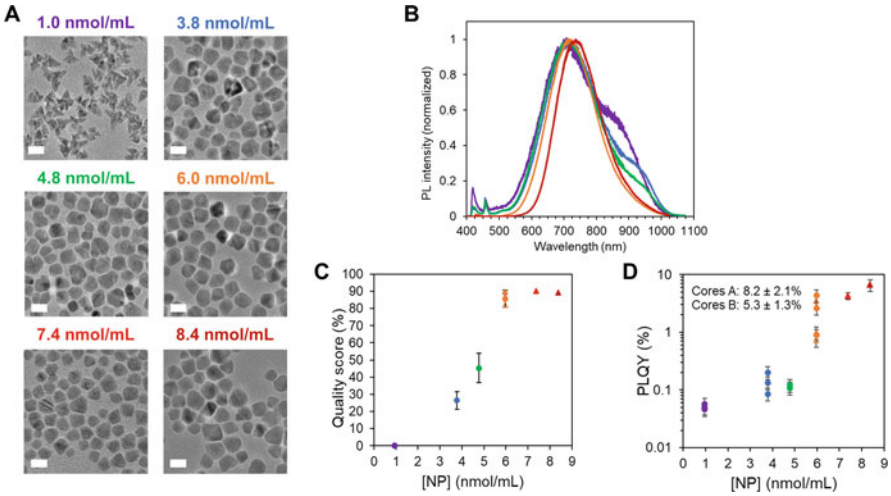


Fig. 2 Varying [NP] for CdTe/CdS synthesis at constant OA:Cd and Cd-S:CdTe core ratios. (**a**) TEM images (scale bars 20 nm) and (**b**) PL spectra for representative CdTe/CdS samples with [NP] of 1.0 (purple), 3.8 (blue), 4.8 (green), 6.0 (orange), 7.4 (red), and 8.4 (maroon) nmol/mL. Plots of (**c**) quality score from TEM analysis and (**d**) PLQY as a function of [NP]. Reproduced from Ref. [16]

we also observed a qualitative improvement in particle morphology and reduced evidence of visible crystal defects, non-uniform shelling, and particle agglomeration as [NP] increases from 3.8 to 6.0 nmol/mL. This enhancement appears to be sustained upon further increasing [NP] to 7.4 and 8.4 nmol/mL.

This qualitative measure of particle quality is supported by the normalized PL spectra, which are shown for representative samples in Fig. 2b. For all samples, the primary PL peak is present at 711–746 nm, with a slight red shift as [NP] increases from 1.0 to 8.4 nmol/mL. With increasing [NP], we also see the disappearance of a large shoulder at ~900–950 nm, which we attribute to elimination of a low-energy defect state. We determined that the low-energy shoulder is not due to particle aggregation because its intensity remained unchanged after sonication for 30 min. There is also a decrease in relative intensity of several high-energy peaks at 420, 460, and 510 nm, which are associated with independent nucleation of CdS [42]. The PL spectra for the 7.4 nmol/mL and 8.4 nmol/mL samples completely overlap and are similar to that for 6.0 nmol/mL, with only a slight red shift in the peak wavelength.

To quantify the quality of the shells as a function of [NP], we developed two complementary measures of particle quality from the TEM and PL data [16]. To quantify the particle quality from TEM, we applied a set of visual criteria (e.g., morphology, agglomeration, crystalline defects) to 500–1000 particles in each sample. From this method we calculated a "quality score" as the percentage of high-quality particles in the total number of particles analyzed, averaged across the

multiple trials of each reaction. While TEM images do not capture every aspect of shell quality, this quality scoring method is a useful measure of the visible features that contribute to particle quality and can be used in conjunction with other tools such as PLQY. The TEM quality scores for this sample set are plotted as a function of [NP] in Fig. 2c. We find that the quality score increases from 0% to 86 ± 5% with increasing [NP] until 6.0 nmol/mL and then levels out within error as [NP] increases further. In addition, the percentage of high-quality particles is consistent across multiple reaction trials for each concentration, indicating a high degree of repeatability.

PLQY also provides a quantitative measure of particle quality because higher PLQY is indicative of reduced non-radiative recombination due to reduced crystal and surface defects. In shelling reactions, the PLQY is known to increase from that of the core when the first few monolayers of shell are added due to increased surface passivation; PLQY then typically decreases upon further shelling [14, 35, 39, 43]. In Fig. 2d the PLQY of each sample is plotted on a log scale as a function of [NP]. We found that PLQY increases exponentially with increasing [NP], returning to or exceeding the PLQY of the CdTe cores. This trend is consistent with our particle quality analysis from TEM. We note that the range of PLQY we measure (0.05–8.2%) is lower than what has been obtained for CdSe/CdS thick-shell particles [39]. This is expected because of the larger lattice mismatch between CdTe and CdS and the type II band structure for CdTe/CdS, which is discussed further in the Supporting Information of Ref. [16].

Collectively, these results show that the hot-injection shelling reaction mechanism is strongly dependent on reaction concentration. For a given shell thickness, uniform spherical shelling occurs only above a certain [NP] threshold. Just above this [NP] threshold, reaction products show poor morphology, particle agglomeration, and independent nucleation. Increasing [NP] improves the particle quality until a second concentration threshold that represents entrance into the regime of highest-quality shelling; beyond this second threshold particle quality does not improve with increasing [NP]. Importantly, we have demonstrated this dependence across reactions with the same target shell thickness (6 nm) rather than only increasing the core input to yield thinner shells. Following this approach, the independent effect of reaction concentration on the quality of a single reaction product can be considered in future synthesis design.

3.2 Separating the Effects of OA and [NP]

For the growth of CdS shells, the reaction mechanism is also dictated by the concentration of oleic acid (OA), which acts as both a ligand and solvent [16]. While cadmium oleate nominally consists of a 2:1 stoichiometric ratio of OA and cadmium, it has been found that a minimum 3:1 ratio is needed for full dissolution of CdO [39]. Nakonechnyi et al. later reported that using a 3:1 OA:Cd ratio resulted in significant independent nucleation of CdS and that a 20:1 ratio suppressed

independent nucleation by increasing the solubility of the Cd-S monomer [42]. However, a high OA concentration can also increase the solubility of the core and core/shell particles, which can lead to particle dissolution and ripening rather than ideal shell growth [27]. Choosing an OA:Cd ratio that balances these competing effects is difficult because there is no standard method to determine the optimal ratio for a given reaction condition or specified shell thickness. Importantly, increasing the OA:Cd ratio also increases the total reaction volume, thus lowering the reaction concentration. The nonorthogonal relationship between OA:Cd ratio and particle concentration is further exacerbated for thicker shell reactions that require higher volumes of ligand.

The dramatic impact of [NP] identified through the first phase of our study, as described above, makes it clear that it is essential to control for [NP] in all subsequent experiments. With this in mind, we designed a study to investigate the OA:Cd ratio while controlling for [NP]. The Cd-S:CdTe core ratio was again held constant for a calculated shell thickness of 6 nm. We varied the OA:Cd ratio for two sets of reactions, each at a constant [NP] value chosen from the previous study to test both below and above the [NP] threshold for high-quality shelling. The amount of CdTe cores was carefully adjusted for each OA:Cd ratio to keep the [NP] constant despite the changing reaction volume, therefore, separating the effects of [NP] and OA:Cd ratio.

We first varied the OA:Cd ratio between 3.5:1 and 9:1 for a set of reactions with [NP] of 3.8 nmol/mL, which is below the [NP] threshold for high-quality shelling [16]. Representative TEM images of the resulting CdTe/CdS NPs are shown in Fig. 3a. The resulting structures are consistent with the 3.8 nmol/mL example in Fig. 2a.[1] However, we notice that the size of the particles increases with increasing OA:Cd ratio. The CdTe/CdS particle diameter is plotted as a function of OA:Cd ratio in Fig. 3b with error bars taken from the standard deviation of the diameter. Both the particle diameter and the % standard deviation increase with increasing OA. We hypothesize that with increasing OA relative to Cd there is an intensified ripening effect, and these larger particles continue to undergo particle agglomeration.

Despite this trend in the particle size, we see no trend with OA:Cd ratio in the PL spectra, as shown in Fig. 3c. The main peak is consistent with the previous set at ~730 nm. In the lowest OA ratio case (3.5:1), the previously mentioned low-energy shoulder at ~950 nm has characteristics of a second peak. At higher OA:Cd ratios, the PL in this region is lower in relative intensity, though it is still present in all spectra and there is no trend with increasing OA. Similarly, the high-energy CdS peaks are present in the spectra for all OA ratios, and there is no trend in the relative intensity with increasing OA.

We performed a similar investigation for reactions with [NP] of 6.0 nmol/mL, which is above the threshold for high-quality shelling [16]. For this series we varied the OA:Cd ratio between 3.5:1 and 7.5:1. Representative TEM images of

[1] Note that the 4.5:1 OA:Cd case reported in Fig. 3 is an identical reaction to that reported for 3.8 nmol/mL in Fig. 2.

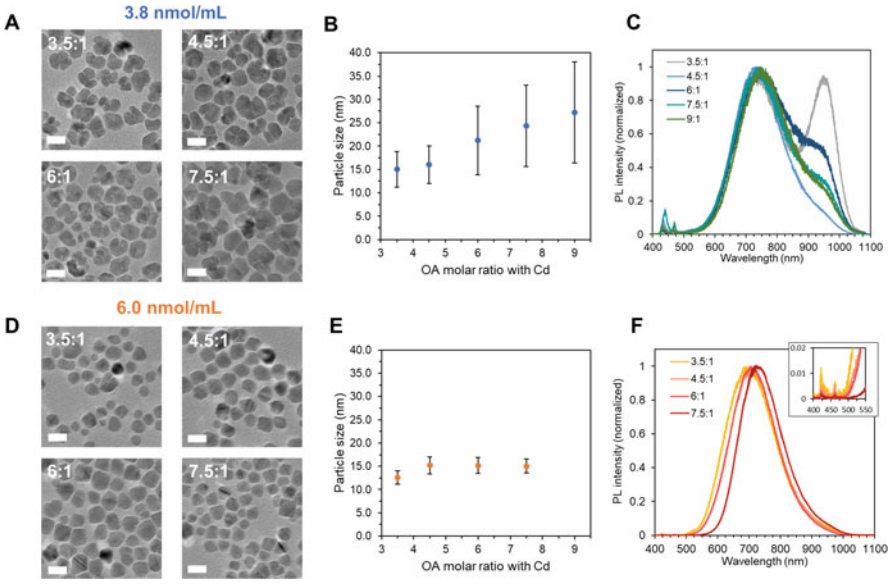


Fig. 3 Varying OA:Cd ratio at constant [NP] and Cd-S:CdTe core ratio. (**a**) TEM images (scale bars 20 nm), (**b**) particle diameter and standard deviation, and (**c**) PL spectra for samples with [NP] of 3.8 nmol/mL at various OA:Cd ratios. (**d**) TEM images (scale bars 20 nm), (**e**) particle diameter and standard deviation, and (**f**) PL spectra for samples with [NP] of 6.0 nmol/mL at various OA:Cd ratios. Reproduced from Ref. [16]

the resulting CdTe/CdS NPs are shown in Fig. 3d. As expected, the 4.5:1 case is comparable to the other 6.0 nmol/mL reactions performed in the previous study. Rather surprisingly, there is no significant variation across the different OA:Cd ratios. The ratio of 3.5:1 results in a slightly smaller particle size, likely due to insufficient solubility and shelling of Cd-S. However, further increasing the OA ratio past 4.5:1 has no effect on size, which is seen in the plot of particle diameters and standard deviations (Fig. 3e). There are also only minimal changes in the PL spectra across this range of OA ratios, shown in Fig. 3f. As the OA content increases, there is a modest red shift in the main PL peak. No spectra show significant evidence of a low-energy defect state or independent nucleation of CdS. The higher-energy peaks associated with CdS are less than ~1% of the main peak in relative intensity and decrease to near zero with increasing OA (as shown in the inset of Fig. 3f).

Finally, we quantified the quality of the samples through TEM analysis and PLQY measurements for both NP concentrations, as shown in Fig. 4. As expected, the quality scores of the 3.8 nmol/mL products as measured by TEM (Fig. 4a) are consistently low, with the worst quality at 3.5:1 OA:Cd. In contrast, the TEM quality scores of all 6.0 nmol/mL reactions are above 80% regardless of OA ratio and are within error of all previous reactions at this NP concentration (see Fig. 2c). We see a similar pattern in the PLQY (Fig. 4b), with consistently low QY values for the 3.8 nmol/mL reactions. However, for the 6.0 nmol/mL reactions there is an

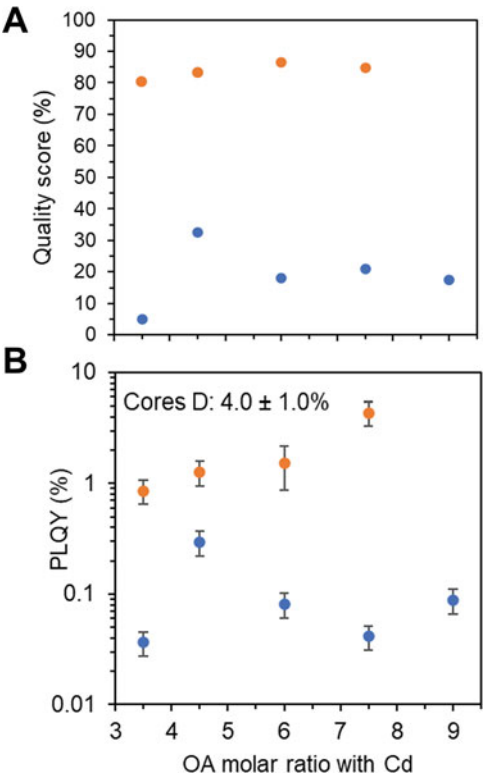


Fig. 4 (**a**) Quality score from TEM analysis and (**b**) PLQY plotted as a function of OA:Cd ratio for samples with [NP] of 3.8 nmol/mL (blue) and 6.0 nmol/mL (orange). Reproduced from Ref. [16]

improvement in PLQY with increasing OA:Cd ratio, which is consistent with the red shift and reduced independent nucleation observed in the PL spectra.

There are several important implications of this data. When the desired shelling process dominates, as in the 6.0 nmol/mL case, increasing the OA:Cd ratio does not lead to increased particle dissolution and ripening as it does at lower [NP]. When a competing ripening process dominates, as in the 3.8 nmol/mL case, increasing the OA further increases that effect. This is slightly surprising: while higher OA concentration is known to increase the dissolution of smaller particles, leading to ripening, we would also expect this higher concentration of ligand to have a stabilizing effect on larger particles [27]. We observe that the effect of reaction concentration dominates, and that particles prone to agglomerate in a low [NP] reaction are not stabilized by increasing the OA. This is shown by the fact that the reactions performed at lower [NP] have consistently low quality across the investigated range of OA ratios, with no improvement as a function of increasing OA. Importantly, from this we can conclude that the reaction concentration [NP] dictates the resulting shelled particle quality. In other words, adjusting the OA:Cd ratio improves the quality of the shell only if the reaction is already above the [NP] threshold required for high-quality shell growth.

3.3 Variation of Optimal Parameters with Increasing Shell Thickness

The shell thickness is controlled through the shelling material to core ratio. In the experiments reported thus far, this ratio was held constant to target a 6 nm CdS shell (corresponding to a Cd-S:CdTe core ratio of 41 μmol/nmol). The results reported above show that [NP] is critical for obtaining high-quality shells. To understand how the [NP] sensitivity depends on the target shell thickness, we conducted [NP] sensitivity experiments analogous to those described above for two higher Cd-S:CdTe core ratios that target shell thicknesses of 9 and 12 nm. The OA:Cd ratios were set at 6:1 and 7.5:1, respectively.

We first varied the [NP] between 0.82 and 3.2 nmol/mL for reactions with a target shell thickness of 9 nm, corresponding to a Cd-S:CdTe core ratio of 107 μmol/nmol [16]. Consistent with our previous results, we observe non-uniform shelling and particle agglomeration at lower [NP] values. The particle quality improves when the [NP] is increased to 3.2 nmol/mL. Below this threshold, we also observe significant evidence of independent nucleation of CdS in the PL spectra. Specifically, the highest energy CdS peak for the 0.82 and 1.4 nmol/mL cases has intensity as high as 30% of the intensity of the main PL peak. With increasing [NP], the intensities of these higher-energy PL peaks decrease substantially. We next targeted 12 nm shells (Cd-S:CdTe core ratio of 224 μmol/nmol) and observed similar effects when varying [NP] between 0.39 and 1.0 nmol/mL. At the lowest concentration, there are also smaller particles (~6 nm in diameter) visible in the TEM images, which we attribute to independent nucleation of CdS. The particle quality improvement with increasing [NP] that is evident in both the TEM images and PL spectra is consistent with our previous results.

We again analyzed the quality of our NPs for both sets of reactions by using TEM and PLQY measurements. The results are plotted for the 12 nm (blue) and 9 nm (green) target shell reactions as a function of [NP] in Fig. 5a–b. The particle concentration data for the 6 nm shell reactions (see Fig. 2) are also plotted in gray for ease of comparison. In all cases we find that the quality score from TEM analysis increases linearly and the PLQY increases exponentially with increasing [NP]. Notably, however, the [NP] threshold values needed to achieve a high-quality shell depends strongly on the target shell thickness. For example, in the target 9 nm case we reach a high TEM quality score at 3.2 nmol/mL, approximately half the [NP] required for a comparable quality result in the target 6 nm case. Similarly high particle quality is achieved at an [NP] of only 1.0 nmol/mL when targeting 12 nm shells. This [NP] threshold for high-quality particles (designated as those with a ≥80% quality score from TEM analysis) is plotted as a function of Cd-S:CdTe core ratio in Fig. 5c.[2] We see a strong correlation between the threshold [NP] and the

[2] We of course do not test every possible value of [NP]. The lower error bars represent the range of possible values within which the [NP] threshold could lie.

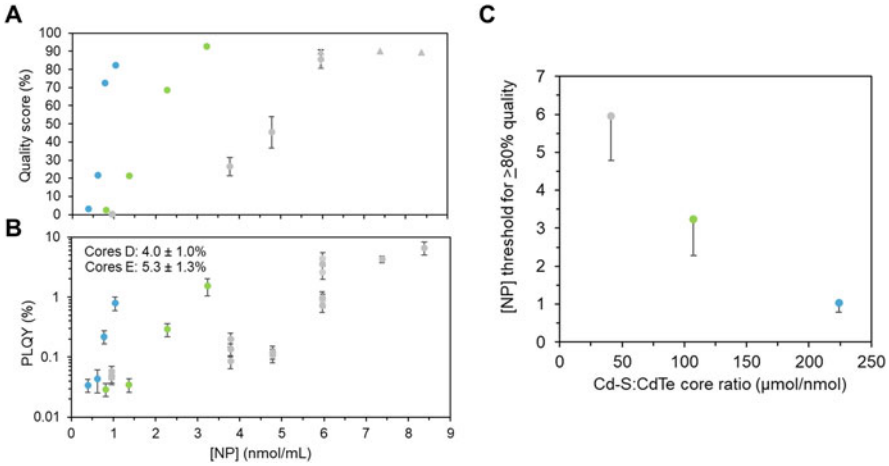


Fig. 5 Varying [NP] at higher Cd-S:CdTe core ratios. (**a**) Quality score from TEM analysis and (**b**) PLQY as a function of [NP] for Cd-S:CdTe core ratio of 224 μmol/nmol (blue), 107 μmol/nmol (green), and 41 μmol/nmol (gray, reproduced from Fig. 2. (**c**) [NP] threshold to synthesize high-quality (≥80% quality score from TEM analysis) particles as a function of Cd-S:CdTe core ratio. Reproduced from Ref. [16]

amount of shelling material present in the reaction per core, indicating that a higher Cd-S:CdTe core ratio lowers the minimum [NP] needed for high-quality shelling.

While increasing the Cd-S:CdTe core ratio (targeting thicker shells) lowers the [NP] threshold for achieving high-quality particles, we also found that saturation limits and unreacted precursors prevent the shells from reaching their target thickness [16]. For example, when targeting 9 nm shells, the diameter of the highest [NP] sample was measured to be 19.9 ± 3.9 nm, corresponding to a slightly below-target CdS shell thickness of 8.1 ± 2.0 nm. We note that the PL spectra for this sample still has a small shoulder at 515 nm and that the main peak is blue shifted from the others in this set. We attribute this to saturation limits of the reagents, specifically of sulfur in TOP, which prevented full incorporation of the precursors into the reaction solution. In the 12 nm shell target case, the highest [NP] sample has a particle diameter of 22.0 ± 3.4 nm, corresponding to a CdS shell thickness of 9.1 ± 1.7 nm. We again found unreacted Cd and S precursors evident from a dark supernatant and insoluble yellow flakes during sample purification. In this case, the OA:Cd ratio likely needs to be higher than 7.5:1 to reach the target shell thickness, analogous to our previous determination that a 3.5:1 OA:Cd ratio was too low to reach a 6 nm target thickness. However, maintaining an [NP] of 1.0 nmol/mL for these reactions would be difficult at higher OA ratios without also adjusting other parameters, such as the TOP and TOPO volumes, due to the saturation limit of sulfur in TOP. We further discuss these additional synthesis considerations below.

Summarizing this section, our results indicate that the observed improvement in particle quality with increasing [NP] is consistent across shells of various

thicknesses. We also find that increasing the availability of Cd-S precursors as compared to the cores by increasing the Cd-S:CdTe core ratio lowers the [NP] threshold required to achieve high-quality shells. However, saturation limits and unreacted precursors prevent the shells from reaching the target thickness. We hypothesize that other reaction parameters need to be further adjusted for one-step growth of high-quality CdS shells with thicknesses beyond 9 nm.

3.4 Insights into the Shelling Reaction Mechanism

Competing reaction processes must be balanced to stay within a successful shelling regime. Our results show that the reaction concentration is a crucial factor in maintaining this balance [16]. As previously discussed, thick shelling reactions are typically performed at lower particle concentrations than thin shelling reactions. However, we can clearly see that having too low [NP] has a detrimental effect on the shelling process. Figure 6 illustrates this impact on the shelling reaction mechanism for a given target shell thickness. At lower concentrations, the shelling reaction shifts to non-ideal growth where there is an insufficient supply of cores (red spheres) and shelling materials (yellow spheres) in solution, and it is less likely for the shelling precursors to "find" the cores. Cd-S consumption by growth is, therefore, reduced, and secondary nucleation and particle dissolution will dominate. It is also worth noting that the Cd-S precursor intermediate is expected to form more slowly at lower CdO and S concentrations, which will also contribute to slow and inefficient shell growth. The reaction then becomes dominated by non-uniform shelling, homogeneous nucleation, particle dissolution, and ripening due to insufficient supply of materials in solution.

The adverse effects of low [NP] can be offset by increasing the amount of shelling material per core, in this case, the Cd-S:CdTe core ratio. The higher availability of shelling materials explains why thick shelling reactions can be done at much lower particle concentrations than typical few monolayer shelling reactions. It is also consistent with previous studies where the number of cores was simply increased without proportionally adjusting the shelling material, resulting in higher-quality, albeit thinner, shells [39]. However, we have found that the effect of too low [NP] cannot be compensated for by increasing the OA ratio. While increasing the OA ratio increases the solubility and thus the availability of Cd-S for shelling, it also causes dissolution and agglomeration of existing particles in unstable, non-optimal conditions. These competing processes are shown schematically in Fig. 6a.

Upon increasing the availability of both cores and shelling materials in the reaction solution, the balance of competing shelling and dissolution processes tilts toward improved shelling and facilitates isotropic shell growth, as depicted in Fig. 6b. Above the [NP] threshold, there is a sufficient supply of materials in the reaction solution and heterogeneous shelling dominates. This stabilized solution reduces homogeneous nucleation, agglomeration, and ripening. For [NP] above the threshold, increasing the OA:Cd ratio does not push the reaction conditions into

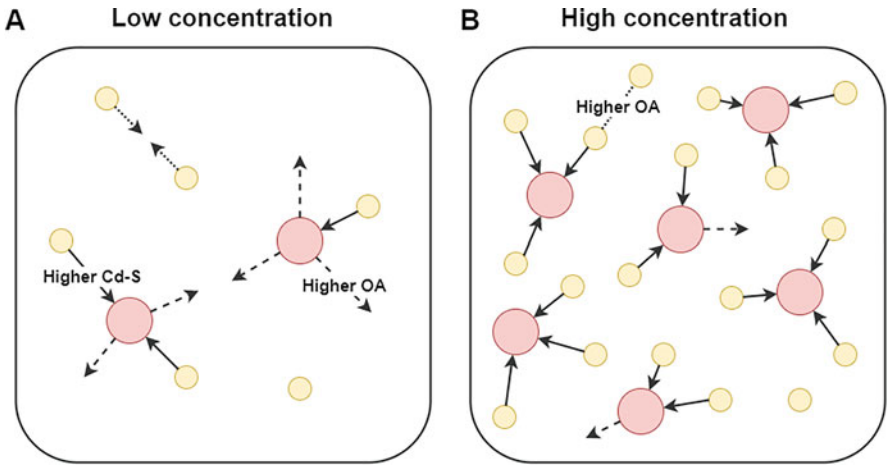


Fig. 6 Schematic of shelling reaction mechanism for the addition of shelling materials (yellow spheres) on cores (red spheres). A constant shell thickness is targeted in the cases of (**a**) low and (**b**) high particle concentration. The system of simultaneous reaction processes is depicted for independent nucleation (dotted arrows), particle dissolution (dashed arrows), and shell growth (solid arrows). Reproduced from Ref. [16]

a non-optimal regime; rather, increasing OA:Cd further suppresses independent nucleation and promotes uniform spherical shelling.

Our findings indicate that reaction concentration dictates the product quality and is, therefore, an especially critical factor to consider when synthesizing giant shelled QDs. We hypothesize that these general mechanistic principles are applicable to core/thick-shell structures beyond giant CdTe/CdS. For this reason, we propose the following optimization sequence when designing or adapting reactions for thick-shell growth. We recommend that the particle concentration at a specified shell thickness be optimized first to ensure high-quality spherical shelling. When the reaction is above the determined [NP] threshold, the OA ratio can then be incrementally adjusted to achieve the desired shell thickness. We do not recommend optimizing the OA ratio first because modulating the OA does not improve the reaction product if the reaction is below the [NP] threshold.

3.5 Additional Synthesis Considerations

An important element of our synthesis approach for the studies above limits the sensitivity of our results to batch-to-batch variation [16]. Identical CdTe cores and reagents from the same supplier and lot were used for each set of experiments and up to five trials were performed for each reaction. The order of reactions was randomly staggered to ensure that variables were not tested in series and that each trial of the

same reaction was performed on a different day. We found that performing multiple reaction trials is especially important for poor-performing samples to ensure that the results are due to the variable being tested, rather than any unknown adverse effect on one particular trial. Importantly, this method also allows us to assess the reliability and repeatability of our results, which is reported via the error bars and confidence intervals in the data.

In addition, we considered several other specific experimental factors [16]. For example, we found the injection method to significantly impact the reaction product. The injection of CdTe cores and S-TOP for reactions performed in a 50-mL flask was done using a 3-inch needle to inject directly into the bottom of the reaction flask, near the stir bar, to ensure rapid and even mixing. Using the same needle for a larger 250-mL flask, the precursors can only be injected on top of the Cd oleate solution rather than directly into it. We found this injection method to result in a hugely varying reaction product in terms of size and particle quality, which was more apparent at higher reaction volumes. For example, we took TEM images from two areas of the same TEM grid for a reaction using the 3-inch needle to inject on top of a reaction volume of 28 mL. The product is extremely heterogeneous in terms of particle size and quality, to the point that the TEM images appear as if they are from two different samples. We found that instead using a 6-inch stainless steel reusable needle to inject directly into the bottom of the 250-mL flask resulted in a significantly more homogeneous product for all larger volume reactions.

We also isolated the effect of total reaction volume by repeating a reaction at half scale. The quality score and PLQY of this reaction are plotted in Fig. 2c as an open orange triangle. We found there is no change in the product for the full as compared to the half scale reaction, indicating that the reaction volume has no effect while all other parameter ratios are kept constant. While it would be useful to perform all larger volume reactions at half scale, it is not practical to work with smaller volumes of TOP when dissolving large amounts of CdTe cores and sulfur.

In addition, we identified solubility limits of sulfur in TOP. The S-TOP solution was typically prepared by stirring sulfur powder in a vial with 1 mL TOP at 100°C until dissolved. We found that as the concentration of sulfur increased past ~0.2 g per 1 mL TOP, the solution needed to be heated to 150°C to ensure dissolution of all powder. We also found that these highly concentrated S:TOP solutions precipitate out of solution within a few seconds of being removed from the heat. Therefore, the removal and injection of the solution must happen very quickly. For reactions requiring greater than ~0.2 g of sulfur, the solution of CdTe cores in 2 mL TOP was also added to the vial and stirred together to better dissolve the sulfur in a larger volume. However, in the highest [NP] case for the reaction targeting 9 nm shells, there was still precipitated sulfur powder remaining in the syringe after the precursors were injected. This solubility limit restricts the range of available shell thicknesses without adjusting other reagent amounts to maintain the required [NP], such as increasing the volume of TOP while decreasing the amount of TOPO or decreasing the number of CdTe cores while decreasing the amount of TOPO.

Lastly, we note that it is recommended to purify ligands and solvents, such as TOPO, through recrystallization before use to remove impurities that may affect

synthesis method reliability [44]. For example, the cadmium oleate used in the CdS shelling reactions for this study was generated in situ. This preparation method could affect batch-to-batch reliability because of variations in the removal of byproducts from cadmium oleate formation. Alternatively, cadmium oleate could be synthesized and isolated before use in subsequent reactions to better control this extraneous variable [26].

4 Conclusions

In this chapter we have discussed advances toward understanding thick-shell growth processes to achieve high synthetic control of giant QDs. When thick shells are synthesized via SILAR, the choices of anneal times, solvents, and ligands all play key roles in determining the resulting structure. Importantly, these impacts are not revealed in studies of SILAR growth of thin-shell structures and must be studied specifically for the thick-shell case. When CdTe/CdS thick-shell structures are synthesized by hot-injection, we reveal the reaction concentration to be the most important factor dictating the product quality, and this result likely generalizes to other core/thick-shell structures. We, therefore, recommend that when performing hot-injection core/thick-shell particle synthesis, the particle concentration for realizing a specific shell thickness should be optimized first to ensure high-quality spherical shelling. When the reaction is above the determined [NP] threshold, the ligand ratio can then be incrementally adjusted to achieve the desired shell thickness.

References

1. F. Pelayo García de Arquer, Dmitri V. Talapin, Victor I. Klimov, Yasuhiko Arakawa, Manfred Bayer, and Edward H. Sargent. Semiconductor quantum dots: Technological progress and future challenges. *Science*, 373(6555):eaaz8541, 8 2021.
2. C B Murray, D J Norris, and M G Bawendi. Synthesis and Characterization of Nearly Monodisperse CdE (E = S, Se, Te) Semiconductor Nanocrystallites. *J. Am. Chem. Soc*, 115:8706–8715, 1993.
3. Jaehyun Kim, Seungho Song, Yong-Hoon Kim, and Sung Kyu Park. Recent Progress of Quantum Dot-Based Photonic Devices and Systems: A Comprehensive Review of Materials, Devices, and Applications. *Small Structures*, 2(3):2000024, 2021.
4. Donghao Wang, Feifei Yin, Zhonglin Du, Dongni Han, and Jianguo Tang. Recent progress in quantum dot-sensitized solar cells employing metal chalcogenides. *J. Mater. Chem. A*, 7:26205, 2019.
5. AHmed A.H. Abdellatif, Hesham M. Tawfeek, Mahmoud A. Younis, Mansour Alsharidah, and Osamah Al Rugaie. Biomedical Applications of Quantum Dots: Overview, Challenges, and Clinical Potential. *International Journal of Nanomedicine*, 17:1951–1970, 2022.
6. Anupam Sahu and Dharmendra Kumar. Core-shell quantum dots: A review on classification, materials, application, and theoretical modeling. *Journal of Alloys and Compounds*, 924:166508, 11 2022.

7. Fabiola Navarro-Pardo, Haiguang Zhao, Zhiming M. Wang, and Federico Rosei. Structure/Property Relations in "Giant" Semiconductor Nanocrystals: Opportunities in Photonics and Electronics. *Accounts of Chemical Research*, 51(3):609–618, 12 2017.
8. Yongfen Chen, Javier Vela, Han Htoon, Joanna L Casson, Donald J Werder, David A Bussian, Victor I Klimov, and Jennifer A Hollingsworth. "Giant" Multishell CdSe Nanocrystal Quantum Dots with Suppressed Blinking. *J. Am. Chem. Soc*, 130:38, 2008.
9. Yagnaseni Ghosh, Benjamin D. Mangum, Joanna L. Casson, Darrick J. Williams, Han Htoon, and Jennifer A. Hollingsworth. New insights into the complexities of shell growth and the strong influence of particle volume in nonblinking "giant" core/shell nanocrystal quantum dots. *Journal of the American Chemical Society*, 134(23):9634–9643, 2012.
10. Haiguang Zhao, Jiabin Liu, François Vidal, Alberto Vomiero, and Federico Rosei. Tailoring the interfacial structure of colloidal "giant" quantum dots for optoelectronic applications. *Nanoscale*, 10:17189, 2018.
11. Krishna P. Acharya, Hue M. Nguyen, Melissa Paulite, Andrei Piryatinski, Jun Zhang, Joanna L. Casson, Hongwu Xu, Han Htoon, and Jennifer A. Hollingsworth. Elucidation of two giants: Challenges to thick-shell synthesis in CdSe/ZnSe and ZnSe/CdS Core/shell quantum dots. *Journal of the American Chemical Society*, 137(11):3755–3758, 3 2015.
12. Christina J. Hanson, Nicolai F. Hartmann, Ajay Singh, Xuedan Ma, William J.I. Debenedetti, Joanna L. Casson, John K. Grey, Yves J. Chabal, Anton V. Malko, Milan Sykora, Andrei Piryatinski, Han Htoon, and Jennifer A. Hollingsworth. Giant PbSe/CdSe/CdSe Quantum Dots: Crystal-Structure-Defined Ultrastable Near-Infrared Photoluminescence from Single Nanocrystals. *Journal of the American Chemical Society*, 139(32):11081–11088, 8 2017.
13. Huidong Zang, Hongbo Li, Nikolay S Makarov, Kirill A Velizhanin, Kaifeng Wu, Young-Shin Park, and Victor I Klimov. Thick-Shell CuInS 2 /ZnS Quantum Dots with Suppressed "Blinking" and Narrow Single-Particle Emission Line Widths. *Nano Lett*, 17:1787–1795, 2017.
14. Sachidananda Krishnamurthy, Ajay Singh, Zhongjian Hu, Anastasia V. Blake, Younghee Kim, Amita Singh, Ekaterina A. Dolgopolova, Darrick J. Williams, Andrei Piryatinski, Anton V. Malko, Han Htoon, Milan Sykora, and Jennifer A. Hollingsworth. PbS/CdS Quantum Dot Room-Temperature Single-Emitter Spectroscopy Reaches the Telecom O and S Bands via an Engineered Stability. *ACS Nano*, 15(1):575–587, 1 2021.
15. Allison M Dennis, Matthew R Buck, Feng Wang, Nicolai F Hartmann, Somak Majumder, Joanna L Casson, John D Watt, Stephen K Doorn, Han Htoon, Milan Sykora, Jennifer A Hollingsworth, A M Dennis, M R Buck, F Wang, N F Hartmann, S Majumder, J L Casson, J D Watt, S K Doorn, H Htoon, J A Hollingsworth, and M Sykora. Role of Interface Chemistry in Opening New Radiative Pathways in InP/CdSe Giant Quantum Dots with Blinking-Suppressed Two-Color Emission. *Advanced Functional Materials*, 29(37):1809111, 9 2019.
16. Tory A Welsch, Jill M Cleveland, D Bruce Chase, and Matthew F Doty. Separating the Effects of Nonorthogonal Variables on the Hot-Injection Synthesis of Core/Thick-Shell ("Giant") CdTe/CdS Quantum Dots. *Chem. Mater.*, 34(23):10721–10731, 2022.
17. Christopher C Milleville, Eric Y Chen, Kyle R Lennon, Jill M Cleveland, Abinash Kumar, Jing Zhang, James A Bork, Ansel Tessier, James M Lebeau, D Bruce Chase, Joshua M O Zide, and Matthew F Doty. Engineering Efficient Photon Upconversion in Semiconductor Heterostructures. *ACS Nano*, 13(1):489–497, 2019.
18. Diane G. Sellers and Matthew F. Doty. Design, synthesis and photophysical properties of InP/CdS/CdSe and CdTe/CdS/CdSe (core/shell/shell) quantum dots for photon upconversion. *2015 IEEE 42nd Photovoltaic Specialist Conference, PVSC 2015*, pages 1–5, 2015.
19. Andrei Piryatinski, Sergei A Ivanov, Sergei Tretiak, and Victor I Klimov. Effect of Quantum and Dielectric Confinement on the ExcitonExciton Interaction Energy in Type II Core/Shell Semiconductor Nanocrystals. *Nano Lett.*, 7(1):108–115, 2007.
20. Sergio Brovelli, Wan Ki Bae, Christophe Galland, Umberto Giovanella, Francesco Meinardi, and Victor I Klimov. Dual-Color Electroluminescence from Dot-in-Bulk Nanocrystals. *ACS Nano Letters*, 14:486–494, 2014.
21. Valerio Pinchetti, Elena V. Shornikova, Gang Qiang, Wan Ki Bae, Francesco Meinardi, Scott A. Crooker, Dmitri R. Yakovlev, Manfred Bayer, Victor I. Klimov, and Sergio Brovelli. Dual-

emitting dot-in-bulk CdSe/CdS nanocrystals with highly emissive core-and shell-based Trions sharing the same resident electron. *Nano Letters*, 19:8846–8854, 2019.
22. Zvicka Deutsch, Lior Neeman, and Dan Oron. Luminescence upconversion in colloidal double quantum dots. *Nature Nanotechnology*, 8(9):649–653, 9 2013.
23. Ayelet Teitelboim and Dan Oron. Broadband Near-Infrared to Visible Upconversion in Quantum DotQuantum Well Heterostructures. *ACS Nano*, 10:446–452, 2015.
24. Gaoling Yang, Miri Kazes, Dekel Raanan, and Dan Oron. Bright Near-Infrared to Visible Upconversion Double Quantum Dots Based on a Type-II/Type-I Heterostructure. *ACS Photonics*, 8:1909–1916, 2021.
25. Jennifer A. Hollingsworth and Victor I. Klimov. "Soft" Chemical Synthesis and Manipulation of Semiconductor Nanocrystals. In *Nanocrystal Quantum Dots*, pages 1–57. 2010.
26. Leslie S. Hamachi, Haoran Yang, Ilan Jen-La Plante, Natalie Saenz, Kevin Qian, Michael P. Campos, Gregory T. Cleveland, Iva Rreza, Aisha Oza, Willem Walravens, Emory M. Chan, Zeger Hens, Andrew C. Crowther, and Jonathan S. Owen. Precursor reaction kinetics control compositional grading and size of CdSe1-: XSx nanocrystal heterostructures. *Chemical Science*, 10(26):6539–6552, 2019.
27. Haoran Yang, Leslie S. Hamachi, Iva Rreza, Wesley Wang, and Emory M. Chan. Design Rules for One-Step Seeded Growth of Nanocrystals: Threading the Needle between Secondary Nucleation and Ripening. *Chemistry of Materials*, 31:17, 2019.
28. Joonhyuck Park, Arun Jayaraman, Alex W. Schrader, Gyu Weon Hwang, and Hee Sun Han. Controllable modulation of precursor reactivity using chemical additives for systematic synthesis of high-quality quantum dots. *Nature Communications*, 11(1):1–9, 11 2020.
29. P Tim Prins, Federico Montanarella, Kim Du, Yolanda Justo, Johanna C Van Der Bok, Stijn O M Hinterding, Jaco J Geuchies, Jorick Maes, Kim De Nolf, Sander Deelen, Hans Meijer, Thomas Zinn, Andrei V Petukhov, Freddy T Rabouw, Celso De, Mello Donega, Daniel Vanmaekelbergh, and Zeger Hens. Extended Nucleation and Superfocusing in Colloidal Semiconductor Nanocrystal Synthesis. *ACS Nano Letters*, 21:2487–2496, 2021.
30. Ellie Bennett, Matthew W Greenberg, Abraham J Jordan, Leslie S Hamachi, Soham Banerjee, Simon J L Billinge, and Jonathan S Owen. Size Dependent Optical Properties and Structure of ZnS Nanocrystals Prepared from a Library of Thioureas. *Chem. Mater*, 34:706–717, 2022.
31. Craig R. Bullen and Paul Mulvaney. Nucleation and growth kinetics of CdSe nanocrystals in octadecene. *NANO LETTERS*, 4(12):2303–2307, 12 2004.
32. Sofie Abe, Richard Karel Capek, Bram De Geyter, and Zeger Hens. Tuning the Postfocused Size of Colloidal Nanocrystals by the Reaction Rate: From Theory to Application. *ACS Nano*, 6(1):42–53, 2012.
33. Emanuele A. Slejko and Vanni Lughi. Size Control at Maximum Yield and Growth Kinetics of Colloidal II-VI Semiconductor Nanocrystals. *Journal of Physical Chemistry C*, 123(2):1421–1428, 2019.
34. Jennifer M. Lee, Rebecca C. Miller, Lily J. Moloney, and Amy L. Prieto. The development of strategies for nanoparticle synthesis: Considerations for deepening understanding of inherently complex systems. *Journal of Solid State Chemistry*, 273:243–286, 5 2019.
35. Yuan Niu, Chaodan Pu, Runchen Lai, Renyang Meng, Wanzhen Lin, Haiyan Qin, and Xiaogang Peng. One-pot/three-step synthesis of zinc-blende CdSe/CdS core/shell nanocrystals with thick shells. *Nano Research*, 10(4):1149–1162, 2017.
36. J Jack Li, Y Andrew Wang, Wenzhuo Guo, Joel C Keay, Tetsuya D Mishima, Matthew B Johnson, and Xiaogang Peng. Large-Scale Synthesis of Nearly Monodisperse CdSe/CdS Core/Shell Nanocrystals Using Air-Stable Reagents via Successive Ion Layer Adsorption and Reaction. *J. Am. Chem. Soc*, 125:12567–12575, 2003.
37. Guiju Liu, Zhibin Ling, Yiqian Wang, and Haiguang Zhao. Near-infrared CdSexTe1-x@CdS "giant" quantum dots for efficient photoelectrochemical hydrogen generation. *International Journal of Hydrogen Energy*, 43(49):22064–22074, 12 2018.
38. James R Mcbride, Nimai Mishra, and Sophia M Click. Role of shell composition and morphology in achieving single-emitter photostability for green-emitting "giant" quantum dots. *J. Chem. Phys*, 152:124713, 2020.

39. Emile Drijvers, Jonathan De Roo, Pieter Geiregat, Krisztina Feher Feher, Zeger Hens, and Tangi Aubert. Revisited Wurtzite CdSe Synthesis: A Gateway for the Versatile Flash Synthesis of Multishell Quantum Dots and Rods. *Chemistry of Materials*, 28:7311–7323, 2016.
40. Curtis B. Williamson, Douglas R. Nevers, Tobias Hanrath, and Richard D. Robinson. Prodigious Effects of Concentration Intensification on Nanoparticle Synthesis: A High-Quality, Scalable Approach. *Journal of the American Chemical Society*, 137(50):15843–15851, 2015.
41. Adam Roberge, John H Dunlap, Fiaz Ahmed, and Andrew B Greytak. Size-Dependent PbS Quantum Dot Surface Chemistry Investigated via Gel Permeation Chromatography. *Chem. Mater.*, 32:6588–6594, 2020.
42. Igor Nakonechnyi, Michael Sluydts, Yolanda Justo, Jacek Jasieniak, and Zeger Hens. Mechanistic Insights in Seeded Growth Synthesis of Colloidal Core/Shell Quantum Dots. *Chemistry of Materials*, 29(11):4719–4727, 6 2017.
43. Yanyan Jia, Jinquan Chen, Kaifeng Wu, Alex Kaledin, Djamaladdin G. Musaev, Zhaoxiong Xie, and Tianquan Lian. Enhancing photo-reduction quantum efficiency using quasi-type II core/shell quantum dots. *Chemical Science*, 7(7):4125–4133, 6 2016.
44. Jonathan De Roo. Chemical Considerations for Colloidal Nanocrystal Synthesis. *Chem. Mater*, 34:5766–5779, 2022.

Emerging Trends in Nanotechnology for Forensic Science



Alexandro Mangueira Lima de Assis, Gerard de Oliveira Deokaran, and Adriana Santos Ribeiro

1 Introduction

Forensic science can be defined as the application of the natural and physical science methods to investigate crimes or examine crime scene evidence that might be presented in a court of law. Thus, forensic science is a critical element of the criminal justice system [16, 35, 43, 44]. Forensic evidence is the result of employing scientific methods through the recognition, collection, identification, analysis, and comparison of physical evidence generated by criminal or illegal civil activity. In an independent and objective way, forensic evidence can link suspects or victims to a crime scene, refute an alibi, exonerate innocent individuals, or even develop and

A. M. L. de Assis
Federal Police, National Institute of Criminalistics, Brasília, Federal District, Brazil

Federal Police, Regional Superintendent Office in Alagoas, Technical and Scientific Section, Maceió, Alagoas, Brazil

Graduate Program in Materials, Technology Centre, Federal University of Alagoas, Maceió, Alagoas, Brazil

G. d. O. Deokaran
Scientific Police of Alagoas, Institute of Criminalistics, Maceió, Alagoas, Brazil

Graduate Program in Materials, Technology Centre, Federal University of Alagoas, Maceió, Alagoas, Brazil

A. S. Ribeiro (✉)
Graduate Program in Materials, Technology Centre, Federal University of Alagoas, Maceió, Alagoas, Brazil

Chemistry and Biotechnology Institute, Federal University of Alagoas, Maceió, Alagoas, Brazil
e-mail: aribeiro@qui.ufal.br

© The Author(s), under exclusive license to Springer Nature Switzerland AG 2024

S. Krishnamoorthy, K. (Kris) Iniewski (eds.), *Advances in Fabrication and Investigation of Nanomaterials for Industrial Applications*,
https://doi.org/10.1007/978-3-031-42700-8_3

validate investigation theories aimed at fully clarifying the facts related to the crime [15, 35, 36].

The scope of forensic science comprises a varied set of disciplines, including forensic chemistry, latent fingerprint examination, forensic molecular biology (DNA), fire and explosive examinations, forensic toxicology, trace evidence examination (fibers, hairs, paints, polymers, glass, soil, and materials in general), firearms, ammunition and tool mark examination, handwriting analysis, digital evidence, etc. [15, 35].

Routinely, forensic practitioners endeavor to ensure the reliability of results and to keep up with new technologies without falling behind in handling forensic caseworks. However, these professionals may find situations that suggest or require the implementation of new technologies or the improvement of existing methods for solving crimes. In these cases, the solution is the use of scientific research as a tool to address these challenges and ensure that forensic science remains a powerful force to support justice and public security [16, 45, 57].

From this perspective, materials science has stood out especially in relation to the advanced research of nanomaterials applied in forensic analysis, such as new colorimetric and electrochemical sensors for illicit drugs, explosives, and other substances of interest, as well as nanocomposites applied as innovative developers of latent fingerprints. In this chapter, some of the most recent advances in nanotechnology with promising potential for application by the forensic science community are presented. The first section is devoted to a brief introduction to forensic science, in addition to an overview about the structure and properties of nanoparticles and its nanocomposites. Next, we focus on recent advances concerning the preparation of polymer nanofibers and nanocomposites by electrospinning technique. Last, we underline the possibilities of innovative applications of these advanced materials in forensic science.

2 Nanostructured Materials and Nanocomposites

2.1 Molecular Structure and Properties

Nanotechnology is the science which involves design, fabrication, and applications of nanostructures and nanomaterials with typical size smaller than 100 nm. As a broad interdisciplinary field, which encompasses the understanding of the fundamental physics, chemistry, biology, and technology of materials, nanotechnology involves the production of new structures, materials, and devices through the manipulation of matter on a near-atomic scale [26, 39].

A nanomaterial is often characterized by a dimension linked either to the dimension of the salient nanofeatures making up the material or to their organization. When some interesting property of a material emerges from the organization or pattern of random or well-ordered nanopatterns, the resultant material is referred to as

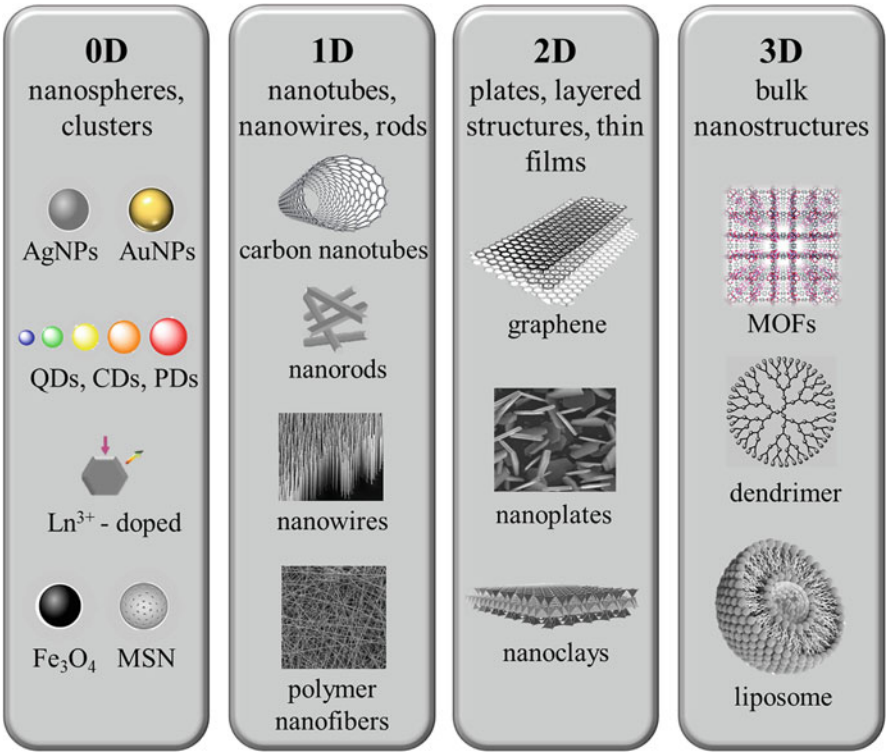


Fig. 1 Classification of nanomaterials according to their dimensions

nanostructure or nanostructured material. Such materials are usually classified based on their dimensionality, morphology, composition, uniformity, and agglomeration.

In terms of their dimensionality, nanomaterials can be classified as zero-dimension (0-D) to three-dimension (3-D). 0-D nanomaterials include metallic nanoparticles, such as gold and silver nanoparticles, quantum dots (CdS, CdSe, CdTe), carbon dots, and polymer dots. These nanoparticles may have shapes such as spherical, cubic, or polygonal with size in the range of 1–50 nm. 1-D nanomaterials, for example, nanotubes, nanofibers, nanorods, or whiskers of metals or oxides, have a very high surface area and aspect ratio, which are useful to prepare nanocomposites. Graphene, nanolayers, nanoclays, nanosheets, nanofilms, platelet-like structure, nanoflakes, or nanoplatelets and silicate nanoplatelets comprise 2-D-type nanomaterials. Materials that are not confined to the nanoscale in any dimension, having all three dimensions >100 nm, are designated 3-D nanostructured materials, also known as bulk nanomaterials. Such materials present a nanocrystalline structure or features at the nanoscale consisting of a multiple arrangement of nanosized crystals in different orientations, typically dispersions of nanoparticles, nanowires, nanotubes, or multinanolayers, in the matrix ([3, 13]; see Fig. 1).

Based on the morphology, nanomaterials are generally classified into high-aspect-ratio and low-aspect-ratio nanoparticles. Nanotubes and nanowires with various shapes are examples of high-aspect-ratio nanoparticles, whereas helical-, spherical-, cubic-, pillar-, and oval-shaped nanoparticles are the examples of low-aspect-ratio nanomaterials. Most of these nanoparticles occur in the form of powder, suspensions, or colloids, which tend to form clusters or agglomerates due to their surface energy. A convenient way to reduce the surface energy and increase dispersion rate is through the modification of the nanoparticle by a polymer, for example, alginate, chitosan, polyethylene glycol (PEG), and pluronic P123, which offers structural diversity and different functionalities [19, 22, 34].

Due to the boundary between atoms/molecules and the macroworld at this size scale, nanomaterials usually exhibit enhanced properties such as higher strength, lighter weight, increased control of light spectrum, and greater chemical reactivity than their larger-scale counterparts. Further advantage of nanoscale materials is the vastly increased ratio of surface area to volume compared to the bulk material, which provides new possibilities in surface-based science aiming at improvement of collection and processing of evidence at crime scenes, including fingerprint enhancement, DNA analysis, and sensors for detection of explosives, illicit drugs, and other substances of forensic interest [2, 7, 17, 41, 42, 48].

The attractive properties of nanomaterials strongly depend on their structural characteristics and mostly lie in their ability to alter the electronic and spectral features of the material upon modifications of its size, incorporation to a matrix producing nanocomposites, or chemical structure through attachment of different functional groups, such as amine and carboxylic acid, amphiphilic moieties, or fluorescent substituents. For example, a series of physical phenomena become noticeably more pronounced as the size of the nanomaterial decreases, including the crystal phase of the material, electron transport properties, its doping properties, and interactions with light [5]. Therefore, rational design and synthesis of the nanomaterials and nanocomposites play an important role in tailoring their properties and functionalities aiming at specific applications.

2.2 Application in Forensic Science

In forensic science, nanotechnology is most effectively applied for latent fingerprint development and forensic toxicology for detection and quantification of different substances of forensic interest. Fluorescent nanomaterials and nanocomposites, such as quantum dots [7, 58], carbon dots [10], polymer dots [4], and rare earth and metallic nanoparticles [2, 62], have been proven to be highly efficient in the visualization and/or detection of crime scene evidence.

Nanomaterials have been applied for detection of illicit drugs, as clonazepam (date rape drug) as demonstrated by A. Lodha et al. [25] that developed a sensor based on melamine-modified gold nanoparticles to identify clonazepam from blood and skeletal remains samples. Similarly, lidocaine hydrochloride was investigated

from vitreous humor as an alternative body fluid for on-spot, portable, lab-on-phone approach of postmortem drug screening which is another advancement to provide the advance platform for the future investigations based on forensic nanotechnology [1, 25].

Colorimetric and fluorescence sensing methods are two kinds of optical sensor systems based on nanomaterials. Graphene quantum dots (GQDs) functionalized with antimorphine were applied to develop a novel turn-on fluorescence nanosensor to detect morphine [32]. Fluorescent GQDs have been synthesized and used as nanosensors to distinguish and determine two of the most frequently used narcotic substances, morphine and methamphetamine. This low-cost sensing device has several advantages, including a quick reaction time (less than 1 min), nontoxicity, and a low limit of detection [31]. Au@Ag-based nanoparticles may be applied as colorimetric nanosensors to determine morphine, cocaine, and methamphetamine [41]. Therefore, sensors developed using nanomaterials are usually portable, low-cost, rapid, reliable, and real-time methods for forensic toxicological drug screening.

For latent fingerprint enhancement, traditional developer powders and commercial wet powder suspensions may present heterogeneous (and sometimes not strictly controlled) particle sizes in the submicrometer to micrometer range (5–100 μm) and various shapes. In contrast, the smaller (and generally more homogeneous size distribution) of nanoparticles means that the adhesion energy required for attachment to the fingermark residue is smaller than that for dry powders. This favors the development process via deposition of a greater number of colored or luminescent nanoparticles along the residue [7, 23]. Additionally, the possibility of functionalization of such nanoparticles may improve their stability and optical properties or even provide the interaction with specific components (e.g., amino acids, fatty acids, etc.) or metabolites within the sweat at cellular and molecular scales [2].

Detection of trace amounts of explosive is a challenging task due to several limitations, such as low quantity of unexploded explosives, contaminated samples, and different sample collection procedure. For example, in a bomb blast, fragmented residues of explosive can be scattered from the actual place of blast, while unfragmented part of explosive remains at the crime scene. In this scenario, nano-based technology can be useful to analyze and identify the unfragmented/trace amount of fragmented explosives from the crime scene. Nanoparticles based on curcumin [37] and amine-terminated functionalities have been applied as highly selective and ultrasensitive fluorescent probes for trinitrotoluene (TNT) [38]. These studies open up a new prospect for rapid, easy, and reliable detection of TNT from environmental samples and also at the crime scenes by measuring the fluorometric intensity.

However, despite the large number of recent papers, books, and reviews devoted to the synthesis and properties of nanomaterials [13, 39] and their application in forensic science [2, 38, 42, 52], there are just a few reports in the literature that describe the application of electrospun polymer nanofibers aiming at forensic purposes.

3 Advances in Electrospun Polymer Nanofibers

As previously stated, nanofibers are 1-D nanomaterials, meaning they are in the nanoscale range for two dimensions and are analogous to long threads. In this world of nanotechnology, nanofibrous structures offer specialized features, such as mechanical strength and a large surface area, which makes them attractive for many applications. As nanofibers have one macroscale dimension, their composition can contain a large number of functional groups, resulting in a higher number of binding sites, in comparison to 0-D nanomaterials. Additionally, when compared to 2-D materials, 1-D nanomaterials have higher-surface-area-to-volume ratios, which makes them highly efficient. Among all the techniques for generating nanofibers, electrospinning is an easy, low-cost fabrication method that allows for variable morphology that is not applicable to other nanomaterials [9, 40].

Importantly, for clarity, the scope of this chapter has been narrowed to electrospun polymer nanofibers with a major focus in systematically incorporating the studies addressing nanocomposites for application in forensic science, even though this kind of material may have other applications, as biomedical hydrogels, textiles, photovoltaics, pharmaceutics, water treatment, catalysis, optical computing, and sensors.

3.1 Electrospinning Technique: Concepts

Fundamentals and advances on electrospun polymer nanofiber research have been described in detail in recent reviews of Ray et al. [40], Xue et al. [61], Islam et al. [20], Cleeton et al. [6], Li et al. [24], and Haider et al. [14]. Overall, electrospinning involves an electrohydrodynamic process in which polymer solutions are sprayed and stretched under the action of static electricity to obtain fibers with diameters ranging from nanometers to micrometers scale [61]. The electrospinning equipment is mainly composed of four parts: a high-voltage power supply, a syringe pump, a spinneret (usually, a hypodermic needle with blunt tip), and a conductive collector. When the electric field force is sufficiently large, the charged polymer droplets overcome the surface tension to form a jet stream that evaporates or solidifies with the solvent during the jetting process. Finally, it falls on the collection substrate to form a fiber mat that is similar to a nonwoven fabric [6, 14, 20, 24, 40, 49, 53] (Fig. 2).

Electrospinning is a highly versatile technique in that the surface topography, fiber morphology, and orientation are largely dictated by solution properties and operating conditions. The characteristics of electrospun nanofibers depend on solution parameters (solution concentration and/or viscosity, solution surface tension, and solution conductivity), process parameters (feed rate, applied voltage, and tip-to-collector distance), and ambient conditions (temperature and humidity). Thus, the

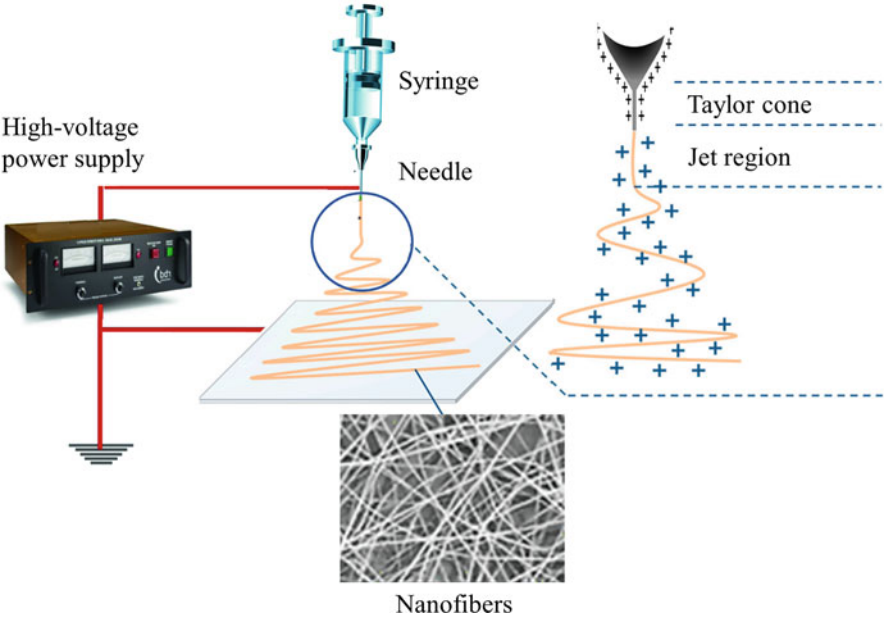


Fig. 2 Schematic representation of electrospinning process. (Adapted from P. Wang et al. [53], under the terms and conditions of the Creative Commons Attribution (CC BY) license (https://creativecommons.org/licenses/by/4.0/))

control of these parameters is important to produce fibers with uniform morphology and size (diameter), absence of defects (beads), and good mechanical properties.

A great number of polymers can be processed by electrospinning, for example, polystyrene, polyvinyl alcohol), polyacrylonitrile, polyurethane, and poly(ε-caprolactone). The choice of an appropriate polymer for nanofiber electrospinning relies on its low degradation rate, nontoxic products of degradation, good mechanical properties, and ability to form blends with various polymers in a wide range of compositions. Preparation of copolymers and composites or functionalization of the polymers allows tailoring their properties to specific applications. According to this approach, fluorescent probes and dyes can be incorporated to the polymer system aiming to achieve materials, which present light emission under a certain stimulus, like ultraviolet light exposure.

3.2 Preparation of Polymer Nanofibers for Latent Fingerprint Development

The fingerprints are widely used as biometric information, being a powerful tool in forensic investigation for identification of an individual, because they are unique

for everyone and immutable throughout the whole life. Even though the fingerprint ridge pattern appears barely visible to the naked eye, it still may produce an invisible impression on the touched surfaces known as latent fingerprint.

Over time, many researchers have explored a variety of methods to promote and improve latent fingerprint development to assist with the efficiency of criminal investigations. Among them, powder dusting, cyanoacrylate fuming, silver nitrate, ninhydrin, 1,8-diazafluoren-9-one, and small particle reagent methods are the most widely used due to their simplicity, efficiency, and ease of operation. The enhancement of latent fingerprint using contrast agent materials may involve spraying, dusting, or vapor deposition techniques which, despite their proven efficacy, may exhibit some downsides such as intricate synthetic procedures of the materials [65], additional posttreatment processes required for visualization of the samples [18], or toxicity of the developing reagents [2, 11, 52].

Recently, new methodologies for latent fingerprint development, such as electrospinning, have been proposed as an alternative strategy to circumvent these drawbacks. The electrospun polymer materials containing a nonfluorescent dye or a fluorophore (a fluorescent organic dye or a fluorescent nanomaterial) incorporated in a polymer matrix may facilitate the sensing and interaction of the developer with the components of the latent fingerprint residues. One of the first examples of the utilization of an electrospun mat for the identification of latent fingerprints was given by S. Yang et al. [63] that prepared an electrospun thermoplastic polyurethane (TPU)/fluorescein nanofiber mat. They have demonstrated a new easy-to-perform and versatile strategy that enables a nondestructive collection and identification of latent fingerprints on various surfaces. In this methodology, latent marks on various surfaces were transferred onto the electrospun mat by softly pressing the mat on the surfaces and then visualized after exposing the mat to hot air (100 °C). Under visible light, the developed fingerprint on the electrospun mat displays a red color in the contact area of the fingerprint ridges [63].

Fluorescein dye was also used in the preparation of electrospun nanofiber mats based on poly(lactic acid)/poly(glycidyl methacrylate)/fluorescein [(PLA)/(PGMA)/fluorescein] [56] for latent fingerprint development. However, in this case, the donor deposited a fingermark directly on the electrospun PLA/PGMA/fluorescein nanofiber mat without transfer from other surfaces commonly found at crime scenes. After exposing the nanofiber mat to hot air (100 °C), the developed latent fingerprint displayed color change from yellow to brownish orange under visible light.

The TPU/fluorescein and (PLA)/(PGMA)/fluorescein electrospun fibrous mats were investigated by laser scanning confocal microscopy (LSCM) showing a bright and well-distributed green fluorescence due to the presence of fluorescein dye. According to the authors, a fluorescence quenching occurs after the interaction with the fingerprint residues due to the crosslink reaction between polymers (TPU, PGMA, and/or PLA) with the carboxyl, hydroxyl, and amino functional groups present in the sweat. These procedures have the advantage of visualizing latent fingerprints by the naked eye, but the process involves a heat treatment with hot air.

Polyvinyl alcohol (PVA)/ninhydrin electrospun mats were also used for the enhancement of latent fingerprints present on glass and ceramics surfaces. In this case, the mats were pressed against the finger marks and subjected to steam from a weak acid bath, in which the marks became purple owing to the color reaction of ninhydrin and the amino acids from the fingerprint residues [55]. Another reported procedure for fingerprint visualization was based on electrospun polyamide nanofiber membranes, in which the latent fingerprints on the surface of different substrates could be transferred by the membranes and be developed after the immersion in a quantum dot solution [21]. This methodology involves time-consuming additional steps necessary to reveal the fingerprints using quantum dots as developer.

Phenothiazine carboxylate salts were prepared by Gal et al. [11] from 10-ethyl-10H-phenothiazine as starting reagent in a three-step synthetic route and combined with polyvinylpyrrolidone (PVP) producing electrospun fluorescent nanofibers. Such materials based on PVP/phenothiazine carboxylate salts of Li, Na, K, and Ca were applied for latent fingerprint development on various surfaces (glass, metal, banknote, ceramic, wood, plastic) after transferred onto the electrospun mat by softly pressing the mat on the surface, followed by visualization on UV or visible light. This procedure afforded highly accurate imaging of the specific fingerprint ridge characteristics unequivocally required for individual identification in forensic investigations (Fig. 3).

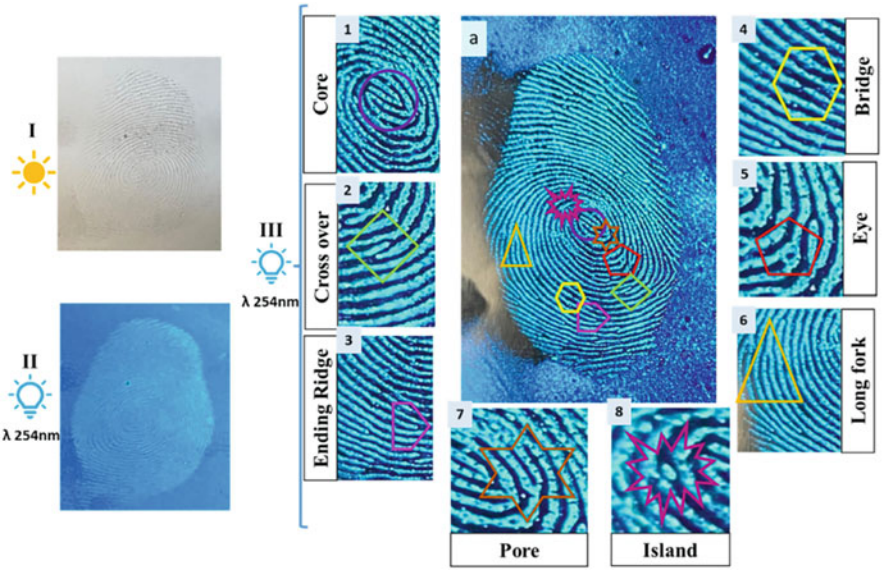


Fig. 3 Image of latent fingerprint transferred onto fluorescent electrospun polymer mat from a metal surface (I) under visible light and (II) under UV irradiation at $\lambda = 254$ nm and (III) image of developed fingerprint ridge characteristics. (Reproduced with permission from Gal et al. [11], Elsevier)

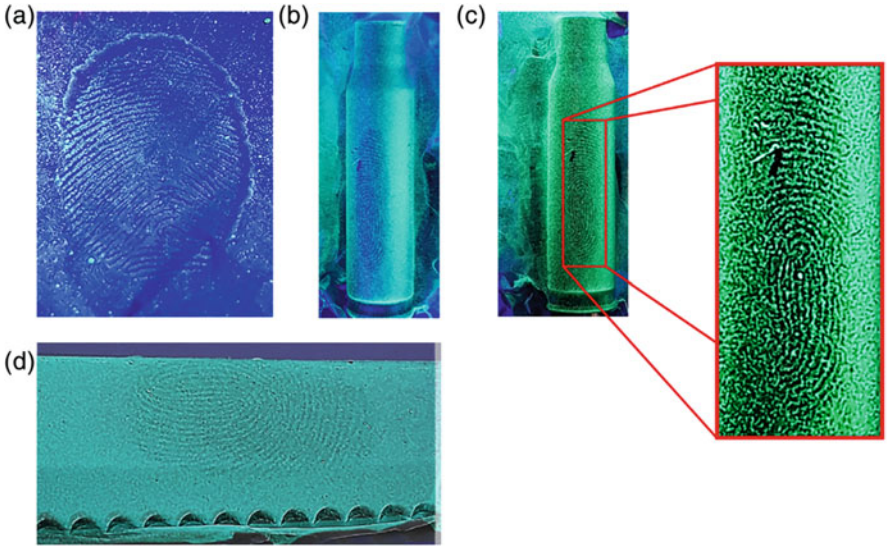


Fig. 4 Images of developed fingerprints by electrospun: (**a**) PCL/DnsCad 2% on aluminum foil, (**b**) PCL/DnsCad 2% on cartridge case, (**c**) PCL/DnsGly 2% on cartridge case and its magnified images, and (**d**) PCL/DnsCad 2% on stainless steel knife blade under UV light (366 nm). (Reproduced with permission from Mazzini Junior et al. [33], Wiley)

An alternative strategy was proposed by Mazzini Júnior et al. [33] that prepared fluorescent electrospun nanofibers based on poly(e-caprolactone) (PCL) and dansyl derivatives for visualization of latent fingerprints present on metallic surfaces, including knife blades and cartridge cases. In this work, the electrospun PCL/dansylcadaverine or PCL/dansylglycine nanofibers were collected directly onto the knife blade or cartridge cases mounted on aluminum foil with a collection time of 5 s. Dansylcadaverine (DnsCad) and dansylglycine (DnsGly) are known as fluorescent probes for determination of certain human proteins, free amino acids, and biologically generated halogenated compounds, since they may react promptly with such compounds with depletion of their intrinsic fluorescence. Likewise, the dansyl derivatives incorporated in PCL matrix were able to interact with the fingerprint residue components by fluorescence quenching, generating a negative image of the fingerprint in that regions in which the residues are present. Such methodology provided a convenient low-cost method for fast fabrication of dansyl-based fluorescent nanofibers for enhancement of the visual contrast of latent fingerprints on metallic surfaces when exposed to UV light [33] (Fig. 4).

Compared with most of known conventional methods for development of latent fingerprints, such as powder dusting and cyanoacrylate fuming, the methodology proposed presented as advantages (i) the use of low toxicity raw materials and solvents, (ii) the easy control of the polymer film formation, and (iii) the acquisition of evidence on fingerprinted metallic surfaces of different shapes and sizes,

Table 1 Fluorescent electrospun polymers applied for latent fingerprint development

Polymer	Fluorophore	Surfaces	Comments	References
TPU	Fluorescein	Quartz, glass, stainless steel, polypropylene film, marble, wood	Exposure mats to hot air	[63]
PLA/PGMA	Fluorescein	–	Exposure mats to hot air	[56]
PVA	Ninhydrin	Glass, ceramics	Subject mats to steam from a weak acid bath	[55]
PA-6	Quantum dots	Aluminum foil, glass, polyethylene film, wood	Immerse mats in QD solution, wash with $CHCl_3$, and place in a vacuum oven for 1h. It is a time-consuming method	[21]
PVP	Phenothiazine carboxylate salts	Glass, Metal, banknote, ceramic, wood, plastic	Involves a three-step synthetic procedure before electrospinning	[11]
PCL	Dansyl derivatives	Aluminum foil, knife blade, cartridge case	Electrospinning directly on the metallic surface containing the latent fingerprint	[33]

TPU thermoplastic polyurethane, *PLA/PGMA* poly(lactic acid)/poly(glycidyl methacrylate), *PVA* polyvinyl alcohol, *PA-6* polyamide-6, *PVP* polyvinylpyrrolidone

depending on settings in the electrospinning collector. As can be seen in Table 1, electrospinning is an emerging technique to be explored aiming at improvement in ease, cost, time, and portability of the latent fingerprint development as an alternative/complementary methodology when compared with the current ones. Therefore, the presented strategies may not only provide a new method to enhancement of latent fingerprints but also open the door to developing electrospinning technique and fluorescent materials for diverse applications in the forensic area, such as explosive detection.

3.3 Fluorescent Sensors for Explosive Detection

Terrorist activities have drawn attention to detect hidden explosives and needs to call for new advanced technologies to combat such type of activities and protect the public. Efficient detection of hidden explosives in luggage, mail, vehicles, aircraft, and toothpaste as well as on suspects is the major challenge for law enforcement

agencies throughout the world. Therefore, great efforts concerning anti-terrorism and national security are toward explosive detection, stimulating the development of novel-sensitive and low-cost materials and devices for this purpose [26].

Detection of nitroaromatic explosives, such as 2,4,6-trinitrotoluene (TNT), 2,4-dinitrotoluene (DNT), and picric acid (PA), is important owing to their broad applications in forensic and criminal investigations. Other explosives of interest are nitramines and nitrate esters, for example, 3,5-trinitroperhydro-1,3,5-triazine (RDX) and pentaerythritol tetranitrate (PETN), since they are the main components of highly energetic plastic explosives, namely, C-4 and Semtex [46, 54]. The main methodologies currently available for detection of these explosives are metal detectors, mass spectrometry (MS), ion mobility spectrometry (IMS), gas chromatography (GC), surface-enhanced Raman spectroscopy, energy dispersive X-ray diffraction, and cyclic voltammetry, which may have some drawbacks, due to requirement of sophisticated protocols, along with poor portability and high cost, making these methodologies not suitable for real-time field detection [59].

Therefore, there is an urgent need to develop low-cost, simple, and field applicable explosive detectors with high performance aiming at practical issues. In recent years, fluorescent sensing based on electron transfer and/or energy transfer mechanisms has become one of the most effective detection methods for explosives, and considerable progress has been made in sensing materials for explosives based on simple small molecule fluorophores incorporated with large surface area nanomaterials to gain increased sensitivity. Therefore, it is a great challenge to fabricate highly sensitive sensors with small molecule fluorophores through facile preparation of sensing materials [50].

Owing to the high sensitivity and fast responses of fluorescent sensors, electrospun nanofiber materials for fluorescence sensing have emerged as a fascinating development of nanomaterials. The first example of the use of electrospun fibrous membranes for TNT detection was reported by Tao et al. [51] that have prepared electrospun silica nanofibers modified with porphyrin [51]. Polymer electrospun nanofibrous sensors using polystyrene (PS) doped with conjugated polymers were developed for detection of trace nitroaromatic explosive vapors, including DNT [28], PA, and TNT [27]. However, the synthesis of these conjugated polymers bearing fluorene and benzothiophene fused rings as the backbone involves several and tedious steps. Well-aligned nanofibers from a conjugated polymer, namely, poly(triphenylamine-alt-biphenylene vinylene) (TPA-PBPV), were prepared by Deng et al. [8] and coated on the surface of electrospun polyacrylonitrile (PAN) nanofiber nonwoven membrane. This material showed highly improved sensory ability to detect TNT vapors, suggesting that nanofibrous structures could be a promising strategy to improve the sensory efficiency of fluorescent chemosensors [8].

A facile sensor for nitroaromatic explosive detection was developed by Y. Yang et al. [64] taking advantage of the ease of the electrospinning technique and simple doping of small molecule fluorophores, in which polystyrene (PS) was doped with tetrakis(4-methoxylphenyl)porphyrin (TMOPP) to produce electrospun nanofibers presenting highly sensitive response toward TNT and PA vapors [64]. Following

the same approach, a porphyrin-based fluorophore was used to prepare nanofibers with distinct luminescent property by electrospinning from porphyrinated polyimide [29]. The authors have demonstrated that this material is able to detect trace TNT vapor.

A series of different fluorophores, such as pyrene (Py) [50, 54] and its derivative 9-(pyren-1-yl)-9H-carbazole (PyCz) [59], has been used to prepare fluorescent nanofibers through electrospinning technique. Wang et al. [54] developed polystyrene (PS)/Py electrospun fluorescent nanofibrous membrane for detection of ultra-trace nitro explosive vapors, explosive residues on handprint, and buried explosives by the naked eye under UV excitation. In this case, a wide spectrum of nitro explosives, as 1,2-dinitrobenzene (DNB), TNT, Tetryl, RDX, PETN, and HMX, could be "visually" detected at their subequilibrium vapors. Such outstanding sensing performance was attributed to the proposed "sandwich-like" conformation between Py and phenyl pendants of PS which may allow efficient long-range energy migration similar to "molecular wire," thus achieving amplified fluorescence quenching. In a similar way, fluorescent polyethersulfone (PES)/Py nanofibers were prepared through electrospinning technique using mixed solvents, being further applied for detection of PA, TNT, DNT, and RDX in aqueous phase [50].

Metal nanoparticles and rare-earth doped materials may also be used to prepare electrospun nanofibers for explosive detection. For example, highly red fluorescent BSA-capped gold clusters (Au.BSA) were incorporated into polyethylene oxide (PEO) nanofibrous membrane termed as Au.BSA@PEO for on-the-spot detection of TNT [47]. Recently, polyvinylpyrrolidone (PVP)/$BaWO_4$ nanofibers doped with Tb^{3+} and Eu^{3+} ions were prepared through a sol-gel electrospinning process, and their emission characteristics and application as a fluorescent probe for the sensing of 2-nitrotoluene and H_2O_2, explosive taggants representing a broad class of explosives, were studied in detail [12].

Owing to their strong electron accepting nature, nitroaromatic explosives have often been detected by fluorescence through a photoinduced electron transfer (PET)-quenching process [60]; hence, as good electron donors, fluorene derivatives are promising candidates to act as sensory materials for such kind of explosives. Additionally, these materials used to exhibit high photoluminescence quantum yields [30]. Following this approach, fluorescent polycaprolactone (PCL) electrospun nanofibers based on a fluorene derivative, namely, 2,2′-(9,9-dioctyl-9H-fluorene-2,7-diyl)bisthiophene (FBT), were prepared for explosive detection through a "turn-off" mechanism presenting excellent results for PA and TNT in vapor, solution, and solid (residue) phases [46]. Figure 5 shows images of a cartridge contaminated with exogenous TNT residues and the fluorescence quenching in regions of the PCL/FBT after the contact with the explosive.

According to the results presented in Table 2, the performance of electrospun nanofibers for explosive detection may be comparable or higher than other sensing systems or conventional methods with the advantage to be used as a free-standing mat in a rapid and facile detection test of explosives present in landmines, airport, and border security and at crime scenes containing nitroaromatic explosives, such as a bank robbery or ATM explosion.

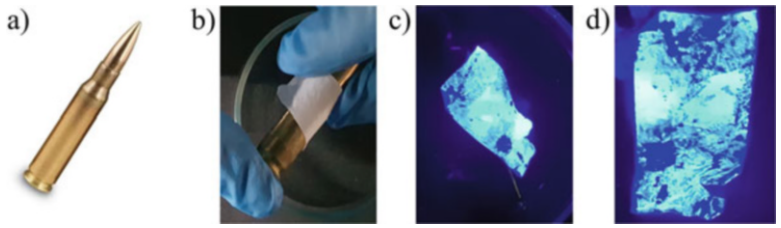


Fig. 5 Images of (**a**) cartridge contaminated with exogenous TNT residues, (**b**) PCL/FBT mat swiped on the cartridge surface, (**c**) PCL/FBT wrapping the cartridge immediately after the contact with the surface, and (**d**) ca. 5 min after the removal of the mat on the cartridge surface. Images (**c**) and (**d**) are under UV light (365 nm). (Reproduced with permission from Santos et al. [46], Elsevier)

Table 2 Fluorescent electrospun nanofibers applied for explosive detection

Polymer	Fluorophore	Explosives	Phase	References
Silica	Porphyrin	TNT	Vapor	[51]
PS	Conjugated polymer	DNT, PA, TNT	Vapor	[27]
PAN	TPA-PBPV	TNT	Vapor	[8]
PS	TMOPP	PA, TNT	Vapor	[64]
Polyimide	Porphyrin	TNT	Vapor	[29]
PS	Pyrene	DNB, HMX, PETN, RDX, tetryl, TNT	Vapor	[54]
PES	Pyrene	DNT, PA, RDX, TNT	Solution	[50]
PS, PEO	PyCz	DNB, DNT, NB, NM, NT, TNT	Vapor	[59]
PEO	Au.BSA	TNT	Solution	[47]
PVP	Tb^{3+}, Eu^{3+}-doped $BaWO_4$	NT, H_2O_2	Solution, vapor, solid	[12]
PCL	FBT	PA, TNT	Solution, vapor, solid	[46]

PS polystyrene, *PAN* polyacrylonitrile, *TPA-PBPV* poly(triphenylamine-alt-biphenylene vinylene), *TMOPP* tetrakis(4-methoxylphenyl)porphyrin, *PES* polyethersulfone, *PEO* polyethylene oxide, *PyCz* 9-(pyren-1-yl)-9H-carbazole, *PVP* polyvinylpyrrolidone, *PCL* polycaprolactone, *FBT* 2,2′-(9,9-dioctyl-9*H*-fluorene-2,7-diyl)bisthiophene

4 Concluding Remarks

Despite the wide range of conventional and commercially available forensic analysis technologies, there are still situations in which it is difficult or even impossible to analyze some types of crime scene traces. Given this context, forensic scientists are dedicated to the research of new technologies and improve the methods already available, in order to offer solutions to the questions that forensic practitioners face in their work routine. This effort includes several scientific research aimed at improving factors such as sensitivity, universality, convenience, and efficiency of materials and methods intended for forensic application.

Regarding latent fingerprint developers, issues related to the chemical composition of the developer materials, possible changes in the molecular structure, and chromatic variation, in addition to their interaction either with the fingerprint residue, with the surface, or both, during the development process, there are characteristics presented in this chapter that should be carefully observed by forensic experts and scientists. As with conventional developers, these characteristics have an influence when choosing which material or technique is most suitable for a particular fingerprint, considering surface, age, waste composition, and environmental conditions (temperature, humidity, etc.), in addition to all information arising from the technical investigation of the crime scene.

It is noteworthy that research into NP-based fingermark detection techniques generally follows the same trends as greenfield materials research, peaking at the "potential application" points in the research life cycle for each new material. While these preliminary investigations are a vital aspect of designing more effective fingermark detection techniques, many remain hidden to the forensic science community as they are published in traditional academic materials, chemistry, or physics journals. Consequently, discussion and collaboration between the disciplines are fragmented, and even the most promising methods are rarely the subject of further evaluation.

Terrorist activities have drawn attention to detect hidden explosives and need to call for new advanced technologies for the purpose of combating terrorism as well as supporting law enforcement actions. Efficient detection of hidden explosives in luggage, mail, vehicles, aircraft, and toothpaste as well as on suspects is the major challenge for government security agencies throughout the world. Therefore, great efforts concerning anti-terrorism and national security are toward explosive detection, stimulating the development of novel-sensitive and low-cost materials and devices for this purpose.

The potential application of nanotechnology in forensic science is notorious, especially in nanosensors for explosive detection or illicit drugs and fingerprint enhancement. Before it comes into the regular applications in the field of forensic science, many other things need to be addressed for the future perspectives like efficiency, cost cutting, accuracy of amalgamation of technology, and safety aspects of health and environment. Nevertheless, the routine use of nanotechnology in the forensic practice is still limited; probably as a consequence of that, many of the reported developments were not applied to samples with the grade of complexity that is required. Therefore, major research efforts should be made in the near future to ensure the use of nanotechnology better equipped for these samples, in order to enhance the robustness and reliability necessary for a real applicability to this field. This technology is going to transform various fields of forensic science including molecular biology, legal medicine, crime scene investigation, fingerprint enhancement, ballistics, and forensic toxicology. In the future, it will clear trends to be taken into account for an effective translation of the laboratory to the real world.

In this context of combining the problems faced by practitioners and the solutions proposed by scientific research, the interaction between the forensic science

institutes, law enforcement agencies, and academy is needful and indispensable for the implementation of new technologies for forensic evidence investigation.

References

1. Ansari, N., Lodha, A., Pandya, A., Sutariya, P. G., & Menon, S. K. (2015). Lab-on-phone citrate-capped silver nanosensor for lidocaine hydrochloride detection from a biological matrix. *Analytical Methods*, *7*(21), 9084–9091. https://doi.org/10.1039/C5AY01977J
2. Assis, A. M. L., Costa, C. V., Alves, M. S., Melo, J. C. S., de Oliveira, V. R., Tonholo, J., Hillman, A. R., & Ribeiro, A. S. (2022). From nanomaterials to macromolecules: Innovative technologies for latent fingerprint development. *WIREs Forensic Science*. https://doi.org/10.1002/wfs2.1475
3. Chen, C., Tang, Y., Vlahovic, B., & Yan, F. (2017). Electrospun Polymer Nanofibers Decorated with Noble Metal Nanoparticles for Chemical Sensing. *Nanoscale Research Letters*, *12*(1), 451. https://doi.org/10.1186/s11671-017-2216-4
4. Chen, Y.-H., Kuo, S.-Y., Tsai, W.-K., Ke, C.-S., Liao, C.-H., Chen, C.-P., Wang, Y.-T., Chen, H.-W., & Chan, Y.-H. (2016). Dual Colorimetric and Fluorescent Imaging of Latent Fingerprints on Both Porous and Nonporous Surfaces with Near-Infrared Fluorescent Semiconducting Polymer Dots. *Analytical Chemistry*, *88*(23), 11616–11623. https://doi.org/10.1021/acs.analchem.6b03178
5. Choi, M. J., McDonagh, A. M., Maynard, P., & Roux, C. (2008). Metal-containing nanoparticles and nano-structured particles in fingermark detection. *Forensic Science International*, *179*(2–3), 87–97. https://doi.org/10.1016/j.forsciint.2008.04.027
6. Cleeton, C., Keirouz, A., Chen, X., & Radacsi, N. (2019). Electrospun Nanofibers for Drug Delivery and Biosensing. *ACS Biomaterials Science & Engineering*, *5*(9), 4183–4205. https://doi.org/10.1021/acsbiomaterials.9b00853
7. Costa, B. M. F., Freitas, D. V, Sousa, F. L. N., Silva, K. D., Dias, J. M. M., Assis, A. M. L., Jesus, A. C., Ribeiro, A. S., & Navarro, M. (2020). SATS@CdTe hierarchical structures emitting green to red colors developed for latent fingerprint applications. *Dyes and Pigments*, *180*(January), 108483. https://doi.org/10.1016/j.dyepig.2020.108483
8. Deng, C., Gong, P., He, Q., Cheng, J., He, C., Shi, L., Zhu, D., & Lin, T. (2009). Highly fluorescent TPA-PBPV nanofibers with amplified sensory response to TNT. *Chemical Physics Letters*, *483*(4–6), 219–223. https://doi.org/10.1016/j.cplett.2009.10.060
9. Feeney, S. G., LaFreniere, J. M. J., & Halpern, J. M. (2021). Perspective on Nanofiber Electrochemical Sensors: Design of Relative Selectivity Experiments. *Polymers*, *13*(21), 3706. https://doi.org/10.3390/polym13213706
10. Feng, Q., Xie, Z., & Zheng, M. (2022). Room temperature phosphorescent carbon dots for latent fingerprints detection and in vivo phosphorescence bioimaging. *Sensors and Actuators B: Chemical*, *351*, 130976. https://doi.org/10.1016/j.snb.2021.130976
11. Gal, M., Cristea, C., Craciun, A. M., Turza, A., Barbu-Tudoran, L., Balazs, B., Lovasz, T., Silaghi-Dumitrescu, L., & Gaina, L. I. (2023). New fluorescent electrospun polymer materials containing phenothiazinyl carboxylate metal salts for versatile latent fingerprint detection. *Dyes and Pigments*, *211*, 111085. https://doi.org/10.1016/j.dyepig.2023.111085
12. George, G., Edwards, C. S., Hayes, J. I., Yu, L., Ede, S. R., Wen, J., & Luo, Z. (2019). A novel reversible fluorescent probe for the highly sensitive detection of nitro and peroxide organic explosives using electrospun BaWO 4 nanofibers. *Journal of Materials Chemistry C*, *7*(47), 14949–14961. https://doi.org/10.1039/C9TC05068J
13. Goyal, R. K. (2017). *Nanomaterials and Nanocomposites*. CRC Press. https://doi.org/10.1201/9781315153285

14. Haider, A., Haider, S., & Kang, I.-K. (2018). A comprehensive review summarizing the effect of electrospinning parameters and potential applications of nanofibers in biomedical and biotechnology. *Arabian Journal of Chemistry*, *11*(8), 1165–1188. https://doi.org/10.1016/j.arabjc.2015.11.015
15. Harris, H. A., & Lee, H. C. (2019). *Introduction to Forensic Science and Criminalistics* (2nd ed.). CRC Press.
16. Houck, M. M. (2019). Open, transparent science helps promote justice. *Forensic Science International: Synergy*, *1*, A275–A276. https://doi.org/10.1016/j.fsisyn.2018.12.001
17. Hou, H. J. M. (2015). Nanoforensics: Forensic application of nanotechnology in illicit drug detection. *Journal of Forensic Research*, *6*(5), 106. https://www.hilarispublisher.com/conference-abstracts-files/2157-7145.C1.018_015.pdf
18. Huang, W., Li, X., Wang, H., Xu, X., Liu, H., & Wang, G. (2015). Synthesis of Amphiphilic Silica Nanoparticles for Latent Fingerprint Detection. *Analytical Letters*, *48*(9), 1524–1535. https://doi.org/10.1080/00032719.2014.984195
19. Hu, Y., Ke, L., Chen, H., Zhuo, M., Yang, X., Zhao, D., Zeng, S., & Xiao, X. (2017). Natural material-decorated mesoporous silica nanoparticle container for multifunctional membrane-controlled targeted drug delivery. *International Journal of Nanomedicine*, *Volume 12*, 8411–8426. https://doi.org/10.2147/IJN.S148438
20. Islam, M. S., Ang, B. C., Andriyana, A., & Afifi, A. M. (2019). A review on fabrication of nanofibers via electrospinning and their applications. *SN Applied Sciences*, *1*(10), 1248. https://doi.org/10.1007/s42452-019-1288-4
21. Kang, H., Ju, Y., Han, T., Ye, S., Zhao, G., & Dong, L. (2021). Sensitive and rapid detection of fingerprints based on electrospun nanofibrous membranes and quantum dots. *Colloids and Surfaces A: Physicochemical and Engineering Aspects*, *623*, 126716. https://doi.org/10.1016/j.colsurfa.2021.126716
22. Kankala, R. K., Han, Y., Na, J., Lee, C., Sun, Z., Wang, S., Kimura, T., Ok, Y. S., Yamauchi, Y., Chen, A., & Wu, K. C.-W. (2020). Nanoarchitectured Structure and Surface Biofunctionality of Mesoporous Silica Nanoparticles. *Advanced Materials*, *32*(23), 1907035. https://doi.org/10.1002/adma.201907035
23. Kanodarwala, F. K., Moret, S., Spindler, X., Lennard, C., & Roux, C. (2019). Nanoparticles used for fingermark detection—A comprehensive review. *Wiley Interdisciplinary Reviews: Forensic Science*, *1*(5), 1–41. https://doi.org/10.1002/wfs2.1341
24. Li, Y., Zhu, J., Cheng, H., Li, G., Cho, H., Jiang, M., Gao, Q., & Zhang, X. (2021). Developments of Advanced Electrospinning Techniques: A Critical Review. *Advanced Materials Technologies*, *6*(11), 2100410. https://doi.org/10.1002/admt.202100410
25. Lodha, A., Pandya, A., Sutariya, P. G., & Menon, S. K. (2013). Melamine modified gold nanoprobe for "on-spot" colorimetric recognition of clonazepam from biological specimens. *The Analyst*, *138*(18), 5411. https://doi.org/10.1039/c3an00184a
26. Lodha, A. S., Pandya, A., & Shukla, R. K. (2016). Nanotechnology: An Applied and Robust Approach for Forensic Investigation. *Forensic Research & Criminology International Journal*, *2*(1). 10.15406/frcij.2016.02.00044
27. Long, Y., Chen, H., Wang, H., Peng, Z., Yang, Y., Zhang, G., Li, N., Liu, F., & Pei, J. (2012). Highly sensitive detection of nitroaromatic explosives using an electrospun nanofibrous sensor based on a novel fluorescent conjugated polymer. *Analytica Chimica Acta*, *744*, 82–91. https://doi.org/10.1016/j.aca.2012.07.028
28. Long, Y., Chen, H., Yang, Y., Wang, H., Yang, Y., Li, N., Li, K., Pei, J., & Liu, F. (2009). Electrospun Nanofibrous Film Doped with a Conjugated Polymer for DNT Fluorescence Sensor. *Macromolecules*, *42*(17), 6501–6509. https://doi.org/10.1021/ma900756w
29. Lv, Y.-Y., Xu, W., Lin, F.-W., Wu, J., & Xu, Z.-K. (2013). Electrospun nanofibers of porphyrinated polyimide for the ultra-sensitive detection of trace TNT. *Sensors and Actuators B: Chemical*, *184*, 205–211. https://doi.org/10.1016/j.snb.2013.04.094

30. Martelo, L., das Neves, T., Figueiredo, J., Marques, L., Fedorov, A., Charas, A., Berberan-Santos, M., & Burrows, H. (2017). Towards the Development of a Low-Cost Device for the Detection of Explosives Vapors by Fluorescence Quenching of Conjugated Polymers in Solid Matrices. *Sensors*, *17*(11), 2532. https://doi.org/10.3390/s17112532
31. Masteri-Farahani, M., & Askari, F. (2019). Design and photophysical insights on graphene quantum dots for use as nanosensor in differentiating methamphetamine and morphine in solution. *Spectrochimica Acta Part A: Molecular and Biomolecular Spectroscopy*, *206*, 448–453. https://doi.org/10.1016/j.saa.2018.08.044
32. Masteri-Farahani, M., & Mosleh, N. (2019). Functionalization of graphene quantum dots with antimorphine: Design of selective nanosensor for detection of morphine. *Materials Letters*, *241*, 206–209. https://doi.org/10.1016/j.matlet.2019.01.057
33. Mazzini Junior, E. G., Cantalice, J. D. de A., Assis, A. M. L. de, Freitas, J. D. de, Costa, L. M. M., & Ribeiro, A. S. (2020). Fluorescent polymer nanofibers based on polycaprolactone and dansyl derivatives for development of latent fingerprints. *Journal of Applied Polymer Science*, *e49804*. https://doi.org/10.1002/app.49804
34. Mehmood, A., Ghafar, H., Yaqoob, S., Gohar, U. F., & Ahmad, B. (2017). Mesoporous Silica Nanoparticles: A Review. *Journal of Developing Drugs*, *06*(02). 10.4172/2329-6631.1000174
35. Morgan, R. M. (2019). Forensic science. The importance of identity in theory and practice. *Forensic Science International: Synergy*, *1*, 239–242. https://doi.org/10.1016/J.FSISYN.2019.09.001
36. Page, H., Horsman, G., Sarna, A., & Foster, J. (2019). A review of quality procedures in the UK forensic sciences: What can the field of digital forensics learn? *Science and Justice*, *59*(1), 83–92. https://doi.org/10.1016/j.scijus.2018.09.006
37. Pandya, A., Goswami, H., Lodha, A., & Menon, S. K. (2012). A novel nanoaggregation detection technique of TNT using selective and ultrasensitive nanocurcumin as a probe. *The Analyst*, *137*(8), 1771. https://doi.org/10.1039/c2an35131e
38. Pandya, A., & Shukla, R. K. (2018). New perspective of nanotechnology: role in preventive forensic. *Egyptian Journal of Forensic Sciences*, *8*(1), 57. https://doi.org/10.1186/s41935-018-0088-0
39. Pomerantseva, E., Bonaccorso, F., Feng, X., Cui, Y., & Gogotsi, Y. (2019). Energy storage: The future enabled by nanomaterials. *Science*, *366*(6468). https://doi.org/10.1126/science.aan8285
40. Ray, S. S., Chen, S.-S., Li, C.-W., Nguyen, N. C., & Nguyen, H. T. (2016). A comprehensive review: electrospinning technique for fabrication and surface modification of membranes for water treatment application. *RSC Advances*, *6*(88), 85495–85514. https://doi.org/10.1039/C6RA14952A
41. Razlansari, M., Ulucan-Karnak, F., Kahrizi, M., Mirinejad, S., Sargazi, S., Mishra, S., Rahdar, A., & Díez-Pascual, A. M. (2022). Nanobiosensors for detection of opioids: A review of latest advancements. *European Journal of Pharmaceutics and Biopharmaceutics*, *179*, 79–94. https://doi.org/10.1016/j.ejpb.2022.08.017
42. Rohatgi, R., & Dominica, F. (2022). Application of Nanotechnology in Forensic Science. *Journal of Forensic Research*, *13*(8), 507. https://www.hilarispublisher.com/open-access/application-of-nanotechnology-in-forensic-science.pdf
43. Roux, C., Bucht, R., Crispino, F., De Forest, P., Lennard, C., Margot, P., Miranda, M. D., NicDaeid, N., Ribaux, O., Ross, A., & Willis, S. (2022). The Sydney declaration – Revisiting the essence of forensic science through its fundamental principles. *Forensic Science International*, *332*, 111182. https://doi.org/10.1016/j.forsciint.2022.111182
44. Roux, C., Crispino, F., & Ribaux, O. (2012). From Forensics to Forensic Science. *Current Issues in Criminal Justice*, *24*(1), 7–24. https://doi.org/10.1080/10345329.2012.12035941
45. Roux, C., & Weyermann, C. (2021). From Research Integrity to Research Relevance to Advance Forensic Science. *Forensic Sciences Research*, *6*(4), 292–294. https://doi.org/10.1080/20961790.2021.1977480
46. Santos, A. P. L. A., Deokaran, G. O., Costa, C. V., Gama, L. I. L. M., Mazzini Júnior, E. G., de Assis, A. M. L., de Freitas, J. D., de Araujo, W. R., Dias, R. P., da Silva, J. C. S., Costa, L. M. M., & Ribeiro, A. S. (2021). A "turn-off" fluorescent sensor based on electrospun polycapro-

lactone nanofibers and fluorene(bisthiophene) derivative for nitroaromatic explosive detection. *Forensic Science International*, *329*, 111056. https://doi.org/10.1016/j.forsciint.2021.111056
47. Senthamizhan, A., Celebioglu, A., & Uyar, T. (2015). Ultrafast on-site selective visual detection of TNT at sub-ppt level using fluorescent gold cluster incorporated single nanofiber. *Chemical Communications*, *51*(26), 5590–5593. https://doi.org/10.1039/C4CC01190B
48. Shuaibu, L., Audu, A. A., & Igenepo, K. J. (2021). The Application of Nanosensors in Illicit Drugs Determination: A Review. *Current Journal of Applied Science and Technology*, 39–59. https://doi.org/10.9734/cjast/2021/v40i2231477
49. Song, J., Lin, X., Ee, L. Y., Li, S. F. Y., & Huang, M. (2023). A Review on Electrospinning as Versatile Supports for Diverse Nanofibers and Their Applications in Environmental Sensing. *Advanced Fiber Materials*, *5*(2), 429–460. https://doi.org/10.1007/s42765-022-00237-5
50. Sun, X., Liu, Y., Shaw, G., Carrier, A., Dey, S., Zhao, J., & Lei, Y. (2015). Fundamental Study of Electrospun Pyrene–Polyethersulfone Nanofibers Using Mixed Solvents for Sensitive and Selective Explosives Detection in Aqueous Solution. *ACS Applied Materials & Interfaces*, *7*(24), 13189–13197. https://doi.org/10.1021/acsami.5b03655
51. Tao, S., Li, G., & Yin, J. (2007). Fluorescent nanofibrous membranes for trace detection of TNT vapor. *Journal of Materials Chemistry*, *17*(26), 2730. https://doi.org/10.1039/b618122h
52. Wang, M., Li, M., Yu, A., Zhu, Y., Yang, M., & Mao, C. (2017). Fluorescent Nanomaterials for the Development of Latent Fingerprints in Forensic Sciences. *Adv. Funct. Mater.*, *27*(14), 1606243. https://doi.org/10.1002/adfm.201606243
53. Wang, P., Lv, H., Cao, X., Liu, Y., & Yu, D.-G. (2023). Recent Progress of the Preparation and Application of Electrospun Porous Nanofibers. *Polymers*, *15*(4), 921. https://doi.org/10.3390/polym15040921
54. Wang, Y., La, A., Ding, Y., Liu, Y., & Lei, Y. (2012). Novel Signal-Amplifying Fluorescent Nanofibers for Naked-Eye-Based Ultrasensitive Detection of Buried Explosives and Explosive Vapors. *Advanced Functional Materials*, *22*(17), 3547–3555. https://doi.org/10.1002/adfm.201200047
55. Wang, Y.-T., Wang, Y., Guo, J., & Zhou, Q.-X. (2020). Preparation of Polyvinyl Alcohol/Ninhydrin Blend Nanomembranes by Needleless Electrospinning and Their Application in Latent Finger Mark Detection. *Journal of Macromolecular Science, Part B*, *59*(1), 49–64. https://doi.org/10.1080/00222348.2019.1687137
56. Wei, J., Yang, S., Wang, L., Wang, C.-F., Chen, L., & Chen, S. (2013). Electrospun fluorescein-embedded nanofibers towards fingerprint recognition and luminescent patterns. *RSC Advances*, *3*(42), 19403. https://doi.org/10.1039/c3ra42328j
57. Weyermann, C., Willis, S., Margot, P., & Roux, C. (2023). Towards more relevance in forensic science research and development. *Forensic Science International*, 111592. https://doi.org/10.1016/j.forsciint.2023.111592
58. Wu, P., Xu, C., Hou, X., Xu, J.-J., & Chen, H.-Y. (2015). Dual-emitting quantum dot nanohybrid for imaging of latent fingerprints: simultaneous identification of individuals and traffic light-type visualization of TNT. *Chemical Science*, *6*(8), 4445–4450. https://doi.org/10.1039/C5SC01497B
59. Wu, W., Shi, N., Zhang, J., Wu, X., Wang, T., Yang, L., Yang, R., Ou, C., Xue, W., Feng, X., Xie, L., & Huang, W. (2018). Electrospun fluorescent sensors for the selective detection of nitro explosive vapors and trace water. *Journal of Materials Chemistry A*, *6*(38), 18543–18550. https://doi.org/10.1039/C8TA01861H
60. Xu, B., Wu, X., Li, H., Tong, H., & Wang, L. (2011). Selective Detection of TNT and Picric Acid by Conjugated Polymer Film Sensors with Donor–Acceptor Architecture. *Macromolecules*, *44*(13), 5089–5092. https://doi.org/10.1021/ma201003f
61. Xue, J., Wu, T., Dai, Y., & Xia, Y. (2019). Electrospinning and Electrospun Nanofibers: Methods, Materials, and Applications. *Chemical Reviews*, *119*(8), 5298–5415. https://doi.org/10.1021/acs.chemrev.8b00593
62. Xu, J., Zhang, B., Jia, L., Fan, Y., Chen, R., Zhu, T., & Liu, B. (2019). Dual-Mode, Color-Tunable, Lanthanide-Doped Core–Shell Nanoarchitectures for Anti-Counterfeiting Inks and Latent Fingerprint Recognition. *ACS Applied Materials & Interfaces*, *11*(38), 35294–35304. https://doi.org/10.1021/acsami.9b10989

63. Yang, S., Wang, C.-F., & Chen, S. (2011a). A Release-Induced Response for the Rapid Recognition of Latent Fingerprints and Formation of Inkjet-Printed Patterns. *Angewandte Chemie*, *123*(16), 3790–3793. https://doi.org/10.1002/ange.201006537
64. Yang, Y., Wang, H., Su, K., Long, Y., Peng, Z., Li, N., & Liu, F. (2011b). A facile and sensitive fluorescent sensor using electrospun nanofibrous film for nitroaromatic explosive detection. *Journal of Materials Chemistry*, *21*(32), 11895. https://doi.org/10.1039/c0jm04444j
65. Zhang, S., Liu, R., Cui, Q., Yang, Y., Cao, Q., Xu, W., & Li, L. (2017). Ultrabright Fluorescent Silica Nanoparticles Embedded with Conjugated Oligomers and Their Application in Latent Fingerprint Detection. *ACS Applied Materials & Interfaces*, *9*(50), 44134–44145. https://doi.org/10.1021/acsami.7b15612

Nanoparticles-Induced Alignment of Nematic Liquid Crystals for Tunable Electro-Optical Devices



Ajay Kumar and Gautam Singh

1 Introduction

The possession of anisotropy due to preferred orientation of certain types of organic molecules along with fluidity (low viscosity) eventually constitutes the "liquid crystal (LC)" mesophases. The LC mesophases can be classified broadly based on their geometrical shape or chemical structure. They are further categorized as nematic (N), cholesteric or chiral nematic (N*), smectic (Sm), and chiral smectic mesophases by considering the arrangement of the constituent molecules [1–3]. The nematic liquid crystal (NLC) phase is the simplest form of LC mesophases that possess only the long-range orientational order and is being used extensively in the fabrication of LC-based display and non-display devices. The presence of suitable chirality to N phase causes the molecular director to rotate in a helical manner, and such modulation results in the formation of chiral nematic (N*) or cholesteric liquid crystal (CLCs) mesophases [4]. The inclusion of a weak positional ordering by LC molecules, along with their orientational order, gives rise to the complex smectic mesophases [5]. For instance, in smectic A (SmA) mesophase, the molecules are arranged in layers with director (n) always parallel to the layer normal (k), whereas the titling of n away from the k results into the smectic C (SmC) mesophase. Various other mesophases with increasing positional order such as SmI, SmJ, SmK, etc. have also been discovered. The chiral additives to the tilted smectic phases (such

A. Kumar
Department of Physics, Dharma Samaj College (Raja Mahendra Pratap Singh State University, Aligarh), Aligarh, Uttar Pradesh, India

G. Singh (✉)
Department of Applied Physics, Amity Institute of Applied Sciences, Amity University, Noida, Uttar Pradesh, India
e-mail: gsingh6@amity.edu

© The Author(s), under exclusive license to Springer Nature Switzerland AG 2024

S. Krishnamoorthy, K. (Kris) Iniewski (eds.), *Advances in Fabrication and Investigation of Nanomaterials for Industrial Applications*,
https://doi.org/10.1007/978-3-031-42700-8_4

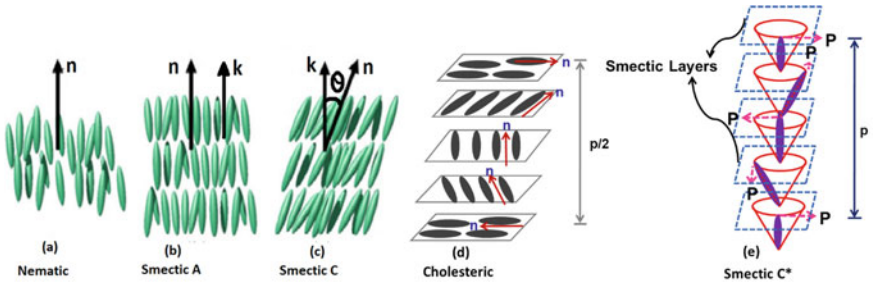


Fig. 1 The schematic of LC phases: (**a**) nematic (N), (**b**) smectic A (SmA), (**c**) smectic C (SmC), (**d**) cholesteric (N*), (**e**) spiraling of the polarization P in the Sm C* phase according to their molecular structure. Here, n represents the director, k and θ denote layer normal and tilt angle, and p represents helical pitch [8]

as SmC*) could give rise to the helicoidal arrangement of molecules with nonzero spontaneous polarization. Such mesophases are termed as ferroelectric LCs (FLCs) and are enriched with advanced characteristics over nematic LCs [6, 7]. Figure 1 shows the arrangement of rodlike molecules in various LC mesophases [8]. The LC mesophases are so "delicate" to offer controllable sensitivity to the external stimuli such as electric, magnetic, electromagnetic, heat, and surface forces [4]. It is the sensitive coupling of the dielectric anisotropy ($\Delta\varepsilon$) of LC materials with the applied electric field that placed them as an essential component of the modern displays and other photonic devices. The electric-field-modulated light transmission through the LC sample is the key phenomenon of the LC-based displays [9, 10].

However, the alignment of the LC molecules in a preferred orientation is very essential for the fabrication of LC-based displays and non-display devices. Various alignment techniques such as rubbing of polyimides, coating of surfactants, magnetic field, oblique evaporation of SiOx, photoalignment, etc. are being used to obtain the uniform alignment of LCs [8–11]. It is worth pointing out here that homogeneous (or planar) and homeotropic (or vertical) alignments of LC molecules are being mainly used in the manufacturing of LC-based devices. The unidirectional rubbing (or buffing) of the alignment layer creates the patterned grooves along which the nearby elongated LC molecules get fixed with parallel (or with some pre-tilt) to the surface, and these molecules guide the bulk molecules to have uniform homogeneous (HMG) alignment of the whole sample. On the other hand, the silane-based surfactant molecules could attach uprightly on the substrate surface to guide the LC molecules to orient vertically to exhibit homeotropic (HMT) alignment. The rubbed polyimide alignment technique has been extensively used in commercially available LC-based displays, photonic devices, and LC-based research investigations. Though the rubbed polyimide or surfactant-based techniques provide uniform and industry quality alignment of LC molecules, they are very prone to add some undesired ionic impurities in the sample. Moreover, such techniques put a limit in the fabrication of the flexible displays. To overcome these challenges, the researchers have explored the exciting benefits of nanotechnology

in aligning LC molecules by nonconventional ways. The evolution of nanotechnology has augmented significantly to the existing research fields, and the LC research has been one of them to receive remarkable advancement [12–15]. As far as alignment is concerned, the collaboration of nanotechnology with LCs was initiated more than a decade ago when Jeng et al. incorporated POSS (polyhedral oligomeric silsesquioxanes) NPs into the NLC matrix and filled into the untreated (polyimide−/surfactant-free) sample cell [16]. When the sample cell was analyzed under the crossed polarizing optical microscope (POM), a uniform HMT alignment of NLC molecules was obtained. This was attributed to the adsorption of the POSS NPs on the substrate surfaces, which eventually guided the NLC molecules to align vertically. Later, this group explored the POSS NPs in various other investigations and observed exciting results on induced alignment of NLC molecules [17–23]. The NPs-induced NLC alignment has motivated the researchers to explore other nanostructured materials such as gold NPs, magnetic NPs, silica NPs, polymeric NPs, zinc oxide NPs, carbon nanotubes (CNTs), and even quantum dots (QDs) for obtaining uniform LC alignment [24–31]. In most of these studies, the interactions among the guest NPs (residing at the substrate surface), the substrate surface, and the NLC molecules have been found to be the deciding factor for the resulting alignment of the NPs-NLC composite [24–31]. Moreover, the material, size, shape, capping legends, concentration, etc. of gust NPs and the host NLC matrix itself have contributed greatly in obtaining the modulated alignment/configuration of NPs-NLCs composites [25, 30]. Also, numerous investigations have been reported where the NPs, instead of dispersing into the bulk, were either coated on the substrate surface or embedded in the polyimide layer or grown on the substrate surface [32–35]. It is worth mentioning that the presence of NPs has induced alignment not only in simplest NLCs; the molecules of highly ordered LCs such as FLCs were aligned too [28, 29, 31]. However, the NPs-induced alignment of LCs is in its nascent stage, and the proper understanding of the underlying mechanisms of such alignments is needed for its commercial applications.

In this chapter, we have systematically presented the comprehensive overview of the NPs-induced alignment of NLCs, the underlying mechanisms involved in achieving polyimide−/silane-free uniform alignment of NLC molecules, and its possible applications in tunable electro-optical devices. To be more specific, we have discussed (i) conventional methods to align LC molecules, (ii) NPs-induced alignment of NLCs, and (iii) conclusion and future perspectives.

2 Conventional Methods to Align Liquid Crystals

The orientation of LC molecules is very sensitive to various external fields, e.g., surface interaction, electric field, magnetic field, etc., and this fact has been greatly utilized to align the LC molecules. Conventionally, there are mainly three alignment configurations, i.e., homogenous (or planar), homeotropic (or vertical), and hybrid

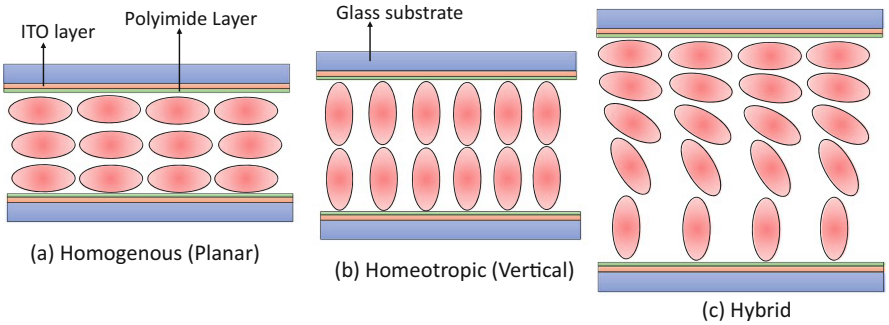


Fig. 2 The schematic of (**a**) homogeneous (or planar), (**b**) homeotropic (or vertical), and (**c**) hybrid (or homogeneous and homeotropic) alignment configurations of NLCs [8]

(or homogeneous + homeotropic) of LCs (Fig. 2) that are being used in different kinds of LC-based displays and other photonic devices [8, 36].

There are certain surface modifications which are used to guide LC molecules to orient vertically or planar using techniques like rubbed polyimide [37, 38], oblique evaporation of silicon oxides [39], deposition of surfactants [40], shearing technique [41], etc. The electromagnetic field has also been utilized to align LC molecules via photoalignment [42–45], UV irradiation [46], and polarized laser light [47]. Among the discussed methods, the rubbed polyimide technique is mainly utilized in laboratories/industries to align LCs in the fabrication of LCDs and other electro-optical devices. In this method, a suitable polymer solution (such as nylon 6/6) is coated (followed by baking) on the indium tin oxide (ITO) electrode surface and is then rubbed/buffed to create microgrooves. These grooves eventually work as a template for the surface LC molecules to align homogeneously (i.e., planar) and which then propagate throughout the bulk of the sample cell. However, this conventional rubbed polyimide method of alignment requires finite processing time and is prone to add defects in the surfaces and undesired static charges into the LC samples [48]. Later, the noncontact alignment techniques, such as magnetic field-assisted alignment and photoalignment, have been developed to avoid undesired ionic inclusions [49, 50].

3 Nanoparticles-Induced LC Alignment

In the preceding section, we reviewed briefly about the initial developments on the alignment of LC molecules. The traditional polyimide coating followed by rubbing produced the HMG alignment, whereas the HMT alignment was achieved by using surface treatment by silane-based chemicals or oxides. In these alignment configurations, the inclusion of undesired ionic contamination could degrade the function of the LC displays and other photonic devices, and this has put a limit

on the conventionally aligned LC systems [48]. The nanostructured materials (materials whose at least one dimension is less than 100 nm) are well known to exhibit exciting characteristic features as compared to their bulk counterparts. Their characteristics could be further tailored significantly by changing the size, shape, concentration, etc. of NPs [51, 52]. The variation in the surface-to-volume ratio and the phenomenon of quantum confinement have been the key factors to envisage the size-dependent electrical and optical properties of nanomaterials (NMs) [51, 52]. Moreover, a minute amount of the suitable NMs have potential to modify remarkably the display features of an LC system [14]. There are plenty of reports where amalgamation of NMs with the LCs has resulted improved characteristics such as lower threshold voltage, faster switching response, enhanced photoluminescence, reduced ionic load, etc. of LC materials [53–58]. The NMs have also showed significant potential in achieving the uniform alignment of LC molecules. Let us begin with the isotropic (shape isotropy) NPs-induced alignment of nematic LCs.

3.1 Isotropic NPs-Induced Alignment of NLCs

The first experimental realization of isotropic NPs-induced spontaneous vertical alignment of NLCs filled into untreated ITO sample cells (i.e., devoid of conventional alignment layers) was demonstrated by Jeng et al. [16]. For this study, authors firstly prepared the composites of phenethyl-polyhedral oligomeric silsesquioxane (phenethyl POSS, ~0.7–30 A°) NPs-doped NLCs (E7, positive dielectric, and MLC6608, negative dielectric) and then tested for the induced vertical alignment using POM and voltage-dependent optical transmission (Fig. 3). The POSS NPs-induced vertical alignment was obtained in both positive and negative dielectric NLCs for dopant concentration (> 3 wt%) as well as type of NLCs. Interestingly,

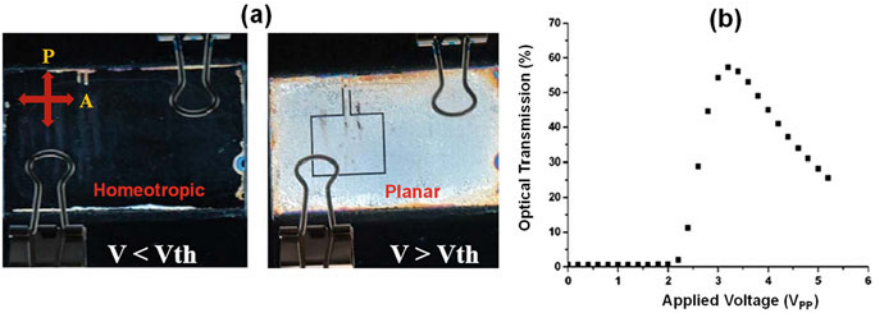


Fig. 3 (**a**) POSS-induced vertical alignment in an LC cell viewed under cross polarizers and (**b**) measured voltage-dependent transmission curves by applying voltage of 60 Hz square wave for the 4 wt% POSS-filled homeotropic LC cell [16]

the electro-optical parameters (threshold voltage and switching response) of NLC device with POSS NPs-induced vertical alignment were more or less the same as that for conventional vertical alignment. However, the switching response of the composite was slower by 1.5 times than conventional vertically aligned NLC device.

This study had opened a new dimension of NPs-induced LC alignment and motivated the researchers to explore the interactions between POSS NPs and ITO-coated substrate as well as with LC molecules to search for a better alternate to the conventional LC alignment techniques. The investigations were extended further to analyze quantitatively the interaction between the POSS NPs and LC molecules for application point of view. By using the hybrid electrode pair, one treated with polyimide layer and the other untreated, Kuo et al. obtained the hybrid alignment nematic (HAN) mode [17]. Jeng et al. [20] utilized the plausible competition between the polyimide layer of HMG aligned LC cell and POSS NPs-induced HMT domains to achieve tunable pre-tilt of NLC (E7) molecules. Based on their measurements, it was pointed out that the magnitude of pre-tilt angle (θp) was strongly dependent on the concentration of POSS NPs and it could be tuned over a wide range (i.e., $0° < \theta p < 90°$). Authors hoped the results to be useful for no bias bend, bistable bend-splay, and super-twisted nematic display devices. Chen et al. [59] reported the fabrication of a trans-reflective LCD with a single cell gap in a dual alignment configuration (i.e., HMG aligned transmissive and hybrid-aligned reflective), using methyl red dye and POSS NPs-induced alignment effects. The fabrication of such a dual structure was obtained by using a single-step laser light exposure via photomask. Authors pointed out the feasibility of the fabrication method of trans-reflective LCDs and could be further extended to the production of multidomain LCDs. Afterward, Huang et al. [22] reported the simple fabrication of adaptive flat LC microlens by using the hybrid-aligned NLC obtained through POSS NPs. In this method, prior to assemble the sample cell, the droplets of PI/POSS solution were sprinkled (microdropped) selectively on the ITO substrates (bottom one) coated with homogeneously aligning polyimide layer. The NLC (positive dielectric, E7) filled in the fabricated cells acquired hybrid (planar and vertical) alignment such that the portions with PI/POSS droplets exhibited vertical and the rest of portion get homogeneously aligned. Therefore, the vertical alignment induced by POSS NPs eventually resulted into the formation of hybrid-aligned NLC layer with concentric nonuniform distribution of the refractive index in the homogeneously anchored sample cell, and consequently a lens was formed with tunable focal length even in the absence of applied bias voltage. It was pointed out that the dimension of such concentric hybrid-aligned nematic structure was dependent on the volume of microdroplet of PI/POSS and concentration of POSS NPs. The voltage-dependent focal length of the fabricated LC microlens was found in the range of -50 mm to -90 mm. Authors hoped that the proposed method has significant potential to obtain the LC microlens using an inkjet printer. Later, Chen et al. [23] demonstrated the use of PEDOT:PSS pretreated with DMSO as a better substrate with higher conductivity and optical transparency than the conventional ITO, for the fabrication of vertically aligned LC devices with the help of POSS NPs. The induced uniform vertical alignment of NLC without any disclination lines in the

sample cells of PEDOT:PSS by the dopant POSS NPs was obtained. Interestingly, the contrast ratio of the sample cell made of PEDOT:PSS/POSS was ~2.3 times higher than the sample cell consisting of ITO/POSS. However, the electro-optical features of vertically aligned sample cells fabricated using PEDOT:PSS/POSS were comparable to that of sample cells of ITO/POSS. Authors predicted that such POSS NP-induced vertical alignment on the rubbed PEDOT:PSS films may be suitable for the fabrication of ITO-free LC displays.

Various NPs, other than POSS NPs, too, have been analyzed for their suitability for polyimide-free, flexible alignment of NLCs. Multiple alignment modes (planar, vertical, and thermally controlled alignment, i.e., switching between planar and vertical via thermal energy) of NLCs were achieved using alky thiol-capped gold nanoparticles (GNPs, size ~1.5–2 nm) [24]. The authors carried out a detailed investigation on the orientation of NLC dispersed with alkyl thiol-capped GNPs on untreated glass slides and treated (rubbed polyimide) and ITO-coated substrates. Unlike the POSS NPs, the GNPs introduced both vertical and planar configurations of alignment in NLC molecules depending on the preconditions. It was proposed that the dispersed GNPs reside on the substrate surface and could modify the ordering of nearby NLC molecules to orient them in different configuration modes.

Ahmed et al. demonstrated the vertical alignment of NLC (E7) and PDLC (PN393/E7) by dispersing them with spherical magnetic NPs (Fe_2O_3, <50 nm) and in the presence of external weak magnetic field (0.1 T, duration, 5 minutes, and irradiation direction, 90°) [60]. This magnetic NPs-induced alignment was analyzed by using POM, FTIR spectroscopy, and optical transmittance of PDLC films. The observed uniform vertical alignment of E7 molecules was attributed to (i) the magnetic NPs that were aligned in the direction of externally applied magnetic field and (ii) the surface bonding between the metal (Fe) atoms and the cyanobenzene chain of E7. Zhao et al. [61] demonstrated the induced uniform vertical alignment of NLC and chiral NLC by dispersion of spherical-shaped Ni NPs (diameter ~ 150 nm), useful in the development of flexible plastic LCDs. Authors proposed that the adsorption of spherical Ni NPs onto the substrate surface of sample cell eventually led to the induction of vertical alignment in NLC. Afterward, authors used this concept to achieve uniform vertical alignment of NLC (5CB) using spherical Ni NPs (diameter ~ 15 nm) and utilized it for the label-free and quantitative monitoring of thrombin protein [62].

Apart from metal and magnetic NPs, the semiconducting QDs have also been investigated for polyimide-free alignment of LC molecules, for instance, the effect of doping of hexa-decylamine-capped CdSe QDs (2.5–5.2 nm) and thioglycolic acid-capped CdTe QDs (3.2–4 nm) on the alignment of phenylpyrimidine-based NLC material (Felix 2900–03) in the sample cells (untreated plain glass slides and rubbed polyimide ITO-coated glass substrates) using optical polarizing microscopy [25]. The CdSe QDs (1 to 2 wt%) were able to induce vertical alignment in untreated plain glass slides, whereas only 1 wt% in planar-anchored ITO sample cells. Only planar alignment in all types of sample cells was induced by CdSe QDs (> 2 wt%) and mainly attributed to the aggregation of QDs. However, CdTe QDs of concentration (>2 wt%) were able to induce vertical alignment in untreated

plain glass slides. Afterward, this group also investigated the impact of three magic-sized CdSe QDs (QD1-CdSe and QD2-CdSe QDs differ by the presence of defects; QD3-CdSe@Zn; size, ~2 nm) on the alignment of NLC in the untreated plain glass slides and planar-anchored ITO sample cells [30]. The vertical alignment of NLC was only shown by QD3 in untreated plain glass slides, whereas QD1 and QD2 showed the planar alignment. However, all three QDs induced the planar alignment of NLC in the planar-anchored ITO sample cells. Moreover, the same research group utilized GNPs (~ 4 nm) having suitable silane conjugation to achieve uniform vertical alignment of NLC [63]. The obtained vertical alignment of NLC molecules showed better stabilization and exhibited faster switching response in comparison to that of conventional polyimide coated cell.

Very recently, Varshney et al. [64] demonstrated the achievement of dual alignment of NLC (5CB) in untreated ITO sample cells by using varying concentrations of the indium tin oxide NPs (ITO NPs, diameter < 50 nm). For instance, the vertical alignment of 5CB was obtained by doping of 0.25 wt% ITO NPs and which further tuned to planar alignment by increasing concentration of ITO NPs to 1 wt%. The achieved tunable dual alignment was attributed to the ITO-ITO interaction and their various arrangements on the ITO substrate.

In Sect. 3.1, we have discussed the investigations on the isotropic NPs-induced polyimide-free alignment of NLCs. In case of isotropic NPs, the surface interaction between the guest NPs (residing on the substrate surface) and the substrate surface had been the dominating factor, which, in turn, guided the nearby LC molecules to orient accordingly in either planar or vertical alignment. The magnetic NPs, on the other hand, followed the direction of applied magnetic field to orient themselves. The protective/capping attachments of the NPs has worked as a template to guide LC molecules via (i) upright orientation of attachments on the substrate (ITO) surface, (ii) interaction with benzene core of LC molecule, and (iii) interaction with elongated alkyl/alkene tails of LC molecules. The surface energy of NLC molecules got minimized on their upright orientation on substrate surface, that is why, a uniform vertical alignment was observed in most of the cases based on isotropic NPs.

3.2 Anisotropic NPs-Induced Alignment of NLCs

Apart from the isotropic NPs, there are numerous reports where anisotropic NPs (such as nanotubes, nanoplatelets, bowl-shaped, etc.) were introduced in the NLC matrix to obtain the polyimide-free alignment of NLC molecules. The CNTs possess large shape anisotropy and are organic wrapping of benzene rings. This has offered a dominant π-π stacking interaction between CNTs and benzene rings present in LC molecules. The π-π stacking interaction causes the nearby NLC molecules to align along the length of the CNTs, and this has appeared as a key to observe CNT-induced alignment and other improvements in the display features of NLCs [65–68]. For instance, the single-walled CNTs (0.01–0.02 wt%, length ~ 100–

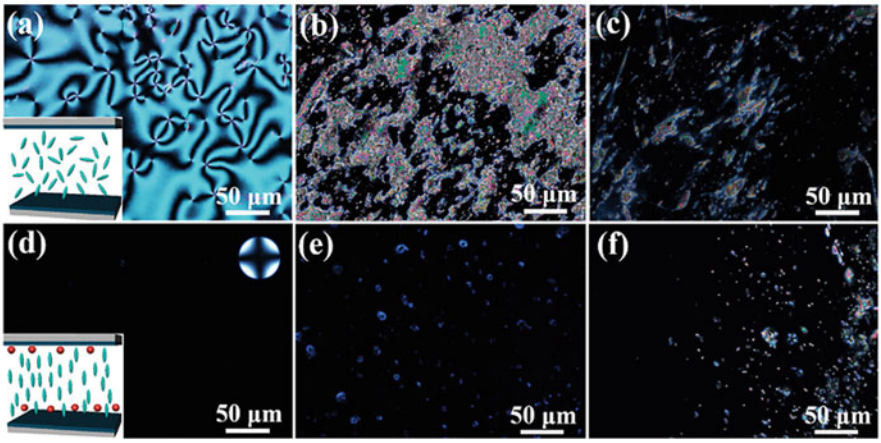


Fig. 4 Polarizing optical microscope (POM) images of 5CB doped with flowerlike CuS at concentrations of (**a**) 0 wt.%, (**b**) 0.01 wt.%, (**c**) 0.03 wt.%, (**d**) 0.05 wt.%, (**e**) 0.07 wt.%, and (**f**) 0.10 wt.%. The insets in **a** and **d** show schematics of the array change of LC molecules doped with CuS NPs in LC cells. All the LC cells have the same cell gap of ~10 μm [35]

300 nm, and diameter ~ 0.8–1.4 nm) were dispersed into an NLC (6CHBT) by Dhar et al. [69]. The display parameters of the composite were improved significantly, and this was attributed to the improved alignment of NLC due to dopant CNTs. The bowl-like, flowerlike, and spherical magnetic Ni NPs (diamtere∼250 nm and shell thickness ∼10 nm) were synthesized using a mild wet chemical method with PVP as stabilizers by Zhou et al. to analyze their effect on the alignment of NLC molecules [70]. These Ni NPs dispersed into NLC material (SLC-1717) induced a uniform planar alignment of NLC molecules. However, the other two structures of Ni NPs (i.e., nanoflowers and nanospheres) caused the vertical alignment of the NLC molecules as that was appeared in the case of POSS NPs, Au NPs, etc. The authors attributed the bowl-like shape and magnetic self-assembly in 1D structure of Ni NPs to be responsible for the observed planar alignment of NLC molecules. Later, the flowerlike and frame-like CuS NPs were introduced into the NLC material (5CB) to analyze the induced alignment [35]. It was observed that the presence of 0.05 wt.% flowerlike CuS NPs induced a uniform vertical alignment of 5CB molecules when filled into a polyimide-free ITO-coated sample cell (Fig. 4), whereas the frame-like CuS NPs were found unable to induce alignment of NLC sample. In case of flowerlike NPs, the 5CB molecules lying close to these nanosheets were oriented normal to the inner surface that, in turn, guided the nearby NLC molecules to result the vertical alignment in the bulk. Authors predicted the use of these composites in the fabrication of flexible LCDs.

In another study, different forms of Cu_2O nanocrystals (cubes, octahedra, and rhombic dodecahedra) of the same size (diameter: ~600 nm) were dispersed into an NLC (5CB) material [71]. A shape-dependent (on Cu_2O nanocrystals) alignment of LC molecules was observed: the cubic Cu_2O nanocrystals induced planar alignment,

whereas vertical alignment was induced by the octahedra and rhombic dodecahedra-shaped Cu_2O nanocrystals. The authors proposed that the cubic nanocrystals formed 1-D self-assembly along the filling direction of Cu_2O/LC nanocomposite due to the flow effect and the microgroove structure formed by Cu_2O cubes induced the planar alignment of LC molecules. On the other hand, the strong interaction between the cyano group of LCs and the surface Cu atoms with dangling bonds favored the vertical alignment. The same group [72] also demonstrated the achievement of thermally stable vertical alignment of NLC (5CB) by using the newly synthesized $CuInS_2$ NPs. They doped two types of $CuInS_2$ NPs (i.e., tremelliform-like and frame-like) into 5CB in unaligned ITO sample cell and reported that tremelliform-like NPs could induce uniform and stable vertical alignment and random alignment by frame-like NPs. The induced vertical alignment was attributed to the low surface energy and the regular morphology of $CuInS_2$ NPs. The crystal structure of used NPs was found to be strongly dependent on the reaction solvents during the preparation process which eventually played an important role in inducing the macroscopic vertical alignment of NLC. Moreover, authors also reported the long-range tunability of pre-tilt angle of NLC in planar-anchored sample cell by the dopant $CuInS_2$ NPs.

Very recently, Mishra et al. [73] reported the use of nanocomposite zinc oxide nanorods capped with oleic acid (ZOR, length ~ 1–1.2 μm and width ~ 50–60 nm, concentration $\geq$ 0.5 wt%) to obtain the vertical alignment of NLC (8CB) in both unaligned and planar-anchored ITO sample cells, confirmed by POM and attenuated total reflection-Fourier transform infrared absorption spectra studies. The achievement of such induced vertical alignment was attributed to the overcoming of surface anchoring energy of the cell substrates due to the van der Waal's interaction between the oleic acid functional group of ZOR and 8CB molecules.

3.3 Induced Alignment of NLCs by Deposition of Isotropic NPs on Substrates

The deposition of various NPs on the substrate surface in place of polyimide/oxide layer, too, could induce alignment of LC molecules. Under this framework, Lee et al. used the random drop casting and capillary injection of QDs ($CuInS_2$-ZnS, ~2.2 nm) on the substrates of the sample cell to align NLCs (positive and negative dielectric anisotropy) [74]. For instance, the vertical and planar alignment of NLCs was obtained by the random drop casting and capillary injection methods, respectively. The induced vertical or planar alignment was attributed to the random or linear diffusion of QD clusters into the ITO defects. Authors suggested that the obtained results could pave a way to cost-effective and practical method to manufacture advanced flexible LCDs. The zinc oxide NP arrays (~50 nm) were synthesized using hydrothermal technique and coated on ITO-coated glass substrates by Chung et al. [75]. The ZnO NP array-coated (thin film) ITO substrates were rubbed to

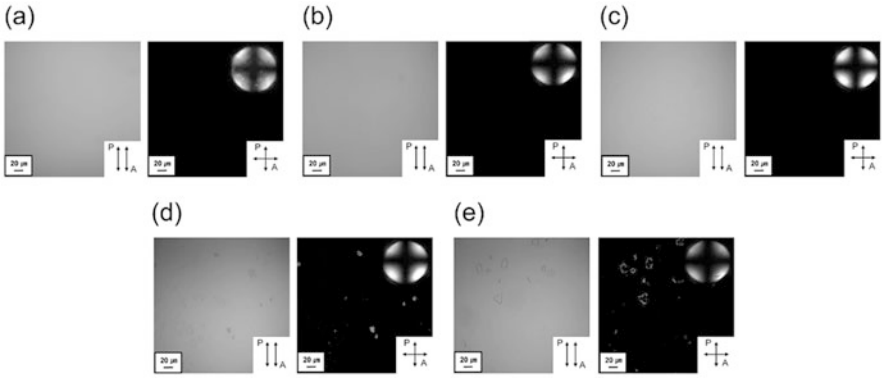


Fig. 5 Polarizing optical microscope (POM) images of the LC devices prepared using (**a**) the conventional PI layer and the nanostructured PI layer and the nanostructured O-GQD layers with an O-GQD concentration of (**b**) 0.05 wt%, (**c**) 0.1 wt%, (**d**) 0.5 wt%, and (**e**) 1.0 wt% [78]

create topographic grooves before assembling the cell. The uniform alignment of NLC molecules with tunable pretilt angles (0.5–88.5°) was observed for cells with ZnO NPs array coating. The authors attributed the observed tunable pretilt to the annealing temperatures (which produces different chemical surface properties of film) of the ZnO NP array film. The proposed method of tuning pretilt angle of NLC molecules could provide a sustainable inorganic alignment material useful for LCDs. Rezinkov et al. have used, for the first time, inkjet printing of dodecane thiolate-capped gold NPs on the substrates and analyzed the alignment of different NLC materials [76]. The uniform and stable vertical alignment was induced for all the used nematic materials (Felix-2900-03, 5CB, MLC-6610, TL203) on the patterned substrates. This was extended further by Sharma et al., who involved the inkjet printing of dodecane thiolate-capped gold NPs (Au1 ~ 1.9 ± 0.4 nm, Au2 ~ 5.0 ± 2.5 nm) and emissive carbon dots (2.5 ± 0.5 nm) with mixed ligand shell of carboxylic acid groups and aliphatic hydrocarbon chains [77]. The authors obtained high-quality vertical alignment of NLCs on such NP printed layers and proposed its applications in adaptive LC Fresnel lenses, Bragg diffraction gratings, VA-LCDs, and flexible LCDs. In another report, the octadecylamine-capped graphene quantum dots (O-GQDs) were deposited on ITO surface, and then the assembled sample cell was filled with negative dielectric NLC material [78]. Interestingly, a uniform vertical alignment of NLC molecules was achieved (Fig. 5). It was pointed out that the hydrophobic O-GQDs spontaneously covered the hydrophilic ITO surface via polar intermolecular interactions and eventually lead to the formation of self-assembled nanostructured O-GQD layer. Such self-assembled nanostructured layer could align NLC molecules vertically on the ITO surface due to the van der Waals interactions of long side chains of O-GQDs and NLC molecules. Authors hoped that such ultrathin nanostructured O-GQDs layers would have potential applications in flexible and functional display devices.

Dogra et al. [79] recently demonstrated the induction of vertical alignment of negative dielectric NLC (MJ98468) using the evaporation-induced self-assembly of silica NPs (SNPs, ~15 nm) on untreated ITO substrates of sample cell. The self-assembly of SNPs on ITO substrates was confirmed through FESEM and FTIR spectroscopic investigations. The induced vertical alignment was attributed to the significant lowering of the surface energy of self-assembled SNP layer on ITO substrates as compared to the bare ITO substrates. The authors predicted the use of such induced vertical alignment of NLCs in the development of futuristic flexible LCDs.

Liu et al. [80] demonstrated the use of ion beam-irradiated spherical $Y_2Sn_2O_7$ NPs as an alignment layer over the ITO-coated glass substrates to achieve the planar alignment of commercial positive dielectric NLC. Such induced planar alignment with a small pre-tilt was attributed to (i) van der Waals interactions between the LCs and the alignment layer, (ii) the interaction between benzene rings of LCs and broken chemical bonds, and (iii) special morphology structure. More importantly, the electro-optical properties of NLCs measured in the sample cells with ion beam-irradiated spherical $Y_2Sn_2O_7$ NPs as an alignment layer were found better than the conventional rubbed PI-coated ITO sample cells.

3.4 Induced Alignment of NLCs by Deposition of Anisotropic NPs on Substrates

There are also several investigations based on alignment of NLC molecules on the substrates deposited/coated with anisotropic NPs such as nanorods, nanowires, nanotubes, nanosheets, etc. For instance, Russell et al. reported the achievement of uniform macroscopic planar alignment of NLC (Licristal K-15, EM industries) by depositing the single-walled carbon nanotubes (SWCNTs, length ~ 2 μm and diameter ~ 0.5 μm) on the ITO-coated glass substrate devoid of any alignment layer using self-assembly and dip-coating methods for dense and sparse CNT films, respectively [81]. In a similar study, Fu et al. utilized CNT (length ~ 250 μm and diameter ~ 10–15 nm) films as an alignment layer and transparent electrode (also used as heating electrode) in the fabrication of LCDs with wider working temperature range [82]. They predicted the use of such CNT films as a substitute of very costly ITO-coated glass substrates in the fabrication of LCDs. Recently, Basu et al. had grown the vertically aligned CNTs (VA-CNTs, length, 2 μm, and density, 2×10^9 cm^{-2}) arrays on the surface of chromium-coated glass substrate using plasma-enhanced chemical vapor deposition [67]. A uniform vertical alignment of negative dielectric anisotropic NLC material (BYVA-01, Instec, USA) was observed (Fig. 6) and attributed to the π-π stacking interaction between the NLC molecules and the VA-CNT arrays. Authors clearly pointed out that such inorganic VA-CNT arrays could be an excellent alternative to the traditional organic PI layers for homeotropic alignment and ITO electrodes.

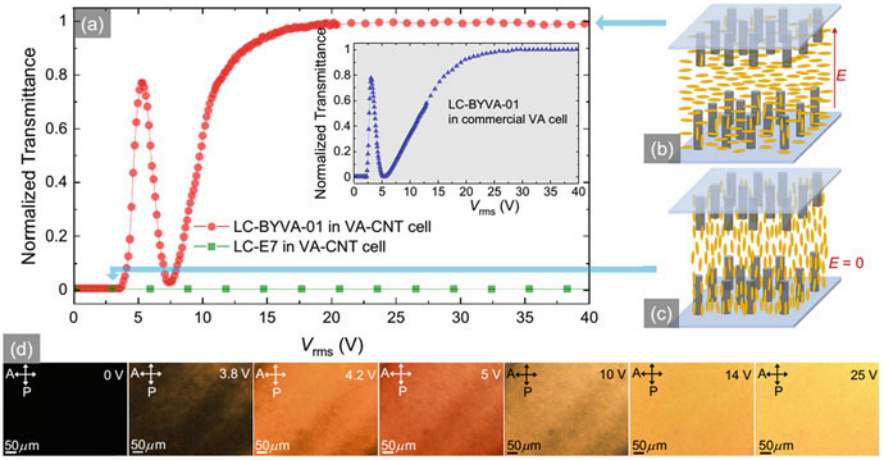


Fig. 6 (**a**) The normalized transmittance of negative anisotropic LC-BYVA01 and positive anisotropic LC E7 in the VA-CNT array-based homeotropic cell (at $T = 22$ °C), listed in the legend, as a function of applied AC voltage ($f = 1000$ Hz); inset: negative anisotropic LC-BYVA01 in a commercial VA cell. Schematic representations of (**b**) voltage on and (**c**) voltage off state of LC-BYVA01 in the VA-CNT array-based homeotropic cell. (**d**) Seven separate micrographs of the VA-CNT array-based homeotropic cell filled with LC-BYVA01 under the crossed-polarized optical microscope at different applied voltages [67]

Besides CNTs, zinc oxide nanorods (ZnO NRs) have also been utilized in guiding the NLC molecules in a preferred orientation [83–85]. Chen et al. had grown ZnO NRs of varying lengths, diameters, and densities on ITO-coated glass substrate using a two-step hydrothermal method [85]. The tunable orientation of NLC molecules on NR grown surface was observed whose pretilt angle was tuned from 89° to 1.7° that corresponds to the vertical and planar alignment of LC molecules, respectively. It was proposed that the contact angle of water on ZnO NRs changed from 93° to 28° on changing their growth time and the same resulted to the tunable alignment of LC molecules. It was also pointed out that ZnO NRs grown on the ITO substrates also enhanced the transmission of LCDs due to the antireflection. Lim et al. reported the growth of ZnO nanorods on ITO-coated substrate using electrochemical deposition and fabricated the LC sample cells [84]. The authors obtained an excellent vertical alignment of the negative dielectric NLC that exhibited the similar electro-optical characteristics as that for conventional LC cell (Fig. 7). Chen et al. [85] fabricated the ZnO nanowire (NWs) arrays on the ITO-coated substrate using the two-step hydrothermal method. The substrates were then assembled as LC sample cell and filled with NLC material. It was found that the NW arrays guided the NLC director to align vertically on the substrate.

There are numerous investigations that reported the polyimide/oxide layer-free NPs-induced uniform alignment of LC materials. In the present chapter, we have covered some of such studies to render the readers the understanding of the basic physics and methodology involved in most of the NPs-induced alignment of

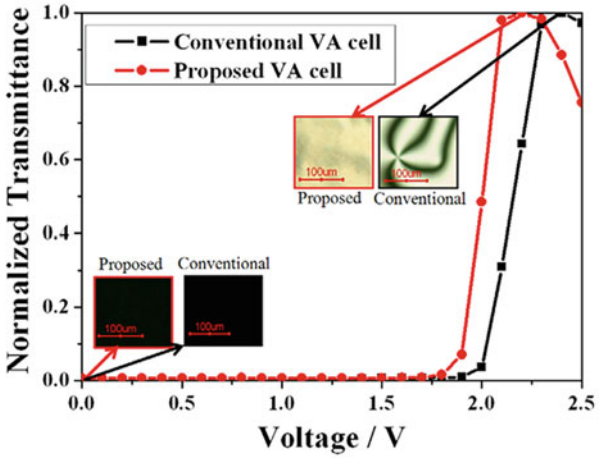


Fig. 7 Measured voltage-dependent normalized transmittance curves for the conventional and proposed vertically aligned cells. The insets are POM images in voltage-off (dark) and voltage-on (white) states for the proposed cell and the conventional vertically aligned cells [84]

simplest form of the LC mesophase, i.e., NLCs. Some recent reviews have provided deep insight on the mechanisms of NPs-induced LC alignment as they contain many such investigations including other forms of mesophases such as cholesteric, discotic, ferroelectric, and antiferroelectric LCs and methods such as dispersion of isotropic/anisotropic NPs in the bulk, coating (film) on the substrate, mixing with alignment layer, deposition (solid state), etc. [8, 11].

4 Conclusion and Future Perspectives

In this chapter, the comprehensive overview of nanoparticle (isotropic- and anisotropic-shaped)-induced alignment of NLCs without using the conventional alignment layers for tunable electro-optical devices is presented. Firstly, the conventional methods to align NLCs are briefly described. Afterward, the induction of alignment to NLCs (positive and negative dielectric anisotropic) by doping of nanoparticles in the bulk and then their coating on the substrates of sample cell has been critically reviewed. For instance, the doping of NPs (isotropic, spherical, and anisotropic, nanotubes, nanorods, nanowires, etc.) into the bulk of NLCs has induced the vertical, planar, and thermally switchable dual alignment in the sample cells devoid of alignment layers. Moreover, the coating/growing of anisotropic NPs on the substrates of the sample cells could also induce the vertical and planar alignments to NLCs. It is worth pointing out here the quality of the alignment and the electro-optical performance of NPs-induced aligned sample cells have been found almost comparable to sample cells aligned with the conventional alignment

techniques. Therefore, it is promising to have NPs-controlled alignment due to their potential applications in high-quality display devices and other photonic devices such as tunable lenses, gratings, filters, lasers, sensors, etc. Despite of such numerous applications, the durability of NPs-induced alignment and the toxicity of used NPs are major concern due to the plausible agglomeration of NPs in NLC matrix and the presence of heavy metals such as Cd, Pb, etc. Therefore, to minimize the agglomeration, the mesogen-functionalized NPs should be utilized. The heavy metal-free NPs should be used to reduce the toxicity in the devices based on NPs-NLC composites [86]. Last but not the least, to further advance and explore the basic and applied aspects of NPs-controlled alignment of NLCs, the detailed experimental, theoretical, and simulation work should be carried out.

Acknowledgments Ajay Kumar is thankful to the principal of D S College for his kind encouragement in the presented work. Gautam Singh thanks Amity University Uttar Pradesh, Noida, India, for its continuous support and encouragement in his research work.

References

1. Stephen M. J.; Straley, J. P. Physics of liquid crystals. *Rev. Mod. Phys.* 1974, 46, 617. https://doi.org/10.1103/RevModPhys.46.617
2. de Gennes, P. G., Prost, J. *The Physics of Liquid Crystals.* (Oxford University Press, New York, 1993).
3. Demus, D.; Goodby, J.; Gray,G. W.; Spiess,H. -W.; Vill,V. *Handbook of Liquid Crystals*. Vol. **2A**., Mol. Liq. Cryst. (1998).
4. S. Kumar, S. *Liquid Crystals: Experimental Study of Physical Properties and Phase Transitions.* (Cambridge University Press, Cambridge, New York, 2001).
5. Collings, P. J.; Hird, M. Introduction to liquid crystals: Chemistry and physics. *Mol. Cryst. Liq. Cryst.* 2017, 339, 273–214.
6. Blinc, R. *Ferroelectric Liquid Crystals, Science, CRC Press, 1984.*
7. Goodby, J. W., *Ferroelectric Liquid Crystals: Principles, Properties and Applications.* Gordon and Breach Science Publishers, Science, 1991.
8. Priscilla, P; Malik, P; Supreet; Kumar, A; Castagna, R; and Singh, G. Recent advances and future perspectives on nanoparticles-controlled alignment of liquid crystals for displays and other photonic devices, *Critical Reviews in Solid State and Materials Sciences* (2023), **48,** 57-92. https://doi.org/10.1080/10408436.2022.2027226
9. Chen, R. H. *Liquid Crystal Displays: Fundamental Physics and Technology*. Wiley, Germany, 2011.
10. DiLisi, G. A. *Phases of liquid crystals: An Introduction to Liquid Crystals*. IOP Publishing, 2019.
11. Prakash, J; Kumar, A; and Chauhan, S. Aligning liquid crystal materials through nanoparticles: A review of recent progress. *Liquids (*2022), **2,** 50–71. https://doi.org/10.3390/liquids2020005
12. Hegman, T. and Qi, H. Nanoparticles in liquid crystals: Synthesis, self-assembly, defect formation, and potential applications. *J. Inorganic and Organometallic Polymers and Materials* (2007), **17,** 483–508.
13. Lagerwall, J. P. F. and Scalia, G. *Liquid crystals with nano and microparticles*. World Scientific publications, vol 1 &2, 2016.
14. Shen, Y. and Dierking, I. Perspectives in liquid-crystal-aided nanotechnology and Nanoscience. *Applied Sciences* (2019) **9,** 2512. https://doi.org/10.3390/app9122512
15. Mirzaei, J.; Reznikov, M.; Hegman, T., Impact of nanoscale particles and carbon nanotubes on current and future generations of liquid crystal displays. *J. Mater. Chem.* (2008), **18**, 3288–

3294. https://doi.org/10.1039/B718920F (b) Stamatoiu, O.; Mirzaei, Nanoparticles in liquid crystals and liquid crystalline nanoparticles. *Top. Curr. Chem.* (2012), **318**, 331–394. https://doi.org/10.1007/128_2011_233
16. Jeng, S. C.; Kuo, C. W.; Wang, H. L.; Liao, C. C. Nanoparticles-induced vertical alignment in liquid crystal cell. *Appl. Phys. Lett.* (2007), **91,** 061112. https://doi.org/10.1063/1.2768309
17. Kuo, C. W.; Jeng, S. C.; Wang, H. L.; Liao, C. C. Application of nanoparticle-induced vertical alignment in hybrid-aligned nematic liquid crystal cell. *Appl. Phys. Lett.*(2007), **91**, 141103. https://doi.org/10.1063/1.2794007
18. Hwang, S. J.; Jeng, S. C.; Yang, C. Y.; Kuo, C. W.; Liao, C. C. Characteristics of nanoparticle-doped homeotropic liquid crystal devices. *J. Phys. D: Appl. Phys.* (2009), **42**, 025102. https://doi.org/10.1088/0022-3727/42/2/025102
19. Teng, W. Y.; Jeng, S. C.; Kuo, C. W.; Lin, Y. R.; Liao, C. C.; Chin, W. K. Nanoparticles-doped guest-host liquid crystal displays. *Opt. Lett.* (2008), **33**, 1663. https://doi.org/10.1364/OL.33.001663
20. Jeng, S. C.; Hwang, S. J.; Yang, C. Y. Tunable pretilt angles based on nanoparticles-doped planar liquid-crystal cells. *Opt. Lett.*(2009), **34**, 455. https://doi.org/10.1364/OL.34.000455
21. Jeng, S. C.; Hwang, S. J.; Chen, T. A.; Liu, H. S.; Chen, M. Z. Controlling the alignment of liquid crystals by nanoparticle-doped and UV-treated polyimide alignment films. *Proc. of SPIE* (2012), **8279**, 827912. https://doi.org/10.1117/12.912827
22. Hwang, S. J.; Shieh, Y. M.; Lin, K. R. Liquid crystal microlens using nanoparticle-induced vertical alignment. *J. Nanomaterials* (2015)**, 2015,** 6. https://doi.org/10.1155/2015/840182
23. Chen, S. H.; Chou, T. R.; Chiang, Y. T.; and Chao, C. Y. Nanoparticle-induced vertical alignment liquid crystal cell with highly conductive PEDOT:PSS films as transparent electrodes. *Mol. Cryst. Liq. Cryst.,* (2017), 646, 107–115.
24. Qi, H.; Hegmann, T. Multiple alignment modes for nematic liquid crystals doped with alkylthiol-capped gold nanoparticles. *ACS Appl. Mater. & Interfaces* (2009), **8**, 1731–1738. https://doi.org/10.1021/am9002815
25. Kinkead, B.; Hegmann, T. Effects of size, capping agent, and concentration of CdSe and CdTe quantum dots doped into a nematic liquid crystal on the optical and electro-optic properties of the final colloidal liquid crystal mixture. *J. Mater. Chem.* (2010), **20**, 448–458. https://doi.org/10.1039/B911641A
26. Dogra, A. R.; Sharma, V.; Gahrotra, R.; Kumar, P. Evaporation induced self-assembly of silica nanoparticles on ITO substrates in a confined cell of vertical alignment of liquid crystals and performance analysis. *Colloids and Surfaces A: Physiochemical and engineering aspects* (2022), **642**, 128712. https://doi.org/10.1016/j.colsurfa.2022.128712
27. Chinky, Kumar, P.; Sharma, V.; Malik, P.; Raina, K. K. Nano particles induced vertical alignment of liquid crystal for display devices with augmented morphological and electro-optical characteristics. *J. Mol. Struct.* (2019), **1196**, 866–873. https://doi.org/10.1016/j.molstruc.2019.06.045
28. Kumar, A.; Prakash, J.; Goel, P.; Khan, T.; Dhawan, S. K.; Silotia, P.; Biradar, A. M. Polymeric-nanoparticles–induced vertical alignment in ferroelectric liquid crystals. *Euro. Phys. Lett.* (2009), **88,** 26003. https://doi.org/10.1209/0295-5075/88/26003
29. Kumar, A.; Silotia, P.; Biradar, A. M. Effect of polymeric nanoparticles on dielectric and electro-optical properties of ferroelectric liquid crystals. *J. Appl. Phys.* (2010), **108,** 024107. https://doi.org/10.1063/1.3452355
30. Mirzaei, J.; Urbanski, M.; Yu, K.; Kitzerow, H.-S.; Hegmann, T. Nanocomposites of a nematic liquid crystal doped with magic-sized CdSe quantum dots. *J. Mater. Chem.* (2011), **21**, 12710–12716. https://doi.org/10.1039/C1JM11832C
31. Kumar, A.; Silotia, P.; Biradar, A. M. Sign reversal of dielectric anisotropy of ferroelectric liquid crystals doped with cadmium telluride quantum dots. *Appl. Phys. Lett.* (2011), **99,** 072902. https://doi.org/10.1063/1.3627179
32. Kundu, S.; Akimoto, M.; Hirayama, I.; Inoue, M.; Kobayashi, S.; Takatoh, K. Enhancement of Contrast Ratio by Using Ferroelectric Nanoparticles in the Alignment Layer of Liquid Crystal Display. *Jpn. J. Appl. Phys.* (2008), **47**, 4751–4754. https://doi.org/10.1143/JJAP.47.4751

33. Fuh, A.Y.G.; Huang, C. Y.; Liu, C. K.; Chen, Y. D.; Cheng, K. T. Dual liquid crystal alignment configuration based on nanoparticle-doped polymer films. *Opt. Exp.* (2011), **19**, 11825. https://doi.org/10.1364/OE.19.011825
34. Akimoto, M.; Kundu, S. K.; Hirayama, I. I.; Kobayashi, S.; Takatoh, K. Improvement of Electro-Optical Characteristics of Liquid Crystal Display by Nanoparticle-Embedded Alignment Layers. *Mol. Cryst. Liq. Cryst.* (2009), **508**, 1/363–13/375. https://doi.org/10.1080/15421400903058130
35. Liu, B.; Ma, Y.; Zhao, D.; Xu, L.; Liu, F.; Zhou, W.; Guo, L. Effects of morphology and concentration of CuS nanoparticles on alignment and electro-optic properties of nematic liquid crystal. *Nano Res.* (2017), **10,** 618–625. https://doi.org/10.1007/s12274-016-1321-5
36. Chen, J.; Cranton, W.; Fihn M. *Handbook of Visual Display Technology* Berlin, Germany: Springer, 2016. https://doi.org/10.1007/978-3-319-14346-0
37. van Aerle, N. A. J. M.; Tol, A. J. W. Molecular Orientation in Rubbed Polyimide Alignment Layers Used for Liquid-Crystal Displays. *Macromolecules* (1994), **27**, 6520–6526. https://doi.org/10.1021/ma00100a042
38. Ishihara, S.; Wakemoto, H.; Nakazima, K.; Matsuo, Y. The effect of rubbed polymer films on the liquid crystal alignment. *Liq. Cryst.* (1989), **4**, 669–675. https://doi.org/10.1080/02678298908033202
39. Meyerhofer, D. New technique of aligning liquid crystals on surfaces. *Appl. Phys. Lett.* (1976), **29**, 691–692. https://doi.org/10.1063/1.88928
40. Cognard, J. *Alignment of Nematic Liquid-Crystals and Their Mixtures. Molecular Crystals and Liquid Crystals.* Gordon and Breach Science Publishers, New York, 1982.
41. Jákli, A.; Jánossy, I.; Bata, L.; Buka, A. A special shear method of alignment for smectic liquid crystals. *Cryst. Res. Technol.* 1988, **23,** 949-954. https://doi.org/10.1002/crat.2170230721
42. Chigrinov, V. G.; Kozenkov, V. M.; Kwok, H. S. *Photoalignment of Liquid Crystalline Materials: Physics and Applications* Wiley SID Series in Display Technology (Wiley, Chichester, England; Hoboken, NJ, 2008. https://doi.org/10.1002/9780470751800
43. Chrzanowski, M. M.; Zielinski, J.; Olifierczuk, M.; Kedzierski, J.; Nowinowski-Kruszelnicki, E. J. Photoalignment-an alternative aligning technique for liquid crystal displays. *Achiev. Mater. Manuf. Eng.* (2011), **48**, 7–13.
44. Yaroshchuk, O.; Reznikov, Y. Photoalignment of liquid crystals: basics and current trends. *J. Mater. Chem.* (2012), **22,** 286. https://doi.org/10.1039/C1JM13485J
45. Babakhanova, G.; Lavrentovich, O. D. The Techniques of Surface Alignment of Liquid Crystals. *Springer Proceedings in Physics* (2019), **223,** 165–197. https://doi.org/10.1007/978-3-030-21755-6_7
46. Hasegawa, M. Azimuthal anchoring energies of photoaligned nematic liquid crystals produced by small dosages of linearly polarized uv light. *Jpn. J. Appl. Phys.* (1999), **38,** L457–L460. https://doi.org/10.1143/JJAP.41.L1167
47. Gibbons, W. M.; Shannon, P. J.; Sun, S. T.; Swetlin, B. J. Patterned optical properties in photopolymerized surface-aligned liquid-crystal films. *Nature* (1991), **351**, 49–50. https://doi.org/10.1038/368532a0
48. Matsuda, H.; Seo, D.-S.; Yoshida, N.; Fujibayashi, K.; Kobayashi, S.; and Yabe, Y. Estimation of the static electricity and optical retardation produced by rubbing polyimide and polyamide films with different fabrics, *Mol. Cyrst. Liq. Cryst.*, (1995), **264**, 23–28. https://doi.org/10.1080/10587259508037298
49. Singh, G.; Prakash, G. V.; Kaur, S.; Choudhary, A.; Biradar, and A. M. Molecular relaxation in homeotropically aligned ferroelectric liquid crystals. *Physica B: Condensed Matter* (2008), **403**, 3316–3319. https://doi.org/10.1016/j.physb.2008.04.026
50. Yaroshchuk, O.; Reznikov, Y. Photoalignment of liquid crystals: basics and current trends. *J. Mater. Chem.* (2012), **22,** 286. https://doi.org/10.1039/C1JM13485J
51. Khan, I.; Saeed, K.; Khan, I. Nanoparticles: Properties, applications, and toxicities. *Arab. J. Chem.* (2019), **12**, 908–931. https://doi.org/10.1016/j.arabjc.2017.05.011 Quantum dots as liquid crystal dopants. *J. Mater. Chem.* (2012), **22**, 22350–22365. https://doi.org/10.1039/C2JM33274D

52. Jeevanandam, J.; Barhoum, A.; Chan, Y. S.; Dufresne, A.; Danquah, M. K. Review on nanoparticles and nanostructured materials: history, sources, toxicity, and regulations. *Beilstein J. Nanotechnol.,* (2018), **9** 1050–1074. https://doi.org/10.3762/bjnano.9.98
53. Bisoyi, H. K.; Kumar, S. Liquid-crystal nanoscience: an emerging avenue of soft self-assembly. *Chem. Soc. Rev.* (2011), **40**, 306–319. https://doi.org/10.1039/B901793N
54. (a) Prakash, J.; Choudhary, A.; Kumar, A.; Mehta, D. S.; Biradar, A. M. Nonvolatile memory effect based on gold nanoparticles doped ferroelectric liquid crystal. *Appl. Phys. Lett.* (2008), **93**, 112904. https://doi.org/10.1063/1.2980037 (b) Kumar, A.; Prakash, J.; Mehta, D. S.; Biradar, A. M.; Haase, W. Enhanced photoluminescence in gold nanoparticles doped ferroelectric liquid crystals. *Appl. Phys. Lett.* (2009), **95**, 023117. https://doi.org/10.1063/1.3179577
55. Choudhary, A.; Singh, G.; Biradar, A. M. Advances in gold nanoparticle–liquid crystal composites. *Nanoscale* (2014), **6**, 7743–7756. https://doi.org/10.1039/C4NR01325E
56. Singh, G.; Fisch, M. R.; Kumar, S. Emissivity and electrooptical properties of semiconducting quantum dots/rods and liquid crystal composites: a review. *Rep. Prog. Phys.* (2016), **79**, 056502. https://doi.org/10.1088/0034-4885/79/5/056502
57. Singh, G.; Fisch, M. R.; Kumar, S. Tunable polarised fluorescence of quantum dot doped nematic liquid crystals. *Liq. Cryst.* (2017), **44**, 444–452. https://doi.org/10.1080/02678292.2016.1217357
58. Dierking, I. Nanomaterials in Liquid Crystals. *Nanomaterials* (2018), **8**, 453. https://doi.org/10.3390/nano8070453
59. Chen, W.-Z.; Tsai, Y.-T.; Lin, T.-H. Single-cell-gap trans-reflective liquid-crystal display based on photo- and nanoparticle-induced alignment effects. *Opt. Lett.* (2009), **34**, 2545. https://doi.org/10.1364/OL.34.002545
60. Ahmad, F.; Jamil, M.; Lee, J. W.; Jeon, Y. J. Magnetically driven vertical alignment of liquid crystals by ferromagnetic particles. *Liq. Cryst.* (2015), **42**, 233–239. https://doi.org/10.1080/02678292.2014.981603
61. Zhao, D.; Zhou, W.; Cui, X.; Tian, Y.; Guo L.; Yang, H. Alignment of liquid crystals doped with nickel nanoparticles containing different morphologies. *Adv. Mater.* (2011), **23,** 5779–5784. https://doi.org/10.1002/adma.201102611
62. Zhao, D.; Peng, Y.; Xu, L.; Zhou, W.; Wang, Q.; Guo, L. Liquid-Crystal Biosensor Based on Nickel-Nanosphere-Induced Homeotropic Alignment for the Amplified Detection of Thrombin. *ACS Appl. Mater. Interfaces* (2015), **7**, 23418–23422. https://doi.org/10.1021/acsami.5b08924
63. Mirzaei, J.; Urbanski, M.; Kitzerow, H.-S.; Hegmann, T. Hydrophobic gold nanoparticles via silane conjugation: chemically and thermally robust nanoparticles as dopants for nematic liquid crystals. *Phil. Trans. R. Soc. A* (2013), **371**, 20120256. https://doi.org/10.1098/rsta.2012.0256
64. Varshney, D.; Prakash, J.; and Singh, G. Indium tin oxide nanoparticles induced tunable dual alignment in nematic liquid crystal. *J. Mol. Liq.* (2023), **374,** 121264. https://doi.org/10.1016/j.molliq.2023.121264
65. Dierking, I.; Scalia, G.; and Morales, P. Liquid crystal-carbon nanotube dispersions. *J. Appl. Phys.* (2005), **97,** 044309. https://doi.org/10.1063/1.1850606
66. Lu, S. -Y.; Chien, L.-C. Carbon nanotube doped liquid crystal OCB cells: physical and electro-optical properties. *Opt. Exp.* (2008), **16,** 12777. https://doi.org/10.1364/OE.16.012777
67. Basu, R.; and Atwood, L. J. Homeotropic liquid crystal device employing vertically aligned carbon nanotube arrays as the alignment agent. *Phys. Rev E* (2020), 102, 022701. https://doi.org/10.1103/PhysRevE.102.022701
68. Kumar, A.; Singh, D. P.; and Singh, G. Recent progress and future perspectives on carbon-nanomaterial-dispersed liquid crystal composites. *J. Phys. D: Appl. Phys.* (2022), **55,** 083002. https://doi.org/10.1088/1361-6463/ac2ced
69. Dhar, R.; Pandey, A. S.; Pandey, M. B.; Kumar, S.; Dabrowski, R. Optimization of the Display Parameters of a Room Temperature Twisted Nematic Display Material by Doping Single-Wall Carbon Nanotubes. *Appl. Phys. Exp.* (2008), **1,** 121501. https://doi.org/10.1143/APEX.1.121501

70. Zhou, W.; Lin, L.; Zhao, D. Synthesis of Nickel Bowl-like Nanoparticles and Their Doping for Inducing Planar Alignment of a Nematic Liquid Crystal. *J. Amer. Chem. Soc.* (2011), **133,** 8389–8391. https://doi.org/10.1021/ja201101p
71. Wang, Q.; Shang, Y.; Yu, L.; Zou, C.; Yao, W.; Zhao, D.; Song, P.; Yang, H.; Guo, L. Facet-dependent Cu_2O nanocrystals in manipulating alignment of liquid crystals and photomechanical behaviors. *Nano Res.* (2016), **9,** 2581–2589. https://doi.org/10.1007/s12274-016-1144-4
72. Zhao, D.; Guo, Y.; Bi, W.; Li, X.; Duan, R.; and Guo, L. Effects of $CuInS_2$ nanoparticles on the alignment control of liquid crystals. *Nano Research,* (2022), **15,** 7542–7548. https://doi.org/10.1007/s12274-022-4338-y
73. Mishra, S.; Manjuladevi, V.; and Gupta, R. K. Zinc oleate nanorod-induced vertical alignment of nematic liquid crystal. *ACS Omega* (2023), **7,** 46466–46474. https://doi.org/10.1021/acsomega.2c05196
74. Lee, W. K.; Hwang, S. J.; Cho, M. J.; Park, H. G.; Han, J. W.; Song, S.; Jang, J. H.; Seo, D. S. CIS–ZnS quantum dots for self-aligned liquid crystal molecules with superior electro-optic properties. *Nanoscale* (2013), **5**, 193–199. https://doi.org/10.1039/C2NR32458J
75. Chung, Y.-F.; Chen, M.-Z.; Yang, S.-H.; Jeng, S.-C. Tunable Surface Wettability of ZnO Nanoparticle Arrays for Controlling the Alignment of Liquid Crystals. *ACS Appl. Mater. Interfaces* (2015), **7**, 9619–9624. https://doi.org/10.1021/acsami.5b01157
76. Reznikov, M.; Sharma, A.; Hegmann, T. Ink-Jet Printed Nanoparticle Alignment Layers: Easy Design and Fabrication of Patterned Alignment Layers for Nematic Liquid Crystals. *Part. Part. Syst. Charact.* (2014), **31**, 257–265. https://doi.org/10.1002/ppsc.201300248
77. Sharma, A.; Hofmann, D.; Hegmann, T. Patterned alignment of nematic liquid crystals generated by inkjet printing of gold nanoparticles and emissive carbon dots on both flexible polymer and rigid glass substrates. *Liq. Cryst.* (2016), **43**, 828–838. https://doi.org/10.1080/02678292.2016.1145268
78. Son, I.; Son, S.-R.; An, J.; Choi, J.-W.; Kim, S.; Lee, W. Y.; Lee, J. H. Photoluminescent surface-functionalized graphene quantum dots for spontaneous interfacial homeotropic orientation of liquid crystals. *J. Mol. Liq.* (2021), **332**, 115901. https://doi.org/10.1016/j.molliq.2021.115901
79. Dogra, A. R.; Sharma, V.; Khanra, P.; and Kumar, P. Evaporative deposition of SiO2 nanoparticles multilayer on ITO substrates and application for vertical alignment of liquid crystals-effect of dichroic dye. *J. Phys: Conference Series,* (2021), **2070**, 012071.
80. Liu, Y.; Park, H. G.; Lee, J. H.; Jang, S. B.; Jung, Y. H.; Jeong, H. C.; Seo, D. S. Homogeneous liquid crystal alignment on ion beam-induced $Y_2Sn_2O_7$ layers. *IEEE Electron Devise Letters,* (2015), **36,** 363–365. https://doi.org/10.1109/LED.2015.2399505
81. Russell, J. M.; Oh, S.; LaRue, I.; Zhou, O.; Samulski, E. T. Alignment of nematic liquid crystals using carbon nanotube films. *Thin Solid Films* (2006), **509**, 53–57. https://doi.org/10.1016/j.tsf.2005.09.099
82. Fu, W.; Liu, L.; Jiang, K.; Li, Q.; Fan, S. Super-aligned carbon nanotube films as aligning layers and transparent electrodes for liquid crystal displays. *Carbon* (2010), **48**, 1876–1879. https://doi.org/10.1016/j.carbon.2010.01.026
83. Chen, M. Z.; Yang, S. H.; and Jeng, S. C. Growth of ZnO nanorods and their applications for liquid crystal devices. *ACS applied Nanomaterials,* (2018), **1,** 1879–1885. https://doi.org/10.1021/acsanm.8b00202
84. Lim, Y. J.; Choi, Y. E.; Kang, S. W.; Kim, D. Y.; Lee, S. H.; Hahn, Y.-B. Vertical alignment of liquid crystals with zinc oxide nanorods. *Nanotechnology* (2013), **24**, 345702. https://doi.org/10.1088/0957-4484/24/34/345702
85. Chen, M. Z.; Liquid crystal alignment on zinc oxide nanowires arrays for LCD applications. *Optics Express* (2013), **21,** 29277–29282.
86. Supreet and Singh, G. Recent advances on cadmium free quantum dots-liquid crystal nanocomposites. *Applied Materials Today* (2020), **21,** 100840. https://doi.org/10.1016/j.apmt.2020.100840

Photoelectrochemical Immunosensor for Carcinoembryonic Antigen Detection: An Attempt for Early Cancer Screening



Longshan Zhao and Chunling Mao

1 Introduction

Photoelctrochemistry (PEC) is a new detection platform based on the change of photocurrent of photoactive materials. The combination of photochemical and electrochemical methods is used to study the phenomena, rules, and applications of redox reaction in the ground state or excited state of molecules or ions. It has the advantages of good selectivity, high sensitivity, and low cost and is user-friendly. In conventional PEC sensing, standard three-electrode electrochemical system is used in the detection process, mainly including working electrode, counter electrode (Pt electrode), and reference electrode (Ag/AgCl or saturated calomel electrode). The material coated on the working electrode is irradiated by light, absorbs the energy of light, and promotes the electrode reaction, which is reflected in the conversion of light energy, electrical energy, and chemical energy. Therefore, the core of PEC method is the photoelectric conversion process.

It is worth noting that the materials coated on the working electrode can be metal materials, semiconductors, etc. In this chapter, CdTe-QDs are compounded with MIL-101 (Cr) and applied on the working electrode to generate photocurrent signals, so as to achieve the purpose of detecting carcinoembryonic antigen (CEA). In general, the concentration of CEA in the human body is closely related to colorectal cancer, gastric cancer, lung cancer, and breast cancer, and the normal level should be less than 5.0 ng•mL^{-1}. If it exceeds the normal level, it may indicate that there is a risk of related cancer. Therefore, the establishment of a rapid and sensitive quantitative CEA method for early diagnosis of cancer is the golden means of cancer treatment.

L. Zhao (✉) · C. Mao
School of Pharmacy, Shenyang Pharmaceutical University, Shenyang, Liaoning, P. R. China

© The Author(s), under exclusive license to Springer Nature Switzerland AG 2024

S. Krishnamoorthy, K. (Kris) Iniewski (eds.), *Advances in Fabrication and Investigation of Nanomaterials for Industrial Applications*,
https://doi.org/10.1007/978-3-031-42700-8_5

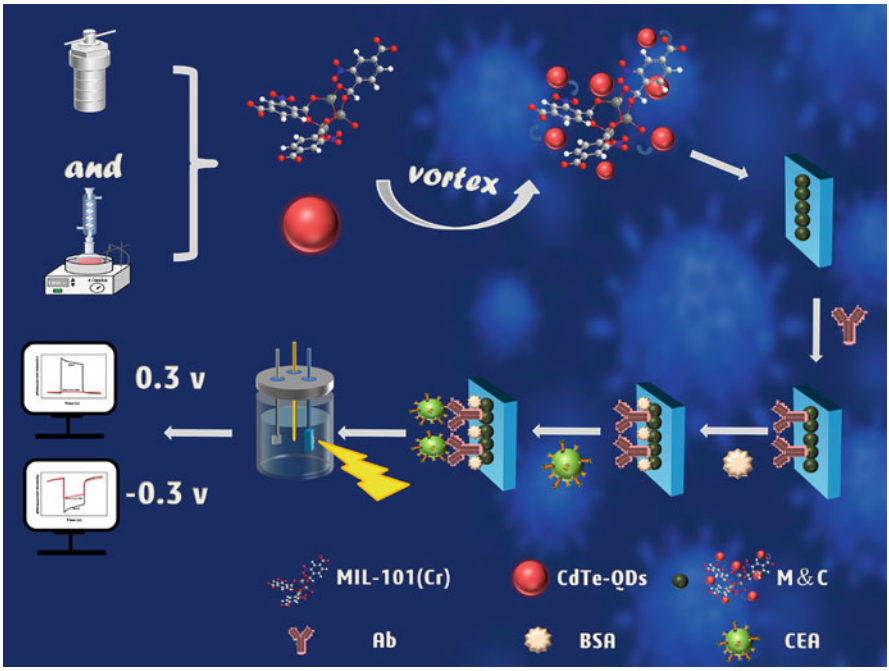


Fig. 1 The test process of CEA

MIL-101(Cr) has superior properties such as larger volume, specific surface area, higher porosity, and adjustable pore size. However, its wide bandgap will lead to a decrease in the density of photogenerated carriers. CdTe-QDs with narrow bandgap have strong light absorption ability, which can sensitize MIL-101(Cr). Therefore, CdTe-QDs and MIL-101(Cr) can be well combined to form M&C composites with certain photoelectric activity. The carboxyl and amino groups on the surface of M&C can be covalently coupled with the antibody (Ab) of CEA, and bovine serum albumin (BSA) is further used to block the nonspecific binding site. Finally, CEA is modified according to the specific recognition immune reaction of antigen (Ag-Ab), which blocks the movement of photogenerated carriers through steric hindrance and the inherent insulation of biological macromolecules, leading to the attenuation of photocurrent signal (Fig. 1). Since the photocurrent intensity of MIL-101 (Cr) varies with the applied working voltage (−0.3 V~0.3 V), a dual photocurrent signal response platform has been established to form an "anodic photocurrent-CEA concentration-cathodic photocurrent" system to realize the self-calibration function of the self-detection results. All the above analytical processes can be integrated into a newly designed portable PEC testing unit for CEA detection.

2 Experimental Method

MIL-101(Cr) was synthesized by hydrothermal method in the absence of hydrofluoric acid (HF) according to the literature [1]. Cr $(NO_3)_3 \bullet 9H_2O$ (2.0 g, 5 mmol) was mixed with terephthalic acid (H_2BDC) (5 mmol) and 20-mL deionized water and ultrasonically treated for 30 min. After mixing, a dark blue suspension with pH 2.58 was obtained. The suspension was placed in Teflon-lined stainless-steel autoclave and heated in an oven at 218 °C for 18 h. After synthesis, it was cooled to room temperature to obtain the suspension, which was filtered to give a dark blue product. The product was washed with hot *N,N-dimethylformamide* (DMF) to remove unreacted terephthalic acid (H_2BDC) and then washed with hot absolute ethanol to displace the pores of DMF molecule. After drying at 60 °C for 2 h in an oven and finally drying at 150 °C for 8 h under vacuum conditions, MIL-101(Cr) was obtained after removing the ethanol molecules adsorbed in the pores.

The synthesis method of CdTe-QDs was improved by the literature [2]. Firstly, $CdCl_2 \bullet 2.5H_2O$ was dissolved in 50-mL ultrapure water, and then 3-mercaptopropionic acid was added. Next, it was stirred vigorously, adjusted to pH 10.5~11.0 with 1 mol•L^{-1} NaOH solution, and added K_2TeO_3 solution. After, $NaBH_4$ solution was added and stirred for 5 min and then stirred and refluxed at 100 °C for 90 min to obtain CdTe-QDs. Finally, the obtained CdTe-QD red solution was dialyzed (500 Da), lyophilized, and used for later use.

Preparation of CdTe − QDs/FTO, MIL − 101 (Cr)/FTO, and M & C/FTO was continued. Firstly, the fluorine-doped tin oxide (FTO) classical electrode was cut into 2 × 2 cm^2 circular slices, followed by rinsing under sonication with acetone, ultrapure water and ethanol for 30 min, respectively. CdTe-QDs (7 mg•mL^{-1}) and MIL-101 (Cr) (3 mg•mL^{-1}) were dissolved in a water-ethanol solution with a ratio of 3:1(*v/v*), separately. 75-μL CdTe-QDs or MIL-101 (Cr) solution was transferred onto FTO and dried at 120 °C to obtain CdTe-QDs/FTO and MIL-101(Cr)/FTO. 7 mg of MIL-101(Cr) and 3 mg of CdTe-QDs were immersed in a water-ethanol solution with a ratio of 3:1(*v/v*) and sonicated for 30 min to obtain an M&C suspension. Similarly, 75 μL of M&C suspension was pipetted onto FTO and dried at 120 °C to obtain M&C/FTO.

The above electrodes were incubated with 45 μL of Ab for 90 min, and then the redundant Ab was washed away using PBS. Secondly, 45-μL BSA (1 wt%) was added to Ab/M&C/FTO to block nonspecific binding sites and incubated for 90 min; then the electrode was thoroughly washed with PBS. Finally, the BSA/Ab/M&C/FTO was co-incubated with 45 μL of CEA for 90 min to generate specific immunobinding of the Ag-Ab. All incubations were performed in an airtight container at 4 °C. The PEC immunosensors were constructed.

Depending on the specific binding of Ag and Ab, the prepared M&C/FTO electrodes were used to quantify CEA in samples with different concentrations. The M&C/FTO electrodes were incubated in CEA samples with different concentrations for 90 min at room temperature. The prepared CEA/M&C/FTO electrodes were used for photocurrent testing after cleaning. A CHI-660E electrochemical

workstation with a three-electrode system was used to conduct the photocurrent measurement. The modified FTO electrode was used as the working electrode, whereas the platinum wire and the Ag/AgCl were used as the auxiliary and reference electrode, respectively. A xenon lamp with a 420-nm filter was used as the light source (CEL-HXF300, Beijing). All tests were performed at room temperature and repeated three times.

Based on the above PEC analysis principle and process, concentration on the above analysis steps in a small analytical detector was tried. Therefore, the basic structure of the small detector was further designed. The internal circuit was concentrated in the center of the overall structure of the detector, and an organic light-emitting diode (OLED) screen was installed outside the detector for reading. The three electrodes were connected with the internal circuit, equipped with the light source set in advance and the prepared PBS buffer solution. At this time, it incubated the M&C working electrode prepared in advance with CEA to complete the detection. In view of the above ideas, a small detector model was preliminarily developed.

The overall design idea was to apply a ± 0.3 V in the solution, and the collected current was amplified and converted into a voltage signal, which was then collected by a single-chip microcomputer (stm32f103) through digital-to-analog conversion (DAC). In the single-chip microcomputer, the collected voltage signal value was inversely converted into the corresponding current value. The relationship table between the current magnitude and the CEA concentration was stored in the microcontroller in advance, and the concentration value corresponding to the current value was obtained by searching the relationship table. The value of the concentration was displayed on the organic light-emitting diode (OLED) screen. Among them, the stable voltage of 0.3 V was realized by the DAC module. Firstly, the pulse width modulation (PWM) digital signal with a specific duty cycle was generated by the external clock signal of the minimum system of the stm32f103, and the external power supply was 12 V. The output voltage of the DAC module was controlled at 0.3 V. The stm32f103 was a 32-bit microcontroller, and the DAC was 12 bits and has a sufficient precision. The signal amplification process used a 510-kΩ transimpedance amplifier. The input signal was a current in the range of 0–3 mA. The current signal of 0–1500 nA can be converted into a voltage signal of 0–0.75 V, and the error did not exceed 1 nA. The inverse conversion process was to divide the corresponding voltage signal by the magnification in the program of the microcontroller. The microcontroller and transimpedance amplifier were powered by 5 V of the voltage regulator module, wherein the battery pack motor was installed inside the detector main body and the output shaft of the battery pack motor was connected to the single-chip microcomputer through a voltage regulator module to generate a stable applied voltage. Convert the analog voltage module to convert the stable voltage output by the microcontroller. One side of the detector was provided with an analog-to-digital converter to generate a stable digital signal with a specific duty cycle, and a transimpedance amplifier component was connected to it to amplify the originally detected low-current signal. The upper part of the main body of the detector was provided with a liquid crystal display screen for

reading out the detection results. The sealed casing was installed on the detector body, and the detector battery pack motor and all microprocessors connected to the detector battery pack motor were arranged in the sealed casing. The three electrodes (auxiliary electrode, reference electrode, working electrode) were connected with the analog voltage module and the transimpedance amplifier to ensure the input of the detection signal. The battery pack motor of the detector was embedded into the sealed casing of the detector through transition fit, all microprocessors were fixed by metal clips and black tape, and the liquid crystal display was fixed on the back with black tape, so as to achieve the combination with the casing of the detector.

In the process of CEA detection, the PBS solution and the external light source can be prepared in advance. The PEC portable detector was immersed in the PBS solution, the external light source was irradiated on the surface of the working electrode, and the voltage was adjusted. The sealed shell of PEC immune-sensing portable detector was realized through 3D printing. The 3D printer model was Chuangxiang 3D Ender-3. The printing material was polylactic acid (PLA), commonly known as corn material, which was a biodegradable environmental protection material. The specific parameters set by 3D printing for the sealed shell of the detector were:

(A) Slice parameters:

1. Layer height: 0.2 mm.
2. Height of the first layer: 0.2 mm.
3. Vertical shell – number of outer rings, 3; helical structure, none.
4. Horizontal shell – physical layer, top layer 3, bottom layer 3.
5. The order of printing the innermost circle or outermost circle: print the innermost circle first.
6. Joint position: all joints are aligned.
7. Filling concentration: 30%.
8. Filling structure: honeycomb filling.

(B) Printing parameters:

1. Printing speed – peripheral speed, 30 mm/s; outer circumference speed, 70%.
2. Filling speed: 60 mm/s.
3. Solid speed: 60 mm/s.
4. Top solid filling speed: 60 mm/s.
5. Support material speed: 60 mm/s.
6. Bridge speed: 60 mm/s.
7. Groove speed: 20 mm/s.

(C) Printer setting:

1. Extrusion head: 0.4.
2. Retract length: 3 mm.
3. Retract speed: 40 mm/s.
4. Layer change and layer retreat: none.

5. Extrusion head temperature: 190 °C, heat.
6. Bed temperature: 50 °C.

3 Experimental Data

3.1 Brunner-Immet-Teller Analysis

Brunner-Immet-Teller (BET) test can obtain the specific surface area, pore volume, pore size distribution, and other information of the prepared materials to determine the successful synthesis of materials and the bonding mode of individual materials to form composite materials. The specific surface area of MIL-101(Cr) was analyzed using BET. As shown in Fig. 2, the trend of adsorption and desorption isotherms of MIL-101(Cr) indicated that MIL-101(Cr) was a mesoporous material. The BET results showed that the specific surface area was 2192.5604 $m^2 \bullet g^{-1}$ and the average pore diameter and volume were 2.5964 nm and 1.5257 $cm^3 \bullet g^{-1}$, respectively. The above results suggested that the ordered channels of MIL-101(Cr) could serve as "microreactors" and stabilize CdTe-QDs when forming nanoscale composites.

3.2 Morphology Analysis

In 1932, Ruska invented the transmission electron microscope (TEM) with the electron beam as the light source. It can be seen that what cannot be seen clearly under the optical microscope is less than 0.2 μm. Therefore, TEM can be used to observe the fine structure of the resulting material or even the structure of only a column of atoms. At present, TEM is an important analytical method in many

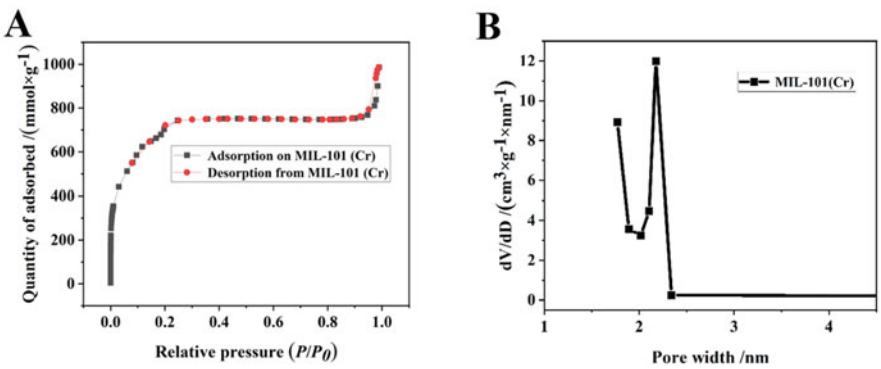


Fig. 2 (**a**) The adsorption/desorption curves of MIL-101(Cr); (**b**) the pore volume distribution of MIL-101(Cr)

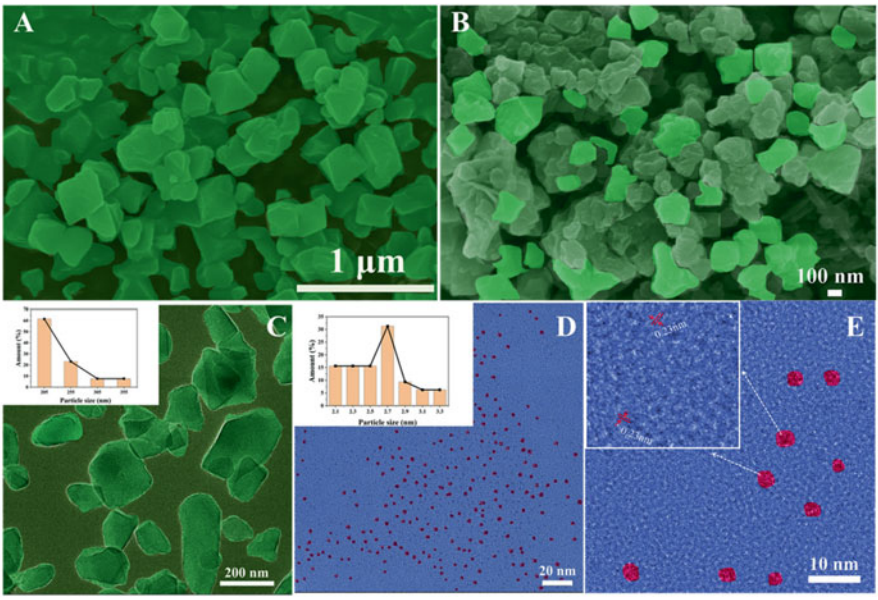


Fig. 3 (**a**) The SEM image of MIL-101(Cr) and (**b**) M&C. (**c**) The TEM image of MIL-101(Cr). (**d**) The SEM image of CdTe-QDs. (**e**) The HR-TEM image of CdTe-QDs

scientific fields related to physics and biology, such as cancer research, virology, materials science, nanotechnology, semiconductor research, etc. High-resolution transmission electron microscope (HR-TEM) is a high-resolution TEM, which can show the crystal plane spacing of materials through light and dark stripes. Compare the measured light and dark stripe spacing with the standard crystal plane spacing of the crystal to determine which crystal plane belongs to. In this way, the crystal plane orientation or material growth direction can be easily calibrated. Scanning electron microscopy (SEM) is an observation method between TEM and optical microscope. It has the advantages of rich kinds of measurable samples, almost no damage and pollution to the original samples, and simultaneous access to morphology, structure, composition, and crystallographic information. It is widely used in the research of nanomaterials and graphite. The microstructures and morphologies of MIL-101(Cr), CdTe-QDs, and M&C were analyzed by TEM, HR-TEM, and SEM. The SEM image of MIL-101(Cr) showed a regular octahedral structure (Fig. 3). The image of TEM showed that the particle size of MIL-101(Cr) ranged from 160 to 360 nm (the number of particles considered was 23). Rough edges of crystals may be attributed to the residual organic solvents in the pores introduced during the synthesis of MIL-101(Cr) [3]. Figure 2 showed smooth spherical shape, uniform size, good dispersibility, high crystallinity, and monodisperse state of CdTe-QDs. The average particle diameter was 2.77 nm (the number of particles considered is 32), which ranged from 2.10 to 3.30 nm. HR-TEM suggested that CdTe-QDs had

high crystallinity with a lattice parameter of 0.23 nm. The SEM of the M&C showed successful recombination of MIL-101(Cr) and CdTe-QDs.

Energy dispersive spectroscopy (EDS) is a chemical analysis method, which is realized by analyzing the wavelength and intensity of the element characteristic X-ray emitted by the sample. The elements contained in the sample are determined according to the different wavelength of the element characteristic X-ray. The content of elements in the sample can be determined by comparing the intensity of spectral lines of different elements. It is an analytical instrument in the fields of physics, chemistry, energy science, and technology. The elements of C, O, and Cr were distributed on the surface of MIL-101(Cr), and the inset was the ratio of each element in the selected area, which proved that the MIL-101 (Cr) was successfully synthesized. The EDS image of M&C and showed that C, O, Cr, Cd, and Te were distributed on the surface of M&C, and the inset showed the proportion of each element in the selected area. This was also solid evidence that M&C was successfully prepared.

3.3 Optical Characteristics

Fourier transform infrared spectroscopy (FT-IR) is an analysis and identification method that combines the mathematical processing of Fourier transform with computer technology and infrared spectroscopy. According to the different characteristics of the spectrogram, it can identify the functional groups of unknown substances, determine the chemical structure, observe the chemical reaction process, distinguish isomers, analyze the purity of substances, etc. It is widely used in chemistry, physics, biology, pharmacy, and other fields and has many applications in the analysis of organic substances in the environment. As shown by FT-IR, the bands at 3345 and 1628 cm^{-1} of the blue curve indicated the presence of guest water adsorbed in the MIL-101(Cr) cage. The bands at 590 and 1405 cm^{-1} correspond to the O-C-O plane bending and symmetry vibrations, respectively, indicating the presence of a dicarboxylate linker in the MIL-101(Cr) framework [4]. The band at 1509 cm^{-1} was attributed to the C=C stretching vibration of the benzene ring in the MIL-101(Cr) framework. For the green curve, the broad absorption peak at 3446 cm^{-1} was attributed to -OH in the carboxyl group [5]. In addition, symmetric and asymmetric vibrational peaks of -COO- (1576 and 1449 cm^{-1}) were observed in CdTe-QDs, suggesting that carboxyl groups may exist on the surface of CdTe-QDs [6]. Overall, MIL-101(Cr), CdTe-QDs, and M&C had strong and broad absorption bands of -OH stretching mode at ~3400 cm^{-1} and C=O peaks at ~1500 cm^{-1} and ~1600 cm^{-1}, which confirmed the presence of −OH and −COOH on the surface of MIL-101(Cr) and CdTe-QDs. The FT-IR (red curve) of M&C was similar to MIL-101(Cr) and CdTe-QDs, indicating MIL-101 (Cr) was successfully combined with CdTe-QDs.

Based on the principle of X-ray diffraction, X-ray diffraction can be used to determine the crystal structure. The crystal has a lattice structure, and the period

of the lattice structure and the wavelength of the X-ray belong to the same order of magnitude. The lattice parameters or the size and shape of the cell can be determined according to the direction of diffraction. Lattice parameters derived from XRD measurements fitted the cubic sphalerite structure of CdTe-QDs crystals. The synthesized CdTe-QDs had three diffraction peaks at $2\theta = 25.7°$, 28.05°, and 45.5°. The standard XRD lines of CdTe-QDs were (111), (200), and (311), which indicated that the prepared CdTe-QDs had a relatively good crystal structure. Five diffraction peaks were found ($2\theta = 5.3°$, 8.6°, 9.2°, 10.4°, 16.6°) on MIL-101(Cr), and the peak shape was consistent with the literature [7], indicating the successful preparation of MIL-101(Cr). MIL-101(Cr) retained the basic structure of the parent MOF after CdTe-QD modification.

X-ray photoelectron spectroscopy (XPS) uses X-ray to radiate the sample, so that the inner layer electrons or valence electrons of atoms or molecules are stimulated to emit. XPS is mainly used to measure the binding energy of electrons to achieve qualitative analysis of surface elements, including valence state, and to achieve quantitative analysis of elements. XPS is used for surface analysis of solid samples to obtain the chemical composition or element composition, atomic valence state, surface energy state distribution, electron cloud distribution, and energy-level structure of surface electrons. XPS spectra of M&C confirmed the existence of C (55.13%), Cd (0.2%), Te (0.2%), O (43.42%), and Cr (1.05%), indicating that CdTe-QDs were successfully loaded on MIL-101(Cr). The C 1-s spectrum showed three peaks at 284.46, 285.34, and 288.57 eV corresponding to C-C/C=O in MIL-101(Cr), C-O, and C=O in CdTe-QDs, respectively. The peaks of Cd 3d appeared at 411.9 and 405.3 eV, corresponding to Cd $3d_{3/2}$ and Cd $3d_{5/2}$ of Cd^{2+}. The peaks of Cr 2p appeared at 587.16 and 577.69 eV were assigned to Cr $2p_{1/2}$ and Cr $2p_{3/2}$ [8], proving the existence of Cr^{3+} in M&C. The binding energies at 582.48 and 572.14 eV in the Te 3d spectrum were attributed to Te $3d_{3/2}$ and Te $3d_{5/2}$ [9]. All the above results indicated the successful preparation of M&C.

UV-Vis diffuse reflectance spectroscopy (UV-Vis DRS) mainly uses the reflection of light on the surface of a substance to obtain information about the substance, which is related to the electronic structure of the substance. It is generally used to study solid materials, which can reflect their structure, oxidation state, coordination state, and coordination symmetry. It can also be used to study the photocatalysis performance of catalysts in photocatalysis or to determine the color difference. In the transition metal ion ligand system, one side is an electron donor, and the other side is an electron acceptor. Under the excitation of light, charge transfer occurs, and the electron absorbs some energy photons from the donor to the acceptor, and the absorption spectrum is generated in the ultraviolet region. When the transition metal ions themselves absorb photons to excite the transition (*d*-*d*) in the internal d orbital, the transition (*d*-*d*) occurs, causing the ligand absorption band, requiring low energy, which is shown as the absorption spectrum in the visible or near-infrared region. For semiconductor materials, energy gap (*E*g) is an important parameter. *E*g is the energy difference between the lowest conduction band and the highest valence band of a semiconductor. The larger the bandgap of a semiconductor is, the harder it is for electrons to be excited from the valence band to the conduction band, the lower the

intrinsic carrier concentration, and the lower the conductivity. The semiconductor's *E*g is generally calculated by UV-Vis DRS. In this study, MIL-101(Cr) exhibited two specific absorption bands centered at 432.5 and 598.5 nm, which were consistent with the study of He et al. [10]. The band of MIL-101(Cr) in the ultraviolet region belonged to the π-π* transition of the ligand, and the band in the visible region can be assigned to the d-d spin permissive transition of Cr^{3+} [11]. It can be seen that the trend of the overall UV-Vis absorption of M&C was consistent with that of MIL-101 (Cr), which was attributed to the absorption of the MIL-101 (Cr), and was consistent with the SEM and other characterizations, indicating that there was no change after compositing. In addition, CdTe-QDs had a broad absorption in the visible region, due to the introduction of CdTe-QDs, which effectively extended the light absorption range of M&C. The results suggested that heterojunction was formed between MIL-101(Cr) and CdTe-QDs, which played a role in enhancing visible light absorption due to the interaction between the MIL-101(Cr) and CdTe-QDs. The bandgap value was calculated by the Tauc plot [11–13], and the formula was as follows:

$$(\alpha h\upsilon)^{1/n} = A\left(h\upsilon - E_g\right) \tag{1}$$

where α is the absorption index, h stands for Planck's constant, υ represents the frequency, A is a constant, E_g is the semiconductor bandgap, and the index n is directly related to the semiconductor type.

The bandgap of M&C was between MIL-101 (Cr) and CdTe-QDs, and the modified M&C with CdTe-QDs was more conducive to light utilization.

3.4 Mechanism Discussion

To further explore the mechanism of the prepared PEC immunosensors, the energy gap (E_g), valence band (E_{VB}), and fermi energy (E_f) of MIL-101(Cr) and CdTe-QDs were investigated using Tauc plot, Mott-Schottky plot (M-S), and ultraviolet photoelectron spectroscopy (UPS). The E_g of MIL-101(Cr) and CdTe-QDs was 2.38 and 1.83 eV, which was similar to the reported results [8, 14]. The M-S curves showed that the flat-band potential (E_{fb}) of MIL-101(Cr) was −0.31 V vs. RHE and the E_{fb} of CdTe-QDs was 1.09 V vs. RHE. Meanwhile, the slope (M-S curve) of MIL-101(Cr) was positive, indicating that it was an n-type semiconductor, and its E_{CB} value was 0.2 eV lower than its E_{fb} value [15]. On the contrary, the slope of CdTe-QDs was negative, revealing that it was a p-type semiconductor, and its E_{VB} value was 0.2 eV higher than its E_{fb} value. The E_{CB} value of MIL-101(Cr) was −0.51 eV vs. RHE, and the E_{VB} value of CdTe-QDs was 1.29 eV vs. RHE, which was calculated using the formula listed below [16]:

$$E_{VB} = E_{CB} + E_g \tag{2}$$

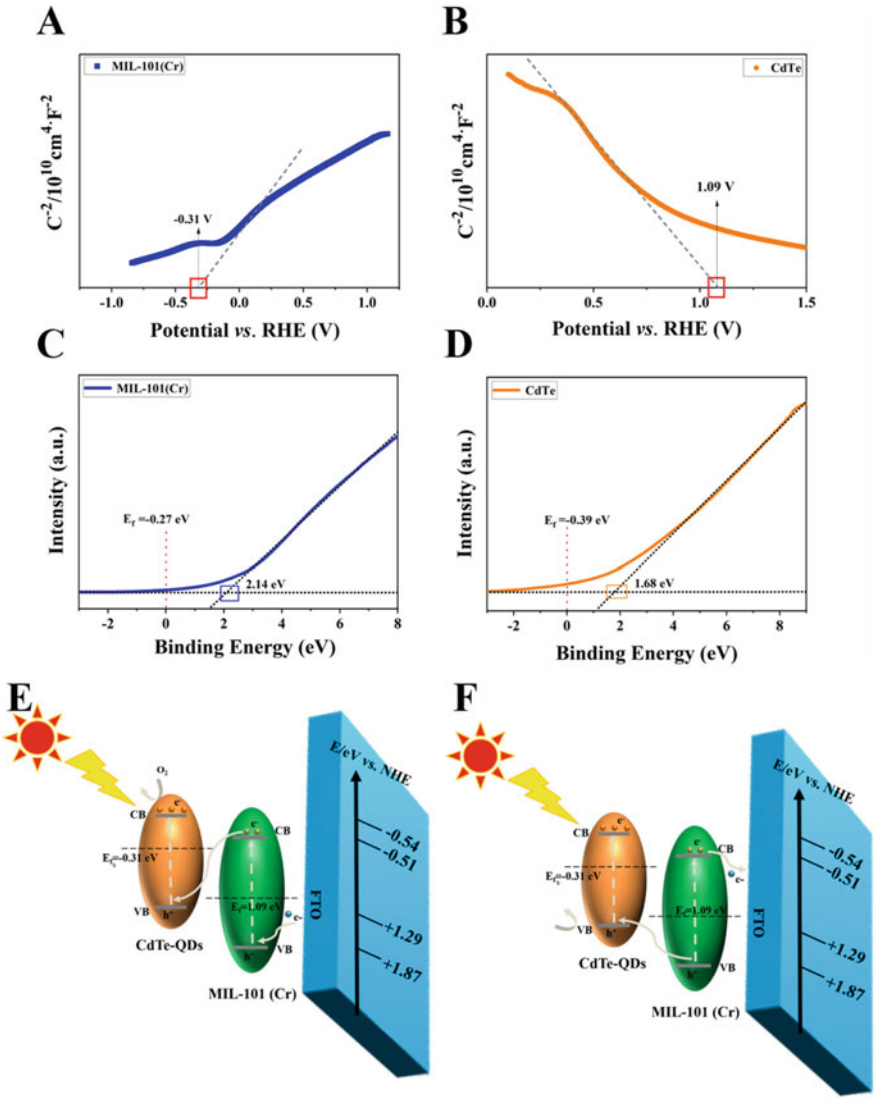


Fig. 4 M-S plots of (**a**) MIL-101(Cr) and (**b**) CdTe-QDs. UPS spectra of (**c**) MIL-101(Cr) and (**d**) CdTe-QDs. Possible electron transport mechanisms for M&C at (**e**) −0.3 V and (**f**) +0.3 V

where E_{CB} is the conduction band (CB) edge potential, E_{VB} stands for the valence band (VB) edge potential, and E_g represents the bandgap energy.

The calculated E_{VB} value of MIL-101(Cr) was 1.87 eV vs. RHE, and the E_{CB} value of CdTe-QDs was −0.54 eV vs. RHE. Therefore, its potential electron transfer path was shown in Fig. 4. When the applied voltage was −0.3 V, the electron transfer path may conform to "II-type" or "Z-type." However, the UPS test results showed

that the E_f of MIL-101(Cr) and CdTe-QDs was −0.39 eV (Fig. 4) and −0.27 eV [17, 18]. Due to their different E_f levels, the charges were redistributed to achieve a balance of E_f levels [19]. Electrons diffused from n-type MIL-101(Cr) (higher E_f) to p-type CdTe-QDs (lower E_f), while holes moved in the opposite direction. Therefore, only a "Z-type" path can be followed [19, 20]. The photogenerated electrons were given from the FTO electrode, at which time the FTO detected the opposite positive charge, resulting in a cathodic photocurrent, after which the electrons were transferred from the VB of MIL-101(Cr) to its CB and then to the VB of CdTe-QDs and finally, reached the CB of CdTe-QDs. Since its CB value was more negative than the potential of $O_2/\cdot O_2^-$ (−0.33 eV) [21], it was able to reduce O_2 in the electrolyte to O_2^-. When the applied voltage was +0.3 V, it was speculated that the applied light source was greater than that of the driving force of the applied voltage on the electrons, and the E_f was not considered, and "II-type" electron transfer pathways were formed. The photogenerated electrons were transported from the CB of CdTe-QDs to the CB of MIL-101(Cr) and finally to FTO surface; thus, the output was in the form of anodic photocurrent. At the same time, the surface electron transfer of CdTe-QDs left electron holes (h^+), and the VB value of CdTe-QDs was more positive than the potential of H_2O/O_2 (1.23 eV), thereby oxidizing H_2O to O_2 in the electrolyte solution [22–24]. Both the photocurrent generation process can be changed by the variation of the applied voltage. The electron-hole recombination rate was reduced, and the PEC performance was improved through the "II-type" and "Z-type" electron transfer pathways.

3.5 Photoelectric Performance Analysis

After the preparation of MIL-101(Cr), the optimum working voltage of MIL-101(Cr) as the working electrode was screened. Applying high potential (anodic or cathodic potential) would adversely affect the surface state of biomaterials and photoelectrodes [25], which was not conducive to the further preparation of PEC immunosensors. Therefore, the applied voltage ranging from −0.3 to +0.3 V was studied. Figure 5a showed that the photocurrent of MIL-101(Cr) changed with the applied voltage and the cathode photocurrent (−34.99 ± 0.02 nA) and anode photocurrent (+ 40.13 ± 0.06 nA) reached the maximum value when the applied voltage was −0.3 V and + 0.3 V, respectively. Apparently, −0.3 V and + 0.3 V were the optimal cathode and anode voltages.

The photocurrent changes of MIL-101(Cr) before and after CdTe-QD modification were also investigated. When the applied voltage was +0.3 V, the anode photocurrent of M&C was 14 times higher than the photocurrent of MIL-101(Cr). In addition, when the applied voltage was −0.3 V, the cathode photocurrent of M&C was 12 times higher than that of MIL-101(Cr). This result demonstrated the efficient separation of photogenerated electron holes.

The effect of CdTe-QD amount on the final photocurrent intensity of M&C was evaluated. The largest photocurrent variation was observed when the CdTe-QDs

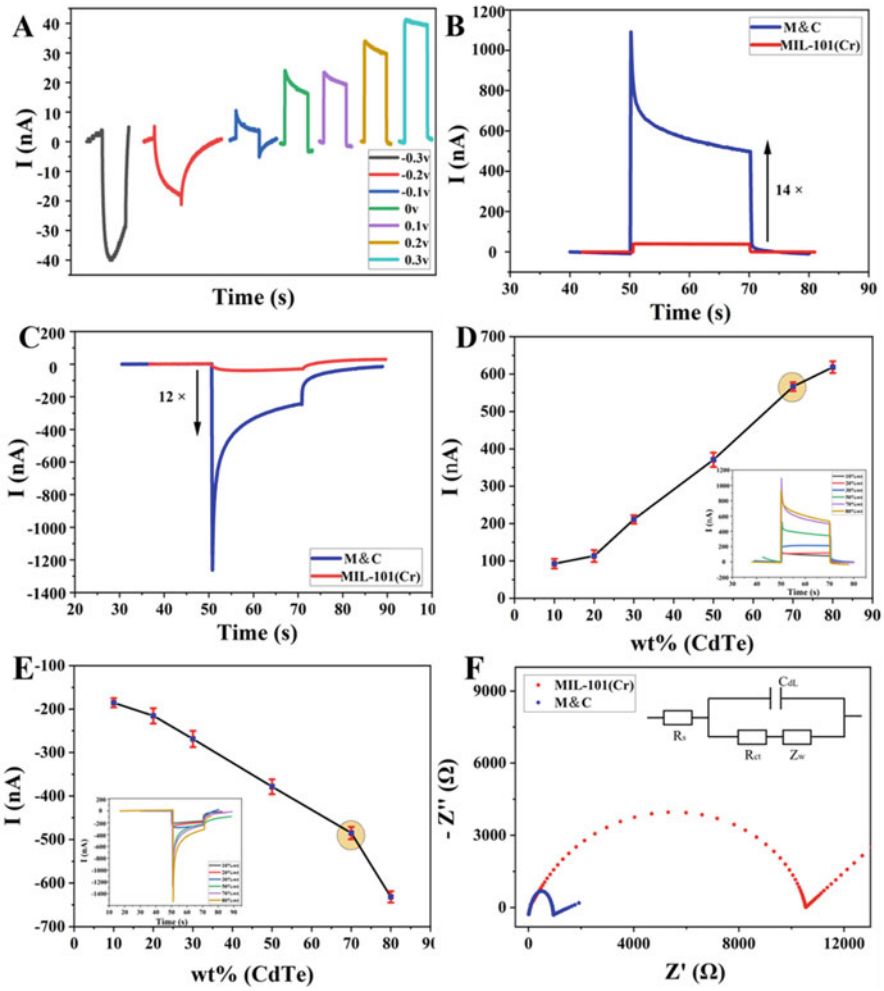


Fig. 5 (**a**) The photocurrent intensity of MIL-101(Cr) changes under different applied voltages. (**b**) Comparison of photocurrent intensities between MIL-101(Cr) and M&C under an applied voltage of +0.3 V and (**c**) –0.3 V. (**d**) Effects of different wt% CdTe-QD additions on M&C photocurrent intensity under the condition of +0.3 V and (**e**) –0.3 V applied voltage. (**f**) EIS spectra of MIL-101(Cr) and M&C. The equivalent circuit including solution resistance (*R*s), charge transfer resistance (*R*ct), Warburg impedance (*Z*ω), and double-layer capacitance (*C*dL) was shown in the illustration

were at 70 wt% in M&C, which was selected as the final working electrode. In addition, electrochemical impedance spectroscopy (EIS) is an effective method to monitor the stepwise fabrication process of the PEC immunosensor. The equivalent circuit was fitted by ZView software, and the results also confirmed each other well with the photocurrent results. The charge transfer resistance (*R*ct) value of

M&C (961.1 Ω) was significantly smaller than that of MIL-101(Cr) (10523.9 Ω), indicating that the electron transport efficiency of M&C was much higher than that of MIL-101(Cr).

During the step-by-step preparation of PEC sensors, the changes in photocurrent and EIS were the key factors to monitor. With the gradual introduction of Ab, BSA, and CEA, the anodic and cathodic photocurrents decreased sequentially, which may be due to the continuously increased steric hindrance of the material interface on the FTO electrode surface, leading to the decrease in excitation efficiency of CdTe-QDs and the photocurrent signal. However, the steric hindrance increased the inhibition rate of CEA on photoelectric conversion. At the same time, with the step-by-step dispensing of the biomaterial, the *Rct* value gradually increased (M&C +Ab, 959.1 Ω; M&C + Ab+ BSA, 977.6 Ω; M&C + Ab+ BSA+ CEA, 1044.1 Ω), which may be caused by the steric hindrance and insulating property of the biomaterial itself that blocked the electron transfer at the interface.

3.6 Optimization of Experimental Conditions

In order to obtain the optimal sensor performance, the optimal use volume of the M&C composites, the ultrasonic mixing time of the composites, the type of solution, the pH of the solution, and the incubation time all needed to be optimized. Experiments were performed at room temperature (25 ± 0.5 °C). Firstly, the effect of the amount of M&C composite material on the performance of the sensor was investigated. The photocurrent response had the largest change trend when the drop-coating volume of the M&C composite material was 75 μL, so 75 μL was selected as the optimal dosage of the M&C composite material. Secondly, the influence of the ultrasonic mixing time of the composite material on the performance of the sensor was investigated. After 30 min of ultrasonication of MIL-101(Cr) and CdTe-QDs, the photocurrent reached the maximum value, and with the extension of the ultrasonic time, the photocurrent strength tended to stabilize. Afterward, the types of solutions were investigated to select the best base solution, M&C had the highest photocurrent intensity in 0.1 M PBS solution, and 0.1 M PBS solution was finally determined as the base solution. The investigation of the photocurrent intensity of M&C in PBS solution under different pH conditions was continued and finally determined that the bottom solution was PBS solution with pH 7.4 as the best buffer solution. Since whether the antigen-antibody can effectively bind had a significant impact on the successful use of the sensor, the optimal incubation time of the antigen-antibody was investigated and selected. The photocurrent achieved the best quenching effect when the antigen-antibody co-incubated for 90 min, and with the prolongation of the incubation time, the photocurrent intensity no longer changed significantly.

3.7 Detection of CEA

Based on the above optimal conditions, a series of concentrations of CEA were detected. The results showed that the photocurrent response changed with the increase of CEA concentration when the applied voltages were +0.3 V and −0.3 V. The signal exhibited good linearity with the concentration in the range from 0.0001 ng·mL^{-1} to 10 ng·mL^{-1}. The anodic photocurrent was fitted to the linear eq. I (nA) = −100.19 log C $_{CEA}$ (ng·mL^{-1}) +59.31 (R^2 = 0.9968, n = 18), and the detection limit was 0.00018 ng·mL^{-1} (S/N = 3). The cathodic photocurrent conformed to the linear eq. I (nA) = 76.17 log C $_{CEA}$ (ng·mL^{-1}) -107.62 (R^2 = 0.9910, n = 18), and the detection limit was 0.00023 ng·mL^{-1} (S/N = 3). For clinical diagnosis, the critical value of CEA was 3 ng•mL^{-1}. Therefore, the prepared PEC immunosensor had sufficient sensitivity to meet the requirement of clinical PEC detection.

3.8 Specificity, Stability, and Reproducibility

Some indicators that may exist in serum and urine sample were selected as interfering substances, bovine serum albumin (BSA), α-fetoprotein (AFP), and prostate antigen (PSA), respectively. Only the sample of 1 ng•mL^{-1} of CEA and the mixed solution of all substances showed large photocurrent changes, whereas the photocurrent response values of other interfering substances exhibited no significant difference to the background noise. Therefore, the prepared immunosensor was specific to CEA.

Stability was an important indicator for evaluating sensor performance. The anodic (with 1 ng•mL^{-1} of CEA) and cathodic (with 0.01 ng•mL^{-1} of CEA) photocurrents did not decay significantly within 600 s. In addition, the prepared immunosensors were stored in a refrigerator at 4 °C. After 15 days, their PEC response value was still preserved at 92%. The above results showed that the prepared sensors were stable during testing. The reproducibility of the sensors was also evaluated. Under the optimized conditions, six electrodes were prepared and incubated with 1 ng•mL^{-1} CEA. When the electrodes were used as the anode, the relative standard deviation (RSD) of the test results was 2.41%. When the electrodes were used as the cathode, the RSD value was 1.20%. The photocurrent intensity of M&C with 1 ng•mL^{-1} CEA for eight repetitive measurements was revealed. The RSD value of the response anodic current is 1.96%, and the RSD value of the response anodic current is 1.16%. These results demonstrated that the PEC sensors had good reproducibility and repeatability for CEA detection.

3.9 Actual Sample Detection

To investigate the feasibility of the prepared M&C PEC sensor in clinical CEA diagnosis, the accuracy of the sensor for CEA detection in actual samples was evaluated by the standard addition method. 0.0005 ng·mL^{-1}, 0.01 ng·mL^{-1}, and 5.00 ng·mL^{-1} of CEA were added to the actual human serum and urine samples. The above results showed that prepared M&C PEC sensor had a recovery of 90.6~103.1% and 90.1~101.2% at the above anodic and cathodic voltage, which covered the practical range of CEA in clinical diagnosis.

4 Tester Model Construction

The PEC immunosensing portable detector was constructed (Fig. 6), wherein the battery pack motor was installed inside the detector main body and the output shaft

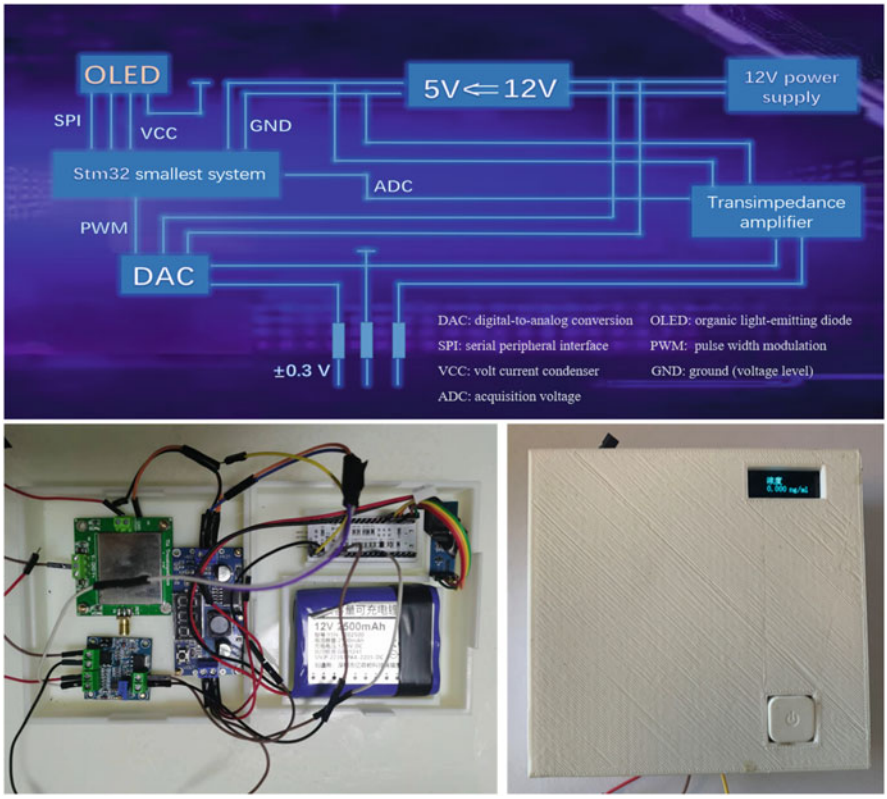


Fig. 6 The internal circuit of the small detector and its actual product structure

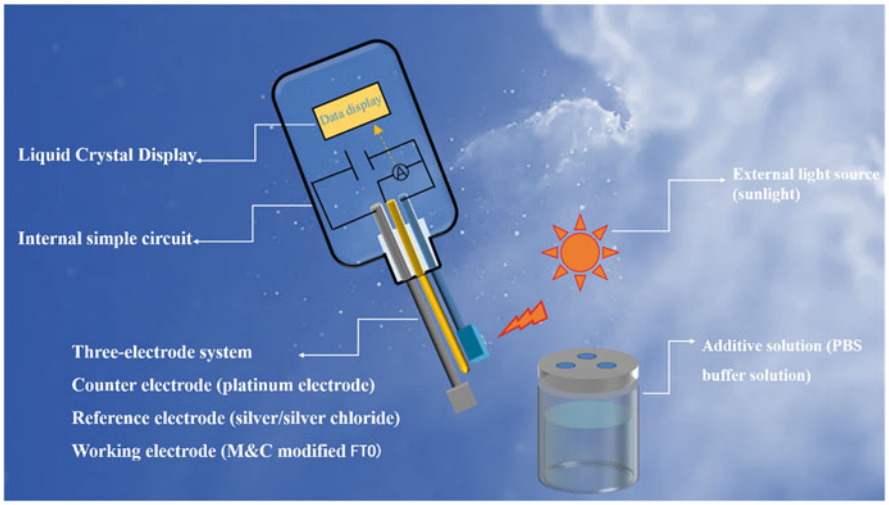


Fig. 7 Structure diagram of CEA small detector

of the battery pack motor was connected to the single-chip microcomputer through a voltage regulator module to generate a stable applied voltage. Convert the analog voltage module to convert the stable voltage output by the microcontroller. One side of the detector was provided with an analog-to-digital converter to generate a stable digital signal with a specific duty cycle, and a transimpedance amplifier component was connected to it to amplify the originally detected low-current signal. The upper part of the main body of the detector was provided with a liquid crystal display screen for reading out the detection results. The sealed casing was installed on the detector body, and the detector battery pack motor and all microprocessors connected to the detector battery pack motor were arranged in the sealed casing. The three electrodes (auxiliary electrode, reference electrode, working electrode) were connected with the analog voltage module and the transimpedance amplifier to ensure the input of the detection signal. The battery pack motor of the detector was embedded into the sealed casing of the detector through transition fit, all microprocessors were fixed by metal clips and black tape, and the liquid crystal display was fixed on the back with black tape, so as to achieve the combination with the casing of the detector.

In the process of CEA detection, the PBS solution and the external light source can be prepared in advance. The PEC portable detector was immersed in the PBS solution, the external light source was irradiated on the surface of the working electrode, and the voltage was adjusted (Fig. 7). The photocurrent intensity corresponded to the concentration of CEA to realize the rapid and portable clinical detection of CEA.

5 Conclusions

A PEC immunosensor for detecting CEA was prepared and validated. However, there are still challenges for the commercial application of the product, and more research is needed for the manufacturing process. The CEA detector is expected to be broadly utilized in the CEA detection in human serum and urine samples.

Acknowledgments This work was supported by the Youqing lift Program of Shenyang Pharmaceutical University (YQ202206) and the Middle-Aged Backbone Personnel Training Program of Shenyang Pharmaceutical University (ZQN2016011).

Credit Authorship Statement **Chunling Mao**: Formal analysis, writing original draft, data curation, performing the experiments, and analyzing the data.

Longshan Zhao: Conceptualization, writing review and editing, conceiving and designing the research.

References

1. Y. Tang, X. Yin, M. Mu, Y. Jiang, T. Ouyang, Colloid Surface A, 596 (2020), p. 124745. https://doi.org/10.1016/j.colsurfa.2020.124745
2. Y. Wang, C. Zhang, X. Chen, B. Yang, L. Yang, C. Jiang, Z. Zhang, Nanoscale, 8 (2016), pp. 5977–5984. https://doi.org/10.1039/C6NR00430J
3. Tan, S.C., Lee, H.K., 2019. Microchim Acta 186(3), 165.
4. Huang, Z., Lee, H.K., 2015. J Chromatogr A. 1401, 9–16.
5. Inoue, K.-I., Ahmed, M., Nihonyanagi, S., Tahara, T., 2020. Nat Commun. 11, 5344.
6. Han, S., Yang, L., Wen, Z., Chu, S., Wang, M., Wang, Z., Jiang, C., 2020. J Hazard Mater. 398, 122894.
7. Mohammadian, R., Amini, M.M., Shaabani, A., 2020. Catal Commun. 136, 105905.
8. Wu, Y., Chen, X., Luo, X., Yang, M., Hou, C., Huo, D., 2021. Anal Chim Acta 1183, 339000.
9. He, Y., Wang, Y., Mao, G., Liang, C., Fan, M., 2022. Anal Chim Acta 1191, 339251.
10. He, J., Yan, Z., Wang, J., Xie, J., Jiang, L., Shi, Y., Yuan, F., Yu, F., Sun, Y., 2013. Chem Commun. 49, 6761–6763.
11. Tauc, J., Grigorovici, R., Vancu, A., 1966. phys. stat. sol. 15, 627–637.
12. Davis, E.A., Mott, N.F., Mag, P., 1970. 22.
13. Tauc, J.F.A.E., 1972. Optical Properties of Solids North-Holland, NJ.
14. Guo, Z., Jiang, K., Jiang, H., Zhang, H., Liu, Q., You, T., 2022. J Hazard Mater. 424, 127498.
15. Zou, X., Dong, Y., Ke, J., Ge, H., Chen, D., Sun, H., Cui, Y., 2020. Chem Eng J. 400, 125919.
16. Jiang, J., Zhang, X., Sun, P., Zhang, L., 2011. J. Phys. Chem. C. 115, 20555–20564.
17. Wen, Z., Zhu, W., You, F., Yuan, R., Ding, L., Hao, N., Wei, J., Wang, K., 2022. Biosens. Bioelectron. 203, 114036.
18. Zhang, Y., Hu, Y., Zhao, J., Park, E., Jin, Y., Liu, Q., Zhang, W., 2019. J Mater Chem A. 7, 16364–16371.
19. Li, Z., Zhao, Y., Guan, Q., Liu, Q., Khan, S., Zhang, L., Wang, X., Chen, L., Yang, X., Huo, M., 2020. Appl Surf Sci 508, 145225.
20. Deng, H., Xiao, M., Chai, Y., Yuan, R., Yuan, Y.J.B., bioelectronics, 2022. Biosens. Bioelectron. 197, 113806.
21. Xue, W., Huang, D., Li, J., Zeng, G., Deng, R., Yang, Y., Chen, S., Li, Z., Gong, X., Li, B., 2019. Chem Eng J. 373, 1144–1157.
22. Di, T., Zhu, B., Zhang, J., Cheng, B., Yu, J., 2016. Appl Surf Sci. 389, 775–782.

23. Wolff, C.M., Frischmann, P.D., Schulze, M., Bohn, B.J., Wein, R., Livadas, P., Carlson, M.T., Jäckel, F., Feldmann, J., Würthner, F. Stolarczyk, J.K., 2018. Nat. Energy. 3, 862–869.
24. Zhang, L., Wang, G., Hao, X., Jin, Z., Wang, Y., 2020. Chem Eng J. 395, 125113.
25. Yang, R., Yan, X., Li, Y., Zhang, X., Chen, J., 2017. ACS Appl Mater Inter. 9, 42482–42491.

Scanning Photodielectric Spectroscopy of CdZnTe Crystals



Oleg Chugai, Oleksii Poluboiarov, Serhii Oliinyk, and Sergei Sulima

1 Introduction

It is well known that the study of localized states (LS) of carriers in semiconductors plays an important role in solving a wide range of problems, both scientific and practical. Although today a number of methods for studying of localized states are known (TEES, PICTS, PL, and others), the improvement of known, as well as development of new, methods is an urgent problem in the physics of semiconductors. The fact is that in recent decades, there has been a rapid expansion of the objects under study, including nanostructures, as well as the types of point defects in crystals that give rise to localized states. Therefore, when choosing one or another method for studying crystals, it is important to take into account the features of their defect-impurity composition and, accordingly, the nature of the indicated states of carriers. In particular, in the presence of bistable and metastable defects in crystals (see, for example, [1, 2]), external impact on the crystal associated with the measurement procedure, including heating [3], should not cause their transition to a new state with a different position of the energy level in the bandgap. An obvious condition for this is the minimum intensity of external impact on the crystal during measurement. Next, we describe the method of scanning photodielectric spectroscopy (SPDS), which makes it possible to measure the energy spectrum of localized states of carriers, as well as the near-surface electrostatic potential of a semiconductor under a weak effect of a light flux and an electric field. Different variants of application of this method in the investigation of crystals $Cd_{1-x}Zn_xTe$ ($x = 0.12$ ... 0.16) are given. Numerous research have been devoted to studies

O. Chugai · O. Poluboiarov (✉) · S. Oliinyk · S. Sulima
National Aerospace University Kharkiv Aviation Institute, Kharkiv, Ukraine

© The Author(s), under exclusive license to Springer Nature Switzerland AG 2024

S. Krishnamoorthy, K. (Kris) Iniewski (eds.), *Advances in Fabrication and Investigation of Nanomaterials for Industrial Applications*,
https://doi.org/10.1007/978-3-031-42700-8_6

of energy spectra of carriers' localized states in connection with the possible application in uncooled gamma radiation detectors.

2 Scanning Photoelectric Spectroscopy Without Additional Impact on the Semiconductor

The photodielectric effect (PDE) has been known as long as the photoconductivity effect. We have proposed new features of PDE registration and presentation of the obtained data, which form the basis of the SPDS method. Thus, when measuring the spectral dependences of this effect, it was proposed for the first time to consistently measure with the highest sensitivity the increments of the real $\Delta\varepsilon'_{ef}$ and imaginary $\Delta\varepsilon''_{ef}$ parts of the complex permittivity effective values under the impact of light. The resulting spectral dependences of the parameters are presented in the form of a diagram in the complex plane. In such a diagram, characteristic sections are distinguished, each of which corresponds to the photoexcitation of one type of localized states with its own depth of occurrence in the crystal bandgap.

$Cd_{1-x}Zn_xTe$ (CdZnTe) crystals were grown by Bridgman technique from melt under high pressure of argon ($P \approx 100$ atm). The content of zinc in the solid solution was measured by the method of electron probe microanalysis using a scanning electron microscope JEOL JSM-820 equipped with a system of the X-ray microanalysis LINK 10000, while the concentration of foreign impurities was measured by the method of laser mass spectrometry using the EMAL-2 device. The integral level of concentration did not exceed 10^{-4} mass% for 75 elements. Structure quality of crystals was controlled by the X-ray diffraction method using a two-crystal X-ray diffractometer on the basis of DRON-3. According to the obtained data, the investigated samples were free of low-angle (~ > 10 arcsec) boundaries and twins, and the mean halfwidth of the diffraction rocking curve was in the range of 16 to 20 arcsec. Thin plates were prepared by chopping off a single crystal parallel to the plane (110) to be used as samples. Two electrical contacts of In were applied to one side of the plate at a distance 5 mm, thus forming a planar system. The open part of the sample surface was exposed to monochromatic light ($\lambda = 0.6...1.8$ μm). The electric capacity and the tangent of the dielectric loss angle of the planar system were measured by the automatic bridge of the alternating current R589 or LCR-meter Instek LCR-819.

In Fig. 1b, one can see that the diagram is represented by a system of linear segments. The numbering corresponds to the increase in photoexcitation wavelength (Table 1). The wavelengths restricting the segments were determined by the method of sectionally linear approximation of the experimental curve (Fig. 1a). It should be emphasized that unlike relative extension of the adjacent segments and the angles between them the wavelengths are well reproduced by repeat measurements (the error is not worse than several tenths of a percent).

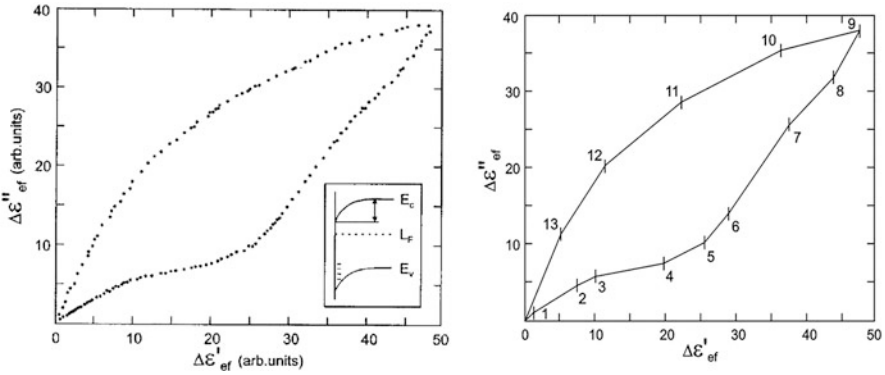


Fig. 1 (**a**) Typical spectral dependence of increments of the real $\Delta\varepsilon'$ and imaginary $\Delta\varepsilon''$ parts of effective dielectric permittivity for $Cd_{0.86}Zn_{0.14}Te$ crystal at the photoexcitation ($\lambda = 0.6...1.8\ \mu m$) and (**b**) the same after sectionally linear approximation of the experimental curve

Table 1 Acceptor levels in CdZnTe crystals revealed by different methods

Method of photodielectric spectroscopy			Other Methods		
Part no.	λ_i (nm)	Energy (eV)	Energy[a] (eV)	Energy[b] (eV)	Probable origin[b]
1	782	$E_v + 0.019(0.091)$	...	...	...
2	795	$E_v + 0.045(0.085)$	...	...	...
3	800	$E_v + 0.055(0.095)$	...	...	...
4	810	$E_v + 0.074(0.106)$	...	...	...
5	830	$E_v + 0.11$	$E_v + 0.12$	$E_v + 0.10 \ldots 0.16$	Complex impurity-V_{Cd}
6	840	$E_v + 0.13$	$E_v + 0.14$	...	A-center
7	850	$E_v + 0.15$	$E_v + 0.15$	...	Impurity in Cd sites
8	870	$E_v + 0.18$	$E_v + 0.20$	$E_v + 0.19$–0.22	V_{Te}
9	895	$E_v + 0.22$	...	...	...
10	908	$E_v + 0.24$	$E_v + 0.25$	$E_v + 0.27 \ldots 0.29$	C, Si atoms
11	930	$E_v + 0.27$	...	...	...
12	960	$E_v + 0.31$	$E_v + 0.32$	$E_v + 0.35 \ldots 0.41$	Complex V_{Cd}
...	...	...	$E_v + 0.43$	$E_v + 0.46 \ldots 0.50$	Structure defect connected with deformation
13	1155–1175	$E_v + 0.53 \ldots 0.55$	$E_v + 0.57$	0.60	Zn atoms in a complex
...	...	...	$E_v + 0.76$	0.75	Phonon impurities and vacancies

[a]See ref. [4]
[b]See ref. [5]

Another essential peculiarity of the diagrams consists of a regular variation of the ratio $\Delta\varepsilon''_{ef}/\Delta\varepsilon'_{ef}$ when passing toward the long-wave region. At the same time,

in the short-wave region of photosensitivity, this ratio has a tendency to decrease, while in the long-wave one its tendency is to increase.

Good reproducibility of the boundary wavelengths of the linear segment of the diagram $\Delta\varepsilon''_{\text{ef}}(\lambda) - \Delta\varepsilon'_{\text{ef}}(\lambda)$ allows one to correlate these segments with the intrinsic structure defects of crystals. Quantitatively, this is confirmed by the data presented in Table 1.

Table 1 shows the long-wave boundaries of the segments λ_i and the corresponding depths of occurrence of the acceptor levels, photoionization of which leads to the formation of a free electron. The manifold of λ_i values was determined by comparison of the mentioned diagrams for several samples having the same composition $Cd_{0.84}Zn_{0.16}Te$. The bandgap used for calculation (1.6 eV) was determined by extrapolation, taking into account the Vegard's rule and the data [5]. As it is seen from Table 1, the majority of the acceptor levels determined by the method of scanning photodielectric spectroscopy coincide well with the known ones obtained by several methods. This being so, a number of levels (corresponding to segments 1–4) were observed for the first time. Comparing these levels with the following four ones, one can see that the difference in their energy position, that is, E_5–E_1, E_6–E_2, E_7–E_3 3, and E_8–E_4 (given in Table 1 in parentheses), represents a nearly constant value for different pairs of levels. In other words, the first four levels are characterized by approximately the same energy shift (~0.094 eV) with respect to the next four ones. The reason for this could be the existence of an additional electric potential near the surface ($\Delta\phi_s$) and the corresponding curvature of the energy bands of the crystal [6] (inset, Fig. 1a). Simultaneously, the condition for the participation of photocarriers excited from the levels in the subsurface region in PDE will be transfer of additional energy $\Delta\phi_s e$ (e is the electron charge) to them, the latter being necessary for the carriers to get into the crystal volume. Let us note that the levels $E_v + 0.43$ eV and $E_v + 0.76$ eV are not revealed by this method. As one of the reasons for this, we can mention peculiarities of the formation of defects and their complexes under certain growth conditions and composition of the background impurities.

Each of the linear segments of the diagram $\Delta\varepsilon''_{\text{ef}}(\lambda) - \Delta\varepsilon'_{\text{ef}}(\lambda)$ can be correlated with the dominating influence of the photoionization centers on the variation of dielectric parameters, those centers being in a particular energy state. At the same time, the increasing of light photoexcitation wavelength within the limits of the segment favors a deeper penetration of light in the crystal volume and leads to weakening of the surface recombination effect. As a result, we see growth of a quantity of free electrons Ne, ionized centers $\sum_i N_i^+$, and neutral centers $\sum_i N_i^0$ but occurring in the excited state after capture of an electron. The contribution to the dielectric parameters made by electrons and the mentioned centers is proportional to their quantity, and this explains the linearity of a separate segment of the diagram.

The qualitative changes in the considered process occur when the energy of the light quantum becomes lower than the ionization energy E_i of the dominating centers. After this, the photodielectric effect will be defined by the states with the closest lower value of E_i. Perhaps, as is the case for hydrogen-like impurity centers [7], polarizability of deep centers in the ground α_o and in the excited α_s states is

defined by E_i. That is why we observe the previously mentioned regular variation of the ratio $\Delta\varepsilon''_{ef}/\Delta\varepsilon'_{ef}$ when passing toward the longer-wavelength region.

It should be specified that with heating (25–100 °C) the response preserves its form but the boundary wavelengths of the linear parts vary. The relative variations of E_i are comparable in the order of value to the analogous variation of the bandgap of CdTe crystals. In our opinion, this gives evidence of a high sensitivity of the scanning photodielectric spectroscopy method.

In order to confirm the correlation of the linear parts of the diagram $\Delta\varepsilon''_{ef}(\lambda) - \Delta\varepsilon'_{ef}(\lambda)$ with the intrinsic structure defects of the studied crystals, we incorporated Ag atoms by means of diffusion from the chipped surface. It was supposed that the atoms would interact with the intrinsic structure defects and that this would be reflected on the diagram. While the form as a whole and the boundary wavelength λ_i of most segments were preserved, the boundaries of some parts changed noticeably due to silver diffusion. There appeared three new segments. In particular, there appeared one with $\lambda_i = 816$ nm, which corresponds to the energy level $E_v + 0.086$ eV. This value is in accordance with the previous data [8] on the depths of occurrence of A centers ($E_v + 0.060$–0.100 eV) formed with the participation of Ag atoms in CdTe crystals. These atoms probably interact with other intrinsic defects, thus explaining the previously mentioned changes of the diagram $\Delta\varepsilon''_{ef}(\lambda) - \Delta\varepsilon'_{ef}(\lambda)$.

3 Scanning Photoelectric Spectroscopy Under Impact of Bias Electric Field

Approbation of the SPDS method on CdZnTe crystals showed that in this case only localized states of the acceptor type with the energy levels located in the lower half of the bandgap are revealed, as well as states with the ionization energy exceeding the bandgap width (~ 1.6 eV [5, 9]). Therefore, it was of interest to expand the energy spectrum of the states identified by the SPDS method, as well as to ascertain the nature of the states with an extraordinary high photoionization energy. To achieve these goals, it was proposed to create structures with a Schottky barrier based on CdZnTe crystals. Applying a biasing electric field to such structure will cause a shift in the Fermi level E_F in the area of the barrier and, as a consequence, recharging of the states close to this level. Due to this, the states will be revealed by the SPDS method.

The samples were rectangular-shaped (12 × 12 × 0.8 mm). After grinding and polishing, their faces were subjected to chemical etching, which provided removal of the damaged layer. We used pressure contacts, one of which was the In plate, and the other was the SnO_2 layer deposited on the fused quartz plate. This electrode is transparent in a wide spectral region. The location of electrodes on the sample and the direction of photoexcitation are schematically shown in Fig. 2. The measurements were carried out under standard conditions using an R5016 AC

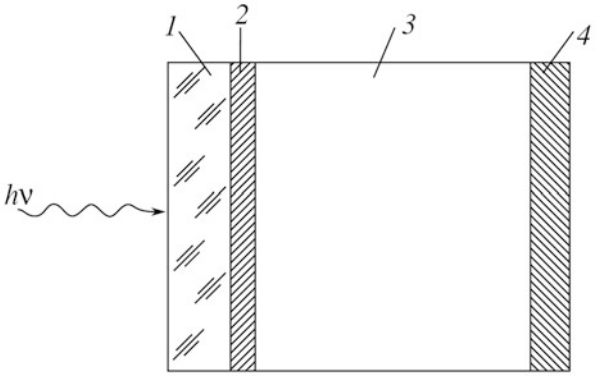


Fig. 2 Arrangement of transparent (*2*) and opaque (*4*) electrodes on the sample (*3*); (*1*) denotes the quartz substrate

bridge. The electric field frequency was 10 kHz, and the voltage across the sample was 9 V. The bias electric field in the sample was induced using the external DC voltage source.

3.1 Spectral Distribution of the Photodielectric Effect and Energy Spectrum of Localized States at Various Bias Voltages

Figure 3 shows the dependences $\Delta\varepsilon''_{\text{ef}}(\lambda) - \Delta\varepsilon'_{\text{ef}}(\lambda)$ in the complex plane typical for the investigated crystals, which were measured in the absence of the bias voltage across the sample and at its opposite polarities. Notice that upon the forward polarity of the mentioned voltage (V_{f}), the negative potential was applied to the illuminated electrode and the positive potential was applied to the *p*-type semiconductor (*p*-type of conductivity of the investigated crystals was specified in [10]). Upon the reverse polarity of the bias voltage (V_{r}), the signs of applied potentials, naturally, were opposite to those mentioned above. It is evident from Fig. 3 that, irrespective of the polarity of the voltage *V*, its application causes the variation in the shape and relative length of the portions of the dependence, which correspond to the same spectral intervals. It is noteworthy that at V_{r} compared with V_{f}, qualitative distinctions of the diagram $\Delta\varepsilon''_{\text{ef}}(\lambda) - \Delta\varepsilon'_{\text{ef}}(\lambda)$ were observed, since $\Delta\varepsilon'_{\text{ef}}\square$ has the negative sign in the shorter-wavelength region in this case.

When determining the boundary wavelengths for characteristic portions λ_i of the mentioned dependences, we used the computer data processing. These quantities were found from the condition of the local extremum of the second-order derivative $\frac{d^2(\Delta\varepsilon''_{\text{ef}})}{d(\Delta\varepsilon'_{\text{ef}})^2}$. The energy levels of localized states were calculated under the assumption

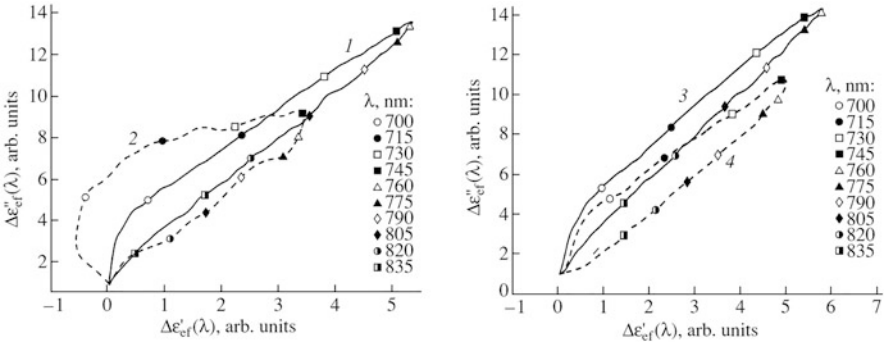


Fig. 3 Spectral dependences of effective values of the real and imaginary parts of CdZnTe crystal dielectric permittivity for (**a**) the reverse and (**b**) forward polarities of the electric bias 150 V (*2*, *4*). (*1*) Initial state of the crystal and (*3*) the state of the crystal after switching off of the reverse bias

that absorption of a photon with the energy E_i causes the electron transfer from the localized state to the conduction band [9].

The energy spectra of the localized states typical of the crystals investigated at various forward biases applied to the sample and the energy spectrum known from the available publications are listed in Table 2. The energies of the states are given relative to the valence band top E_v. It is evident that, irrespective of V_f, the energy levels of a series of states agree well with those observed previously. However, there are states for which E_i is close to E_g and even exceeds this magnitude, due to which the levels which are associated with them are located near or below the valence band top. We should also note the whole series of values of E_i, which are coupled to each other by "the rule of shift by ΔE." The essence of this rule is that the level turns out to be shifted relative to any level which is observed at the lower V_f, by the same magnitude ΔE, i.e., $E_i(V_2) = E_i(V_1) + \Delta E$ (indices V_1 and V_2 correspond to the lower and higher V_f). In Table 2, the levels coupled by the mentioned rule are marked by identical superscripts or subscripts. The multiplication ΔE is given in brackets to the right of $E_i(V_f)$. It should be noted that a series of energy levels in the upper part of Table 1 vanishes or emerges under the effect of the electric field not following the rule of "shift by ΔE." However, the levels which are located close to the valence band top E_v compared with the level $E_v + 0.16$ eV, as a rule, retain their location at various values of V_f.

Another essential feature of the presented energy spectra consists in the vanishing of a series of levels which are distant from the valence band top more than $E_v + 0.16$ eV, under the effect of the bias field (see Table 2). This phenomenon is accompanied by the formation of a range free of energy levels, which is extended with V_f. The described features of the energy spectra were also observed in the case of applying V_f to the structure under study. However, the sign of the shift of the levels ΔE was negative in this case.

In order to reveal the nature of the levels, which do not follow the above-described rule, the diagram $\Delta\varepsilon''_{ef}(\lambda) - \Delta\varepsilon'_{ef}(\lambda)$ for the sample with the highest sensitivity was investigated depending on the duration of the effect of the bias

Table 2 Energy spectra of localized states in the $Cd_{0.86}Zn_{0.14}Te$ crystals measured by various methods

Possible nature [5]	Energy, eV				
	The TSC, TEES, and PICTS methods	Method of scanning photodielectric spectroscopy			
		$V_f = 0$ V	$V_f = 100$ V	$V_f = 150$ V	$V_f = 200$ V
					−0.98
		−0.81[1]			
					−0.74
			-0.67^{1}_{a}(0.14)		
		−0.62[2]		-0.60^{1}_{a}(0.07)	
		−0.57[3]			−0.56[1] (0.04)
		−0.54[4]	-0.53_{b}		
				−0.49[2]	
		−0.45[5]	-0.46^{2}_{c}(0.16)		−0.46[2] (0.03)
			-0.42^{3}_{d}(0.15)	-0.43_{b} (0.10)	−0.42
		−0.38[6]	−0.39[4] (0.15)		
		−0.36[7]	−0.37	-0.36^{3}_{c}(0.10)	−0.36
			-0.35_{e}		
				-0.34_{d} (0.08)	−0.33[3] (0.03)
		−0.30[8]	-0.31^{5}_{f}(0.14)		
		−0.28[9]		-0.28^{4}_{e}(0.07)	−0.29
		−0.27			−0.26
		−0.25	-0.25_{g}		
		−0.24	−0.24[6] (0.14)	-0.24^{5}_{f}(0.07)	−0.24[4] (0.04)
			-0.23^{7}_{h}(0.14)	−0.23	
		−0.21	−0.20	−0.21	−0.21[5] (0.03)
		−0.19[10]	−0.18		−0.18
		−0.17[11]		-0.17_{g} (0.08)	
			−0.16[8] (0.14)	-0.16_{h} (0.07)	
			-0.15^{9}_{i}(0.13)		
		−0.14[12], −0.13			
		−0.10[13], −0.08[14]		-0.08^{6}_{i}(0.07)	
			−0.06[10] (0.13)		−0.06[6] (0.02)
		−0.04, −0.02	−0.02[11] (0.15)		−0.03
			−0.01[12] (0.13)	−0.01	
		0.02[15]	0.04[13] (0.14)		
		0.06[16], 0.07[17]	0.07[14] (0.15)		

(continued)

Table 2 (continued)

Possible nature [5]	Energy, eV				
	The TSC, TEES, and PICTS methods	Method of scanning photodielectric spectroscopy			
Impurity–V_{Cd} complex		0.09[18], 0.11			
A center	0.10–0.16				
Impurity at the Cd sites		0.15	0.17[15] (0.15)	0.16, 0.17	0.16
			0.18, 0.19	0.18, 0.19	0.18, 0.19
V_{Tc}	0.19–0.22	0.20	0.20[16] (0.14)	0.20	0.20
		0.21, 0.22	0.21[17] (0.14)	0.21, 0.22	0.21, 0.22
		0.23, 0.24	0.24[18] (0.15)	0.23	0.23
		0.25, 0.26		0.25	
C and Si atoms	0.27–0.29	0.27			
				0.32	
			0.33, 0.34		
V_{Cd} complex	0.35–0.41				0.36, 0.38
Structural defect associated with deformation	0.46–0.50	0.49			

voltage $V_f = 100$ V. The energy spectra of localized states obtained in this case are given in Table 3. One can see that the prolonged electrical bias mainly affects the spectral components located above the level $E_v + 0.10$ eV.

3.2 The Schottky Barrier in the Region of Illuminated Electrode: The Condition for the Effect of the Barrier on the Results of Measurements

The described systematic trends in the effect of the bias electric field on the diagrams $\Delta\varepsilon''_{ef}(\lambda) - \Delta\varepsilon'_{ef}(\lambda)$ can be interpreted using the notions of the potential barrier in the metal-semiconductor contact region (the Schottky barrier). A substantial effect of such a barrier on the photodielectric effect is evidenced by the abovementioned observation of negative values of $\Delta\varepsilon'_{ef}$, since a decrease in the capacitance under the effect of illumination is characteristic of the structures with the Schottky barrier [11].

Table 3 Energy spectra of localized states in one of the $Cd_{0.86}Zn_{0.14}Te$ crystals at various durations of the effect of the electric bias

Crystal without bias	Crystal after prolonged bias		
	1 h	3 h	17 h
−1.52			
−1.31			
	−1.28		
		−1.20	−1.22
	−1.19		
−1.12		−1.10	−1.12
	−1.09		−1.09
−1.06			−1.06
−1.02	−1.03		
	−0.99	−1.00	
−0.96			−0.94
−0.91	−0.90		
			−0.88
−0.84			
	−0.80	−0.81	−0.79
−0.76	−0.76	−0.77	
−0.73, −0.69			
−0.32	−0.30	−0.29	−0.30
	−0.25	−0.23	−0.25
−0.22, −0.19	−0.19	−0.19	
−0.17, −0.16	−0.17, −0.16	−0.17	−0.17
	−0.14, −0.13	−0.13	
−0.11	−0.11	−0.10	−0.11
−0.07	−0.07	−0.06	−0.07
			−0.04
−0.02	−0.01		
0.01, 0.03	0.02	0.03	0.02
0.06	0.05, 0.06	0.05	0.05, 0.06
		0.07	0.07, 0.08
0.09	0.10, 0.11	0.10, 0.11	0.10, 0.11
0.12, 0.14		0.2	
0.16	0.16	0.16	0.15, 0.16
0.17, 0.18	0.17, 0.18	0.17, 0.18	0.17, 0.18
0.19	0.19, 0.20	0.19, 0.20	0.19, 0.20
0.21, 0.22	0.21	0.21, 0.22	0.21, 0.22
0.23, 0.24	0.23	0.23	0.23, 0.24
0.25	0.25	0.25, 0.26	0.25, 0.26
0.27	0.27	0.28	
	0.31		0.30
0.44	0.43		0.42
		0.48	
	0.57		0.55

Strictly speaking, the investigated structures involve two such barriers formed by each of the electrodes and the semiconductor. However, it will be further shown that only the barrier in the region of the illuminated contact exerts a determining effect on the diagrams $\Delta\varepsilon''_{\text{ef}}(\lambda) - \Delta\varepsilon'_{\text{ef}}(\lambda)$. For further consideration, it is important to estimate the width of the mentioned barrier, which, in the approximation of an abrupt boundary of the depletion layer, is determined by the formula [12].

$$W = \sqrt{\frac{2\varepsilon_0\varepsilon'\left(V_{\text{bi}} - V_{\text{bf,br}} - \frac{kT}{e}\right)}{e\,(N_a - N_d)}}. \tag{1}$$

Here, ε_0 is the permittivity of free space, ε' is the relative permittivity, e is the elementary charge, $(N_a - N_d)$ is the concentration difference of charged acceptors and donors, V_{bi} is the contact potential difference, $V_{\text{bf,br}}$ is the potential drop in the barrier region upon forward or reverse polarity of V, k is the Boltzmann constant, and T is the absolute temperature. According to the results of our measurements, ε' is in the range of 12–15. Assuming that $(N_a - N_d)$ is 10^{14}–10^{15} cm^{-3} [13] and $(V_{\text{bi}} - V_{\text{bf,br}} - kT/e)$ is 1 V, according to relation (1), we find that the value of W for the investigated crystals is on the order of several micrometers. It is evident that, when realizing the SPDS method, the Schottky barrier plays the determining role only if the states are excited by strongly absorbing light. In this case, for the optical absorption coefficient α, the following inequality is satisfied:

$$\alpha W \geq 1. \tag{2}$$

If the structure is exposed to weakly absorbing light, the states in the crystal bulk will make the main contribution to the quantities $\Delta\varepsilon'_{ef}$ and $\Delta\varepsilon''_{ef}$, and the effect of the barrier on the results of measurements can be disregarded. This circumstance is also equally related to the potential barrier in the region of the nontransparent electrode. For the given value of W according to relation (2), we find that, in the case of strongly absorbing light, α should exceed 10^{-3} cm^{-1}. Our measurements showed that such large values of α correspond to photon energies exceeding 1.53 eV. Such photons excite the states with energy levels located above the level $E_{\text{v}} + 0.10$ eV.

3.3 Energy Spectrum of Localized States at Opposite Bias Polarities

3.3.1 The Bias Is Absent

Considering the dependences $\Delta\varepsilon''_{\text{ef}}(\lambda) - \Delta\varepsilon'_{\text{ef}}(\lambda)$ for the CdZnTe crystals under various experimental conditions, let us initially consider the energy band diagram of the metal-*p*-semiconductor contact in the absence of V (Fig. 4a). As the wavelength of light is decreased, starting with the long-wavelength edge of photosensitivity, the first revealed portions would be those corresponding to electron transitions from

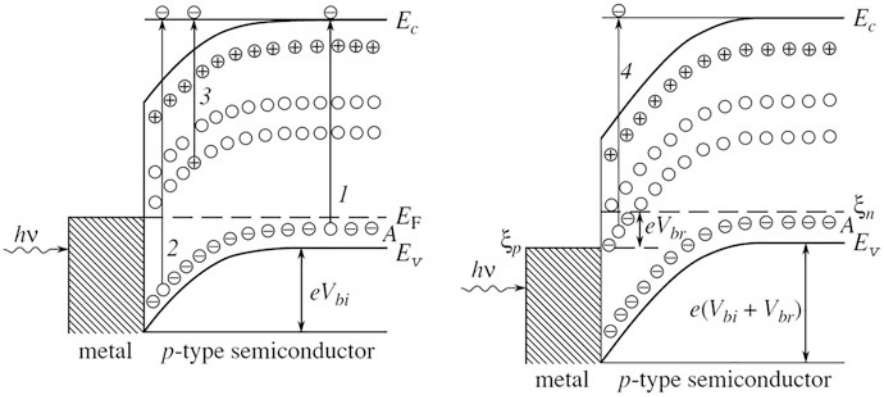


Fig. 4 Band diagrams of the Schottky barrier near the surface of *p*-type semiconductor (**a**) in the absence of the bias and (**b**) under the reverse bias

the energy levels A in the bandgap (transitions 1). As λ decreases, levels located increasingly nearer to the valence band top will be revealed in the energy spectrum. The effect of the Schottky barrier on the localized states will manifest itself in the fact that the levels located near the valence band top will be "repeated" with the further decrease in λ with the shift by the energy value approximately equal to eV_{bi} (transition 2). This circumstance is caused by both the almost complete absorption of the short-wavelength light in the potential barrier region and by the necessity to transfer the electrons to the conduction band bottom E_c in the crystal bulk.

We can conventionally associate the energy levels with the transition 2. Some of them will be located below the valence band top. We find these very levels under all measurement conditions (see Tables 2 and 3). In this context, it is of fundamental significance whether the levels corresponding to largest values of E_i are associated with ionization of electrically neutral acceptors (transitions 3) or not. The level $E_v - 0.98$ eV, which is observed at $V_f = 200$ V (see Table 2), in principle, can be interpreted as the result of the effect of high contact potential difference on one of the known acceptor levels. However, in this case, we should assume that V_{bi} exceeds 1 V. This assumption seems to be unrealistic from the viewpoint of the known data. For example, the largest value of V_{bi} (0.81 V) was found for the contact of CdTe with Ag [12]. However, Table 2 involves the levels located above the level $E_v - 1.00$ eV.

3.3.2 The Bias Is Applied

The given interpretation of the energy spectrum of localized states is confirmed by the results obtained under the effect of the bias voltage on the investigated structures. It is known that, at the bias V, the Fermi level in the Schottky barrier region is split into the quasi-Fermi levels of electrons (ξ_n) and holes (ξ_p) (Fig. 4b). Let us assume

[14] that both quasilevels are horizontal, ξ_n coincides with E_F in the crystal bulk, and ξ_p coincides with E_F in the metal. In addition, the conditions [15] are satisfied, according to which filling of the centers is determined only by their location relative to ξ_n.

The effect of the bias voltage will apparently affect only the states excited by the strongly absorbed light. In this case, the energy levels exert the shift equal to $eV_{bf,br}$. The abovementioned shift of the energy levels, whose sign is determined by polarity of V, can be attributed to this fact. The specific feature of the energy spectrum at $V_f = 100$ V (see Table 2) is the fact that a series of levels with superscripts 8–12, due to the shift, coincide with the levels in the crystal bulk, which correspond to transitions 1 (see Fig. 4a).

The states located sufficiently close ($\sim eV_{bf,br}$) to E_F exert radically different variations under the effect of V. For example, due to the application of V_f, the states located below E_F will shift above ξ_n and become electrically neutral. As a result, transitions 4 will be impossible (see Fig. 4b), and the corresponding energy level will vanish. Disappearance of the level $E_v + 0.49$ eV from the spectrum on the application of V_f to the structure under study can possibly be attributed to this fact. Alternatively, on the application of V_r, the states can shift below ξ_n. This phenomenon will give rise to a new energy level, which was observed in our experiments.

3.3.3 Various Effects of the Bias Voltage on the Localized States

Strictly speaking, the described recharging of the localized states also affects the transitions 3 (see Fig. 4a) which occur with the involvement of electrically neutral states near E_F. In this case, application of V_f should cause vanishing of the spectral levels which correspond to the largest values of E_F. However, the above data do not allow us to identify such variations in the energy spectrum unambiguously. This is caused by the existence of states which do not follow the abovementioned rule of "shift by ΔE." This feature of the effect of the electric field on separate localized states can be interpreted in the context of the model of the deep-level defect with a nonmonotonic dependence of the constant of the electron-vibration interaction on the charged state of the center [16]. In this case, the external field determines the shift of sites of the charged states of the defect in the crystal lattice. Due to this, the variation in the energy of photoionization of the defect additional to $eV_{bf,br}$ takes place. Since such metastable defects are observed in crystals of various compositions [17–19], including CdTe [20] and CdZnTe:Cl [21], their presence is also possible in the investigated CdZnTe crystals. However, we believe that the determining role in the mentioned feature of the effect of the electric field on the localized states belongs to the metastable state of the centers of another nature. We have in view the variation in the system of localized states due to the drift of charged defects in the electric field. For example, in the CdS crystals, the electric field ($\sim 10^2$ V/cm) causes the drift of preferentially interstitial Cd atoms, which leads to the formation of the layer with increased electrical resistivity in the near-anode region [22]. Due to the spatial redistribution of mobile defects in one or

another local region of the crystal, the formation of new defects and decay of the initial ones becomes energetically favorable. In addition to mobile charged defects, mainly electrically neutral defects turn out to be involved into this process. This is confirmed by the abovementioned (see Table 3) variation in the energy spectrum of the localized states under the prolonged effect of V_f. The lag of these variations is apparently determined by the mobility of charged defects and field strength. The twofold difference of energy shifts of the levels ΔE, which correspond to opposite polarities of the electric bias 200 V, is in agreement with the stated assumptions. In addition, the nonuniform distribution of the electric field found in the CdTe and CdZnTe crystals [23, 24] can be attributed to the formation of the region with the increased electrical resistance near one of electrodes. The above-described disappearance of the levels in a certain energy range from the spectrum under the effect of electric bias (see Table 3) can apparently be caused by ionization of the centers by a high electric field. In this case, both the energy location and the electron-phonon interaction of the center [25], as well as the symmetry of the center, which is determined by its interaction with the nearest energy bands [26], are of primary significance.

Thus, the investigation of structures with a Schottky barrier based on CdZnTe crystals by the SPDS method under the conditions of applying a bias electric field to the structures allows one to obtain additional information on the localized states in the crystals. At the same time, the interpretation of the data obtained in this case is complicated due to the transformation of metastable defects under the impact of the field, as well as by the migration of charged defects. The influence of these factors could be weakened, for example, by reducing the duration of the exposure to the structure of bias electric field.

4 Scanning Photodielectric Spectroscopy of Crystals with Additional Non-monochromatic Illumination

It was shown above that a structure with a Schottky barrier created on the basis of investigated crystal, with a bias electric field applied during the measurement, can be used to expand the energy spectrum of the localized states measured by the SPDS method. However, in the case of high-resistive crystals, this method of broadening the energy spectrum of the localized states is insufficiently effective due to the fact that a small part of the voltage applied to the structure falls on the barrier area. As a result, only states that are located sufficiently close to the Fermi level undergo recharge. Therefore, it was of interest to use additional non-monochromatic illumination for recharging the localized states.

A feature of our experiments was the measurement of the dependences $\Delta\varepsilon'_{ef}(\lambda)$ and $\Delta\varepsilon''_{ef}(\lambda)$ not only under exposure of the specimen to monochromatic (scanning) light with an intensity of I_λ but also under additional exposure of the specimen to non-monochromatic light with an intensity $I_0 \approx 20$ mW/cm^2. In all cases, the

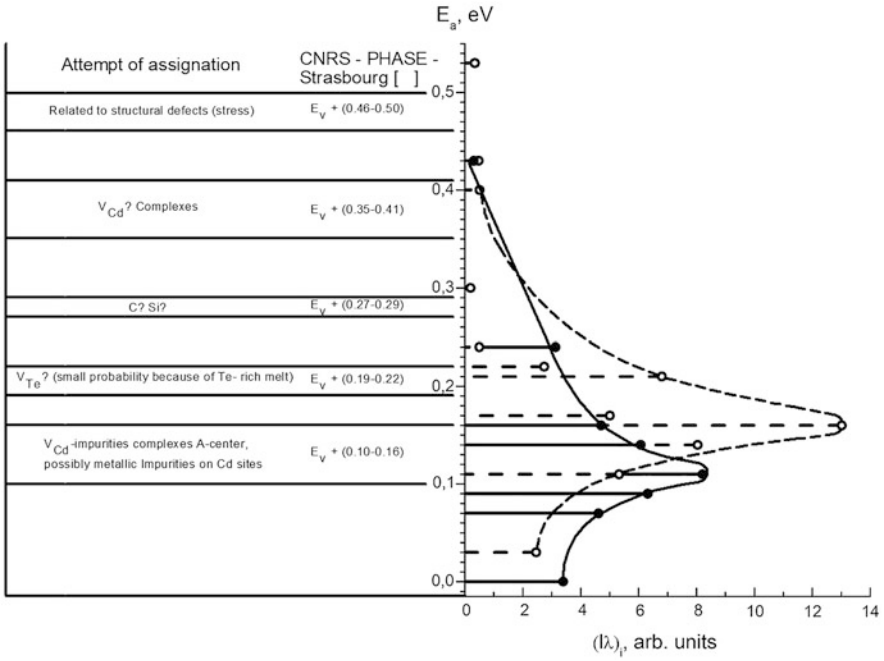


Fig. 5 Energy spectrum and the parameter $(\ell\lambda)_i$ of the localized states in CdZnTe crystals

light impinged normally on the specimen surface. Moreover, the intensity I_λ was varied from one experiment to another, with values of 5, 10, and 20 mW/cm^2. Obviously, at the highest value of I_λ, sections of the dependences are observed corresponding to the lowest photosensitivity of the specimen, and vice versa. When plotting the $\Delta\varepsilon''_{\text{ef}}(\lambda) - \Delta\varepsilon'_{\text{ef}}(\lambda)$ diagram being common for different I_λ on the complex plane, the sections were fused, provided that their edges corresponded to the same spectral interval. In present work, separate influence of monochromatic and non-monochromatic light photons to initially occupied states is not determined. The role of non-monochromatic illumination in this study is to ensure the recharging of states above the Fermi level by throwing electrons at them from the valence band.

Another feature of our studies was a new parameter – the spectral density of a section of the photodielectric effect (PDE) diagram $(\ell\lambda)_i$. This parameter is defined as the ratio of the length of an individual section $\Delta\ell_i$ of the diagram $\Delta\varepsilon''_{\text{ef}}(\lambda) - \Delta\varepsilon'_{\text{ef}}(\lambda)$ to the corresponding wavelength interval $\Delta\lambda_i = \lambda_{i+1} - \lambda_i$. A change in this parameter with any given additional effect on the crystal, obviously, is indicative of the change in the contribution of those localized states that condition the piece $\Delta\ell_i$ of the photodielectric effect diagram.

Figure 5 shows typical spectrum of the localized states and the corresponding values of the parameter $(\ell\lambda)_i$ for studied crystals measured with or without additional illumination. Besides, the information on the energy position and nature of

the states known from the literature is provided. A variety of crystalline specimens were studied to gather data and acquire the spectrum. It mainly consists data for $Cd_{0.9}Zn_{0.1}Te$ and $Cd_{0.88}Zn_{0.12}Te$. Also, the concentration of the deep energy-level defects could be obtained from parameter $(\ell\lambda)_i$. An increase or a decrease in this parameter characterizes a corresponding change in the occupation density of localized states, which are excited under light exposure on crystal.

Three features of the energy position and the parameter $(\ell\lambda)_i$ of the states are noteworthy. The first is an increase in the number of states and – for some of them – in the values $(\ell\lambda)_i$ under illumination. In this regard, it is important to note the appearance of the states at $E_V + 0.49$ eV and $E_V + 0.53$ eV, which are the deepest of observed ones. Note that the depths of the observed localized states agree with the known data. Thus, most of the levels we have observed fall in the ranges reported in [27]. Meanwhile, some individual levels, e.g., $E_v + 0.25$ eV, do not fall into those ranges but were reported elsewhere. Particularly, in [4], this level was detected by CL, DLTS, DLOS, and PICT methods.

The second feature of the data in Fig. 5 is that the line drawn through the ends of the segments corresponding to the localized state parameter $(\ell\lambda)_i$ is bell-shaped. What is more, primarily this feature was characteristic of all observed states and under additional non-monochromatic illumination – of most of them. Finally, the third feature of the data presented is that when illuminating the specimens, the curve shifts toward deeper states.

In explaining the above features of PDE on CdZnTe crystals, in our opinion, it is important to consider several factors. Thus, photons with a high enough energy E_i, which is close to bandgap E_g, induce recharging of the detected states.

Therefore, much of those photons are absorbed in subsurface region I (Fig. 6), where the charge carriers are exposed to the electric field of the surface states. Moreover, according to [28], in CdZnTe, the field bends the edges of the energy bands down.

In the absence of an additional illumination, the photons of the scanning light cause electron transitions from the charged acceptor states ***a*** in the bandgap to some states near the conduction band edge (transitions 1 and $1'$ in Fig. 6a). Further, the states' depth of occurrence with regard to the bottom of the conduction band observed in the crystal's surface region (I) exceeds the occurrence depth in the bulk (II) by the amount $e\varphi_0$. It is important that in this case, the deeper states ***b*** (with regard to the top of the valence band) are electrically neutral and hence are not involved in PDE.

Non-monochromatic illumination has a significant effect on the generation and recombination processes in region I of the crystal. In particular, due to interband transitions 3 (see Fig. 6b), which are localized mostly in this region, and transitions $1'$ in region II, electrons will tend to accumulate in the subsurface region of the crystal. This is due both to the spatial separation of nonequilibrium electrons and holes by the electrostatic field of surface states and to the diffusion of electrons from the bulk (i.e., from region II) to region I. Resulting from the accumulation of electrons in this region, the balance between generation and recombination

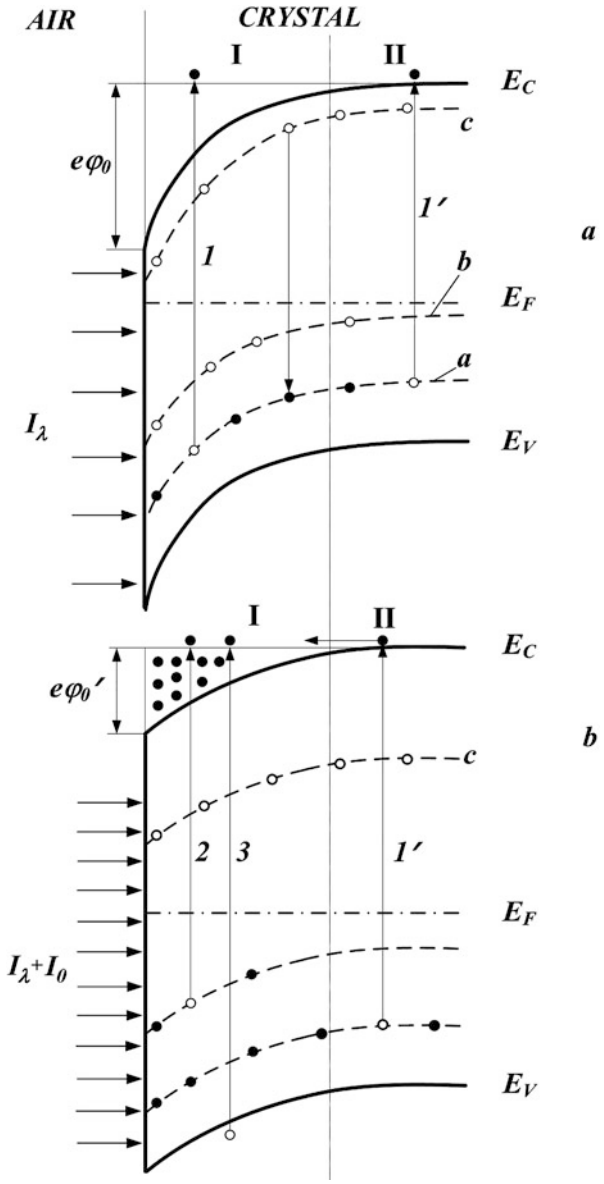


Fig. 6 Band diagram of CdZnTe crystal near its surface: (**a**) under monochromatic (scanning) light, (**b**) with additional non-monochromatic illumination

processes is achieved at a higher concentration of electrons at the localized states in the bandgap. Consequently, the charging will take effect on the acceptor state ***b*** with a greater depth by contrast to the absence of illumination. Thus, when variating

the wavelength of light, the electron transitions from these states to the conduction band will become possible (transitions 2 in Fig. 6b), and the parameter $(\ell\lambda)_i$ will increase for some states that were observed initially. Another consequence of the accumulation of electrons in region I will be a decrease in the subsurface potential φ_o [29]. Obviously, it is this phenomenon that caused the shift of the envelope peak for the parameter $(\ell\lambda)_i$ to the mid-gap (see Fig. 5).

The bell shape of this line, in our opinion, may be explained by the peculiarities of photon absorption by the localized states, as well as by a change in their polarizability α_i due to an increase in the occurrence depth E_i relative to the top of the valence band. Note that the last parameter is related to the energy E_f of the photon absorbed by the given localized state and to the bandgap width by the relation

$$E_i = E_g - E_f. \tag{3}$$

Most likely, as a result of the electron capture during the self-compensation (transitions from the states ***c*** to the states ***a*** in Fig. 6a), the polarizability of a state becomes much lower than the initial polarizability α_i. Hence, the value $\Delta\varepsilon'_{ef}$ has a positive sign. According to [30], the states' polarizability changes with E_i in conformity with the relation

$$\alpha_i = \frac{c\hbar^2 e^2}{2m E_i^2}, \tag{4}$$

where $\hbar$ is the Planck constant divided by 2π; e and m are the electron charge and mass, respectively; and c is a coefficient depending on the type of the potential near the localized state. In Fig. 7, curve 1 corresponds to the dependence $\alpha_i(E_i)$. Note that in this figure, the energy positions of the localized states relative to the top of the valence band are plotted along the horizontal axis.

We emphasize that the increments of the real and imaginary parts of ε^* measured in the experiment are effective values, since photons of an arbitrary wavelength λ are inhomogeneously absorbed in the specimen bulk. Nevertheless, it can be assumed that for the i^{th} grade states, these increments are proportional to the parameter α_i and the number of states ΔN_i that underwent recharging under the action of the scanning light. Thus, for the measured values, the following relations are valid:

$$\Delta\varepsilon'_{efi} \sim \alpha_i \Delta N_i \tag{5}$$

$$\Delta\varepsilon''_{efi} \sim K''_i \alpha_i \Delta N_i. \tag{6}$$

The coefficient K''_i appearing in the relation (6) characterizes the ratio of the states' contributions to the quantities $\Delta\varepsilon'_{ef}(\lambda)$ and $\Delta\varepsilon''_{ef}(\lambda)$. Assuming that the wavelength interval $\Delta\lambda_i$ of photons, whose absorption causes the recharging of the i^{th} grade localized states, along with the coefficient K''_i is weakly dependent on the

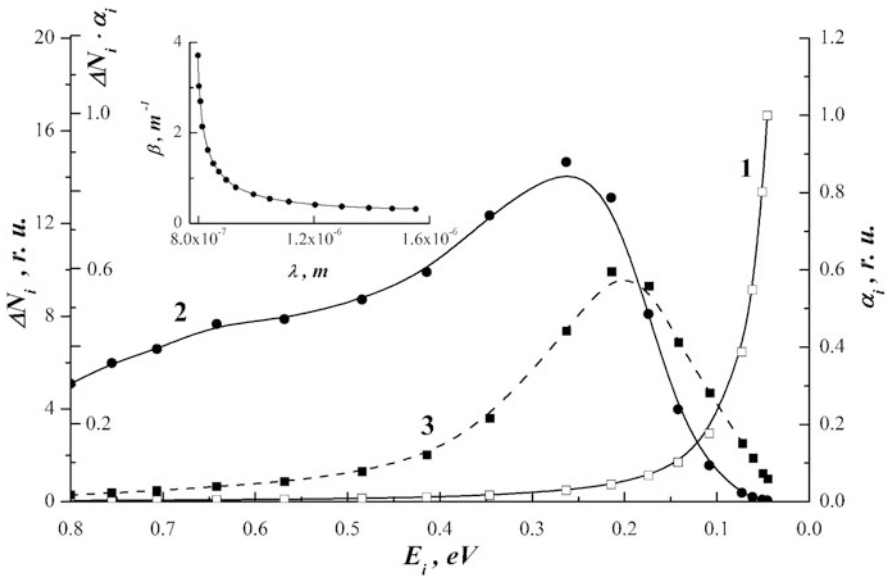


Fig. 7 Dependence of quantities α_i and ΔN_i and their product from the depth of the acceptor localized states. Insertion – spectral dependence of light coefficient in CdZnTe crystals

depth of the states, i.e., on E_i, then for the parameter $(\ell\lambda)_i$ the below relation will be valid:

$$(\ell\lambda)_i \sim \sqrt{\Delta\varepsilon'_{\mathrm{efi}} + \Delta\varepsilon''_{\mathrm{efi}}} \sim \sqrt{1 + K''_i}\,\Delta N_i \alpha_i . \tag{7}$$

Thus, with the assumptions made, the product $\Delta N_i \alpha_i$ is of our main interest. We also assume that the centers are uniformly distributed throughout the specimen and the flux of incident monochromatic light is independent of λ. This being the case, the elementary number of the states that underwent recharging upon absorption of

$$dN_i = I_\lambda D_i n_i S dx, \tag{8}$$

where S is the area of the specimen's facet being illuminated, I_λ is the light intensity at the depth x, n_i is the concentration of centers of the i^{th} grade, and D_i is a dimensionless coefficient equal to the fraction of the i^{th} grade states in the volume Sdx that undergo recharging at a unit light intensity. Neglecting the reflection of light from the front and back surfaces of the specimen, we can assume that the change in the value I_λ as the light penetrates into the specimen follows Beer-Lambert law:

$$I_\lambda = I_{0\lambda} \exp\left(-\beta_\lambda x\right). \tag{9}$$

Here, β_λ is the absorption coefficient of light with the wavelength λ.

Given both law (6) and relation (5), the total number of localized states that underwent recharging under the action of light with the wavelength λ in the h long specimen will be expressed as

$$\Delta N_i = \int_0^h D_i I_0 N_i S \exp(-\beta_\lambda x)\, dx. \tag{10}$$

Integrating the right-hand side of this expression under the assumption that D_i is a constant gives

$$\Delta N_i = \frac{D_i I_{0\lambda} n_i S}{\beta_\lambda} (1 - \exp(\beta_\lambda h)). \tag{11}$$

Since in the spectral region of interest β_λ depends substantially on λ, then the value of ΔN_i is also spectrally dependent. As to this dependence, in Fig. 7, it corresponds to curve 2. This curve was plotted with an approximation of the spectral dependence of the coefficient β_λ for the CZT crystals (inset in Fig. 7), based on the data of [31]. Curve 3 in Fig. 7 is the spectral dependence of the product of the quantities ΔN_i and α_i, which, as noted above, is proportional to the parameter $(\ell\lambda)_i$. When comparing curve 3 with the spectral dependence $(\ell\lambda)_i$ acquired experimentally (see Figs. 5 and 7), we can see their qualitative similarity.

Thus, involving an additional non-monochromatic illumination in the implementation of scanning photodielectric spectroscopy made it possible to measure a wider energy spectrum of localized states in $Cd_{1-x}Zn_xTe$ crystals. The new parameter "spectral density of a section of the photodielectric effect diagram" is introduced, reflecting changes in the occupation of localized states in a crystal that are caused by non-monochromatic illumination or another external action.

5 Conclusion

We have shown that this technique, scanning photodielectric spectroscopy for semiconductors, allows to obtain important information about localized states in high-resistance crystals while minimizing interference of the probe on the semiconductor electronic configuration (e.g., via heating). Carrying out tuning of the wavelengths allowed to specify in detail the importance of this factor to separate bulk vs. interface and pre-interface effects, as well as to focus on the energy states of interest. Either we have discussed effect of bias voltage on localized states which is of special importance for CZT-based devices. It can be assumed that the information content of the data obtained by this method will increase when measurements are performed under special conditions, when using linearly polarized light or uniaxial compression of the sample. The rapid progress observed in recent decades in the creation of instruments for measuring electrical capacity and dielectric loss tangent of various semiconductor structures will also contribute to an

increase in the information content of the data. This technique could be a powerful tool to benchmark different crystal growth recipes based on the energy spectrum of localized state information it reveals.

References

1. Makarenko L. F. et al. Formation of a Bistable Interstitial Complex in Irradiated p-Type Silicon //physica status solidi (a). – 2019. – V. 216. – №. 17. – C. 1900354. https://doi.org/10.1002/pssa.201900354
2. Besleaga C. et al. Bistability of the BiOi complex and its implications on evaluating the "acceptor removal" process in p-type silicon //Nuclear Instruments and Methods in Physics Research Section A: Accelerators, Spectrometers, Detectors and Associated Equipment. – 2021. – V. 1017. – C. 165809. https://doi.org/10.1016/j.nima.2021.165809
3. José Coutinho Theory of the Thermal Stability of Silicon Vacancies and Interstitials in 4H–SiC *Crystals***2021**, *11*(2), 167; https://doi.org/10.3390/cryst11020167
4. A. Costaldini, A. Cavallini, B. Fraboni, P. Fernandez, J. Appl. Phys. **83**, 2121 (1998). https://doi.org/10.1063/1.366946
5. P. Fougeres, P. Siffert, M. Hageali, J. M. Koebel, and R. Regal, Nucl.Instrum. Methods Phys. Res. A **428**, 38 (1999). https://doi.org/10.1016/S0168-9002(98)01578-2
6. F. Bechstedt, *Semiconductor Surfaces and Interfaces. Their Atomic and Electron Structures*, Physical Research Vol. 5, edited by R. Enderlein (Academic, Berlin, 1988), p. 488.
7. F. A. D'Altroy and N. Y. Fan, Phys. Rev. **103**, 1671 (1956). https://doi.org/10.1103/PhysRev.103.1671
8. D. M. Hofmann, W. Stadler, P. Christmann, and B. K. Meyer, Nucl. Instrum. Methods Phys. Res. A **380**, 117 (1996). https://doi.org/10.1016/S0168-9002(96)00287-2
9. V. K. Komar, V. P. Migal, O. N. Chugai, et al., Appl. Phys. Lett. 81, 4195 (2002). https://doi.org/10.1063/1.1525883
10. H. Hermon, M. Schieber, R. B. James, et al., Nucl. Instrum. Methods Phys. Res. A 428, 30 (1999). https://doi.org/10.1016/S0168-9002(98)01577-0
11. N. A. Penin, Fiz. Tekh. Poluprovodn. (St. Petersburg) 30, 626 (1996) [Semiconductors 30, 340 (1996)].
12. S.M. Sze, Physics of Semiconductor Devices, 2nd ed. (Wiley, New York, 1981; Mir, Moscow, 1984), Vol. 1. https://doi.org/10.1002/0470068329
13. L. N. Davydov, O. A. Datsenko, G. P. Kovtun, et al., Funct. Mater. 8, 255 (2001).
14. E. H. Rhoderick, Metal–Semiconductor Contacts (Clarendon, Oxford, 1978; Radio i Svyaz', Moscow, 1982). https://doi.org/10.1049/ip-i-1.1982.0001
15. J. S. Blakemore, Semiconductor Statistics (Pergamon, Oxford, 1962; Mir, Moscow, 1964).
16. N. T. Bagraev and V. A. Mashkov, Solid State Commun. 65, 1111 (1988). https://doi.org/10.1016/0038-1098(88)90904-0
17. N. T. Bagraev, R. M. Mirsaatov, I. S. Polovtsev, and A. Yusupov, Fiz. Tekh. Poluprovodn. (St. Petersburg) 26, 481 (1992) [Sov. Phys. Semicond. 26, 271 (1992)]
18. N. T. Bagraev, R. M. Mirsaatov, I. S. Polovtsev, et al., Fiz. Tekh. Poluprovodn. (St. Petersburg) 26, 427 (1992) [Sov. Phys. Semicond. 26, 242 (1992)].
19. N. T. Bagraev, Zh. Éksp. Teor. Fiz. 100, 1378 (1991) [Sov. Phys. JETP 73, 764 (1991)].
20. P. N. Tkachuk, V. I. Tkachuk, P. N. Bukivskioe, and M. V. Kurik, Fiz. Tverd. Tela (St. Petersburg) **46**, 804 (2004) [Phys. Solid State **46**, 825 (2004)]. https://doi.org/10.1134/1.1744955
21. Tineke Thio, J. W. Bennett, D. J. Chadi, et al., J. Cryst. Growth **159**, 345 (1996). https://doi.org/10.1016/0022-0248(95)00681-8

22. V. V. Kislyuk, N. E. Korsunskaya, I. V. Markevich, et al., Fiz. Tekh. Poluprovodn. (St. Petersburg) **30**, 1884 (1996) [Semiconductors **30**, 986 (1996)].
23. P. De Antonis, E. J. Morton, and E. J. W. Podd, IEEE Trans. Nucl. Sci. **43**, 1487 (1996). https://doi.org/10.1109/23.507089
24. A. Zumbiehl, M. Hage-Ali, P. Fougeres, et al., J. Cryst. Growth **197**, 650 (1999). https://doi.org/10.1016/S0022-0248(98)00764-7
25. V. Karpus, Pis'ma Zh. Eksp. Teor. Fiz. **44**, 334 (1986) [JETP Lett. **44**, 430 (1986)].
26. O. V. Kurnosova and I. N. Yassievich, Fiz. Tverd. Tela (Leningrad) **26**, 3307 (1984) [Sov. Phys. Solid State **26**, 1988 (1984)].
27. P. Fougeres, Crystal growth and characterization of $Cd_{1-x}Zn_xTe$ crystals elaborated by the High Pressure Bridgman Method: application to X and γ ray detection, Thesis, Louis Pasteur University, Strasbourg, 1998.
28. V.K. Komar', V.M. Puzikov, O.N. Chugai, D.P. Nalivaiko, S.V. Sulima, Effect of thebias electric field on the spectral distribution of the photodielectric effect in theSchottky-barrier structures based on the cadmium-zinc telluride crystals, Semiconductors 41 (2007) 689–695, https://doi.org/10.1134/S1063782607060140
29. O.V. Konstantinov, V.V. Tsarenkov, Changes in the surface potential of a semiconductor under illumination, Semiconductors 24 (1990) 2126–2131.
30. Yu. N. Demkov, G.F. Drukarev, Decay and polarizability of a negative ion in an electric field, JETP 20 (1964) 918–924.
31. A.J. Syllaios, P.K. Liao, B.E. Dean, Optical absorption coefficient of CdZnTe, Proc. SPIE 2274, Optics, Photonics (1994) 49–54, https://doi.org/10.1117/12.189248

Photoinduced Electron Transfer Dynamics in Hybrid Quantum Dot/Molecular Catalyst Systems for Artificial Photosynthesis



Thomas Michael Khazanov, Niharika Krishna Botcha, and Anusree Mukherjee

1 Introduction

Over the last few decades, nanomaterials have gained significant attention in fundamental research in physical science because of their range of potential applications. Quantum dots, in particular, have shown great promise for photonic and photovoltaic applications owing to their ease of synthesis and tunable optical properties [1]. This is especially true regarding their use as light-harvesting materials, as the number of papers involving quantum dots has dramatically increased within the areas of photovoltaics and artificial photosynthesis [2]. The goal of this chapter is to highlight some of the recent advances in quantum dot photophysics relevant to artificial photosynthesis as an introduction to specialists in other areas.

2 Artificial Photosynthesis

Photosynthesis is the process through which green plants and some bacteria and algae convert solar energy into storable chemical energy in the form of carbohydrates [3–5]. Inspired by photosynthesis in nature, the artificial conversion of

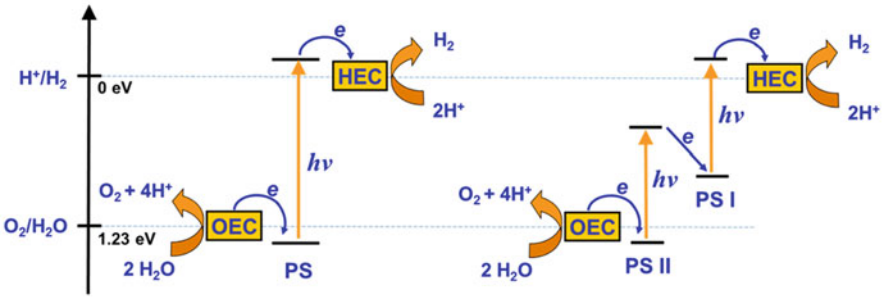
T. M. Khazanov
Department of Chemistry and Chemical Biology, Cornell University, Ithaca, NY, USA

N. K. Botcha
Department of Chemistry, Carnegie Mellon University, Pittsburgh, PA, USA

A. Mukherjee (✉)
Department of Chemistry and Geosciences, Jacksonville State University, Jacksonville, AL, USA
e-mail: amukherjee@jsu.edu

© The Author(s), under exclusive license to Springer Nature Switzerland AG 2024

S. Krishnamoorthy, K. (Kris) Iniewski (eds.), *Advances in Fabrication and Investigation of Nanomaterials for Industrial Applications*,
https://doi.org/10.1007/978-3-031-42700-8_7



Scheme 1 Schematic representation of photocatalytic water splitting with one photosensitizer (left) and two photosensitizers (right). (Reproduced with permission from *Acc. Chem. Res.***2014**, 47, 7, 2177–2185. Copyright 2014 American Chemical Society)

sunlight to chemical fuels has attracted attention for several decades as a green approach to store and transport energy [6]. The term *artificial photosynthesis* has been used to refer to any scheme that incorporates concepts derived from natural photosynthesis, though it typically refers to the splitting of water into its constituent elements, molecular hydrogen and oxygen [7]. The study of artificial photosynthesis generally treats the carbon dioxide reduction reaction (CO_2RR), the oxygen evolution reaction (OER), and the hydrogen evolution reaction (HER) separately, the latter being the focus of this chapter. Photocatalytic hydrogen evolution has emerged as a promising strategy for chemical energy conversion and storage owing to the large enthalpy of combustion of molecular hydrogen and because of its benign combustion product, water [4, 5].

Three basic processes dictate the design of any artificial photocatalytic system: light harvesting, charge separation, and redox catalysis [8, 9]. Simply put, the HER requires excitation of the photosensitizer and subsequent transfer of the photoexcited electron from the photosensitizer to the catalytic site to participate in the redox chemistry necessary to produce hydrogen from protons. It is challenging to design a system with a single photosensitizer that drives both hydrogen and oxygen evolution reactions and can only be achieved with ultraviolet photons that comprise less than 5% of the solar spectrum [5]. To overcome these issues, two-photosensitizer systems (Scheme 1) mimicking the Z-scheme configuration of natural photosynthesis are often proposed. It is then possible to study each half-reaction separately under simpler conditions. For the HER, this is typically accomplished by the combination of a photosensitizer, catalyst, and sacrificial electron donor.

For this process to be effective, the excited state energy levels of the photosensitizer have to match the redox potentials of the catalyst responsible for water splitting, which in turn has to be aligned with the water redox potential. That is, an ideal photosensitizer must possess a more positive excited state reduction

potential than the water oxidation potential (+0.82V vs. NHE at pH 7) for the OER, and meanwhile, a more negative excited state oxidation potential than the water reduction potential (−0.41V vs. NHE at pH 7) is needed for the HER [5, 10, 11]. Beyond this, however, the photosensitizer must exhibit long-term photostability, maximal overlap of the photosensitizer absorption and the solar spectrum, and long excited state lifetimes for effective charge separation. A variety of photoactive materials have been investigated for use as photosensitizers such as organic and organometallic chromophores, lead halide perovskites, as well as semiconductor quantum dots, though most of these works have focused more on the efficiency of the photocatalyst [3, 12, 13]. While the selection of ideal photosensitizer remains a challenge, we have chosen to highlight recent advances in the use of semiconductor nanocrystals as photosensitizers, with emphasis on understanding how the photophysical properties of nanomaterial-based photosensitizers contribute to the photophysics of the artificial photocatalytic system.

2.1 Quantum Dots as Light-Harvesting Materials

Semiconductor nanocrystals (NCs) are nanometer-scale crystalline particles containing approximately 100–100,000 atoms whose properties are heavily dependent on their size and morphology. They can be fabricated through chemical synthesis to yield approximately spherical particles termed quantum dots (QDs) or nanostructures of more complex shapes, with near atomic precision [14]. By combining different materials in one nanocrystal, various heterostructures can be formed, such as all-semiconductor hetero-nanoparticles or hybrid semiconductor-metal structures.

In bulk semiconductors, electronic excitations are often discussed in terms of excitons, in which a bound electron-hole (e-h) pair is treated according to the quasiparticle formalism. The exciton is a neutral, hydrogenic quasiparticle comprising a negative conduction band electron and a positive valence band hole that are fundamental to the study of phenomena such as carrier transport or charge separation. Excitons are typically classified by their Bohr radius, which is dictated by the strength of the e-h Coulomb interaction. As the size of the nanocrystal approaches the exciton Bohr radius, it is the dimensions of the particle itself, rather than solely the e-h interaction strength, that govern the size of the exciton and thus the energetics of electronic states within the particle [14]. In a quantum dot, the spatial confinement of the structure itself imposes a potential that can be thought of, to first order, as analogous to a particle in a spherical box. This spherical potential gives rise to discrete energy levels that replace the continuous energy bands of a bulk material (Fig. 1), and the exact energetics of the electronic manifold vary continuously with particle size, with bandgap roughly proportional to $1/a^2$, where a is the radius of the quantum dot [14, 15].

The large dielectric screening and low quasiparticle effective mass in bulk semiconductors result in small exciton binding energies on the scale of a few meV

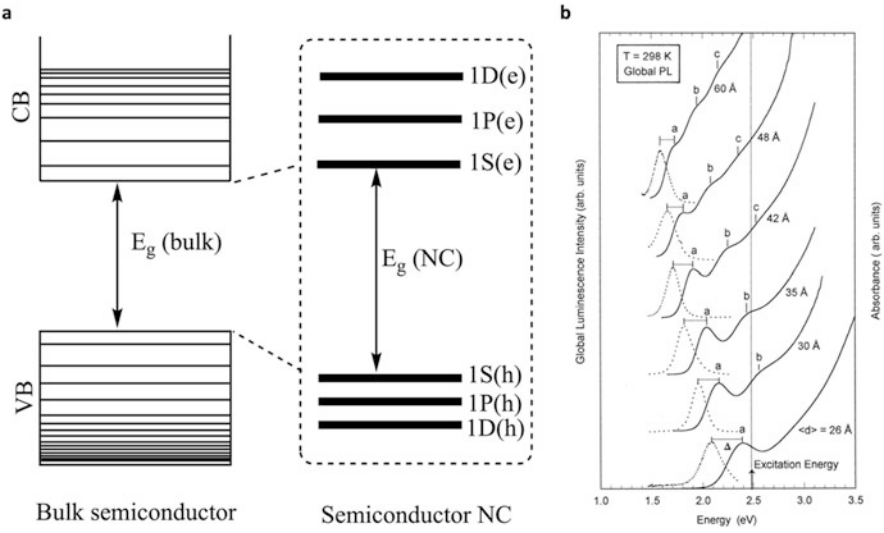


Fig. 1 (**a**) Valence band (VB) and conduction band (CB) of a bulk semiconductor with a fixed bandgap separated into discrete atomic-like states with a size-dependent bandgap [14]. (**b**) Absorption and photoluminescence spectra of InP QDs illustrating the size dependence of the bandgap across a range of QD radii spanning 2.6–6 nm. (Reproduced with permission from *J. Phys. Chem. B* **1997**, 101, 25, 4904–4912. Copyright 1997 American Chemical Society)

[16]. In semiconductor nanocrystals, however, the spatial confinement results in strong e-h Coulomb interactions which, coupled with reduced dielectric screening, leads to higher exciton binding energies compared to the bulk and thus longer exciton radiative lifetimes. This is beneficial for applications in artificial photosynthetic systems because the enhanced exciton lifetime allows for electron transfer to compete with e-h recombination as a relaxation pathway. The spatial confinement in semiconductor NCs also results in a size dependence of the bandgap as discussed above, allowing the bandgap to be easily tuned according to both the optical requirements of the artificial photosynthetic system and the thermodynamic requirements of the overall photocatalytic process. Unlike conventional organic dye photosensitizers, QDs can support simultaneous generation of multiple excitons and produce multiple excitons from a single high-energy photon, termed carrier multiplication, allowing for quantum efficiencies to exceed 100% [14, 15]. The larger surface area of QDs compared to organic dyes also allows for a single QD to interact with multiple photocatalysts, which can even be covalently bound to the QD surface with organic linkers, resulting in highly efficient charge separation and electron transfer. Overall, quantum dots occupy an intermediate regime between bulk semiconductor and molecular photosensitizers and possess many of the advantages of both for use in artificial photosynthetic systems such as broadband absorption of the solar spectrum, tunable bandgaps, long exciton lifetimes, and economic fabrication [5, 17–20].

3 Electron Transport Dynamics in Hybrid QD/Catalyst Systems

The question of electron transfer in artificial photosynthetic systems is typically investigated through various time-resolved spectroscopic methods. Cadmium chalcogenide QDs (of the form CdX, X = S, Se, Te, etc.), in particular, have been studied extensively, and their photophysics are well understood [14, 17, 21–33]. While a detailed discussion of QD electronic structure is beyond the scope of this work, the photophysics of wide-gap CdX QDs such as CdSe or CdTe are typically discussed in the literature in terms of the model presented below (Fig. 2) within the framework of the multiband effective mass approximation [14, 21–23, 32, 33]. The linear absorption spectra of CdX QDs exhibit excitonic features near the band edge, of which three or four are typically resolvable in the visible region in the case of CdSe (Fig. 2). These excitons can be interpreted as bound pairs of electrons and holes occupying discrete single-particle states in the QD valence and conduction bands that are often referred to as quantum size levels (QSLs) [33]. The manifold of hole QSLs is more complex than that described by the case of a particle in a spherical potential. In a simple tight-binding picture, the valence band of CdX QDs is derived from atomic p orbitals and thus carries an internal angular momentum equal to unity, resulting in splitting and state-mixing of the hole QSLs due to the spin-orbit interaction [32]. The resulting hole QSLs are labeled according to standard atomic notation nQ_j where n is the principal quantum number, $Q = S,P,D,...$ is the spectroscopic notation for the lowest value of the internal or orbital angular momentum L, and j is the total angular momentum. The electron QSLs are labeled simply as nQ, and transitions to the first $1S$ level are allowed from any hole QSL that has mixed s-d symmetry. Similarly, transitions to the first $1P$ level are allowed

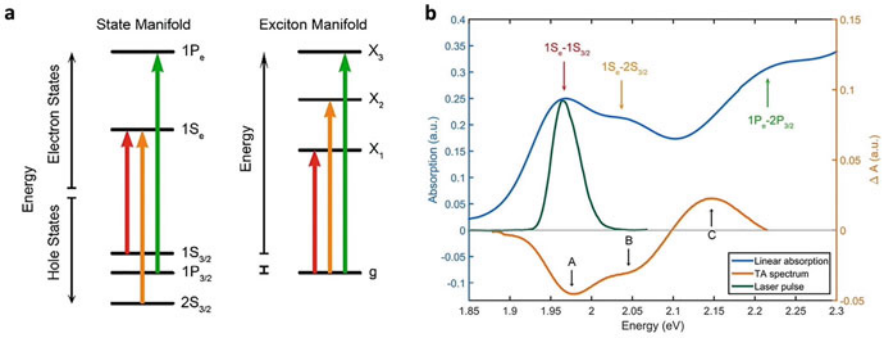


Fig. 2 (**a**) Electronic energy levels of CdSe QDs. (**b**) Linear spectrum of CdSe QDs (blue line) overlaid with excitation laser pulse (green line) and TA spectrum at $t = 100$ ps (orange line) showing negative features related to the X_1 (A) and X_2 (B) excitons and positive photoinduced absorption (C) redshifted by the biexcitonic binding energy. (Adapted with permission from *Chemical Physics* **2016**, 481, 157–164. Copyright 2016 Elsevier B.V.)

from any hole QSL with mixed *p-f* symmetry [33]. Because of this intersubband mixing, transitions may also be allowed from hole QSLs labeled as nS_j to electron QSLs labeled *nD*, as well as *nF-nPj* transitions, though these features are generally less resolved and outside of the typical visible probe region.

Ultrafast transient absorption spectroscopy has been applied to study the dynamics of processes in CdX QDs such as Auger recombination or the cooling dynamics of hot excitons and is a powerful technique for studying charge carrier dynamics [24]. Transient absorption (TA) spectroscopy is a nonlinear spectroscopic technique in which absorption spectra are collected at defined delay times after initial photoexcitation. They are typically presented as either differential absorption or transmission spectra because they are acquired by measuring the differential transmission of the probe through the sample with and without photoexcitation. The ultrafast TA spectra of ideal CdX QDs excited resonantly with the X_1 transition are comprised of three main features, here labeled A, B, and C (Fig. 2). The assignments of these features can be made by considering the physical mechanisms of transient absorption. Transient absorption signals in semiconductor nanocrystals primarily arise from state filling and Coulomb interactions [14]. State filling results in the bleaching of the corresponding optical transitions and manifests as negative features in differential absorption spectra, while the Stark effect associated with photoexcited carriers results in shifts to the energy of optical transitions and their oscillator strength [14]. These can be understood as arising from the Coulomb interactions between e-h pairs generated by the pump pulse and the e-h pair generated by the probe pulse. While state filling selectively affects only transitions involving populated states, the carrier-induced Stark effect modifies all NC transitions. Features A and B are negative in the differential absorption spectrum and appear at the same energies as the X_1 and X_2 excitonic features in the linear absorption spectrum and are therefore assigned as ground-state bleach (GSB). Feature C is positive, however, and thus results from photoinduced absorption (PA) attributed to biexciton formation. Biexciton formation in semiconductor NCs typically manifests as redshifts of optical absorptions with an associated PA at the position of the shifted transition and here can be observed below the X_3 transition (Fig. 2) in feature C. Bleaching arising from filling of the $1P_e$ QSL is not observed here only because the probe range considered does not extend to sufficiently high energy. With realistic semiconductor NCs, broad PA may be observed below the bandgap and is typically rationalized by the absorption of photogenerated charge carriers [26]. While it is difficult to extract information from these features, such as if they arise from electrons or holes, free carriers, or trapped carriers, they have typically been attributed to surface-localized holes through both experimental and theoretical studies [25, 34–38].

Understanding the rate of electron transfer (ET) is of fundamental importance in the study of hybrid QD/molecular catalyst systems and is often quantified through TA spectroscopy. Here, we consider a study investigating the ET process between dihydrolipoic acid (DHLA)-capped CdSe QDs as the photosensitizer and Ni-DHLA as the catalyst [18]. The linear absorption spectra of the QD, catalyst, and QD/catalyst system are presented in Fig. 3. Two excitonic features at the band edge

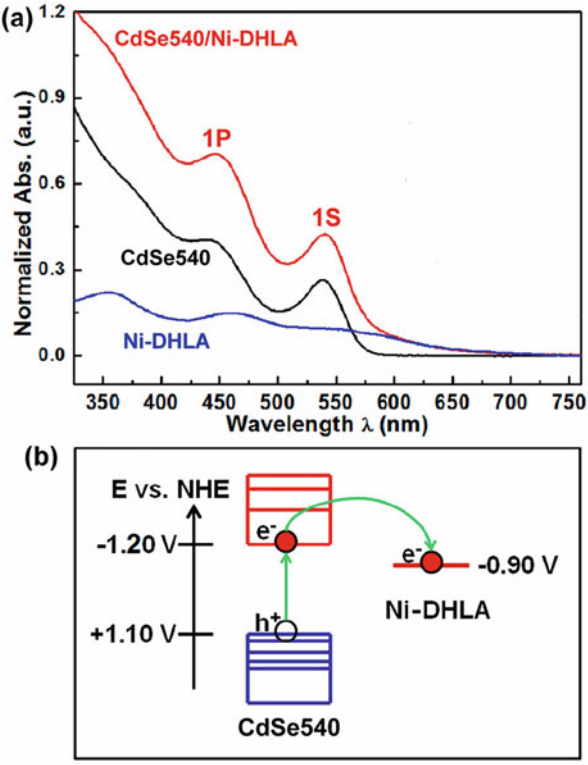


Fig. 3 (**a**) Absorption spectra of the Ni-DHLA catalyst and CdSe540 QDs with (red, [QD]:[Ni-DHLA] = 1:20) and without (black) the presence of Ni-DHLA catalyst. (**b**) Potentials of 1S electron and hole states of CdSe540 QDs and the reduction potential of the Ni-DHLA. Potential values given versus normal hydrogen electrode (NHE). (Reprinted with permission from *J. Phys. Chem. B.* **2015**, 119 (24), 7349–7357. Copyright 2014 American Chemical Society)

are clearly resolvable and are labeled 1S and 1P, corresponding to transitions to $1S_e$ and $1P_e$ QSLs.

Femtosecond TA spectroscopy with an excitation wavelength of 400 nm was performed to understand the dynamics of ET from the QD to the Ni complex. In the TA spectra of the bare CdSe QDs (Fig. 4a), bleaching of the 1S and 1P bands are observed, which manifests as positive features in the differential transmission spectrum. The splitting of the 1S band into two distinct features is not observed in the linear absorption spectrum, though here it can be clearly resolved. Two PA bands are observed around 470 and 580 nm, which the authors attribute to biexciton formation. The 1S exciton photobleaching signal only recovers 40% of its maximum value in 1 ns, indicating that the excited state has a lifetime of greater than 1 ns. However, when the CdSe QDs are excited in the presence of Ni-DHLA (Fig. 4b), the 1S exciton bleach has recovered by 95% within 1 ns, indicating rapid depopulation

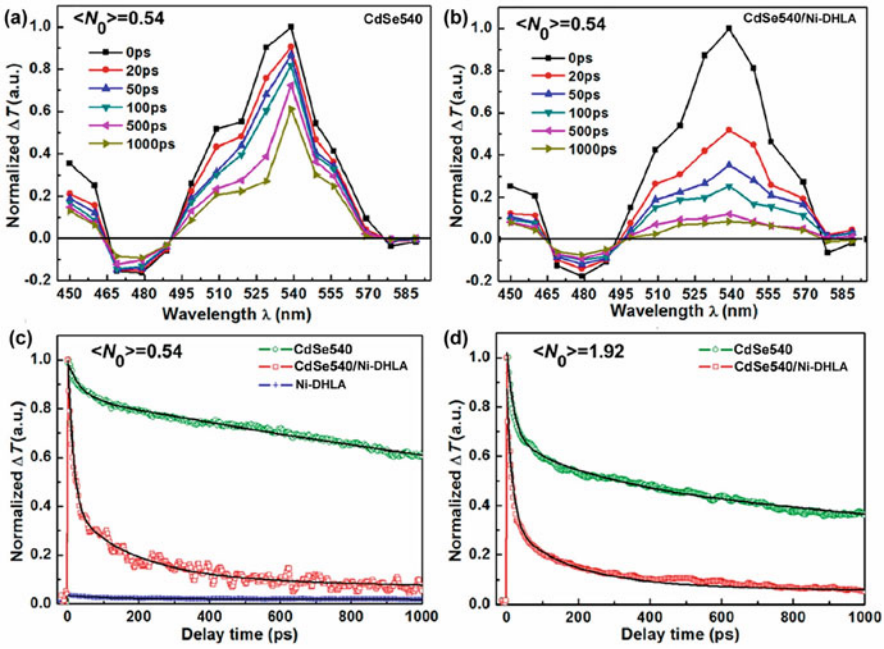
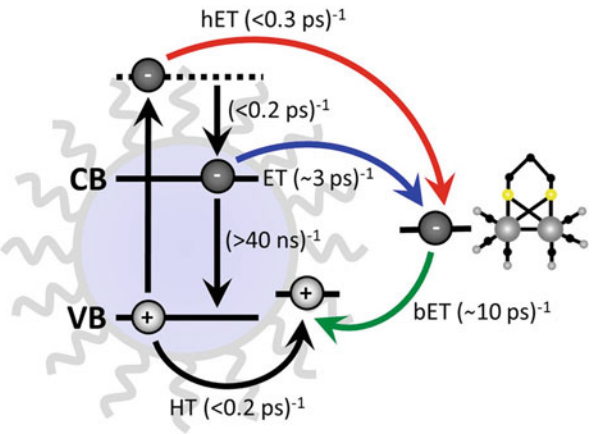


Fig. 4 TA spectra of CdSe540 QDs (**a**) without and (**b**) with Ni-DHLA catalyst ([QD]:[Ni-DHLA] = 1:20) under $\langle N_0 \rangle = 0.54$. TA transients probed at 540 nm with (red) and without (green) the presence of the Ni-DHLA catalyst under (**c**) $\langle N_0 \rangle = 0.54$ and (**d**) $\langle N_0 \rangle = 1.92$, respectively. The blue line in panel c is the TA signal of pure Ni-DHLA probed at 540 nm. Solid black lines in panels c and d are multiexponential fits. (Reprinted with permission from *J. Phys. Chem. B.* **2015**, 119 (24), 7349–7357. Copyright 2014 American Chemical Society)

of the 1S state compared to the bare QD. This suggests ET from the QD to the Ni catalyst. Additional control experiments were performed to confirm ET.

Kinetic traces of the 1S photobleaching signal with and without Ni-DHLA were fit with a multiexponential model (Fig. 4c, d) to further quantify the ET process. Without the Ni-DHLA catalyst present, the 1S bleach exhibits a biexponential decay with time constants 37 ± 2 ps and 3.1 ± 0.1 ns. Addition of Ni-DHLA results in an additional fast decay component in the 1S bleach (Fig. 4c). Control experiments with only Ni-DHLA without photosensitizer did not exhibit any fast component, and the signal is nearly 60 times weaker, indicating that the observed signal in the QD/Ni-DHLA system is not associated with the pure catalyst. Holding the intrinsic lifetime of the relaxation processes in the pure QD constant, the 1S bleach recovery in the presence of Ni-DHLA was fit with a multiple exponential model. A single exponential could not model the rapid decay of the QD excited state dynamics in the presence of Ni-DHLA, though the data could be nicely fit with two exponentials with time constants 15 ± 1 ps and 180 ± 6 ps and exponential prefactors 0.59 and 0.29, respectively. The authors attribute this deviation from monoexponential decay to the presence of multiple ET pathways, giving rise to relaxation processes with



Scheme 2 Summary of the photophysics of the combined CdSe/HM system. (Reprinted with permission from *J. Phys. Chem. Lett.* **2021**, 12, 18, 4385–4391. Copyright 2021 American Chemical Society)

different dynamics. This has been observed in other studies in which the QD was excited well above the bandgap, resulting in a population of hot electrons that can also undergo transfer [34]. It is important to note, however, that multiexponential models of TA kinetics are not without their weaknesses and some cases may require further analysis [28]. From the exponential prefactors, it was concluded that the majority of electrons are transferred within ca. 15 ps, while the remainder transfers at a slower rate. The amplitude-weighted average lifetime for ET from the QD to the catalyst was determined to be 69 ± 2 ps and account for nearly 90% of the 1S bleach recovery. The relatively large percentage of electrons undergoing ET from the QD to the catalyst has been invoked to rationalize the unusually high catalytic efficiency of the CdSe/Ni-DHLA system.

Understanding back ET is relevant in the design of artificial photosynthetic systems as it can occur on much faster timescales than the subsequent catalysis, and thus maximizing forward ET while simultaneously minimizing back ET is an important consideration when optimizing such systems. Quantifying back ET can be challenging because it involves the dynamics of surface-localized holes and TA bleach signals of QDs are dominated by conduction band state filling, while the hole contribution is weaker and difficult to extract [27, 39]. However, the sub-bandgap PA in the TA spectra of CdX QDs contains information regarding trapped hole dynamics that other experiments may not provide. Consider, for example, the case of a hybrid QD/molecular catalyst system employing CdSe quantum dots and a synthetic [FeFe]-hydrogenase mimic (HM) (Scheme 2) [34].

Here, femtosecond transient absorption spectroscopy was performed with an excitation wavelength of 390 nm (above the bandgap) on CdSe QDs in the absence and presence of equimolar HM (Fig. 5). The TA spectra in the absence of HM exhibit two negative features centered at 400 and 450 nm, assigned to bleaching

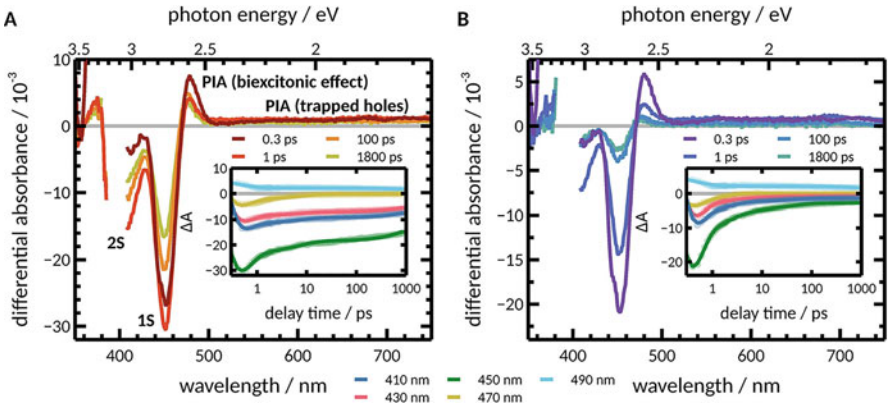


Fig. 5 Transient absorption spectra of CdSe QDs in the (**a**) absence and (**b**) presence of equimolar HM. Kinetic traces at selected wavelength depicted in the inset. (Reprinted with permission from *J. Phys. Chem. Lett.* **2021**, 12, 18, 4385–4391. Copyright 2021 American Chemical Society)

arising from transitions to the $1S_e$ QSL. The intense PA recorded at 450 nm is attributed to biexciton formation, while the broad PA in the range of 520–750 nm has been assigned to trapped holes. Electron transfer between the QD and the catalyst was established in a similar manner as with the Ni-DHLA catalyst and occurs on the sub-ps to ps timescale. This broad PA signal is formed with a rise time of less than 0.2 ps in the absence of HM and can be described by two time constants of 103 ± 8 and >1800 ps. The decay is attributed to e-h recombination with conduction band electrons. The amplitude of this PA signal is reduced in the presence of HM. Direct hole transfer to HM was ruled out due to the energetic band position. Modeling of the trapped hole PA in the presence of HM resulted in a single time constant of 10.1 ± 0.4 ps, assigned to back ET. This is in agreement with other experiments investigating back ET to shallow hole traps on a timescale of 10s of ps [29]. This process is fast enough to compete with the hydrogen evolution reaction, and optimization of artificial photosynthetic systems involving QDs will require careful understanding of back ET processes that may limit their efficiency.

While some investigations have focused on systematic studies of the dependence of QD properties such as size on ET kinetics, there are few reports of systematic studies varying the molecular catalyst in these systems. A study comparing the hydrogen production efficiency between nickel hydrogen evolution catalysts supported by a series of polypyridyl ligands revealed trends in catalytic efficiency ascribed to the variation of ligand structure and catalyst M^{II}/M^{I} redox potential [40]. This is in agreement with the conventional understanding of the effect of band energetics on ET kinetics. In the case of the analogous copper catalysts, however, no trend could be established, despite demonstrating the same trend in catalyst M^{II}/M^{I} redox potential. This suggests that the relevant factors influencing hydrogen evolution by artificial photosynthetic systems include, but are not limited to, tuning

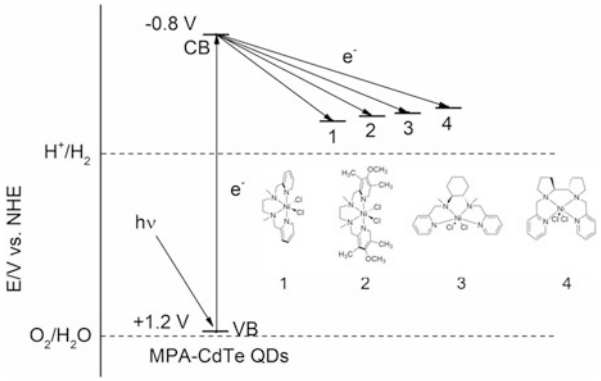


Fig. 6 Energy-level diagram of the cathodic peak potentials (vs. NHE) of Ni complexes *1–4* relative to the redox potential of the MPA-CdTe QDs (vs. NHE) [41]

of the catalyst and photosensitizer energetics and that further mechanistic analysis is required.

A model system consisting of mercaptopropionic acid-capped CdTe quantum dots (MPA-CdTe QDs) and nickel molecular catalysts was constructed to investigate ET from the photosensitizer to the hydrogen evolution catalyst decoupled from the full catalytic cycle [41]. The series of nickel(II) complexes supported by N4 tetradentate ligands (Fig. 6) were synthesized such that the reduction potential of the metal center could be systematically varied. In this study, the photoluminescence (PL) lifetime of the MPA-CdTe QDs was investigated in the presence of complexes **1–4** with varied concentrations**.** Photoluminescence arises only from radiative recombination processes, allowing for the selective measurement of processes such as recombination of valence band electrons with conduction band holes. This is often useful in deconvoluting the TA response of a system and for fully characterizing its photophysics across the range of relevant timescales. Time-resolved PL can be measured in a few different ways but can often be easily implemented through methods such as time-correlated single photon counting (TCSPC), in which emitted photons at a single detection wavelength are counted at a defined delay relative to the excitation pulse. TCSPC systems can be excellent for measuring PL on the ns timescale with sub-ns resolution [42, 43]. This can serve as an indirect probe of ET in hybrid QD/catalyst systems, as it directly monitors the relaxation of valence band electrons into the conduction band (Scheme 2). When additional competing decay pathways are available, such as ET to the catalyst, the depopulation of the excited state undergoing e-h recombination is accelerated, resulting in a quenching of the observed PL intensity and lifetime.

Time-resolved PL ($\lambda_{ex} = 450$ nm) measurements in the absence and increasing concentrations of **1** resulted in subsequently shorter dynamics as the concentration was increased, consistent with ET from the QD to the catalyst. The PL lifetime decayed with biexponential kinetics on the ns timescale, from which mean time

Table 1 Effect of catalyst concentration on QD mean PL lifetime reported in ns

	Catalyst **1**	Catalyst **2**	Catalyst **3**	Catalyst **4**
0 mM	24	24	24	24
0.15 mM	16	15	16	19
0.30 mM	14	13	14	17
0.75 mM	13	11	12	15

constants were reported (Table 1). However, while similar experiments with **2–4** repeated with the same concentrations of QD and catalyst resulted in the same reduction of the QD PL lifetime, there was no significant difference in QD PL lifetime between **1** and **4** at the same catalyst concentration (Table 1). This suggests that in the case of the nickel hydrogen evolution catalysts, the catalytic efficiency is limited by another step in the cycle, as the electron transfer kinetics do not differ significantly in this case as a function of Ni^{II}/Ni^{I} redox potential, as was previously expected. Additionally, when the PL lifetime measurements were repeated with the analogous Cu^{II} complexes, the results were ambiguous, and no significant difference in PL lifetime was observed, despite having similar M^{II}/M^{I} redox potentials to **1–4** below that of the QD conduction band [44]. This might be attributed to small variations in experimental conditions due to the reduced solubility of the copper complexes, though overall the results are challenging to interpret. Together, this suggests that the ET dynamics between the photosensitizer and the catalyst may depend on additional factors related to the electron acceptor such as ligand functionalization that are not currently well understood. A clear understanding of the ET step in such cases will be fundamental in establishing rational design principles for improved artificial photosynthetic systems.

4 Concluding Remarks

The diversification of our energy supplies is one of the great challenges of the twenty-first century. Hydrogen-based energy has gained significant attention as it produces only water upon combustion. However, in order to move toward a realistic integration of hydrogen-based energy sources into our energy supply, we must ensure that hydrogen is produced in a sustainable fashion. Obtaining hydrogen through stream-reforming fossil fuel is energy-intensive and environmentally harmful. The benign alternative is hydrogen production from water reduction, a key target within the field of artificial photosynthesis.

It is our position that a fundamental understanding of each individual process in artificial photosynthetic systems will lead to more efficient and scalable hydrogen production. There are excellent reviews available in the literature that report on the efficiency of photocatalytic water splitting with multicomponent systems, but a comprehensive analysis of photoinduced electron transfer processes for these systems is lacking [3, 12]. We have tried to bridge that gap by introducing such hybrid nanomaterial/molecular systems from a fundamental photophysical

perspective and have narrowed our discussion based on the cost-effectiveness and stability of the individual components. While clear design principles have yet to be established for such systems, we believe that detailed study of the electron transfer mechanism will make the process less random and more systematic.

References

1. Hammer, N. I.; Emrick, T.; Barnes, M. D. Quantum Dots Coordinated with Conjugated Organic Ligands: New Nanomaterials with Novel Photophysics. *Nanoscale Res Lett* **2007**, *2* (6), 282–290. https://doi.org/10.1007/s11671-007-9062-8.
2. Kamat, P. V. Quantum Dot Solar Cells. Semiconductor Nanocrystals as Light Harvesters. *J. Phys. Chem. C* **2008**, *112* (48), 18737–18753. https://doi.org/10.1021/jp806791s.
3. Liu, J.; Ren, Y.-Y.; Wu, J.; Xia, W.; Deng, B.-Y.; Wang, F. Hybrid Artificial Photosynthetic Systems Constructed Using Quantum Dots and Molecular Catalysts for Solar Fuel Production: Development and Advances. *Journal of Materials Chemistry A* **2021**, *9* (35), 19346–19368. https://doi.org/10.1039/D1TA02673A.
4. Han, Z.; Eisenberg, R. Fuel from Water: The Photochemical Generation of Hydrogen from Water. *Acc. Chem. Res.* **2014**, *47* (8), 2537–2544. https://doi.org/10.1021/ar5001605.
5. Xu, Y.; Zhang, B. Hydrogen Photogeneration from Water on the Biomimetic Hybrid Artificial Photocatalytic Systems of Semiconductors and Earth-Abundant Metal Complexes: Progress and Challenges. *Catal. Sci. Technol.* **2015**, *5* (6), 3084–3096. https://doi.org/10.1039/C5CY00365B.
6. Lewis, N. S. Toward Cost-Effective Solar Energy Use. *Science* **2007**, *315* (5813), 798–801. https://doi.org/10.1126/science.1137014.
7. Mazzeo, A.; Santalla, S.; Gaviglio, C.; Doctorovich, F.; Pellegrino, J. Recent Progress in Homogeneous Light-Driven Hydrogen Evolution Using First-Row Transition Metal Catalysts. *Inorganica Chimica Acta* **2021**, *517*, 119950. https://doi.org/10.1016/j.ica.2020.119950.
8. Wang, X.; Li, C. Interfacial Charge Transfer in Semiconductor-Molecular Photocatalyst Systems for Proton Reduction. *Journal of Photochemistry and Photobiology C: Photochemistry Reviews* **2017**, *33*, 165–179. https://doi.org/10.1016/j.jphotochemrev.2017.10.003.
9. Liu, S.; Lei, Y.-J.; Xin, Z.-J.; Lu, Y.-B.; Wang, H.-Y. Water Splitting Based on Homogeneous Copper Molecular Catalysts. *Journal of Photochemistry and Photobiology A: Chemistry* **2018**, *355*, 141–151. https://doi.org/10.1016/j.jphotochem.2017.09.060.
10. Wu, L.-Z.; Chen, B.; Li, Z.-J.; Tung, C.-H. Enhancement of the Efficiency of Photocatalytic Reduction of Protons to Hydrogen via Molecular Assembly. *Acc. Chem. Res.* **2014**, *47* (7), 2177–2185. https://doi.org/10.1021/ar500140r.
11. Tachibana, Y.; Vayssieres, L.; Durrant, J. R. Artificial Photosynthesis for Solar Water-Splitting. *Nature Photon* **2012**, *6* (8), 511–518. https://doi.org/10.1038/nphoton.2012.175.
12. Eckenhoff, W. T.; Eisenberg, R. Molecular Systems for Light Driven Hydrogen Production. *Dalton Trans.* **2012**, *41* (42), 13004–13021. https://doi.org/10.1039/C2DT30823A.
13. Lee, S.; Jang, G. Y.; Kim, J. K.; Park, J. H. Solar-Harvesting Lead Halide Perovskite for Artificial Photosynthesis. *Journal of Energy Chemistry* **2021**, *62*, 11–26. https://doi.org/10.1016/j.jechem.2021.02.025.
14. Klimov, V. I. Spectral and Dynamical Properties of Multiexcitons in Semiconductor Nanocrystals. *Annual Review of Physical Chemistry* **2007**, *58* (1), 635–673. https://doi.org/10.1146/annurev.physchem.58.032806.104537.
15. Ghimire, S.; Biju, V. Relations of Exciton Dynamics in Quantum Dots to Photoluminescence, Lasing, and Energy Harvesting. *Journal of Photochemistry and Photobiology C: Photochemistry Reviews* **2018**, *34*, 137–151. https://doi.org/10.1016/j.jphotochemrev.2018.01.004.

16. Xiao, J.; Zhao, M.; Wang, Y.; Zhang, X. Excitons in Atomically Thin 2D Semiconductors and Their Applications. *Nanophotonics* **2017**, *6* (6), 1309–1328. https://doi.org/10.1515/nanoph-2016-0160.
17. Masumoto, Y.; Sonobe, K. Size-Dependent Energy Levels of CdTe Quantum Dots. *Phys. Rev. B* **1997**, *56* (15), 9734–9737. https://doi.org/10.1103/PhysRevB.56.9734.
18. Liu, C.; Qiu, F.; Peterson, J. J.; Krauss, T. D. Aqueous Photogeneration of H2 with CdSe Nanocrystals and Nickel Catalysts: Electron Transfer Dynamics. *J. Phys. Chem. B* **2015**, *119* (24), 7349–7357. https://doi.org/10.1021/jp510935w.
19. Chica, B.; Wu, C.-H.; Liu, Y.; Adams, M. W. W.; Lian, T.; Dyer, R. B. Balancing Electron Transfer Rate and Driving Force for Efficient Photocatalytic Hydrogen Production in CdSe/CdS Nanorod–[NiFe] Hydrogenase Assemblies. *Energy Environ. Sci.* **2017**, *10* (10), 2245–2255. https://doi.org/10.1039/C7EE01738C.
20. Han, Z.; Qiu, F.; Eisenberg, R.; Holland, P. L.; Krauss, T. D. Robust Photogeneration of H2 in Water Using Semiconductor Nanocrystals and a Nickel Catalyst. *Science* **2012**, *338* (6112), 1321–1324. https://doi.org/10.1126/science.1227775.
21. Norris, D. J.; Bawendi, M. G. Measurement and Assignment of the Size-Dependent Optical Spectrum in CdSe Quantum Dots. *Phys. Rev. B* **1996**, *53* (24), 16338–16346. https://doi.org/10.1103/PhysRevB.53.16338.
22. Caram, J. R.; Zheng, H.; Dahlberg, P. D.; Rolczynski, B. S.; Griffin, G. B.; Dolzhnikov, D. S.; Talapin, D. V.; Engel, G. S. Exploring Size and State Dynamics in CdSe Quantum Dots Using Two-Dimensional Electronic Spectroscopy. *The Journal of Chemical Physics* **2014**, *140* (8), 084701. https://doi.org/10.1063/1.4865832.
23. Ekimov, A. I.; Kudryavtsev, I. A.; Efros, Al. L.; Yazeva, T. V.; Hache, F.; Schanne-Klein, M. C.; Rodina, A. V.; Ricard, D.; Flytzanis, C. Absorption and Intensity-Dependent Photoluminescence Measurements on CdSe Quantum Dots: Assignment of the First Electronic Transitions. *J. Opt. Soc. Am. B* **1993**, *10* (1), 100. https://doi.org/10.1364/JOSAB.10.000100.
24. Zhang, C.; Do, T. N.; Ong, X.; Chan, Y.; Tan, H.-S. Understanding the Features in the Ultrafast Transient Absorption Spectra of CdSe Quantum Dots. *Chemical Physics* **2016**, *481*, 157–164. https://doi.org/10.1016/j.chemphys.2016.08.027.
25. Jasrasaria, D.; Philbin, J. P.; Yan, C.; Weinberg, D.; Alivisatos, A. P.; Rabani, E. Sub-Bandgap Photoinduced Transient Absorption Features in CdSe Nanostructures: The Role of Trapped Holes. *J. Phys. Chem. C* **2020**, *124* (31), 17372–17378. https://doi.org/10.1021/acs.jpcc.0c04746.
26. Rawalekar, S.; Kaniyankandy, S.; Verma, S.; Ghosh, H. N. Ultrafast Charge Carrier Relaxation and Charge Transfer Dynamics of CdTe/CdS Core−Shell Quantum Dots as Studied by Femtosecond Transient Absorption Spectroscopy. *J. Phys. Chem. C* **2010**, *114* (3), 1460–1466. https://doi.org/10.1021/jp909118c.
27. Morgan, D. P.; Kelley, D. F. What Does the Transient Absorption Spectrum of CdSe Quantum Dots Measure? *J. Phys. Chem. C* **2020**, *124* (15), 8448–8455. https://doi.org/10.1021/acs.jpcc.0c02566.
28. Taheri, M. M.; Elbert, K. C.; Yang, S.; Diroll, B. T.; Park, J.; Murray, C. B.; Baxter, J. B. Distinguishing Electron and Hole Dynamics in Functionalized CdSe/CdS Core/Shell Quantum Dots Using Complementary Ultrafast Spectroscopies and Kinetic Modeling. *J. Phys. Chem. C* **2021**, *125* (1), 31–41. https://doi.org/10.1021/acs.jpcc.0c07037.
29. Thomas, A.; Sandeep, K.; Somasundaran, S. M.; Thomas, K. G. How Trap States Affect Charge Carrier Dynamics of CdSe and InP Quantum Dots: Visualization through Complexation with Viologen. *ACS Energy Lett.* **2018**, *3* (10), 2368–2375. https://doi.org/10.1021/acsenergylett.8b01532.
30. Klimov, V. I.; McBranch, D. W.; Leatherdale, C. A.; Bawendi, M. G. Electron and Hole Relaxation Pathways in Semiconductor Quantum Dots. *Phys. Rev. B* **1999**, *60* (19), 13740–13749. https://doi.org/10.1103/PhysRevB.60.13740.
31. Klimov, V.; Hunsche, S.; Kurz, H. Biexciton Effects in Femtosecond Nonlinear Transmission of Semiconductor Quantum Dots. *Phys. Rev. B* **1994**, *50* (11), 8110–8113. https://doi.org/10.1103/PhysRevB.50.8110.

32. Jacak, L.; Wójs, A.; Hawrylak, P. *Quantum Dots*; Springer Berlin Heidelberg: Berlin, Heidelberg, 1998. https://doi.org/10.1007/978-3-642-72002-4.
33. Efros, Al. L.; Rosen, M. The Electronic Structure of Semiconductor Nanocrystals. *Annu. Rev. Mater. Sci.* **2000**, *30* (1), 475–521. https://doi.org/10.1146/annurev.matsci.30.1.475.
34. Schleusener, A.; Micheel, M.; Benndorf, S.; Rettenmayr, M.; Weigand, W.; Wächtler, M. Ultrafast Electron Transfer from CdSe Quantum Dots to an [FeFe]-Hydrogenase Mimic. *J. Phys. Chem. Lett.* **2021**, *12* (18), 4385–4391. https://doi.org/10.1021/acs.jpclett.1c01028.
35. Lian, S.; Weinberg, D. J.; Harris, R. D.; Kodaimati, M. S.; Weiss, E. A. Subpicosecond Photoinduced Hole Transfer from a CdS Quantum Dot to a Molecular Acceptor Bound Through an Exciton-Delocalizing Ligand. *ACS Nano* **2016**, *10* (6), 6372–6382. https://doi.org/10.1021/acsnano.6b02814.
36. Morris-Cohen, A. J.; Frederick, M. T.; Cass, L. C.; Weiss, E. A. Simultaneous Determination of the Adsorption Constant and the Photoinduced Electron Transfer Rate for a Cds Quantum Dot–Viologen Complex. *J. Am. Chem. Soc.* **2011**, *133* (26), 10146–10154. https://doi.org/10.1021/ja2010237.
37. Lian, S.; Christensen, J. A.; Kodaimati, M. S.; Rogers, C. R.; Wasielewski, M. R.; Weiss, E. A. Oxidation of a Molecule by the Biexcitonic State of a CdS Quantum Dot. *J. Phys. Chem. C* **2019**, *123* (10), 5923–5930. https://doi.org/10.1021/acs.jpcc.9b00210.
38. Schnitzenbaumer, K. J.; Labrador, T.; Dukovic, G. Impact of Chalcogenide Ligands on Excited State Dynamics in CdSe Quantum Dots. *J. Phys. Chem. C* **2015**, *119* (23), 13314–13324. https://doi.org/10.1021/acs.jpcc.5b02880.
39. Grimaldi, G.; Geuchies, J. J.; van der Stam, W.; du Fossé, I.; Brynjarsson, B.; Kirkwood, N.; Kinge, S.; Siebbeles, L. D. A.; Houtepen, A. J. Spectroscopic Evidence for the Contribution of Holes to the Bleach of Cd-Chalcogenide Quantum Dots. *Nano Lett.* **2019**, *19* (5), 3002–3010. https://doi.org/10.1021/acs.nanolett.9b00164.
40. Kankanamalage, P. H. A.; Ekanayake, D. M.; Singh, N.; Morais, A. C. P. de; Mazumder, S.; Verani, C. N.; Mukherjee, A.; Lanznaster, M. Effect of Ligand Substituents on Nickel and Copper [N4] Complexes: Electronic and Redox Behavior, and Reactivity towards Protons. *New J. Chem.* **2019**, *43* (32), 12795–12803. https://doi.org/10.1039/C9NJ01283D.
41. Botcha, N. K.; Gutha, R. R.; Sadeghi, S. M.; Mukherjee, A. Synthesis of Water-Soluble Ni(II) Complexes and Their Role in Photo-Induced Electron Transfer with MPA-CdTe Quantum Dots. *Photosynth Res* **2019**. https://doi.org/10.1007/s11120-019-00668-z.
42. Millar, D. P. Time-Resolved Fluorescence Spectroscopy. *Current Opinion in Structural Biology* **1996**, *6* (5), 637–642. https://doi.org/10.1016/S0959-440X(96)80030-3.
43. Smith, D. A.; McKenzie, G.; Jones, A. C.; Smith, T. A. Analysis of Time-Correlated Single Photon Counting Data: A Comparative Evaluation of Deterministic and Probabilistic Approaches. *Methods Appl. Fluoresc.* **2017**, *5* (4), 042001. https://doi.org/10.1088/2050-6120/aa8055.
44. Botcha, N. K.; Gutha, R. R.; Sadeghi, S. M.; Mukherjee, A. Exploring the Potential of Water-Soluble Cu(II) Complexes with MPA–CdTe Quantum Dots for Photoinduced Electron Transfer. *Catalysts* **2022**, *12* (4), 422. https://doi.org/10.3390/catal12040422.

Interparticle Charge Transport Enhances Electrochemiluminescence of Quantum Dots



Xuwen Gao and Bin Cai

1 Introduction

Quantum dots (QDs) exhibit exceptional optical and electronic properties that can be precisely tailored by their size, shape, and surface chemistry [1, 2]. With these luminescence properties superior to that of molecular counterparts [3, 4], QDs have attracted significant interest for fundamental studies of exciton and charge dynamics [5–8] and for practical applications including light-emitting diodes [9, 10], solar cells [11, 12], and biomedical diagnostics [13, 14]. Besides photo and electrical excitations, the emissive states of QDs can also be generated electrochemically based on the charge-transfer reactions of electrogenerated reactive species, known as electrochemiluminescence (ECL) [15, 16]. The combination of electrochemistry and spectroscopy brings intriguing features to ECL such as low background, wide dynamic range, and high controllability, thus leading to the great commercial success of the ECL technique in various fields [17, 18].

The current understanding of ECL generation upon QDs is largely inherited from the theories developed by Bard and coworkers [16, 17, 19] and has been extended to other ECL luminophores [20–22]. There are two possible reaction routes proposed for QD-based ECL in the presence of coreactants according to existing ECL mechanisms developed by Miao et al. [23], where the final charge-transfer step to generate exciton could be (i) reaction between coreactant radical and QD radical (i.e., intraparticle charge transfer, left of Fig. 1) or (ii) reaction between QD radicals (i.e., interparticle charge transfer, middle of Fig. 1).

For the intraparticle charge-transfer route (left of Fig. 1), coreactant radical (i.e., coreactant$^{\bullet}$) is generated via electrochemical oxidation which is mostly followed

X. Gao · B. Cai (✉)
School of Chemistry and Chemical Engineering, Shandong University, Jinan, China
e-mail: bin.cai@sdu.edu.cn

© The Author(s), under exclusive license to Springer Nature Switzerland AG 2024

S. Krishnamoorthy, K. (Kris) Iniewski (eds.), *Advances in Fabrication and Investigation of Nanomaterials for Industrial Applications*,
https://doi.org/10.1007/978-3-031-42700-8_8

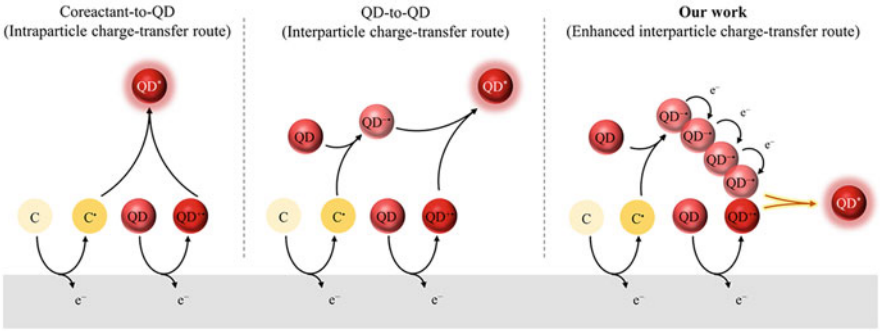


Fig. 1 Scheme of the possible charge-transfer routes for ECL generation in the presence of coreactant (left and middle), as well as the selectively enhanced interparticle charge-transfer route which corresponds to our work based on QD aerogels (right)

by subsequent deprotonation (Eq. 1), while the QD cation radical (i.e., $QD^{+\bullet}$) is generated via electrochemical oxidation of QD (Eq. 2). Then the intraparticle charge-transfer reaction between coreactant$^{\bullet}$ and $QD^{+\bullet}$ produces the excited states QD^{*} (Eq. 3) which eventually emits light (Eq. 4):

$$\text{coreactant} \rightarrow \text{coreactant}^{\bullet} + e^{-} + H^{+} \tag{1}$$

$$QD \rightarrow QD^{+\bullet} + e^{-} \tag{2}$$

$$\text{coreactant}^{\bullet} + QD^{+\bullet} \rightarrow QD^{*} \tag{3}$$

$$QD^{*} \rightarrow QD + h\nu \tag{4}$$

As shown in the middle of Fig. 1, the excitons could also be generated via an interparticle charge-transfer route which involves the generation of coreactant$^{\bullet}$ and $QD^{+\bullet}$ radicals (Eqs. 1 and 2). Specifically, when the diffusing coreactant$^{\bullet}$ radicals collide with ground-state QDs, oppositely charged QD radicals (i.e., $QD^{-\bullet}$) are formed (Eq. 5), which could then annihilate with $QD^{+\bullet}$ radicals to generate excitons (Eq. 6):

$$\text{coreactant}^{\bullet} + QD \rightarrow QD^{-\bullet} \tag{5}$$

$$QD^{-\bullet} + QD^{+\bullet} \rightarrow QD^{*} \tag{6}$$

The extremely short lifetime of radicals and their stochastic collisions make the investigation of these charge-transfer processes particularly challenging, thus leading to the long-term ambiguity in mechanistic understanding of modern coreactant-based ECL systems [24]. Thus, it is of fundamental interest to manipulate the

charge-transfer pathways and elucidate the unique mechanisms for exciton generation in ECL systems.

In this chapter, this challenge are addressed by electronically coupling individual QDs into an aerogel structure to facilitate interparticle charge transport, which leads to the generation of highly efficient ECL based on the selectively enhanced interparticle charge-transfer route (right of Fig. 1). In this regard, the QD aerogel luminophore could efficiently accept holes from electrode and electrons from coreactant$^{\bullet}$ radicals. And the charge carriers were transported within the aerogel network to annihilate into excitons.

CdSe QDs can be self-assembled into all-inorganic and impurity-free aerogel monolith with large surface area, ultralow density, and high porosity via a novel water-induced gelation strategy. The removal of insulating organic ligands aids the fusion and electronic coupling of adjacent QDs, enabling efficient charge transport within the aerogel networks. As a demonstration, the resultant CdSe QD aerogel shows a 126-fold improved ECL efficiency. The charge-transport-promoted ECL mechanism upon aerogel is further verified by designing a CdSe-CdTe mixed QD aerogel and clearly decoupled the two routes for ECL generation for the first time. When applying a coreactant that is solely suitable for CdTe QD, the ECL signal from both CdSe and CdTe QDs can be observed, confirming the electron transfer from CdTe QD to CdSe QD toward ECL generation.

2 Experimental

2.1 Chemicals and Reagents

Cadmium oxide (CdO, 99.99%), oleic acid (OA, 90%), 1-octadecene (ODE, 90%), 2-ethylhexanoic acid (≥99%), myristic acid (98.5%), triethylene glycol dimethyl ether (99%), thiourea (99%), sodium borohydride ($NaBH_4$, 99%), tellurium powder (Te, 200 mesh, 99.8%), cadmium chloride ($CdCl_2$, 99%), 3-mercaptopropionic acid (MPA, 99%), sodium hydroxide (NaOH, 98%), and ammonium sulfide solution (20 wt% $(NH_4)_2S$ in H_2O) were purchased from Sigma-Aldrich. Zinc 2-ethylhexanoate (ca. 80% in mineral spirits) and selenium powder (Se, 99.99%) were purchased from Alfa Aesar. The solvents, including *N*-methylformamide (NMF), isopropanol, acetonitrile, and hexane, were purchased from VWR Chemicals. All reagents were used as received without further purification.

2.2 Apparatus and Measurements

Bright-field transmission electron microscopy (TEM), HAADF-STEM, and EDXS analysis were performed at a Talos F200X microscope equipped with an X-FEG

electron source and a Super-X EDX detector system (FEI). Prior to transmission electron microscopy (TEM) analysis, the specimen mounted in a high-visibility holder was treated for 2 s into a Model 1020 Plasma Cleaner (Fischione) to remove possible contamination. The UV-vis absorption and Tauc plot were recorded on Agilent Cary 5000 spectrophotometer (Agilent, USA). The photoluminescence (PL) spectra were measured with F-320 spectrofluorimeter (Tianjin Gangdong Sci. & Tech. Co., China). The PL lifetime were recorded on an FLS920 fluorescence spectrometer equipped with matching point ball (Edinburgh Instruments, UK). X-ray photoelectron spectroscopy (XPS) was conducted with monochromatic Al Kα radiation (Thermo Fisher Scientific Co., USA). X-ray diffraction (XRD) was carried out on a Siemens D5000 X-ray diffractometer with Cu Kα radiation ($\lambda = 1.5406$ Å). Thermogravimetric analysis (TGA) was conducted by a Diamond TG-DTA/Spectrum GX with a heating rate of 10 K min^{-1} under N_2 atmosphere. Fourier transform infrared spectroscopy (FT-IR) was recorded using a Thermo Nicolet 8700 spectrometer. Nitrogen adsorption was performed with a Quantachrome NOVA 3000e system at 77 K. The sample was degassed at 373 K for ~72 h under vacuum before the measurement. Scanning electron microscopy (SEM) was performed on a Zeiss DSM 982 Gemini instrument.

Accumulated and spooling ECL spectra were obtained on a homemade ECL spectrometer consisting of an Acton SP2300i monochromator equipped with a liquid N_2-cooled PyLoN 400BR-eXcelon digital charge-coupled device (CCD) detector (Princeton Instruments, USA) and a VersaSTAT 3 electrochemical analyzer (Princeton Applied Research, USA). The solid-state ECL was constructed by deposition of luminophores at the Au electrode surface with a diameter of 5 mm which was polished 0.3- and 0.05-μm alumina slurry before use. The QD or QD aerogel powers were sonicated in acetonitrile to form an ink with a concentration of 0.5 mg_{QD} mL^{-1}. The working electrode was obtained by drop-casting 2.0 μL of freshly prepared ink onto the Au disk electrode and drying under N_2 atmosphere. For all the electrochemistry and ECL measurement, a typical three-electrode system was involved by using saturated Ag/AgCl as reference electrode and Pt wire as counter electrode. To evaluate the ECL intensity, the electrochemical cell was placed on a holder attached to photomultiplier tube (PMT) in the cassette dedicated to the MPI-II ECL analyzer (Remex Analytical Instrument Co., Ltd., China). The ECL generation was driven by the potential scan at 0.1 V s^{-1} for one cycle in the range between 0 and 1.60 V. To collect ECL spectra, the electrochemical cell was placed into a homemade holder attached to a spectrograph with a CCD camera cooled to −120 °C. The ECL generation was also driven by the potential scan at 0.1 V/s for one cycle in the range between 0 and 1.60 V. As for the spooling ECL, the spectra were recorded every 0.1 V during the potential scan, which is equivalent to 2 s. The ECL emission was collected with an objective lens before it was delivered to the ECL spectrum system.

2.3 Synthesis and Preparation

2.3.1 CdSe-OA QDs

In a 100-mL three-neck flask, 4 mmol of CdO, 12 mmol of myristic acid, and 20 mL of ODE were degassed at room temperature for 15 min. After filling the flask with Ar, the mixture was heated up to 270 °C until CdO was fully dissolved. Then, the mixture was cooled down to 90 °C and degassed for 1 h, and 20 mL of dried ODE (degassed at 80 °C for 1 h) were added. The temperature was increased to 240 °C, and 2 mmol of Se suspended in 2 mL of ODE were quickly injected. The solution was kept at 240 °C for 5 min for CdSe QDs growth. Then, the temperature was decreased to 180 °C, and 1 mL of 2-ethylhexanoic acid and 4 mL of OA were added into the reaction system.

The surface of CdSe QDs was passivated by CdZnS. Specifically, 7 mmol of thiourea in 6 mL of triethylene glycol dimethyl ether were mixed with 2.88 mL of zinc 2-ethylhexanoate, and the obtained solution was divided into three parts. The first part of the solution was slowly injected into the reaction system at 180 °C for 1 h using a syringe pump. Fifteen minutes after injection of the first part, the second part was slowly injected for 30 min. Ten minutes after the complete injection of the second part, the third part was injected at the same speed. The reaction system was kept at 180 °C after the complete addition of the solution. The surface-passivated CdSe QDs were washed twice with acetonitrile and stored in hexane.

2.3.2 CdSe-S^{2-} QDs

The organic ligands of CdSe QDs were exchanged for S^{2-} ions to achieve a stable dispersion in polar solvent according to previous reports [25]. Specifically, the 10-mg OA-capped CdSe QDs dispersed in hexane (2 mL) were added on top of 4-mL NMF containing 1 mmol $(NH_4)_2S$. The amount of sulfide precursor was in excess of that required to form a complete S^{2-}-terminated surface via a self-limiting reaction. After vigorous stirring, pristine organic ligands were replaced with S^{2-} ions, accompanied by QD transfer from a nonpolar (hexane) to a polar (NMF) phase, which could be observed by color change. The NMF phase was washed for three times using fresh hexane. The resulting S^2-capped QDs dispersed in a 4-mL NMF were precipitated by adding 8-mL acetone, centrifuged, and then redispersed in a 2-mL NMF for subsequent gelation.

2.3.3 CdSe Aerogel

The resulting S^{2-}-capped QDs form a stable dispersion in NMF, which serves as a sol for the following sol-gel process (Fig. 2a). Specifically, the gelation of QDs

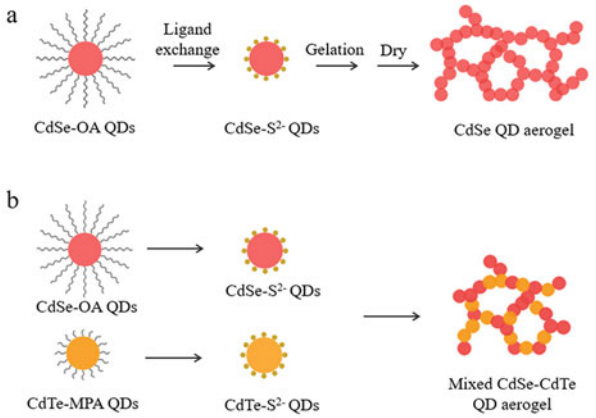


Fig. 2 Schematic representation of (**a**) the water-induced gelation route for aerogel synthesis and (**b**) the synthesis strategy toward CdSe-CdTe mixed aerogels

into gel structure was triggered by adding a 20-μL deionized water to a 1-mL NMF solution of CdSe-S^{2-} QDs (about 4 mg). The system was kept still for about 3 days, after which a gel monolith was formed and settled down in the bottom of the vial. After aging for several days, the resulting solvogel was solvent-exchanged by more than 20 times with copious ethanol to remove possible residues, leading to the QD gel solvated in ethanol. Afterward, the ethanol solvent was exchanged with liquid CO_2 in autoclave, followed by supercritical drying at 100 bar and 45 °C using a critical point dryer 13200J0AB (SPI Supplies) equipped with a CO_2 pump.

2.3.4 CdTe-MPA QDs

In a typical synthesis, two solutions were prepared at the same time. The Te precursor (i.e., NaHTe) solution was prepared by injection of a 10-mL water into a mixture of 0.1 mmol of Te powder and 0.5 mmol of $NaBH_4$ in a three-necked flask under N_2 atmosphere, which was further heated to 85 °C and kept for 15 min to obtain a dark red transparent NaHTe solution. On the other hand, the Cd precursor solution was prepared by dissolving 0.2 mmol of $CdCl_2$ and 23 μL of MPA in 10 mL of deionized water, followed by adjusting the pH to 11 ~ 12 by dropwise addition of 1-M solution of NaOH. The solution is placed in a three-necked flask and deaerated by N_2 bubbling for 30 min. Then, 2 mL of fresh NaHTe solution were injected into the Cd precursor solution and refluxed at 90 °C for 16 h under N_2 atmosphere. The CdTe-MPA QDs were washed twice with isopropanol and stored in 0.2 mL of deionized water.

2.3.5 CdTe-S^{2-} QDs

The surface MPA ligand of the CdTe-MPA QDs was replaced by S^{2-} ions for the synthesis of mixed aerogel, ensuring the formation of CdSe-CdTe heterojunctions. Specifically, 0.02 mL of MPA-capped CdTe QDs solution was diluted by adding 1 mL of NMF solution containing a 5-mM $(NH_4)_2S$ under N_2 atmosphere at 40 °C. The mixture was stirred at 40 °C for 5 h to achieve the surface modification of S^{2-} ions and a passivation layer of CdS [26].

2.3.6 CdSe-CdTe Mixed Aerogel

The obtained CdTe-S^{2-} QDs in NMF solution were directly applied to the subsequent gelation process to prepare the CdSe-CdTe mixed QD aerogel. As shown in Fig. 2b, the as-obtained CdTe QDs were ligand-exchanged by S^{2-} ions and then mixed with CdSe QDs to form a mixed QD sol. Next, the CdSe-CdTe mixed aerogels were synthesized via water-induced gelation strategy.

3 Results and Discussion

To realize the aerogel architecture, a novel water-induced gelation strategy was developed for the synthesis of all-inorganic, impurity-free QD aerogels (Fig. 2a). The CdSe QDs (surface-passivated with CdZnS) were chosen as the building blocks, as they are among the most efficient ECL luminophores [27]. Previously, the gelation of anion-capped QDs was achieved by appropriate metal-ion-assisted complexation [28, 29]. However, the involvement of hetero-metal ions may lead to unintentional cation exchange or surface contamination, which is detrimental to photoluminescence (PL) properties [30]. Generally, the surface of chalcogenide QDs is partially hydroxylated by environmental water, thus providing proper affinity to water molecules [8]. Herein, adding a trace amount of water into the QD sol could trigger the sol-gel process, which slowly turns the QD colloids into multibranched gel networks. Afterward, the CdSe QD aerogel monolith was obtained by supercritical drying.

3.1 Characterization of CdSe QDs and Aerogel

3.1.1 Structure and Specific Surface

Some conventional techniques have been used for the characterization of aerogels. In FTIR spectra, the prominent peak stretching vibration of $–CH_2$ from hydrocarbon species disappeared to a large extent after the ligand exchange and completely after

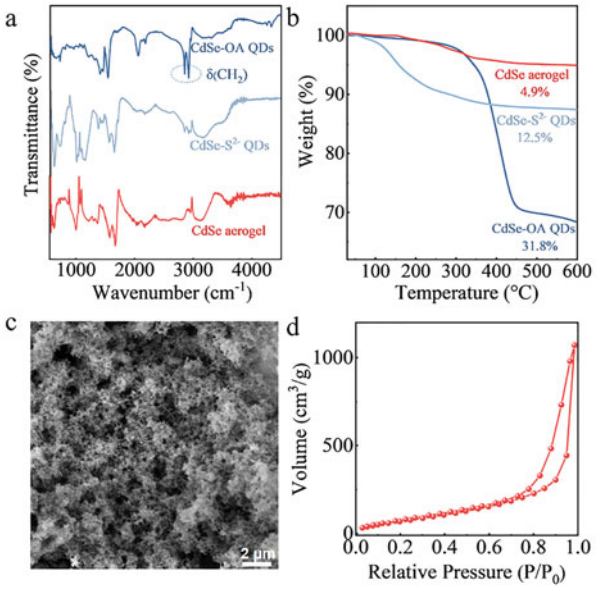


Fig. 3 (**a**) FTIR of the CdSe-OA QDs, CdSe-S^{2-} QDs, and CdSe aerogel. (**b**) TGA of the CdSe-OA QDs, CdSe-S^{2-} QDs, and CdSe aerogel with a heating rate of 10 K min^{-1} under N_2 atmosphere. (**c**) SEM image of the as-synthesized CdSe QD aerogel. (**d**) Nitrogen adsorption isotherms of the as-synthesized CdSe QD aerogel at 1 bar, 77 K

the gelation and drying (Fig. 3a), thus proving an efficient elimination of the OA molecules from the QD surface. Furthermore, the TGA results indicate that the CdSe aerogel lost only ca. 4.9% of its weight after heating up to 600 °C (Fig. 3b). This behavior is another indirect evidence of the fact that there are almost no ligands associated with the aerogel surface. The high porosity, impurity-free surface, and high specific surface area were confirmed by SEM and N_2 physisorption analysis (Fig. 3c,d).

3.1.2 Morphology and Optical Properties

The as-synthesized CdSe-OA QDs with narrow particle-size distributions were initially capped with insulating organic ligands (Fig. 4a). Afterward, the long-chain OA was completely replaced with S^{2-} ions to achieve a stable colloidal dispersion in a polar solvent (Fig. 4b). The usage of S^{2-} ligands facilitates the decrease of surface traps by avoiding midgap states in comparison with the widely used thiol ligands [31]. The TEM for CdSe QD aerogel shows a well-defined 3D network array composed of interconnected nanowires with a diameter similar to the original CdSe QDs (Fig. 4c,d).

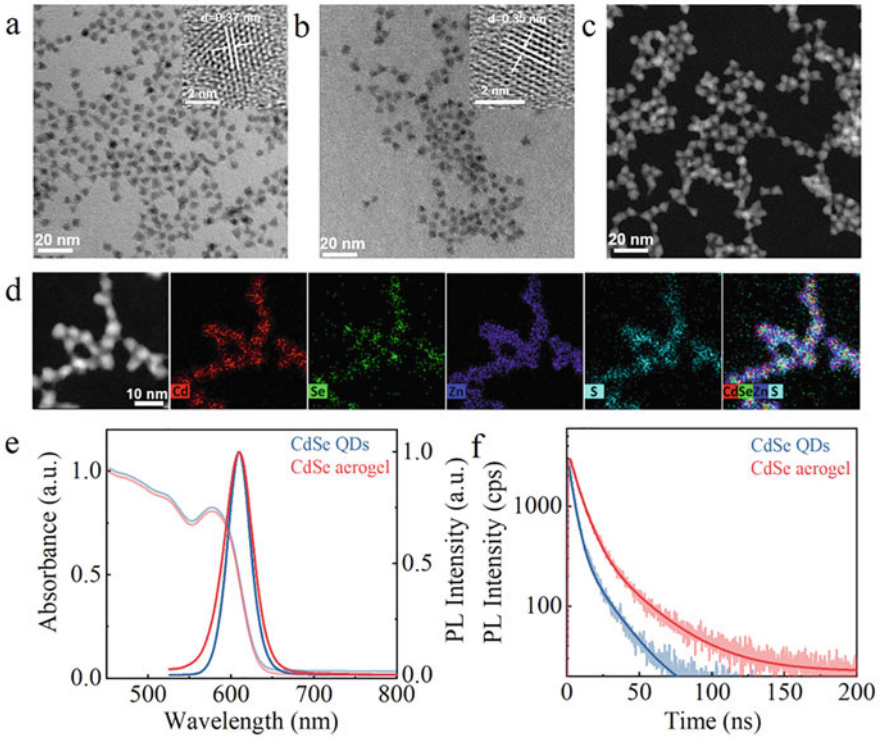


Fig. 4 TEM image of individual (**a**) CdSe-OA QDs and (**b**) CdSe-S^{2-} QDs. (**c**) HAADF-STEM images of the monolithic CdSe aerogel. (**d**) HAADF-STEM image and corresponding EDXS-based element maps for the CdSe QD aerogel. (**e**) UV-vis and PL spectra. (**f**) PL decay curves of the CdSe QDs and aerogel, respectively. The absorption and PL measurements were performed in the diffuse reflection mode with a sample thickness of 0.1 mm and a diameter of 5 mm

It has been well demonstrated that epitaxially fused connections of QDs is an effective route to increase inter-dot coupling and enhance electron mobility between QDs [6, 32]. The crystalline nature of the fused junction area revealed the strong electronic coupling between adjacent CdSe QDs (Fig. 4c,d) [8, 33], which contributes to fast charge transport within the aerogel structure [34, 35]. The quantitative water-induced strategy is a key to gelation process, and the introduction of water facilitates the gelation process in two aspects: (i) assisting surface hydroxylation and water adsorption, thus facilitating the close attachment and epitaxial fusion between QDs, and (ii) decreasing the colloidal stability by reducing the electrical double layer of QDs owing to the smaller dielectric constant of water.

The absorption and emission properties of the CdSe QDs before and after the formation of aerogel were further investigated. Both CdSe QDs and aerogel exhibit similar absorption onsets and PL profiles (Fig. 4e), indicative of the retention of

the quantum confinement property in the macroscopic aerogel. The monolithic QD aerogel is characterized by an increased PL lifetime (17.40 ns) in comparison to that of the isolated QDs (11.75 ns) (Fig. 4f). The distinct properties of prolonged exciton lifetimes have been attributed to a delocalization of the excited electrons throughout the aerogel network [36–38].

3.1.3 Electrochemistry and ECL Properties

The redox of luminophore could be conveniently achieved via electrochemically injecting conduction band (CB) electrons and valence band (VB) holes under given potentials, the electrochemical redox involved charge injection of both CdSe QDs, and aerogel is consequently investigated with the surface-confined states. Both the isolated QDs and the aerogel exhibit obvious oxidation processes around 1.16 V (Fig. 5b), manifesting the direct injection of holes into their VB. More impressively, the CdSe aerogel shows a remarkably enhanced anodic current density at 1.16 V compared to the isolated CdSe QDs, indicative of a more efficient hole injection into the VB of the aerogel. This is explainable as the electronic coupling between the QDs provides efficient charge transport pathways within the aerogel network. In other words, the QDs that are far away from the electrode can still be efficiently oxidized.

Compared to conventional ECL where luminophores diffuse freely in solution, solid-state ECL confines luminophores at the electrode surface, which favors charge transport and device engineering [39]. Here, a solid-state device was constructed to evaluate ECL generation using triethanolamine (TEOA) as coreactant (Fig. 5). In particular, ECL was generated via an oxidative-reduction route, where the QD luminophore receives a hole from the electrode and an electron from the reducing radical $TEOA^{\bullet}$ generated from electro-oxidation of TEOA (Eqs. 7–9):

$$QD_{CdSe} + TEOA - 2e^{-} \rightarrow {QD_{CdSe}}^{+\bullet} + TEOA^{\bullet} \tag{7}$$

$${QD_{CdSe}}^{+\bullet} + TEOA^{\bullet} \rightarrow {QD_{CdSe}}^{*} \tag{8}$$

$${QD_{CdSe}}^{*} \rightarrow QD_{CdSe} + h\upsilon_{610\ nm} \tag{9}$$

During the anodic scan, both entities exhibit a distinct oxidative-reduction ECL around 1.20 V upon employing TEOA as coreactant. The CdSe QD aerogel demonstrates an ECL efficiency of 86% relative to ${Ru(bpy)_3}^{2+}$ [40, 41] that is 126-fold higher than that of the isolated CdSe QDs (Fig. 5c). The ECL spectra reveal similar maximum emission wavelengths for both CdSe QDs and aerogel (~610 nm, FWHM = 55 nm), indicative of the preservation of the exciton properties in the form of aerogel (inset of Fig. 5c). Notably, the ECL properties of both QDs and aerogel are similar to their PL properties (Fig. 4f). As shown in the spooling

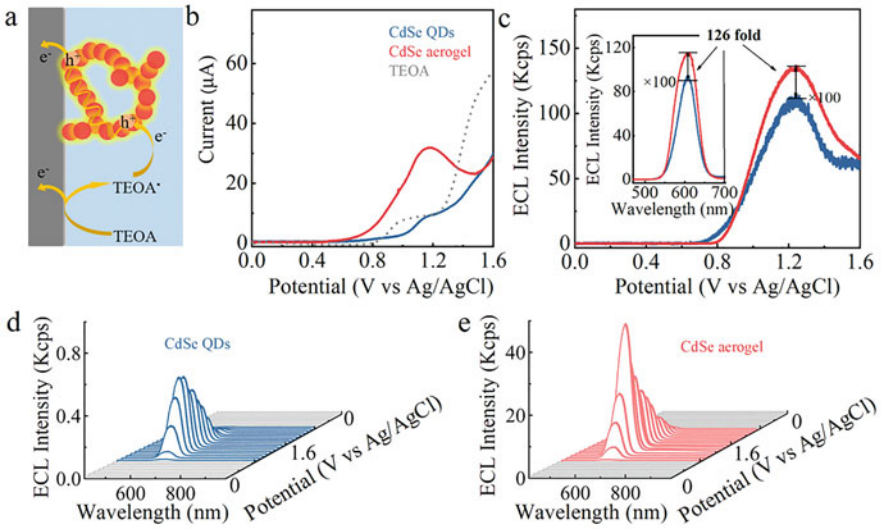


Fig. 5 (**a**) Schematic illustration of a solid-state ECL device using QD aerogel as luminophore. (**b**) DPV and (**c**) ECL intensity-potential profiles of CdSe QDs and CdSe QD aerogel. *Inset of panel (c)* shows the ECL spectra, where the ECL intensity of CdSe QDs is multiplied by 100 for comparison. Spooling ECL spectra of (**d**) the CdSe QDs and (**e**) the CdSe QD aerogel. The ECL was evaluated under 0.1 M pH 7.4 borate buffer containing a 10-mM TEOA by scanning the potential from 0 to 1.6 V at 100 mV s^{-1}. The DPV and ECL were recorded using Au disk electrode, saturated Ag/AgCl, and Pt wire as working, reference, and counter electrodes, respectively

ECL spectra, both entities demonstrate ECL peak sets centered at ~610 nm with increasing intensity during the potential scan up to 1.20 V (Fig. 5d,e).

The drastically enhanced ECL efficiency has been ascribed to the aerogel structure. In contrast, ECL built from isolated QDs can only inject holes into the electrode-contacted QDs owing to the interparticle charge-transfer barriers. The delocalization of charge carriers also applies for the electrons donated from the coreactant radicals. The fast charge transport in the aerogel greatly facilitates the utilization efficiency of the holes or electrons for ECL generation via the interparticle charge-transfer route (Eqs. 10–12):

$$\mathrm{QD_{Aerogel}} + \mathrm{TEOA^{\bullet}} \rightarrow \mathrm{QD_{Aerogel}}^{-\bullet} \tag{10}$$

$$\mathrm{QD_{Aerogel}} - \mathrm{e^{-}} \rightarrow \mathrm{QD_{Aerogel}}^{+\bullet} \tag{11}$$

$$\mathrm{QD_{Aerogel}}^{+\bullet} + \mathrm{QD_{Aerogel}}^{-\bullet} \rightarrow \mathrm{QD_{CdSe}}^{*} \tag{12}$$

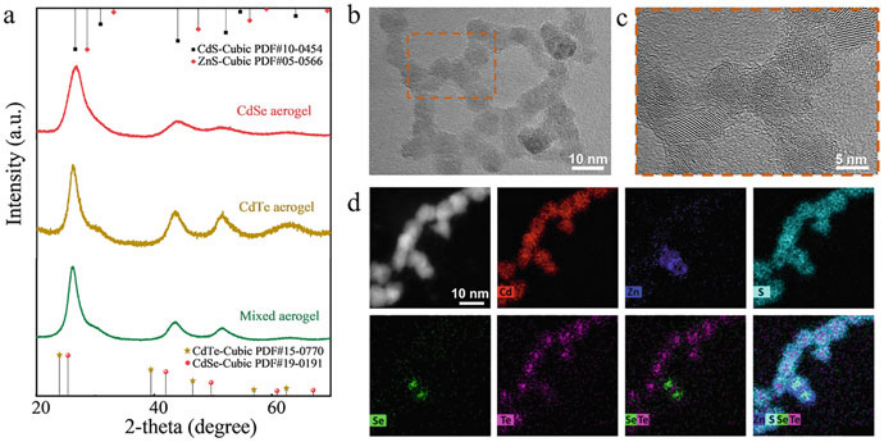


Fig. 6 (**a**) XRD characterization of the CdSe QDs, the CdTe QDs, and the CdSe-CdTe mixed QD aerogels. XRD were recorded at Siemens D5000 X-ray diffractometer using CuKα radiation ($\lambda = 1.5406$ Å) with step size of 0.02° and for $2\theta = 2$–35°. (**b**, **c**) TEM images, as well as (**d**) HAADF-STEM image and corresponding EDXS-based element maps of the CdSe-CdTe mixed aerogel, highlighting the abundant heterojunctions within the aerogel

3.2 Characterization of CdSe-CdTe Mixed Aerogel

3.2.1 Structure and Morphology

The charge-transport-promoted ECL mechanism is further verified by designing CdSe-CdTe mixed QD aerogels, where the interparticle charge-transfer route could be clearly decoupled from the intraparticle charge-transfer route. The CdTe QDs (surface passivated with CdS) were selected to mix with CdSe QDs (surface passivated with CdZnS), as their excitons can be clearly differentiated by ECL properties.

The XRD pattern of mixed aerogel that displays peaks with 2θ value similar to those of both CdSe and CdTe aerogels confirms the preservation of both CdSe and CdTe QD components. The CdSe-CdTe mixed QD aerogels preserve the zinc blende crystal structure of both CdSe and CdTe aerogel (Fig. 6a). The mixed aerogel possesses a typical network structure composed of interconnected nanowires (Fig. 6b,c). The mixed aerogel inherits the diameter of the precursor QDs, ensuring the preservation of nanoscopic quantum confinement properties. Evidenced by the elemental maps (Fig. 6d), the two QD components are randomly distributed within the mixed aerogel networks, demonstrating the existence of numerous CdSe-CdTe heterojunctions.

3.2.2 ECL Properties and Mechanism

A proper selection of the coreactants provides an effective way for electron injection into the specific QD components of the mixed aerogel (Fig. 7a). According to the coreactant mechanism, electron injection from a coreactant radical into the QDs plays an essential role in generating ECL. It is clear that the CdSe QDs generate efficient ECL with maximum emission wavelength of 610 nm using TEOA as coreactant (Figs. 5c,d, and 7b). However, no any ECL signal was detected when 2-(dibutylamino)ethanol (DBAE) was employed as coreactant (Fig. 7b), indicating an inappropriate energy alignment between CdSe QDs and the DBAE$^{\bullet}$ radicals. In contrast, using DBAE as coreactant, conspicuous ECL with maximum emission

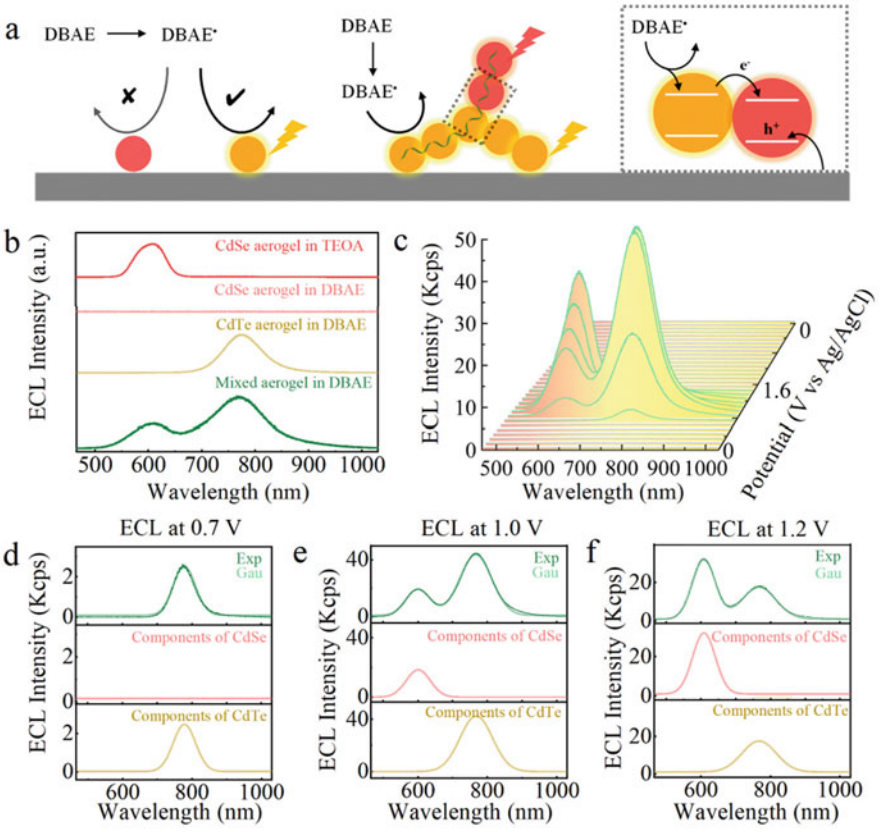


Fig. 7 (**a**) Scheme of the charge-transfer-mediated ECL mechanism. (**b**) ECL spectra of the CdSe, CdTe, and mixed aerogels. (**c**) Spooling ECL spectra of the mixed aerogel in 0.1 M pH 7.4 borate buffer containing a 10-mM DBAE. Corresponding ECL spectra of the mixed aerogel at potentials of (**d**) 0.7 V, (**e**) 1.0 V, and (**f**) 1.2 V. Exp and Gau represent the experiment and Gaussian fit, respectively. The ECL generation was evaluated using Au disk electrode, Ag/AgCl, and Pt wire as working, reference, and counter electrodes, respectively

wavelength of 775 nm was generated upon CdTe QDs, demonstrating an effective electron injection from DBAE$^{\bullet}$ radicals into the CdTe QDs (Fig. 7b).

Impressively, when applying DBAE as coreactant that is solely suitable for CdTe, the accumulated ECL upon the CdSe-CdTe mixed aerogel demonstrates two well-defined ECL peaks located at ca. 610 and 775 nm (Fig. 7b), whose peak profile, maximum emission wavelength, and FWHM are almost identical to the emission spectra of the CdSe and CdTe aerogels, respectively. Both QD components can generate ECL within the mixed aerogel, despite that the DBAE coreactant is not suitable for the CdSe QD component. Therefore, it is reasonable to deduce the electron transfer pathway from CdTe to CdSe (Fig. 7a). The ECL signal at 775 nm (refers to CdTe QD component) of the CdSe-CdTe mixed aerogel is slightly lower than the pure CdTe QD aerogel, which could be ascribed to (i) a lower loading of CdTe QDs (50 wt %) and (ii) a lower utilization of electrons (transferred into CdSe components).

Potential-resolved ECL spectra show two groups of distinguishable peaks without obvious shift and broadening in the potential range between 0.7 and 1.4 V (Fig. 7c).To gain more insights into the ECL mechanism, three representative transient ECL spectra at different potentials were deconvoluted (Fig. 7d–f). During the potential scan from 0 to 0.7 V, the ECL was dominated by CdTe with a maximum at 775 nm. When the potential increased to a more oxidative range (i.e., 0.8 to 1.0 V), the ECL at 610 nm based on CdSe can be observed, while the ECL at 775 nm based on CdTe reaches a maximum at 1.0 V. As the potential is further increased to 1.2 V, the ECL became dominated by the CdSe component. The evolution of the ECL spectra agrees well with the oxidation processes of the CdSe aerogel during the potential scan from 0 to 1.6 V (Fig. 5b,c).These results demonstrate that the DBAE$^{\bullet}$ radical injects electrons into the CdTe component, which could be transferred to the CdSe component to generate ECL. The facilitated interparticle electron transfer for ECL has been further demonstrated by varying the components (data not shown). The ECL generation mechanism from both CdTe and CdSe components is proposed as follows (Eqs. 13–17):

$$\mathrm{QD_{CdTe}} + \mathrm{QD_{CdSe}} + \mathrm{DBAE} - 3\mathrm{e}^{-} \rightarrow \mathrm{DBAE}^{\bullet} + \mathrm{QD_{CdTe}}^{+\bullet} + \mathrm{QD_{CdSe}}^{+\bullet} \tag{13}$$

$$\mathrm{DBAE}^{\bullet} + \mathrm{QD_{CdTe}} \rightarrow \mathrm{QD_{CdTe}}^{-\bullet} \tag{14}$$

$$\mathrm{QD_{CdTe}}^{-\bullet} + \mathrm{QD_{CdSe}} \rightarrow \mathrm{QD_{CdTe}} + \mathrm{QD_{CdSe}}^{-\bullet} \tag{15}$$

$$\mathrm{QD_{CdSe}}^{-\bullet} + \mathrm{QD_{CdSe}}^{+\bullet} \rightarrow \mathrm{QD_{CdSe}}^{*} \rightarrow \mathrm{QD_{CdSe}} + h\upsilon_{610\ \mathrm{nm}} \tag{16}$$

$$\mathrm{QD_{CdTe}}^{+\bullet} + \mathrm{DBAE}^{\bullet} \rightarrow \mathrm{QD_{CdTe}}^{*} \rightarrow \mathrm{QD_{CdTe}} + h\upsilon_{775\ \mathrm{nm}} \tag{17}$$

3.3 Experimental and Theoretical Results

To further verify the electron transfer from CdTe to CdSe, the energy-level alignments were estimated experimentally and theoretically (Fig. 8). The bandgap (E_g) of the CdSe and CdTe QDs can be calculated from the intercept of the tangents

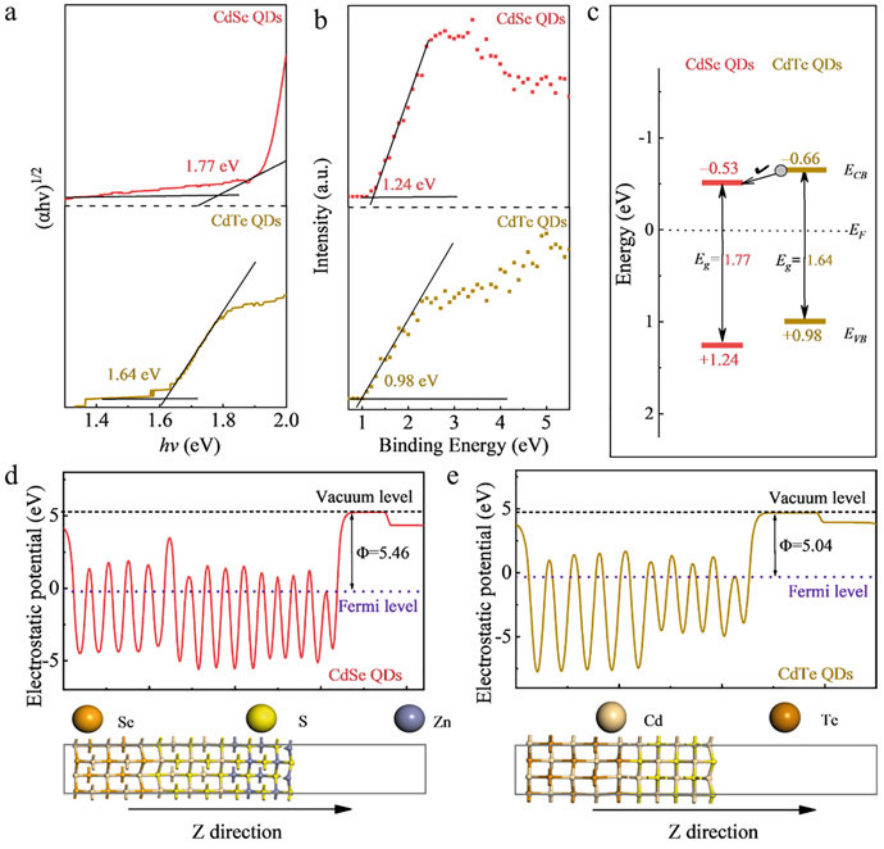


Fig. 8 (**a**) Tauc plots of the CdSe and CdTe QDs. (**b**) Determination of valence band edges by XPS spectra of the CdSe and the CdTe QDs. (**c**) Schematic energy-level alignment at the interface between CdSe and CdTe QDs. The calculated work function and corresponding structure model for the (220) plane of (**e**) CdSe QDs and (**f**) CdTe QDs. The original bulk structures of CdSe and CdTe (including surface passivation) have been optimized with the Monkhorst-Pack k-point of 4 × 4 × 4. Geometry optimizations were performed with the force convergency smaller than 0.02 eV/Å. The Vienna Ab initio Simulation Package (VASP) and the Perdew-Burke-Ernzerhof (PBE) function were employing to perform all density functional theory (DFT) calculations with the generalized gradient approximation (GGA). The projected augmented wave (PAW) potentials were chosen to describe the ionic cores, and valence electrons have been taken into account using a plane wave basis set with a kinetic energy cutoff of 450 eV

to a taut plot of $(\alpha h\nu)^{1/2}$ versus the photon energy ($h\nu$), and the intrinsic E_g of the CdSe and CdTe QDs were determined to be 1.77 and 1.64 eV, respectively (Fig. 8a). As revealed by the XPS spectra (Fig. 8b), the valence band energy (E_{VB}) of the CdSe and CdTe QDs were measured as +1.24 and + 0.98 eV, respectively. Based on the calculated E_g and the measured E_{VB}, the energy-level alignments at the interface between CdSe and CdTe QDs can be outlined (Fig. 8c). The conduction band edges (E_{CB}) of the CdSe and CdTe QDs were determined as −0.53 V and − 0.66 V, respectively. Notably, the more negative E_{CB} of the CdTe QDs than that of CdSe QDs provides supports for the charge transfer from the CdTe component to the CdSe component in the CdSe-CdTe mixed aerogel.

In addition, DFT calculations were adopted to directly evaluate the work functions (Φ) to further understand the interfacial charge separation and transfer within the CdSe-CdTe mixed QD aerogel. The theoretical work functions of the CdSe and CdTe QDs are 5.46 eV and 5.04 eV (with respect to vacuum), respectively (Fig. 8d,e), inferring that the Fermi level of the CdTe (−5.04 eV) is higher than the CdSe QDs (−5.46 eV). The difference in Fermi levels facilitates electron transfer from CdTe to CdSe upon contact until they are closely aligned, confirming the proposed electron transfer mechanism within the mixed aerogel, which participates in the ECL generation of the CdSe QDs.

4 Conclusions

This chapter developed a versatile water-induced gelation strategy for the synthesis of all-inorganic and impurity-free chalcogenide QD aerogels and elucidated the interparticle charge-transfer route in coreactant-based ECL systems by employing QD aerogels as luminophores. The interparticle charge-transfer route can be selectively enhanced based on the fast interparticle charge transport, which relies on the strong electronic coupling between adjacent QDs within the aerogel structures. The resulting CdSe QD aerogel exhibited a 126-fold enhanced ECL efficiency. When applying a coreactant that is solely suitable for CdTe, the ECL signals from both CdSe and CdTe components can be observed in the CdSe-CdTe mixed QD aerogel, confirming the electron transfer from CdTe QDs to CdSe QDs toward ECL generation. The ECL signal of the CdSe QD component was generated by an explicit interparticle charge-transfer route, which accepts electrons from the CdTe QD component and holes from the electrode. Thus, the two charge-transfer routes were clearly decoupled in the conventional coreactant mechanisms, confirming the charge-transport-promoted ECL mechanism. The CdTe QD component acts as a catalyst to drive the electron transfer reaction between DBAE radicals and CdSe QD components. This study is anticipated to advance the mechanistic understanding of electrochemical exciton generation in QDs and provides synthetic perspectives for novel nanocrystal aerogels.

Acknowledgments This study was supported by the National Natural Science Foundation of China (22174087, 52201262), Guangdong Basic and Applied Basic Research Foundation (2021A1515110920), Natural Science Foundation of Shandong Province (ZR2022QE001), Taishan Scholars Program of Shandong Province (tsqn202211042), Fundamental Research Funds of Shandong University (ZY202006), and Jinan Bureau of Science and Technology (2021GXRC127). The author (DNT) wishes to thank Prof. Guizheng Zou, School of Chemistry and Chemical Engineering at Shandong University for UV-Vis, PL, electrochemistry, ECL analysis, and DFT calculation. DNT acknowledges Drs. Guocan Jiang and Anatol Prudnikau, Physical Chemistry at Technische Universität Dresden, for the synthesis of samples and corresponding characterizations used in this study. DNT acknowledges René Hübner, Institute of Ion Beam Physics and Materials Research at Helmholtz-Zentrum Dresden-Rossendorf, for TEM analysis. The author thanks Prof. Alexander Eychmüller for fruitful discussion in this work.

References

1. Kagan, C. R.; Lifshitz, E.; Sargent, E. H.; Talapin, D. V., Building devices from colloidal quantum dots. *Science***2016,***353* (6302), aac5523.
2. Boles, M. A.; Ling, D.; Hyeon, T.; Talapin, D. V., The surface science of nanocrystals. *Nat. Mater.***2016,***15* (3), 364.
3. Owen, J.; Brus, L., Chemical synthesis and luminescence applications of colloidal semiconductor quantum dots. *J. Am. Chem. Soc.***2017,***139* (32), 10939–10943.
4. Resch-Genger, U.; Grabolle, M.; Cavaliere-Jaricot, S.; Nitschke, R.; Nann, T., Quantum dots versus organic dyes as fluorescent labels. *Nat. Methods***2008,***5* (9), 763–775.
5. Zhang, Z.; Sung, J.; Toolan, D. T. W.; Han, S.; Pandya, R.; Weir, M. P.; Xiao, J.; Dowland, S.; Liu, M.; Ryan, A. J.; Jones, R. A. L.; Huang, S.; Rao, A., Ultrafast exciton transport at early times in quantum dot solids. *Nat. Mater.***2022,***21* (5), 533–539.
6. Whitham, K.; Yang, J.; Savitzky, B. H.; Kourkoutis, L. F.; Wise, F.; Hanrath, T., Charge transport and localization in atomically coherent quantum dot solids. *Nat. Mater.***2016,***15* (5), 557–563.
7. Zherebetskyy, D.; Scheele, M.; Zhang, Y. J.; Bronstein, N.; Thompson, C.; Britt, D.; Salmeron, M.; Alivisatos, P.; Wang, L. W., Hydroxylation of the surface of PbS nanocrystals passivated with oleic acid. *Science***2014,***344* (6190), 1380–1384.
8. Kagan, C. R.; Murray, C. B., Charge transport in strongly coupled quantum dot solids. *Nat. Nanotechnol.***2015,***10* (12), 1013–1026.
9. Sayevich, V.; Robinson, Z. L.; Kim, Y.; Kozlov, O. V.; Jung, H.; Nakotte, T.; Park, Y. S.; Klimov, V. I., Highly versatile near-infrared emitters based on an atomically defined HgS interlayer embedded into a CdSe/CdS quantum dot. *Nat. Nanotechnol.***2021,***16* (6), 673–679.
10. Kim, T.; Kim, K.; Kim, S.; Choi, S. M.; Jang, H.; Seo, H. K.; Lee, H.; Chung, D. Y.; Jang, E., Efficient and stable blue quantum dot light-emitting diode. *Nature***2020,***586* (7829), 385–389.
11. Meinardi, F.; McDaniel, H.; Carulli, F.; Colombo, A.; Velizhanin, K. A.; Makarov, N. S.; Simonutti, R.; Klimov, V. I.; Brovelli, S., Highly efficient large-area colourless luminescent solar concentrators using heavy-metal-free colloidal quantum dots. *Nat. Nanotechnol.***2015,***10* (10), 878–885.
12. Chuang, C.-H. M.; Brown, P. R.; Bulović, V.; Bawendi, M. G., Improved performance and stability in quantum dot solar cells through band alignment engineering. *Nat. Mater.***2014,***13* (8), 796–801.
13. Howes, P. D.; Chandrawati, R.; Stevens, M. M., Colloidal nanoparticles as advanced biological sensors. *Science***2014,***346* (6205), 54–62.
14. Bruns, O. T.; Bischof, T. S.; Harris, D. K.; Franke, D.; Shi, Y.; Riedemann, L.; Bartelt, A.; Jaworski, F. B.; Carr, J. A.; Rowlands, C. J.; Wilson, M. W. B.; Chen, O.; Wei, H.; Hwang, G. W.; Montana, D. M.; Coropceanu, I.; Achorn, O. B.; Kloepper, J.; Heeren, J.; So, P. T. C.;

Fukumura, D.; Jensen, K. F.; Jain, R. K.; Bawendi, M. G., Next-generation in vivo optical imaging with short-wave infrared quantum dots. *Nat. Biomed. Eng.***2017,***1* (4), 0056.
15. Wu, P.; Hou, X.; Xu, J. J.; Chen, H. Y., Electrochemically generated versus photoexcited luminescence from semiconductor nanomaterials: bridging the valley between two worlds. *Chem. Rev.***2014,***114* (21), 11027–11059.
16. Ding, Z.; Quinn, B. M.; Haram, S. K.; Pell, L. E.; Korgel, B. A.; Bard, A. J., Electrochemistry and electrogenerated chemiluminescence from silicon nanocrystal quantum dots. *Science***2002,***296* (5571), 1293–1297.
17. Richter, M. M., Electrochemiluminescence (ECL). *Chem. Rev.***2004,***104*, 3003−3036.
18. Ma, C.; Cao, Y.; Gou, X.; Zhu, J. J., Recent progress in electrochemiluminescence sensing and imaging. *Anal. Chem.***2020,***92* (1), 431–454.
19. J., M. W., Electrogenerated chemiluminescence and its biorelated applications. *Chem. Rev.***2008,***108*, 2506–2553.
20. Hesari, M.; Ding, Z., A grand avenue to Au nanocluster electrochemiluminescence. *Acc. Chem. Res.***2017,***50* (2), 218–230.
21. Zhu, D.; Zhang, Y.; Bao, S.; Wang, N.; Yu, S.; Luo, R.; Ma, J.; Ju, H.; Lei, J., Dual intrareticular oxidation of mixed-ligand metal-organic frameworks for stepwise electrochemiluminescence. *J. Am. Chem. Soc.***2021,***143* (8), 3049–3053.
22. Tan, X.; Zhang, B.; Zou, G., Electrochemistry and electrochemiluminescence of organometal halide perovskite nanocrystals in aqueous medium. *J. Am. Chem. Soc.***2017,***139* (25), 8772–8776.
23. Miao, W. J.; Choi, J. P.; Bard, A. J., Electrogenerated chemiluminescence 69: the tris(2,2'-bipyridine)ruthenium(II), $(Ru(bpy)_3{}^{2+})$/tri-n-propylamine (TPrA) system revisited-a new route involving $TPrA^{\cdot}$ cation radicals. *J. Am. Chem. Soc.***2002,***124* (48), 14478–14485.
24. Dong, J.; Lu, Y.; Xu, Y.; Chen, F.; Yang, J.; Chen, Y.; Feng, J., Direct imaging of single-molecule electrochemical reactions in solution. *Nature***2021,***596* (7871), 244–249.
25. Nag, A.; Kovalenko, M. V.; Lee, J. S.; Liu, W.; Spokoyny, B.; Talapin, D. V., Metal-free inorganic ligands for colloidal nanocrystals: S^{2-}, HS^{-}, Se^{2-}, HSe^{-}, Te^{2-}, HTe^{-}, $TeS_3{}^{2-}$, OH^{-}, and $NH_2{}^{-}$ as surface ligands. *J. Am. Chem. Soc.***2011,***133* (27), 10612–10620.
26. Fan, X. B.; Yu, S.; Wang, X.; Li, Z. J.; Zhan, F.; Li, J. X.; Gao, Y. J.; Xia, A. D.; Tao, Y.; Li, X. B.; Zhang, L. P.; Tung, C. H.; Wu, L. Z., Susceptible surface sulfide regulates catalytic activity of CdSe quantum dots for hydrogen photogeneration. *Adv. Mater.***2019,***31* (7), 1804872.
27. Cao, Z.; Shu, Y.; Qin, H.; Su, B.; Peng, X., Quantum dots with highly efficient, stable, and multicolor electrochemiluminescence. *ACS. Cent. Sci.***2020,***6* (7), 1129–1137.
28. Sayevich, V.; Cai, B.; Benad, A.; Haubold, D.; Sonntag, L.; Gaponik, N.; Lesnyak, V.; Eychmuller, A., 3D assembly of all-inorganic colloidal nanocrystals into gels and aerogels. *Angew. Chem. Int. Ed.***2016,***55* (21), 6334–6338.
29. Singh, A.; Lindquist, B. A.; Ong, G. K.; Jadrich, R. B.; Singh, A.; Ha, H.; Ellison, C. J.; Truskett, T. M.; Milliron, D. J., Linking semiconductor nanocrystals into gel networks through all-inorganic bridges. *Angew. Chem. Int. Ed.***2015,***54* (49), 14840–14844.
30. Geng, X.; Li, S.; Mawella-Vithanage, L.; Ma, T.; Kilani, M.; Wang, B.; Ma, L.; Hewa-Rahinduwage, C. C.; Shafikova, A.; Nikolla, E.; Mao, G.; Brock, S. L.; Zhang, L.; Luo, L., Atomically dispersed Pb ionic sites in PbCdSe quantum dot gels enhance room-temperature NO_2 sensing. *Nat. Commun.***2021,***12* (1), 4895.
31. Kovalenko, M. V.; Scheele, M.; Talapin, D. V., Colloidal nanocrystals with molecular metal chalcogenide surface ligands. *Science***2009,***324* (5933), 1417–1120.
32. Abelson, A.; Qian, C.; Salk, T.; Luan, Z.; Fu, K.; Zheng, J. G.; Wardini, J. L.; Law, M., Collective topo-epitaxy in the self-assembly of a 3D quantum dot superlattice. *Nat. Mater.***2020,***19* (1), 49–55.
33. Coropceanu, I.; Janke, E. M.; Portner, J.; Haubold, D.; Nguyen, T. D.; Das, A.; Tanner, C. P. N.; Utterback, J. K.; Teitelbaum, S. W.; Hudson, M. H.; Sarma, N. A.; Hinkle, A. M.; Tassone, C. J.; Eychmuller, A.; Limmer, D. T.; de la Cruz, M.; Ginsberg, N. S.; Talapin, D. V., Self-assembly of nanocrystals into strongly electronically coupled all-inorganic supercrystals. *Science***2022,***375*, 1422–1426.

34. Mohanan, J. L.; Arachchige, I. U.; Brock, S. L., Porous semiconductor chalcogenide aerogels. *Science***2005,***307* (5708), 397–400.
35. Hewa-Rahinduwage, C. C.; Geng, X.; Silva, K. L.; Niu, X.; Zhang, L.; Brock, S. L.; Luo, L., Reversible electrochemical gelation of metal chalcogenide quantum dots. *J. Am. Chem. Soc.***2020,***142* (28), 12207–12215.
36. Arachchige, I. U.; Brock, S. L., Sol-gel assembly of CdSe nanoparticles to form porous aerogel networks. *J. Am. Chem. Soc.***2006,***128* (24), 7964–7971.
37. Rusch, P.; Zambo, D.; Bigall, N. C., Control over structure and properties in nanocrystal aerogels at the nano-, micro-, and macroscale. *Acc. Chem. Res.***2020,***53* (10), 2414–2424.
38. Sanchez-Paradinas, S.; Dorfs, D.; Friebe, S.; Freytag, A.; Wolf, A.; Bigall, N. C., Aerogels from CdSe/CdS Nanorods with ultra-long exciton lifetimes and high fluorescence quantum yields. *Adv. Mater.***2015,***27* (40), 6152–6156.
39. Peng, H.; Huang, Z.; Deng, H.; Wu, W.; Huang, K.; Li, Z.; Chen, W.; Liu, J., Dual enhancement of gold nanocluster electrochemiluminescence: electrocatalytic excitation and aggregation-induced emission. *Angew. Chem. Int. Ed.***2020,***59* (25), 9982–9985.
40. Hesari, M.; Swanick, K. N.; Lu, J. S.; Whyte, R.; Wang, S.; Ding, Z., Highly efficient dual-color electrochemiluminescence from BODIPY-capped PbS nanocrystals. *J. Am. Chem. Soc.***2015,***137* (35), 11266–11269.
41. Swanick, K. N.; Ladouceur, S.; Zysman-Colman, E.; Ding, Z. F., Self-enhanced electrochemiluminescence of an iridium(III) complex: mechanistic insight. *Angew. Chem. Int. Ed.***2012,***52* (44), 11079–11086.

Optical Structural and Phonon Characteristics of Epitaxially Grown II–VI/III–V Films and Superlattices

Devki N. Talwar

1 Introduction

II–VI cadmium chalcogenides (CdX, X = S, Se, Te) and III–V indium pnictides (InY, Y=P, As, Sb) with tunable structural and electrical characteristics are considered as the device engineering marvels. Hardly any of these materials are useful in their natural zinc-blende (zb) forms. By exploiting epitaxial growth processing and finishing techniques [1–16], it is possible to transform them into device-grade epilayers, multiple quantum wells (MQWs), and superlattices (SLs) having targeted electrical and optical traits. With the molecular beam epitaxy (MBE), one can achieve a pseudomorphic growth of II–VI/III–V semiconductors provided the lattice constant of epilayer is closer to that of the substrate [17–21]. Lattice mismatch can limit not only the coherent hetero-epitaxial structure to within a certain critical thickness – it may also cause intrinsic defects to degrade the quality of materials [22–28].

Cadmium telluride (CdTe) of energy bandgap E_g ~ 1.51 eV (at 300 K) is considered as an attractive semiconductor to design a broad range of device structures for photovoltaic and photodetection applications [1–16]. As compared to the traditional Si and Ge detectors, requiring cryogenic cooling and consuming high power, the II–VI-based devices are compact, expend less power, operate at room temperature, and display unique features for processing more than one million photons/second/mm^2. In recent years, the growing interest for exploiting $Cd_{1-x}Zn_xTe$ (CZT) epifilms over group IV semiconductors has been its ability to concoct alloys with accurate control

D. N. Talwar (✉)
Department of Physics, University of North Florida, Jacksonville, FL, USA

Department of Physics, Indiana University of Pennsylvania, Indiana, PA, USA
e-mail: d.talwar@unf.edu

© The Author(s), under exclusive license to Springer Nature Switzerland AG 2024

S. Krishnamoorthy, K. (Kris) Iniewski (eds.), *Advances in Fabrication and Investigation of Nanomaterials for Industrial Applications*,
https://doi.org/10.1007/978-3-031-42700-8_9

of composition x and thickness d. Another advantage of utilizing these materials in device engineering includes the accessibility of low-cost, large-area, and electrically conductive substrates, such as GaAs and InSb. Although CZT material is used to design γ-ray detector with energy resolution better than 1% at 662 keV, its deployment in the large-scale industrial electronics is hampered, however, due to complications in producing device-grade materials for growing chemically pure and structurally perfect alloys and SLs. The key interest in $Cd_{1-x}Zn_xTe$ alloys and $(CZT)_m/(ZnTe)_n$ superlattices (SLs) aspires assessing their electrical and optical characteristics by controlling x, m, and n – the film thickness d plays an equally important role in regulating the efficiency of electro-optical devices, e.g., an accurate thickness d of buffer and epifilm is required for fabricating sensors, detectors, and solar cells. The II–VI-based electronics demand high-quality crystalline materials with fewer defects. In the as-grown CZT alloys, the constraints of phase diagram necessitating higher growth temperatures usually instigate intrinsic defects.

Indium antimonide (InSb), on the other hand, possesses the highest electron mobility (~7.8×10^4 cm^2/V-s), larger breakdown field (~10^3 V/cm), higher saturated electron drift velocity (~5×10^7 cm/s), smaller effective mass ($m_e^* \sim 0.013\ m_o$), and the lowest energy bandgap $E_g \sim 0.18$ eV (300 K) [17, 18]. InSb-based ternary and/or quaternary alloys are regarded as useful materials for realizing mid-wavelength infrared (MWIR) detectors. There has been a growing interest in developing InSb-based quantum dots (QDs) and nanostructured laser diodes (LDs) for optoelectronic and photonic applications in the 3–5-μm wavelength range for room temperature (RT) operations [19–23]. Both CdTe and InSb semiconductors are almost perfectly lattice matched ($\Delta a/a \equiv < 0.05\%$) with closer thermal expansion coefficients and thus viewed as the most attractive combination in the growth of epilayers, MQWs, and SLs to design faster electronic devices. As CdTe and InSb belong to different groups having atypical electronegativities of constituent atoms, some complications are expected, however, in the preparation of CdTe/InSb epifilms [17–28]. The intricacies are mostly caused by the interdiffusion of In/Te and/or Cd/Sb atoms to stimulate III/VI or II/V bonding for inducing structural deterioration at the interfaces [29–36].

Using soft X-ray photoelectron spectroscopy (S-XPS) and Raman scattering spectroscopy (RSS), there are reports that indicate the erection of In_2Te_3 precipitates and creation of clusters with segregated Sb atoms at the CdTe-InSb boundary [31, 32]. Comprehending the atomic structure at the interface has been and still is a challenge despite the existence of transmission electron microscopy (TEM) with high spatial resolution [29–36]. An accurate estimation of CdTe film thickness on InSb substrate is of paramount importance for using it in device engineering [37–40]. In the far-infrared (FIR) region, 5 meV $\leq E \leq$ 100 meV, while SE is considered an efficient method for exploring lattice dynamics and free-carrier concentration in semiconductors, it has not yet been applied to study the phonons of CZT alloys. No SE measurements are available for assessing film thickness of either $Cd_{1-x}Zn_xTe$/GaAs or CdTe/InSb epilayers. Traditionally, the electronic characteristics of epifilms are characterized by Hall measurements [37], high-resolution X-ray diffraction (HR-XRD), ultraviolet-visible spectrophotometry (UVS) [38], cross-

sectional scanning electron microscopy (X-SEM) [40], etc. Most of these methods, being destructive, are inconvenient for assessing the material quality required in electronic industry for device fabrications. Several nondestructive methods used for characterizing the large-area epitaxially grown wafers include the atomic force microscopy (AFM), energy-dispersive X-ray spectroscopy, secondary ion mass spectrometry (SIMS), SE, etc. High-resolution synchrotron radiation X-ray absorption spectroscopy (HR-SXAS) [39], FIR reflectivity, and RSS [31, 32] are equally valuable tools for evaluating constructive information about the phonon characteristics, including epifilm thickness and structural attributes.

The purpose of this work is to report the results of a comprehensive experimental (cf. Sect. 2) and theoretical (cf. Sect. 3) study not only to extract the epifilm thickness but also to comprehend both phonons and structural traits of several Bridgman-grown CZT alloys (see Sect. 2.1) and MBE-prepared CdTe/InSb (001) epilayers (see Sect. 2.2) by exploiting FIR reflectivity, RSS, and HR-SXAS measurements (cf. Sects. 2.3 and 2.4). A realistic lattice dynamical method is adopted to study phonons and thermodynamical characteristics (cf. Sect. 3). The Brüker IFS 66 v/s spectrometer was used to acquire the RT FIR spectra of CZT and CdTe/InSb (001) epifilms. These materials are also examined by using an HR-SXAS and collecting data at the Cd K-edge (~26,717 eV) covering energy region between 26,500 eV and 27,700 eV in the X-ray fluorescence yield mode. By adopting a traditional multilayer optics within the three-phase (ambient/film/substrate) model, we have simulated thickness-dependent reflectance and transmission spectra of ultrathin CdTe/InSb epilayers and $(CdTe)_m/(ZnTe)_n$/GaAs SLs both at near normal and oblique incidence (cf. Sects. 3.1, 3.2, and 3.3). Model dielectric functions derived from the SE data are meticulously incorporated to fit the reflectivity and transmission spectra of ultrathin binary and ternary alloys in the range of ~1.0 to 6 eV (cf. Sects. 4.1 and 4.2). Careful data analysis of the HR-SXAS spectra (cf. Sect. 4.3) is found quite imperative for not only mapping the local atomic structures of the bond lengths (i.e., the first nearest-neighbor Cd-Te and second nearest-neighbor Cd-Cd atomic bonding) but also estimating the coordination numbers. Theoretical results of the FIR reflectivity, RSS, and HR-SXAS spectra are compared and discussed with the experimental data in Sect. 4 with concluding remarks presented in Sect. 5.

2 Experimental

The ternary alloy samples of $Cd_xZn_{1-x}Te$ ($0 \leq x \leq 1$) were grown by Bridgman technique (cf. Sect. 2.1), while six CdTe/InSb epifilms (cf. Sect. 2.2) were prepared using the MBE method. For optimizing the performance of optoelectronic device structures, the most essential criterion used here is to comprehend the optical behavior of materials at the boundaries of individual epitaxial layers, stacked in a device configuration. The fundamental parameters of such arrangements required careful assessment of the electronic, vibrational, interfacial potentials, electric

field strengths, and widths of the free-carrier depletion layers. For the ideal and atomically abrupt interfaces, the base for such assemblies is to carefully characterize them by using FIR reflectivity/transmission, RSS (cf. Sect. 2.3), XRD, SE (cf. Sect. 2.4), TEM, reflection high-energy electron diffraction (RHEED), time-resolved PL (TRPL), and HR-SXAS (cf. Sect. 2.5) measurements.

2.1 *Bridgman-Grown $Cd_{1-x}Zn_xTe$ Ternary Alloys*

The ternary alloy samples of $Cd_{1-x}Zn_xTe$ ($0 \leq x \leq 1$) used in the FIR (5 meV $\leq E \leq$ 100 meV: 1 meV $\cong$ 8 cm^{-1}), RSS, PL, and XRD measurements were grown at the Massachusetts Institute of Technology by using the Bridgman technique. The CZT alloys were prepared by reacting the 99.9999% pure elemental constituents in the evacuated sealed quartz tubes at ~1150 °C. The Cd composition determined from the mass densities and precast alloys was regrown by directional solidification at the rates of 1.2 mm/h in adiabatic zone of a Bridgman-Stockbarger-type furnace with temperature gradient set at ~15 °C/cm. The resultant boules cut into 1–2-mm-thick slices perpendicular to the growth axis were annealed at 600 °C in a Cd-saturated atmosphere for about 5 d to improve crystalline perfection. Finally, the surfaces of CZT sample were prepared by lapping, mechanical polishing, and etching in a bromine-methanol solution. The alloy composition x, set by the ratio of constituents before growth, was confirmed by XRD and transmission measurements after preparation. All the CZT alloys were found to be single crystal (see Fig. 1) having zb structures.

2.2 *MBE Growth of CdTe/InSb (001) Epifilms*

Prior to the MBE growth of six CdTe epifilms on InSb (001) [37, 38] used in this study, the substrate was required an ion beam cleaning. The ion beam bombardment on InSb was done by using a voltage of 500 V with temperature ranging from 25 °C to 250 °C and varying time from 0.5 h to 2.25 h. An angle ψ between the incident beam and the surface of the substrate was set at around 10° – close to the grazing angle. Before the growth of epifilms, all ion beam cleaned substrates were annealed for 20 min at 225 °C. The CdTe depositions on InSb (001) were carried out at a substrate temperature of 185 °C for 90 min except for the sample # S_1 (which was done for 96 min) while keeping the source (high-purity polycrystalline CdTe) temperature at 600 °C. A set of six MBE-grown CdTe/InSb (001) samples (#S_1–S_6) of different film thickness d ranging between 1.13 μm and 1.31 μm were prepared under nearly identical conditions (see Table 1). The FIR and HR-SXAS measurements (Sects. 2.3 and 2.4) were performed on all these samples for comprehending their thickness-dependent spectra to assess their structural characteristics.

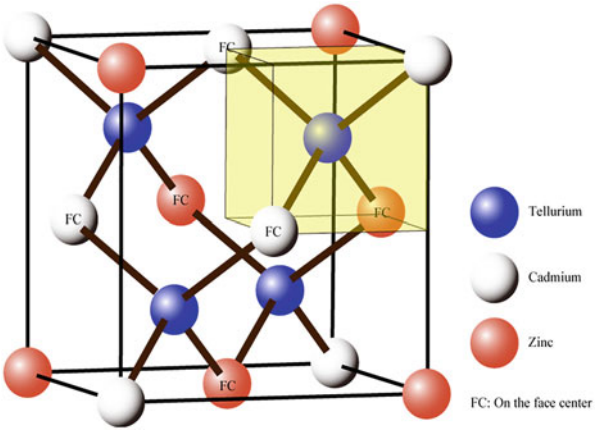


Fig. 1 An ideal image of zinc-blende (zb) structure of $Cd_{1-x}Zn_xTe$ alloy. Here, we have indicated the blue-colored circles with the tellurium (Te), white-colored circles by cadmium (Cd), and pink-colored circles with the zinc (Zn) atoms. In the perfect binary case of CdTe with $x = 0$, each Cd (Te) atom is surrounded by four Te (Cd) atoms occupying the tetrahedral sites. For $x \neq 0$, the Cd atoms are assumed replaced by the Zn atoms (see text)

Table 1 Summary of information for the six MBE-grown CdTe/InSb samples used in the far-infrared reflectivity and high-resolution synchrotron extended X-ray absorption fine structure measurements (see text)

	Ion beam cleaning		MBE-grown CdTe films
Sample #	Time (hr.)	Temperature °C	Thickness (μm)
S_1	2.25	RT	1.14
S_2	0.5	RT	1.25
S_3	1	RT	1.25
S_4	1	100	1.31
S_5	1	230	1.13
S_6	1	250	1.21

2.3 FIR Reflectivity and Raman Scattering Measurements

2.3.1 FIR Reflectivity of $Cd_{1-x}Zn_xTe$ Alloys and CdTe/InSb Epilayers

High-resolution FIR reflectivity measurements were performed on the Bridgman-grown $Cd_{1-x}Zn_xTe$ samples with different composition ($0 \leq x \leq 1$). The Brüker IFS 66 V/S spectrometer was employed with the KBr beam-splitter and using the deuterated triglycine sulfate (DTGS) detector to achieve a very good signal-to-noise ratio in the energy region of 5 meV $\leq E \leq$ 100 meV (where 1 meV ~ 8 cm^{-1}). The experimental details (cf. Sect. 3) were reported by setting the incident beam angle at ~9° from the near normal incidence. A gold mirror with ~300-nm-thick layer of gold deposited on the glass was used as a reference having nearly ~99%

of the reflectance. The successive measurements were performed to normalize the FIR spectra for both the reference gold mirror and the CZT samples. Final spectra with a relative error of <0.2% was achieved by dividing the results of CZT with the reflectivity spectra of the reference gold mirror. For $Cd_{1-x}Zn_xTe$ materials in the reflectivity curves, two (CdTe-like and ZnTe-like) composition-dependent maxima are clearly visible. Similar measurements were also carried out on the six MBE-grown CdTe/InSb (001) epifilms.

2.3.2 Raman Scattering Measurements

Micro-Raman spectra on $Cd_{1-x}Zn_xTe$ alloys were recorded at 80 K in the backscattering geometry by using a Jobin-Yvon T64000 system equipped with customary optics and electronics. Light scattered from the spectrometer was detected by a liquid nitrogen-cooled charged couple detector (CCD) device. An argon-ion (Ar^+) laser source operating at $\lambda = 532$ nm was used to excite vibrational spectra over the 100–400 cm^{-1}.

In Sect. 3, we have compared the simulated spectra with the experimental data by using a classical three-phase "Drude-Lorentz" model. Experimental reflectance spectra of each sample are analyzed theoretically using a classical "Drude-Lorentz" methodology (cf. Sect. 4.1) by creating appropriate effective MDFs which included contributions from the composition-dependent optical lattice phonons.

2.4 Spectroscopic Ellipsometry

Besides reflectivity studies, the SE, time-resolved PL (TRPL) and HR-SXAS measurements were considered as excellent experimental techniques for investigating the optical response in solids.

2.5 Time-Resolved Photoluminescence

Time-resolved PL (TRPL) measurements are performed by exciting luminescence from the CZT samples with a pulsed light source – measuring subsequent decay in the PL as a function of time [38]. The luminescence was achieved using an optic parameter generator laser – pumped by Nd:YAG (Eksma, model PL 2143B) with a 25-ps pulse and a 10-Hz repeat rate. In the near backscattering geometry, all $Cd_{1-x}Zn_xTe$ ternary alloys ($0.005 \leq x \leq 1$) were excited with a pulsed laser - detecting the PL spectra by exploiting a synchro-scan streak-camera combination having the spectral (< 0.2 nm) and temporal (30 ps) resolution. The experimental results are carefully interpreted theoretically in Sec. 3.

2.6 High-Resolution HR-SXAS Results of CdTe/InSb (001) Epifilms

High-resolution synchrotron radiation X-ray absorption measurements were performed to study the local atomic structure of the six MBE-grown CdTe/InSb (001) epifilms. For thin CdTe films, the high-resolution X-ray absorption fine structure (XAFS) data were collected in the X-ray fluorescence yield mode at the 01 C1 beamline of the National Synchrotron Radiation Research Center in Hsinchu, Taiwan. The X-ray photon energy covered the range between 26,500 eV and 27,700 eV. The extended X-ray absorption fine structure (EXAFS) measurements at the Cd K-edge were accomplished for extracting the local structures of CdTe/InSb (001) thin films. The X-ray intensity was monitored by using a liquid N_2-filled ionization chamber, and the fluorescence emitted from the samples were measured by an argon-filled Stern-Held-Lytle detector. A Si (111) double-crystal monochromator with a 0.5-mm entrance slit was used. A filter was inserted between the sample and the detector window to reduce the noise from scattering, improving the spectrum quality. The incident photon direction was set at 45° to the surface of the sample, and the flux I_0 of the incident photons was monitored simultaneously by an ion chamber located just before the sample compartment. All the measurements were made at RT, and the X-ray absorption spectra were normalized to I_0.

3 Theoretical

For the design and analysis of electronic and photonic devices based on II–VI materials, the knowledge of their optical properties plays an important role. Besides FIR reflectivity [39], the SE and TRPL are also considered as an excellent experimental methods for investigating [38] the optical response in solids.

3.1 Spectroscopic Ellipsometry

Spectroscopic ellipsometry is a commonly used method for monitoring the epitaxial growth process of semiconductor materials. As compared to the reflected and transmission intensity approach, the SE is quite meticulous. In this methodology, the customary SE parameters Ψ and Δ are allied with the ratio ρ of complex Fresnel reflection coefficients $\tilde{r}^p$ and $\tilde{r}^s$ for the incident light polarized parallel (||) and perpendicular ($\perp$) to the plane of incidence [35]:

$$\rho \equiv \frac{\tilde{r}^p}{\tilde{r}^s} = \tan\Psi \exp(i\Delta). \tag{1}$$

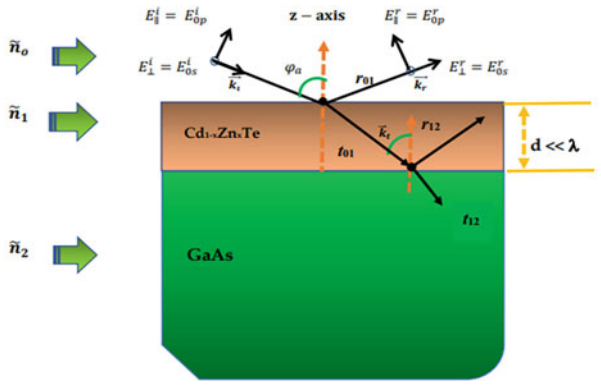


Fig. 2 The sketch of an ideal three-phase model used to calculate the reflectivity and transmission spectra of ultrathin $Cd_{1-x}Zn_xTe$ films of thickness d grown on a thick GaAs substrate. The direction of incident (reflected) far-infrared radiation is shown with s and p electric field components ($E_{\perp}^{i(r)} = E_{0s}^{i(r)}$ and $E_{\parallel}^{i(r)} = E_{0p}^{i(r)}$) of wave vector $\vec{k}_{i(r)}$ at an oblique angle φ_a to the surface of the thin film (see text)

The values of Ψ and Δ are measured by using a suitable angle of incidence φ_a over the appropriate range of photon energies E. While the SE parameters depend on material crystalline structure and optical properties [37–45], a pseudo-dielectric function $\tilde{\varepsilon}(E)$ is commonly employed, however, to interpret the data with a two-phase (ambient/substrate) model by setting the ambient dielectric constant $\tilde{\varepsilon}_a \left(\equiv 1 \right)$:

$$\tilde{\varepsilon}(E) = \tilde{\varepsilon}_a \left[\left\{ \left(\frac{1-\rho}{1+\rho} \right) \right\}^2 \sin^2\varphi_a + \cos^2\varphi_a \right] \tan^2\varphi_a. \tag{2}$$

Here, we have used a three-phase (ambient/film/substrate) model (see Fig. 2) to simulate the optical properties of $Cd_{1-x}Zn_xTe$ alloys (cf. Sect. 4) for assessing its epifilm thickness d grown pseudomorphically on GaAs substrate [35–39].

3.2 *Refractive Index $\tilde{n}$ and Dielectric Function $\tilde{\varepsilon}$*

In semiconductors, the reflection, refraction, transmission, and absorption coefficients are linked to the complex refractive index $\tilde{n}(E)$ $[\equiv n(E) + i\,k(E)]$ or dielectric function $\tilde{\varepsilon}(E)$ $[\equiv \varepsilon_1(E) + i\,\varepsilon_2(E)]$ at the photon energy E $(\equiv \hbar\omega)$. The measurements of absorption coefficient can provide imaginary part $k(E)$ of $\tilde{n}(E)$, while the reflectivity $R(E)$ is allied to a complicated combination of $\varepsilon_1(E)$ and $\varepsilon_2(E)$. Once $\varepsilon_1(E)$ or $\varepsilon_2(E)$ is known from SE, the $\varepsilon_2(E)$ or $\varepsilon_1(E)$ can be determined by

using Kramers-Krönig relationships over a wide energy range [39]:

$$\epsilon_1(E) = 1 + \frac{2}{\pi}\,\mathcal{P}\iint_0^{\infty} \frac{E\prime\epsilon_2\left(E'\right)}{(E\prime)^2 - E^2}\,dE' \,, \tag{3}$$

and

$$\epsilon_2(E) = -\frac{2}{\pi}\,\mathcal{P}\iint_0^{\infty} \frac{E'\epsilon_1\left(E'\right)}{(E\prime)^2 - E^2}\,dE' \,. \tag{4}$$

where the term $\mathcal{P}$ represents the principal value. From Eqs. (3) to (4), it is obvious that the main contributions to $\varepsilon_1(E)$ come from the behavior of $\varepsilon_2(E^{'})$ near $E' \approx E$ due to the resonant term in the denominator. To acquire $\varepsilon_1(E)$, $\varepsilon_2(E^{'})$ should be known for all E'. Once $\varepsilon_1(E)$ and $\varepsilon_2(E)$ are available, it is straightforward to simulate both real and imaginary parts of $\widetilde{n}(E)$:

$$n(E) = \left\{\frac{\left[\varepsilon_1(E)^2 + \varepsilon_1(E)^2\right]^{1/2} + \ \varepsilon_1(E)}{2}\right\}^{1/2}, \tag{5}$$

$$k(E) = \left\{\frac{\left[\varepsilon_1(E)^2 + \varepsilon_1(E)^2\right]^{1/2} - \varepsilon_1(E)}{2}\right\}^{1/2}. \tag{6}$$

From Eqs. (5) to (6), one can calculate the absorption coefficient $\alpha(E)$.

$$\alpha(E) = \frac{4\pi}{\lambda}\,k(E), \tag{7}$$

and reflectivity $R(E)$

$$R(E) = \frac{[n(E) - 1]^2 + k(E)^2}{[n(E) + 1]^2 + k(E)^2}. \tag{8}$$

at near normal incidence.

3.3 *FIR Reflectivity of Binary Compounds, Epilayers, and Superlattices*

For accurately assessing the thickness of the nanostructured CZT epifilms and $(CdTe)_m/(ZnTe)_n$ SLs (cf. Sect. 4) grown pseudomorphically on the GaAs substrates, one needs to simulate the optical constants of the binary CdTe, ZnTe, GaAs, and ternary $Cd_{1-x}Zn_xTe$ materials [35–39, 45]. A three-phase model (ambient

(air)/film/substrate) is adopted here by pretending that the isotropic $Cd_{1-x}Zn_xTe$ film of refractive index$\tilde{n}_1$with thickness d is grown on a thick GaAs substrate of refractive index $\tilde{n}_2$. This method can also be applied to CdTe/InSb epilayers. The light of wavelength λ at an angle φ_a incident from the ambient (air) $\tilde{n}_0$ ($\equiv 1$) can causes (see Fig. 2) many reflections and transmissions at the substrate/film and film/air interfaces. Due to multiple reflections within the film, the reflected electric fields parallel (||) and perpendicular ($\perp$) to the plane of incidence add up by a geometric series giving an airy formula for reflection $\tilde{r}^x$ coefficient ($x \equiv s$-, p-polarization) [45]:

$$\tilde{r}^x = \frac{\tilde{r}^x_{01} + \tilde{r}^x_{12} e^{2i\beta}}{1 + \tilde{r}^x_{01}\tilde{r}^x_{12} e^{2i\beta}}, \tag{9}$$

where $\tilde{r}^x_{01}, \tilde{r}^x_{12}$ are the Fresnel coefficients at the respective interfaces between media of indices $\tilde{n}_0, \tilde{n}_1$ and $\tilde{n}_1, \tilde{n}_2$.

In the s-polarized mode with electric field vector $\boldsymbol{E}$ perpendicular to the optic axis, the $\tilde{r}^s$ spectra contain information about the ordinary dielectric function exhibiting comparable spectral shapes under different angles of incidence except the intensities. In p-polarized case, the electric field vector $\boldsymbol{E}$ is parallel to the plane of incidence and instigates reflectivity $\tilde{r}^p$of the extraordinary mode. This means that the p-polarized reflectance is sensitive to the angles of incidence exhibiting unique spectral response with anisotropic optical properties. Film thickness d and angle of incidence φ_a are restricted to the phase factor $\beta = 2\pi \frac{d}{\lambda}\sqrt{\tilde{n}_1^2 - \tilde{n}_0^2 \sin^2\varphi_a}$. From Eq. (9), we have calculated the polarization-dependent reflectivity $R^x = |\tilde{r}^x|^2$ spectra of ultrathin $Cd_{1-x}Zn_xTe$ films and $(CdTe)_m$/ $(ZnTe)_n$ SLs grown epitaxially on GaAs (001) substrate [39]. Similar calculations of the polarization-dependent transmission $T^x = \left|\tilde{t}^x\right|^2$ can also be accomplished (cf. Sect. 4).

3.4 *Lattice Dynamics and Thermal Properties*

Accurate knowledge of phonon dispersions of solids plays an indispensable role for correlating their macroscopic properties to microscopic traits. Complete results [39] of lattice dynamics exist for CdTe, ZnTe, GaAs, and InSb materials from the inelastic neutron scattering technique. Earlier, we have successfully employed a computationally efficient rigid ion model (RIM) to simulate phonon dispersions $\omega_j\left(\overrightarrow{q}\right)$ to address not only the site selectivity of various defects in semiconductors but also comprehending their pressure-dependent and thermodynamical properties.

3.5 *Phonon and Thermodynamical Properties*

For understanding thermodynamical properties of CdTe and ZnTe semiconductor materials, we preferred RIM over the atomistic and/or density-functional approaches as the latter methods are computationally exorbitant and difficult to justify its use a priori. As compared to IV–IV and III–V semiconductors, the specific heat of iso-row II–VI materials is lower due to the impacts of their respective lattice phonons on $C_v(T)$ [39]. For accurately obtaining $C_v(T)$, it is necessary to estimate Helmholtz free energy Φ_{vib} of atomic vibrations $\omega_j\left(\vec{q}\right)$ by using

$$\Phi_{\text{vib}} = \frac{1}{2}\sum\nolimits_{j,\vec{q}} \hbar\omega_j\left(\vec{q}\right) + k_B T \sum\nolimits_{j,\vec{q}} \ln\left[1 - e^{-\frac{\hbar\omega_j\left(\vec{q}\right)}{k_B T}}\right], \tag{10}$$

where k_B is the Boltzmann constant and the entropy (S_{vib}) of vibrating lattice follows from the Helmholtz free energy as $S_{\text{vib}} \equiv -\partial\Phi_{\text{vib}}/\partial T|V$. The knowledge of Φ_{vib} and S_{vib} allows one to calculate internal energy U of the crystal using a relationship $\Phi_{\text{vib}} = U - S_{\text{vib}}T$. The Helmholtz free energy of the crystalline lattice can be used to define the heat capacity at constant volume either by $C_v(T)$ ($\equiv T\left(\partial S_{\text{vib}}/\partial T|_V\right)$) or $\{\equiv -T\left(\partial\Phi^2_{vib}/\partial T^2\big|_V\right)\}$. In the quasi-harmonic approximation and using the complete phonon dispersions, one can also obtain $C_v(T)$ (cf. Sect. 4.2) by differentiating Eq. (10) with respect to temperature, i.e.,

$$C_v(T) = \sum\nolimits_{j,\vec{q}} k_B \left(\frac{\hbar\omega_j\left(\vec{q}\right)}{k_B T}\right)^2 \left(\frac{e^{\frac{\hbar\omega_j\left(\vec{q}\right)}{k_B T}}}{\left[e^{\frac{\hbar\omega_j\left(\vec{q}\right)}{k_B T}} - 1\right]^2}\right) \tag{11}$$

From the Debye equation of specific heat C_v(T)

$$C_v(T) = 9rk_B\left(\frac{T}{\Theta_D(T)}\right)^3 \int^{\Theta_D(T)/T} \frac{x^4 e^x}{(e^x - 1)^2} dx, \tag{12}$$

it is possible to simulate Debye temperature Θ_D(T), (cf. Sect. 4.1) where the term r in Eq. (12) stands for the number of atoms per unit cell.

4 Numerical Calculation Results and Discussions

To comprehend the optical characteristics of $Cd_{1-x}Zn_xTe$/GaAs (001) or CdTe/InSb epifilms and $(CdTe)_m/(ZnTe)_n$ SLs in the FIR → MIR and NIR → UV range, one needs to have the dielectric functions known in the respective energy regions.

The complex dielectric function $\widetilde{\varepsilon}(\omega)$ or refractive index $\widetilde{n}(\omega)$ of binary materials CdTe, ZnTe, InSb, and GaAs can be extorted theoretically by fitting SE data and expending well-known KK analyses (cf. Eqs. 3 and 4). In the absence of SE results, however, one cannot acquire the optical constants of $Cd_{1-x}Zn_xTe$/GaAs epifilms. It is to be noted that the transmission/reflectance methods adopted by others [35–39] are equally impractical for obtaining the dielectric constants of ultrathin films due to very small and feeble interference patterns. Results of realistic phonon dispersions for CZT alloys and their thermodynamical characteristics are reported (cf. Sect. 4.1). We also extorted the energy-dependent dielectric constants by using accurate MDFs (cf. Sects. 4.2 and 4.3) of binary CdTe, ZnTe, InSb, and GaAs and ternary $Cd_{1-x}Zn_xTe$ alloys and systematically evaluated film thickness in $Cd_{1-x}Zn_xTe$/GaAs (001) or CdTe/InSb and $(CdTe)_m/(ZnTe)_n$/GaAs (001) SLs by assimilating the procedure outlined in Sect. 3.

4.1 Lattice Dynamics

By adopting a realistic rigid ion model (RIM), we have appraised the interatomic interactions of both CdTe and ZnTe by assimilating lattice parameters, elastic constants, phonon frequencies, and other measurable quantities [39]. The simulated results of phonon dispersions $\omega_j\left(\overrightarrow{q}\right)$, density of states, $\Theta_D(T)$, and lattice heat capacities $C_v(T)$ for CdTe, $Cd_{0.8}Zn_{0.6}Te$, $Cd_{06}Zn_{0.4}Te$, $Cd_{0.4}Zn_{0.6}Te$, $Cd_{0.2}Zn_{0.8}Te$, and ZnTe reported in Fig. 3a–d were compared reasonably well with experimental and theoretical data.

4.2 Model Dielectric Functions

By using appropriate MDFs in different energy regions, we have reported comprehensive results of $\widetilde{\varepsilon}(\omega)$ and $\widetilde{n}(\omega)$ for $Cd_{1-x}Zn_xTe$ alloys, InSb and GaAs. To simulate optical response for the binary materials, three parameters are exploited which include energies, strength, and their broadening at critical points (CPs) in the Brillouin zone (BZ) [39]. For achieving the best-fit values of MDFs, an efficient Levenberg-Marquardt algorithm is followed using a nonlinear least square fitting procedure to minimize the error function Ξ over $\aleph$ data points:

$$\Xi^2 = \frac{1}{\aleph}\sum_{i=1}^{\aleph}\left|\mathfrak{R}_i^{\exp} - \mathfrak{R}_i^{\mathrm{cal}}\right|^2, \tag{13}$$

where $\mathfrak{R}_i^{\exp}$ and $\mathfrak{R}_i^{\mathrm{cal}}$ are the experimental and calculated values, respectively.

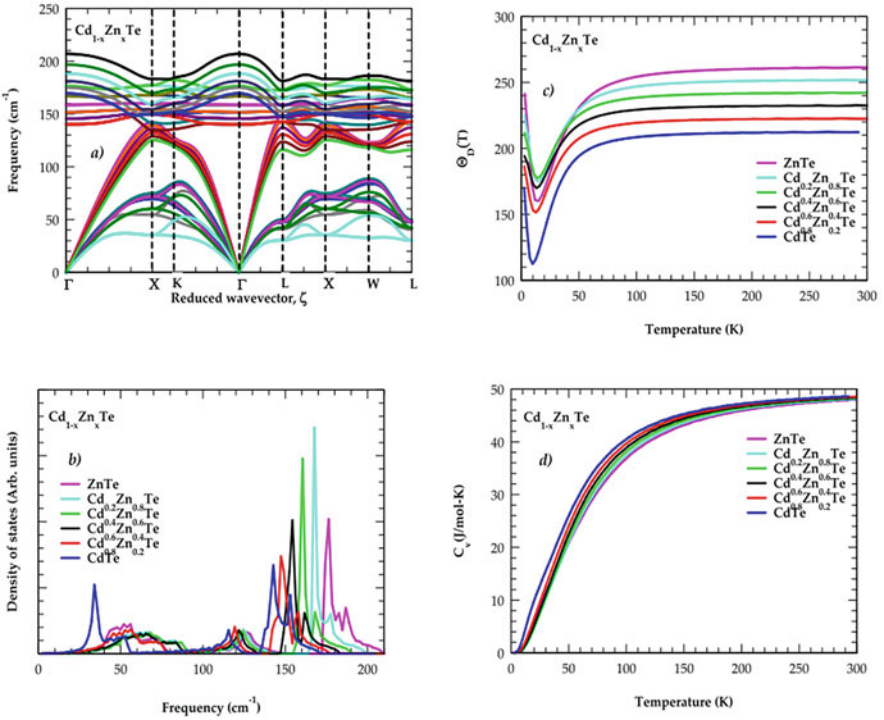


Fig. 3 (**a**) Calculated phonon dispersions $\omega_j\left(\overrightarrow{q}\right)$, (**b**) one-phonon density of states, (**c**) $\Theta_D(T)$, and (**d**) $C_v(T)$ of CdTe $Cd_{0.8}Zn_{0.6}Te$, $Cd_{06}Zn_{0.4}Te$, $Cd_{0.4}Zn_{0.6}Te$, $Cd_{0.2}Zn_{0.8}Te$, and ZnTe based on a RIM

4.2.1 MDFs for FIR → MIR Energy Range

In the FIR→ MIR region, the dielectric $\widetilde{\varepsilon}_L(\omega)$ function of the perfect $Cd_{1-x}Zn_xTe$ alloy is calculated by exploiting a classical "Drude-Lorentz" model by fitting the measured reflectivity data (see Table 2a and b). Appropriate contributions of the longitudinal optical (ω_{LO}) and transverse optical (ω_{TO}) phonons linked to the Lyddane-Sachs-Teller relationship $\left(\frac{\varepsilon_o}{\varepsilon_\infty} = \frac{\omega_{LO}^2}{\omega_{TO}^2}\right)$ at Γ critical point in the BZ are considered [39]:

$$\widetilde{\varepsilon}_L(\omega) = \varepsilon_{\infty x} + \sum\nolimits_{j=1,2} \frac{S_{jx}\omega_{TOxj}^2}{\omega_{TOjx}^2 - \omega^2 - i\Gamma_{jx}\omega}. \tag{14}$$

In Eq. (14), the term $\varepsilon_{\infty x}$ represents the weighted high-frequency dielectric function; ω_{TOjx} is the composition-dependent experimentally observed CdTe-like, ZnTe-like, and GaAs-like TO-mode frequencies from the FIR spectroscopy (cf.

Table 2 The room temperature (300°K) FTIR data was fitted by exploiting a dielectric response model. The set of parameters were evaluated using least square fitting procedure (**a**) for the bulk ternary $Cd_{1-x}Zn_xTe$ alloys and (**b**) GaAs in the long-wavelength limit (see text)

(a) **FTIR parameters for $Cd_{1-x}Zn_xTe$ samples $0 \leq x \leq 1$**							
			CdTe-like mode			**ZnTe-like mode**	
X	ε_∞	S_1	$\omega_{TO1}(cm^{-1})$	$\Gamma_1(cm^{-1})$	S_2	$\omega_{TO2}(cm^{-1})$	$\Gamma_2(cm^{-1})$
0	9.44	4.45	140.69	8.62			
0.1	6.66	3.67	144.81	9.29			
0.2	8.52	3.25	145.86	9.42	0.55	171.59	13.1
0.3	9.4	2.9	151.28	11.14	0.96	175.61	11.51
0.4	7.99	2.36	152.21	11.64	1.07	178.62	10.33
0.5	8.15	2.21	152.03	13.72	1.41	182.07	9.83
0.9	10.02	0.16	158	3.25	3.46	177.03	7.72
1	9.54				3.64	181.9	5.48
(b) GaAs 300 K							
ε_∞		S		$\omega_{TO}\,(cm^{-1})$		$\Gamma_{(cm^{-1})}$	
11.1		1.95		268.2		2.0	

Sect. 2.2; see Fig. 4a); S_{jx} represents the oscillator strength; and Γ_{jx} is the broadening value (see Table 2a and b) of the TO phonon.

4.2.2 FTIR Spectra of Bulk $Cd_{1-x}Zn_xTe$ Alloys

By using appropriate parameters of Table 2a and b for bulk materials, we have carefully analyzed the near normal incidence FIR reflectivity spectra for all $Cd_{1-x}Zn_xTe$ alloys and GaAs. The results displayed in Fig. 4b, c, and d for $x = 1.0$, ZnTe [ω_{TO} = ~176 cm^{-1} (~22 meV), ω_{LO} = 208 cm^{-1} (~26 meV)], $x = 0.0$, CdTe [ω_{TO} = 140 cm^{-1} (~17.5 meV), ω_{LO} = 169 cm^{-1} (~21.3 meV)], and GaAs [ω_{TO} = 269 cm^{-1} (~33.6 meV), ω_{LO} = 292 cm^{-1} (~36.5 meV)] helped us simulate their optical constants [$\widetilde{\varepsilon}_L(\omega)$, $\tilde{n}_L(E)$]. The calculated results of ε_1, ε_2; n, k displayed in Fig. 5a–d for CdTe, ZnTe, and GaAs have revealed the long-wavelength TO phonon energies at the peaks of $\varepsilon_2(\omega)$ and the LO-phonon modes appearing near $n = k$, $\varepsilon_1(\omega) = 0$.

Analyses of the reflectivity spectra for $Cd_{1-x}Zn_xTe$ alloys disclosed the CdTe-like (TO_1, LO_1) and ZnTe-like (TO_2, LO_2) modes in excellent affirmation with the Raman scattering spectroscopy (RSS) data. The results corroborated earlier elucidations of the two-phonon-mode behavior for $Cd_{1-x}Zn_xTe$ and validated predictions of the modified random element iso-displacement (MREI) model [39]. In the absence of FIR-SE data for $Cd_{1-x}Zn_xTe$ alloys, our simulations of ε_1 and ε_2 are found in fairly good agreement with the recent spectroscopic ellipsometry results of $Cd_{0.8}Zn_{0.2}Te$.

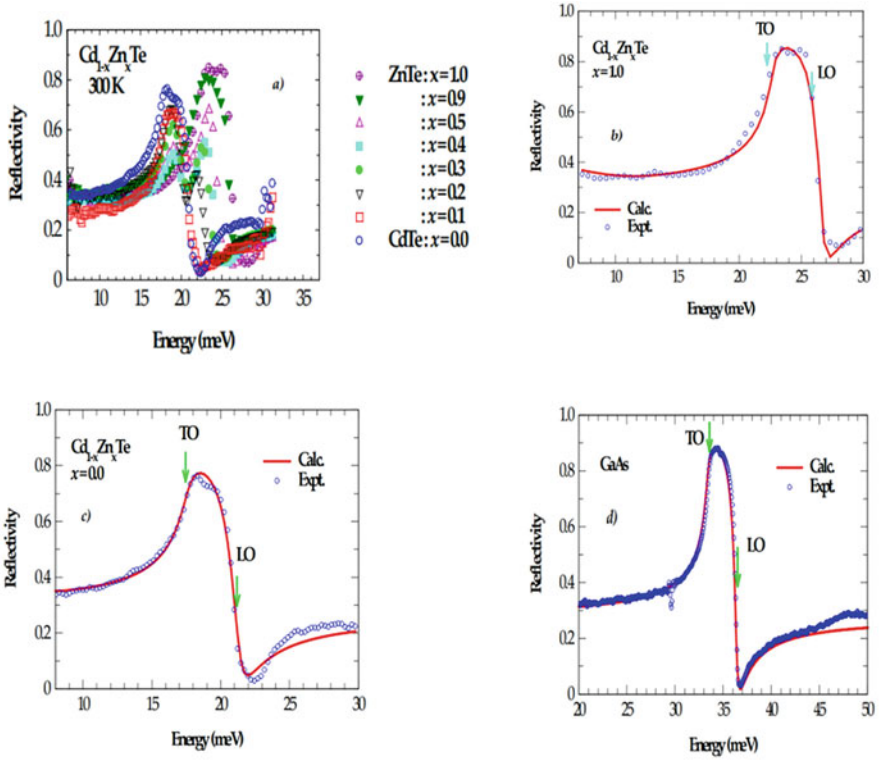


Fig. 4 (**a**) Far-infrared reflectivity spectra for Bridgman-grown samples of $Cd_{1-x}Zn_xTe$ ternary alloys; (**b**) best-fit results for ZnTe using the classical Drude-Lorentz model (Eq. 14) with parameter values of Table 2a – the green-colored vertical arrows represent TO and LO phonons of ZnTe; (**c**) same as (**b**) for CdTe; (**d**) same as (**b**) for GaAs

4.2.3 FTIR Spectra of CdTe/GaAs, ZnTe/GaAs, and $Cd_{1-x}Zn_xTe$/GaAs Epifilms and $(CdTe)_m/(ZnTe)_n$/GaAs Superlattices

For polar materials of thickness d smaller than λ (i.e., $d/\lambda << 1$), Berreman [43] applied judicious reasoning and simple theoretical deliberations to successfully demonstrate observing strong minimum at the zone-center TO phonon in the FIR transmission measurements performed at near normal incidence $\varphi_a = 0$. However, at oblique incidence $\varphi_a > 0$, two minima are detected [39] – a strong minimum emerged near the TO phonon and a relatively weaker minimum centered at the LO mode. Although the TO phonon occurred in both s- and p- polarizations, the LO mode was seen, however, in the p-polarization only. By using standard methodology of multilayer optics, we have calculated transmittance $T_{s(p)}$ and reflectance $R_{s(p)}$ of ZnTe, CdTe, and $Cd_{1-x}Zn_xTe$ epifilms and $(CdTe)_m/(ZnTe)_n$ SLs grown on GaAs (001) substrate.

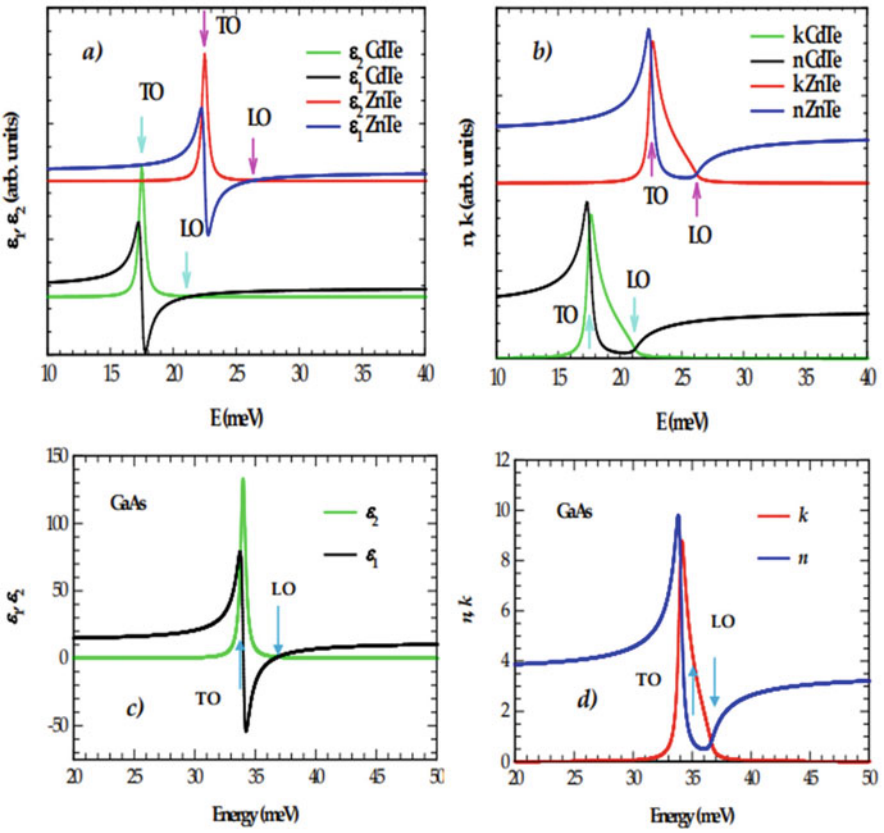


Fig. 5 (**a**) Simulated values of ε_1 *and* ε_2 for ZnTe (upper panel) and CdTe (lower panel) with magenta-colored (blue-colored) arrows representing the TO and LO phonons of ZnTe (CdTe); (**b**) same as (**a**) but of n and k for ZnTe (upper panel) and CdTe (lower panel) with magenta-colored (blue-colored) arrows representing the TO and LO phonons of ZnTe (CdTe); (**c**) simulated values of ε_1 and ε_2 for GaAs with blue-colored arrows representing the TO and LO phonons of GaAs; (**d**) same as (**c**) but for n *a*nd k of GaAs with blue-colored arrows representing the TO and LO phonons

Theoretical results of $T_{s(p)}$ and $R_{s(p)}$ for a 1-μm-thick binary ZnTe/GaAs (001) (upper panel) and CdTe/GaAs (001) epilayers (lower panel) are displayed in Fig. 6a and b, respectively, for $\varphi_a = 30^o$. In the transmission $T_{s(p)}$ spectra, while a stronger dip centered at the TO mode of ZnTe (CdTe) ~177.5 cm^{-1} (~140 cm^{-1}) is perceived in both *s*- and *p*-polarizations (cf. Fig. 6a), a weaker dip near the LO mode ~ 208.3 cm^{-1} (~169.4 cm^{-1}) appeared, however, only in the *p*-polarization (Berreman effect [43]). Not only the calculated optical phonons of ZnTe are found in good agreement with the Raman scattering (TO = 181 cm^{-1}, LO = 210 cm^{-1}) and inelastic neutron scattering data (TO = 177 cm^{-1}, LO = 208 cm^{-1}) – the phonon values also satisfied the well-known Lyddane-Sachs-Teller relationship

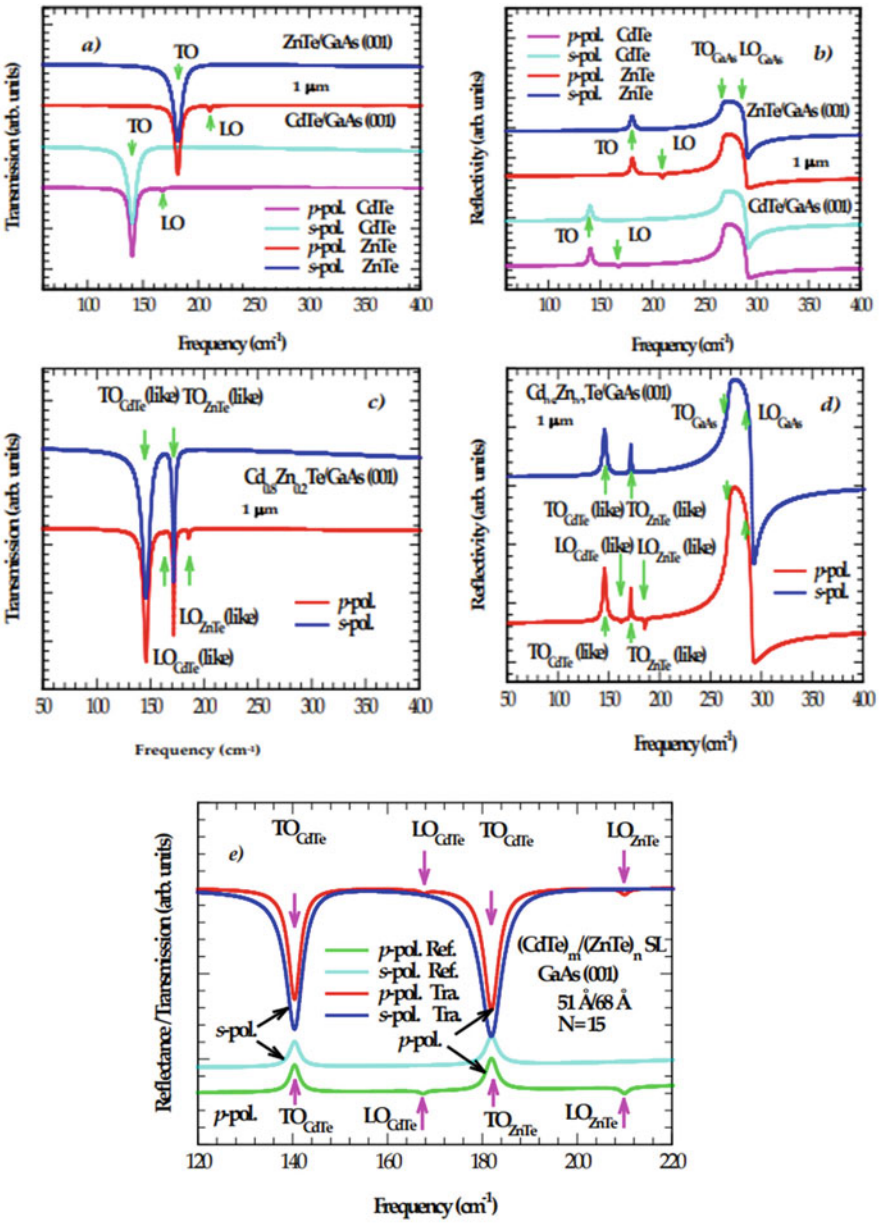


Fig. 6 (**a**) *s*- (blue-colored line) and *p*-polarization-dependent (red-colored line) transmission $T_{s,p}$ spectra of 1-μm ZnTe/GaAs (001) (upper panel) with $\varphi_a = 30^o$; *s*- (sky-blue colored) and *p*-polarization-dependent (magenta-colored) transmission $T_{s,p}$ spectra of 1-μm CdTe/GaAs (001) (lower pane) with $\varphi_a = 30^o$. The green-colored vertical arrows represent TO and LO modes of ZnTe (CdTe); (**b**) same as (**a**) but for the reflectivity $R_{s,p}$ spectra of 1-μm ZnTe/GaAs (001) (upper panel) and of 1-μm CdTe/GaAs (001) (lower pane)*;* (**c**) same as (**a**) but for 1-μm-thick $Cd_{0.8}Zn_{0.2}Te$/GaAs (001); (**d**) same as (**b**) but for 1-μm-thick $Cd_{0.8}Zn_{0.2}Te$/GaAs (001). (**e**) *s*-(blue-colored) and *p* (red-colored)-polarization-dependent transmission $T_{s,p}$ (upper panel) and *s*-(light blue-colored) and *p*-polarization-dependent (green-colored) reflectance spectra (lower panel) of $(CdTe)_m/(ZnTe)_n$/GaAs (001) SL – with n (= 15) repeat periods of m (= 16) monolayer (ML) of CdTe ($d_1 = 51$ Å) and n (= 23) ML of ZnTe ($d_2 = 68$ Å) with $\varphi_a = 30^o$ – two CdTe-like and ZnTe-like TO confined phonon peaks (dips) in the $R_{s,p}$ ($T_{s,p}$) spectrum and the weaker LO confined phonon dips in the R_p, T_p spectrum, respectively

$^{\omega}_{LO}/^{\omega}_{TO} = (\varepsilon_o/\varepsilon_\infty)^{1/2}$. Similar accuracy in our calculations of $T_{s(p)}$ is also seen in the LO and TO phonons of CdTe.

The simulated results of reflectivity spectra $R_{s(p)}$ for a 1-μm-thick binary ZnTe/GaAs (001) (upper panel) and CdTe/GaAs (001) epilayers (lower panel) are displayed in Fig. 6b. Clearly, the perusal of Fig. 6b has revealed a peak centered at the TO mode of ZnTe (CdTe) in both *s*- and *p*-polarizations of $R_{s(p)}$ – a weak dip also appeared near the LO mode of ZnTe (CdTe) only in the *p*-polarization of R_p spectra. The effect of composition on $T_{s(p)}$ and $R_{s(p)}$ spectra displayed in Fig. 6c, d for 1-μm-thick epifilm of $Cd_{0.8}Zn_{0.2}Te$ alloy overlaying the GaAs (001) substrate with $\varphi_a = 30^o$ uncovered four phonon features (cf. Fig. 6c, d) – two representing the CdTe-like (TO_1, LO_1) and two signifying the ZnTe-like (TO_2, LO_2) modes, respectively. The expected shifts of composition-dependent CdTe-like and ZnTe-like optical phonons have clearly offered an unambiguous support of the two-phonon mode behavior for the $Cd_{1-x}Zn_xTe$ ternary alloys. Obviously, for the 1-μm-thick binary and ternary epilayers, the peaks (dips) representing the TO modes in R_p (T_p) are strong, while the dips representing the LO modes are rather frail. One must also note that while the oblique transmission $T_{s(p)}$ spectra supported the Berreman effect [43], our $R_{s(p)}$ simulations are equally valuable being complementary to the $T_{s(p)}$ data – encourage spectroscopists to perform reflectance measurements at oblique incidence.

In Fig. 6e, we have displayed the calculated $T_{s(p)}$ (upper panel) and $R_{s(p)}$ (lower panel) spectra for an MBE-grown sample of $(CdTe)_m/(ZnTe)_n$/GaAs (001) SL – consisting of n (= 15) repeat periods of m (= 16) monolayer (ML) of CdTe (d_1 = 51 Å) and n (= 23) ML of ZnTe (d_2 = 68 Å). The perusal of Fig. 5e has undoubtedly distinguished the two most prominent CdTe-like and ZnTe-like TO confined phonon peaks (dips) in the $R_{s,p}$ ($T_{s,p}$) spectrum and the corresponding weaker LO confined phonon dips in the R_p, T_p spectrum, respectively.

4.2.4 Near Normal Incidence FIR Spectra of CdTe/InSb Epifilms

At near normal incidence, the results of FIR spectra in the frequency range of 40 cm^{-1} to 220 cm^{-1} are presented in Fig. 7a–f for the six MBE-grown CdTe/InSb (001) samples (#S_1–S_6). While the experimental data in each sample are displayed with blue-colored open circles, the simulated reflectivity results are shown with red-colored solid lines. In our calculations, we have followed a three-phase "Lorentz-Drude" model [44, 45] and incorporated appropriate experimental data to obtain the best-fit parameters (see Table 3) using apposite procedures. Theoretical outcomes of all the samples (see Fig. 7a–f) compared reasonably well with the experimental data. In the FIR study, two well-pronounced features (see Fig. 7a–f) are observed near ~140 cm^{-1} and ~ 184 cm^{-1} close to the ω_{TO} (Γ) values observed in the inelastic neutron scattering data of the bulk CdTe [47] and InSb [48], respectively.

Clearly, the observations of ω_{TO} modes and their line shapes have implied that the MBE-grown CdTe layers are well aligned to the InSb (001) substrate. From

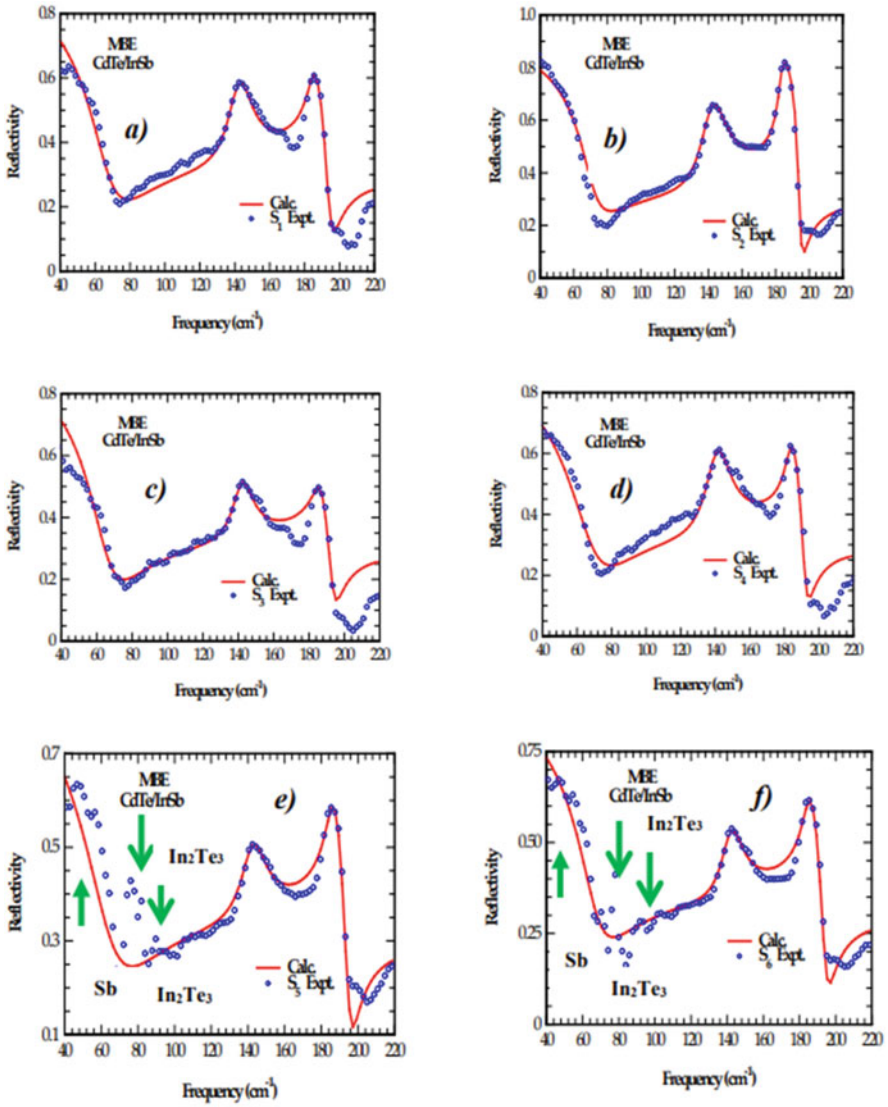


Fig. 7 (**a**–**f**) Comparison of room temperature (300 K) experimental far-infrared reflectivity (open blue circles) spectra of six MBE-grown samples CdTe/InSb (001) with theoretically fitted results (red-colored lines) obtained by using a "Lorentz-Drude" model with a set of parameters (see Table 3). In samples #S_5 and S_6, we have also labeled low-energy phonon features with green-colored vertical arrows triggered possibly by the intrinsic Sb clusters or In_2Te_3-like precipitates at the CdTe-InSb interface

Table 3 Summary of the fitting parameters used in simulating the room temperature far-infrared reflectivity spectra of six MBE-grown CdTe/InSb samples (see text)

MBE-grown sample	# S_1	# S_2	# S_3	# S_4	# S_5	# S_6
	CdTe film					
ε_∞	7.1	7.1	7.1	7.1	7.1	7.1
S, oscillator strength	2.39	2.31	2.38	2.72	3.45	3.31
ω_{TO} (cm^{-1})	142.2	142.19	142.2	141	142.5	142
Γ, damping constant	9.80	8.97	9.70	9.44	10.1	9.91
η, carrier concentration ($10E^{18}$)	0.073	0.12	0.24	0.073	0.059	0.094
μ, (cm^2/V.s)	1634	2721	1610	1090	733	1112
m_e^*, effective mass	0.13	0.09	0.11	0.09	0.11	0.11
d, thickness (μm)	1.14	1.25	1.25	1.31	1.13	1.21
	InSb substrate					
ε_∞	15.3	15.3	15.3	15.3	15.3	15.3
S, oscillator strength	1.515	1.71744	0.63764	1.3586	1.535	1.56
ω_{TO} (cm^{-1})	184.3	183.053	185.7	183.2	185.4	184.4
Γ, damping constant	6.81	2.81253	5.4759	5.51	6.8	6.3
η, carrier concentration ($10E^{18}$)	0.013	0.014	0.008	0.015	0.013	0.013
μ, (cm^2/V.s)	24,007	35,575	32,084	20,600	19,431	29,318
m_e^*, effective mass	0.014	0.014	0.015	0.015	0.014	0.014

Table 3, one may notice relatively large oscillator strengths (S) for samples S_5 and S_6. We believe that these S values are most likely caused by poor crystalline qualities of CdTe/InSb epilayers having the possibilities of interfacial defects. Diffusion of intrinsic Te and/or Sb atoms at the CdTe-InSb boundaries can create either clusters of segregated Sb atoms or In_2Te_3-like precipitates [31, 32]. In the FIR spectra of samples S_5 and S_6, we noticed additional phonon features at lower ($<\boldsymbol{\omega_{TO}}$) frequency sides near ~60 cm^{-1}, ~80 cm^{-1}, and ~ 95 cm^{-1}. In corroboration with the existing RSS data [31, 32], these phonon traits (drawn by vertical green-colored arrows) are ascribed to the Sb clusters or In_2Te_3-like precipitates at the CdTe-InSb interface.

4.2.5 FIR at Oblique Incidence for CdTe/InSb Epifilms and Superlattices

The study of reflectivity and transmission at near normal incident is commonly used to obtain the optical constants in semiconductors [49–53]. In polar materials, the IR absorption and Raman scattering results (i.e., at $\varphi_i \approx 0$) delineate ω_{TO} and ω_{LO} optical phonons, respectively. In the transmission studies at oblique incidence (i.e., $\varphi_a \neq 0$), it was anticipated observing $\boldsymbol{\omega_{TO}}$ phonon in the s-polarization while perceiving both $\boldsymbol{\omega_{TO}}$ and $\boldsymbol{\omega_{LO}}$ modes in the p-polarization (Berreman effect) [43].

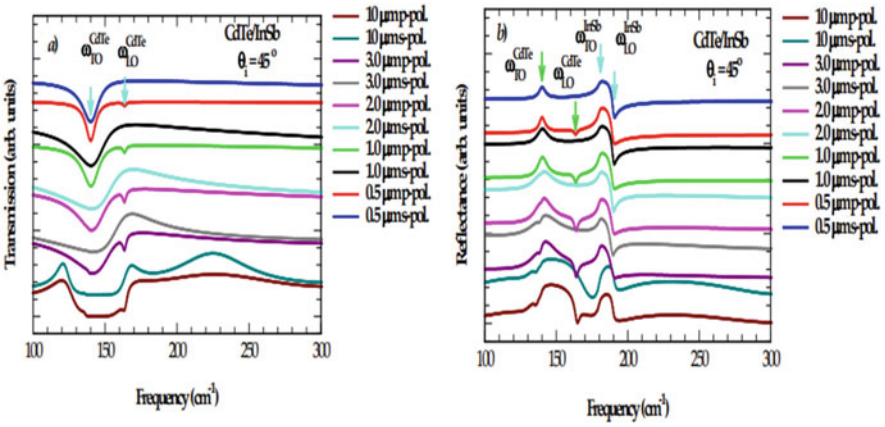


Fig. 8 Thickness-dependent simulated (**a**) transmission and (**b**) reflectance spectra of CdTe/InSb (001) epilayers at oblique incidence ($\varphi_i = 45^\circ$). The *s*- and *p*-polarization spectra are displayed for films with increasing thickness from 0.5 μm, 1.0 μm, 2.0 μm, 3.0 μm, and 10 μm corroborating the Berreman effect

However, at $\varphi_a \approx 0$, one expects only one minimum at $\boldsymbol{\omega_{TO}}$ irrespective of the polarization. Earlier, Sciacca et al. [54] have validated Berreman effect [43] by investigating optical phonons in thin semiconductor epilayers. The observation of transmission minima at $\boldsymbol{\omega_{LO}}$ and $\boldsymbol{\omega_{TO}}$ modes for oblique incidence is limited to samples significantly thinner than the wavelength of electromagnetic radiation corresponding to the Reststrahlen band of the material. One must note that this condition can be easily fulfilled in epilayers and heterostructures prepared by MBE or chemical vapor deposition methods – providing an alternative means of establishing both $\boldsymbol{\omega_{TO}}$ and $\boldsymbol{\omega_{LO}}$ phonons in polar III-N's (GaN, AlN, and AlGaN) and other technologically important structures [55, 56].

Here, we have reported our simulated results for both transmission and reflectivity spectra at oblique incidence on a series of CdTe/InSb epifilms. In Fig. 8a and b, the results of transmission and reflectivity spectra are displayed at oblique incidence ($\varphi_a = 45^\circ$) for epilayers of different thicknesses (e.g., 0.5 μm, 1.0 μm, 2 μm, 3.0 μm, and 10.0 μm), respectively. In these studies, we have meticulously followed our procedures outlined in [45] by incorporating values of CdTe-like (and InSb-like) phonons and their broadening parameters from Table 3.

Clearly, the transmission spectra (see Fig. 8a) in *s*-polarization (T_s) has revealed dips near the transverse optical mode of CdTe marked as $\boldsymbol{\omega_{TO}}$ ($\equiv$ ~140 cm^{-1}), while the transmission (T_p) spectra in the *p*-polarization provided dips near $\boldsymbol{\omega_{TO}}$ ($\equiv$ ~140 cm^{-1}) and $\boldsymbol{\omega_{LO}}$ ($\equiv$ ~168 cm^{-1}) – in good agreement with the inelastic neutron scattering [47] and Raman scattering data [31, 32]. Moreover, our simulations have clearly demonstrated a progression of narrow transmission dip for an ultrathin film (0.5 μm) covering a broader region of the entire reststrahlen band for relatively thicker films (e.g., 10.0 μm). Like transmission spectra, we have also displayed

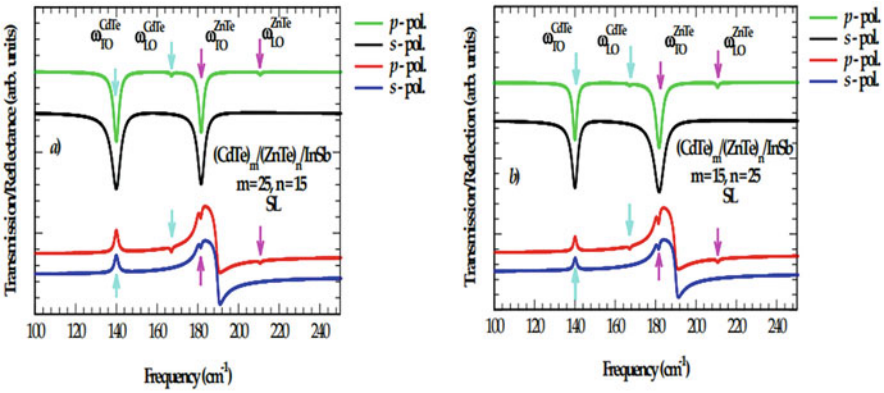


Fig. 9 Simulated results of transmission (upper panel) and reflectivity spectra (lower panel) at oblique incidence ($\varphi_a = 45°$) for $(CdTe)_m/(ZnTe)_n$/InSb (001) superlattices (SLs). To corroborate Berreman effect, we have displayed theoretical results for an SL structure consisting of (**a**) 100 repeat periods m (= 9) monolayers of CdTe and n (= 5) monolayers of ZnTe on InSb (001) and (**b**) 100 repeat periods m (= 5) of CdTe and n (= 9) of ZnTe on InSb (001) (see text)

simulated results of reflectivity spectra (see Fig. 8b) at the oblique incidence ($\varphi_a = 45°$) for CdTe/InSb epilayers with thicknesses identical to the one used in Fig. 8a. It should be noted that in semiconductors the reflectance spectra (R_s) generally drop to a minimum at the plasma edge which depends upon carrier concentration to exhibit a peak near $\boldsymbol{\omega_{TO}}$ mode. In semi-insulating polar materials, the $\boldsymbol{\omega_{TO}}$ phonon peak dominates at near normal incidence, while at the oblique incidence ($\varphi_a = 45°$) a maximum occurs at $\boldsymbol{\omega_{TO}}$ and a dip near ~$\boldsymbol{\omega_{LO}}$ (Berreman effect [43]) in the *p*-polarization (R_p) reflectivity (see Fig. 8b).

Here, we have demonstrated to confer theoretical results of transmission and reflectivity spectra [45] at oblique incidence ($\varphi_a = 45°$) for $(CdTe)_m/(ZnTe)_n$/InSb SLs. To differentiate simulated results, we have examined two SL structures consisting of (*a*) 100 repeat periods for m (= 9) monolayers of CdTe and n (= 5) monolayers of ZnTe on InSb (001), and (*b*) 100 repeat periods for m (= 5) of CdTe and n (= 9) of ZnTe on InSb (001), respectively. In Fig. 9a and b, the results of *s*- and *p*-polarized transmission and reflectance spectra are displayed in the upper and lower panels, respectively.

As expected [39], the transmission (reflectance) spectra in the *s*-polarization revealed minima (maxima) occurring near $\boldsymbol{\omega_{TO}}$ phonons of CdTe (~140 cm^{-1}) and ZnTe (~ 180 cm^{-1}), while in the *p*-polarization spectra the $\boldsymbol{\omega_{LO}}$ phonons show dips of CdTe (e.g., ~168 cm^{-1}) and ZnTe (e.g., ~210 cm^{-1}), respectively, in a very good agreement with the inelastic neutron scattering [47, 48] and Raman scattering data [32]. It is to be noted that as m and n increases (decreases), the transmission (reflectance) dips show increase (decrease) near the $\boldsymbol{\omega_{LO}}$ phonons of CdTe and ZnTe, respectively.

4.3 MDF's Near-IR → UV Energy Range

In the NIR to UV (0. 5 eV to >7.0 eV) spectral range, the dielectric behaviors of crystalline materials are strongly allied to their energy band structures [21]. It has been well established that in semiconductors both direct and indirect bandgap transitions near the critical points (CPs) affect optical dispersion relations. In the indirect bandgap semiconductors, while the transitions take place at energies below the onset of the lowest direct transitions, in the direct bandgap materials, the transitions take part at energies above the onset of the lowest direct transitions [21]. The electronic energy band structures of CdTe, ZnTe, and GaAs have been extensively studied both theoretically [39] and experimentally [21]. In the experimental studies, several interband transitions related to CPs at different parts of the Brillouin zone (BZ) have been identified by exploiting reflectivity [35], SE [21], electro-reflectance, thermo-reflectance, and wavelength-modulated reflectivity techniques.

In our simulations of the complex dielectric functions $\tilde{\varepsilon}(\omega)$ for the direct bandgap binary compounds CdTe, ZnTe, and GaAs, we instigated Adachi's [21] optical dispersion mechanisms by exploiting the modified model dielectric functions. Based on the Kramers-Krönig (KK) transformation, this methodology [39] predicts very well the distinct optical features of the perfect materials near CPs in the BZ. In this approach, one anticipates obtaining three fitting constraints for each CP transitions: the energy, strength, and broadening parameter. For instance, the transition energies at CPs near Γ (i.e., at the center of the BZ), Λ or L (in the <111>), and X (in the <100>) points are labeled as E_0, $E_0 + \Delta_0$; E_1, $E_1 + \Delta_1$; and E_2, respectively [21]. While the E_0, $E_0 + \Delta_0$ transitions at Γ point are of the three-dimensional (3D) M_0-type, the E_1, $E_1 + \Delta_1$ transitions, which take place in the <111> direction near Λ or L points in the BZ, are of 3D M_1-type. Since the M_1-CP longitudinal effective mass is much larger than its transverse counterparts, one can treat 3D-M_1 CPs as two-dimensional (2D) minimum M_0 [21]. Again, a pronounced structure in the optical spectra of CdTe and ZnTe near X point in the <100> direction having energy higher than $E_1 + \Delta_1$ is labeled as E_2. In general, the E_2 transition does not correspond to a single well-defined CP – it has been characterized by a damped harmonic oscillator. For calculating the optical constants of ternary $Cd_{1-x}Zn_xTe$ alloys, the CP energies are represented by quadratic expressions involving binary energy values and composition x, while the strength and broadening parameters are assumed varying linearly with x. The relevant expressions of MDFs reported elsewhere [39] for each energy gaps are used in assessing the spectral dependence of various optical constants (cf. Sect. 3) – linked to the dielectric function $\tilde{\varepsilon}(\omega)$.

One must note that $\varepsilon_1(\omega)$ describes the refraction of photons at any energy range, while $\varepsilon_2(\omega)$ plays a crucial role near the characteristic resonances where the material absorbs electromagnetic radiation. For instance, in polar semiconductors, the distinct resonances in the FIR energy region arise from the transverse optical (ω_{TO}) (cf. Sect. 3) vibrational modes. In bulk materials, the optical constants can be appraised by SE and other experiments [21] – exploiting specific wavelengths

ranging from FIR → NIR → UV. Theoretically, the dielectric functions $\tilde{\varepsilon}(\omega)$ or refractive indices $\tilde{n}(\omega)$ are extorted fitting SE data by expending the well-known KK analysis [39]. However, such a methodology cannot be offered to explicate the optical properties of epilayers prepared on a substrate. Again, from the traditional transmission/reflectance methods adopted by others [35], it is equally impractical acquiring optical parameters of ultrathin films due to small and feeble interference patterns. Here, we have extorted the energy-dependent dielectric constants by using accurate MDFs for both the binary GaAs and ternary $Cd_{1-x}Zn_xTe$ alloys and successfully evaluated epifilm thickness by assimilating a procedure outlined in Sect. 3

4.3.1 Optical Constants in the NIR-UV Region

By exploiting Adachi's formalisms [21] (cf. Sect. 3.1 b) and using the modified MDFs, we have numerically simulated ε_1,ε_2, n, k at the photon energy range of 6 eV $\geq E \geq$ 0.5 eV for both binary and ternary alloy semiconductors. Theoretical results of the optical constants shown in Fig. 10a–e for CdTe, ZnTe, and GaAs are compared with the best-fit spectra for CdTe.

Not only the dispersions of the pseudo-dielectric functions (cf. Fig. 10a–e) concurred well with the experimental data for the binary materials, the results have clearly revealed distinct CP features from the band structures arising from inter-band transitions. In calculating the optical constants for the $Cd_{1-x}Zn_xTe$ ternary alloys with $x = 0.0$, 0.11, 0.64, 0.86, and 1.0 (cf. Fig. 11a, b, we have evaluated the CP energy parameters from the values of its binary counterparts and used the quadratic expressions involving x, while the energy strength and broadening parameters are obtained deliberating linear dependence articulations on x. Once again, the results (see Fig. 11a, b) of the optical parameters for ternary $Cd_{1-x}Zn_xTe$ alloys not only are found consistent with the limited SE data [21] but has also provided clear revelations of the composition-dependent CP energy shifts and widths.

4.3.2 Reflectivity and Transmission Spectra of Thin Epifilms

By incorporating the energy-dependent optical constants (cf. Sect. 4.3) and following the methodology outlined in Sect. 3, we have calculated (cf. Fig. 12a–d) the optical reflectivity [$R(\lambda)$] (blue line) and transmission [$T(\lambda)$] spectra (green line) as a function of photon wavelength λ (~ 150–1800 nm) for several ultrathin $Cd_{1-x}Zn_xTe$ epifilms prepared on n-type GaAs (001). Theoretical results of $R(\lambda)$ appraised at near normal incidence are displayed and compared against the existing experimental data (red squares) for various ultrathin ZnTe/GaAs (001) and $Cd_{0.89}Zn_{0.11}Te$/GaAs (001) epifilms [35] having thicknesses ranging between 22 nm and 129 nm. The perusal of Fig. 11a–d clearly revealed that the simulated reflectivity spectra not only concurred well with the experiments – the theoretical results have certainly

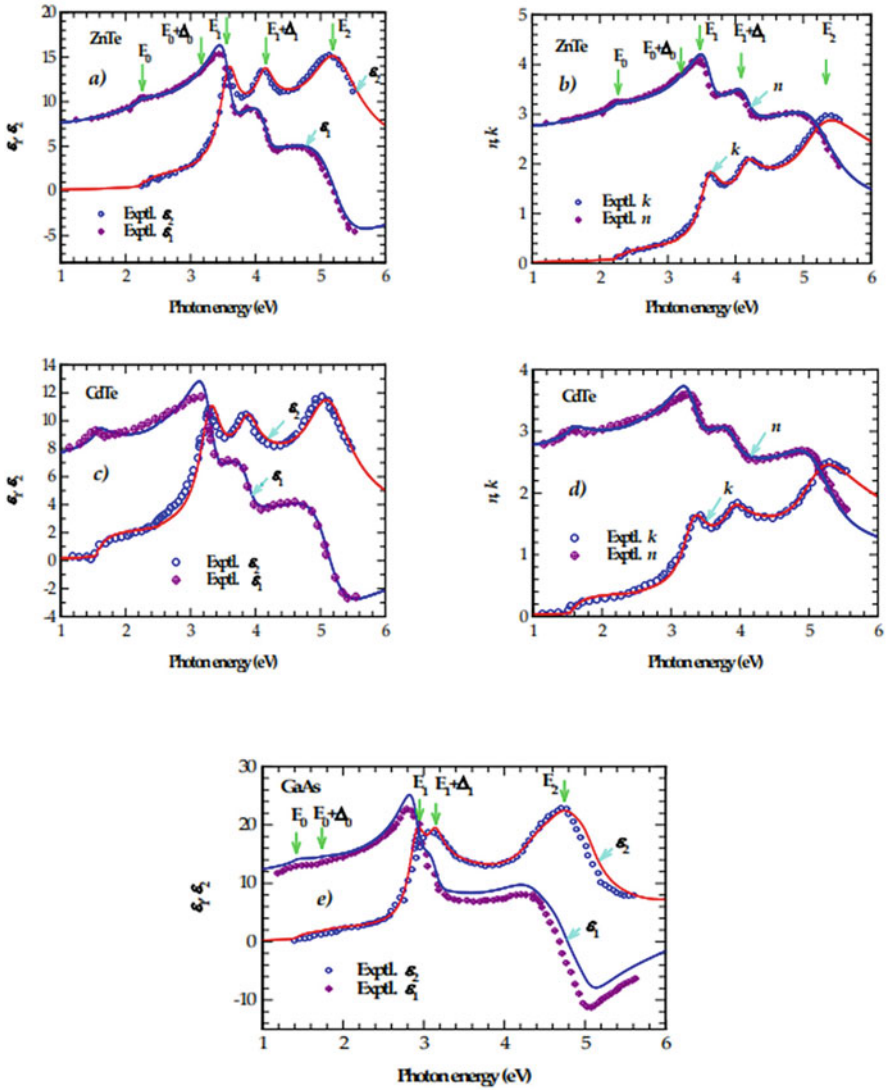


Fig. 10 (**a**) Comparison of the SE data for the complex dielectric function $\widetilde{\varepsilon}(\omega)$ with the best-fit simulated spectra based on a modified MDF for ZnTe; (**b**) the comparison of the experimental data with the best-fit spectra for the complex refractive index $\widetilde{n}(\omega)$ of ZnTe (see text); (**c**) similar results [as of (**a**)] showing comparison of the experimental complex dielectric function $\widetilde{\varepsilon}(\omega)$ with the best-fit spectra for CdTe; (**d**) similar results [as of (**b**)] showing comparison of the experimental complex refractive index $\widetilde{n}(\omega)$ with (**e**) similar results [as of (**a**)] showing comparison of the experimental complex dielectric function $\widetilde{\varepsilon}(\omega)$ with the best-fit spectra for GaAs, the existing SE data [21]

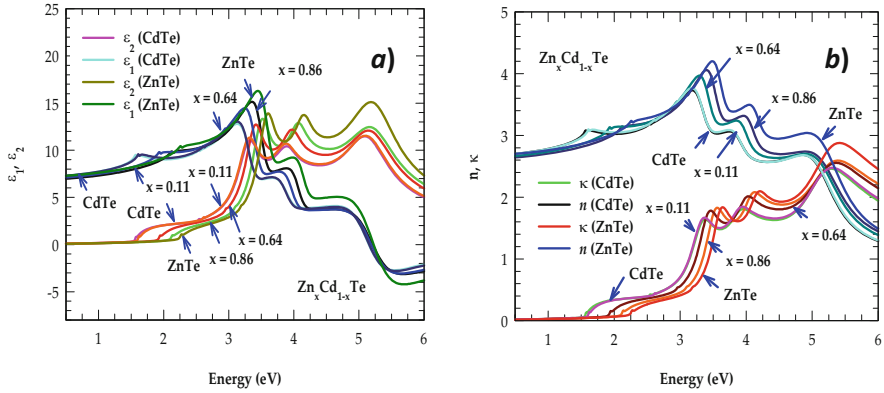


Fig. 11 (**a**) Calculated complex dielectric function $\tilde{\varepsilon}(\omega)$ spectra based on a modified model dielectric functions for $Cd_{1-x}Zn_xTe$ ($x = 0.11$, 0.64, and 0.86); (**b**) the calculated complex refractive index $\tilde{n}(\omega)$ spectra based on modified MDFs for $Cd_{1-x}Zn_xTe$ ($x = 0.11$, 0.64, and 0.86)

encapsulated all the major observed features. One must note that as the ZnTe ($Cd_{1-x}Zn_xTe$)/GaAs (001) epifilms are too lean, the simulated (cf. Fig. 12a–d) reflectivity [$R(\lambda)$] and transmission [$T(\lambda)$] spectra have divulged no interference fringes in the transparent photon energy region – except that they disclosed the broad intensity modulations. Moreover, for all the material samples studied here, the film thicknesses d assessed by reflectivity studies have concurred copiously with the apparent values appraised from the HR-XRD $\omega/2\theta$ scans and other measurements [37–39].

4.3.3 Reflectivity/Transmission: Thickness Dependence

In Fig. 13a and b, we have displayed the results of our model calculations for the optical reflectivity and transmission spectra of ZnTe/GaAs (001) as a function of λ (100–2500 nm) for film thicknesses d varied between 100 nm and 1000 nm. The reflectivity $R(\lambda)$ and transmission $T(\lambda)$ spectra have clearly revealed interference fringes in the highly transparent photon energy region ($\lambda > 548$ nm). As expected for thicker films, we perceived the emergence of fringes when the conditions of constructive and destructive interferences are met between the light waves reflected off the top and bottom of the film – causing maxima and minima, respectively. From the calculated results of transmission $T(\lambda)$ spectra for ZnTe/GaAs films, we also noticed that with the increase of film thickness from 100 nm to 1000 nm, the transmittance (cf. Fig. 13b) decreased – eliciting a sharp absorption edge near $\lambda \equiv$ 548 nm. For ZnTe films with thickness $d > 400$ nm, our assessed optical bandgap E_g ($\equiv$ 2.26 eV) from the absorption band edge concurred very well with the PL measurement of E_g for the bulk material. In thinner films ($d < 400$ nm), we noticed the absorption band edge divulging a slight blue shift, i.e., veering toward the

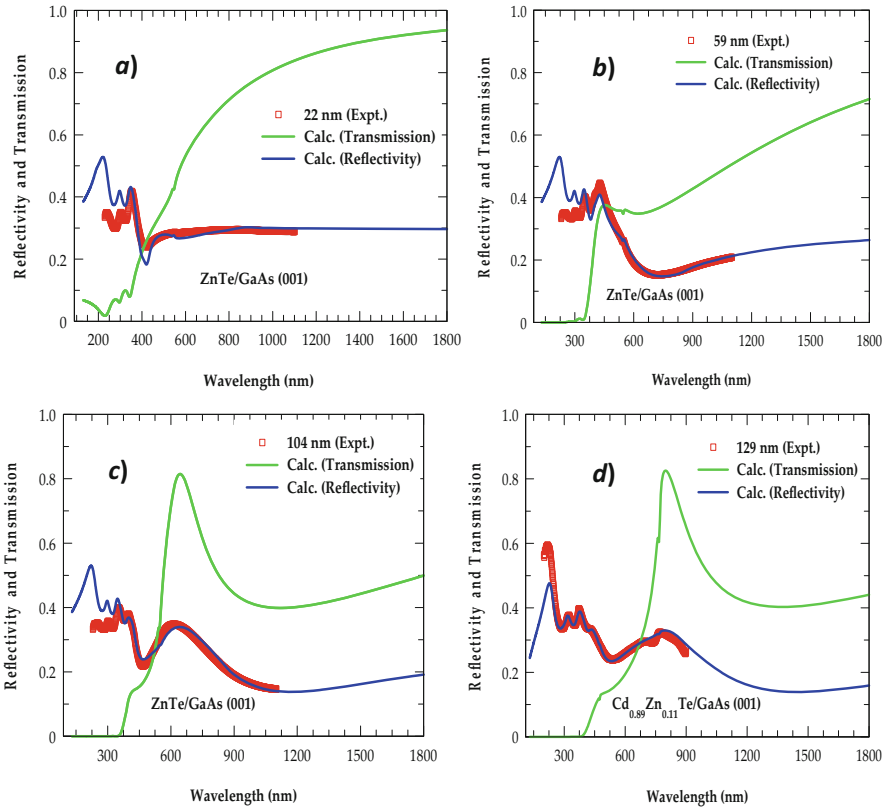


Fig. 12 Comparison of the experimental reflectivity (open red square Ref. [26]) spectra with the simulated reflectivity (solid blue lines) and transmission (solid green lines) spectra for different $Cd_{1-x}Zn_xTe$/GaAs (001) epifilms: (**a**) for $x = 1$ and $d = 22$ nm, (**b**) for $x = 1$ and $d = 59$ nm, (**c**) for $x = 1$ and $d = 104$ nm, (**d**) for $x = 0.11$ and $d = 129$ nm

lower λ – possibly prompting slightly larger optical bandgaps. This manifestation in ultrathin ZnTe/GaAs films while not clearly implicit has been recognized, however, in a few recent experiments [35] and attributed to the probable misfit strain between the films and substrate.

4.4 Analysis of SR-XAS Data for $Cd_{1-x}Zn_xTe$ and CdTe/InSb Epifilms

4.4.1 EXAFS Study for Local Structure in CZT Alloys

The Zn K-edge EXAFS data, displayed in Fig. 14a, b for CZT alloys, were recorded in X-ray fluorescence yield in the energy range between 9500 and 10,700 eV. The

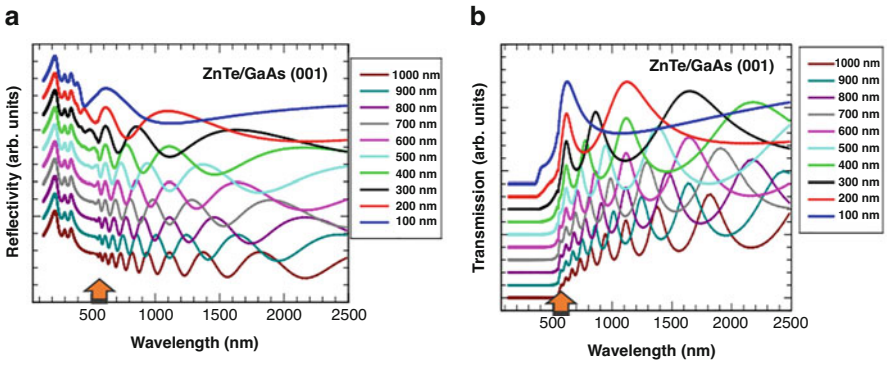


Fig. 13 (**a**) Thickness-dependent reflectivity and (**b**) transmission spectra for ZnTe/GaAs (001) epifilms with *d* ranging from 100 nm to 1000 nm

X-ray absorption coefficient μ as a function of E shown in Fig. 14a has revealed sharp rise in intensity at the Zn K-edge (~9659 eV) – initiating almost a steplike function having weak oscillatory wiggles beyond several hundred eV above the absorption edge. The region closer to the edge is often dominated by the strong scattering processes including the local atomic resonances. The X-ray absorption near edge structures (XANES) are customarily excluded from EXAFS. Our interest here has only been in the fine structures which contained precise information on the local structures around the atom that absorbed X-rays. The smooth "bare atom" background $\mu_o(E)$ has been subtracted off and divided by the "edge step" $\Delta\mu_o(E_o)$ to give oscillations (Fig. 14b) normalized to the one absorption event. The ATHENA package codes are exploited for removing the background contributions using AUTOBK for extracting the EXAFS oscillations from the k-space signals. The information for local atomic structure is obtained by utilizing FEFF 8.2 codes implemented in the ARTEMIS software.

Figure 15 shows the magnitudes of Fourier-transformed EXAFS data with major peaks corresponding to atomic shells from the Zn ions. The best-fit x-dependent results for the $Cd_{1-x}Zn_xTe$ alloys displayed by red open squares are found to be in very good agreement with the experimental data which are indicated using blue lines. Perusal of Fig. 15 clearly reveals that the observed signal of NN "Zn-Te" shell in the Fourier transform absorption exhibits no significant changes in its character over the range of Zn composition. The x-dependent results revealing bimodal behavior (Fig. 16) for the NN "Zn-Te" bond lengths along with the coordination number N and mean-square displacement σ^2 are included in Table 4 while retaining an overall amplitude parameter S_o^2 to 0.94 for all the CZT samples.

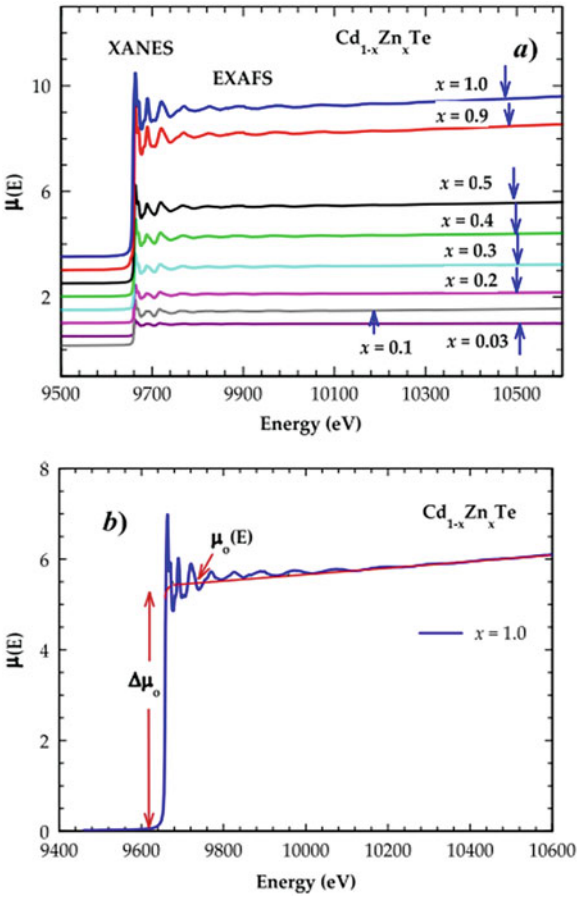


Fig. 14 (**a**) Zn K-edge EXAFS absorption coefficient μ(E) versus X-ray photon energy for $Cd_{1-x}Zn_xTe$ alloys $x = 0.03$, 0.1, 0.2, 0.3, 0.4, 0.5, 0.9, and 1. The spectra are processed by using pre-edge and post-edge lines and spline-fitted background $\mu(E_o)$ subtraction. (**b**) Same as (**a**) for $Cd_{1-x}Zn_xTe$ alloy with $x = 1.00$. Here, $\mu(E_o)$ is the bare atom background absorption and $\Delta\mu(E_o)$ is the edge step

4.4.2 EXAFS Study for Local Structure in CdTe/InSb Epifilms

By exploiting the Cd K-edge EXAFS data, we have assessed local atomic structure around Cd atoms in CdTe with different ion cleaning time and temperature for the six MBE-grown CdTe/InSb (001) epifilms. The results of Cd K-edge data for CdTe are displayed in Fig. 17a near 26,717 eV. The EXAFS spectra for all samples were collected to 1200 eV beyond the Cd K-edges and carefully analyzed (cf. Fig. 17b) for the photoelectron momentum $k = 1.0$ Å^{-1} to $k = 10.0$ Å^{-1}. The background contributions to EXAFS were removed appropriately by using AUTOBK [46]. Replicating scans were coadded for improving the signal-to-noise ratio. Due to numerous diffraction peaks in the Cd-EXAFS spectra, the samples were spun to average out the diffraction peaks. The chi data were $k^2\ \chi\ (k)$ weighted (cf. Fig. 17c) and Fourier transformed with a window width of k 0.5 Å^{-1} to yield the R-space data. The simulated results were generated using the conventional and documented crystallographic properties of Cd and Te by employing the Green's function theory

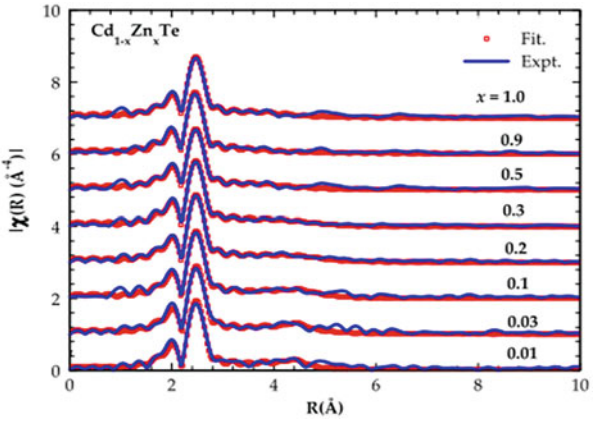


Fig. 15 Fourier transform magnitudes of Zn K-edge k2-weighed EXAFS data (blue solid lines) along with the fitted (red squares) results for eight $Cd_{1-x}Zn_xTe$ samples of different composition $x = 0.01., 0.03, 0.1, 0.2, 0.3, 0.5, 0.9$, and 1, respectively

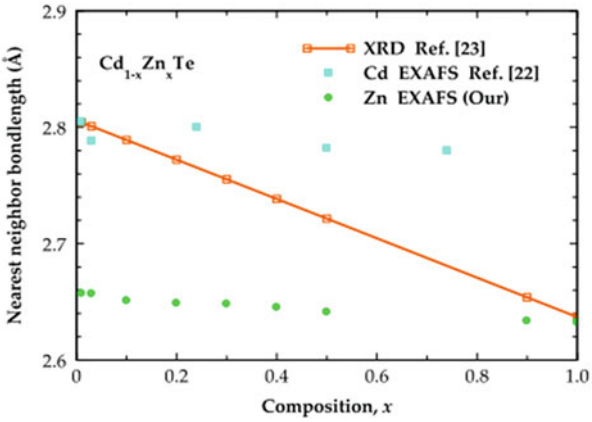


Fig. 16 Local NN bond lengths of Cd-Te (blue-filled squares) from [21] and Zn-Te (green-filled circles) deviate strongly from Vegard's law as given by X-ray diffraction (XRD) [21] data (orange open square)

involving FEFF 8.2 program and implementing it in the ARTEMIS software. The analysis of EXAFS data required empirical standards in conjunction with the Fourier filter techniques. For extorting the nearest-neighbor (Cd-Te) and second nearest-neighbor (Cd-Cd) bond lengths, a structural model was constructed by employing a commercial IFEFFIT package. The fitting results of Fourier transforms have provided very good agreements with the experimental measurements (see Fig. 17c). From the well-defined first neighbor peak in the Cd absorption, we were able to extract the Cd-Te bond lengths listed in Table 5. The fitting results of $R_{Cd\text{-}Te}$ and coordination number (CN) of the first Cd-Te shell are assessed around ~2.80 Å

Table 4 Composition-dependent results of the EXAFS data fit (see text) for first coordination shell around Zn atom of the bulk Bridgman-grown $Cd_{1-x}Zn_xTe$ samples. Calculated results are reported for the amplitude reduction factor S_0^2, the mean coordination number (CN) around the first Cd-Te shell, the nearest-neighbor bond length $R_{Cd\text{-}Te}$, and the relative square displacements (σ^2)

$Cd_{1-x}Zn_xTe$ samples x	$S_0{}^2$	$CN_{Cd\text{-}Te}$	$R_{Cd\text{-}Te}$(Å)	σ^2(Å^2)
0.01	0.94	3.659	2.657	0.0062
0.02	0.94	3.633	2657	0.0063
0.1	0.94	3.598	2.651	0.0063
0.2	0.94	3.490	2.650	0.0061
0.3	0.94	3.444	2.650	0.0062
0.4	0.94	3.357	2.650	0.0061
0.5	0.94	3.250	2.641	0.0061
0.9	0.94	3.295	2.634	0.0052
1.0	0.94	3.132	2.633	0.0058

and nearly ~3.8, respectively. From the second neighbor peaks, we also obtained $CN_{Cd\text{-}Cd}$ and $R_{Cd\text{-}Cd}$ of the second neighbor Cd-Cd shell around ~4.70 Å and nearly ~12 (see Table 6), respectively. The fitting of Cd K-edge spectra for six samples yielded an average value of Cd- as 3.79 neighboring atoms to agree with an expected value of 4 to within 5.25%.

5 Conclusions

In summary, we have performed comprehensive experimental and theoretical studies on several MBE-grown CdTe/InSb (001) samples for assessing their vibrational and structural traits. Simulated results of phonon dispersions $\omega_j\left(\overrightarrow{q}\right)$, density of states, $\Theta_D(T)$, and lattice heat capacities $C_v(T)$ for CdTe, $Cd_{0.8}Zn_{0.6}Te$, $Cd_{06}Zn_{0.4}Te$, $Cd_{0.4}Zn_{0.6}Te$, $Cd_{0.2}Zn_{0.8}Te$, and ZnTe compared reasonably well with experimental and theoretical data. Thickness-dependent FIR spectroscopy investigations have revealed accurate frequency and line shapes of the transverse optical modes for both epilayers and substrates. These reports implied that the MBE-grown CdTe epilayers are well aligned to InSb. In two of the six (#S_5 and S_6) samples besides observing ω_{TO} modes, we have also detected several weak phonon features in the low-frequency $< \omega_{TO}$ region. In the framework of a traditional multilayer optics with three-phase model (ambient/film/substrate), our simulated FIR spectra for S_5 and S_6 extorted relatively large values of oscillator strengths (S) (see Table 3) – indicating poor crystalline qualities of the samples. In such cases, one would expect diffusion of Te/In and/or Sb atoms at the CdTe-InSb boundaries. In corroboration with Raman scattering measurements [31, 32], our FIR studies have clearly validated observing low-frequency modes near ~60 cm^{-1}, ~80 cm^{-1}, and ~ 95 cm^{-1} – triggered by clusters of segregated Sb atoms and/or In_2Te_3-like pre-

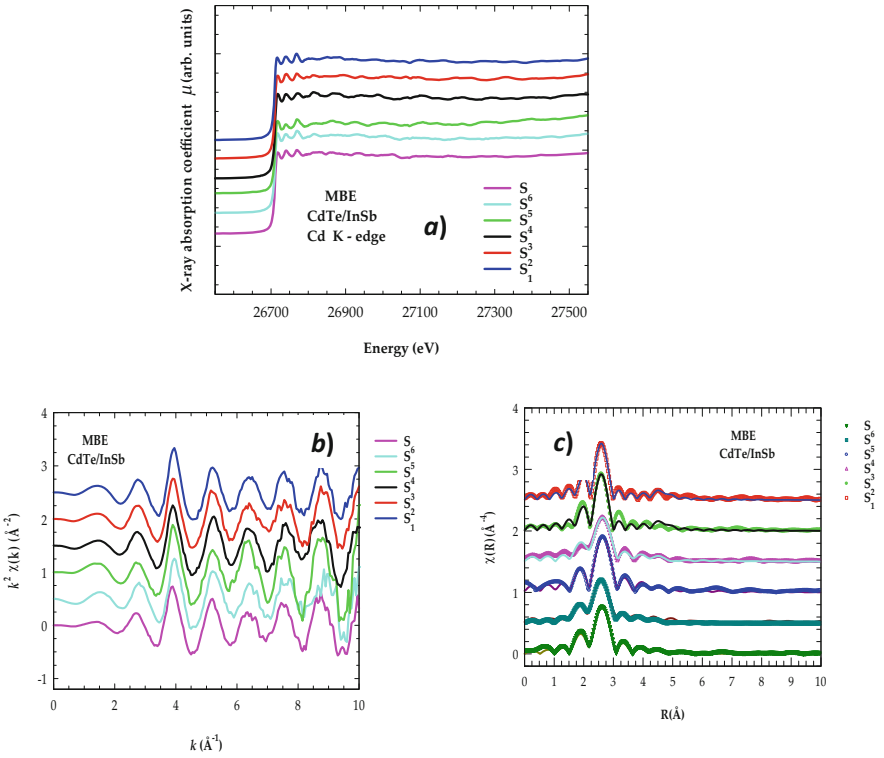


Fig. 17 (**a**) X-ray absorption spectra of Cd-K edge (26,717 eV), (**b**) the experimental Cd K-edge oscillation $k^2\chi(k)$, and (**c**) the magnitude of the measured Fourier transforms (open symbols) and fitted results (lines) for six MBE-grown CdTe/InSb samples (see text)

cipitates at the CdTe-InSb interface. To substantiate Berreman effect, we have also calculated the transmission and reflectivity spectra at oblique incidence ($\varphi_a = 45°$) for CdTe/InSb epilayers of different thickness and $(CdTe)_m/(ZnTe)_n$/InSb SLs. The study has not only confirmed perceiving ω_{TO} phonons in s-polarization and recognizing ω_{TO} and ω_{LO} modes in the p-polarization but also established clearly a simple way of identifying long-wavelength optical phonons in technologically important materials. From the comprehensive analyses of advanced SR-XAS data, we have assessed atomic scale bond lengths and coordination numbers of six MBE-grown CdTe/InSb samples. The small discrepancies in our EXAFS study with respect to the bulk CdTe nearest-neighbor and next-nearest-neighbor Cd-Cd bond lengths are attributed to the possibility of the existence of intrinsic segregated Sb atoms and/or disorder on the surface/interface in CdTe/InSb (001) epifilms.

Table 5 Summary of EXAFS fitting results for six (# S_1–S_6) MBE-grown CdTe/InSb samples. The calculated results are reported (see text) for the amplitude reduction factor S_0^2, the mean coordination number (CN) around the first Cd-Te shell, the nearest-neighbor bond length $R_{Cd\text{-}Te}$, and the relative square displacements (σ^2)

CdTe/InSb samples	$S_0{}^2$	$CN_{Cd\text{-}Te}$	$R_{Cd\text{-}Te}$(Å)	σ^2(Å^2)
S_1	0.895	3.78	2.8020	0.0063
S_2	0.850	3.81	2.8003	0.0058
S_3	0.990	3.76	2.8121	0.0105
S_4	0.949	3.80	2.8137	0.0045
S_5	0.989	3.80	2.7782	0.0114
S_6	0.940	3.76	2.8127	0.0066

Table 6 Summary of EXAFS fitting results for six (#S_1–S_6) MBE-grown CdTe/InSb samples. Calculated results are reported (see text) for the amplitude reduction factor S_0^2, the mean coordination number (CN) around the second Cd-Cd shell, the second-neighbor bond length $R_{Cd\text{-}Cd}$, and the relative square displacements (σ^2)

CdTe/InSb samples	$S_0{}^2$	$CN_{Cd\text{-}Cd}$	$R_{Cd\text{-}Cd}$(Å)	σ^2(Å^2)
S_1	1.000	12.0	4.7022	0.0225
S_2	1.000	12.0	4.6887	0.0373
S_3	1.000	12.0	4.7776	0.0350
S_4	0.990	11.0	4.5338	0.0297
S_5	1.000	12.9	4.6294	0.0453
S_6	1.000	12.2	4.8018	0.0330

Acknowledgments The author (DNT) wishes to thank Dr. Deanne Snavely, Dean of the College of Natural Science and Mathematics at Indiana University of Pennsylvania, for the travel support and the Innovation Grant that he received from the School of Graduate Studies, making this research possible. DNT acknowledges Drs. R. F. C. Farrow, W. J. Choyke, H. H. Lin and P. Becla for the MBE, Bridgman-grown samples used in this study. The author thanks Dr. Z.C. Feng for fruitful discussion and is grateful to Dr. Jyh-Fu Lee for the help on synchrotron radiation X-ray absorption measurements reported in this work.

References

1. Chuang Li, Xia Hao, Yulu He, Jingquan Zhang, Lili Wu, Wei Li, Wenwu Wang, Lianghuan Feng, Islam Muhammad Monirul, Katsuhiro Akimoto, "Identification of deep level defects in CdTe solar cells using transient photo-capacitance spectroscopy" *Jpn. J. Appl. Phys.***60** (2021) SBBF01.
2. H. N. Desai, P. B. Patel, J. M. Dhimmar, and B. P. Modi, "Approaching new photo-electrics: CdTe nano-crystallite thin film" Sol. Stat. Commun. **313** (2020) 113910.
3. B. K. Ghosh, I. Saad, K. T. K. Teo, and S. K. Ghosh, "mcSi and CdTe solar photovoltaic challenges: Pathways to progress" Optik 206 (2020) 164278.
4. G. M. Wilson et al., "The 2020 photovoltaic technologies roadmap", J. Phys. D: Appl. Phys. **53** (2020) 493001.

5. M. A. Green, E. D. Dunlop, J. Hohl-Ebinger, M. Yoshita, N. Kopidakis, and A. W. Y. Ho-Baillie, "Solar cell efficiency tables (Version 55)" Prog. Photovolt. **28** (2019) 3.
6. Budhika G. Mendis, Quentin M. Ramasse, Thomas P. Shalvey, Jonathan D. Major, and Ken Durose, "Optical Properties and Dielectric Functions of Grain Boundaries and Interfaces in CdTe Thin-Film Solar Cells" Appl. Energy Mater. **2** (2019) 1419−1427.
7. Chee Leong Tan and Hooman Mohseni, "Emerging technologies for high performance infrared detectors" Nanophotonics **7** (2018) 169–197.
8. Tao Song, Ana Kanevce, and James R. Sites, "Design of Epitaxial CdTe Solar Cells on InSb Substrates", IEEE J. Photovoltaics, **5** (2015) 1762-1768; R. M. Geisthardt, M. Topic, and J. R. Sites, Status and Potential of CdTe Solar-Cell Efficiency IEEE J. Photovolt. **5** (2015) 1217; J. R. Sites, A. Munshi, J. Kephart, D. Swanson, and W. S. Sampath, IEEE 43rd Photovoltaic Specialists Conf. (Portland, OR, USA), (2016) June 5–10, 10.1109/PVSC.2016.7750351;Tao Song, "Design strategies for high-efficiency CdTe solar cells", PhD thesis (2017) Colorado State University.
9. C. U. Vyas, Pratik Pataniya, Chetan K. Zankat, V. M. Pathak, K. D. Patel, G. K. Solanki, "Transient photo-response properties of CdTe thin films synthesized by screen printing technique" Mat. Sci. Semicond. Process. **71** (2017) 226-231.
10. Samira Abbaspour, Babak Mahmoudian, and Jalil Pirayesh Islamian, "Cadmium Telluride Semiconductor Detector for Improved Spatial and Energy Resolution Radio-isotopic Imaging", World J Nucl Med. **16** (2017) 101–107.
11. Minoru Isshiki and Jifeng Wang, "II-IV Semiconductors for Optoelectronics: CdS, CdSe, CdTe" in Springer Handbook of Electronic and Photonic Materials: Kasap S., Capper P. (eds) (2017) Springer, Cham. https://doi.org/10.1007/978-3-319-48933-9_33.
12. A. Polman, M. Knight, E. C. Garnett, B. Ehrler, and W. C. Sinke, Photovoltaic materials: Present efficiencies and future challenges Science **352** (2016) aad4424.
13. O. de Melo, A. Domínguez, K. Gutiérrez Z-B, G. Contreras-Puente, S. Gallardo-Hernández, A. Escobosa, J.C. González, R. Paniago, J. Ferraz Dias, M. Behar, "Graded composition $Cd_xZn_{1-x}Te$ films grown by Isothermal Close Space Sublimation technique", Solar Energy Materials & Solar Cells **138** (2015) 17–21; E. M. Larramendi, F. Purón, O, Melo O, "Thickness measurement and optical properties of $Cd_{1-x}Zn_xTe$" Semicond Sci Technol **17**, 8-12 (2002).
14. J. Kang, E. I. Parsai, D. Albin, V. G. Karpov, and Diana Shvydka, "From photovoltaics to medical imaging: Applications of thin-film CdTe in x-ray detection" Appl. Phys. Lett. **93** (2008) 223507.
15. O. Limousin, "New trends in CdTe and CdZnTe detectors for X- and gamma-ray applications", Nucl. Instr. Meth. Phys. Res. 504 (2003) 24-37.
16. Christian Scheiber, and George C. Giakos, "Medical applications of CdTe and CdZnTe detectors", Nucl. Instr. Meth. Phys. Res. 458 (2001) 12-25.
17. Yong-Hang Zhang and David J. Smith, "Heterovalent semiconductor structures and devices grown by molecular beam epitaxy" J. Vac. Sci. Technol. **A 39** (2021) 030803.
18. Akihiro Ohtake, Takaaki Mano and Yoshiki Sakuma, "Strain relaxation in InAs heteroepitaxy on lattice-mismatched substrates", Scientific Reports, **10** (2020) 4606.
19. Jiaming Li, Chenjia Tang, Peng Du, Yilan Jiang, Yong Zhang, Xuyi Zhao, Qian Gong, and Xufeng Kou, "Epitaxial growth of lattice-matched InSb/CdTe heterostructures on the GaAs(111) substrate by molecular beam epitaxy" Appl. Phys. Lett. **116** (2020) 122102.
20. Roger E. Welser, Stephen J. Polly, Mitsul Kacharia, Anastasiia Fedorenko, Ashok K. Sood and Seth M. Hubbard, "Design and Demonstration of High Efficiency Quantum Well Solar Cells Employing Thin Strained Superlattices" Scientific Reports **9** (2019) 13955.
21. Sadao Adachi, "Properties of Semiconductor Alloys: Group-IV, III-V and II-VI Semiconductors" Wiley (2009), wiley.com; Sadao Adachi, Toshifumi Kimura, and Norihiro Suzuki, "Optical properties of CdTe: Experiment and modeling", J. Appl. Phys. **74**, 3435 (1993); Kohzo Sato and Sadao Adachi, "Optical properties of ZnTe", J. Appl. Phys. **73**, 926 (1993).
22. T Garcia, "Heterojunction Engineering for Next Generation Hybrid II-VI Materials" PhD Thesis (2017) The City University of New York (CUNY); M. B. Lassise, "Monolithic Heterovalent Integration of Compound Semiconductors and Their Applications" PhD thesis (2019) Arizona State University.

23. Vladimir L. Tassev, "Heteroepitaxy, an Amazing Contribution of Crystal Growth to the World of Optics and Electronics" *Crystals7* (2017) 178. https://doi.org/10.3390/cryst7060178
24. Jonathan Faugier-Tovar, Florica Lazar, Catherine Marichy and Christian Brylinski, "Influence of the Lattice Mismatch on the Atomic Ordering of ZnO Grown by Atomic Layer Deposition onto Single Crystal Surfaces with Variable Mismatch (InP, GaAs, GaN, SiC)" Condens. Matter **1** (2017) 3; doi:https://doi.org/10.3390/condmat2010003.
25. Peter Capper, Stuart Irvine and Tim Joyce, "Epitaxial Crystal Growth: Methods and Materials" in Kasap S., Capper P. (eds) (2017) Springer Handbook of Electronic and Photonic Materials. Springer Handbooks. Springer, Cham. https://doi.org/10.1007/978-3-319-48933-9_14.
26. Qihang Liu , Xiuwen Zhang , L. B. Abdalla and Alex Zunger "Transforming Common III–V and II–VI Semiconductor Compounds into Topological Heterostructures: The Case of CdTe/InSb Superlattices" Adv. Funct. Mater. **26** (2016) 3259-3267.
27. Matthew P. Lumb, Igor Vurgaftman, Chaffra A. Affouda , Jerry R. Meyer , Edward H. Aifer and Robert J. Walters, "Quantum wells and superlattices for III-V photovoltaics and photodetectors" in Proceedings of SPIE - The International Society for Optical Engineering **8471** (2012) 8471 0A1.
28. D. Gerthsen, K. Tillmann and M. Lentzen, "Structural properties of lattice-mismatched compound semiconductor heterostructures" in: Helbig R. (eds) Festkörperprobleme : Advances in Solid State Physics **34** (1995) Springer, Berlin, Heidelberg. https://doi.org/10.1007/BFb0107532
29. R. G. van Welzenis, F. M. van Setten and O. F. Z. Schannen, "InSb/CdTe heterostructures grown by MBE" Applied Physics **A 52** (1991) 19–27.
30. Ebadollah Naderi, Sachin Nanavati, Chiranjib Majumder and S. V. Ghaisas, "Diffusion of Cd and Te adatoms on CdTe(111) surfaces: A computational study using density functional theory" AIP Advances **5** (2015) 017134; https://doi.org/10.1063/1.4906794
31. D. Drews, J. Sahm, W. Richter and D. R. T. Zahn, "Molecular-beam-epitaxy growth of CdTe on InSb (110) monitored in situ by Raman spectroscopy", J. Appl. Phys. **78** (1995) 4060.
32. K. J. Mackey, Dietrich R. T. Zahn, P. M. G. Allen, R. H. Williams, W. Richter and Stan Williams, "InSb–CdTe interfaces: A combined study by soft x-ray photoemission, low-energy electron diffraction, and Raman spectroscopy", J. Vac. Sci. Tech. **B 5** (1987) 1233 – 1238.
33. J. Huerta, M. López, and O. Zelaya, "MBE growth of CdTe epilayers on InSb (111) substrates" Superficies y Vacio **8** (1999) 125-129.
34. David J. Smith, Jing Lu,Toshihiro Aoki, Martha R. McCartney and Yong-Hang Zhang "Observation of compound semiconductors and heterovalent interfaces using aberration-corrected scanning transmission electron microscopy" J. Mat. Res. **32** (2017) 297; DOI: https://doi.org/10.1557/jmr.2016.297
35. E. M. Larramendi, O. de Melo, M. Hernández Vélez and M. C. Tamargo, "Adsorption, desorption, and interdiffusion in atomic layer epitaxy of CdTe and CdZnTe", J. Appl. Phys. **96** (2004) 7164.
36. Youngjin Jang, Arthur Shapiro, Faris Horani, Yaron Kauffmann and Efrat Lifshitz, "Towards low-toxic colloidal quantum dots" De Gruyter **232** (2018) 1443-1455.DOI: https://doi.org/10.1515/zpch-2018-1148; ibid: "Cation Exchange Combined with Kirkendall Effect in the Preparation of SnTe/CdTe and CdTe/SnTe Core/Shell Nanocrystals" J. Phys. Chem. Lett. 13 (2016) 2602–2609.
37. R. F. C. Farrow, G. R. Jones, G. M. Williams, and I. M. Young, "Molecular beam epitaxial growth of high structural perfection, heteroepitaxial CdTe films on InSb (001)" Appl. Phys. Lett. **39** (1981) 954.
38. A T S Wee, Z C Feng, H H Hng, K L Tan, R F C Farrow and W J Choyke, "XPS and SIMS studies of MBE grown CdTe/InSb(001) heterostructures", J. Phys.: Condens. Matter **7** (1995) 4359-4369.
39. Devki Talwar, Zhe Chuan Feng, Jyh-Fu Lee, P. Becla, "Extended x-ray absorption fine structure and micro-Raman spectra of Bridgman grown $Cd_{1-x}Zn_xTe$ ternary alloys", Materials Research Express **1** (2014) 015018; Yingda Qian, Yuanlan Liang, Xuguang Luo, Kaiyan He, Wenhong Sun, Hao-Hsiung Lin, Devki N. Talwar, Ting-Shan Chan, Ian Ferguson, Lingyu Wan, Qingyi

Yang, and Zhe Chuan Feng, "Synchrotron Radiation X-Ray Absorption Spectroscopy and Spectroscopic Ellipsometry Studies of InSb Thin Films on GaAs Grown by Metal Organic Chemical Vapor Deposition" Advances in Materials Science and Engineering (2018) 5016435, 11 pages https://doi.org/10.1155/2018/5016435; Devki N. Talwar, Na Lu, Ian T. Ferguson and Zhe Chuan Feng, High resolution synchrotron extended x-ray absorption fine structure and infrared spectroscopy analysis of MBE grown CdTe/InSb epifilms, J. Vac. Sci. Technol. A 39, 063401 (2021); doi: https://doi.org/10.1116/6.0001145

40. D. G. Diso, "Research and Development of CdTe based Thin Film PV Solar Cells" PhD thesis (2011) Sheffield Hallam University http://shura.shu.ac.uk/id/eprint/4941
41. I.F. Almog, M.S. Bradley, and V. Bulovi'c, "The Lorentz Oscillator and its Applications" https://ocw.mit.edu/courses/electrical-engineering-and-computer-science/6-007-electromagnetic-energy-from-motors-to-lasers-spring-2011/readings/MIT6_007S11_lorentz.pdf
42. Z. G. Hu, M. B. M. Rinzan, S. G. Matsik, A. G. U. Perera, G. Von Winckel, A. Stintz, and S. Krishna, "Optical characterizations of heavily doped p-type $Al_xGa_{1-x}As$ and GaAs epitaxial films at terahertz frequencies" J. Appl. Phys. **97** (2005) 093529
43. D. W. Berreman, "Infrared absorption at longitudinal optic frequency in cubic crystal films," Phys. Rev. **130** (1963) 2193–2198.
44. O. E. Piro, "Optical properties, reflectance, and transmittance of anisotropic absorbing crystal plates" Phys. Rev. **B 36** (1987) 3427.
45. Devki N. Talwar, Tzuen-Rong Yang, Zhe Chuan Feng and P. Becla, "Infrared reflectance and transmission spectra in II-VI alloys and superlattices" Phys. Rev. **B 84** (2011) 174203.
46. Matthew Newille, "IFEFFIT: Interactive XAFS analysis and FEFF fitting", J. Sync. Rad. **8** (2001) 322-324.
47. J. M. Rowe, R. M. Nicklow, D. L. Price, and K. Zanio, "Lattice dynamics of cadmium telluride", Phys. Rev. **B 10** (1974) 671; N. Vagelatos, D. Wehe, and J. S. King, "Phonon dispersion and phonon densities of states for ZnS and ZnTe", J. Chem. Phys. **60** (1974) 3613.
48. D. L. Price, J. M. Rowe and R. M. Nicklow, "Lattice dynamics of grey tin and indium antimonide", Phys. Rev. B **3** (1971) 1268.
49. E. S. Koteles, W. R. Datars and G. Dolling, "Far-infrared phonon absorption in InSb", Phys. Rev. B **9** (1974) 572.
50. E. S. Koteles and W. R. Datars, "Two-phonon absorption in InSb, InAs and GaAs", Can. J. Phys. **54** (1976) 1676-1682.
51. N. L. Rowell, D. L. Lockwood and Guolin Yu, "Optical phonons in $InSb_{1-x}As_x$/InSb", J. Vac Sci and Tech. **A 22** (2004) 935.
52. D. L. Lockwood, Guolin Yu and N. L. Rowell, Optical phonon frequencies and damping of AlAs, GaP, GaAs, InP, InAs and InSb studied by oblique incidence infrared spectroscopy", Sol. State Commun. **136** (2005) 404-409.
53. Romuald Brazis and Romas Raguotis, "Electron and phonon dynamics in indium antimonide crystals" Opt. Quan. Elect. **40** (2008) 249–252.
54. M. D. Sciacca, A. J. Mayur, E. Oh, A. K. Ramdas, S. Rodriguez, J. K. Furdyna, M. R. Melloch, C. P. Beetz, and W. S. Yoo, "Infrared observation of transverse and longitudinal polar optical modes of semiconductor films: Normal and oblique incidence", Phys. Rev. **B 51** (1995) 7744.
55. J. Iba'nez, E. Tarhan, A. K. Ramdas, S. Hern˜andez, R. Cusc'o, L. Artus, M. R. Melloch, and M. Hopkinson, "Direct observation of LO phonon plasmon coupled modes in the infrared transmission spectra of n-GaAs and n-$In_{1-x}Ga_x$ As", Phys. Rev. **B 69** (2004) 075314.
56. J. Iba'nez, S. Hern˜andez, E. Alarc'on-Llad'o, R. Cusc'o, L. Art'us, S. V. Navikov, C. T. Foxon, and E. Calleja, "Far-infrared transmission in GaN, AlN and AlGaN thin films grown by molecular-beam epitaxy", J. Appl. Phys. **104** (2008) 033544.

Defect Engineering in Epitaxially Grown Cd(Zn)Te Thin Films on Lattice-Mismatch Substrates



Wenwu Pan, Lorenzo Faraone, and Wen Lei

1 Introduction

1.1 Overview of II–VI HgCdTe and Cd(Zn)Te Semiconductors and Their Applications

II–VI semiconductors (highlighted in red in Fig. 1) are composed of elements from Group II and Group VI of the periodic table and are a group of common semiconductor materials [1]. In particular, cubic zincblende HgCdTe and Cd(Zn)Te semiconductors are significant materials with a wide range of applications in high-end infrared (IR) sensing/imaging, radiation detectors, and solar cells. For example, II–VI HgCdTe, alloyed by closely lattice-matched CdTe and HgTe, is well known as a material system with a widely tunable working wavelength range (1–30 μm), large absorption coefficient, long carrier lifetimes, and high mobilities, which established it as the leading semiconductor for fabricating high-performance IR detectors and imaging focal plane arrays (FPAs) [2]. Apart from the IR applications, HgCdTe epilayers grown by molecular beam epitaxy (MBE) have also emerged as attractive materials in developing integrated terahertz photonic systems [3] and topological electronics [4].

Cd(Zn)Te is also a representative II–VI compound with a bandgap well-suited for solar cell applications [5]. Currently, CdTe is the second most widely used material for thin-film photovoltaic solar cells, after silicon. CdZnTe also is a high-density material with high atomic numbers making it an excellent candidate for fabricating

W. Pan (✉) · L. Faraone · W. Lei
ARC Centre of Excellence for Transformative Meta-Optical Systems (TMOS), Department of Electrical, Electronic and Computer Engineering, The University of Western Australia, Perth, WA, Australia
e-mail: wenwu.pan@uwa.edu.au; lorenzo.faraone@uwa.edu.au; wen.lei@uwa.edu.au

© The Author(s), under exclusive license to Springer Nature Switzerland AG 2024

S. Krishnamoorthy, K. (Kris) Iniewski (eds.), *Advances in Fabrication and Investigation of Nanomaterials for Industrial Applications*,
https://doi.org/10.1007/978-3-031-42700-8_10

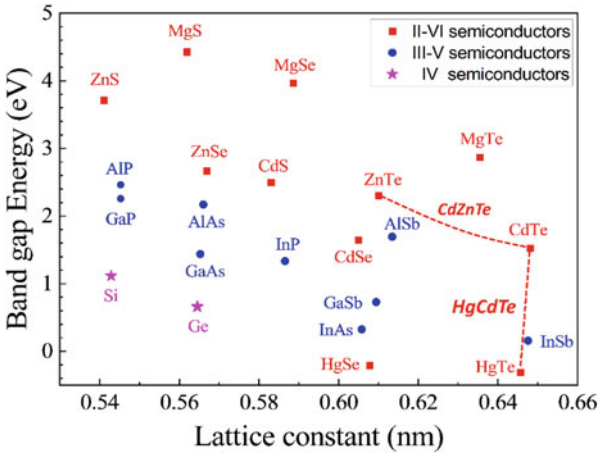


Fig. 1 A lattice constant vs. bandgap plot of common semiconductor materials [1]

radiation detectors used for gamma-ray spectroscopy, X-ray imaging, and medical imaging applications [6]. The lattice constant of CdZnTe can be tuned by adjusting the Zn composition of the alloy material, and $Cd_{0.96}Zn_{0.04}Te$ (CZT) has long been the baseline substrate for lattice-matched MBE growth of high-quality HgCdTe for fabricating state-of-the-art IR FPAs [7].

1.2 Limitations of the HgCdTe-CZT-Based IR Technology

Despite the fact that the unparalleled device performance is achieved based on the epitaxial growth of HgCdTe on lattice-matched CZT substrates, HgCdTe-CZT-based technology suffers severe limitations such as high cost, small array format size, and low mechanical strength, which are fundamentally caused by the unfavorable features of CZT substrates including high cost, small size, more fragile, and less commercial availability [2].

The soft and brittle nature of II–VI materials makes them more challenging to handle, process, and fabricate compared to more common IV and III–V semiconductor substrates, which are more robust and durable [8]. Consequently, CZT substrates are generally more expensive and less commercially available than other common semiconductor substrates, such as Si and GaAs.

The size of CZT substrates is also typically smaller than other standard semiconductor substrates, limiting the number of devices that can be fabricated on them and the ability to produce large format size HgCdTe FPAs for high-resolution IR imaging applications. In addition, the quality of CZT substrates can also be a concern as they are often subject to relatively high levels of defects, which can reduce the yield and reliability of devices fabricated on them. These substrate

issues hinder HgCdTe and Cd(Zn)Te from being widely adopted in applications demanding compact, sensitive, and inexpensive optoelectronic devices.

1.3 Advantages and Challenges in Heteroepitaxy of (Hg)Cd(Zn)Te Films on Alternative Substrates

With the development of IR technologies and their applications, there is a growing demand for high-performance HgCdTe IR detectors with larger array size and lower cost, which has fuelled the hetero-epitaxial growth of HgCdTe on CdTe buffer layers on large-area, high-quality, cost-effective, and commercially available substrates such as Si [9], Ge [10], and GaAs [11]. Compared to the conventional growth on CZT substrates, the growth of II–VI HgCdTe and Cd(Zn)Te films on these alternative substrates (AS) offers several advantages, including increased wafer size for the processing of numerous FPAs per wafer and/or larger format size of FPAs. In addition, the AS can offer lower surface defect density/impurities and better mechanical properties than CZT substrates, thus benefiting the detector yield and reducing the production cost. This approach is promising to increase the FPA format size, deliver higher FPA yield and operability, and dramatically lower the costs, providing the IR imaging industry with a viable solution to meet the growing demands for advanced IR imaging systems.

Despite these advantages, one of the major challenges associated with the heteroepitaxial growth of single-crystalline HgCdTe thin film on AS is their large lattice mismatch (f_l) between HgCdTe and these AS ($f_l = -19.3\%, -14.3\%, -14.4\%$ for Si, Ge, and GaAs, respectively, as shown in Fig. 2), which inevitably generate

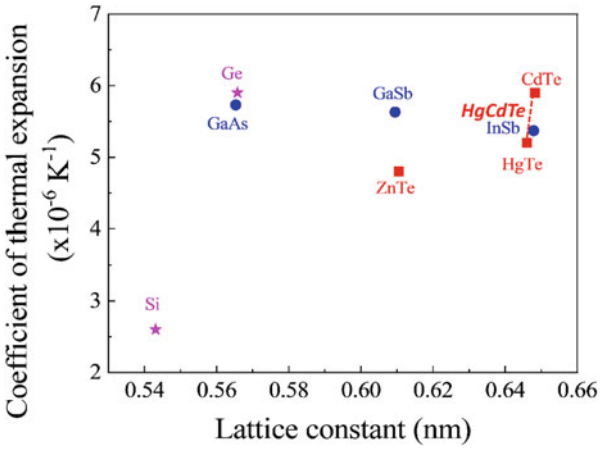


Fig. 2 Lattice constant and CTE (coefficient of thermal expansion) mismatches between HgCdTe and several semiconductor substrates

misfit dislocations (>10^8 cm^{-2}) in the vicinity of the CdTe/AS interface. The misfit dislocations (MDs) form threading dislocations (TDs) that can propagate into the CdTe buffer layer and the subsequent HgCdTe epitaxial layer, which eventually limit the performance of HgCdTe devices and, therefore, the FPA operability. Another concern is their mismatch in CTE (thermal expansion coefficient, f_t), which can also result in strain, defects, or dislocations in HgCdTe thin film grown on these AS. As evident from Fig. 2, III–V InSb has almost the same lattice constant of CdTe, exhibiting the minimum lattice and CTE mismatches with HgCdTe in comparison to other AS. The preliminary studies on MBE growth of HgCdTe on InSb have shown that the crystal quality of (Hg)CdTe grown on InSb substrates can exceed that of (Hg)CdTe grown on CdTe substrates [12–14]. However, a significant complication with the use of InSb substrates is the potential necessity for substrate removal and epitaxial film transfer [13]. This is because InSb can absorb IR light due to its narrow bandgap (0.17 eV at 300 K and 0.23 eV at 80 K) and thus is not compatible with current state-of-the-art backside-illuminated HgCdTe device technology. III–V GaSb is IR transparent and has a relatively smaller lattice mismatch with HgCdTe ($f_l = -6\%$) compared to previously studied AS (Si, Ge, and GaAs). Experimentally, (Hg)CdTe layers grown on GaSb substrates have generally demonstrated material quality comparable to those on GaAs substrates [15–17]. Further growth studies are hampered by the fact that III-Sb substrates are vulnerable to thermal decomposition during the deoxidation thermal process without a background group V Sb flux, which usually is not available in II–VI MBE system. Even better (Hg)CdTe layers would be expected on III–V AS by optimizing the thermal cleaning process, such as using a dual chamber III–V and II–VI MBE system [18, 19].

To reduce the threading dislocation density (TDD) in HgCdTe grown on lattice-mismatched AS, an intermediate CdTe buffer layer is commonly interposed between these AS and HgCdTe to accommodate their large f_l and f_t. Providing thick buffer layers is unlikely to yield very high-quality material, so different approaches have been studied to reduce the TDD in CdTe and HgCdTe epitaxial layers grown on AS. These include using low-temperature nucleation layers of ZnTe or CdTe [20] and various forms of cyclic thermal annealing (CTA) [9].

Screening techniques such as X-ray diffraction (XRD) and etch pit density (EPD) analysis are usually used to evaluate the material quality of (Hg)CdTe epilayers [21, 22]. For example, lattice-matched HgCdTe/CZT typically demonstrates XRD full-width-half-maximum (XRD FWHM) of 25–50 arcsec and EPD of ~10^4–10^5 cm^{-2}. For the conventional CdTe buffers (5 ~ 10 microns thick) grown with optimal nucleation layer and cyclic thermal annealing processes, the resultant XRD FWHM and EPD are in the range of 60–80 arcsec and low-10^6 to low-10^7 cm^{-2}, respectively. Moreover, since the direct growth of HgCdTe on CdTe substrates (EPD ~ low-10^4 cm^{-2}) can result in an EPD around low-10^6 cm^{-2} in HgCdTe due to the small lattice mismatch ($f_l = 0.24\%$) between HgCdTe and CdTe [23], it is essential to reduce the HgCdTe/CdTe lattice mismatch in order to fabricate high-performance detectors, especially for long-wave IR (LWIR) detectors because LWIR detectors are much more sensitive to material defects due to their narrower

bandgap. In the past, an approach to reducing the HgCdTe/CdTe lattice mismatch was incorporating Zn and/or Se into the CdTe buffer layer. However, high-quality Cd(Zn, Se)Te alloy buffer layers were difficult to obtain by MBE [24].

Overall, due to the limited dislocation confining efficiency of the CdTe buffer and the residual HgCdTe/CdTe lattice mismatch, none of these approaches yields HgCdTe with material quality, detector performance, and FPA operability comparable to those grown on CZT, especially for LWIR detectors in which EPD levels below mid-10^5 cm^{-2} are required [25]. This book chapter will discuss a recently developed CdTe buffer layer process based on strained CdZnTe/CdTe superlattices for dislocation filtering aimed at resolving the problem mentioned above [26].

2 Strained CdTe/CdZnTe Superlattice-Based Dislocation Filtering Layers (DFL)

2.1 Working Principle of DFL

A strained-layer superlattice (SLS), consisting of alternating strained hetero-layers and generally referred to as a DFL, has been observed to be able to block TD propagation and thus reduce TDD in the overlaying epitaxial layer [27–29]. Although the dislocation filtering efficiency varies with experimental conditions, modeling results indicate that the minimum TDD obtained in any given structure is likely to be limited by kinetic effects to approximately 10^4–10^5 cm^{-2}. Movement of TDs in response to misfit strain combined with thermal energy has been shown to be the best way to enhance the dislocation annihilation probability. The SLS-based DFL technology has been successfully demonstrated in the growth of III–V semiconductors on lattice-mismatched substrates for many years. For example, the TDD has been reduced from ~10^9 cm^{-2} to ~10^5 cm^{-2} for GaAs buffer layers grown on Si by incorporating four sets of 10-nm $In_{0.18}Ga_{0.18}As$/10-nm GaAs SLS-based DFLs, leading to high-performance InAs/GaAs quantum dot lasers [30]. In contrast to the CTA techniques used in the heteroepitaxial growth of (Hg)CdTe on AS, DFL technology will allow thinner buffer layer thickness, shorter processing time, and lower processing temperature to achieve similar EPD levels due to the high dislocation filtering efficiency.

2.2 Structure Design of CdTe DFL Buffer Layers and the MBE Growth

Figure 3a shows a typical sample structure for a CdTe buffer layer on a 2-inch GaAs (211)B substrate with five sets of $Cd_{1-x}Zn_xTe$/CdTe SLS-based DFL. Compared to nonpolar group IV substrates such as Si and Ge, “epi-ready” GaAs is more

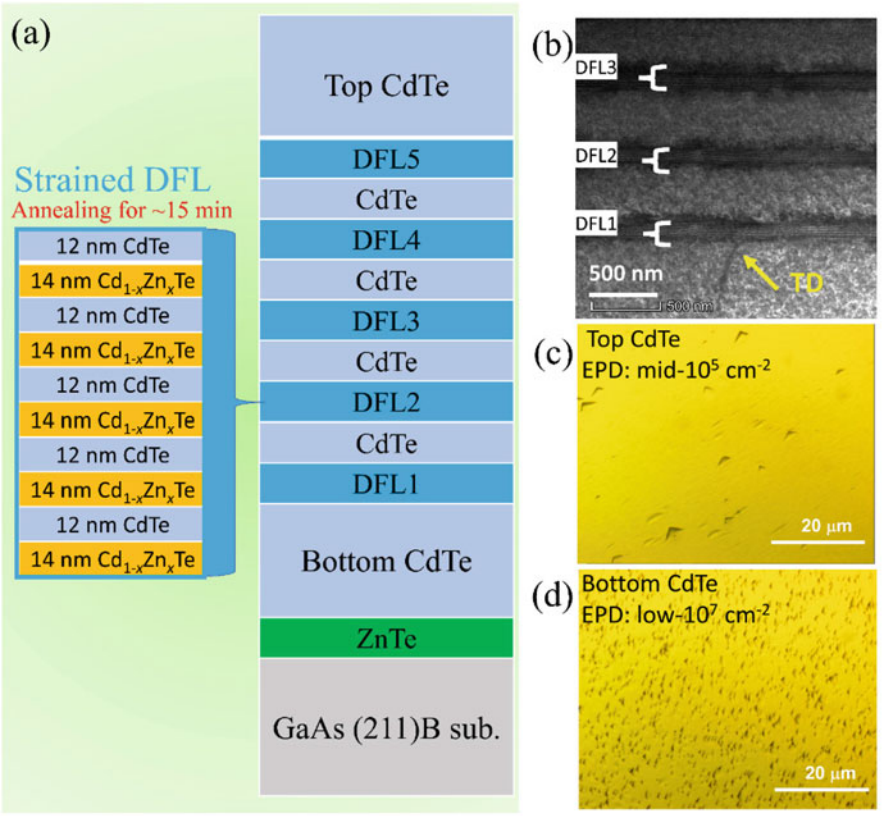


Fig. 3 (**a**) Schematic DFL-based buffer layer structure, (**b**) Transmission electron microscopy (TEM) evidence for dislocation filtering by the DFLs, (**c**) and (**d**) CdTe EPD results after and before the incorporation of the DFLs, respectively

readily available for epitaxial growth of II–VI materials and has smaller f_l and f_t with (Hg)CdTe. MBE growth of the DFL buffer structure was first demonstrated on III–V GaSb substrates [31]. However, further growth studies on GaSb are hampered by the fact that GaSb substrates are vulnerable to decomposition during the thermal deoxidation process without a background Sb flux, which is not available in II–VI MBE system. Then, GaAs substrates were used and found to be more "epi-ready" than GaSb after thermal cleaning.

The (211)B orientation has been widely used for growing high-quality HgCdTe since it requires much lower Hg flux than either (001) or (111)A orientations to maintain the same MBE growth rate, and it is less sensitive to micro-twin formation in comparison to (111) A/B [32]. As mentioned above, the purpose of the SLS layer structure is to increase the likelihood of dislocation annihilation and inhibit dislocation multiplication and/or propagation. The key to a significant reduction in TDD is TD movement using misfit stress, i.e., in layers with a finite strain-thickness

product (εh). Moreover, a good rule of thumb for DFL design in heteroepitaxial growth is given by $\varepsilon_c h_c < \varepsilon h < 4\varepsilon_c h_c$, where $\varepsilon_c h_c$ is a constant (experimentally, $\varepsilon_c h_c$ is ~0.24 nm in the GaInAs system) [29]. This can be understood by considering that the stress in the DFL needs to be high enough to divert TDs but not enough to generate additional TDs. In a layer with constant composition, dislocation multiplication is expected to commence when the strain-thickness product exceeds ~ $4\varepsilon_c h_c$, which places an upper limit on the strain and thickness of a DFL. In addition, $Cd_{1-x}Zn_xTe$ layers that are too thick and/or have more Zn content (x) may increase the risk of Zn segregation.

In calculating this product, the superlattice structure of each DFL set can be considered to be equivalent to a single $Cd_{1-y}Zn_yTe$ layer having the same total thickness of $h = 5d_1 + 4d_2$, and having a mean Zn content of $y = xd_1/(d_1 + d_2)$, and therefore a mean misfit strain of $\varepsilon = yf_l$, where $d_1 = 14$ nm and $d_2 = 12$ nm are the thicknesses of the $Cd_{1-x}Zn_xTe$ layers and CdTe layers, respectively, and $f_l = -5.8\%$ is the lattice mismatch of ZnTe/CdTe. Hence, the DFL has a strain-thickness product of $\varepsilon h = 3.1x$ nm, and the constraint condition determines a limited Zn content range of $0.08 < x < 0.30$ for our DFL design, assuming $\varepsilon_c h_c = 0.24$ nm for the $Cd_{1-x}Zn_xTe$ system.

CdTe buffer layers were grown on 2-inch GaAs (211)B substrates in a Riber 32P II–VI MBE system where elementary Zn, Te, and compound CdTe were loaded in standard Knudsen cells as sources, and the individual fluxes (beam equivalent pressures (BEP)) were controlled by adjusting the cell temperatures. To evaluate the in situ oxide desorption process of GaAs substrates prior to MBE growth, reflection high-energy electron diffraction (RHEED) was used to monitor the transition from a spotty pattern to a streaky pattern as the substrate temperature was raised to ~580 °C.

After the oxide desorption at ~580 °C for 3 min, the substrates were cooled down to 220 °C, and a thin ZnTe nucleation layer (<10 nm) was grown at this temperature and then processed by in situ thermal annealing with a background Te BEP of 3×10^{-6} Torr at 380 °C for 15 min. Note that ZnTe has a lattice constant intermediate between those of GaAs and CdTe, contributing to better nucleation on GaAs in comparison to CdTe nucleation layer. The thin ZnTe nucleation layer was used in order to suppress a three-dimensional growth and preserve a good (211)B interface for the subsequent CdTe growth. After the growth of a 2 ~ 5-μm-thick CdTe bottom layer, several sets of CdZnTe/CdTe SLS-based DFL were grown, separated by 500-nm-thick CdTe spacer layers. Each set of CdZnTe/CdTe DFL consisted of five periods of ~14-nm CdZnTe (20 s MBE growth)/~12-nm CdTe (20 s MBE growth). In situ thermal annealing for 15 min was undertaken after each DFL growth. The samples were completed by the growth of 4 ~ 20-μm-thick CdTe top layer. Both the CdZnTe and CdTe layers were grown at about 270 °C under Te-rich conditions with the Te/CdTe BEP ratio of approximately 1.5.

The CdTe DFL buffer layers were grown with different structural designs and annealing conditions to explore their impact on the final EPD of the top CdTe layer. The growth process/parameters consistently resulted in (211)B-orientated CdTe epilayers, while unexpected changes in substrate temperature during growth might result in (133)B-orientated layers [33].

2.3 Dislocation Filtering Effect

After MBE growth, there are various methods for characterizing the dislocation filtering effect in the CdTe DFL buffer layers. TEM characterizations are straightforward as they can visualize individual defects such as TDs. Apparent TD redirection and termination at the CdZnTe/CdTe hetero-interfaces are evident, as indicated by the yellow arrows in Fig. 3b. TEM has a lower detection limit of TDD of 10^7–10^8 cm^{-2} due to the relatively small volume being analyzed. Defect decoration based on chemical etching, known as EPD etching, significantly extends the lower detection limit. For example, 1 min of Everson-etching (composition of the etchant: 48% HF/HNO_3/lactic acid =1:4:25) for CdTe (211)B surface (etching rate ~ 1.9 μm min^{-1}) decorates TDs by forming larger surface etch pits, which can be easily detected and counted at lower magnification, thereby facilitating the inspection of larger sample areas. The EPD measurements show that a DFL-based buffer can reduce the EPD of CdTe grown on GaAs from low-10^7 (Fig. 3d) to low-10^6 cm^{-2} (5×10^5 cm^{-2} for the best layer, as shown in Fig. 3c), which approaches the critical EPD level required for fabricating high-performance LWIR HgCdTe detectors.

3 Structural and Optical analysis of the CdTe DFL Buffer Layers [34]

A better understanding of the CdTe DFL buffers in terms of their detailed structural properties and associated dislocation filtering effects may allow them to be optimized sufficiently to achieve high-quality HgCdTe epilayers. Although TEM can characterize the epitaxial layers in detail, it is destructive and time-consuming, and TEM specimen preparation of (Hg)CdTe structures can be challenging due to the fragile nature of the material compared with other semiconductors [35]. EPD measurements are destructive, and for CdTe buffer layers containing strained DFL structures, it was found that the chemical etching rate for the $Cd_{1-x}Zn_xTe$/CdTe DFL region is a factor of 2 ~ 5 times (depending on the x value) lower than that for CdTe, and the defect decoration effect appears to be less pronounced if the etching stops within the DFL region, causing difficulties in characterizing TD evolution within the CdTe layer between each DFL set. Instead, rapid and nondestructive methods such as XRD, photoluminescence (PL), and cathodoluminescence (CL) spectroscopy have been widely used in developing optoelectronic devices. As will be discussed in the following, these nondestructive techniques have yielded unique insight into both the defect density and the lattice strain presented in the CdTe DFL buffer, which is crucial for the subsequent high-quality growth of HgCdTe.

3.1 XRD Characterizations

As shown in Fig. 4, high-resolution XRD characterizations with X-ray beam direction aligned with the $[1\overline{1}1]$ direction of the substrate were carried out for reciprocal space mapping (RSM), $\omega{-}2\theta$ and ω scans for a CdTe DFL buffer structure ($x = 0.178$, EPD $= 5 \times 10^5$ cm^{-2}, 5-μm-thick top CdTe layer). Based on the RMS analysis, it was found that CdTe layers in/near the DFL region can

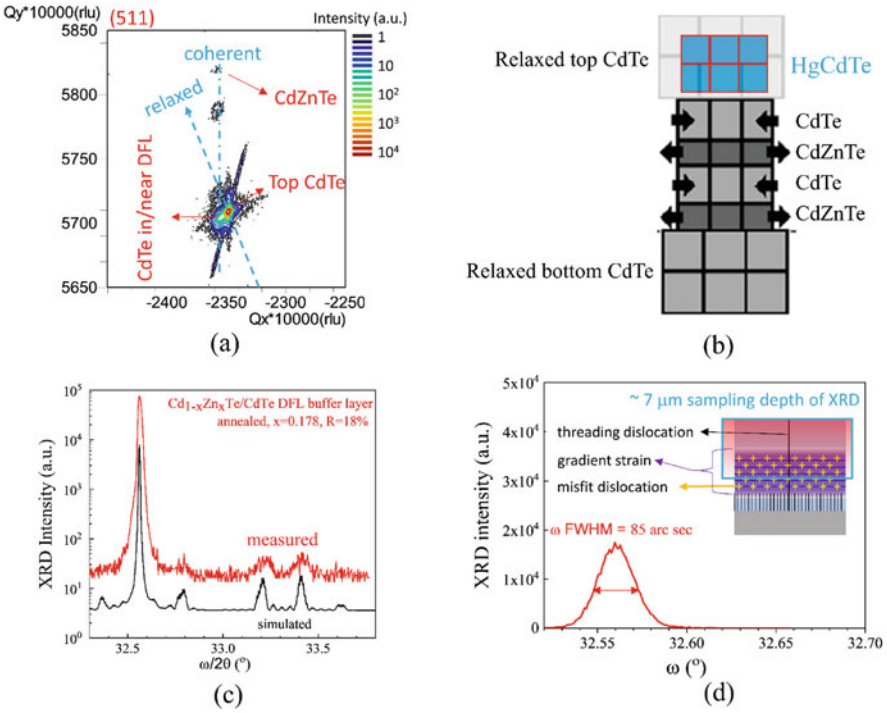


Fig. 4 (**a**) Reciprocal space mapping of asymmetric (511) reflection of a CdTe DFL buffer. The dominant bottom peak corresponds to the relaxed top CdTe layer, and the nearby sub-peak with lower intensity corresponds to the CdTe layers in/near the DFL region. The upper features consist of several interference fringes corresponding to the strained CdZnTe/CdTe DFLs. The tilted line (azure dash) crossing the top CdTe layer peak points toward the origin of reciprocal space and marks the line of fully relaxed (cubic) materials. The vertical line (azure dash-dot) represents reciprocal lattice points where the parallel lattice constant of the CdZnTe superlattice is equal to that of the CdTe in/near the DFL region: that is, a coherently strained superlattice. (**b**) Schematic illustration of stress relaxation in the SLS-DFL region: CdTe layers in/near the DFL region can be compressively strained to partially compensate the large tensile strain presented in the CdZnTe layers. (**c**) (422) $\omega{-}2\theta$ diffraction spectra collected from the CdTe DFL buffer layer and the theoretical simulation. The curves are shifted vertically for better visibility. (**d**) (422) ω diffraction spectrum collected for the CdTe buffer layer and the inset indicates that three mechanisms are presumably responsible for the XRD FWHM spread: (1) threading dislocations in top CdTe, (2) compressively strained CdTe in/near DFL region, and (3) misfit dislocations in DFLs

be compressively strained to partially compensate the large tensile strain presented in the $Cd_{1-x}Zn_xTe$ layers (Fig. 4b). Similar coherent growth has been previously observed in InGaN/GaN superlattice structures grown on GaN [36]. The in-plane lattice parameter from the coherently grown DFL region shows a lattice mismatch of -0.14% with respect to the top relaxed CdTe, which is close to the target value of -0.24% for the in-plane lattice-matched growth of MWIR and LWIR HgCdTe. The coherent growth of the DFL is therefore advantageous in comparison to the conventional pseudomorphic growth in terms of better lattice matching with HgCdTe.

From the RSMs, the relaxation (R) of the CdZnTe layers with respect to the relaxed top CdTe layer is calculated to be $R = 18\%$. With the R value, the structural parameters such as the Zn content (x) and the thicknesses of the $Cd_{1-x}Zn_xTe$/CdTe in the DFL layers can be determined by comparing measured and simulated (422) $\omega-2\theta$ diffraction curves shown in Fig. 4c. From the fitting for the DFL buffer, the thicknesses of the CdZnTe/CdTe layers and x value in the $Cd_{1-x}Zn_xTe$ layer are derived to be 14 nm/12 nm and 0.178, respectively.

The XRD FWHM extracted from ω diffraction has been widely used to screen epilayers in terms of TDD, based on the empirical observation that a decrease in EPD is generally associated with smaller XRD FWHM as observed for the relaxed CdTe buffers and HgCdTe layers. Figure 4d shows the high-resolution XRD (422) ω diffraction spectrum measured for the CdTe DFL buffer ($x = 0.178$, EPD $= 5 \times 10^5$ cm^{-2}, XRD FWHM of ~85 arcsec) with a top CdTe thickness of 5 μm. It is worth noting that the CdTe DFL buffer layer doesn't exhibit any noticeable XRD FWHM reduction compared with the reference CdTe buffer layer without DFL (EPD of ~2×10^7 cm^{-2}, XRD FWHM of ~73 arcsec). The main reason is that XRD measurement has a relatively large sampling depth of ~7 μm, so the XRD FWHM essentially samples both the top CdTe layer and the DFL region. As discussed previously, the in-plane lattice of the CdTe in/near the DFL region appears to be partially compressively strained to compensate the large tensile strain in their neighboring CdZnTe layers. With the top CdTe layer growth, the lattice of the top CdTe layer would be relaxed gradually. As a result, both the residual TDs and the lattice gradient of the CdTe layers contribute to the XRD FWHM spread. On the other hand, as will be discussed later, the more dislocations that are blocked by the DFLs, the more MDs will be generated in the DFL region due to the TD filtering process, presumably contributing to the XRD FWHM spread as well.

As shown in Fig. 5a and b, the correlation between the XRD FWHM spread and the strain related to the DFL buffer design has been investigated. Both the CdTe DFL grown with the thickest top CdTe layer (~20 μm) and the CdTe DFL buffer grown with the lowest Zn content of $x = 0.08$ (top CdTe layer thickness ~ 5 μm) have small XRD FWHM that are very close to the expected range of 40–50 arcsec predicted based on the empirical correlation ($\boldsymbol{\rho} = \mathbf{10}^{\left[-14.6+20.8\left(1-e^{-\frac{X_f}{11.3}}\right)+2\left(1-e^{-\frac{X_f}{104.5}}\right)\right]}$) established in the previous work [26]. An XRD FWHM broadening rate of 3±1 arcsec/Zn% is deduced for the DFL buffer layers grown with a 5-μm top CdTe

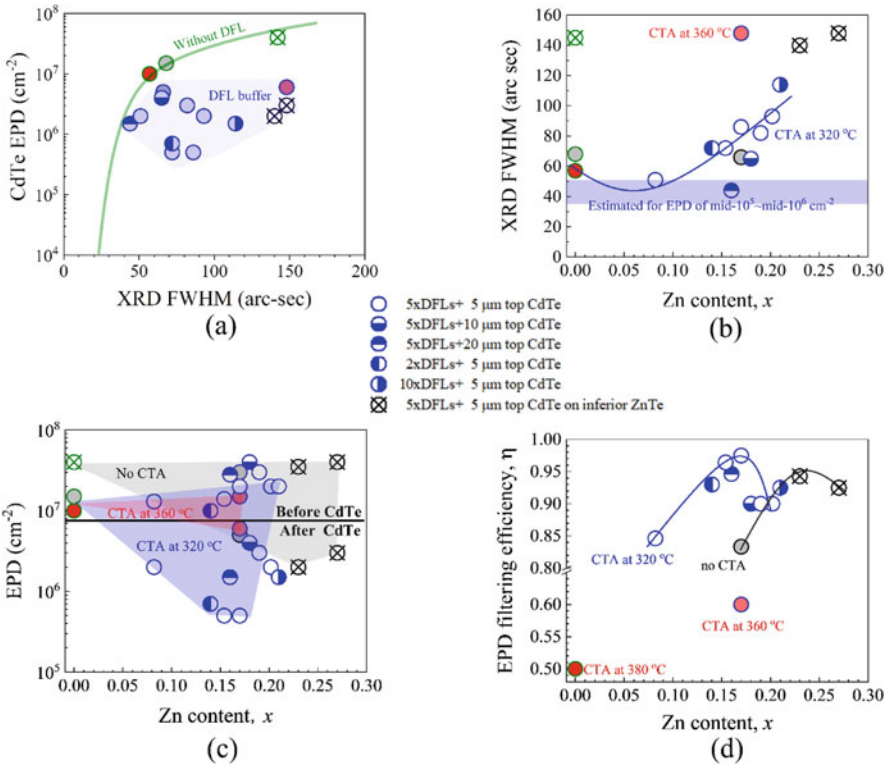


Fig. 5 (**a**) EPD of CdTe buffer layers/GaAs with DFL and some CdTe reference samples, plotted as a function of XRD FWHM and compared to the empirical correlation (solid red curve) established in previous work and (**b**) plotted as a function of Zn content, (**c**) EPD values measured for the top CdTe (EPD_t) and bottom CdTe (EPD_b) layers for DFL buffer layers grown with different DFL designs and plotted as a function of Zn content (x), and (**d**) corresponding EPD filtering efficiency (η) calculated by $\eta=(EPD_b - EPD_t)/EPD_b$

layer and CTA at 320 °C. Other parameters, such as the thickness of the top CdTe layer, the DFL annealing temperature, the number of DFLs, and the thickness of the bottom CdTe layer, are also suspected to affect the XRD FWHM values.

3.2 Correlation Between Structural/Growth Parameters and Dislocation Filtering Efficiency

Several parameters, such as x value in $Cd_{1-x}Zn_xTe$ layers, CTA temperature, and the number of DFL, as summarized in Fig. 5c, were found to affect the dislocation filtering efficiency (η) and therefore the final EPD value of the top CdTe layer. In the case of buffer layers with five sets of DFL grown with CTA at 320 °C, an optimal x

range of $0.16 < x < 0.18$ is observed, which leads to a low EPD level ranging from mid-10^5 to low-10^6 cm^{-2} and the highest EPD filtering efficiency of ~98% within the Zn composition range of $0.08 < x < 0.27$ studied. It is generally assumed that moderate thermal annealing for DFL structures can further improve their efficiency of filtering defects due to the combined effect of increasing the mobility of defects and introducing thermal strain (ε_t) for more efficient defect annihilation. The data in Fig. 5d suggests that in CdTe DFL buffer layers without CTA, the optimal x value in $Cd_{1-x}Zn_xTe$ is relatively high at around 0.23 (η=94%, EPD_t of 2×10^6 cm^{-2}). This is to be expected since higher x value, and therefore more lattice-mismatch strain in the DFL, can compensate for the lack of benefits associated with CTA.

Excessive annealing can result in net surface evaporation of CdTe, surface roughening, Te deficiency-related defects, and potential nucleation points for additional dislocations. However, this is unlikely to occur for nearly relaxed CdTe when the CTA is carried out at temperatures below 400 °C under Te overpressure. Experimentally, we found that the EPD of a CdTe/GaAs buffer without DFL can be reduced from 2×10^7 to 1×10^7 cm^{-2} after introducing CTA at temperatures up to 380 °C, corresponding to a TD reduction efficiency of ~50%. Furthermore, EPD reduction from low-10^7 to mid-10^5 cm^{-2} was observed by other workers for CdTe/Si ($f_t = -92\%$) with ten cycles of CTA at high temperatures up to ~500 °C [37]. In this case, both additional Te and CdTe fluxes were supplied during the CTA process to prevent surface roughening/evaporation. Note that the EPD reported for CdTe/Ge ($f_t = 14\%$) and CdTe/GaAs ($f_t = 14\%$) with the use of CTA at ~400 °C varied in the range of $10^6 \sim 10^7$ cm^{-2} [38, 39]. These values are relatively high compared to the best-reported values for CdTe/Si, which may be explained by the differences in the thermal annealing temperature (ΔT) as well as f_t since $\varepsilon_t \propto f_t \Delta T$.

The above discussion suggests that strained CdZnTe layers in the DFL may be more sensitive to CTA and thus the effect of excessive heating on the strained CdZnTe layers should be considered. It has been found in many lattice-mismatched systems, such as strained InGaAs/GaAs and strained SiGe/Ge, that annealing of the strained layers helps to generate MDs that relax the strain and reduce critical thickness [40]. Therefore, the decrease of dislocation filtering efficiency observed in the CdTe DFL buffer with CTA at 360 °C could be attributed to thermal annealing-assisted MD formation and strain relaxation/leakage in the CdZnTe layers. Further detailed control of the annealing temperature and/or annealing duration, as well as Te flux, could be effective in providing CdTe DFL buffers with $EPD_t <$ mid-10^5 cm^{-2}. The CdTe DFL buffer layers demonstrate higher efficiency in TD reduction at much lower temperature CTA in comparison to conventional CdTe/AS, which may be beneficial in reducing the risk of structural damage during cooling with highly mismatched CTE, such as CdTe/Si, as well as reducing the risk of Ga contamination in HgCdTe layers grown on GaAs substrates.

As evident from Fig. 5d, other parameters, such as thicknesses of the top and bottom CdTe layers and the number of DFLs, are also expected to affect the EPD_t values. It is interesting that considerable EPD reduction can be achieved by using only two sets of DFL, providing much shorter processing times and thinner buffer layers compared with conventional CdTe buffer layers grown with complex CTA

procedures. Moreover, the EPD_t of CdTe DFL buffer layers with thicker top CdTe layer (> 10 μm) appears to be slightly larger than that with 5 μm, which may be related to lattice relaxation in the top CdTe layer. In principle, the thicknesses of the bottom CdTe as well as the top CdTe can be reduced for the subsequent growth of HgCdTe without affecting dislocation filtering while improving the lattice matching for HgCdTe/CdTe.

3.3 Optical Properties of the CdTe Buffer Layers

Optical techniques such as scanning electron microscopy-based cathodoluminescence (SEM-CL) and microscopy-based photoluminescence (μPL) also provide a fast and nondestructive approach for evaluating dislocation evolution in the heteroepitaxial CdTe buffer layers with and without DFLs. In contrast to volumetric XRD FWHM measurements, these optical techniques offer much higher spatial resolution due to their much less sampling/penetrating depth of laser used in μPL or electron beam used in SEM-CL. Despite nonideal surfaces, interfaces, and background impurities that dominate the overall recombination velocity and screen the impact of bulk TDD, a comparison of luminescence intensities for similar structures grown in the same batch of samples and/or within a short time interval remains relevant to TDD measurements as the MBE growth conditions in terms of background impurities and fluxes can be assumed to be unchanged. In order to evaluate the dislocation filtering effect caused by the DFLs, surface PL and cross-sectional SEM-CL spectroscopies were used to examine the direct bandgap emission from the CdTe buffer layers at room temperature (RT), making use of the fact that dislocations normally behave as non-radiative recombination centers that are harmful to optical emission.

As shown in Fig. 6a and b, a comparison of RT-PL spectroscopy was undertaken for CdTe buffer samples grown within the same MBE growth session. These PL intensities of the CdTe peak at around 1.5 eV are very well correlated with the EPD values in the range from low-10^7 to mid-$10^5 cm^{-2}$, suggesting that this optical method provides a fast and reliable nondestructive approach for evaluating the TDD for CdTe buffer layers with and without DFL. In contrast, a larger XRD FWHM does not necessarily imply higher TDD for the CdTe buffer layers with DFLs due to the gradient strain of the CdTe layers in/near the DFL region.

Figure 6c shows a depth dependence of cross-sectional SEM-CL for a DFL-based buffer layer grown on GaAs. Five CL quenching areas in series along the growth direction are visible for the CdTe DFL sample, corresponding to the 110-nm-thick DFL layers separated by the 500-nm-thick CdTe spacers. In addition, the CL intensity of the CdTe peak at around 810 nm (1.530 eV) appears to increase from bottom to top after each DFL, whereas it remains almost unchanged in the CdTe reference sample without DFL [34], suggesting that each DFL acts as a barrier to TD propagation.

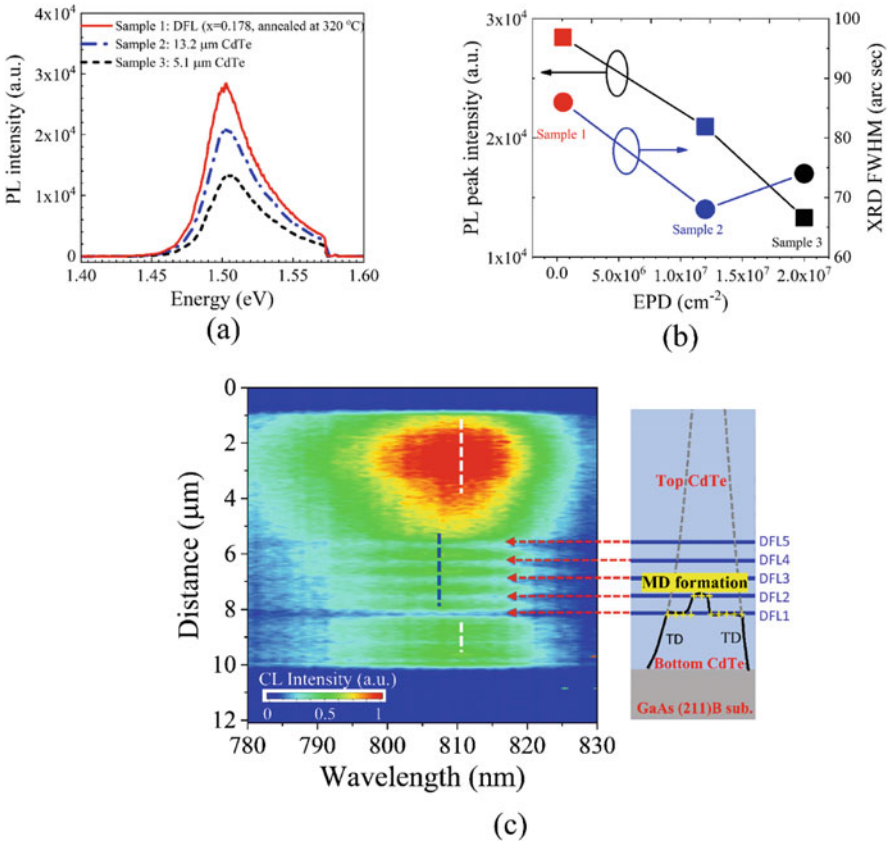


Fig. 6 (**a**) RT-PL spectra of CdTe buffer layers with/without DFL. (**b**) PL peak intensity and XRD FWHM plotted as a function of the measured EPD for different buffer layers. (**c**) Left, depth dependence of cross-sectional SEM-CL for a DFL-based buffer layer grown on GaAs; right, schematic representation of approximate dislocation evolution in a CdZnTe/CdTe DFL-based buffer layer

The TDs in a heteroepitaxial CdTe layer grown on lattice-mismatched GaAs are expected to propagate during the growth process and thus extend into the upper layer. However, as illustrated in Fig. 6c, if lattice misfit strain is introduced by inserting lattice-mismatched CdZnTe layers within the CdTe, the TDs experience a lateral force resulting from the Peach-Koehler interaction with the mismatch stress field [41]. The TD segments are thus driven to glide away, and the glide of TD segments produces MDs at the CdZnTe/CdTe interfaces. As glide proceeds, the gliding dislocations encounter others and react with them to eliminate the TDs, or the threading segments escape to the edge of the sample. In either case, TDs are converted into more MDs confined in the DFL layers, which facilitates non-radiative recombination and hence decreases the CL efficiency of the DFL layers

while increasing the CL emissions from the upper CdTe layer. Similar MD-induced CL quenching has been observed in InAs/GaAs quantum dot lasers [42].

4 Conclusions

In conclusion, this book chapter provides a comprehensive overview of the current state of research on defect engineering in the epitaxially grown Cd(Zn)Te thin films on lattice-mismatch alternative substrates. We have reviewed our findings concerning using strained CdZnTe/CdTe superlattice layers as dislocation filtering layers for the heteroepitaxial growth of CdTe buffer layers on AS, such as III–V GaAs. The DFL approach has reduced the routine EPD from low-10^7 cm^{-2} to low-10^6 cm^{-2} and 5×10^5 cm^{-2} for the best layer, which approaches the critical EPD level required for fabricating high-performance LWIR HgCdTe detectors. The structural and optical properties of the CdTe buffer layers were characterized, and the correlation between the structural/growth parameters and the dislocation filtering efficiency was explored. The dislocation filtering efficiency is found to be highly dependent on the balance between stress and thermal annealing, and even lower EPD can be expected with further optimization of the DFL structural design, growth parameters, and annealing conditions. Moreover, the in-plane lattice of the CdTe layers near the DFL region is found to be compressively strained, leading to a spread in XRD FWHM but better in-plane lattice-matching with HgCdTe, in comparison to conventional single-layer CdTe buffers/AS.

More work needs to be done to investigate the impact of growth and annealing temperature, and the thickness and composition of superlattice layers on the final EPD of the top HgCdTe layer, and their impact on HgCdTe device performance. The beneficial effects of CdZnTe/CdTe DFL are not limited to III–V substrates but could also be applied to the growth of CdTe buffer layers on other alternative substrates such as Si and Ge, which would be a feasible approach for growing high-quality CdTe and HgCdTe materials on large-area alternative substrates for next-generation HgCdTe IR detectors and imaging FPAs with lower cost and larger array format. The results presented in this chapter have significant implications for future research and development in the field of general heteroepitaxial growth of II–VI semiconductors.

References

1. Capper, P., *Narrow Bandgap II-VI Semiconductors: Growth*. Springer Handbook of Electronic and Photonic Materials, 2nd Edition, ed. S. Kasap and P. Capper. 2017. 343-364.
2. Lei, W., J. Antoszewski, and L. Faraone, *Progress, challenges, and opportunities for HgCdTe infrared materials and detectors.* Applied Physics Reviews, 2015. **2**(4): p. 041303.
3. Ruffenach, S., et al., *HgCdTe-based heterostructures for terahertz photonics.* APL Materials, 2017. **5**(3): p. 035503.

4. Bernevig, B.A., T.L. Hughes, and S.C. Zhang, *Quantum spin Hall effect and topological phase transition in HgTe quantum wells.* Science, 2006. **314**(5806): p. 1757-1761.
5. Metzger, W.K., et al., *Exceeding 20% efficiency with in situ group V doping in polycrystalline CdTe solar cells.* Nature Energy, 2019. **4**(10): p. 837-845.
6. Schlesinger, T.E., et al., *Cadmium zinc telluride and its use as a nuclear radiation detector material.* Materials Science and Engineering: R: Reports, 2001. **32**(4-5): p. 103-189.
7. Berding, M.A., et al., *Critical thickness in the HgCdTe/CdZnTe system.* Journal of Electronic Materials, 2000. **29**(6): p. 676-679.
8. Adachi, S., *Properties of semiconductor alloys: group-IV, III-V and II-VI semiconductors*. Vol. 28. 2009: John Wiley & Sons.
9. Wijewarnasuriya, P.S. *Dislocation reduction in HgCdTe grown on CdTe/Si*. in *Image Sensing Technologies: Materials, Devices, Systems, and Applications III*. 2016. International Society for Optics and Photonics.
10. Badano, G., et al., *Lattice Relaxation and Dislocation Reduction in MBE CdTe (211) B/Ge (211).* Journal of electronic materials, 2010. **39**(7): p. 908-911.
11. Carmody, M., et al., *Recent Progress in MBE Growth of CdTe and HgCdTe on (211)B GaAs Substrates.* Journal of Electronic Materials, 2012. **41**(10): p. 2719-2724.
12. Seyedmohammadi, S., et al., *Molecular beam epitaxial re-growth of CdTe, CdTe/CdMgTe and CdTe/CdZnTe double heterostructures on CdTe/InSb(100) substrates with As cap.* Journal of Crystal Growth, 2015. **425**: p. 181-185.
13. De Lyon, T.J., et al., *MBE Growth and Transfer of HgCdTe Epitaxial Films from InSb Substrates.* Journal of electronic materials, 2010. **39**(7): p. 1058-1062.
14. Liu, S., et al., *Minority carrier lifetime of lattice-matched CdZnTe alloy grown on InSb substrates using molecular beam epitaxy.* Journal of Vacuum Science & Technology B, Nanotechnology and Microelectronics: Materials, Processing, Measurement, and Phenomena, 2015. **33**(1): p. 011207.
15. Lei, W., et al., *Low dislocation density MBE process for CdTe-on-GaSb as an alternative substrate for HgCdTe growth.* Infrared Physics & Technology, 2018. **92**: p. 96-102.
16. Lei, W., et al., *MBE growth of mid-wave infrared HgCdTe layers on GaSb alternative substrates.* Journal of Electronic Materials, 2015. **44**(9): p. 3180-3187.
17. Lei, W., et al., *GaSb: A new alternative substrate for epitaxial growth of HgCdTe.* Journal of electronic materials, 2014. **43**(8): p. 2788-2794.
18. Zhao, Y., et al., *Monocrystalline CdTe solar cells with open-circuit voltage over 1V and efficiency of 17%.* Nature Energy, 2016. **1**.
19. Lassise, M.B., et al., *Growth of II-VI/III-V heterovalent quantum structures.* Journal of Vacuum Science & Technology B, Nanotechnology and Microelectronics: Materials, Processing, Measurement, and Phenomena, 2018. **36**(2): p. 02D110.
20. Jaime-Vasquez, M., et al., *Nucleation of ZnTe on the As-terminated Si (112) surface.* Journal of electronic materials, 2007. **36**(8): p. 905-909.
21. Everson, W.J., et al., *Etch Pit Characterization of CdTe and CdZnte Substrates for Use in Mercury Cadmium Telluride Epitaxy.* Journal of Electronic Materials, 1995. **24**(5): p. 505-510.
22. Yang, J.R., et al., *Traces of HgCdTe defects as revealed by etch pits.* Journal of electronic materials, 2008. **37**(9): p. 1241-1246.
23. Benson, J.D., et al., *Growth and Analysis of HgCdTe on Alternate Substrates.* Journal of Electronic Materials, 2012. **41**(10): p. 2971-2974.
24. Chen, Y.P., G. Brill, and N.K. Dhar, *MBE growth of CdSeTe/Si composite substrate for long-wavelength IR HgCdTe applications.* Journal of crystal growth, 2003. **252**(1-3): p. 270-274.
25. Johnson, S.M., et al., *Effect of dislocations on the electrical and optical properties of long-wavelength infrared HgCdTe photovoltaic detectors.* Journal of Vacuum Science & Technology B: Microelectronics and Nanometer Structures Processing, Measurement, and Phenomena, 1992. **10**(4): p. 1499-1506.
26. Pan, W., et al., *Defect Engineering in MBE-Grown CdTe Buffer Layers on GaAs (211) B Substrates.* Journal of Electronic Materials, 2022: p. 1-15.

27. Dodson, B.W., *Dislocation filtering: why it works, when it doesn't.* Journal of electronic materials, 1990. **19**(6): p. 503-508.
28. Gourley, P.L., T.J. Drummond, and B.L. Doyle, *Dislocation filtering in semiconductor superlattices with lattice-matched and lattice-mismatched layer materials.* Applied physics letters, 1986. **49**(17): p. 1101-1103.
29. Ward, T., et al., *Design rules for dislocation filters.* Journal of Applied Physics, 2014. **116**(6): p. 063508.
30. Chen, S., et al., *Electrically pumped continuous-wave III–V quantum dot lasers on silicon.* Nature Photonics, 2016. **10**(5): p. 307.
31. Pan, W., et al., *Strained CdZnTe/CdTe superlattices as threading dislocation filters in lattice mismatched MBE growth of CdTe on GaSb.* Journal of Electronic Materials, 2020. **49**(11): p. 6983-6989.
32. Faurie, J.-P., *Molecular beam epitaxy of Hg1−xCdxTe: growth and characterization.* Progress in crystal growth and characterization of materials, 1994. **29**(1-4): p. 85-159.
33. Iso, K., et al., *Vapor Phase Epitaxy of (133) and (211) CdTe on (211) Si Substrates Using Metallic Cd Source.* Journal of Electronic Materials, 2019. **48**(1): p. 454-459.
34. Pan, W., et al., *Non-invasive and non-destructive characterization of MBE-grown CdZnTe/CdTe superlattice-based dislocation filtering layers.* Journal of Applied Physics, 2022. **131**(20): p. 205304.
35. Wang, C.Z., et al., *Understanding ion-milling damage in Hg1-xCdxTe epilayers.* Journal of Vacuum Science & Technology A, 2006. **24**(4): p. 995-1000.
36. Moram, M.A. and M.E. Vickers, *X-ray diffraction of III-nitrides.* Reports on progress in physics, 2009. **72**(3): p. 036502.
37. Chen, Y., et al., *Dislocation reduction in CdTe/Si by molecular beam epitaxy through in-situ annealing.* Journal of Crystal Growth, 2008. **310**(24): p. 5303-5307.
38. Bakali, E., Y. Selamet, and E. Tarhan, *Effect of Annealing on the density of defects in epitaxial CdTe (211)/GaAs.* Journal of Electronic Materials, 2018. **47**: p. 4780-4792.
39. Badano, G., et al., *Reduction of the dislocation density in molecular beam epitaxial CdTe (2 1 1) B on Ge (2 1 1).* Journal of crystal growth, 2010. **312**(10): p. 1721-1725.
40. Zou, J., D. Cockayne, and B. Usher, *Misfit dislocations and critical thickness in InGaAs/GaAs heterostructure systems.* Journal of applied physics, 1993. **73**(2): p. 619-626.
41. Peach, M. and J. Koehler, *The forces exerted on dislocations and the stress fields produced by them.* Physical Review, 1950. **80**(3): p. 436.
42. Selvidge, J., et al., *Defect filtering for thermal expansion induced dislocations in III–V lasers on silicon.* Applied Physics Letters, 2020. **117**(12): p. 122101.

Defect-Influenced Modeling of Photophysics in Lead-Based Hybrid and All-Inorganic Perovskites



Irina Gushchina and Masaru Kuno

1 Introduction

This chapter presents a discussion on the optoelectronic characteristics of lead halide perovskites, which show great promise as materials for solar photovoltaic applications. Hybrid/all-inorganic perovskites exhibit an ABX_3 stoichiometry, where A represents an organic or inorganic monovalent cation such as methylammonium ($CH_3NH_3^+$, MA), formamidinium ($CH(NH_2)_2^+$, FA), or Cs^+, B denotes Pb^{2+}, and X stands for I^-, Br^-, or Cl^-. Examples of such materials include the families of $MAPbX_3$, $FAPbX_3$, and $CsPbX_3$, with the possibility of creating mixed-cation, mixed-anion, or mixed-cation/mixed-anion alloys.

$APbX_3$ perovskites have gained significant attention in recent years due to their exceptional optical response and their demonstrated utility in high-efficiency photovoltaics. Power conversion efficiencies (PCEs) now reach a maximum of 26.1%, greatly surpassing their initial value of 3.8% in 2009. As such, these materials are now comparable to crystalline silicon in terms of PCE.

While perovskite properties such as solution processability, crystallinity despite low-temperature processing, and large absorption efficiencies contribute to their promising use in solar cells, performance bottlenecks still exist. Among them is the need to better understand the impact of defects on perovskite optoelectronic response as this is essential to fully realizing their photovoltaic potential.

I. Gushchina (✉)
Department of Chemistry and Biochemistry, University of Notre Dame, Notre Dame, IN, USA
e-mail: igushchi@nd.edu

M. Kuno
Department of Chemistry and Biochemistry, University of Notre Dame, Notre Dame, IN, USA

Department of Physics and Astronomy, University of Notre Dame, Notre Dame, IN, USA

© The Author(s), under exclusive license to Springer Nature Switzerland AG 2024

S. Krishnamoorthy, K. (Kris) Iniewski (eds.), *Advances in Fabrication and Investigation of Nanomaterials for Industrial Applications*,
https://doi.org/10.1007/978-3-031-42700-8_11

2 Absorption

Lead halide perovskites possess highly favorable absorption properties with significant absorption coefficients (α), tunable absorption edges in mixed-halide alloys, and band edges that are close to the desired Shockley-Queisser value of 1.55 eV. Figure 1a displays reported absorption spectra for common $APbX_3$ systems that illustrate perovskite band gap (E_g) sensitivities to choice of halide anion. Optical transitions are primarily established by the perovskite's inorganic $[PbI_6]^{4-}$ framework, with A-site cations playing a minor role. Choice of cation stoichiometry does, however, alter band gaps [1, 2].

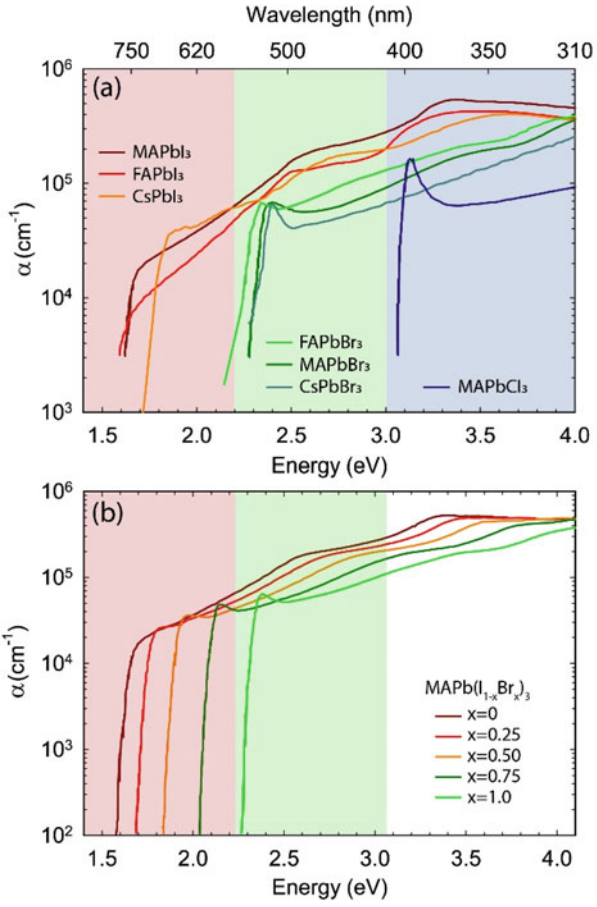


Fig. 1 Summary of the linear absorption spectra of various $APbX_3$ perovskites. (Data extracted from Refs. [8–11]. Spectral band edges highlighted using colored regions)

Figure 1b demonstrates how increasing the Br fraction (x) in a $MAPb(I_{1-x}Br_x)_3$ alloy shifts its E_g toward that of $MAPbBr_3$. Similar trends are observed in $MAPb(Cl_{1-x}Br_x)_3$ [3] and $FAPb(I_{1-x}Br_x)_3$ [30]. Continuous $MAPb(I_{1-x}Cl_x)_3$ alloys cannot be formed due to a large difference in I^- and Cl^- ionic radii. Consequently, such systems are denoted $MAPbI_3(Cl)$ in what follows [4]. Fig. 1b thus illustrates how mixed-halide alloys with composition-dependent band gaps have potential uses in tandem solar cells.

Figure 1 summarizes the absorption coefficients of $APbX_3$ perovskites. Evident is that perovskite α-values are comparable to those of other photovoltaic-relevant semiconductors such as GaAs. References [5–7, 11] provide visual comparisons of perovskite absorption coefficients to those of other semiconductors.

The optical properties of various $APbX_3$ perovskites, including $MAPbI_3$, $FAPbI_3$, and $CsPbI_3$, exhibit significant variability in their reported E_g-values, binding energies, and α. E_g spreads are approximately 150 meV, accompanied by wide variations in α, as demonstrated in prior literature [11, 12]. These discrepancies can be attributed to differences in sample quality, arising from preparation methods that lead to varying degrees of crystallinity, thicknesses, grain sizes, and surface roughness. $APbX_3$ single crystals are generally of higher quality than thin films, display larger grains, and exhibit reduced morphological disorder. However, they still exhibit measurement variations due to differences in sample preparation. Moreover, their surface roughness can cause significant light scattering, leading to an underestimation of band gaps.

Figure 1 shows that $MAPbI_3$, $FAPbI_3$, and $CsPbI_3$ exhibit no excitonic features, while Br- and Cl-based $APbX_3$ materials do. Observations of excitonic behavior or lack of are corroborated by estimated exciton binding energies. Perovskite valence to conduction band transitions occur at the R symmetry point and involve antibonding combinations of halide p and Pb (6s) orbitals. Corresponding conduction bands mainly originate from Pb (6p) orbitals.

Of note is that perovskite band gaps increase with increasing temperature. This is unlike traditional, tetrahedrally coordinated semiconductors.

3 Carrier Dynamics

We now illustrate carrier recombination processes in $APbX_3$ materials following photoexcitation. These processes play a crucial role in understanding the operation and efficiency of perovskite devices. We develop a kinetic model that incorporates experimental observations of emission and absorption dynamics [13, 43]. The resulting model encompasses both numerical simulations and analytical approximations to yield predictive trends in emission intensities and decays. Notably, while the model does not consider device operation, readers may find Ref. [53] useful where the model has been extended to include charge extracting interfaces.

The primary recombination processes considered are radiative electron-hole recombination, carrier trapping, and non-radiative Auger recombination (Fig. 2). We

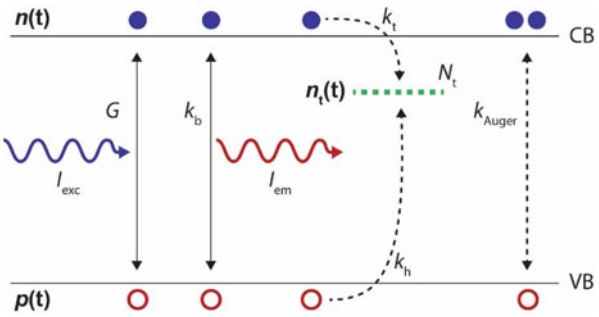


Fig. 2 Schematic illustration of photophysical processes occurring in lead halide perovskites, following photoexcitation [53]

assume that trap states in $APbX_3$ primarily function as electron traps. Other versions of the model are available that account for exciton dissociation, unintentional doping, and carrier diffusion [22, 26].

Corresponding kinetic expressions are:

$$\frac{dn}{dt} = G - k_t\,(N_t - n_t)\,n - k_b np - \frac{1}{2}k_{\text{Auger}}\left[n^2 p + np^2\right]$$

$$\frac{dp}{dt} = G - k_h n_t\,p - k_b np - \frac{1}{2}k_{\text{Auger}}\left[n^2 p + np^2\right]$$

$$\frac{dn_t}{dt} = k_t\,(N_t - n_t)\,n - k_h n_t\,p, \tag{1}$$

where G is the initial charge generation rate ($\text{cm}^{-3}\ \text{s}^{-1}$), linked to excitation intensity (I_{exc}, W cm^{-2}) [i.e., $G = \frac{I_{\text{exc}}\alpha}{h\nu}$ with α the absorption coefficient (cm^{-1}) and $h\nu$ the photon energy (J)], n (p) is the electron (hole) concentration (cm^{-3}) in the perovskite conduction (valence) band, k_t is an electron trapping rate constant ($\text{cm}^3\ \text{s}^{-1}$), N_t is a corresponding trap density (cm^{-3}), n_t is the trap population (cm^{-3}), k_b is a bimolecular radiative recombination rate constant ($\text{cm}^3\ \text{s}^{-1}$, referred to as k_2 in the literature), and k_{Auger} is an Auger, three-carrier rate constant ($\text{cm}^6\ \text{s}^{-1}$, referred to as k_3 in the literature).

Equation 1 and Fig. 2 have been the subject of numerous studies, with a multitude of estimates provided for the various rate constants. Table 1 provides a compilation of these literature estimates across various $APbX_3$ systems. Examining the table reveals that most research efforts have concentrated on $MAPbI_3$ and $MAPbI_3(Cl)$ thin films with fewer investigations carried out on corresponding FA-based materials.

Table 1 Literature rate constants for various lead halide perovskites

	$MAPbI_3$	$MAPbI_3(Cl)$	$MAPbBr_3$	$FAPbI_3$	$FAPb(I_{1-x}Br_x)_3$	$FAPbBr_3$	FAMACs
$k_1 \approx k_t N_t$ ($\times 10^7$ s^{-1})	0.091 (TOPO) [41] 0.66 [41] 0.72–1.3 [14] 1.4–1.5 [15] 1.5 [16, 17] 1.8 [31]	0.49 [15] 1.2 [16] 2.0 [18]	–	7×10^6 [16]	–	2.1×10^7 [16]	4×10^6 [19]
N_t ($\times 10^{16}$ cm^{-3})	10^{-4}–10^{-3} (emissive) [20] 0.90–86 [43] 5.0–16 [21] 6.0 [22]	<0.05 [22] <0.1–4.0 [23] 1.0 [24] 2.5 [32]	–	–	–	–	0.54–60 [53]
k_b ($\times 10^{-10}$ cm^3 s^{-1})	0.1–1.0 [17] 0.35 [41] 0.4 (TOPO) [41] 0.60 [16] 1.5 [29] 1.7 [31] 3.5 [22] 6.0 [25] 6.2–37 [14] 9.2–9.4 [15] 13 [26] 23 [27]	0.23–0.78 [23] 0.87 [15] 1.1 [16, 18] 4.9 [22] 11 [28]	4.9 [29]	1.1 [16]	1.0–30 [30] ($x = 0$–1)	11 [16]	0.30 [19]
k_{Auger} ($\times 10^{-28}$ cm^6 s^{-1})	0.37–1.3 [15] ~1 [17] 1.6 [16] 3.4 [29] ~10 [25]	0.20 [16] 0.23 [18] 0.99 [15] 3.8 [28]	13.5 [29]	0.20 [16]	0.20–1.5 [30] ($x = 0$–1)	1.5 [16]	0.01 [19]

Table 1 makes evident that consistent rate constants exist across different materials. Bimolecular radiative rate constants hover about 10^{-10} cm^3 s^{-1}. Auger rate constants take order of magnitude values of 10^{-28} cm^6 s^{-1}. Electron trapping rate constants are in the range of $k_1 \sim 10^7$ s^{-1}, where $k_1 \approx k_t N_t$. This yields $k_t \sim 10^{-10}$ cm^3 s^{-1} for estimated trap densities of $N_t \sim 10^{-16}$ cm^{-3}.

In what follows, photogenerated carrier dynamics, as predicted by Eq. 1, are presented for continuous wave excitation. An analysis assuming pulsed excitation can be found in Refs. [34 and 35].

4 Low Excitation Intensities

At low excitation intensities, carrier trapping dominates radiative recombination. Low photogenerated carrier densities further mean that non-radiative Auger pathways can be ignored. Consequently, under the assumption that the material is intrinsic, Eq. 1 reduces to

$$\frac{dn}{dt} \approx G - k_t N_t n$$

$$\frac{dp}{dt} \approx G - k_h p^2.$$

These equations make apparent that at steady state $n = \frac{G}{k_t N_t} \propto G$ and $p = \sqrt{\frac{G}{k_h}} \propto \sqrt{G}$. Since the emission rate and corresponding intensity, I_{em}, are proportional to the product of n and p, I_{em} grows with increasing I_{exc} (G) in a power law fashion. Its growth exponent is ~3/2, i.e., $I_{em} \propto G^{\frac{3}{2}}$. A power law plot therefore yields a slope, $m = 3/2$.

Figure 3a shows that I_{em} grows as $G^{1.6}$ for low G and $N_t = 10^{16}$ cm^{-3}. Assumed parameters are $k_b = 10^{-10}$ cm^3 s^{-1}, $k_t = 10^{-9}$ cm^3 s^{-1}, $k_h = 10^{-11}$ cm^3 s^{-1}, and $k_{Auger} = 10^{-28}$ cm^6 s^{-1}. Figure 3b confirms identical I_{em} power law growth as G^m for $N_t = 10^{15}$–10^{18} cm^{-3}, with $m = 1.5$–1.6. Experimental data in Fig. 3c for $MAPbI_3$ single crystals and thin films also show $m \sim 1.5$, with slight variations due to underlying N_t-values. $m \sim 1.5$ power law growth is also observed for $MAPbI_3$ and $MAPbI_3$(Cl) at low $G^{1.3}$. Note that under pulsed excitation I_{em} power growth as G^2 is predicted [35].

Next, by assuming above-simplified kinetic expressions for n and p, corresponding (normalized) photoluminescence decays take the form

$$\mathrm{PL}(t) = \frac{I_{em}(t)}{I_{em,max}} \approx \frac{e^{-k_t N_t t}}{1 + k_h G t}. \tag{2}$$

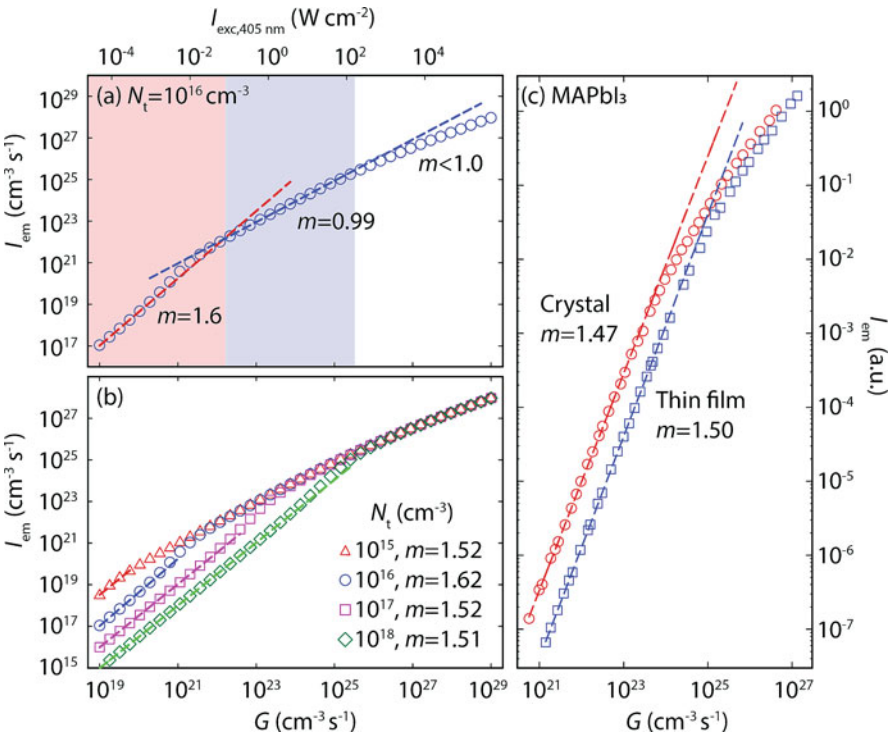


Fig. 3 (**a**) I_{em} versus G for $N_t = 10^{16}$ cm^{-3}. Dashed lines are linear fits to the data in a given growth regime (shaded regions). Fit-extracted growth exponents shown. G-values are linked to associated I_{exc}, assuming 405 nm excitation with $a = 10^5$ cm^{-1}. (**b**) I_{em} versus G for N_t varying between $N_t = 10^{15}$–10^{18} cm^{-3}. Dashed lines are linear fits in the trap-mediated recombination regime. Fit-extracted growth exponents shown. (**c**) I_{em} versus G data for a $MAPbI_3$ single crystal and thin film. [Data from Ref. [43]. Dashed lines are fits to the data at smaller G with fit-extracted growth exponents shown]

Equation 2 is characterized by a numerator that predominates at small G or at short times and which yields near-exponential decays when $k_t N_t \sim 10^7$ s^{-1} (as indicated in Table 1). Figure 4a corroborates this behavior by plotting a model-predicted decay for $G = 10^{15}$ cm^{-3} s^{-1}. Supporting this are additional studies conducted on different perovskite systems, which report near-exponential photoluminescence decays at low I_{exc} [15, 31].

5 Intermediate Excitation Intensities

As I_{exc} increases, progressive filling of traps ($n_t \rightarrow N_t$) reduces electron trapping rates. This means that $n \rightarrow p$. Equation 1 can therefore be simplified to yield the

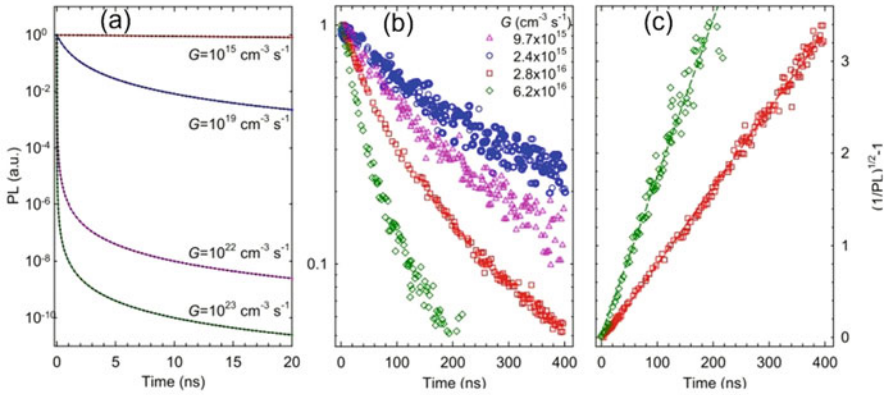


Fig. 4 (**a**) Predicted PL decays from Eq. 1 for variable G between $G = 10^{15}$–10^{23} cm^{-3} s^{-1}. Superimposed over the data are analytical predictions from Eqs. 2–4 (dashed lines). (**b**) $MAPbI_3$ PL decays from Reference [31]. (**c**) Large G $MAPbI_3$ PL decays from Ref. [31] replotted. Dashed lines are linear fits to the data

following effective rate expressions:

$$\frac{dn}{dt} \approx G - k_b n^2$$

$$\frac{dp}{dt} \approx G - k_h N_t p - k_b p^2.$$

Invoking steady-state conditions then means that $n = \sqrt{\frac{G}{k_b}} \propto \sqrt{G}$ with $p = \frac{-k_t N_t + \sqrt{(k_t N_t)^2 + 4G}}{2} \propto \sqrt{G}$.

Figure 3a shows that a transition of I_{em} occurs toward power law growth with $m \sim 1$. A fit-extracted m-value is $m = 0.99$. Figure 3b confirms this pattern for different N_t-values. Moreover, as N_t increases, the region of trap-mediated recombination ($m \sim 1.5$) extends to higher G-values before bimolecular recombination ($m \sim 1.0$) dominates (Fig. 3c). For decays, application of above-simplified rate expressions yields the following bimolecular photoluminescence decay:

$$\mathrm{PL}(t) = \frac{I_{em}(t)}{I_{em,max}} = \frac{1}{(1 + k_b G t)\left[1 + (k_t N_t + k_b G t)\right]}. \tag{3}$$

Figure 4a shows model-predicted decays at high I_{exc} for $G = 10^{19}$–10^{22} cm^{-3} s^{-1}, where there is excellent agreement with Eq. 3. Figure 4b demonstrates the transition in PL(t) from near-exponential to near-bimolecular

for $G = 10^{15}$–10^{16} cm^{-3} s^{-1} for a $MAPbI_3$ thin film. Similar transitions have been reported in the literature [22, 31, 32, 33].

6 High Excitation Intensities

At high excitation intensities, trap saturation leads to a dominance of bimolecular (radiative) recombination. In this limit, Eq. 1 effectively simplifies to

$$\frac{dn}{dt} \approx G - k_b n^2$$

$$\frac{dp}{dt} \approx G - k_b p^2.$$

As a result, $n = p = \sqrt{\frac{G}{k_b}} \propto \sqrt{G}$. This causes I_{em} to grow in a power law fashion with a growth exponent of $m \sim 1$. Figure 3a illustrates this for $N_t = 10^{16}$ cm^{-3}. It is worth noting that a growth exponent of $m \sim 1$ is also predicted for pulsed excitation in this intensity regime [34, 35, 36].

An associated (normalized) photoluminescence decay takes the bimolecular form

$$\text{PL}(t) = \frac{I_{\text{em}}(t)}{I_{\text{em,max}}} \approx \frac{1}{(1 + k_b G t)^2}. \tag{4}$$

Figure 4a shows $\text{PL}(\tau)$ for $G = 10^{23}$ and reveals quantitative agreement with Eq. 4. Equation 4 further suggests that $k_b G t + 1 = \sqrt{\frac{I_{\text{em,max}}}{I_{\text{em}}(t)}}$ from where plotting $\sqrt{\frac{I_{\text{em,max}}}{I_{\text{em}}(t)}} - 1$ versus time yields linear behavior. Figure 4c confirms this for the experimental data in Fig. 4b.

At excitation regimes above a certain threshold, emission efficiencies decrease due to the onset of Auger-mediated non-radiative recombination. Figure 3a shows that the onset of Auger non-radiative recombination causes I_{em} to grow sublinearly with $m < 1$. In this regime, linear behavior is observed when plotting $\left[\frac{I_{\text{em,max}}}{I_{\text{em}}(t)} - 1\right]$ versus time [37].

7 Emission Quantum Yields

Equation 1 allows internal emission quantum yields (QYs) to be estimated through the ratio of the bimolecular, radiative recombination rate to the initial carrier generation rate, i.e.,

$$\mathrm{QY} = \frac{k_b np}{G}. \tag{5}$$

In $APbX_3$ photovoltaics, achieving high emission efficiencies is crucial for their optimal performance. The external emission quantum efficiency (EQE) is defined as the product of the internal quantum yield and the photon extraction efficiency ($\mathrm{EQE} = \eta_e \mathrm{QY}$ where η_e is a photon extraction efficiency). EQE is directly linked to a solar cell's maximum achievable open-circuit voltage and PCE [38]. Good solar cells must therefore be good emitters [39]. Figure 5 now shows model-predicted internal QYs and EQEs as functions of N_t, ranging from 10^{15} cm^{-3} to 10^{18} cm^{-3}, using the following rate constants $k_b \sim 10^{-10}$ cm^3 s^{-1}, $k_t \sim 10^{-9}$ cm^3 s^{-1}, and $k_h \sim 10^{-11}$ cm^3 s^{-1}. Predicted EQEs are calculated using $\mathrm{EQE} = \frac{\eta_e (k_b np)}{G}$.

At low excitation intensity, carrier trapping dominates and leads to low EQE-values, as observed in Table 2 and Fig. 5. Experimental 1 sun EQE-values for perovskite thin films are typically a few percent, with some exceptions. This stands in contrast to perovskite nanocrystals, which exhibit near-unity or unity EQEs.

Figure 5 illustrates that when carrier trapping is present, high excitation intensities are needed to achieve maximal QY or EQE-values. For $N_t = 10^{16}$ cm^{-3}, near-unity QYs are predicted at approximately 1 sun. Increasing N_t means larger

Table 2 Literature $APbX_3$ EQEs under effective 1 sun conditions

Material	EQE film (%)	EQE film treated (%)	EQE device (%)
$MAPbI_3$	0.92 [40] 3 [41] 5 [42] 5.8 [43] 10 [44]	12–13 (TOPO) [45] 20.3 (TOPO) [40] 35 (TOPO) [41]	5 [45]
$MAPbI_3$(Cl)	20 [42] 50–60 [46]	24–25 (pyr) [47]	–
$MAPbBr_3$	2–3 [48] 15 [42]	1.2 [49] 2 (TPPO) [50] 85 (SPPO) [50]	–
FAMACs	2.4 [51] 66 (K) [52]	3.6 (Rb) [51]	0.43–2.83 [53] 14.5 (K) [52]
$FAMAPb(I_{1-x}Br_x)_3$			0.1–3.0 [54]

Additives shown in parenthesis (*K* potassium, *Rb* rubidium, *TOPO* trioctylphosphine oxide, *pyr* pyridine, *TPPO* triphenylphosphine oxide, *SPPO* 9,9-spirobifluoren-2-yl-diphenyl-phosphine oxide)

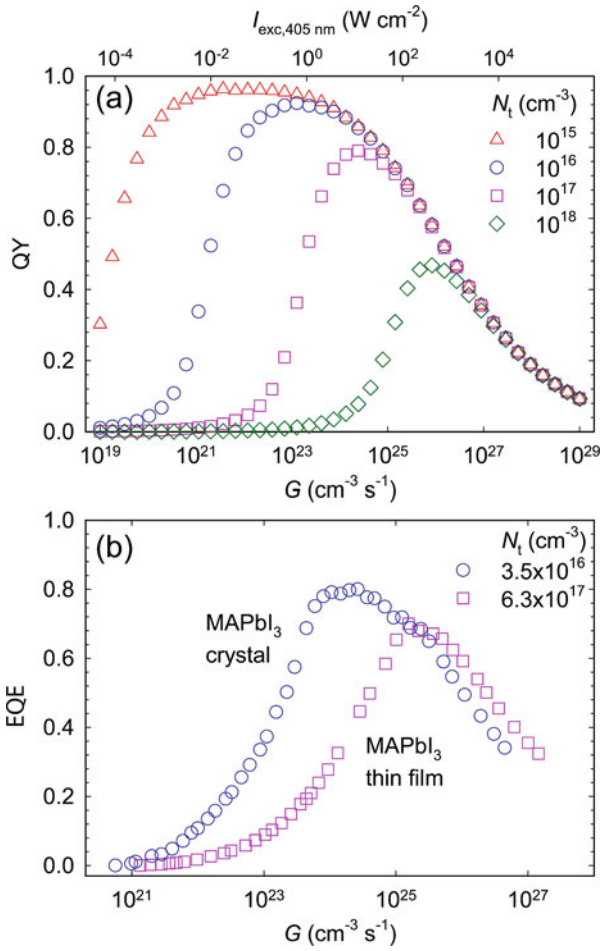


Fig. 5 (**a**) Predicted (internal) QYs for variable G between $G = 10^{19}$–10^{29} cm^{-3} s^{-1} and N_t between 10^{15} and 10^{18} cm^{-3}. G-values are linked to associated I_{exc} assuming 405 nm excitation with $\alpha = 10^5$ cm^{-1}. (**b**) Experimental EQE estimates for a $MAPbI_3$ single crystal and thin film. [Data from Ref. [43]. Fit extracted N_t-values shown]

I_{exc} are required to maximize QY/EQE. Beyond a critical I_{exc}, the onset of Auger-mediated carrier recombination causes all QYs/EQE-values to decrease.

This QY/EQE behavior has previously been modeled by reducing Eq. 1 to [55]

$$\frac{dN}{dt} = G - AN - BN^2 - CN^3. \tag{6}$$

In Eq. 6, N is an effective electron-hole density, A is a generic first-order rate constant that describes non-radiative, trap-mediated recombination of photogener-

ated carriers, B is a second-order (radiative) rate constant, and C is a third-order rate constant that accounts for non-radiative Auger recombination. The rate constants A, B, and C are effectively k_1, k_b, and k_{Auger} in Table 1. A corresponding internal QY is then

$$QY = \frac{BN^2}{AN + BN^2 + CN^3}. \tag{7}$$

Equation 7 can be recast in terms of EQE via $EQE = \frac{\eta_e BN^2}{AN+\eta_e BN^2+CN^3}$. For either QY or EQE, peak values are found by taking their derivative with respect to N to find a critical point (i.e., $\frac{dQY}{dN} = \frac{dEQE}{dN} = 0$) [55]. A resulting optimal carrier density (N_{opt}) is then

$$N_{opt} = \sqrt{\frac{A}{C}} \sim \sqrt{\frac{k_1}{k_{Auger}}} \tag{8}$$

and is linked to a corresponding maximum internal QY of

$$QY_{max} = \frac{1}{1 + \frac{2\sqrt{AC}}{B}} \sim \frac{1}{1 + \frac{2\sqrt{k_1 k_3}}{k_2}} \tag{9}$$

with a corresponding maximum EQE of $EQE_{max} = \frac{1}{1+\frac{2\sqrt{AC}}{\eta_e B}} \sim \frac{1}{1+\frac{2\sqrt{k_1 k_3}}{\eta_e k_2}}$.

In addition to trap-mediated recombination, photon trapping within the perovskite also contributes to small external QYs compared to internal QYs. This is due to refractive index mismatches with the surrounding medium, which become prominent in perovskite crystals and films. Under these circumstances, associated photon extraction efficiencies (η_e) are approximately 10%. Perovskite nanocrystals, in contrast, behave as dipole emitters. This rationalizes why they often exhibit unity/near-unity EQEs.

8 Conclusions

$APbX_3$ perovskites exhibit desirable optoelectronic properties advantageous for their implementation in applications such as solar cells. Figure 1 displays their tunable absorption that is dependent on cation or anion compositions. Despite reported defect tolerances [56], Table 1 indicates that perovskites possess carrier traps that lead to undesired losses in photogenerated carrier density. Through appropriate kinetic modeling, Eq. 1 and Figs. 3–4 demonstrate that $APbX_3$ behavior

under illumination can be established. This facilitates a deeper understanding of the impact carrier traps have on perovskite photoresponse, including emission quantum yields and external quantum efficiencies.

A comprehensive assessment of other defect-related $APbX_3$ instabilities is warranted for their possible application. Notably, intrinsic instabilities in $APbX_3$ optoelectronic response stem from ion migration. It is observed that both cations and anions migrate/segregate in $APbX_3$ materials under bias or illumination. Mixed-halide perovskite anion photosegregation, in particular, remains an area of active research. References [57, 58, 59] provide readers critical reviews of this crucial and ongoing topic. Beyond this, the relationship between perovskite ion instabilities and their impact on aforementioned optoelectronic response remain underexplored. Consequently, the connection should be established in future investigations to ensure the successful commercialization of this unique materials system.

Acknowledgments I.G. and M.K. thank the Division of Materials Sciences and Engineering, Office of Basic Energy Sciences, US Department of Energy (DOE) under Award DE-SC0014334 for financial support of this work.

References

1. Pellet, N., Gao, P., Gregori, G., Yang, T., Nazeeruddin, M., Maier, J., Grätzel, M. Mixed-Organic-Cation Perovskite Photovoltaics for enhanced solar-light harvesting. Angewandte Chemie International Edition. 2014 53, 3151–3157.
2. Ono, L., Juarez-Perez, E., Qi, Y. Progress on perovskite materials and solar cells with mixed cations and halide anions. ACS Applied Materials & Interfaces. 2017 9, 30197–30246.
3. Sadhanala, A., Ahmad, S., Zhao, B., Giesbrecht, N., Pearce, P., Deschler, F., Hoye, R. L. Z., Gödel, K. C., Bein, T., Docampo, P., Dutton, S. E., De Volder, M. F. L., Friend, R. H. Blue-green color tunable solution processable organolead chloride–bromide mixed halide perovskites for optoelectronic applications. Nano Letters. 2015 15, 6095–6101.
4. Colella, S., Mosconi, E., Fedeli, P., Listorti, A., Gazza, F., Orlandi, F., Ferro, P., Besagni, T., Rizzo, A., Calestani, G., Gigli, G., De Angelis, F., Mosca, R., Gigli, G. $MAPbI_{3-x}Cl_x$ mixed halide perovskite for hybrid solar cells: the role of chloride as dopant on the transport and structural properties. Chemistry of Materials. 2013 25, 4613–4618.
5. De Wolf, S., Holovsky, J., Moon, S. J., Löper, P., Niesen, B., Ledinsky, M., Haug, F. J., Yum, J. H., Ballif, C. Organometallic halide perovskites: sharp optical absorption edge and its relation to photovoltaic performance. Journal of Physical Chemistry Letters. 2014 5, 1035–1039.
6. Ziang, X., Shifeng, L., Laixiang, Q., Shuping, P., Wei, W., Yu, Y., Li, Y., Zhijian, C., Shufeng, W., Honglin, D., Minghui, Y., Qin, G. G. Refractive index and extinction coefficient of $CH_3NH_3PbI_3$ studied by spectroscopic ellipsometry. Optical Materials Express. 2015 5, 29–43.
7. Xie, Z., Sun, S., Yan, Y., Zhang, L., Hou, R., Tian, F., Qin, G. G. Refractive index and extinction coefficient of $NH_2CH{=}NH_2PbI_3$ perovskite photovoltaic material. Journal of Physics: Condensed Matter. 2017 29, 245702.
8. Fujiwara, H., Collins, R. W. Organic-inorganic hybrid perovskites, Spectroscopic Ellipsometry for Photovoltaics, 2018, 2, 471–493.
9. Yan, W., Guo, Y., Beri, D., Dottermusch, S., Chen, H., Richards, B. S. Experimental determination of complex optical constants of air-stable inorganic $CsPbI_3$ perovskite thin films. Physica Status Solidi (RRL)–Rapid Research Letters. 2020 14, 2000070.

10. Yan, W., Mao, L., Zhao, P., Mertens, A., Dottermusch, S., Hu, H., Jin, Z., Richards, B. S. Determination of complex optical constants and photovoltaic device design of all-inorganic $CsPbBr_3$ perovskite thin films. Optics Express. 2020 28, 15706–15717.
11. Fujiwara, H., Kato, M., Tamakoshi, M., Miyadera, T., Chikamatsu, M. Optical characteristics and operational principles of hybrid perovskite solar cells. Physica Status Solidi (a). 2018 215, 1700730.
12. Green, M. A., Jiang, Y., Soufiani, A. M., Ho-Baillie, A. Optical properties of photovoltaic organic–inorganic lead halide perovskites. Journal Physical Chemistry Letters. 2015 6, 4774–4785.
13. Saba, M., Cadelano, M., Marongiu, D., Chen, F., Sarritzu, V., Sestu, N., Figus, C., Aresti, M., Piras, R., Lehmann, A. G., Cannas, C. Musinu, A. Quochi, F., Mura, A., Bongiovanni, G. Correlated electron–hole plasma in organometal perovskites. Nature Communications. 2014 5, 5049.
14. D'Innocenzo, V., Srimath Kandada, A. R., De Bastiani, M., Gandini, M., Petrozza, A. Tuning the light emission properties by band gap engineering in hybrid lead halide perovskite. Journal of the American Chemical Society. 2014 136, 17730–17733.
15. Wehrenfennig, C., Eperon, G. E., Johnston, M. B., Snaith, H. J., Herz, L. M. High charge carrier mobilities and lifetimes in organolead trihalide perovskites. Advanced Materials. 2014 26, 1584–1589.
16. Johnston, M. B., Herz, L. M. Hybrid perovskites for photovoltaics: charge-carrier recombination, diffusion, and radiative efficiencies. Accounts of Chemical Research. 2016 49, 146–154.
17. Milot, R. L., Eperon, G. E., Snaith, H. J., Johnston, M. B., Herz, L. M. Temperature-dependent charge-carrier dynamics in $CH_3NH_3PbI_3$ perovskite thin films. Advanced Functional Materials. 2015 25, 6218–6227.
18. Wehrenfennig, C., Liu, M., Snaith, H. J., Johnston, M. B., Herz, L. M. Charge-carrier dynamics in vapour-deposited films of the organolead halide perovskite $CH_3NH_3PbI_{3-x}Cl_x$. Energy & Environmental Science. 2014 7 2269–2275.
19. Wolff, C. M., Bourelle, S. A., Phuong, L. Q., Kurpiers, J, Feldmann, S., Caprioglio, P., Marquez, J. A., Wolansky, J, Unold, T, Stolterfoht, M, Shoaee, S., Deschler, F., Neher, D. Orders of recombination in complete perovskite solar cells-linking time-resolved and steady-state measurements. Advanced Energy Materials. 2021 45, 2101823.
20. Dobrovolsky, A., Merdasa, A., Li, J., Hirselandt, K., Unger, E. L., Scheblykin, I. G. Relating defect luminescence and nonradiative charge recombination in $MAPbI_3$ perovskite films. Journal of Physical Chemistry Letters. 2020 11, 1714–1720.
21. Xing, G., Mathews, N., Lim, S. S., Yantara, N., Liu, X., Sabba, D., Grätzel, M., Mhaisalkar, S., Sum, T. C. Low-temperature solution-processed wavelength-tunable perovskites for lasing. Nature Materials. 2014 13, 476–480.
22. Hutter, E. M., Eperon, G. E., Stranks, S. D., Savenije, T. J. Charge carriers in planar and meso-structured organic–inorganic perovskites: mobilities, lifetimes, and concentrations of trap states. Journal of Physical Chemistry Letters. 2015 6, 3082–3090.
23. de Quilettes, D. W., Vorpahl, S. M., Stranks, S. D., Nagaoka, H., Eperon, G. E., Ziffer, M. E., Snaith, H. J., Ginger, D. S. Impact of microstructure on local carrier lifetime in perovskite solar cells. Science. 2015 348, 683–686.
24. Samiee, M., Konduri, S., Ganapathy, B., Kottokkaran, R., Abbas, H. A., Kitahara, A., Joshi, P., Zhang, L., Noack, M., Dalal, V. Defect density and dielectric constant in perovskite solar cells. Applied Physics Letters. 2014 105, 153502.
25. Guo, Z., Manser, J. S., Wan, Y., Kamat, P. V., Huang, L. Spatial and temporal imaging of long-range charge transport in perovskite thin films by ultrafast microscopy. Nature Communications. 2015 6, 7471.
26. Savenije, T. J., Ponseca, Jr C. S., Kunneman, L., Abdellah, M., Zheng, K., Tian, Y., Zhu, Q., Canton, S. E., Scheblykin, I. G., Pullerits, T., Yartsev, A., Sundström, V. Thermally activated exciton dissociation and recombination control the carrier dynamics in organometal halide perovskite. Journal of Physical Chemistry Letters. 2014 5, 2189–2194.

27. Manser, J. S., Kamat, P. V. Band filling with free charge carriers in organometal halide perovskites. Nature Photonics. 2014 8, 737–743.
28. Trinh, M. T., Wu, X., Niesner, D., Zhu, X. Y. Many-body interactions in photo-excited lead iodide perovskite. Journal of Materials Chemistry A. 2015 3, 9285–9290.
29. Chen, X., Lu, H., Yang, Y., Beard, M. C. Excitonic effects in methylammonium lead halide perovskites. Journal of Physical Chemistry Letters. 2018 9, 2595–2603.
30. Rehman, W., Milot, R. L., Eperon, G. E., Wehrenfennig, C., Boland, J. L., Snaith, H. J., Johnston, M. B., Herz, L. M. Charge-carrier dynamics and mobilities in formamidinium lead mixed-halide perovskites. Advanced Materials. 2015 27, 7938–7944.
31. Yamada, Y., Nakamura, T., Endo, M., Wakamiya, A., Kanemitsu, Y. Photocarrier recombination dynamics in perovskite $CH_3NH_3PbI_3$ for solar cell applications. Journal of the American Chemical Society. 2014 136, 11610–11613.
32. Stranks, S. D., Burlakov, V. M., Leijtens, T., Ball, J. M., Goriely, A., Snaith, H. J. Recombination kinetics in organic-inorganic perovskites: excitons, free charge, and subgap states. Physical Review Applied. 2014 2, 034007.
33. Stranks, S. D. Nonradiative losses in metal halide perovskites. ACS Energy Letters. 2017 2, 1515–1525.
34. Vietmeyer, F., Frantsuzov, P. A., Janko, B., Kuno, M. Carrier recombination dynamics in individual CdSe nanowires. Phys. Rev. B. 2011 83, 115319.
35. Morozov, Y. V., Draguta, S., Zhang, S., Cadranel, A., Wang, Y., Janko, B., Kuno, M. Defect-mediated CdS nanobelt photoluminescence up-conversion. J. Phys. Chem. C. 2017 121, 16607–16616.
36. Saba, M., Cadelano, M., Marongiu, D., Chen, F., Sarritzu, V., Sestu, N., Figus, C., Aresti, M., Piras, R., Lehmann, A. G., Cannas, C. Musinu, A. Quochi, F., Mura, A., Bongiovanni, G. Correlated electron–hole plasma in organometal perovskites. Nature Communications. 2014 5, 5049.
37. Puthussery, J., Lan, A., Kosel, T. H., Kuno, M. Band-filling of solution-synthesized CdS nanowires. ACS Nano. 2008 2, 357–367.
38. Ross, R. T. Some thermodynamics of photochemical systems. The Journal of Chemical Physics. 1967 46, 4590–4593.
39. Miller, O. D., Yablonovitch, E., Kurtz, S. R. Strong internal and external luminescence as solar cells approach the Shockley–Queisser limit. IEEE Journal of Photovoltaics. 2012 2, 303–311.
40. Braly, I. L., de Quilettes, D. W., Pazos-Outón, L. M., Burke, S., Ziffer, M. E., Ginger, D. S., Hillhouse, H. W. Hybrid perovskite films approaching the radiative limit with over 90% photoluminescence quantum efficiency. Nature Photonics. 2018 12, 355–361.
41. DeQuilettes, D. W., Koch, S., Burke, S., Paranji, R. K., Shropshire, A. J., Ziffer, M. E., Ginger, D. S. Photoluminescence lifetimes exceeding 8 μs and quantum yields exceeding 30% in hybrid perovskite thin films by ligand passivation. ACS Energy Letters. 2016 1, 438–444.
42. Richter, J. M., Abdi-Jalebi, M., Sadhanala, A., Tabachnyk, M., Rivett, J. P., Pazos-Outón, L. M., Gödel, K. C., Price, M., Deschler, F., Friend, R. H. Enhancing photoluminescence yields in lead halide perovskites by photon recycling and light out-coupling. Nature Communications. 2016 7, 13941.
43. Draguta, S., Thakur, S., Morozov, Y. V., Wang, Y., Manser, J. S., Kamat, P. V., Kuno M. Spatially non-uniform trap state densities in solution-processed hybrid perovskite thin films. Journal of Physical Chemistry Letters. 2016 7, 715–721.
44. Pazos-Outón, L. M., Szumilo, M., Lamboll, R., Richter, J. M., Crespo-Quesada, M., Abdi-Jalebi, M., Beeson, H. J., Vrućinić, M., Alsari, M., Snaith, H. J., Ehrler, B., Friend, R. H., Deschler, F. Photon recycling in lead iodide perovskite solar cells. Science. 2016 351, 1430–1433.
45. Liu, Z., Krückemeier, L., Krogmeier, B., Klingebiel, B., Márquez, J. A., Levcenko, S., Öz, S., Mathur, S., Rau, U., Unold, T., Kirchartz, T. Open-circuit voltages exceeding 1.26 V in planar methylammonium lead iodide perovskite solar cells. ACS Energy Letters. 2018 4, 110–117.
46. Deschler, F., Price, M., Pathak, S., Klintberg, L. E., Jarausch, D. D., Higler, R., Hüttner, S., Leijtens, T., Stranks, S. D., Snaith, H. J., Atatüre, M., Phillips, R. T., Friend, R. H. High

photoluminescence efficiency and optically pumped lasing in solution-processed mixed halide perovskite semiconductors. Journal of Physical Chemistry Letters. 2014 5, 1421–1426.
47. Noel, N. K., Abate, A., Stranks, S. D., Parrott, E. S., Burlakov, V. M., Goriely, A., Snaith, H. J. Enhanced photoluminescence and solar cell performance via Lewis base passivation of organic–inorganic lead halide perovskites. ACS Nano. 2014 8, 9815–9821.
48. Kojima, K., Ikemura, K., Matsumori, K., Yamada, Y., Kanemitsu, Y., Chichibu, S. F. Internal quantum efficiency of radiation in a bulk $CH_3NH_3PbBr_3$ perovskite crystal quantified by using the omnidirectional photoluminescence spectroscopy. APL Materials. 2019 7, 071116.
49. Droseros, N., Longo, G., Brauer, J., Sessolo, M., Bolink, H., Banerji, N. Origin of the enhanced photoluminescence quantum yield in $MAPbBr_3$ perovskite with reduced crystal size. ACS Energy Letters. 2018 3, 1458–1466.
50. Longo, G., La-Placa, M., Sessolo, M., Bolink, H. J. High photoluminescence quantum yields in organic semiconductor-perovskite composite thin films. Chem Sus Chem. 2017 10, 3788–3793.
51. Saliba, M., Matsui, T., Domanski, K., Seo, J. Y., Ummadisingu, A., Zakeeruddin, S. M., Correa-Baena, J. P., Tress, W. R., Abate, A., Hagfeldt, A., Grätzel, M. Incorporation of rubidium cations into perovskite solar cells improves photovoltaic performance. Science. 2016 354, 206–209.
52. Abdi-Jalebi, M., Andaji-Garmaroudi, Z., Cacovich, S., Stavrakas, C., Philippe, B., Richter, J. M., Alsari, M., Booker, E. P., Hutter, E. M., Pearson, A. J., Lilliu, S., Savenije, T. J., Rensmo, H., Divitini, G., Ducati, C., Friend, R. H., Stranks, S. D. Maximizing and stabilizing luminescence from halide perovskites with potassium passivation. Nature. 2018 555, 497–501.
53. Draguta, S., Christians, J. A., Morozov, Y. V., Mucunzi, A., Manser, J. S., Kamat, P. V., Luther, J. M., Kuno, M. A quantitative and spatially resolved analysis of the performance-bottleneck in high efficiency, planar hybrid perovskite solar cells. Energy & Environmental Science. 2018 11, 960–969.
54. Kramarenko, M., Ferreira, C. G., Martínez-Denegri, G., Sansierra, C., Toudert, J., Martorell, J. Relation between fluorescence quantum yield and open-circuit voltage in complete perovskite solar cells. Solar RRL. 2020 4, 1900554.
55. Johnston, M. B., Herz, L. M. Hybrid perovskites for photovoltaics: charge-carrier recombination, diffusion, and radiative efficiencies. Accounts of Chemical Research. 2016 49, 146–154.
56. Kang, J., Wang, L.-W. High defect tolerance in lead halide perovskite CsPbBr3. *J. Phys. Chem. Lett.* 2017 8, 2, 489–493
57. Brennan, M., Ruth, A., Kamat, P., Kuno, M. Photoinduced anion segregation in mixed halide perovskites. Trends in Chemistry. 2020 2, 282–301
58. Brennan, M. C., Draguta, S., Kamat, P. V., Kuno, M. Light-induced anion phase segregation in mixed halide perovskites. ACS Energy Letters. 2017 3, 204–213.
59. Wang, Y., Quintana, X., Kim, J., Guan, X., Hu, L., Lin, C. H., Jones, B. T., Chen, W., Wen, X., Gao, H., Wu, T. Phase segregation in inorganic mixed-halide perovskites: from phenomena to mechanisms. Photonics Research. 2020 8, A56–71.

Charge Carrier Dynamics of Halide Perovskite Nanocrystals: Application Toward X-Ray/Gamma-Ray Radiation Detection



Zheng Zhang

1 Introduction

The detection of ionizing radiation (e.g., X-ray and γ-ray detection) plays a pivotal role for a wide range of practical applications, including medical imaging, national security, astrophysics and particle physics, national security, and high-tech and consumer electronics [1–3]. Recently, three-dimensional (3D) metal halide perovskites (MHPs, Fig. 1a) with the general chemical formula ABX_3 (where A = methylammonium, formamidinium, or Cs^+; B = Pb^{2+}; X = I^-, Br^-, Cl^-) have shown great promise for radiation detection due to their suitable bandgap energies, high bulk crystal resistivity, superior charge carrier transport properties, and preparation using simple and low-cost solution-processing methods [4–6] (Fig. 2). However, the instability of semiconducting 3D halide perovskites under ambient air, irradiation, and heat exposure is a major concern; therefore, lower-dimensional perovskites (e.g., two-dimensional (2D), one-dimensional (1D), zero-dimensional (0D)), which incorporate larger organic spacers that serve as electrically insulating layers along the vertical direction (Fig. 1b), have been studied as alternatives to 3D perovskites. Among notable high-performance 3D perovskites is $CsPbBr_3$, which shows encouraging gamma photon detection performance with a superior detector energy resolution of 1.4% for 662 keV γ-ray radiation [7]. While materials and device performance-focused studies dominate the field, in-depth understanding of the charge carrier transport dynamics of halide perovskites is still limited [8]. This is at least in part due to the unusual fundamental chemical and physical properties of this new class of materials including the halide ion migration issues. The inherent limitations of the moderate charge carrier mobility of MHPs are not still fully

Z. Zhang (✉)
Department of Chemistry, Tulane University, New Orleans, LA, USA
e-mail: zzhang55@tulane.edu

© The Author(s), under exclusive license to Springer Nature Switzerland AG 2024

S. Krishnamoorthy, K. (Kris) Iniewski (eds.), *Advances in Fabrication and Investigation of Nanomaterials for Industrial Applications*,
https://doi.org/10.1007/978-3-031-42700-8_12

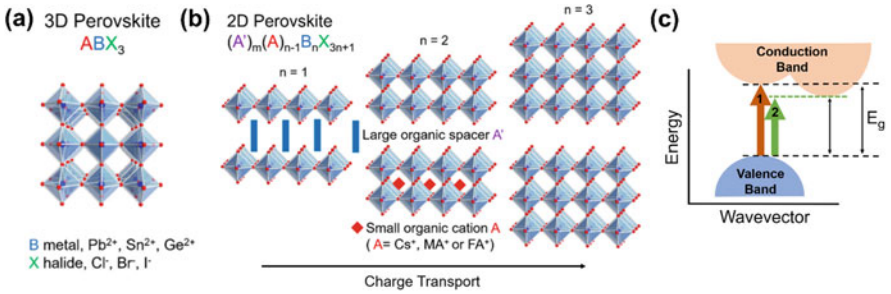


Fig. 1 (**a**) A polyhedral representation of the 3D crystal structure of the parent ABX_3 perovskite. (**b**) Sample 2D perovskite structures containing variable thickness inorganic layers; charge transport in 2D perovskites is expected to be anisotropic with the preferred charge transport direction along the inorganic layers. (Reproduced with permission from Ref. [12], American Chemical Society, Copyright 2019.). (**c**) Illustration of the direct and indirect band to band transitions. (Reproduced with permission from Ref. [6], AIP Publishing, Copyright 2021)

explored and understood. In addition, the reported experimentally measured mobility values, even for the same material composition and stoichiometry, show a vast variation in literature. In this chapter, we aim to summarize the literature-reported carrier mobility values for MHPs and provide an explanation for the origin of the unusually high variation in the reported mobilities. Further, we outline several future research directions to ensure the accurate elucidation of the charge carrier dynamics and reveal the charge carrier mobility of MHPs. Meanwhile, when transitioning from bulk perovskite single crystals (usually millimeter to centimeter sized) to nanocrystals (nanometer sized, referred to as quantum dots), owing to the quantum confinement phenomena, perovskites have demonstrated bright luminescence for scintillation X-ray imaging applications compared to the bulk single-crystal counterparts. In fact, taking $CsPbBr_3$ and $CH_3NH_3PbBr_3$ as examples, bulk perovskite single crystals do not usually exhibit noticeable emissions under the same X-ray excitation conditions [9]. Hence, perovskite quantum dots (QDs) have attracted broad interests as scintillation X-ray sensors, which involve the X-ray photon excitation to light emission mechanism (i.e., the process of charge carriers from generation through the X-ray photon interactions to radiative recombination for light-emitting). This chapter will cover the basics of charge carrier dynamics in both semiconductors and scintillators including halide perovskites, measurement techniques and methods for determining the carrier mobility, and the current limitations in understanding the charge carrier dynamics of MHPs. Readers are further referred to the previous discussion of charge carrier dynamics in perovskite semiconducting single crystals for more details (see Chapter 6 "Charge Carrier Mobility of Metal Halide Perovskites: From Fundamentals to Ionizing Radiation Detection," published in the book *Metal-Halide Perovskite Semiconductors: From Physical Properties to Opto-electronic Devices and X-ray Sensors*).

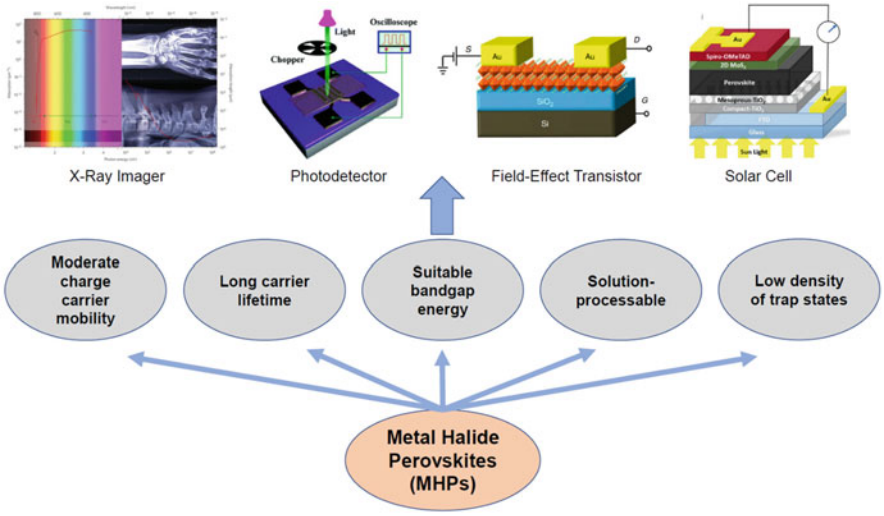


Fig. 2 Metal halide perovskites (MHPs) are an exciting new class of semiconductors with favorable chemical and physical properties that allow their consideration for several optical and electronic applications including ionizing radiation detection. (Reproduced with permission from Ref. [71], Springer Nature, Copyright 2020; [25], Springer Nature, Copyright 2018; [72], Royal Society of Chemistry, Copyright 2017; [73], Springer Nature, Copyright 2015)

2 Basics of Charge Carrier Transport

2.1 Optical Bandgap and Electron-Hole Pair Creation Energy

The charge carrier electron-hole pair creation energy (W) depends on the bandgap energy (E_g) of a semiconductor [10]:

$$W = 2E_g + 1.43 \tag{1}$$

In intrinsic semiconductors, carrier densities are low with most of the charge carrier electrons sitting in the valence band (VB). Through heat/photon excitation (including ionizing radiation such as X-rays, γ-rays), electrons gain sufficient energy and move to the conduction band (CB), and thus, they become free charge carriers. According to the bandgap nature of semiconductors, the VB to CB band-to-band transitions could be either direct or indirect type (Fig. 1c). For indirect bandgap semiconductors, the transition of electrons from VB to CB requires the participation of phonons to conserve the momentum. Therefore, direct bandgap semiconductors are preferred for applications that involve photo-absorption.

2.2 Defects, Doping, and Crystal Structures

For the charge transport dynamics, it could be impacted by the temperature, structural phase transition, carrier concentration, doping levels, and material defects. For instance, measurements on $MAPbBr_3$ single crystals suggest that the measured Hall mobility is highly temperature-dependent across the cubic-to-tetragonal structural phase transition region [11]. The results suggest that acoustic-phonon and space-charge carrier scattering mechanisms dominate at the cubic phase and tetragonal phase regions, respectively. The impurity dopants could serve as either donors or acceptors to enhance the majority or minority carrier concentration and thus influence the charge transport dynamics. For Sn-doped $MA_3Sb_2I_9$, the mobility is twofold raised to 43.05 cm^2/V-s in comparison to 16.68 cm^2/V-s for undoped $MA_3Sb_2I_9$ [52], although the inherent mechanisms seem to have not been fully explored. In addition, material defects play a pivotal role that impacts the charge carrier transport dynamics. Examples include detrimental deep vacancy-type defects could trap the charge carriers and dislocations enhance the scattering probability of charge carriers. As a result, the charge collection efficiency between the semiconductor detector metal contact electrodes is at some extent influenced by either the intrinsic or extrinsic defects. Although benign shallow defects are known to form in 3D halide perovskites such as $MAPbX_3$, given the rich chemistry and crystal structures of MHPs, some members may exhibit more harmful defects, e.g., deep-level electron traps V_{Br} and Bi_{Ag} with formation energies above the thermal energy have been reported for the double perovskite $Cs_2AgBiBr_6$ [75].

2.3 Bulk Single Crystals vs. Nanocrystal Thin Films

For applications targeting semiconducting and scintillation radiation sensing, studies on both bulk single crystals and polycrystalline MHP thin films have been carried out [4, 74]. As the name suggests, single crystal is a continuous undisrupted crystal lattice, whereas polycrystalline films are comprised of many small crystallites (or crystal grains) that can have various orientations and sizes (nanocrystals). Compared to single-crystal perovskites, carrier transport through thin-film samples can be significantly impacted by the grain boundaries, which are the interfaces between neighboring grains. Hence, the mobility for thin films is usually orders of magnitude lower in contrast to single-crystal counterparts. In addition, the compositional and structural uniformity of the thin-film sample, film thickness, surface roughness, grain sizes, and their distribution all could influence the measured mobility to some extent. In terms of the crystal synthesis, single-crystal perovskites can be grown from solutions using methods including inverse temperature crystallization (ITC), temperature lowering, anti-solvent slow diffusion, and slow evaporation. Perovskite thin films are most often fabricated by using the spin coating method, which deposits thin layers (approximately nanometer to micron thicknesses) onto glass substrates using the perovskite precursor solutions.

2.4 Radiative vs. Non-radiative

The charge carrier recombination process could either be radiative or non-radiative. For radiative recombination, charge carrier electrons and holes recombine and emit the energy as photons (i.e., scintillation light emission), which is the detection mechanism for perovskite scintillator X-ray photon counting/imaging detectors. In addition, perovskite light-emitting diodes (LEDs), in which minority and majority carriers recombine at the junction interface, are operated based on this principle. Contrary to radiative recombination, non-radiative process refers to the recombination process that emits phonons (heat) rather than photons. Auger recombination is an example of a non-radiative process, though this process is more favored for high carrier concentration semiconductors. In the Auger recombination, after electrons are excited from valence to conduction band, part of the energy could be transferred to nearby electrons, and then the energy is lost through thermal vibrations (in the form of phonons) due to the unstable energetic state. Alternatively, excited electrons by X-rays or light from valence band in semiconducting perovskites could decay back to valence band and recombine with the holes. Or along the decay route, electrons encounter the intermediate energy levels formed by defects and get trapped and then delocalize; the carrier recombination rate is thus significantly reduced. Nonetheless, although the recombination rate is reduced, such trapping-detrapping process could be beneficial for enhancing the carrier lifetime. In other cases, electrons recombine with holes in the defect sites and emit photons; the rest energy is again lost as phonons.

3 Mobility Characterization Methods

3.1 Contact-Required Methods

The time-of-flight (ToF) method has been widely used to separately determine the mobility of electrons and holes for semiconductors, including leading room-temperature radiation detector material cadmium zinc telluride (CdZnTe) [63], thallium bromide (TlBr) [65], and lead halide perovskites such as cesium lead bromide $CsPbBr_3$ [45]. This technique essentially measures the carrier drift time from a typical ToF pulse trace (see Fig. 3a); then the carrier mobility could be easily calculated using the below equation:

$$\mu = \frac{v}{t} = \frac{L/t}{t} = \frac{L}{t^2} \tag{2}$$

where L is the carrier drift distance, which could be simply taken as the sample thickness. The carrier drift time t is read from the ToF pulse trace as the time interval between 10% and 90% of the pulse amplitude or as double of the time it requires to

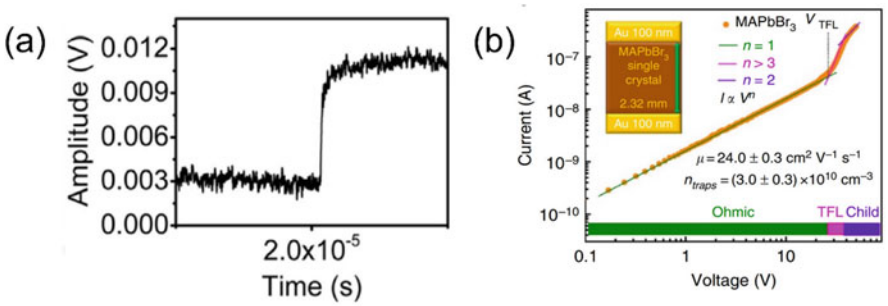


Fig. 3 (**a**) A measured ToF pulse trace using the $TlSn_2I_5$ halide anti-perovskite detector for estimating the mobility. (Reproduced with permission from [15], American Chemical Society, Copyright 2017.) (**b**) SCLC curve for a solution-grown $MAPbBr_3$ perovskite single crystal with Ohmic, TFL, and Child transition regimes identified to extract the density of trap states and carrier mobility. (Reproduced with permission from Ref. [16], Nature Publishing Group, Copyright 2015)

reach half of the maximum pulse amplitude. Readers are further directed to read the ToF mobility studies of CdZnTe single crystals [63, 64].

Since the emergence of metal halide perovskites in 2010s, space-charge-limited-current (SCLC) technique has been the most often used method in literature for characterization of the charge carrier mobilities. This is due to the ease of measurement by using the SCLC technique, although the suitability of this method for mobility measurement of halide perovskites is questionable (see below). The SCLC method is essentially based on the balance between the injected charge carrier concentration from metal contact electrodes and the intrinsic charge carrier concentration of perovskite semiconductors. To use this method for mobility extraction, a perovskite single crystal is sandwiched between two metal contact electrodes, and then voltage bias is applied to the two electrode areas. By varying the applied bias voltage, a SCLC curve (i.e., a current vs. voltage curve, Fig. 3b) that contains three transition regimes (namely, Ohmic, trap-filled-limited (TFL), and Child) could be identified. In the Ohmic regime, the current is linearly proportional to the applied voltage bias. Thus, the bulk crystal resistivity (which is a basic and yet important property to evaluate semiconductor's potential for ionizing radiation detector leakage current reduction) could be determined from this regime. Following the Ohmic regime, all intrinsic defect traps are filled by the injected charge carriers from metal contact electrodes; therefore the second regime is named as TFL region. The onset voltage (i.e., V_{TFL}) of the TFL regime could be used to estimate the density of trap states n_{trap} in halide perovskites using the Eq. (3) [13]

$$n_{trap} = \frac{2\varepsilon\varepsilon_0}{eL^2} V_{TFL} \tag{3}$$

where ε is the dielectric constant, ε_0 is the vacuum permittivity, e is the electronic charge, and L is the sample thickness or the distance between two electrodes. The

carrier mobility could be determined from the third Child region, where the intrinsic charge carrier concentration is dominated over by the injected charge carriers from metal contacts, and thus, the carrier mobility is no longer a function of intrinsic carrier concentration. The mobility μ is evaluated from this regime using the Mott-Gurney law [14]:

$$\mu = \frac{8J_D L^3}{9\varepsilon\varepsilon_0 V^2} \tag{4}$$

where J_D is the current density and V is the applied bias voltage.

Hall effect technique is the gold standard method for mobility measurement of semiconductors, e.g., detailed Hall effect measurements have been performed for beta-gallium oxide (β-Ga_2O_3) [76] and gallium arsenide (GaAs) [77]. The Hall effect evaluates the charge carrier behaviors under a combination of the electrical and magnetic fields. Under the electrical field, charge carriers are being pulled toward one side of the semiconductor solids depending on if the charge is positive/negative. The addition of magnetic field produces a Lorentz force on charge carriers, and thus the moving direction of charge carriers is deflected. Magnitude of the produced Lorentz force on one electron could be described using the below formula [17]:

$$\vec{\mathrm{F}} = -\mathrm{e}\left[\vec{\mathrm{E}} + \vec{\mathrm{v}} \times \vec{\mathrm{B}}\right] \tag{5}$$

where e is the electronic charge, E is the electrical field, v is the velocity of electrons, and B is the magnetic field. A same equation can be written for holes with positive charge. The mobility can be determined from Hall effect using the below Eq. (6):

$$\mu = \frac{R_H}{\rho} \tag{6}$$

where R_H is the Hall coefficient (could be calculated using the electrical field, current density, and magnetic field) and ρ is the semiconductor resistivity (Ω·cm). The Hall effect method has been used for measuring the mobility of halide perovskites such as $MAPbI_3$, $MAPbBr_3$, and tin perovskite $CsSnI_3$ [11, 14, 56].

Fabrication of a field-effect transistor (FET) is another contact-required technique that may be used to determine the mobility; however, this method is more suitable for assessing the mobility of halide perovskites for transistor applications (i.e., the device-oriented mobility). Note that the charge carrier transport behaviors across the electrode-semiconductor interface (either being Ohmic or Schottky type) is another research topic that requires further studies for halide perovskites. The FET technique evaluates the carrier mobility from the saturation regime using the relationship between I_{DS} (drain current) and V_{GS} (gate voltage) through the equation below [25, 26]:

$$I_{DS} = \frac{W}{2L} C_i \mu (V_{GS} - V_{TH})^2 \tag{7}$$

where W refers to the channel width, L is the channel length, C_i is the capacitance of gate electrode, and V_{TH} is the threshold voltage. Carrier mobility extracted by the FET method is related to the surface morphology, temperature, grain size, and the electrode materials [25].

3.2 Contact-Free Techniques

The time-resolved terahertz spectroscopy (TRTS) and time-resolved microwave conductivity (TRMC) are both contactless measurement techniques [18–21] that can be used to determine carrier mobilities of materials. The TRTS technique essentially uses visible excitations to excite the samples and then record the transient photoconductivity. TRTS method requires the sample to be transparent; for this reason, this method is usually used for studying the perovskite thin films. Nonetheless, using the TRTS technique, few successful measurements are made to determine the mobility of perovskite single crystals [18, 19]. As an alternative to TRTS, for the TRMC method, a nanosecond laser pulse is used to photoexcite the sample, and then the transient change in microwave reflectivity that is induced by the charge carriers is monitored [22]. Carrier mobility can be determined from the TRMC method using Eq. (8) (according to the relative change of microwave power) [23, 24]:

$$\frac{\Delta P(t)}{P} = Ae \sum_i \Delta n_i(t) \mu_i = Ae \left(\Delta n_e(t) \mu_e + \Delta n_h(t) \mu_h \right) \tag{8}$$

where μ_e and μ_h are electron and hole mobilities, respectively. Note that the mobility determined above from the TRMC measurement is a sum of electron and hole mobilities, although Eq. (8) has separated the contributions from the two types of charge carriers.

4 Discussion of the Reported Carrier Mobility

Though many studies have been carried out for metal halide perovskites such as $MAPbI_3$, $FAPbI_3$, and $CsPbBr_3$, the literature reported charge carrier mobility for the same perovskite material composition, and structure shows a large variance (see Table 1 for comparison of the reported mobility for single crystals). Therefore, this leads to an intuitive question: what causes this large variance in the reported carrier mobility even if the perovskite composition is the same? In part, some discrepancy is expected to originate from the measurement methods used for determining the

Table 1 Summary of the mobility measured by different methods for metal halide perovskite single crystals. Note the mobility reported here is measured at room temperature, unless otherwise mentioned

Perovskite	Mobility (cm^2/V-s)	Method	References
Three-dimensional (3D) perovskites			
$MAPbI_3$	105 ± 35 (h)	Hall	[14]
	164 ± 25 (h)	SCLC	
	24.0 ± 6.8 (e)	ToF	
	65 ± 6	SCLC	[33]
	60	TRTS	[34]
	620	TRTS	[18]
	35	TRTS	[35]
	130 ± 20 (n-type)	TRMS	[36]
	42 ± 5 (p-type)	FET	[25]
	< 4.7		
$MASnI_3$	2320 (e) 322 (h)	Hall	[37]
	200 (at 250 K)	Hall	[38]
$MAPbBr_3$	35 ± 2 (h)	SCLC	[39]
	24.0	SCLC	[16]
	15 (at 80 K)	FET	[67]
$MAPbCl_3$	42 ± 9	SCLC	[40]
$FAPbI_3$	4.4	SCLC	[41]
	35 ± 7	SCLC	[42]
	40 ± 5	SCLC	[43]
	150 ± 15	SCLC	[33]
$FAPbBr_3$	62 ± 11 (h)	SCLC	[42]
	0.12	SCLC	[44]
$FAPbBr_{2.23}Cl_{0.77}$	12	SCLC	[44]
$FAPb_{0.97}Sn_{0.03}Br_3$	0.22	SCLC	[44]
$MA_{0.45}FA_{0.55}PbI_3$	271 ± 60	SCLC	[33]
$CsPbBr_3$	181 (e) 56.5 (h)	ToF	[45]
	63 (e) 49 (h)	ToF	[46]
	1.78 (h)	ToF	[47]
	9.71–38.5	Hall	[48]
	< 2.3	FET	[69]
	0.32	FET	[70]
$CsPbCl_3$	28 ± 1 (e) 20 ± 1 (h)	ToF	[49]
$FA_{0.9}Cs_{0.05}MA_{0.05}PbI_{2.7}Br_{0.3}$	197 (e)	SCLC	[27]
$KTaO_3$	219 ± 18 (h)	FET	[68]
	0.4		

(continued)

Table 1 (continued)

Perovskite	Mobility (cm^2/V-s)	Method	References
$Cs_2AgBiBr_6$	7.02	SCLC	[50]
	3.17	SCLC	[51]
	5	ToF	[2]
Two-dimensional (2D) perovskites			
$MA_3Sb_2I_9$	16.68	SCLC	[52]
Sn-doped $MA_3Sb_2I_9$	43.05	SCLC	[52]
$Rb_3Sb_2I_9$	0.32 (e)	ToF	[53]
$Cs_3Sb_2I_9$	0.14 (h)	ToF	[53]
$(NH_4)_3Bi_2I_9$	213	SCLC	[54]
$PEA_2MA_2Pb_3I_{10}$	4.4×10^{-2}	SCLC	[55]
$(BA)_2MAPb_2I_7$	0.5 (at 80 K)	FET	[66]
One-dimensional (1D) perovskites			
$(DME)PbBr_4$	> 4.51	SCLC	[56]
Zero-dimensional (0D) perovskites			
$Cs_3Bi_2I_9$	4.3 (e) 1.7 (h)	ToF	[53]
$FA_3Bi_2I_9$	4	Hall	[57]
$MA_3Bi_2I_9$	70	Hall	[58]
	1–6 (h) 2–8 (e)	ToF	
Metal-free perovskites			
$DABCO\text{-}NH_4Br_3$	2.00 (h) 0.67 (e)	SCLC	[59]
	2.08	Hall	

Reproduced with permission from Ref. [6], AIP Publishing, Copyright 2021
h hole and *e* electron

mobility. As having been discussed above, drift mobility differs from the Hall mobility. In addition, this observation could be related to the unusual chemistry and physics of MHPs. Many of these studies used the facile SCLC method to estimate the carrier mobility of halide perovskites [16, 27, 28]. Although the SCLC method is relatively simple and straightforward, it is known that the halogen ionic migration is a critical issue for this class of materials [29, 30], e.g., the ionic migration negatively impacts the fabricated perovskite-based device performance including X-ray detectors and photodetectors. The device efficiency deteriorates under continuous operation due to the charge screening effect. Given the fact that MHPs may demonstrate changing chemistry under measurement conditions due to the movement of halide ions, the suitability of using SCLC method to measure the mobility becomes a question that should be addressed. In fact, this issue has long been observed in other halide-based radiation detector materials, such as thallium bromide (TlBr) [78]. Under external added bias, the halogen ions drift and form an electrical counter-field. Thus, the TFL and Child regimes could have been incorrectly identified if the migration of halogen ions is not considered. To

understand the mechanism that drives the halogen migration, few studies have been carried out [29–31]. Pulsed SCLC is proposed as an alternative to traditional SCLC to reliably measure the carrier mobility [32].

It could be noticed that contact-free methods TRTS and TRMC yield very high mobility values up to 620 cm^2/V-s for $MAPbI_3$. Note that TRTS and TRMC measurements are conducted on a localized small area from the sample in contrast to ToF and SCLC measurements. Thus, the contact-free measurements are less likely to be influenced by the material defects and grain boundaries (for thin-film samples). As a result, the carrier mobility determined by contactless methods could serve as a guidance for the further material optimization. However, contactless methods will probably be less beneficial to reveal the carrier mobility for practical applications as most of these fabricated devices, including ionizing radiation detectors, require to have electrode contacts.

5 Perovskite Nanocrystals for Scintillation X-Ray Detection

Since the wide study on halide perovskites emerged from 2010s, perovskites have resided in applications which are not limited to semiconducting radiation detection. They were first reported in 2015 as the form of perovskite quantum dots (QDs). They have been proven to be extremely sensitive compared to the bulk counterparts for scintillation light-emitting X-ray detection. In fact, not limited to X-ray scintillator counting, perovskite quantum dots may in the meantime find use in light-emitting diodes, lasers, solar cells, and quantum computing applications. A noteworthy work that may be of interest to readers is the study of all-inorganic 3D $CsPbX_3$ ($X = Br^-$, Cl^-) nanocrystals for scintillation imaging by Chen et al. in 2018 [9]. By tuning the halide compositions in $CsPbX_3$ (i.e., relative ratio of Br^- to Cl^- or Br^- to I^- content), a multicolored radioluminescence emission by X-ray excitation was observed (see Fig. 4a). Note that in traditional semiconductors such as cadmium selenium (CdSe), the light emission (such as red and blue light emissions) is tuned by changing the quantum dot's size (i.e., tune the optical bandgap energy). However, changing the perovskite nanocrystal's size tunes the bandgap only at some extent. In Fig. 4b, Chen et al. have fabricated a prototype perovskite quantum dots-based scintillator detector, which comprises of $CsPbBr_3$ nanocrystal thin films as detection media and a photomultiplier tube (PMT) for converting the light photons into measurable electronic signals. The PMT signal will then be typically fed into preamplifier and other associated processing electronics to achieve X-ray photon counting or imaging purposes. For X-ray detection, detection limit and detector sensitivity are the main parameters for evaluating the detector performance. Detection limit refers to the lowest detectable dose rate when the detector is at zero bias, and detector sensitivity reflects how sensitive the scintillator responds to X-ray photon interactions. In Chen et al. work, X-ray imaging by perovskite nanocrystals scintillators was demonstrated by using an insect as imaging sample.

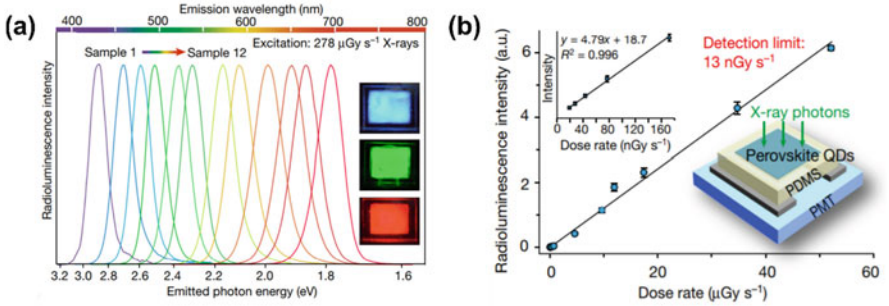


Fig. 4 (**a**) Radioluminescence spectra for samples 1–12 with compositions $CsPbCl_3$, $CsPbCl_2Br$, $CsPbCl_{1.5}Br_{1.5}$, $CsPbClBr_2$, $CsPbCl_{2.5}Br_{0.5}$, $CsPbBr_3$, $CsPbBr_2I$, $CsPbBr_{1.8}I_{1.2}$, $CsPbBr_{1.5}I_{1.5}$, $CsPbBr_{1.2}I_{1.8}$, $CsPbBrI_2$, and $CsPbI_3$ under the same X-ray illumination conditions. (**b**) Radioluminescence intensity vs. X-ray illumination dose rate to extract the detection limit for $CsPbBr_3$ nanocrystal thin films. Inset shows a prototype $CsPbBr_3$ nanocrystal-based scintillator X-ray detector, which consists of ~120 um thick thin films coupled with a photomultiplier tube (PMT) for converting the emitted light photons into measurable signals. (Reproduced with permission from Ref. [9], Nature Publishing Group, Copyright 2018)

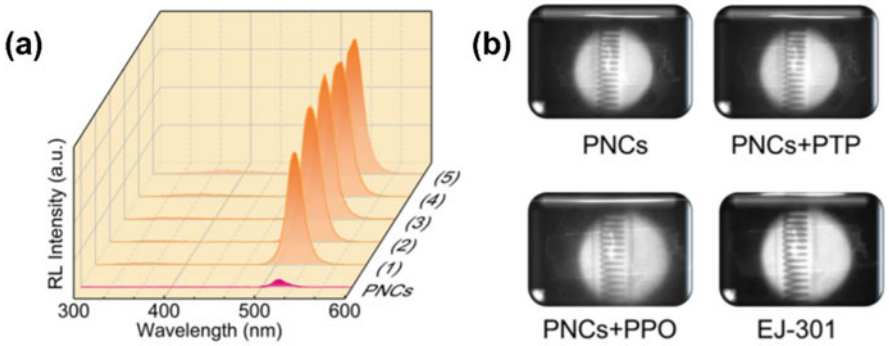


Fig. 5 (**a**) Enhanced radioluminescence intensity of perovskite nanocrystals (PNCs) mixed with organic p-terphenyl (PTP) dyes at five different concentrations (from 1 to 5, 1, 5, 10, 50, 100 mg/L, respectively) compared to PNCs only. (**b**) X-ray images of the sample obtained using PNCs liquid scintillators only and PNCs mixed with different organic dyes, where PPO is 2,5-diphenyloxazole and EJ-301 is the commercial liquid scintillator from Eljen Technology. (Reproduced with permission from Ref. [79], American Chemical Society, Copyright 2023)

In another work published recently by Liu et al. in 2023 [79], $CsPbBr_3$ perovskite nanocrystals mixed with organic dyes as liquid scintillators were used for photon counting and imaging applications. One parameter which can be used for scintillator detector performance comparison is the photon light yield. Bright luminescence of metal halide perovskites is a direct indication of high photoluminescence quantum yield (PLQY). In the study by Liu et al., organic dyes were mixed with perovskite nanocrystals, respectively, as liquid scintillators to investigate the enhancement of radioluminescence intensity (Fig. 5a) and record the light yield (reaching 16,740

photons/MeV when the organic dye PTP was mixed). As a comparison, the commercial liquid scintillator EJ-301 was also studied to record the light yield. Meanwhile, this work recorded the X-ray images obtained by the prepared liquid scintillators (see Fig. 5b), which demonstrated the applicability of using halide perovskite nanocrystals for X-ray scintillation counting and imaging. Readers are referred to the related references for more details if it is of interest.

6 Conclusions and Future Development

This chapter discusses the application and progress of perovskite nanocrystals for scintillation X-ray counting and imaging, from detection principle to the broad tunability of halide compositions for multicolored X-ray scintillation. In the meantime, this chapter summarizes the measured mobilities of metal halide semiconductors from recent reports and discusses the inherent reasons for the large variance of the measured mobility in literature. Even though the pursuit of ideal semiconductor detector materials has been ongoing for over half a century, there is yet no single material that possesses all desirable properties, while offering excellent detector energy resolution and low costs. The recently developed halide perovskites have achieved some success over the past few years yet understanding the carrier transport properties of this novel class of new materials is still at an early stage. The reported carrier mobility values, even for the same perovskite composition and structure, exhibit a notably large variance. In addition, for application of halide perovskites for semiconducting radiation detection, the carrier mobility is relatively low as compared to the traditional detector material CdZnTe, which has electron mobility above 1000 cm^2/V-s but suffers from poor hole transport. Thus, there is an urgent demand to understand the inherent factors that limit the charge transport to ensure the fabrication of high-performance detectors based on this class of materials. Polaron formation (dielectric electron-phonon coupling) has been investigated by computational tools and experimental studies [60, 61], yet the impact of polaron theory on carrier transport remains to be under debate. Polaron formation is relatively fast within femtoseconds in halide perovskites, and large polarons localize the charge carriers and thus reduce the carrier mobility. The polaron theory in part explains the moderate carrier mobility of halide perovskites, yet the measured mobility reported in literatures remains to be lower than the theoretical mobility predicted using the polaron theory [62]. This might indicate that more fundamental limitations (mainly should be from carrier scatterings) should be explored. To fully reveal the carrier scattering mechanisms and charge localization that limit the charge carrier mobility, temperature-dependent measurements may be carried out as the polaron formation and charge carrier behaviors vary with temperature.

To transform the perovskite technology from lab research to commercial applications, the detrimental influence of halide ion migration on mobility measurement should not be overlooked. In fact, as having been discussed by Corre et al. [32], the traditional manner of conducting SCLC measurement with no consideration

of the halogen migration should be revisited. This should at least in part explain the vast disagreement of the reported carrier mobility among literatures. In the meantime, perovskite nanocrystals have shown bright luminescence with high light yield that may have the great potential to rival commercial scintillator technologies. However, a rational and meanwhile conservative viewpoint is commercialization of perovskite nanocrystal technology may require further efforts. For instance, the environmental stability of nanocrystals could be a concern that requires more surface engineering studies [80, 81]. However, it can be envisioned that with its low-cost and facile solution-processing methodology, long carrier lifetime and moderate mobility, and high photon light yield, halide perovskites have demonstrated great possibilities to rival the current market technologies and may be used as next-generation semiconducting and scintillation X-ray, gamma-ray ionizing radiation detector materials.

References

1. Matt, G. J.; Levchuk, I.; Knüttel, J.; Dallmann, J.; Osvet, A.; Sytnyk, M.; Tang, X.; Elia, J.; Hock, R.; Heiss, W.; Brabec, C. J. Sensitive Direct Converting X-Ray Detectors Utilizing Crystalline CsPbBr3 Perovskite Films Fabricated via Scalable Melt Processing. *Adv. Mater. Interfaces* **2020**, *7* (4), 1901575.
2. Zhang, Z.; Cao, D.; Huang, Z.; Danilov, E. O.; Chung, C. C.; Sun, D.; Yang, G. Gamma-Ray Detection Using Bi-Poor Cs2AgBiBr6 Double Perovskite Single Crystals. *Adv. Opt. Mater.* **2021**, *9* (8), 2001575.
3. Weber, M. J. Inorganic Scintillators: Today and Tomorrow. *J. Lumin.* **2002**, *100* (1–4), 35–45.
4. Yakunin, S.; Dirin, D. N.; Shynkarenko, Y.; Morad, V.; Cherniukh, I.; Nazarenko, O.; Kreil, D.; Nauser, T.; Kovalenko, M. V. Detection of Gamma Photons Using Solution-Grown Single Crystals of Hybrid Lead Halide Perovskites. *Nat. Photonics* **2016**, *10* (9), 585–589.
5. López, C. A.; Abia, C.; Alvarez-Galván, M. C.; Hong, B. K.; Martínez-Huerta, M. V.; Serrano-Sánchez, F.; Carrascoso, F.; Castellanos-Gómez, A.; Fernández-DÍaz, M. T.; Alonso, J. A. Crystal Structure Features of CsPbBr3 Perovskite Prepared by Mechanochemical Synthesis. *ACS Omega* **2020**, *5* (11), 5931–5938.
6. Zhang, Z.; Saparov, B. Charge Carrier Mobility of Halide Perovskite Single Crystals for Ionizing Radiation Detection. *Appl. Phys. Lett.* **2021**, *119* (3), 030502.
7. He, Y.; Petryk, M.; Liu, Z.; Chica, D. G.; Hadar, I.; Leak, C.; Ke, W.; Spanopoulos, I.; Lin, W.; Chung, D. Y.; Wessels, B. W.; He, Z.; Kanatzidis, M. G. CsPbBr3 Perovskite Detectors with 1.4% Energy Resolution for High-Energy γ-Rays. *Nat. Photonics* **2021**, *15* (1), 36–42.
8. Herz, L. M. Charge-Carrier Dynamics in Organic-Inorganic Metal Halide Perovskites. *Annu. Rev. Phys. Chem.* **2016**, *67*, 65–89.
9. Chen, Q.; Wu, J.; Ou, X.; Huang, B.; Almutlaq, J.; Zhumekenov, A. A.; Guan, X.; Han, S.; Liang, L.; Yi, Z.; Li, J.; Xie, X.; Wang, Y.; Li, Y.; Fan, D.; Teh, D. B. L.; All, A. H.; Mohammed, O. F.; Bakr, O. M.; Wu, T.; Bettinelli, M.; Yang, H.; Huang, W.; Liu, X. All-Inorganic Perovskite Nanocrystal Scintillators. *Nature* **2018**, *561* (7721), 88–93.
10. Devanathan, R.; Corrales, L. R.; Gao, F.; Weber, W. J. Signal Variance in Gamma-Ray Detectors-A Review. *Nucl. Instruments Methods Phys. Res. Sect. A Accel. Spectrometers, Detect. Assoc. Equip.* **2006**, *565* (2), 637–649.
11. Yi, H. T.; Wu, X.; Zhu, X.; Podzorov, V. Intrinsic Charge Transport across Phase Transitions in Hybrid Organo-Inorganic Perovskites. *Adv. Mater.* **2016**, *28* (30), 6509–6514.

12. Mao, L.; Stoumpos, C. C.; Kanatzidis, M. G. Two-Dimensional Hybrid Halide Perovskites: Principles and Promises. *J. Am. Chem. Soc.* **2019**, *141* (3), 1171–1190.
13. Bube, R. H. Trap Density Determination by Space-Charge-Limited Currents. *J. Appl. Phys.* **1962**, *33* (5), 1733–1737.
14. Dong, Q.; Fang, Y.; Shao, Y.; Mulligan, P.; Qiu, J.; Cao, L.; Huang, J. Electron-Hole Diffusion Lengths > 175 μm in Solution-Grown CH3NH3PbI3 Single Crystals. *Science (80-.).* **2015**, *347* (6225), 967–970.
15. Lin, W.; Stoumpos, C. C.; Liu, Z.; Das, S.; Kontsevoi, O. Y.; He, Y.; Malliakas, C. D.; Chen, H.; Wessels, B. W.; Kanatzidis, M. G. TlSn2I5, a Robust Halide Antiperovskite Semiconductor for γ-Ray Detection at Room Temperature. *ACS Photonics* **2017**, *4* (7), 1805–1813.
16. Saidaminov, M. I.; Abdelhady, A. L.; Murali, B.; Alarousu, E.; Burlakov, V. M.; Peng, W.; Dursun, I.; Wang, L.; He, Y.; MacUlan, G.; Goriely, A.; Wu, T.; Mohammed, O. F.; Bakr, O. M. High-Quality Bulk Hybrid Perovskite Single Crystals within Minutes by Inverse Temperature Crystallization. *Nat. Commun.* **2015**, *6* (1), 1–6.
17. Dunlap, R. A. Electrons in Solids: Contemporary Topics. *Electrons Solids Contemp. Top.* **2019**, 1–114. https://doi.org/10.1088/2053-2571/ab2f2c.
18. Valverde-Chávez, D. A.; Ponseca, C. S.; Stoumpos, C. C.; Yartsev, A.; Kanatzidis, M. G.; Sundström, V.; Cooke, D. G. Intrinsic Femtosecond Charge Generation Dynamics in Single Crystal CH3NH3PbI3. *Energy Environ. Sci.* **2015**, *8* (12), 3700–3707.
19. C. Q. Xia, Q. Lin, J. B. Patel, A. D. Wright, T. W. Crothers, R. L. Milot, L. M. Herz, and M. B. Johnston, in *International Conference on Infrared, Millimeter, and Terahertz Waves, IRMMW-THz* (IEEE Computer Society, **2019**).
20. Savenije, T. J.; Guo, D.; Caselli, V. M.; Hutter, E. M. Quantifying Charge-Carrier Mobilities and Recombination Rates in Metal Halide Perovskites from Time-Resolved Microwave Photoconductivity Measurements. *Adv. Energy Mater.* **2020**, *10* (26), 1903788.
21. Guse, J. A.; Soufiani, A. M.; Jiang, L.; Kim, J.; Cheng, Y. B.; Schmidt, T. W.; Ho-Baillie, A.; McCamey, D. R. Spectral Dependence of Direct and Trap-Mediated Recombination Processes in Lead Halide Perovskites Using Time Resolved Microwave Conductivity. *Phys. Chem. Chem. Phys.* **2016**, *18* (17), 12043–12049.
22. Brenot, R.; Vanderhaghen, R.; Drevillon, B.; French, I.; Roca I Cabarrocas, P. Time Resolved Microwave Conductivity Measurements for the Characterization of Transport Properties in Thin Film Micro-Crystalline Silicon. *Thin Solid Films* **1997**, *296* (1–2), 94–97.
23. Peng, J.; Chen, Y.; Zheng, K.; Pullerits, T.; Liang, Z. Insights into Charge Carrier Dynamics in Organo-Metal Halide Perovskites: From Neat Films to Solar Cells. *Chem. Soc. Rev.* **2017**, *46* (19), 5714–5729.
24. Colbeau-Justin, C.; Valenzuela, M. A. Time-Resolved Microwave Conductivity (TRMC) a Useful Characterization Tool for Charge Carrier Transfer in Photocatalysis: A Short Review. *Rev. Mex. Fis.* **2013**, *59* (3), 191–200.
25. Yu, W.; Li, F.; Yu, L.; Niazi, M. R.; Zou, Y.; Corzo, D.; Basu, A.; Ma, C.; Dey, S.; Tietze, M. L.; Buttner, U.; Wang, X.; Wang, Z.; Hedhili, M. N.; Guo, C.; Wu, T.; Amassian, A. Single Crystal Hybrid Perovskite Field-Effect Transistors. *Nat. Commun.* **2018**, *9* (1), 1–10.
26. Matsushima, T.; Leyden, M. R.; Fujihara, T.; Qin, C.; Sandanayaka, A. S. D.; Adachi, C. Large Metal Halide Perovskite Crystals for Field-Effect Transistor Applications. *Appl. Phys. Lett.* **2019**, *115* (12), 120601.
27. Liu, Y.; Zhang, Y.; Zhu, X.; Yang, Z.; Ke, W.; Feng, J.; Ren, X.; Zhao, K.; Liu, M.; Kanatzidis, M. G.; Liu, S. Inch-Sized High-Quality Perovskite Single Crystals by Suppressing Phase Segregation for Light-Powered Integrated Circuits. *Sci. Adv.* **2021**, *7* (7).
28. Liu, Y.; Zhang, Y.; Zhu, X.; Feng, J.; Spanopoulos, I.; Ke, W.; He, Y.; Ren, X.; Yang, Z.; Xiao, F.; Zhao, K.; Kanatzidis, M.; Liu, S. Triple-Cation and Mixed-Halide Perovskite Single Crystal for High-Performance X-Ray Imaging. *Adv. Mater.* **2021**, *33* (8).
29. Oranskaia, A.; Yin, J.; Bakr, O. M.; Brédas, J. L.; Mohammed, O. F. Halogen Migration in Hybrid Perovskites: The Organic Cation Matters. *J. Phys. Chem. Lett.* **2018**, *9* (18), 5474–5480.

30. Liu, G.; Wu, Y.; Liu, Y.; Cai, B.; Dong, Y.; Zhang, S.; Zeng, H. Halide Ion Migration in Lead-Free All-Inorganic Cesium Tin Perovskites. *Appl. Phys. Lett.* **2021**, *119* (3), 031902.
31. Meggiolaro, D.; Mosconi, E.; De Angelis, F. Formation of Surface Defects Dominates Ion Migration in Lead-Halide Perovskites. *ACS Energy Lett.* **2019**, *4* (3), 779–785.
32. Le Corre, V. M.; Duijnstee, E. A.; El Tambouli, O.; Ball, J. M.; Snaith, H. J.; Lim, J.; Koster, L. J. A. Revealing Charge Carrier Mobility and Defect Densities in Metal Halide Perovskites via Space-Charge-Limited Current Measurements. *ACS Energy Lett.* **2021**, *6* (3), 1087–1094.
33. Li, W. G.; Rao, H. S.; Chen, B. X.; Wang, X. D.; Kuang, D. Bin. A Formamidinium-Methylammonium Lead Iodide Perovskite Single Crystal Exhibiting Exceptional Optoelectronic Properties and Long-Term Stability. *J. Mater. Chem. A* **2017**, *5* (36), 19431–19438.
34. Xia, C. Q.; Lin, Q.; Patel, J. B.; Wright, A. D.; Crothers, T. W.; Milot, R. L.; Herz, L. M.; Johnston, M. B. Time-Resolved THz Spectroscopy of Metal-Halide Perovskite Single Crystals and Polycrystalline Thin Films. *Int. Conf. Infrared, Millimeter, Terahertz Waves, IRMMW-THz* **2019**, *2019-September*.
35. Valverde-Chávez, D. A.; Ponseca, C. S.; Stoumpos, C.; Yartsev, A.; Kanatzidis, M. G.; Sundström, V.; Cooke, D. G. Optical Pump – Multi-THz Probe Spectroscopy of a Single Crystal Organic Hybrid Lead Halide Perovskite. *CLEO Sci. Innov. CLEO-SI 2015* **2015**, 2267.
36. Semonin, O. E.; Elbaz, G. A.; Straus, D. B.; Hull, T. D.; Paley, D. W.; Van Der Zande, A. M.; Hone, J. C.; Kymissis, I.; Kagan, C. R.; Roy, X.; Owen, J. S. Limits of Carrier Diffusion in N-Type and p-Type CH3NH3PbI3 Perovskite Single Crystals. *J. Phys. Chem. Lett.* **2016**, *7* (17), 3510–3518.
37. Stoumpos, C. C.; Malliakas, C. D.; Kanatzidis, M. G. Semiconducting Tin and Lead Iodide Perovskites with Organic Cations: Phase Transitions, High Mobilities, and near-Infrared Photoluminescent Properties. *Inorg. Chem.* **2013**, *52* (15), 9019–9038.
38. Takahashi, Y.; Hasegawa, H.; Takahashi, Y.; Inabe, T. Hall Mobility in Tin Iodide Perovskite CH3NH3SnI 3: Evidence for a Doped Semiconductor. *J. Solid State Chem.* **2013**, *205*, 39–43.
39. Rong, S.; Xiao, Y.; Jiang, J.; Zeng, Q.; Li, Y. Strongly Enhanced Photoluminescence and Photoconductivity in Erbium-Doped MAPbBr3 Single Crystals. *J. Phys. Chem. C* **2020**, *124* (16), 8992–8998.
40. Maculan, G.; Sheikh, A. D.; Abdelhady, A. L.; Saidaminov, M. I.; Haque, M. A.; Murali, B.; Alarousu, E.; Mohammed, O. F.; Wu, T.; Bakr, O. M. CH3NH3PbCl3 Single Crystals: Inverse Temperature Crystallization and Visible-Blind UV-Photodetector. *J. Phys. Chem. Lett.* **2015**, *6* (19), 3781–3786.
41. Han, Q.; Bae, S. H.; Sun, P.; Hsieh, Y. T.; Yang, Y.; Rim, Y. S.; Zhao, H.; Chen, Q.; Shi, W.; Li, G.; Yeng, Y. Single Crystal Formamidinium Lead Iodide (FAPbI3): Insight into the Structural, Optical, and Electrical Properties. *Adv. Mater.* **2016**, *28* (11), 2253–2258.
42. Zhumekenov, A. A.; Saidaminov, M. I.; Haque, M. A.; Alarousu, E.; Sarmah, S. P.; Murali, B.; Dursun, I.; Miao, X. H.; Abdelhady, A. L.; Wu, T.; Mohammed, O. F.; Bakr, O. M. Formamidinium Lead Halide Perovskite Crystals with Unprecedented Long Carrier Dynamics and Diffusion Length. *ACS Energy Lett.* **2016**, *1* (1), 32–37.
43. Liu, Y.; Sun, J.; Yang, Z.; Yang, D.; Ren, X.; Xu, H.; Yang, Z.; Liu, S. F. 20-Mm-Large Single-Crystalline Formamidinium-Perovskite Wafer for Mass Production of Integrated Photodetectors. *Adv. Opt. Mater.* **2016**, *4* (11), 1829–1837.
44. Ng, M.; Halpert, J. E. Single Crystals of Mixed Br/Cl and Sn-Doped Formamidinium Lead Halide Perovskites: Via Inverse Temperature Crystallization. *RSC Adv.* **2020**, *10* (7), 3832–3836.
45. Feng, Y.; Pan, L.; Wei, H.; Liu, Y.; Ni, Z.; Zhao, J.; Rudd, P. N.; Cao, L. R.; Huang, J. Low Defects Density CsPbBr3single Crystals Grown by an Additive Assisted Method for Gamma-Ray Detection. *J. Mater. Chem. C* **2020**, *8* (33), 11360–11368.
46. He, Y.; Liu, Z.; McCall, K. M.; Lin, W.; Chung, D. Y.; Wessels, B. W.; Kanatzidis, M. G. Perovskite CsPbBr 3 Single Crystal Detector for Alpha-Particle Spectroscopy. *Nucl. Instruments Methods Phys. Res. Sect. A Accel. Spectrometers, Detect. Assoc. Equip.* **2019**, *922*, 217–221.

47. Pan, L.; Feng, Y.; Huang, J.; Cao, L. R. Comparison of Zr, Bi, Ti, and Ga as Metal Contacts in Inorganic Perovskite CsPbBr Gamma-Ray Detector. *IEEE Trans. Nucl. Sci.* **2020**, *67* (10), 2255–2262.
48. Zhang, B. Bin; Wang, F.; Zhang, H.; Xiao, B.; Sun, Q.; Guo, J.; Hafsia, A. Ben; Shao, A.; Xu, Y.; Zhou, J. Defect Proliferation in CsPbBr3 Crystal Induced by Ion Migration. *Appl. Phys. Lett.* **2020**, *116* (6), 063505.
49. He, Y.; Stoumpos, C. C.; Hadar, I.; Luo, Z.; McCall, K. M.; Liu, Z.; Chung, D. Y.; Wessels, B. W.; Kanatzidis, M. G. Demonstration of Energy-Resolved γ-Ray Detection at Room Temperature by the CsPBCl3 Perovskite Semiconductor. *J. Am. Chem. Soc.* **2021**, *143* (4), 2068–2077.
50. Zhang, Z.; Chung, C. C.; Huang, Z.; Vetter, E.; Seyitliyev, D.; Sun, D.; Gundogdu, K.; Castellano, F. N.; Danilov, E. O.; Yang, G. Towards Radiation Detection Using Cs2AgBiBr6 Double Perovskite Single Crystals. *Mater. Lett.* **2020**, *269*, 127667.
51. Pan, W.; Wu, H.; Luo, J.; Deng, Z.; Ge, C.; Chen, C.; Jiang, X.; Yin, W. J.; Niu, G.; Zhu, L.; Yin, L.; Zhou, Y.; Xie, Q.; Ke, X.; Sui, M.; Tang, J. Cs2AgBiBr6 Single-Crystal X-Ray Detectors with a Low Detection Limit. *Nat. Photonics* **2017**, *11* (11), 726–732.
52. Ju, D.; Jiang, X.; Xiao, H.; Chen, X.; Hu, X.; Tao, X. Narrow Band Gap and High Mobility of Lead-Free Perovskite Single Crystal Sn-Doped MA3Sb2I9. *J. Mater. Chem. A* **2018**, *6* (42), 20753–20759.
53. McCall, K. M.; Liu, Z.; Trimarchi, G.; Stoumpos, C. C.; Lin, W.; He, Y.; Hadar, I.; Kanatzidis, M. G.; Wessels, B. W. α-Particle Detection and Charge Transport Characteristics in the A3M2I9 Defect Perovskites (A = Cs, Rb; M = Bi, Sb). *ACS Photonics* **2018**, *5* (9), 3748–3762.
54. Zhuang, R.; Wang, X.; Ma, W.; Wu, Y.; Chen, X.; Tang, L.; Zhu, H.; Liu, J.; Wu, L.; Zhou, W.; Liu, X.; Yang, Y. (Michael). Highly Sensitive X-Ray Detector Made of Layered Perovskite-like (NH4)3Bi2I9 Single Crystal with Anisotropic Response. *Nat. Photonics* **2019**, *13* (9), 602–608.
55. Zhang, Y.; Sun, M.; Zhou, N.; Huang, B.; Zhou, H. Electronic Tunability and Mobility Anisotropy of Quasi-2D Perovskite Single Crystals with Varied Spacer Cations. *J. Phys. Chem. Lett.* **2020**, *11* (18), 7610–7616.
56. Liu, T.; Tang, W.; Luong, S.; Fenwick, O. High Charge Carrier Mobility in Solution Processed One-Dimensional Lead Halide Perovskite Single Crystals and Their Application as Photodetectors. *Nanoscale* **2020**, *12* (17), 9688–9695.
57. Li, W.; Xin, D.; Tie, S.; Ren, J.; Dong, S.; Lei, L.; Zheng, X.; Zhao, Y.; Zhang, W. H. Zero-Dimensional Lead-Free FA3Bi2I9Single Crystals for High-Performance X-Ray Detection. *J. Phys. Chem. Lett.* **2021**, *12* (7), 1778–1785.
58. Zheng, X.; Zhao, W.; Wang, P.; Tan, H.; Saidaminov, M. I.; Tie, S.; Chen, L.; Peng, Y.; Long, J.; Zhang, W. H. Ultrasensitive and Stable X-Ray Detection Using Zero-Dimensional Lead-Free Perovskites. *J. Energy Chem.* **2020**, *49*, 299–306.
59. Song, X.; Cui, Q.; Liu, Y.; Xu, Z.; Cohen, H.; Ma, C.; Fan, Y.; Zhang, Y.; Ye, H.; Peng, Z.; Li, R.; Chen, Y.; Wang, J.; Sun, H.; Yang, Z.; Liu, Z.; Yang, Z.; Huang, W.; Hodes, G.; Liu, S.; Zhao, K. Metal-Free Halide Perovskite Single Crystals with Very Long Charge Lifetimes for Efficient X-Ray Imaging. *Adv. Mater.* **2020**, *32* (42), 2003353.
60. Zheng, F.; Wang, L. W. Large Polaron Formation and Its Effect on Electron Transport in Hybrid Perovskites. *Energy Environ. Sci.* **2019**, *12* (4), 1219–1230.
61. Miyata, K.; Meggiolaro, D.; Tuan Trinh, M.; Joshi, P. P.; Mosconi, E.; Jones, S. C.; De Angelis, F.; Zhu, X. Y. Large Polarons in Lead Halide Perovskites. *Sci. Adv.* **2017**, *3* (8).
62. Bonn, M.; Miyata, K.; Hendry, E.; Zhu, X. Y. Role of Dielectric Drag in Polaron Mobility in Lead Halide Perovskites. *ACS Energy Lett.* **2017**, *2* (11), 2555–2562.
63. Erickson, J. C.; Yao, H. W.; James, R. B.; Hermon, H.; Greaves, M. Time of Flight Experimental Studies of CdZnTe Radiation Detectors. *J. Electron. Mater.* **2000**, *29* (6), 699–703.

64. Karasyuk, P.; Shepelytskyi, Y.; Semeniuk, O.; Bubon, O.; Juska, G.; Blevis, I.; Reznik, A. Investigation of Photoconductivity and Electric Field Distribution in CZT Detectors by Time-of-Flight (TOF) and Charge Extraction by Linearly Increasing Voltage (CELIV). *J. Mater. Sci. Mater. Electron.* **2018**, *29* (16), 13941–13951.
65. Suzuki, K.; Shorohov, M.; Sawada, T.; Seto, S. Time-of-Flight Measurements on TlBr Detectors. *IEEE Trans. Nucl. Sci.* **2015**, *62* (2), 433–436.
66. Liu, F.; Wang, L.; Wang, J.; Wang, F.; Chen, Y.; Zhang, S.; Sun, H.; Liu, J.; Wang, G.; Hu, Y.; Jiang, C. 2D Ruddlesden–Popper Perovskite Single Crystal Field-Effect Transistors. *Adv. Funct. Mater.* **2021**, *31* (1), 2005662.
67. Wang, J.; Senanayak, S. P.; Liu, J.; Hu, Y.; Shi, Y.; Li, Z.; Zhang, C.; Yang, B.; Jiang, L.; Di, D.; Ievlev, A. V.; Ovchinnikova, O. S.; Ding, T.; Deng, H.; Tang, L.; Guo, Y.; Wang, J.; Xiao, K.; Venkateshvaran, D.; Jiang, L.; Zhu, D.; Sirringhaus, H. Investigation of Electrode Electrochemical Reactions in CH3NH3PbBr3 Perovskite Single-Crystal Field-Effect Transistors. *Adv. Mater.* **2019**, *31* (35), 1902618.
68. Ueno, K.; Inoue, I. H.; Yamada, T.; Akoh, H.; Tokura, Y.; Takagi, H. Field-Effect Transistor Based on KTaO3 Perovskite. *Appl. Phys. Lett.* **2004**, *84* (19), 3726–3728.
69. Liu, J.; Liu, F.; Liu, H.; Hou, R.; Yue, J.; Cai, J.; Peng, Z.; Impundu, J.; Xie, L.; Li, Y. J.; Sun, L. Direct Growth of Perovskite Crystals on Metallic Electrodes for High-Performance Electronic and Optoelectronic Devices. *Small* **2020**, *16* (3), 1906185.
70. Huo, C.; Liu, X.; Song, X.; Wang, Z.; Zeng, H. Field-Effect Transistors Based on van-Der-Waals-Grown and Dry-Transferred All-Inorganic Perovskite Ultrathin Platelets. *J. Phys. Chem. Lett.* **2017**, *8* (19), 4785–4792.
71. Liang, M.; Ali, A.; Belaidi, A.; Hossain, M. I.; Ronan, O.; Downing, C.; Tabet, N.; Sanvito, S.; EI-Mellouhi, F.; Nicolosi, V. Improving Stability of Organometallic-Halide Perovskite Solar Cells Using Exfoliation Two-Dimensional Molybdenum Chalcogenides. *npj 2D Mater. Appl.* **2020**, *4* (1), 1–8.
72. Li, Y.; Shi, Z. F.; Li, S.; Lei, L. Z.; Ji, H. F.; Wu, D.; Xu, T. T.; Tian, Y. T.; Li, X. J. High-Performance Perovskite Photodetectors Based on Solution-Processed All-Inorganic CsPbBr3 Thin Films. *J. Mater. Chem. C* **2017**, *5* (33), 8355–8360.
73. Yakunin, S.; Sytnyk, M.; Kriegner, D.; Shrestha, S.; Richter, M.; Matt, G. J.; Azimi, H.; Brabec, C. J.; Stangl, J.; Kovalenko, M. V.; Heiss, W. Detection of X-Ray Photons by Solution-Processed Lead Halide Perovskites. *Nat. Photonics* **2015**, *9* (7), 444–449.
74. Tsai, H.; Liu, F.; Shrestha, S.; Fernando, K.; Tretiak, S.; Scott, B.; Vo, D. T.; Strzalka, J.; Nie, W. A Sensitive and Robust Thin-Film X-Ray Detector Using 2D Layered Perovskite Diodes. *Sci. Adv.* **2020**, *6* (15).
75. Li, T.; Zhao, X.; Yang, D.; Du, M. H.; Zhang, L. Intrinsic Defect Properties in Halide Double Perovskites for Optoelectronic Applications. *Phys. Rev. Appl.* **2018**, *10* (4), 041001.
76. Ahrling, R.; Boy, J.; Handwerg, M.; Chiatti, O.; Mitdank, R.; Wagner, G.; Galazka, Z.; Fischer, S. F. Transport Properties and Finite Size Effects in β-Ga2O3 Thin Films. *Sci. Rep.* **2019**, *9* (1).
77. Stillman, G. E.; Wolfe, C. M.; Dimmock, J. O. Hall Coefficient Factor for Polar Mode Scattering in N-Type GaAs. *J. Phys. Chem. Solids* **1970**, *31* (6), 1199–1204.
78. Datta, A.; Fiala, J.; Becla, P.; Motakef, S. Stable Room-Temperature Thallium Bromide Semiconductor Radiation Detectors. *APL Mater.* **2017**, *5* (10), 106109.
79. Liu, M.; Huang, L.; Yuan, D.; Li, Z.; Teng, Y.; Zhang, J.; Huang, S.; Liu, B. Perovskite Nanocrystals and Dyes for High-Efficiency Liquid Scintillator Counters To Detect Radiation. *ACS Appl. Nano Mater.* **2023**, *6* (1), 370–378.
80. Ahmed, G. H.; Yin, J.; Bakr, O. M.; Mohammed, O. F. Successes and Challenges of Core/Shell Lead Halide Perovskite Nanocrystals. *ACS Energy Lett.* **2021**, *6* (4), 1340–1357.
81. Meena, M. L.; Gupta, K. K.; Dutta, S.; Kumar, R.; Singh, R. K.; Lu, C. H.; Lin, S. D.; Som, S. Short Review on the Instability and Potential Solutions for Perovskite Quantum Dots. *Curr. Res. Green Sustain. Chem.* **2022**, *5* (December 2021), 100321.

Development of Thallium-Based Semiconductors and Scintillators for High Energy Radiation Detection



Ge Yang, Doup Kim, and Ibrahim Hany

1 Introduction

Advanced radiation detectors have attracted many attentions in a wide variety of fields, such as homeland security, medical diagnosis and imaging, nuclear safety control, nondestructive industrial inspection, and basic physical research [1–5]. In this regard, room temperature radiation detector technologies are highly desired since no cooling is required to suppress electronic noises. Among different types of room temperature radiation detector materials, semiconductors and scintillators have received considerable interest. The semiconductor radiation detectors operate through a direct detection process, where the incident radiation is directly converted to charge carriers, i.e., electrons and holes. The scintillator radiation detectors function through an indirect detection mechanism where scintillation light is firstly formed through the interaction between scintillator materials and incident radiation, followed by the generation of readable electrical signal from scintillator lights using the photosensors. In this process the radiation-induced scintillation light is converted into the electrical signal for the sequent processing [6].

As a promising class of materials for semiconductor and scintillator radiation detectors, thallium (Tl)-based materials have been actively investigated, thanks to its high stopping power, high atomic number, appealing charge transport properties, and other physical properties suitable for radiation detection systems. This chapter provides the readers with various aspects of Tl-based radiation detectors, which are categorized by Tl-based semiconductor materials and Tl-based scintillator materials.

G. Yang (✉) · D. Kim · I. Hany
Department of Nuclear Engineering, North Carolina State University, Raleigh, NC, USA
e-mail: gyang9@ncsu.edu

© The Author(s), under exclusive license to Springer Nature Switzerland AG 2024

S. Krishnamoorthy, K. (Kris) Iniewski (eds.), *Advances in Fabrication and Investigation of Nanomaterials for Industrial Applications*,
https://doi.org/10.1007/978-3-031-42700-8_13

2 Tl-Based Semiconductor Detector Materials

2.1 TlBr (Thallium Bromide)

Historically, one of the first Tl-based radiation detector materials is TlBr, which was developed by Hofstadter in 1947 [7]. Owing to its high density of 7.56 g/cm^3, which can provide high stopping power to high energy radiation, and the development of material purification processes, such as the zone-refining technology, which led to the advancement of TlBr's charge transport properties and the improvement of the corresponding radiation detection performance, this material has been continuously investigated [8]. TlBr has a reasonable bandgap energy of 2.68 eV [9], guaranteeing minimization of noise signals. Meanwhile, TlBr can be grown using traditional melt growth methods since this material has a relatively low melting temperature of 480 °C [10]. It should be noted that the phase transition in the TlBr structure rarely occurs under the melting temperature [8]. These advantages directly contribute to the cost-effectiveness of TlBr manufacturing and, thus, help attract further interest to develop TlBr for radiation detection.

The purification of raw materials, prior to the crystal growth, has played an important role in the development of TlBr semiconductor radiation detector. This purification step can significantly reduce the level of impurities and improve the quality of as-grown TlBr. Among the various purification methods, e.g., directed crystallization [10] and vacuum-based techniques [11], the zone-refining purification technique is one of the most widely used ways to purify the raw materials in the purification of TlBr [8]. The zone-refining purification process is easy to implement, in which the molten zone moves along the ingot length of synthesized raw material ingots until approaching to the end. To this end, the impurities can be accumulated together at one end of the ingots, due to the segregation effects. This impurity-rich ingot end can be removed through cutting. The zone-refining process can be used repeatedly on the same ingot to further improve the purification results. After the purification, several growth methods can be used to grow TlBr single crystals, such as the Bridgman-Stockbarger method, the hydrothermal growth method, and the traveling molten zone (TMZ) method. The most common method for growing the TlBr semiconductor is the Bridgman-Stockbarger method, which has been used to grow large size of TlBr crystals (Fig. 1).

The fabrication of TlBr semiconductor radiation detectors includes a series of procedures such as cutting, lapping, polishing, chemical etching, and electrode/contact deposition [14]. The as-fabricated TlBr detector devices are widely studied for gamma-ray detection. Table 1 summarizes the performance of some reported TlBr gamma-ray detectors, with a focus on mobility-lifetime product ($\mu\tau$) and energy resolution (full width at half-maximum: FWHM) when being exposed to radiation sources.

Although TlBr has exhibited great potential as a promising candidate material for room temperature radiation detection, it faces the challenge of polarization, which many semiconductors have suffered from [23]. This kind of long-standing

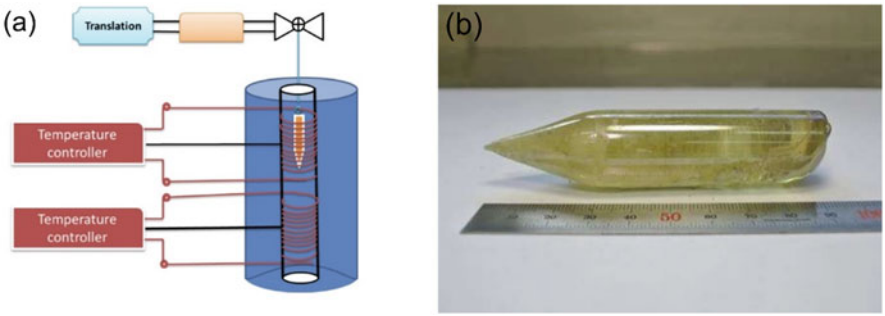


Fig. 1 (**a**) Schematic diagram of the vertical Bridgman-Stockbarger method [12]. (**b**) TlBr single-crystal ingot with diameter of 1 inch grown by the vertical Bridgman-Stockbarger method [13]

Table 1 The performance of TlBr detectors for gamma-ray detection

Device (structure)	Growth method	$\mu\tau$ product [$cm^2\ V^{-1}$]	FWHM/source	Ref.
Au/TlBr/Au (planar)	Bridgman	2×10^{-4}	5.2%/Co^{57} 122 keV 2.5%/Cs^{137} 662 keV	[15]/2006
Au/TlBr/Au (planar)	TMZ	9.1×10^{-4}	11.0%/Am^{241} 59.5 keV	[16]/2007
Au/TlBr/Au (pixel)	TMZ	3×10^{-3}	5.5%/Co^{57} 122 keV 1.66%/Cs^{137} 662 keV	[14]/2009
Au/Cr/TlBr/Cr/Au (planar)	Bridgman	6×10^{-3}	1.3%/Cs^{137} 662 keV	[17]/2010
Tl/TlBr/Tl (pixel)	TMZ	2.93×10^{-3}	4.4%/Co^{57} 122 keV 1.5%/Cs^{137} 662 keV	[18]/2014
Tl/TlBr/Tl (pixel)	Bridgman	–	2–2.5%/Cs^{137} 662 keV	[19]/2018
Tl/TlBr/Tl (planar)	TMZ	–	1.8%/Cs^{137} 662 keV	[20]/2019
Au/Cr/TlBr/Cr/Au (planar)	Horizontal zone	–	5.8%/Cs^{137} 662 keV	[21]/2020
Au/Cr/TlBr/Cr/Au (planar)	TMZ	–	3%/Cs^{137} 662 keV	[22]/2022

polarization issue directly results in the performance degradation of TlBr semiconductor radiation detectors over time, even if these detectors could show excellent results initially. In this process, once the bias voltage is applied across the TlBr detector materials, positive ions (Tl^+) and negative ions (Br^-) could migrate and accumulated to cathode and anode, respectively. Due to the movement of ions to electrodes, this unwanted physical behavior has been called as the polarization phenomena. Especially, compared with diffusion of Tl^+ ions, Br^- ions can contribute more to ion migration, due to the fact that Br^- ions interact more frequently with most of electrode materials [24]. This type of ion migration phenomenon, often observed in ion-type semiconductors, leads to the long-term instability issue of the TlBr detector materials. One way to suppress ion migration from the polarization phenomena is to cool down the detectors, i.e., keeping the operation temperature

under the room temperature, such as −20 °C, which can alleviate ion diffusion and metal-bromide formation [25, 26]. However, even though the cooling method can be a useful way to mitigate the polarization effect, this will compromise the design objective of TlBr radiation detectors, i.e., providing high energy resolution detection capabilities to high energy radiation at room temperature. To this end, other approaches have been actively explored to address the polarization issue of TlBr semiconductors. Considering the fact that the major contribution of ion diffusion comes from Br^- ions, applying the electrodes of gold (Au), thallium (Tl), platinum (Pt), and palladium (Pd) or fabrication of heterojunction with the form of $TlBr_{1-x}Cl_x$ should help suppress the migration behavior of Br^- ions [24]. The effect of doping certain elements, such as lead (Pb), into TlBr semiconductors was also studied to understand the dopants' role for adjusting the conductivity of this class of ion-type semiconductors [27]. The impact of external factors, e.g., humidity, on the stability and degradation of TlBr semiconductors was also investigated [26], which can provide useful information for improving fabrication and packaging processes of TlBr radiation detectors.

2.2 $TlPbI_3$ (Thallium Lead Iodide)

$TlPbI_3$ is another Tl-based material which has recently been explored for radiation detection. $TlPbI_3$ is a type of perovskite materials. Over the past few years, perovskite materials have attracted strong interest in the radiation detector community due to their excellent physical properties for the radiation detection, such as high stopping power, high resistivity, suitable bandgap, low trap density, and appealing charge transport property. Among the perovskite-based radiation detector materials, the general formula of ABX_3 (A = Cs, CH_3NH_3, and $CH(NH_2)_2$; B = Pb, Sn, and Bi; X = I, Br, and Cl) has been extensively studied due to their facile growth approaches and their promising performance. The Tl-based $TlPbI_3$ is a less explored all-inorganic perovskite, which has lattice parameter of $\boldsymbol{a}$ = 4.6096(9) Å, $\boldsymbol{b}$ = 14.874(3) Å, and $\boldsymbol{c}$ = 11.831(2) Å, and the $[PbI_3]^-$ layers are isolated by $[Tl]^+$ positive ions, as depicted in Fig. 2a [28, 29]. $TlPbI_3$ has a wide bandgap of up to 2.3 eV, which helps suppress noise signal; a low melting point of around 360 °C, which is desired for cost-effective growth; and a high density of 6.6 g/cm^3, which offers a high attenuation coefficient for the radiation detection [29].

Due to the relatively low melting temperature of 360 °C, $TlPbI_3$ perovskite crystal has been grown using the Bridgman method. To this end, thallium iodide (TlI) and lead iodide (PbI_3) are normally used as the raw materials, owing to the fact that they are not expected to experience phase transitions during the temperature range from the melting point to room temperature [30–32]. As described in Fig. 2b, the as-grown $TlPbI_3$ single crystal by the Bridgman method is of dark-red color and cylindrical shape with around 1 cm diameter.

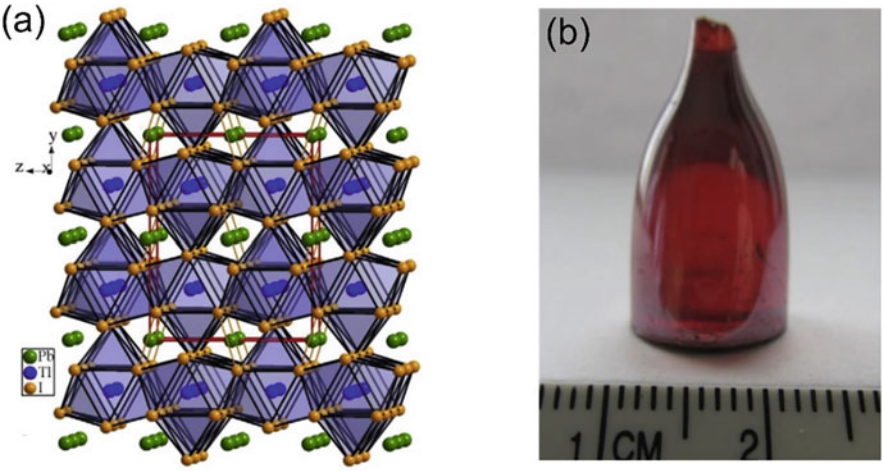


Fig. 2 (**a**) The crystal structure of $TlPbI_3$ [29]. (**b**) As-grown single crystal of $TlPbI_3$ perovskite [29]

Table 2 The investigated electrical properties of $TlPbI_3$ planar detector devices

Device	Growth method	Bandgap [eV]	Resistivity [Ω cm]	$\mu\tau$ product [$cm^2\ V^{-1}$]	Ref.
Cu/$TlPbI_3$/Cu	Bridgman	2.20	2.5×10^{12}	–	[31]/2000
Au/$TlPbI_3$/Au	Bridgman	–	~ 10^{11}	–	[32]/2003
C/$TlPbI_3$/C	Bridgman	2.25	4.0×10^{12}	1.8×10^{-5}	[28]/2021
Ag/$TlPbI_3$/Ag	Bridgman	2.17	2.0×10^{11}	3.43×10^{-5}	[33]/2021

$TlPbI_3$ perovskite has been investigated for the high energy radiation (X-ray and gamma-ray) detection using various fabrication methods and configurations. The corresponding electrical properties are listed in Table 2. As a relatively new detector material, the detector performance of $TlPbI_3$ perovskite, such as the energy resolution of gamma-ray spectra, is still inferior than that of TlBr. However, there are much progress in the development of $TlPbI_3$ material for radiation detection. Kocsis et al. reported a resistivity of 10^{12} Ω•cm from $TlPbI_3$ single crystal, which is higher than that of CdZnTe semiconductor and suitable for suppressing the noise signal. This detector device exhibited a signal-to-noise ratio (SNR) of 276 and showed a linear X-ray-induced conductivity (XRIC) response, which can lead to a promising candidate material for X-ray detector and imaging applications [31]. As shown in Fig. 3, Hitomi et al. investigated the spectra from γ-ray (Co^{57}) and alpha-particle (Am^{241}) using a Au/$TlPbI_3$/Au detector device in 2003. There was no peak observed from γ-ray, while a peak of 5.48 MeV, corresponding to alpha-particle from Am^{241},

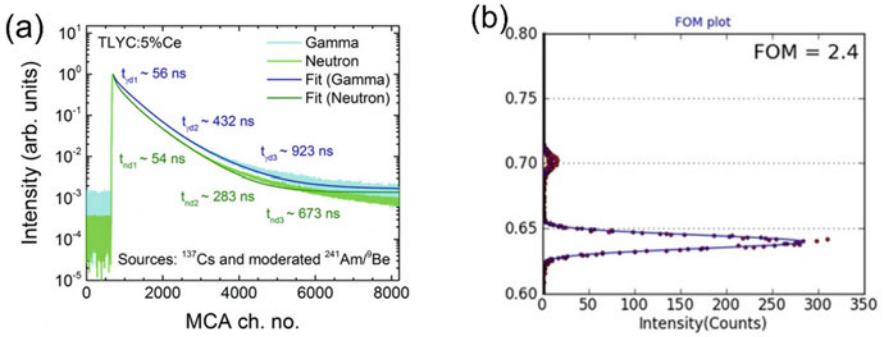


Fig. 3 (**a**) TLYC's time profiles and calculated decay time for the interaction with gamma-rays (Cs^{137} 662 keV) and neutrons (Am^{241}/Be^{9}) [47]. (**b**) Projected PSD scatter plot, which indicates distinguished intensity separation between gamma-rays and neutrons [47]

was collected [32]. Yang et al. reported that the $TlPbI_3$ single crystal can suffer from the deep-level traps, which can affect the mobility of charge carrier and the spectra. In 2021, Hany et al. prepared a Ag/$TlPbI_3$/Ag detector device with a resistivity of 10^{11} Ω•cm and explored its use for radiation detection [33].

Even though a series of investigations have been conducted and good progress has been made for developing $TlPbI_3$-based radiation detectors, there are a few challenges that have to be overcome. Further research should focus on understanding the correlation between material defects and detector performance. More purification efforts could be used to improve the properties of as-grown $TlPbI_3$.

3 Tl-Based Scintillator Detector Materials

For a quite long time, Tl has been widely used as the dopant to enhance the performance of traditional scintillators, such as $Cs_3Cu_2I_5$ and NaI, because Tl^+ ions can serve as an activator for alkali-based scintillators, leading to the improvement of the scintillator performance including light yield, luminescence efficiency, and energy resolution. Tl-based materials have excellent intrinsic properties suitable for the radiation detection, i.e., high density, high atomic number, and relatively low melting temperature; various Tl-based scintillators have also been actively investigated for the detection of high energy radiation, such as X-ray, gamma-ray, neutrons, and alpha-particle. A series of reports of Tl-based scintillators have shown improved performance over the conventional scintillators. The emerging Tl-based scintillators can be categorized into four classes based on their chemical/material structure and properties.

- Class A: Tl_2ALX_6 [A = alkali metal (Li and Ni); L = rare earth element (Sc, Y, La, Gd, and Lu); X = halogen (F, Br, Cl, and I)] elpasolites with/without Ce^+ ion doping
- Class B: TlL_2X_7, Tl_2LX_5, Tl_3LX_6 with/without Ce^+ ion doping
- Class C: TlM_2X_5 and $TlMX_3$ [M = alkaline-earth metal (Mg, Ca, and Sr)] with/without Eu^+ ion doping and $TlCdCl_3$ and $TlAlF_4$
- Class D: Tl_2BX_6 [B = transition metal (Hf and Zr)]
- Class E: $TlPbI_3$ perovskite

Tl-based scintillators have traditionally been grown using the Bridgman method with high-purity materials. To this end, the modified Bridgman techniques have been developed to address crystal growth issues, i.e., segregation of impurities and inhomogeneous chemical composition. As starting materials for this class of materials are highly hygroscopic, they are generally processed in the moisture-free environment and should experience drying process before the beginning of crystal growth. The thermodynamic properties of Tl-based scintillators, particularly their melting points and phase transitions through the temperature change, have been explored using differential scanning calorimetry (DSC) and thermogravimetric analysis (TGA). The results demonstrated the lack of secondary phases and investigated the melting behavior over the temperature ranging from 400 °C to 800 °C. The knowledge helps understand the phase stability of this material, which is closely related to the growth process.

3.1 Class A: Tl_2ALX_6 Elpasolites with/Without Ce^+ Doping

Elpasolites have received continued interest as one class of classical scintillators, which have exhibited fast decay time and high light yield. Due to the fact that elpasolites contain alkali metal halides, such as cesium and potassium, many of elpasolites are based on cesium metal halides. Cesium-based inorganic scintillators with Ce^+ doping, such as Cs_2LiYCl_6:Ce (CLYC), $Cs_2LiLaBr_6$:Ce (CLLB), and $Cs_2LiLa(Br,Cl)_6$:Ce (CLLBC), have been widely investigated considering their excellent ability to detect gamma-rays, neutrons, and charged particles. However, the low density of these scintillators needs to be addressed to improve their performance [34–40]. In this regard, Tl can be an excellent substitute for cesium to improve performance, especially to achieve higher energy resolution and faster decay time for high energy radiation detection [41].

A series of *class A* scintillators, which have been investigated recently, are listed in Table 3. Because lanthanum (La) contributes to the enhancement of the light

Table 3 A summary of the performance of "Tl-based class A" scintillators interacting with gamma-ray or neutron

Scintillator	Doping	Energy resolution [%]	Light yield [ph/MeV]	Radioluminescence emission peak [nm]	Decay time [ns]/contribution [%]		PSD FOM	Ref.
$Tl_2LiGdCl_6$	Ce 10%	4.6	58,000	380	34 (81) 191 (10) 1200 (9)		–	[42]
$Tl_2LiGdBr_6$	Ce 10%	17	17,000	422	29 (92) 197 (8)		–	[43]
$Tl_2LiLaBr_6$	Ce 1%	5.7	53,000	410	–		–	[44]
Tl_2LiYCl_6	Ce 1%	4.8	30,500	430	69 (3) 460 (74) 1400 (23)		–	[45, 46]
	Ce 3%	4.2	–	440	57 (3) 431 (64) 1055 (33)		–	[44, 47, 48]
	Ce 5%	3.8	26,000 (γ)78,000 (n)	–	γ-ray 56 (3) 432 (65) 923 (32)	Neutron 54 (7) 283 (33) 673 (60)	2.4	
$Tl_2LiLuCl_6$	Ce 1%	5.6	27,000	428	72 (8) 366 (30) 1500 (62)		–	[49]
$Tl_2LiScCl_6$	None	8.3	26,000	385	1147 (100)		–	[50]
Tl_2NaYCl_6	None	6.3	23,000	430	350 (80) 2500 (20)		–	[51]
	Ce 5%	4.1	27,800	430	91 (34) 462 (52) 2100 (15)		–	[52]

yield, the energy resolution, and the stability, most of Cs-based scintillators have contained La in their material structure. However, La has the intrinsic radioactivity, which can affect the exact measurement of the incident radiation. Thus, most of Tl-based scintillators tend not to add La. Kim et al. [42] reported $Tl_2LiGdCl_6$:Ce (TLGC) with 10% Ce doping, which showed excellent light yield of 58,000 ph/MeV, the most highest value in *class A*. Tl_2LiYCl_6:Ce (TLYC) with 5% Ce doping was reported by Hawrami et al. [47]. Compared with other types of Tl-based scintillators, this new material shows great potential for neutron detection, as depicted in Fig. 3a. The pulse shape discrimination figure-of-merit (PSD FOM) is an important parameter to evaluate if the scintillators can be used to distinguish different types of radiation, such as gamma-ray and neutron. As described in Fig. 3b, the TLYC showed a PSD FOM of 2.4, which means it is able to differentiate well between gamma-rays and neutrons. Very recently, new types of *class A* scintillators, i.e., $Tl_2LiScCl_6$ Tl_2NaYCl_6, have been explored, and they have demonstrated interesting light yield of over 20,000 ph/MeV. Further studies are still needed to improve the light yield to obtain higher energy resolution [51, 52].

3.2 *Class B: TlL_2X_7, Tl_2LX_5, and Tl_3LX_6 with/Without Ce^+ Ion Doping*

In the past few years, traditional thallium-doped scintillators, such as NaI and CsI, have been employed widely, due to the higher attenuation, the cost-effective growth of large-size crystals, and the increased energy resolution by the contribution of thallium [53]. As a relatively new type of radiation detectors, *class B* scintillators including rubidium (Rb)- and potassium (K)-based scintillators have been developed owing to their reasonable light yield and excellent detection efficiency [54]. In this regard, Tl-based class B scintillators have been studied actively in the scientific community, because they can leverage the strength of both intrinsic properties of thallium suitable for the radiation detection and structural merits of *class B* scintillators.

The recently investigated Tl-based *class B* scintillator materials are listed in Table 4. $TlGd_2Cl_7$:Ce (TGC) was introduced by Khan et al. [56], and the Ce^{3+} doping level for the TGC scintillator was optimized as 5% by X-ray-induced emission spectra. The 5% Ce ions doped TGC showed the highest detection performance among the TlL_2X_7 family, indicated by high light yield of 50,000 ph/MeV and reasonable energy resolution of 6.0%. Compared with TlL_2X_7, the family of $Tl_2L_2X_5$ have been demonstrated with better radiation detection performance, i.e., higher light yield, better energy resolution for the gamma-ray, and fast decay time. Khan et al. [59] reported Tl_2LaCl_5:Ce (TLC) with different Ce^{3+} doping levels and obtained excellent light yield of 82,000 ph/MeV, which have been the highest value among all kinds of Tl-based scintillators. They achieved an outstanding energy resolution of 3.3% under gamma-ray of Cs^{137} 662 keV, as described in Fig. 4a, b.

Table 4 The performance of Tl-based class B scintillators interacting with gamma-ray (Cs^{137} 662 keV)

Scintillator	Doping	Energy resolution [%]	Light yield [ph/MeV]	Radioluminescence emission peak [nm]	Decay time [ns]/contribution [%]	PSD FOM	Ref.
$TlGd_2Cl_7$	Ce 1%	7.0	40,000	412	24 (28) 87 (54) 364 (28)	–	[55]
	Ce 5%	6.0	50,000	405	89 (20) 358 (21) 1780 (58)	–	[56]
TlY_2Cl_7	Ce 5%	9.0	38,000	395	95 (48) 422 (36) 1200 (16)	–	[55]
Tl_2LaCl_5	Ce 3%	3.4	76,000	383	36 (89) 217 (11) 1500 (11)	–	[57]
	Ce 3%	3.3	82,000	370 384	–	–	[58, 59]
	Ce 10%	3.2	68,000	378	44 (98)	–	[60, 61]
Tl_2LaBr_5	Ce 1%	2.8	78,000	400	–	–	[60, 61]
	Ce 5%	6.3	43,000	375 415	25 (100)	–	[62]
Tl_2GdCl_5	Ce 5%	5.0	53,000	388	32 (76) 271 (10) 1600 (14)	–	[63, 64]

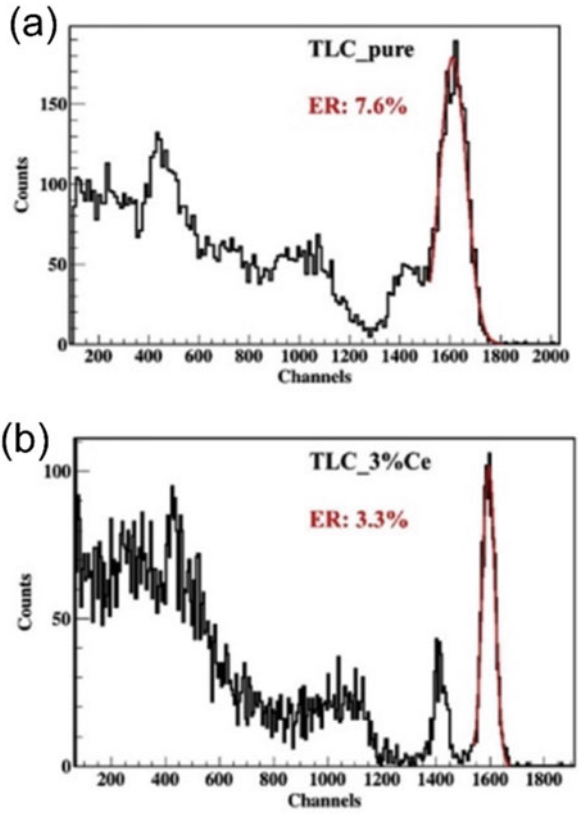


Fig. 4 (**a**) Pulse height spectra of pure Tl_2LaCl_5:Ce scintillator and (**b**) 3% Ce Tl_2LaCl_5:Ce scintillator, which show the 662 keV peak from Cs^{137} gamma-ray source [59]

Other types of Tl-based class B scintillators, such as Tl_3GdCl_6 and Tl_3YCl_6, which belong to the Tl_3LX_6 family, were hard to fabricate and characterize due to their relatively poor crystal quality and opaque nature of polycrystals [55].

3.3 Class C: $TlMX_3$ and TlM_2X_5 with/Without Eu^+ Ion Doping and $TlCdCl_3$ and $TlAlF_4$

Table 5 summarizes a series of recently explored *class C* scintillators. In particular, the results of $TlMX_3$ scintillators, such as $TlMgCl_3$, $TlCdCl_3$, $TlCaCl_3$, and $TlAlF_4$ without any dopants, have been actively reported since 2016. Even though they did not contain any dopants, these scintillators achieved reasonable energy resolution

Table 5 The performance of Tl-based class C scintillators interacting with gamma-ray (Cs^{137} 662 keV)

Scintillator	Doping	Energy resolution [%]	Light yield [ph/MeV]	Radioluminescence emission peak [nm]	Decay time [ns]/contribution [%]	PSD FOM	Ref.
$TlMgCl_3$	None	5.0	46,000	405	60 (25) 350 (75)	–	[65]
$TlCdCl_3$	None	–	2200	450	2.6 (8) 45 (47.8) 170 (45)	–	[66]
$TlCaCl_3$	None	5.0	30,600	425	317 (44) 727 (56)	–	[67]
$TlAlF_4$	None	14.0	11,800	390	194 (13.1) 992 (84.6) 3500 (2.3)	–	[68, 69]
$TlSr_2Br_5$	None	4.6	37,600	441	390 (66) 1900 (34)	–	[70]
$TlSr_2I_5$	Eu 1%	2.8	76,000	383	36 (89) 217 (11) 1500 (11)	–	[71]
	Eu 3%	4.2	72,000	460–470	500 (90)	–	[72]
	Eu 5%	2.6	54,000	420	395 (89%) 2000 (11%)	–	[73]

and light yield for high energy radiation detection [65–69]. Among the TlM_2X_5 scintillator family, $TlSr_2I_5$:Eu (TSI) have shown great potential for gamma-ray detection. As compared with Sr_2I_5:Eu (SI) scintillators, which have shown high light yield and energy resolution to gamma-ray, TSI provides enhanced density (4.5 g/cm^3 to 5.3 g/cm^3) and better linearity between its light yield and the corresponding incident gamma-ray energy [71–73]. TSI scintillator, despite being less developed than SI, has exhibited interesting properties as a gamma-ray detector material for homeland security and high-energy physics. However, self-absorption has been detected from the overlap between the excitation and emission bands of photoluminescence (PL) measurement [72]. This issue needs to be addressed to further develop this class of scintillators.

3.4 Classes D and E: Tl_2BX_6 and $TlPbI_3$

As listed in Table 6, the Tl_2BX_6 scintillator family is one of the emerging Tl-based scintillators and has been explored in many fields, due to the possibility of dual-mode application by PSD and the fast decay time. Tl_2HfCl_6 is considered as a promising candidate scintillator for radiation detection. It offers a relatively good energy resolution and a PSD FOM of 2.6 for alpha-particle and gamma-ray for the discrimination of different types of radiation. Especially, in the case of Tl_2ZrCl_6 scintillator, an energy resolution of 4.3% and a PSD FOM of 3.5 have been achieved for alpha-particle and gamma-ray, which have been among the highest values of the reported Tl-based scintillators. There is little report to study the effects of dopant on Tl_2BX_6 scintillators. To this end, the addition of dopants provides a possibility to improve the performance of *class D* scintillators.

Class E scintillators, as representative as $TlPbI_3$ perovskites, have been investigated for the use of high energy radiation detectors as not only semiconductor but also scintillator. Like other perovskites scintillators, they also have intensive radioluminescence (RL), high sensitivity to X-ray, and fast response/decay time. According to the research by Singh [79] and Du et al. [80], among $TlSnI_3$, $TlGeI_3$, and $TlPbI_3$, $TlPbI_3$ has the most promising properties, and its performances can be facilitated by adding Sn^{2+} activator to the $TlPbI_3$. At this time, there are much less studies regarding Tl-based scintillators compared to other types of classical scintillators. Tl-based scintillators should be further investigated to acquire a deep understanding of their material structure-physical property-scintillator performance correlation for developing the corresponding radiation detection devices.

Table 6 The performance factors of Tl-based class D scintillators interacting with gamma-ray (Cs^{137} 662 keV)

Scintillator	Doping	Energy resolution [%]	Light yield [ph/MeV]	Radioluminescence emission peak [nm]	Decay time [ns]/contribution [%]	PSD FOM	Ref.
Tl_2ZrCl_6	None	5.6	50,800	450–470	696 (−) 2360 (−)	–	[74]
	None	4.3	47,000	468	2700 (−)	3.5(α, γ)	[75, 76]
Tl_2HfCl_6	None	17.7	24,200	465	288 (−) 6340 (−)	–	[77]
	None	4.0	32,000	398	1000 (−)	2.6(α, γ)	[78]
	None	5.0	20,000	425	262 (34)	–	[61]
Tl_2HfBr_6	None	> 5.0	< 20,000	550	22 (99)	–	[61]

References

1. Klann, Raymond T., Jason Shergur, and Gary Mattesich. "Current state of commercial radiation detection equipment for homeland security applications." *Nuclear technology* 168.1 (2009): 79–88.
2. Zentai, George. "X-ray imaging for homeland security." *International Journal of Signal and Imaging Systems Engineering* 3.1 (2010): 13–20.
3. Sordo, Stefano Del, et al. "Progress in the development of CdTe and CdZnTe semiconductor radiation detectors for astrophysical and medical applications." *Sensors* 9.05 (2009): 3491–3526.
4. Lu, Lu, et al. "High energy X-ray radiation sensitive scintillating materials for medical imaging, cancer diagnosis and therapy." *Nano Energy* 79 (2021): 105437.
5. Szeles, Csaba. "CdZnTe and CdTe materials for X-ray and gamma ray radiation detector applications." *physica status solidi (b)* 241.3 (2004): 783–790.
6. Kim, Doup, and Ge Yang. "Perovskite materials: from single crystals to radiation detection." *CrystEngComm* 24.30 (2022): 5383–5399.
7. R. Hofstadter, "Thallium halide crystal counter," *Physical Review*, vol. 72, no. 11. American Physical Society, pp. 1120–1121, 01-Dec-1947.
8. Churilov, Alexei V., et al. "Thallium bromide nuclear radiation detector development." *IEEE Transactions on Nuclear Science* 56.4 (2009): 1875–1881.
9. Farrell, R., et al. "Advances in semiconductor photodetectors for scintillators." *Nuclear Instruments and Methods in Physics Research Section A: Accelerators, Spectrometers, Detectors and Associated Equipment* 387.1-2 (1997): 194–198.
10. Kouznetsov, M. S., et al. "Development of the technology for growing TlBr detector crystals." *Nuclear Instruments and Methods in Physics Research Section A: Accelerators, Spectrometers, Detectors and Associated Equipment* 531.1-2 (2004): 174–180.
11. Zheng, Zhiping, et al. "An effective method for thallium bromide purification and research on crystal properties." *Nuclear Instruments and Methods in Physics Research Section A: Accelerators, Spectrometers, Detectors and Associated Equipment* 676 (2012): 26–31.
12. Jauhar, Ro Mu, et al. "Thermoelectric transport properties in ternary chalcogenide (CuBiSe2) crystal grown by Bridgman-Stockbarger method for thermo-electric applications." *Journal of Crystal Growth* 578 (2022): 126427.
13. Kim, Dong Jin, et al. "Characteristics of TlBr single crystals grown using the vertical Bridgman-Stockbarger method for semiconductor-based radiation detector applications." *Materials Science-Poland* 34.2 (2016): 297–301.
14. Kim, H., et al. "Developing larger TlBr detectors—detector performance." *IEEE Transactions on Nuclear Science* 56.3 (2009): 819–823.
15. Dmitriev, Yuri, et al. "Recent progress in TlBr radiation Detectors." 2006 *IEEE Nuclear Science Symposium Conference Record*. Vol. 6. IEEE, 2006.
16. Hitomi, Keitaro, Toshiyuki Onodera, and Tadayoshi Shoji. "Influence of zone purification process on TlBr crystals for radiation detector fabrication." *Nuclear Instruments and Methods in Physics Research Section A: Accelerators, Spectrometers, Detectors and Associated Equipment* 579.1 (2007): 153–156.
17. Churilov, Alexei V., et al. "TlBr and TlBrxI1− x crystals for γ-ray detectors." *Journal of crystal growth* 312.8 (2010): 1221–1227.
18. Hitomi, Keitaro, et al. "Characterization of pixelated TlBr detectors with Tl electrodes." *Nuclear Instruments and Methods in Physics Research Section A: Accelerators, Spectrometers, Detectors and Associated Equipment* 747 (2014): 7–12.
19. Datta, Amlan, Piotr Becla, and Shariar Motakef. "Large area thallium bromide semiconductor radiation detectors with thallium contacts." *Hard X-Ray, Gamma-Ray, and Neutron Detector Physics XX*. Vol. 10762. SPIE, 2018.
20. Nogami, Mitsuhiro, et al. "Fabrication of Small-Volume Thallium Bromide Gamma-Ray Detectors for High-Intensity Radiation Fields." *Proceedings of the Second International Symposium on Radiation Detectors and Their Uses (ISRD2018)*. 2019.

21. Kim, Hadong, et al. “Thallium bromide gamma-ray spectrometers and pixel arrays.” *Frontiers in Physics* 8 (2020): 55.
22. Kim, H., et al. “Improved performance and longevity of large volume thallium bromide devices.” *Hard X-Ray, Gamma-Ray, and Neutron Detector Physics XXIV*. Vol. 12241. SPIE, 2022.
23. Hitomi, Keitaro, et al. “Thallium bromide optical and radiation detectors for X-and gamma-ray spectroscopy.” *2001 IEEE Nuclear Science Symposium Conference Record (Cat. No. 01CH37310)*. Vol. 4. IEEE, 2001.
24. Datta, Amlan, Piotr Becla, and Shariar Motakef. “Novel electrodes and engineered interfaces for halide-semiconductor radiation detectors.” *Scientific reports* 9.1 (2019): 1–10.
25. B. Dnmez, Z. He, H. Kim, L. J. Cirignano, and K. S. Shah, “The stability of TlBr detectors at low temperature,” *Nucl. Instruments Methods Phys. Res. Sect. A Accel. Spectrometers, Detect. Assoc. Equip.*, vol. 623, no. 3, pp. 1024–1029, Nov. 2010.
26. da Costa, Fábio Eduardo, Carlos Henrique de Mesquita, and Margarida Mizue Hamada. “Temperature dependence in the long-term stability of the TlBr detector.” *IEEE Transactions on Nuclear Science* 56.4 (2009): 1817–1822.
27. Bishop, S. R., et al. “The defect and transport properties of donor doped single crystal TlBr.” *Journal of The Electrochemical Society* 158.2 (2010): J47.
28. Lin, Wenwen, et al. “Inorganic halide perovskitoid TlPbI3 for ionizing radiation detection.” *Advanced Functional Materials* 31.13 (2021): 2006635.
29. Khyzhun, O. Y., et al. “Single crystal growth and electronic structure of TlPbI3.” *Materials Chemistry and Physics* 172 (2016): 165-172.
30. Stoeger, W. “Die Kristallstrukturen von TlPbI3 und Tl4PbI6/The Crystal Structures of TlPbI3 and Tl4PbI6.” *Zeitschrift für Naturforschung B* 32.9 (1977): 975-981.
31. Kocsis, M. “Proposal for a new room temperature X-ray detector-thallium lead iodide.” *IEEE Transactions on Nuclear Science* 47.6 (2000): 1945-1947.
32. Hitomi, Keitaro, et al. “Thallium lead iodide radiation detectors.” *IEEE Transactions on Nuclear Science* 50.4 (2003): 1039-1042.
33. Hany, Ibrahim, et al. “Thallium lead iodide (TlPbI3) single crystal inorganic perovskite: Electrical and optical characterization for gamma radiation detection.” *Materials Science in Semiconductor Processing* 121 (2021): 105392.
34. Kaufman, R. Gilbert, Wayne B. Hadley, and Herbert N. Hersh. “The scintillation mechanism in thallium doped alkali halides.” *IEEE Transactions on Nuclear Science* 17.3 (1970): 82-88.
35. Voronov, A. P., et al. “Influence of thallium doping on scintillation characteristics of mixed KDP/ADP crystals.” *Radiation measurements* 42.4-5 (2007): 553-556.
36. Stand, Luis, et al. “Crystal growth and scintillation properties of pure and Tl-doped Cs3Cu2I5.” *Nuclear Instruments and Methods in Physics Research Section A: Accelerators, Spectrometers, Detectors and Associated Equipment* 991 (2021): 164963.
37. R. S. Woolf, B. F. Phlips, and E. A. Wulf, “Characterization of the internal background for thermal and fast neutron detection with CLLB,” *Nucl. Instruments Methods Phys. Res. Sect. A Accel. Spectrometers, Detect. Assoc. Equip.*, vol. 838, pp. 147–153, Dec. 2016.
38. G. Hull, F. Camera, G. Colombi, M. Josselin, B. Million, and N. Blasi, “Detection properties and internal activity of newly developed La-containing scintillator crystals,” *Nucl. Instruments Methods Phys. Res. Sect. A Accel. Spectrometers, Detect. Assoc. Equip.*, vol. 925, pp. 70–75, May 2019.
39. R. S. Woolf, B. F. Phlips, J. E. Grove, R. J. Murphy, and G. M. Share, “Novel inorganic scintillators for future space-based solar gamma-ray and neutron research,” in *Hard X-Ray, Gamma-Ray, and Neutron Detector Physics XXI*, 2019, vol. 11114, no. 9, p. 7.
40. K. Biswas and M. H. Du, “Energy transport and scintillation of cerium-doped elpasolite Cs 2LiYCl 6: Hybrid density functional calculations,” *Phys. Rev. B – Condens. Matter Mater. Phys.*, vol. 86, no. 1, p. 014102, Jul. 2012.
41. Kim, HongJoo, et al. “Thallium-based heavy inorganic scintillators: recent developments and future perspectives.” *CrystEngComm* 24.3 (2022): 450–464.

42. H. J. Kim, G. Rooh, H. Park, and S. Kim, "Luminescence and scintillation properties of the new Ce-doped Tl2LiGdCl6 single crystals," *J. Lumin.*, vol. 164, pp. 86–89, 2015.
43. H. J. Kim, G. Rooh, H. Park, and S. Kim, "Investigations of scintillation characterization of Ce-activated Tl2LiGdBr6 single crystal," *Radiat. Meas.*, vol. 90, pp. 279–281, 2016.
44. R. Hawrami, E. Ariesanti, L. S. Pandian, J. Glodo, and K. S. Shah, "Tl2LiLaBr6:Ce and Tl2LiYCl6:Ce: New elpasolite scintillators," in *2015 IEEE Nuclear Science Symposium and Medical Imaging Conference, NSS/MIC 2015*, 2016.
45. H. J. Kim, G. Rooh, H. Park, and S. Kim, "Tl2LiYCl6 (Ce3+): New Tl-based Elpasolite Scintillation Material," *IEEE Trans. Nucl. Sci.*, vol. 63, no. 2, pp. 439–442, Apr. 2016.
46. G. Rooh, H. J. Kim, H. Park, and S. Kim, "Crystal growth and scintillation characterizations of Tl2LiYCl6: Ce3+," *J. Cryst. Growth*, vol. 459, pp. 163–166, 2017.
47. R. Hawrami, E. Ariesanti, H. Wei, J. Finkelstein, J. Glodo, and K. Shah, "Tl2LiYCl6: Large Diameter, High Performing Dual Mode Scintillator," *Cryst. Growth Des.*, vol. 17, no. 7, pp. 3960–3964, Jul. 2017.
48. R. Hawrami, E. Ariesanti, L. Soundara-Pandian, J. Glodo, and K. S. Shah, "Tl2LiYCl6:Ce: A New Elpasolite Scintillator," *IEEE Trans. Nucl. Sci.*, vol. 63, no. 6, pp. 2838–2841, Dec. 2016.
49. G. Rooh, H. J. Kim, J. Jang, and S. Kim, "Scintillation characterizations of Tl2LiLuCl6:Ce 3+ single crystal," *J. Lumin.*, vol. 187, pp. 347–351, Jul. 2017.
50. M. J. Kim, H. J. Kim, J. Y. Cho, A. Khan, D. J. Daniel, and G. Rooh, "Characterizations of a New Tl-based Elpasolite Scintillator: Tl2LiScCl6," *J. Korean Phys. Soc.*, vol. 76, no. 8, pp. 706–709, Apr. 2020.
51. M. Arai *et al.*, "Tl2NaYCl6: a new self-activated scintillator possessing an elpasolite structure," *J. Mater. Sci. Mater. Electron.*, pp. 1–7, Feb. 2021.
52. Hawrami, R., E. Ariesanti, and A. Burger. "Characterization of Tl2NaYCl6: Ce scintillation crystals as gamma-ray detectors." *Journal of Crystal Growth* 565 (2021): 126150.
53. E. V.D. Van Loef, P. Dorenbos, C. W. E. Van Eijk, K. Krämer, and H. U. Güdel, "High-energy-resolution scintillator: Ce3+ activated LaBr3," *Appl. Phys. Lett.*, vol. 79, no. 10, pp. 1573–1575, 2001.
54. E. Loef, H. Güdel, P. Dorenbos, K. Kraemer, and C. W. Eijk, "Scintillation properties of LaBr3:Ce3+ crystals: fast, efficient and high-energy-resolution scintillators," *Nucl. Instrum. Methods Phys. Res., A*, vol. 486, pp. 254–258, 2002.
55. E. van Loef *et al.*, "Crystal growth, density functional theory, and scintillation properties of Tl3LnCl6:Ce3+ and TlLn2Cl7:Ce3+ (Ln = Y, Gd)," *Nucl. Instruments Methods Phys. Res. Sect. A Accel. Spectrometers, Detect. Assoc. Equip.*, vol. 995, p. 165047, 2021.
56. A. Khan, G. Rooh, H. J. Kim, and S. Kim, "Scintillation Properties of TlGd2Cl7 (Ce3+) Single Crystal," *IEEE Trans. Nucl. Sci.*, vol. 65, no. 8, pp. 2152–2156, Aug. 2018.
57. R. Hawrami, E. Ariesanti, H. Wei, J. Finkelstein, J. Glodo, and K. S. Shah, "Tl2LaCl5:Ce, high performance scintillator for gamma-ray detectors," *Nucl. Instruments Methods Phys. Res. Sect. A Accel. Spectrometers, Detect. Assoc. Equip.*, vol. 869, pp. 107–109, 2017.
58. H. J. Kim, G. Rooh, and S. Kim, "Tl2LaCl5 (Ce3+): New fast and efficient scintillator for X- and γ-ray detection," *J. Lumin.*, vol. 186, pp. 219–222, 2017.
59. A. Khan, P. Q. Vuong, G. Rooh, H. J. Kim, and S. Kim, "Crystal growth and Ce3+ concentration optimization in Tl2LaCl5: An excellent scintillator for the radiation detection," *J. Alloys Compd.*, vol. 827, 2020.
60. U. Shirwadkar *et al.*, "Thallium-based scintillators for high-resolution gamma-ray spectroscopy: Ce 3+-doped Tl 2 LaCl 5 and Tl 2 LaBr 5," *Nucl. Inst. Methods Phys. Res.*, vol. 962, p. 163684, 2020.
61. E. V van Loef, G. Ciampi, U. Shirwadkar, L. Soundara Pandian, and K. S. Shah, "Crystal growth and scintillation properties of Thallium-based halide scintillators," *J. Cryst. Growth*, vol. 532, 2020.
62. H. J. Kim, G. Rooh, A. Khan, and S. Kim, "New Tl2LaBr5: Ce3+ crystal scintillator for γ-rays detection," *Nucl. Instruments Methods Phys. Res. Sect. A Accel. Spectrometers, Detect. Assoc. Equip.*, vol. 849, pp. 72–75, 2017.

63. A. Khan, G. Rooh, H. J. Kim, and S. Kim, "Ce3+-activated Tl2GdCl5: Novel halide scintillator for X-ray and γ-ray detection," *J. Alloys Compd.*, vol. 741, pp. 878–882, Apr. 2018.
64. G. Rooh, A. Khan, H. J. Kim, H. Park, and S. Kim, "Tl2GdCl5 (Ce3+): A New Efficient Scintillator for X-and γ -Ray Detection," *IEEE Trans. Nucl. Sci.*, vol. 65, no. 8, pp. 2157–2161, Aug. 2018.
65. Y. Fujimoto, M. Koshimizu, T. Yanagida, G. Okada, K. Saeki, and K. Asai, "Thallium magnesium chloride: A high light yield, large effective atomic number, intrinsically activated crystalline scintillator for X-ray and gamma-ray detection," *Jpn. J. Appl. Phys.*, vol. 55, no. 9, p. 090301, Sep. 2016.
66. Y. Fujimoto, K. Saeki, T. Yanagida, M. Koshimizu, and K. Asai, "Luminescence and scintillation properties of TlCdCl3 crystal," *Radiat. Meas.*, vol. 106, pp. 151–154, 2017.
67. A. Khan, G. Rooh, H. J. Kim, H. Park, and S. Kim, "Intrinsically activated TlCaCl3: A new halide scintillator for radiation detection," *Radiat. Meas.*, vol. 107, pp. 115–118, 2017.
68. D. J. Daniel, A. Khan, M. Tyagi, and H. J. Kim, "Scintillation Properties of Tetrafluoroaluminate Crystal," *IEEE Trans. Nucl. Sci.*, vol. 67, no. 6, pp. 898–903, Jun. 2020.
69. D. J. Daniel, J. Cho, H. Won, and H. J. Kim, "TSL kinetic parameters and dosimetric properties of TlAlF4 crystal grown by Bridgman technique," *Opt. Mater. (Amst).*, vol. 111, p. 110636, Jan. 2021.
70. G. Rooh, A. Khan, H. J. Kim, H. Park, and S. Kim, "TlSr2Br5: New intrinsic scintillator for X-ray and γ-ray detection," *Opt. Mater. (Amst).*, vol. 73, pp. 523–526, 2017.
71. L. Soundara Pandian *et al.*, "TlSr2I5:Eu2+- A new high density scintillator for gamma-ray detection," *Nucl. Instruments Methods Phys. Res. Sect. A Accel. Spectrometers, Detect. Assoc. Equip.*, vol. 988, p. 164876, 2021.
72. H. J. Kim, G. Rooh, A. Khan, H. Park, and S. Kim, "Scintillation performance of the TlSr2I5 (Eu2+) single crystal," *Opt. Mater. (Amst).*, vol. 82, pp. 7–10, 2018.
73. R. Hawrami, E. Ariesanti, V. Buliga, and A. Burger, "Thallium strontium iodide: A high efficiency scintillator for gamma-ray detection," *Opt. Mater. (Amst).*, vol. 100, p. 109624, Feb. 2020.
74. Y. Fujimoto, K. Saeki, D. Nakauchi, T. Yanagida, M. Koshimizu, and K. Asai, "New intrinsic scintillator with large effective atomic number: Tl2HfCl6 and Tl2ZrCl6 crystals for x-ray and gamma-ray detections," *Sensors Mater.*, vol. 30, no. 7, pp. 1577–1583, 2018.
75. Q. V. Phan, H. J. Kim, G. Rooh, and S. H. Kim, "Tl2ZrCl6 crystal: Efficient scintillator for X- and γ-ray spectroscopies," *J. Alloys Compd.*, vol. 766, pp. 326–330, 2018.
76. P. Q. Vuong, H. J. Kim, H. Park, G. Rooh, and S. H. Kim, "Pulse shape discrimination study with Tl2ZrCl6 crystal scintillator," *Radiat. Meas.*, vol. 123, pp. 83–87, Apr. 2019.
77. Y. Fujimoto, K. Saeki, D. Nakauchi, T. Yanagida, M. Koshimizu, and K. Asai, "New intrinsic scintillator with large effective atomic number: Tl2HfCl6 and Tl2ZrCl6 crystals for x-ray and gamma-ray detections," *Sensors Mater.*, vol. 30, no. 7, pp. 1577–1583, 2018.
78. P. Q. Vuong, M. Tyagi, S. H. Kim, and H. J. Kim, "Crystal growth of a novel and efficient Tl2HfCl6 scintillator with improved scintillation characteristics," *CrystEngComm*, vol. 21, no. 39, pp. 5898–5904, 2019.
79. Singh, David J. "Electronic structure of TlGeI 3, TlSnI 3, and TlPbI 3: Potential use for spectroscopic radiation detection." *Journal of Applied Physics* 112.8 (2012): 083509.
80. Du, Mao-Hua, Koushik Biswas, and David J. Singh. "Electronic structure, energy transport, and optical properties of halide scintillators." *Hard X-Ray, Gamma-Ray, and Neutron Detector Physics XIV*. Vol. 8507. SPIE, 2012.

Printable Organic and Hybrid Semiconductors: A New Frontier for Detecting Ionizing Radiation



Jessie A. Posar and Matthew J. Griffith

1 Introduction

Ionizing radiation is an extremely powerful and dangerous source of energy. When harnessed safely, the use of ionizing radiation improves our quality of life through applications in medical imaging and treatment and nuclear energy and by enabling high-tech innovations to aid space exploration and national security. However, the rapidly increasing use of radiation in recent decades has correlated to higher radiation exposure in the population, resulting in an increase in harmful health effects to workers and patients. Active monitoring of radiation doses has now become compulsory in many countries to instantaneously detect, evaluate, and correct for any deviations from planned exposure events. Current technologies for detecting ionizing radiation are composed of thick and mechanically rigid solid-state semiconductors, including silicon, selenium, and cadmium telluride; however, these materials are expensive to manufacture and cannot be easily fabricated into flexible or large-area sensing arrays. While such technologies exhibit excellent performance, they cannot satisfy all the demands for real-time monitoring of radiation in complex environments, where materials and devices should ideally be portable, lightweight, flexible, and with low operating power requirements [1]. New hybrid materials must therefore be developed for radiation detection, combining the performance of inorganic semiconductors with these other desirable properties (Fig. 1).

J. A. Posar · M. J. Griffith (✉)
Future Industries Institute, University of South Australia, Mawson Lakes, SA, Australia

Sydney Nano Institute, University of Sydney, Camperdown, NSW, Australia
e-mail: matthew.griffith@unisa.edu.au

© The Author(s), under exclusive license to Springer Nature Switzerland AG 2024

S. Krishnamoorthy, K. (Kris) Iniewski (eds.), *Advances in Fabrication and Investigation of Nanomaterials for Industrial Applications*,
https://doi.org/10.1007/978-3-031-42700-8_14

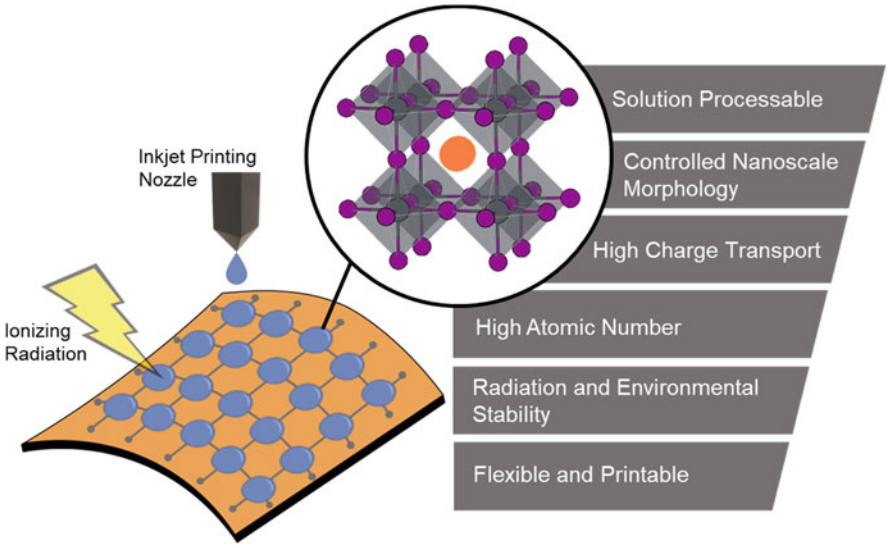


Fig. 1 Schematic summary of material and device properties for scalable direct ionizing radiation detectors. (Figure reproduced with permission from Ref. [1]. Copyright Springer Nature 2023)

Solution-processable alternative materials such as organic semiconductors have attracted substantial recent interest for radiation detection due to the appealing prospect of low-cost processing via industrial-scale printing techniques [2–4]. However, the low atomic number of organic materials results in weak radiation attenuation, and the unique photophysics of organic materials typically results in poor photon-to-electronic conversion performance in comparison to inorganic semiconductors. Accordingly, there has been substantial recent interest devoted to hybrid organic/inorganic metal-halide perovskites. These materials couple the performance benefits of inorganic semiconductors (high atomic number elements for strong radiation attenuation and high mobility-lifetime products for good electrical performance) with the solution state processability of organic semiconductors, thus offering an exciting avenue to achieve low-cost flexible x-ray detectors with high performance [5].

Despite the impressive radiation detection performances that have been achieved with perovskite single-crystal detectors, the research in this arena currently does not exploit one of their most significant advantages: the ability to be printed into flexible detectors with low-cost processing techniques. Significant gaps in performance still exist between perovskite materials and devices fabricated from complex deposition techniques on rigid substrates compared to the same materials deposited onto flexible substrates with innovative printing techniques [6]. To fully unlock the potential of perovskite materials for flexible radiation detection, translation of the precise nanostructures successfully achieved in controlled laboratory environments

to devices fabricated with printing techniques across large areas and demonstration of practical stability of devices in demanding environments is still required.

2 Tuning Perovskite Materials for Radiation Detection

Materials for ionizing radiation detectors must perform three key tasks: (1) efficiently absorb incident radiation, (2) convert this energy into free charge carriers, and (3) output an electrical signal from the free carriers. Metal-halide perovskites are a class of materials of the form ABX_3, where A is a monovalent cation (such as Cs^+ or a small organic molecule), B is a divalent metal cation (usually Pb^{2+}), and X is the halide anion (usually Cl^-, Br^-, or I^-) [7]. The crystal structure of three-dimensional (3D) perovskites can be understood as a network of corner-sharing metal-halide octahedra, as illustrated in Fig. 1 for the aristotype $Pm3^-m$ cubic structure [8]. The material composition defines the probability of different interaction mechanisms for specific radiation sources and energies. During each direct interaction, a certain amount of energy is deposited into the material, termed absorbed dose. Charged particles interact through the Coulomb force, depositing energy along their path as defined by the stopping power $S = -\frac{dE}{dx} \sim NZ$ where NZ is the electron density of the material [9]. Photons can interact by transferring all their energy (photoelectric effect) or only part of their energy (Compton effect or coherent scattering) to the bound electrons of the detecting material [10]. The attenuation coefficient for radiation is shown in Fig. 2 as a function of incident energy, with the inset displaying where the probability of each type of interaction becomes dominant. There is a clear dependence of the attenuation on the energy of the incident photons, E, and the atomic number of the absorbing material, Z. Specifically, the photoelectric effect is dominant for the majority of practical ionizing radiation energies for high-Z materials such as perovskites.

As the interaction probability with ionizing radiation increases exponentially with atomic number, the traditional approach to developing direct radiation detectors is to employ high-Z electronic materials. However, this approach becomes more complex when considering the wide range of demands from modern applications. Wearable and flexible monitoring for dosimetry aims to determine the energy deposited in a target material to measure radiation exposure in real time and thus permit advanced healthcare decisions. However, since the human body is formed mostly of water and carbon, it can be extremely complex to calibrate the energy deposited in a singular high-Z material into the equivalent response for human tissue. The interaction probabilities of detecting materials with ionizing radiation vary with distance from the source, radiation energy, dose rate, temperature, and incident angle, meaning multiple calibration factors are required to convert the signals measured by high-Z materials into the equivalent response from the low-Z human body [12, 13]. Figure 2 compares the energy dependence of silicon ($Z = 14$, $\rho = 2.33$ g/cm^3), which exhibits a sevenfold overresponse, and lead

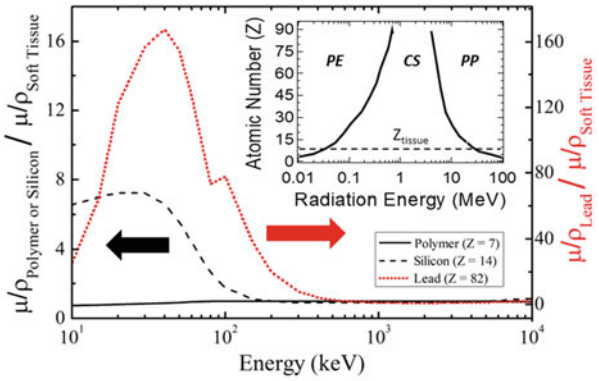


Fig. 2 Attenuation coefficient of materials in radiation detectors polymers (solid black line), silicon (dotted black line), and lead (dotted black line) normalized to soft tissue as a function of energy. The inset displays the interaction type between the incident photons and absorbing material. Data from the National Institute of Standards and Technology (NIST) database [11]. (Figure reproduced with permission from Ref. [1]. Copyright Springer Nature 2023)

($Z = 82$, $\rho = 11.29$ g/cm^3), exhibiting a 170-fold overresponse, for the relatively low energies typical of medical imaging (E < 100 keV) in comparison to the human body when normalized to the higher energies typical of space or radiation therapy (E > 1 MeV). This is advantageous for sensors developed for specifically targeted and narrow energy ranges, for example, x-ray imaging where high-Z materials increase likelihood of the photoelectric effect, improving contrast resolution [14]. However, such environments are not typical in high radiation environments where monitoring or dosimetry is usually required, such as in outer space, medical clinics, or industrial applications of nuclear radiation. Here it is beneficial to use a sensing material with similar Z and ρ to human tissue, targeting a response independent of energy or other beam properties [15].

To accommodate the variation in demands for radiation sensors, a material would exhibit a high interaction probability with incident radiation and target a flat energy response for widespread use in mixed radiation fields and superior electronic performance (defined by the material's ability to convert, transport, and extract free charge carriers) while balancing the ability to be developed using simple fabrication protocols at low manufacturing costs. Ideally, such protocols would have avenues toward pixelated arrays of these small detecting volumes onto a range of flexible substrates to meet the demand for low-cost and lightweight x-ray sensors by acting as a portable and/or wearable electronic for a wide range of applications not limited to personal radiation monitoring (for industries including nuclear energy and space exploration), border security scanning, curved digital x-ray imagers, and in vivo dosimetry.

Many of these requirements for next-gen radiation detectors can be uniquely solved with solution-processable materials. Solution processability allows materials to be combined with a high degree of control to tune the detection properties,

forming new electroactive inks that can be cast onto flexible substrates with a variety of simple deposition techniques at low temperatures [16]. Such inks have been extensively explored in solar cell research for low-cost manufacturing toward industrial-scale roll-to-roll printing techniques. Solution-processable perovskites are a unique class of semiconducting materials that have the potential to maintain crystalline, polycrystalline, or nanocrystal structures during solution-processable fabrication and deposition. The crystalline structure of perovskites facilitates their superior mobility, long carrier lifetimes, high carrier diffusion lengths, and low trap density, and they are recognized as the top-performing solution-processable material in a range of applications. Their high-Z composition results in a high interaction probability with ionizing radiation from extremely thin layers (on the order of hundreds of nanometers), and they exhibit high bandgaps attributed to intrinsically superior radiation tolerance [17]. Accordingly, the material composition, structure, and bandgap of perovskites are key tools that should be considered when tuning detector materials for radiation absorption cross sections that are desirable for specific beam properties, including source type and energy.

3 Printing Perovskite Devices

3.1 Perovskite Film Fabrication Methods

Metal-halide perovskite films can be fabricated into large-scale arrays on flexible substrates using low-cost printing and coating. Accordingly, numerous deposition techniques have been developed over the years, each targeting unique advantages in the control of various parameters such as uniform thin-film deposition, uniform thick layers, or tunable layer thickness by controlling the deposition parameters. At the heart of each technique is the challenge to translate the exquisite control of film nanostructure that can be obtained at the laboratory scale with spin coating in inert environments through to open atmosphere solution printing and coating techniques [16, 18]. In addition to this challenge, the need to develop new methods that can upscale materials, fabrication, and assessment tools must be simultaneously solved, which has proven to be a longstanding challenge in the fabrication of photodiodes from printable semiconductors [19–22].

3.2 Printing Techniques

3.2.1 Spray Coating

The spray coating technique has been widely applied in organic photovoltaic and metal oxide thin-film deposition and provides a promising pathway for low-cost scalable perovskite film fabrication. The spray coating system operates via a two-

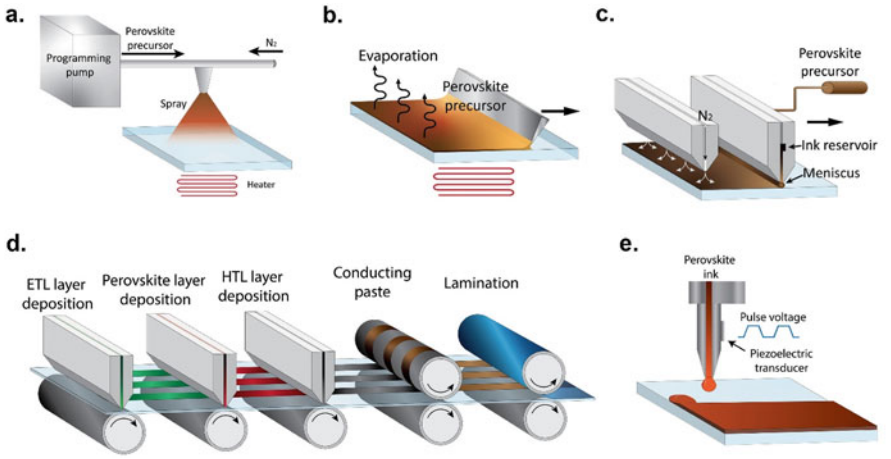


Fig. 3 The illustrations of different printing techniques, (**a**) spray coating, (**b**) blade coating, (**c**) slot-die printing, (**d**) roll-to-roll printing, and (**e**) inkjet printing, for perovskite film fabrication

step procedure, which includes atomizing and deposition systems as shown in Fig. 3a. Spray-coated perovskite x-ray detectors have exhibited thicknesses from 10 to 100 μm, and recently unique in situ deposition reached large areas above 10×10 cm^2 [23–25]. A significant advantage of this technique is that the bottom-up crystal growth process results in compact columnar grains with limited grain boundaries in the direction of charge collection, enabling improved charge transport and collection in radiation detection devices [26, 27]. Spray coating is emerging as a powerful process for next-generation industrial-scale translation of perovskite technologies due to its ability to produce uniform, thick, and large-area films from a wide range of materials, including 3D ($CsPbI_2Br$ and $MAPbI_3$), 2D [$(PEA)_2PbI_4$], quasi-2D [$(PEA)_2MA_3Pb_4I_{13}$], and 0D ($Cs_3Sb_2I_9$) perovskites [24, 28].

3.2.2 Doctor-Blade Coating

Doctor blading is a simple, cheap, and versatile continuous fabrication technique that has been applied extensively to the fabrication of perovskite films for photodiode detectors. This technique operates by spreading the precursor solution across the substrate with a blade, which can be moved at various speeds to control the thickness of the subsequent films. Typically doctor blading is suited to highly viscous films and thus has been most frequently applied to fabricating thick active layer films (500 μm–1 mm) that are used for high attenuation direct radiation detectors [29]. Following film deposition, a heating process is applied to evaporate the solvent and construct a uniform film with the desired nanostructure, as shown in Fig. 3b. While doctor blading has been shown to synthesize devices with areas over 10 cm^2 [30], the blade-coated layer can often incorporate significant porosity due

to solvent evaporation from a thick film, which in turn limits both the attenuation of x-rays and the strength of adhesion of subsequent layers [31]. Attempts to address these limitations include a soft-pressing posttreatment of doctor-bladed perovskite films used to make a TFT array to remove porosity and improve the dark current and device signal-to-noise ratio [32]. The technique has also been used recently to fabricate a series of low-dimensional perovskite materials, including 2D $(PEA)_2MA_8Pb_9I_{28}$ and the 0D material $MA_3Bi_2I_9$, with results indicating a significant reduction in the device dark current due to a suppression of ion migration [33, 34].

3.2.3 Slot-Die Coating

The ability of slot-die coating to create large-area devices has been widely demonstrated in the scalable fabrication of perovskite photovoltaic devices [35, 36]. This method involves containing the perovskite precursor ink inside a pressurized vessel, with a pump used to force ink out of this reservoir through a thin customized slit onto a moving substrate. The film thickness and lateral dimensions are controlled by the pump pressure and reservoir exit slits, respectively. This technique is a highly promising translation toward roll-to-roll printing given the ability to couple the coating procedure with a moving substrate, with previous research on printable photodiodes providing a rich suite of information on the ability to obtain constant uniform ink flow by adjusting the angle of the ink reservoir, solution pumping velocity, flow rate, and substrate pre-wetting [37, 38]. However, unlike doctor blading, the wet film thickness is determined by the flow rate instead of the gap height. Thus, it is crucial to have a continuous meniscus for high-quality perovskite film.

3.2.4 Inkjet Printing

Inkjet printing is a high-resolution digital printing technique based on drop-on-demand transfer of picoliters of material onto a substrate in an extremely material-efficient and contactless deposition procedure [39, 40]. A typical inkjet printing process is shown in Fig. 3e. This method can be divided into drop-on-demand (DOD), continuous inkjet (CIJ), and field- or flow-induced tip streaming (FITS) techniques [41]. The DOD printer is the most advanced technology widely used for large-area perovskite thin-film fabrication. The small volume of delivered droplets has seen this technique find strong benefits in low-temperature (<100 °C) perovskite thin-film deposition process on a flexible substrate for high-performance x-ray detectors [42–44]. Furthermore, the ability of inkjet printing to achieve mask-free patterned perovskite deposition has strong potential to create complex device architectures such as folded perovskite x-ray detectors, as recently proposed [45].

3.2.5 Roll-to-Roll Printing

A particularly attractive route for processing perovskite films with large areas at low cost is to couple the printing and coating techniques described above with high-throughput roll-to-roll (R2R) fabrication [46]. Recently, gravure [47], doctor blading [48], and slot-die coating [49] methods have been applied in roll-to-roll printing to fabricate perovskite photodetector devices. In principle, the addition of R2R capabilities to solution processing is simple, consisting of a motorized substrate control with an unwinder reel that feeds the flexible substrate through the printing or coating station and a rewinder reel that collects the substrate on another reel. In the middle of these two reels, several printing or coating units can be mounted, as shown in Fig. 3d. However, in practice there are a substantial number of challenges that must be solved to enable full R2R fabrication of perovskite films. These include the alteration of thickness of the layers that is introduced by parameters in the R2R system, such as the velocity the substrate is fed and its relationship with the printing or coating solution flow rate [50]. Additionally, the tension of the flexible substrate created by the winding and unwinding reels can influence the interactions between the substrate and the solution as it is deposited, which has a corresponding effect on the uniformity and thickness of the deposited layer [51]. Perhaps one of the larger practical challenges of R2R techniques is the trade-off between speed of substrate movement and the effective drying time required to cure the perovskite film. If the substrate moves too slowly, then layer deposition becomes uncontrollably thick; however, if it moves too rapidly, then the films transit the drying stations too quickly to dry before reaching the rewinder reel [52].

3.3 Challenges for Printable and Flexible Metal-Halide Perovskite Films

Despite steady research progress on materials and device performance at the laboratory scale, long-term durability concerns, toxicity issues of both materials and manufacturing process, and a lack of robust high-throughput production technology for fabricating efficient large-area modules remain major obstacles toward commercialization of these materials using industrial-scale solution processing techniques [53].

The significant stability issues currently facing conventional lab-scale fabrication of perovskite materials including thermal, oxygen, and moisture exposure will remain problematic and likely become more difficult to overcome when upscaling due to the limited control levers available during printing deposition [54]. Therefore, stability studies on large-area devices will need to be extensively explored and understood. Moreover, the printing industry is currently focused on transitioning away from the toxic chemical solvents in which many perovskite inks are currently formulated, in particular halogenated organic solvents, for greener manufacturing

processes [55–57]. A substantial materials challenge for solution-processable perovskites will be their suspension in greener solvents while maintaining desirable nanoscale morphologies once deposited with high device efficiencies.

On the manufacturing side of the equation, although an enormous number of high-performance perovskite systems continue to be developed in the laboratory, the major restriction on transitioning these materials to low-cost and large-area devices remains an inability to control the precise film nanoscale using these printing and coating techniques [31]. This can lead to inhomogeneous crystallization across the large-area perovskite film resulting in poor charge transport properties [58]. Large-area perovskite films also suffer from an increase in series resistance [59], requiring new device designs to be explored including isolated pixels, subcells, or metal grids [53].

4 Printable Metal-Halide Perovskites for Radiation Detection

The application of printable materials such as perovskites for radiation detection has gained significant momentum in recent years [2, 31]. The impacts of ionizing radiation on perovskite devices, both in terms of performance (sensitivity) and stability (radiation hardness), are key parameters that have been the focus of recent characterization efforts. This behavior is particularly dependent on photon energy, though most studies to date have focused on the performance of perovskite radiation detectors at low energy. However, due to the emerging applications in both space and advanced medical treatment protocols, the high-energy regime is beginning to attract significance in the development of novel materials for x-ray detection [60, 61]. In this section we will discuss breakthroughs in printed perovskite radiation detector performance. Those seeking a more detailed review of stability considerations are directed to recent exhaustive reviews elsewhere [1, 62].

Radiation detection capabilities of perovskites have focused on harnessing the excellent carrier mobility and high Z of thick single-crystal perovskites to maximize their absorption and detection performance. The highest radiation sensitivity reported to date was 1.22×10^5 μCGy^{-1} cm^{-2}, demonstrated for an 800 μm-thick $MAPbI_3$ wafer at an operational voltage of 10 V [63]. Ultralow detectable dose rate limits have also been demonstrated with perovskites as low as 7.6 $nGys^{-1}$ with a 2 mm-thick Cl-doped $MAPbBr_3$ single crystal at -5 V; however there is some ongoing contention regarding the correct processes for determination of the detection limit [64, 65]. However, perovskite single crystals are mechanically rigid and require complex and expensive synthesis procedures that include high-vacuum deposition techniques that do not translate to low-cost and large-area production onto flexible substrates. In the remainder of this section, we will focus on solution-processable perovskites as an innovative solution to combine high-performance radiation sensing with large-area and flexible electronics. To evaluate the potential

of these materials, we will expand the figures of merits from radiation sensitivity and detection limit to include flexibility, printability, and operational voltage.

The first solution-processed perovskite photodiode for x-ray detection was achieved by spin coating four layers onto ITO-coated glass, with the perovskite sandwiched between charge-selective interlayers to form a p-i-n diode structure from the materials PEDOT:PSS/$MAPbI_3$/PCBM/ZnO/Ag [23]. Three different perovskite layer thicknesses were chosen for this study, 260 nm, 360 nm, and 600 nm. The 600 nm-thick device demonstrated a competitive sensitivity of 25×10^3 μCGy^{-1} cm^{-3} (or 1.5 μCGy^{-1} cm^{-2}) at short circuit from a radiation source generated at 75 kVp (<E > ~ 37 keV). Recent work has explored how the material composition of the perovskite layer can be optimized to improve the detection performance. Basiricò et al. demonstrated that Cs mixed triple-cation perovskites $Cs_{0.05}FA_{0.79}MA_{0.1}Pb(I_{0.8}\ Br_{0.2})_3$ increased the sensitivity to 3.7 μCGy^{-1} cm^{-2} at short circuit and 97 μCGy^{-1} cm^{-2} with a small operational voltage of −0.4 V [66]. The enhanced sensitivity was suggested to be due to differences in the charge transport and collection properties of the perovskite layer including an increase in grain size from 60 nm for $MAPbI_3$ to 200 nm as shown in Fig. 4a, a longer carrier lifetime, and a decrease in the nonradiative surface defects, with no differences observed for the radiation absorption properties of the two films. The perovskite film thickness in this study was tuned to 450 nm, suggesting that while thicker films can absorb a higher percentage of incident ionizing radiation, they significantly reduce the charge collection and transport within the bulk of the film. This is likely due to poor crystallinity of the thicker films during spin coating deposition compared to single-crystal synthesis [67]. Bruzzi et al. presented the first investigation of drop-cast $CsPbBr_3$ films for medical applications as illustrated in Fig. 4b. This work demonstrated clinically acceptable reconstruction (within 5%) of the dose profile across the treatment field [68]. The authors showed that perovskites are capable of theoretically superior radiation sensitivities compared to materials found in commercial radiation sensors (e.g., silicon and diamond) due to their high density and low ionization energy (lower energy loss when creating electron-hole pairs). However, experimentally the drop-cast perovskite film sensitivity was significantly lower, with per unit area value of 1.4 μCGy^{-1} cm^{-2} reported for 6 MV photons. The sensitivity was 15-fold higher for single-crystal perovskite films prepared with the same device architecture and tested in the same conditions, suggesting drop-cast films form highly disordered structures [71]. It is clear from both spin-coated and drop-cast perovskite films studied for radiation sensing that lab-scale solution-processed deposition techniques result in poor film morphology and reduced charge transport properties compared to single crystals. Novel strategies to increase film morphology and crystallization of spin-coated or drop-cast films have recently been explored, including dissolution-recrystallization [72] and intermittent or two-step spin coating methods [67, 73] that may be advantageous for radiation sensing, especially when thicker films are desired to absorb a higher percentage of incident ionizing radiation. Low-dimensional perovskites have also been explored for radiation sensing, which may also mitigate the crystallinity issues of spin-coated or drop-cast layers [74]. A recent study demonstrated 2D PEA_2PbBr_3

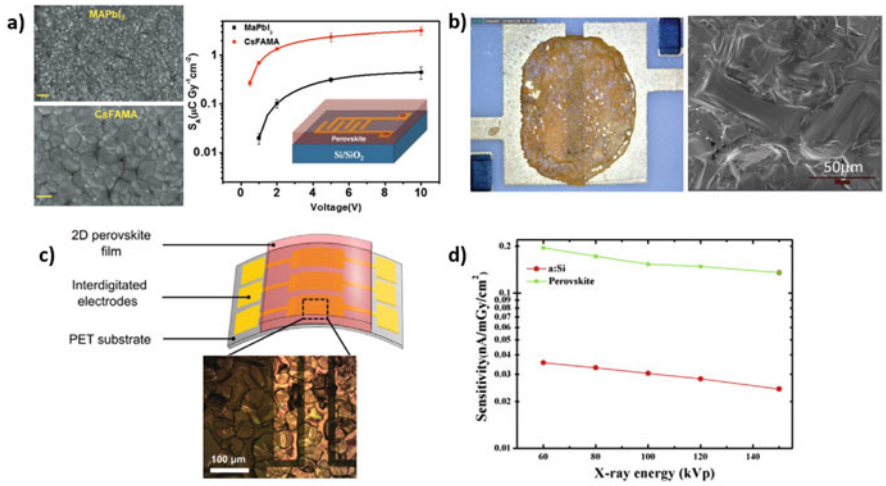


Fig. 4 Small-scale deposition of solution-processable perovskites for radiation sensing. (**a**) Comparison of spin-coated deposition of triple-cation CsFAMA perovskite and $MAPbI_3$ showing differences in the gain sizes (SEM on LHS) and radiation sensitivity (RHS) to a 35 kV Mo source. Reproduced from Ref. [66] with permission from Copyright © 2019 WILEY-VCH Verlag GmbH & Co. KGaA, Weinheim. (**b**) Picture (LHS) and SEM image (RHS) of a drop-cast $CsPbBr_3$ film developed for clinical radiation treatment applications. Reproduced from Ref. [68] under a CC-BY 4.0 Copyright © 2022 AIP Publishing LLC. (**c**) Schematic (top) and microscope image (bottom) of a novel 2D PEA_2PbBr_4 perovskite demonstrating microcrystalline film morphology after spin coating deposition. Reproduced from Ref. [69] under a CC-BY Copyright © 2021 to Wiley-VCH GmbH. d) Energy response of a 270 nm-thick spin-coated $MAPbI_2Cl$ photovoltaic device from a tungsten-rhenium target compared to amorphous silicon. Reproduced from Ref. [70] under a CC BY 4.0

($PEA = C_6H_5C_2H_4NH_3^+$) formed microcrystalline films after standard spin coating deposition onto flexible PET substrates, as shown in Fig. 4c [69]. The crystalline form led to a high radiation sensitivity of 806 μCGy^{-1} cm^{-2} and an ultralow detection limit of 42 $nGys^{-1}$ at 150 kVp using a 1.9 μm-thick layer. The device was deposited onto flexible PET, demonstrating promising capacity to confirm to complex contours; however, the detector was biased with a high operational voltage of 80 V, requiring a large power source which raises safety concerns for wearable electronics.

Throughout the literature, only the theoretical x-ray mass attenuation coefficients across a wide energy range have been referenced to demonstrate superior absorption qualities of high-Z materials in perovskite films. It would be valuable to experimentally determine the energy dependence of a range of perovskite materials to use as a guide to develop a device that exhibits a flat response across a desired energy range as achieved with other novel sensing materials [75]. One study presented an order of magnitude increase in the sensitivity between an x-ray source accelerated at 40 kVp and 150 kVp, respectively, for a 10 μm-thick $MAPbI_3$ film as shown in Fig. 4c. This work confirms a strong energy dependence for perovskite materials in the

low-energy (10–200 keV) regime [76]. Another study compared the response of a 270 nm-thick $MAPbI_2Cl$ between 60 kVp and 150 kVp [70]. Figure 4d shows that the response of this device follows a similar shape to amorphous silicon, suggesting that if similar overresponse issues occur when compared to high x-ray energies, further consideration of the material composition of perovskite films will need to be adjusted to flatten out the energy response across a desired range.

Scalable deposition techniques have become gradually more studied for perovskite radiation sensors for large-area imaging. The first method in 2015 spray coated $MAPbI_3$ onto glass substrates with interdigitated electrodes in a photoconductor device configuration [23]. Spray coating allows thicker films (10–100 μm) to be deposited as uniform films compared to spin coating. A 60 μm-thick single-element (non-pixelated) perovskite photoconductor demonstrated well-resolved images when scanned across the x-y plane of the field at a 40 V operational voltage, with the resolution limited to the size of the single cell. For thicker films, large grain sizes in the polycrystalline structures must be fabricated to ensure printed perovskite films function efficiently. Kim et al. demonstrated that printed $MAPbI_3$ films as thick as 830 μm with an average grain size of 30 μm fabricated via doctor blading exhibited optoelectronic characteristics approaching that of single crystals, with a $\mu\tau$ product of 1×10^{-4} cm^2V^{-1} [29]. The article optimized the perovskite detector by adding additional layers between the contacts (polyimide perovskite composites) to lower the dark current and thus increase the signal-to-noise ratio for high-quality x-ray imaging when coupled with a rigid TFT backplane. A single-cell detector was capable of sensitivities as high as 11×10^3 μCGy^{-1} cm^{-2} from an 830 μm-thick film; however the device required a large operational bias of 200 V. The sensitivity of the pixelated device was lower than the single cell, reaching 3.8×10^3 μCGy^{-1} cm^{-2}. This reduced performance for the pixelated device was suggested by the authors to result from incomplete charge collection in the gaps between the pixels, imperfect device contacts, and insufficient applied bias. In recent years, Qian and colleagues have fabricated a 6×6 64 mm^2 pixelated in situ spray-coated $CsPbI_2Br$ 40 μm-thick x-ray detector. The sensitivity from a 50 kV x-ray source was ~1.48×10^5 μCGy_{air}^{-1} cm^{-2} with a dose rate limit of 280 $nGys^{-1}$ at a low operational voltage of 5 V [24].

Solution-processable perovskites can also be deposited onto flexible substrates, opening avenues toward wearable technology. Ciavatti et al. deposited $MAPbI_3$ nanocrystals onto PEN by doctor-blading multiple layers on top of the previous film to sequentially maximize the perovskite layer thickness for high x-ray attenuation while maintaining high uniformity for efficient charge transport [76]. To further improve the optoelectronic performance, PCBM was added on top of the perovskite layer to fill the gaps in the porous film and passivate any surface traps. The flexible single cell exhibited a good performance up to an active layer thickness of 10 μm, with sensitivities of 494 μCGy^{-1} cm^{-2} from a 150 kVp x-ray source at an operational voltage of 4 V as shown in Fig. 5b. Thicker films exhibited high resistivity and electrical instability, unable to extract charges at the electrodes across the large bulk film with extremely large dark currents above 2 V. The sensitivity was 3.5 times smaller than the same devices on glass substrates, and

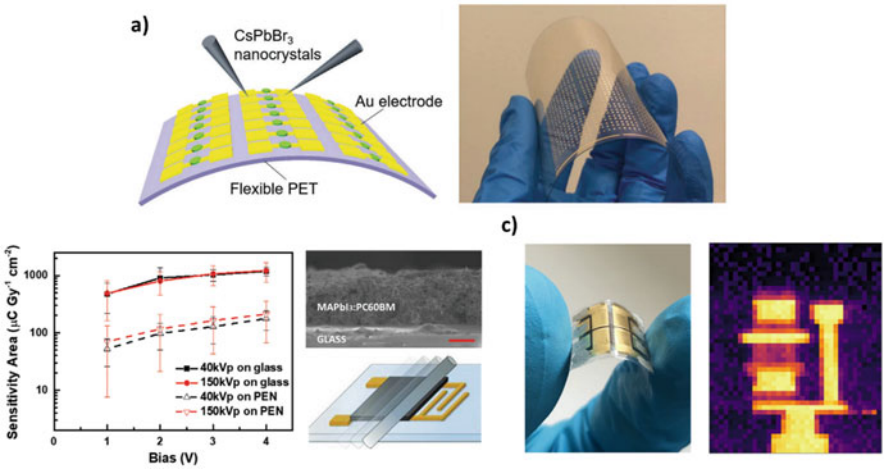


Fig. 5 Scalable deposition techniques solution-processable perovskites for radiation sensing. (**a**) Schematic (LHS) and picture (RHS) of an inkjet-printed array of $CsPbBr_3$ quantum dots deposited onto a flexible substrate. Reproduced from Ref. [42] with permission from Copyright © 2019 WILEY-VCH Verlag GmbH & Co. KGaA, Weinheim. (**b**) Highly uniform $MAPbI_3$ film (SEM image top RHS) via blade coating deposition (schematic bottom RHS). The image on the LHS presents the sensitivity at two radiation energies (40 kVp and 150 kVp) for substrates deposited onto glass and flexible PEN. Reproduced from Ref. [76] with permission from Copyright © 2021 WILEY-VCH Verlag GmbH & Co. KGaA, Weinheim. (**c**) Flexible inkjet-printed triple-cation $CsFAMAPb(BrI)_3$ perovskite (LHS) used to image a pneumatic connector with a single pixel under 70 kVp x-ray radiation. Reproduced from Ref. [43] with permission from Copyright © 2020 American Chemical Society

there was a significant variation in the x-ray performance across all ten flexible devices, suggesting instability and reproducibility issues need to be addressed during fabrication. Bending cycles at a radius of 0.63 mm resulted in a larger dark current after the first bend; however it remained stable with subsequent bending. Furthermore, the sensitivity remained constant in these mechanical robustness tests, a promising result suggesting steady x-ray performance can be achieved in monitoring devices for wearable electronics. Perovskite x-ray detectors have also been doctor-bladed onto a flexible pressure-sensitive air-dielectric IGZO TFT backplane for innovative two-sensing modalities [77]. Guanidinium-doped $MAPbI_3$ was chosen as the x-ray sensing layer for its higher environmental stability, and the authors suggested its increased charge carrier lifetime will also benefit x-ray detection [78]. The sensitivity to 50 kV x-rays was 6.74×10^3 μCGy^{-1} cm^{-2} at 30 V. A thick 300 μm perovskite film was used; however it demonstrated excellent stability to bending after 2000 cycles, suggesting thicker films can be used for flexible sensors.

Inkjet printing has been explored for larger-area flexible perovskite x-ray detectors due to its high spatial deposition control and compatibility with roll-to-roll printing for industrial translation. Mescher et al. demonstrated an inkjet-

printed single-cell triple-cation perovskite $Cs_{0.1}(FA_{0.83}MA_{0.17})_{0.9}Pb(Br_{0.17}I_{0.83})_3$ could achieve sensitivities as high as 59.9 μCGy^{-1} cm^{-2} with a detection limit of 12 μGy/s to a 70 kVp x-ray source at a low operational voltage of 0.1 V, suggesting safe use for wearable electronics [43]. The flexible device was scanned under a metal pneumatic connector showing a clear x-ray image (Fig. 5c). A triple-cation perovskite was chosen for translation to large-area printing due to their improved air stability, reproducibility, and high x-ray performances when spin coated [66, 79]. The device exhibited high reproducibility after multiple bending cycles, stable down to a radius of 6 mm with a slight change after bending around a high radius of 3 mm. However, significant variation in the x-ray performance across 46 different devices was detected compared to analogous devices deposited onto glass. Pixelated and flexible perovskite x-ray detectors have also been realized with inkjet printing. Lui et al. developed a pixelated perovskite device (Fig. 5a) from an extremely thin (~20 nm) film of $CsPbBr_3$ quantum dots, which reached a high sensitivity per unit area of 17.7 μCGy^{-1} cm^{-2} when inkjet-printed onto PET under synchrotron x-rays between 0.1 keV and 2.5 keV with a low operational bias of 0.1 V [42]. The flexible device was also bent up to an angle of 120°, exhibiting a 25% reduction in the device current. The sensitivity of the flexible device was lower than achieved for a rigid substrate under the same conditions at 83 μCGy^{-1} cm^{-2}. The ability to pixelate perovskite x-ray sensors while maintaining extremely high x-ray sensitivities from ultrathin and flexible active layers is an exciting development that is at this stage unique among the high-Z absorbing materials used for radiation detection.

5 Future Outlook

Extensive research efforts in perovskite photodetector materials have seen a recent transition to the application radiation detectors. Increasing exposure to high levels of radiation from emerging applications in space, personal dosimetry, and medicine has led to a drive for more efficient and low-cost materials capable of monitoring and measuring these increased radiation doses. In this chapter we have described the key materials physics of perovskites under ionizing radiation beams, discussing first the materials innovations to improve detector performance and then outlining the key printing and coating techniques that can translate these materials to industrially relevant devices before finishing with an overview of the status of solution-processed radiation detection devices.

Although these materials exhibit excellent performance and have shown some compatibility with R2R printing and coating techniques, a considerable gap remains with respect to optimizing material performance and nanostructure with large-scale fabrication techniques. Controlling the nanoscale morphology of perovskite films has been shown to be essential in the creation of high-performance radiation detectors, with substantial further work required in order to translate the high-precision laboratory fabrication procedures into the large-scale printed fabrication arena where the length scales rapidly increase and temperature, atmospheric

composition, and other similar variables become far less controlled. Unlocking new printing fabrication procedures for these solution-processable perovskite materials provides an avenue toward upscaled low-cost manufacture of radiation detectors using roll-to-roll machinery, which is an exciting prospect for future industrial translation of these technologies.

References

1. Posar, J. A., Liao, C., Tegg, L., Ho-Baillie, A., Petasecca, M., Griffith, M. J. (2023)., in *Metal-Halide Perovskite Semiconductors* (Eds.: W. Nie, K. Iniewski), Springer Nature pp. 141.
2. Griffith, M. J., Cottam, S., Stamenkovic, J., Posar, J. A., Petasecca, M., (2020). *Frontiers in Physics*, *8*.
3. Posar, J. A., Davis, J., Alnaghy, S., Wilkinson, D., Cottam, S., Lee, D. M., Thompson, K. L., Holmes, N. P., Barr, M., Fahy, A., Nicolaidis, N. C., Louie, F., Fraboni, B., Sellin, P. J., Lerch, M. L. F., Rosenfeld, A. B., Petasecca, M., Griffith, M. J., (2021). *Advanced Materials Technologies*, *6*, 2001298.
4. Large, M. J., Posar, J. A., Mozer, A. J., Nattestad, A., Alnaghy, S., Carolan, M., Sellin, P. J., Davies, J., Pastuovic, Z., Lerch, M. L. F., Guatelli, S., Rosenfeld, A. B., Griffith, M. J., Petasecca, M., (2021). *ACS Applied Materials and Interfaces*.
5. Wei, H., Huang, J., (2019). *Nature communications*, *10*, 1066.
6. Basiricò, L., Ciavatti, A., Fraboni, B., (2021). *Advanced Materials Technologies*, *6*, 2000475.
7. Zhao, Y., Zhu, K., (2016). *Chemical Society Reviews*, *45*, 655.
8. Kim, T. W., Park, N.-G., (2020). *Materials Today*, *38*, 67.
9. Attix, F. H. (1986), *Introduction to radiological physics and radiation dosimetry*, Wiley, New York.
10. Knoll, G. F. (2010). *Radiation detection and measurement*, 4th ed., John Wiley, Hoboken, N.J.
11. Hubbell, J. H., Seltzer, S. M. (2004). Radiation Physics Division, PML, NIST.
12. De Martin, E., Alhujaili, S., Fumagalli, M. L., Ghielmetti, F., Marchetti, M., Gallo, P., Aquino, D., Padelli, F., Davis, J., Alnaghy, S., Carrara, M., Fariselli, L., Rosenfeld, A. B., Petasecca, M., (2021). *Physica Medica*, *89*, 20.
13. Fidanzio, A., Azario, L., Miceli, R., Russo, A., Piermattei, A., (2000). *Medical Physics*, *27*, 2589.
14. Martin, C., (2007). *Biomedical Imaging and Intervention Journal*, *3*, e38.
15. Posar, J. A., Davis, J., Brace, O., Sellin, P., Griffith, M. J., Dhez, O., Wilkinson, D., Lerch, M. L. F., Rosenfeld, A., Petasecca, M., (2020). *Physics and Imaging in Radiation Oncology*, *14*, 48.
16. Griffith, M. J., Holmes, N. P., Elkington, D. C., Cottam, S., Stamenkovic, J., Kilcoyne, A. L. D., Andersen, T. R., (2019). *Nanotechnology*, *31*, 92002.
17. Klein, C. A., (1968). *Journal of Applied Physics*, *39*, 2029.
18. Carlé, J. E., Helgesen, M., Madsen, M. V., Bundgaard, E., Krebs, F. C., (2014). *Journal of materials chemistry. C, Materials for Optical and Electronic Devices*, *2*, 1290.
19. Cooling, N. A., Barnes, E. F., Almyahi, F., Feron, K., Al-Mudhaffer, M. F., Al-Ahmad, A., Vaughan, B., Andersen, T. R., Griffith, M. J., Hart, A. S., Lyons, A. G., Belcher, W. J., Dastoor, P. C., (2016). *Journal of Materials Chemistry. A, 4*, 10274.
20. Griffith, M. J., Cooling, N. A., Vaughan, B., O'Donnell, K. M., Al-Mudhaffer, M. F., Al-Ahmad, A., Noori, M., Almyahi, F., Belcher, W. J., Dastoor, P. C., (2015). *Energy Technology*, *3*, 428.
21. Al-Ahmad, A. Y., Almayhi, F., Al-Mudhaffer, M. F., Griffith, M. J., Liu, W., Li, S., Sivunova, K., Elkington, D., Cooling, N. A., Feron, K., Shi, M., Belcher, W., Chen, H., Dastoor, P., Andersen, T. R., (2020). *Sustainable Energy and Fuels*, *4*, 94.

22. Carlé, J. E., Helgesen, M., Hagemann, O., Hösel, M., Heckler, I. M., Bundgaard, E., Gevorgyan, S. A., Søndergaard, R. R., Jørgensen, M., García-Valverde, R., Chaouki-Almagro, S., Villarejo, J. A., Krebs, F. C., (2017). *Joule*, *1*, 274.
23. Yakunin, S., Sytnyk, M., Kriegner, D., Shrestha, S., Richter, M., Matt, G. J., Azimi, H., Brabec, C. J., Stangl, J., Kovalenko, M. V., Heiss, W., (2015). *Nature Photonics*, *9*, 444.
24. Qian, W., Xu, X., Wang, J., Xu, Y., Chen, J., Ge, Y., Chen, J., Xiao, S., Yang, S., (2021). *Matter*, *4*, 942.
25. Haruta, Y., Ikenoue, T., Miyake, M., Hirato, T., (2020). *MRS Advances*, *5*, 395.
26. Haruta, Y., Ikenoue, T., Miyake, M., Hirato, T., (2019). *Applied Physics Express*, *12*.
27. Haruta, Y., Wada, S., Ikenoue, T., Miyake, M., Hirato, T., (2021). *Crystal Growth & Design*, *21*, 4030.
28. Xu, X., Qian, W., Wang, J., Yang, J., Chen, J., Xiao, S., Ge, Y., Yang, S., (2021). *Advanced Science*, *8*, 2102730.
29. Kim, Y. C., Kim, K. H., Son, D.-Y., Jeong, D.-N., Seo, J.-Y., Choi, Y. S., Han, I. T., Lee, S. Y., Park, N.-G., (2017). *Nature*, *550*, 87.
30. Deng, Y., Peng, E., Shao, Y., Xiao, Z., Dong, Q., Huang, J., (2015). *Energy and Environmental Science*, *8*, 1544.
31. Haruta, Y., Kawakami, M., Nakano, Y., Kundu, S., Wada, S., Ikenoue, T., Miyake, M., Hirato, T., Saidaminov, M. I., (2022). *Chemistry of Materials*, *34*, 5323.
32. Xia, M., Song, Z., Wu, H., Du, X., He, X., Pang, J., Luo, H., Jin, L., Li, G., Niu, G., Tang, J., (2022). *Advanced Functional Materials*, *32*, 2110729.
33. Dong, S., Xin, D., Zhang, M., Tie, S., Cai, B., Ma, Q., Zheng, X., (2022). *Journal of materials chemistry. C, Materials for Optical and Electronic Devices*, *10*, 6236.
34. He, X., Xia, M., Wu, H., Du, X., Song, Z., Zhao, S., Chen, X., Niu, G., Tang, J., (2022). *Advanced Functional Materials*, *32*, 2109458.
35. Huang, S. H., Guan, C. K., Lee, P. H., Huang, H. C., Li, C. F., Huang, Y. C., Su, W. F., (2020). *Advanced Energy Materials*, *10*, 2001567.
36. Li, J., Dagar, J., Shargaieva, O., Flatken, M. A., Köbler, H., Fenske, M., Schultz, C., Stegemann, B., Just, J., Többens, D. M., Abate, A., Munir, R., Unger, E., (2021). *Advanced Energy Materials*, *11*, n/a.
37. Andersen, T. R., Cooling, N. A., Almyahi, F., Hart, A. S., Nicolaidis, N. C., Feron, K., Noori, M., Vaughan, B., Griffith, M. J., Belcher, W. J., Dastoor, P. C., (2016). *Solar Energy Materials and Solar Cells*, *149*, 103.
38. Andersen, T. R., Almyahi, F., Cooling, N. A., Elkington, D., Wiggins, L., Fahy, A., Feron, K., Vaughan, B., Griffith, M. J., Mozer, A. J., Sae-kung, C., Wallace, G. G., Belcher, W. J., Dastoor, P. C., (2016). *Journal of Materials Chemistry A, 4*, 15986.
39. Griffith, M. J., Cooling, N. A., Elkington, D. C., Wasson, M., Zhou, X., Belcher, W. J., Dastoor, P. C., (2021). *Nanomaterials*, *11*, 1185.
40. Griffith, M. J., Cooling, N. A., Elkington, D. C., Muller, E., Belcher, W. J., Dastoor, P. C., (2014). *Applied Physics Letters*, *105*, 143301.
41. Basaran, O. A., Gao, H., Bhat, P. P., (2013). *Annual Review of Fluid Mechanics*, *45*, 85.
42. Liu, J., Shabbir, B., Wang, C., Wan, T., Ou, Q., Yu, P., Tadich, A., Jiao, X., Chu, D., Qi, D., Li, D., Kan, R., Huang, Y., Dong, Y., Jasieniak, J., Zhang, Y., Bao, Q., (2019). *Advanced Materials*, *31*.
43. Mescher, H., Schackmar, F., Eggers, H., Abzieher, T., Zuber, M., Hamann, E., Baumbach, T., Richards, B. S., Hernandez-Sosa, G., Paetzold, U. W., Lemmer, U., (2020). *ACS Applied Materials and Interfaces*, *12*, 15774.
44. Glushkova, A., Andričević, P., Smajda, R., Náfrádi, B. L., Kollár, M. R., Djokić, V., Arakcheeva, A., Forró, L. S., Pugin, R., Horváth, E., (2021). *ACS Nano*, *15*, 4077.
45. Mescher, H., Hamann, E., Lemmer, U., (2019). *Scientific Reports*, *9*, 5231.
46. Griffith, M. J., Cooling, N. A., Vaughan, B., Elkington, D. C., Hart, A. S., Lyons, A. G., Quereshi, S., Belcher, W. J., Dastoor, P. C., (2016). *IEEE Journal of Selected Topics in Quantum Electronics*, *22*, 112.

47. Kim, Y. Y., Yang, T. Y., Suhonen, R., Välimäki, M., Maaninen, T., Kemppainen, A., Jeon, N. J., Seo, J., (2019). *Advanced Science*, *6*, 1802094.
48. Dou, B., Whitaker, J. B., Bruening, K., Moore, D. T., Wheeler, L. M., Ryter, J., Breslin, N. J., Berry, J. J., Garner, S. M., Barnes, F. S., Shaheen, S. E., Tassone, C. J., Zhu, K., van Hest, M. F. A. M., (2018). *ACS Energy Letters*, *3*, 2558.
49. Galagan, Y., Di Giacomo, F., Gorter, H., Kirchner, G., de Vries, I., Aniessen, R., Groen, W. A., (2018). *Advanced Energy Materials*, *8*, 1801935.
50. Li, H., Zuo, C., Angmo, D., Weerasinghe, H., Gao, M., Yang, J., (2022). *Nano-micro Letters*, *14*, 79.
51. Lee, C., Kang, H., Kim, C., Shin, K., (2010). *Journal of Microelectromechanical Systems*, *19*, 1243.
52. Benitez-Rodriguez, J. F., Chen, D., Gao, M., Caruso, R. A., (2021). *Solar RRL*, *5*, 2100341.
53. Kim, J., Yun, J. S., Cho, Y., Lee, D. S., Wilkinson, B., Soufiani, A. M., Deng, X., Zheng, J., Shi, A., Lim, S., Chen, S., Hameiri, Z., Zhang, M., Lau, C. F. J., Huang, S., Green, M. A., Ho-Baillie, A. W. Y., (2017). *ACS Energy Letters*, *2*, 1978.
54. Shi, L., Bucknall, M. P., Young, T. L., Zhang, M., Hu, L., Bing, J., Lee, D. S., Kim, J., Wu, T., Takamure, N., McKenzie, D. R., Huang, S., Green, M. A., Ho-Baillie, A. W. Y., (2020). *Science*, *368*.
55. Anderson, D., Cottam, S., Heim, H., Zhang, H., Holmes, N. P., Griffith, M. J., (2019). *MRS Communications*, *9*, 1206.
56. Sunahara, K., Griffith, M. J., Uchiyama, T., Wagner, P., Officer, D. L., Wallace, G. G., Mozer, A. J., Mori, S., (2013). *ACS Applied Materials and Interfaces*, *5*, 10824.
57. van der Salm, H., Lind, S. J., Griffith, M. J., Wagner, P., Wallace, G. G., Officer, D. L., Gordon, K. C., (2015). *Journal of Physical Chemistry C*, *119*, 22379.
58. Rong, Y., Hu, Y., Mei, A., Tan, H., Saidaminov, M. I., Seok, S. I., McGehee, M. D., Sargent, E. H., Han, H., (2018). *Science*, *361*, 1214.
59. Chen, Y., Zhang, L., Zhang, Y., Gao, H., Yan, H., (2018). *RSC advances*, *8*, 1489.
60. Posar, J. A., Large, M., Alnaghy, S., Paino, J. R., Butler, D. J., Griffith, M. J., Hood, S., Lerch, M. L. F., Rosenfeld, A., Sellin, P. J., Guatelli, S., Petasecca, M., (2021). *Journal of Synchrotron Radiation*, *28*, 1444.
61. Ho-Baillie, A. W. Y., Sullivan, H. G. J., Bannerman, T. A., Talathi, H. P., Bing, J., Tang, S., Xu, A., Bhattacharyya, D., Cairns, I. H., McKenzie, D. R., (2021). *Advanced Materials Technologies*, 2101059.
62. Posar, J. A., Petasecca, M., Griffith, M. J., (2021). *Flexible and Printed Electronics*.
63. Hu, M., Jia, S., Liu, Y., Cui, J., Zhang, Y., Su, H., Cao, S., Mo, L., Chu, D., Zhao, G., Zhao, K., Yang, Z., Liu, S. F., (2020). *ACS Applied Materials and Interfaces*, *12*, 16592.
64. Pan, L., Shrestha, S., Taylor, N., Nie, W., Cao, L. R., (2021). *Nature Communications*, *12*, 5258.
65. Wei, H., DeSantis, D., Wei, W., Deng, Y., Guo, D., Savenije, T. J., Cao, L., Huang, J., (2017). *Nature Materials*, *16*, 826.
66. Basiricò, L., Senanayak, S. P., Ciavatti, A., Abdi-Jalebi, M., Fraboni, B., Sirringhaus, H., (2019). *Advanced Functional Materials*, *29*, 1902346.
67. Hamukwaya, S. L., Hao, H., Zhao, Z., Dong, J., Zhong, T., Xing, J., Hao, L., Mashingaidze, M. M., (2022). *Coatings*, *12*, 252.
68. Bruzzi, M., Talamonti, C., Calisi, N., Caporali, S., Vinattieri, A., (2019). *APL Materials*, *7*, 51101.
69. Lédée, F., Ciavatti, A., Verdi, M., Basiricò, L., Fraboni, B., (2022). *Advanced Optical Materials*, *10*, 2101145.
70. Gill, H. S., Elshahat, B., Kokil, A., Li, L., Mosurkal, R., Zygmanski, P., Sajo, E., Kumar, J., (2018). *Physics in Medicine*, *5*, 20.
71. Bruzzi, M., Talamonti, C., (2021). *Frontiers in Physics*, *9*.
72. Li, X., Yu, D., Cao, F., Gu, Y., Wei, Y., Wu, Y., Song, J., Zeng, H., (2016). *Advanced Functional Materials*, *26*, 5903.

73. Yan, Y., Yang, Y., Liang, M., Abdellah, M., Pullerits, T., Zheng, K., Liang, Z., (2021). *Nature Communications*, *12*, 6603.
74. Xiao, B., Sun, Q., Wang, F., Wang, S., Zhang, B.-B., Wang, J., Jie, W., Sellin, P., Xu, Y., (2021). *Journal of Materials Chemistry. A, 9*, 1329.
75. Posar, J. A., Davis, J., Large, M. J., Basiricò, L., Ciavatti, A., Fraboni, B., Dhez, O., Wilkinson, D., Sellin, P. J., Griffith, M. J., Lerch, M. L. F., Rosenfeld, A., Petasecca, M., (2020). *Medical Physics*, *47*, 3658.
76. Ciavatti, A., Sorrentino, R., Basiricò, L., Passarella, B., Caironi, M., Petrozza, A., Fraboni, B., (2021). *Advanced Functional Materials*, *31*, 2009072.
77. Jang, J., Ji, S., Grandhi, G. K., Cho, H. B., Im, W. B., Park, J. U., (2021). *Advanced Materials*, *33*, 2008539.
78. Kubicki, D. J., Prochowicz, D., Hofstetter, A., Saski, M., Yadav, P., Bi, D., Pellet, N., Lewiński, J., Zakeeruddin, S. M., Grätzel, M., Emsley, L., (2018). *Journal of the American Chemical Society*, *140*, 3345.
79. Saliba, M., Matsui, T., Seo, J.-Y., Domanski, K., Correa-Baena, J.-P., Nazeeruddin, M. K., Zakeeruddin, S. M., Tress, W., Abate, A., Hagfeldt, A., Grätzel, M., (2016). *Energy and Environmental Science*, *9*, 1989.

Halide Perovskite Thin Films for Neutron and X-Ray Detection



Leunam Fernandez-Izquierdo, Martin G. Reyes-Banda, Mahsa Shekarnoush, Zeshaan H. Shamsi, Jesus A. Caraveo-Frescas, and Manuel Quevedo-Lopez

1 Introduction

Cesium lead bromide ($CsPbBr_3$) is a promising material for radiation sensing used as a scintillator or direct detector [1–3]. Besides its high stability, $CsPbBr_3$ possesses interesting electronic and optoelectronic properties such as high attenuation above the band gap, good photoresponse, large electron and hole mobility, long lifetimes, low excitation binding energy, halogen self-passivation, defect tolerance, luminosity, etc. [1, 4–12]. Device quality single crystals have been prepared using many methods, including a high-temperature process [4], solution-based methods such as antisolvent vapor crystallization (AVC) [8, 9, 11], and inverse temperature crystallization (ITC) [13]. The carrier concentration (holes) of these crystals varies in the range 5×10^7 to 1×10^8 cm^{-3} [10, 11] and about 1×10^9 cm^{-3} for electrons [10], resulting in nearly intrinsic crystals with resistivities in the range 1–3 GΩ-cm [11]. As a reference, Bridgman-grown crystals show resistivities as high as ~340 GΩ-cm [4, 14] and mobility-lifetime ($\mu\tau$) product for electrons and holes in the range 1.7×10^{-3} to 4.5×10^{-4} cm^2V^{-1} and 1.3×10^{-3} to 9.5×10^{-4} cm^2V^{-1}, respectively [4, 15, 16]. These $\mu\tau$ values are better than that of CdZnTe (CZT) and CdTe. It is important to note that the electron $\mu\tau$ products of CZT and CdTe [12] are in the lower range of the corresponding values for $CsPbBr_3$, while the hole $\mu\tau$ product is only 0.1% that of $CsPbBr_3$.

L. Fernandez-Izquierdo · M. G. Reyes-Banda · M. Shekarnoush · Z. H. Shamsi · J. A. Caraveo-Frescas · M. Quevedo-Lopez (✉)
Department of Material Science & Engineering, University of Texas at Dallas, Richardson, TX, USA
e-mail: mquevedo@utdallas.edu

© The Author(s), under exclusive license to Springer Nature Switzerland AG 2024

S. Krishnamoorthy, K. (Kris) Iniewski (eds.), *Advances in Fabrication and Investigation of Nanomaterials for Industrial Applications*,
https://doi.org/10.1007/978-3-031-42700-8_15

The reported use of $CsPbBr_3$ for radiation sensing is limited to single crystals, except for its use as a thin film in X-ray scintillators [1, 3]. There are few reports for direct radiation detection using thin-film diodes based on $CsPbBr_3$. This is related to the lack of deposition techniques for thick $CsPbBr_3$ films. The close-space sublimation (CSS) process reported here addresses this problem. Although the intrinsic phase purity and crystal quality of single crystals offer improved optoelectronic properties, the high cost of the single-crystal approach renders this option nonviable for portable and large-area applications; hence thin films are a better option. Furthermore, the photon attenuation coefficient of $CsPbBr_3$ is linear and comparable to that of CZT for energies up to 1000 keV [4]. Still, no exhaustive studies exist for the interaction of $CsPbBr_3$ with charged particles (alphas, betas, etc.) or for higher photon energies such as gamma rays. The interaction of $CsPbBr_3$ 2D nanosheets with ionizing radiation has been reported recently, showing scintillation performance comparable to commercial crystals [1]. The observed luminosity of ~21,000 photons/MeV is comparable with commercial Cs_2LiYCl_6 (CLYC) crystals, but the luminescence decay time of <15 ns is much shorter than that of NaI:Tl (~200 ns), CLYC (>50 ns), and $LaBr_3$(Ce) (>16 ns) [17]. Recently gamma- and alpha-particle spectroscopy using $CsPbBr_3$ single crystals were reported [15].

There are a few reports for $CsPbBr_3$ thin-film deposition using solution processing [1, 18, 19], chemical vapor deposition (CVD) [20], vacuum evaporation [21], and even a hybrid vacuum-solution process [22]. Although a solution process approach is "simple," economic, and more flexible, the stability and electronic properties of the resulting materials might be compromised by impurities and solvents incorporated from the precursor solution. On the other hand, physical vapor deposition methods, such as CVD and vacuum processes, eliminate solvents and yield higher-quality materials, but precursor utilization is low and not practical for depositing thick films, necessary for efficient high-energy electromagnetic radiation and neutron sensing [23]. To overcome the aforementioned deficiencies, we have worked on developing a solution-free, simple, high growth rate, scalable, and inexpensive CSS process to deposit high-quality $CsPbBr_3$ films. Furthermore, this method can also be used for other material systems. $CsPbBr_3$ melts congruently at ~570 °C [4]; therefore, sublimation from $CsPbBr_3$ powder or crystals can produce stoichiometric films. The fact that CSS is a near-thermal-equilibrium deposition process results in films with reduced defects, large grain, high material utilization, and high growth rates. The films are used to demonstrate a thin-film solid-state alpha particles, neutron, and X-ray detectors using an ITO/Ga_2O_3/$CsPbBr_3$/Au diode.

Planar $CsPbBr_3$/Ga_2O_3 p-n junction diodes coupled with ^{10}B neutron conversion film have been demonstrated by showing a thermal neutron detection efficiency of 2.5% [24]. The theoretical neutron detection efficiency of planar detectors is limited to <4.5% due to the self-absorption of reaction products within the neutron conversion layer [25]. Higher efficiencies (20%–35%) have been demonstrated when using microstructured silicon diodes backfilled with a neutron conversion material [26–28]. Microstructured detectors fabricated using thin-film semiconductors can be easily scaled for large-area applications than detectors using single-crystal

semiconductors. Neutron detection efficiency using microstructured detectors has also been demonstrated recently [28]. $CsPbBr_3$ diodes have also been used as X-ray detectors, yielding very good performance. $CsPbBr_3/Ga_2O_3$ p-n planar junction diodes have been shown to have an X-ray sensitivity of about 10,000 $\mu C/Gy_{air}cm^2$ at an applied electric field of 375 V/mm.

2 $CsPbBr_3$ Film Deposition Using Close-Space Sublimation

Figure 1a shows a diagram of the process to obtain perovskite thin films. $CsPbBr_3$ films with thicknesses between 8 and 20 μm can be deposited by the CSS process from $CsPbBr_3$ powder obtained by solid-state reaction in a ball milling system. Figure 1b shows the XRD patterns of the $CsPbBr_3$ precursor powder and the resulting $CsPbBr_3$ film. The CSS-deposited $CsPbBr_3$ films have the same crystallographic nature and phase purity as the precursor powder. High incident angle (2 degrees) XRD analyses confirmed the phase purity in the bulk of the CSS-deposited $CsPbBr_3$ films with the orthorhombic perovskite structure [9, 10,

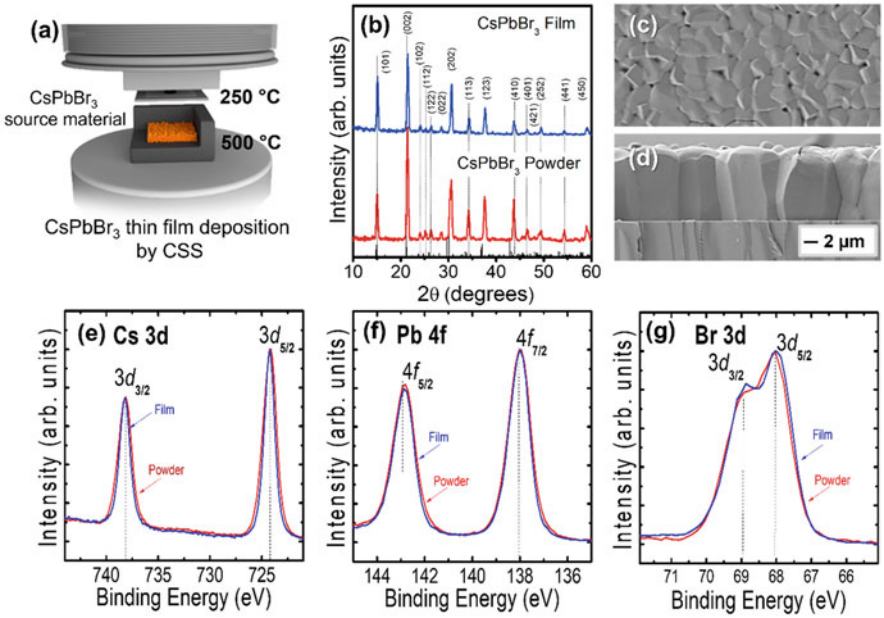


Fig. 1 (**a**) CSS process using the $CsPbBr_3$ powder as the source material; (**b**) XRD patterns of the $CsPbBr_3$ film and powder used as the source material; the reference XRD pattern corresponds to ICSD #97851; (**c**) top-view and (**d**) cross-sectional SEM images of the as-deposited $CsPbBr_3$ thin film; (**e**–**g**) corresponding XPS spectra of Cs 3d, Pb 4 f, and Br 3d showing identical chemical bonding for powder and films

13, 29]. No diffraction peaks for polymorphs Cs_4PbBr_6 and $CsPb_2Br_5$ [30] were observed, further demonstrating the phase purity of the deposited $CsPbBr_3$ films. The crystallite size of the as-deposited $CsPbBr_3$ was in the range of ~245 nm with lattice constants $a = 8.205$, $b = 11.694$, and $c = 8.268$ Å, consistent with the orthorhombic $CsPbBr_3$ phase [10].

Surface morphology of as-deposited films (Fig. 1c), evaluated by scanning electron microscopy (SEM), shows grains with an average size of ~2.5 μm x ~ 6.5 μm with dense columnar growth (Fig. 1d). Recrystallization is evident after annealing at 450 °C for 30 min. This annealing was introduced further to increase the grain size and density of the films. The grain size and columnar growth of the CSS-deposited $CsPbBr_3$ are in sharp contrast with the smaller grains observed in films deposited by solution process or physical methods such as CVD and co-evaporation [19, 31]. EDXS analysis was performed across the film cross section at five points to examine any possible variation in stoichiometry. The composition is maintained constant throughout the film thickness. The surface roughness of the $CsPbBr_3$ film may result in discontinuities at the interface due to poor coverage of the contact films. To avoid this, a polishing process to reduce the surface roughness was introduced, reducing the roughness from ~270 nm to <50 nm.

The X-ray photoelectron spectroscopy (XPS) spectra of the $CsPbBr_3$ film and powder are shown in Fig. 1e–g. The binding energies for the Cs 3d, Pb 4 f, and Br 3d regions are consistent with $CsPbBr_3$ [32]. Furthermore, the binding energies match for both the source powder and the thin films, indicating that the $CsPbBr_3$ stoichiometry/composition and crystalline structure of the powder are maintained during the CSS deposition process.

3 Ga_2O_3/$CsPbBr_3$ Diodes and Performance Characteristics

A schematic of the device configuration along with the band diagram is shown in Fig. 2a–b. Conduction (E_c) and valence band (E_v) edge energies of −3.0 and − 5.3 eV, respectively, were estimated for the $CsPbBr_3$ film using data from photoelectron spectroscopy in air (PESA), Kelvin probe, and optical transmittance. From Hall measurements, the resistivity, mobility, and carrier concentration for the $CsPbBr_3$ film were determined as 1×10^{11} Ω-cm, 0.013 cm^2 $(V\ s)^{-1}$, and 5×10^9 cm^{-3}, respectively. The corresponding values for the n-Ga_2O_3 are ~5×10^6 Ω-cm, 1 cm^2 $(V\ s)^{-1}$, and ~ 10^{15} cm^{-3}, respectively.

To demonstrate charged particle and photons sensing, a p-n junction diode with the configuration ITO/Ga_2O_3/$CsPbBr_3$/Au was fabricated. The resulting diode showed leakage (reverse bias) current of 5×10^{-8} A/mm^2 and is fully depleted at −5 V (Fig. 2c and inset) with negligible I-V hysteresis and rectification of 10^4. The favorable band alignments and the high band gap of Ga_2O_3 enabled low leakage current and diode rectification >10^4, which is significantly superior to that reported for $CsPbBr_3$/ZnO [33] and ZnO/$CsPbBr_3$/MoO_3 diodes [34].

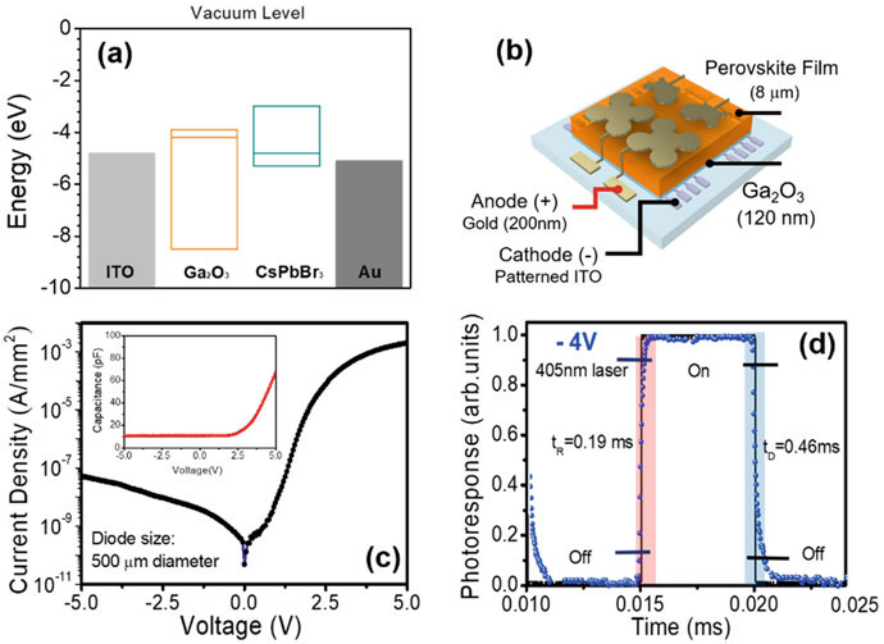


Fig. 2 (**a**) The band edge positions of different layers as determined experimentally and (**b**) schematic of the ITO/Ga_2O_3/$CsPbBr_3$/Au device; (**c**) current-voltage characteristics (dark) for the Ga_2O_3/$CsPbBr_3$ diode; the inset shows the complete depletion of the device with a ~ 8 mm-thick $CsPbBr_3$ film at low reverse bias; (**d**) rise/decay time estimation

The rise and decay times for the $CsPbBr_3$ diode are shown in Fig. 2d. The device shows an on/off ratio of 10^2 at −4 V (E = 5 kV/cm) when exposed to a 405 nm laser (Fig. 2d). The estimated rise/decay time for the diode was 190/460 μs, which is much shorter than previously reported for $CsPbBr_3$-based diodes [33, 34] and photoresistors [8, 10, 35]. The superior performance of the fabricated devices, even without a hole transport layer, is attributed to the phase purity, large columnar grains of the CSS-deposited $CsPbBr_3$ films, as well as the large band gap of the Ga_2O_3 n-layer.

4 Alpha and Neutron Sensing with $CsPbBr_3$ Diodes

The diodes were evaluated as charged particle detectors, specifically for thermal neutron sensing using ^{10}B layer as conversion film. Neutron detectors normally include a "conversion" material such as ^{10}B in which a transmutation reaction produces an ionizing particle which in turn creates e-h pairs in the detector material [36]. The transmutation reaction includes a neutron captured by the ^{10}B that then

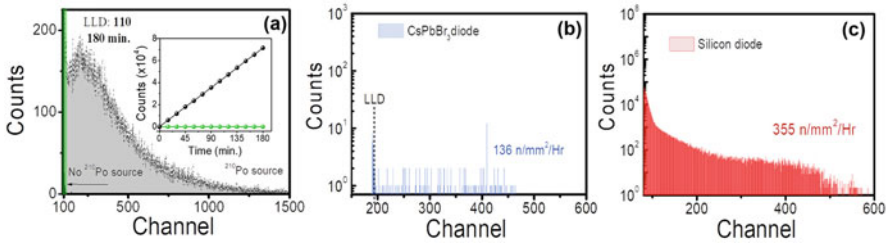


Fig. 3 (**a**) Alpha-particle response when exposed to the ^{210}Po source, data collected for 180 minutes with a shaping time constant of 3 microseconds; inset, counts above LLD for alpha particles (black) and noise (green) recorded every 15 minutes; (**b**) normalized neutron response of $CsPbBr_3$-fabricated devices; (**c**) silicon-based neutron detector

becomes ^{11}B in an excited state that splits into ^{7}Li and an alpha particle (^{4}He) as shown in the reaction from Eq. 1 [36]:

$$^{10}B + n \rightarrow \left\{ \begin{array}{c} 94\%\, ^{7}Li\ \ (0.840\, MeV) + \alpha\, (1.470\ MeV) + \gamma\ \ (0.48\ MeV) \\ 6\%\, ^{7}Li\ \ (1.02\ MeV) + \alpha\, (1.77\ MeV) \end{array} \right\} \tag{1}$$

The results for alpha and neutron response are shown in Fig. 3. The alpha peak is clearly observed after exposing the diodes to ^{210}Po (5.3 MeV) (Fig. 3a), demonstrating the $Ga_2O_3/CsPbBr_3$ diode sensitivity to alpha particles. The measured alpha response corresponds to 16% of that of a commercial OPF480 Si diode when exposed to the same ^{210}Po source. The peak broadening (Fig. 3a) can be due to various factors, such as the attenuation of alpha particles by the air and the top electrode, charge trapping in semiconductors, and electronic noise [37]. Next, the diode was exposed to thermal neutrons using a ^{252}Cf source. Results show neutron counts one order of magnitude higher than the background noise. Background noise measurements were performed before the exposure to the ^{252}Cf source. No increase in the background counts was observed for alpha particle or neutron exposure, indicating that the increase in the counts with time is a result of energetic particles absorbed in the $Ga_2O_3/CsPbBr_3$ diode, as seen in Fig. 3a (inset). No counts were detected above LLD. This confirms that the counts are originating from the alphas generated in the ^{10}B layer after neutron interaction and absorbed in the diode and not due to gammas from the ^{252}Cf source. Figure 3b shows neutron response of the $CsPbBr_3$ diodes when exposed to a ^{252}Cf source. Calculated efficiency shows approx. 1% for $CsPbBr_3$ detectors represents 38.3% of the obtained silicon efficiency (Fig. 3c). To the best of our knowledge, the demonstrated results are the first report of neutron detection using a thin-film $CsPbBr_3$-based device.

5 Composition Tuning in $CsPbBr_3$ Films

The X-ray diffraction results for $CsPbBr_3$ films before and after solid-state ion exchange with chlorine (Cl) are shown in Fig. 4a. The characteristic XRD patterns of $CsPbBr_3$ shift depending on the annealing time under a $PbCl_2$ atmosphere. When annealed in $PbCl_2$ atmosphere, the characteristic peaks $CsPbBr_3$ (101) and (002) shift toward higher 2θ values (Fig. 4a), indicating a smaller lattice constant resulting from the Cl atoms substituting Br in the $CsPbBr_3$ lattice. This indicates that Cl effectively incorporates in the crystalline structure of $CsPbBr_3$ [38, 39]. In fact, in $PbCl_2$-treated films, the lattice parameter is inversely proportional to the Cl content and follows a linear relationship.

The XPS spectra of the $CsPbBr_3$ films before and after annealed with $PbCl_2$ are shown in Fig. 4b–c. The binding energies of the Cs 3d region do not change for as-deposited or ion-exchanged films. This is demonstrated in the 723.66 and 737.66 eV peaks, corresponding to Cs $3d_{5/2}$ and $3d_{3/2}$ core levels [32, 40]. The shifting of Pb 4 f core levels to higher binding energies for $PbCl_2$-treated samples indicates stronger binding of the halogen with Pb, which is attributed to the higher electronegativity of Cl [41].

The binding energies of Br $3d_{5/2}$ and $3d_{3/2}$ for $CsPbBr_3$ are shown in Fig. 4b. No significant change is observed for ion-exchanged films with either $PbCl_2$; however, the attenuation of Br 3d doublet and the presence in the Cl 2p doublet intensity (Fig. 4c) in $PbCl_2$-treated films demonstrate a successful ion exchange [42]. As

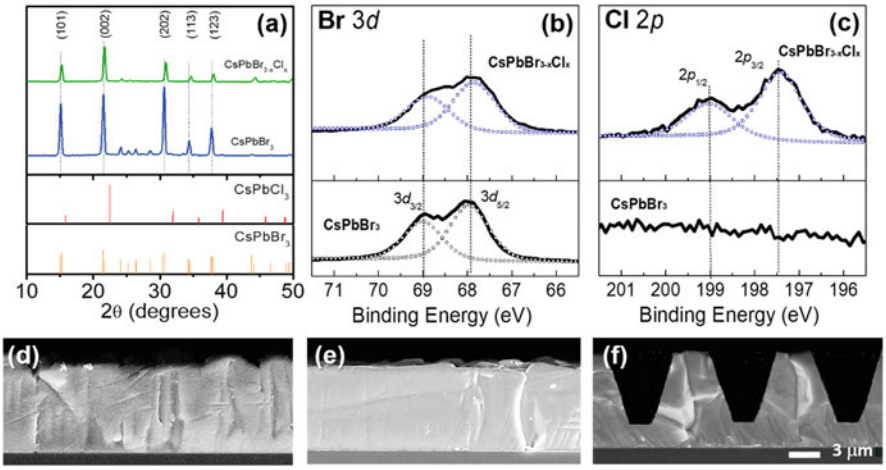


Fig. 4 (**a**) $CsPbBr_3$ films after thermal processing under the vapors of $PbCl_2$. The duration of annealing (120 min.) is given in each case. The two bottom panes in each figure correspond to the ICSD patterns used as reference; (**b**) XPS spectra revealing Br 3d at 67.96 and 68.96 eV and (**c**) XPS spectra of Cl 2p at 197.3 and 198.9 eV for films treated in $PbCl_2$ vapors; (**d**) cross section of as-deposited $CsPbBr_3$ film; (**e**) cross section of films annealed for 120 min. in $PbCl_2$ vapors; (**f**) Cross section of etched microstructures in $CsPbBr_3$ thin films

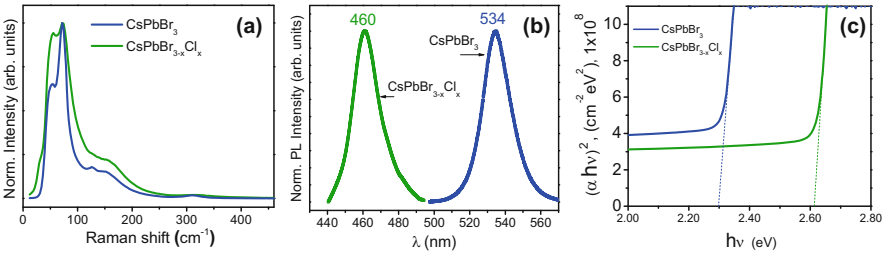


Fig. 5 (**a**) Raman spectra of the $CsPbBr_3$ and $CsPbBr_{3-x}Cl_x$ films; (**b**) PL bands of the as-deposited $CsPbBr_3$ and $CsPbBr_{3-x}Cl_x$ films; (**c**) estimated band gap of the $CsPbBr_3$ and ion-exchanged films. The band gap was determined using the relation $(\alpha E)^2 = A(E\text{-}E_g)$, and the absorption coefficient (α) was obtained from the UV-Vis spectral measurements

expected, the atomic concentration Cl in films treated with $PbCl_2$ varies linearly with annealing time.

Figure 4d shows the cross section of the as-deposited $CsPbBr_3$ films (8 μm). The film exhibits large grains, with an average size of ~5 μm. Annealing of this film at 425 °C under vacuum in the absence of PbX_2 results in the formation of voids without any grain growth. Recrystallization and grain growth are evident when annealed at the same temperature in the presence of $PbCl_2$ vapor (Fig. 4e), with a remarkable change for the films annealed. For films annealed in $PbCl_2$ (Fig. 4e) after 120 min, grain size increased to ~12 μm. This recrystallization is much larger than that obtained by methods such as solution-based treatments [43, 44] and CVD, where the maximum reported grain size was in the order of 0.3 to 0.5 μm [45]. The recrystallization in the presence of $PbCl_2$ vapor not only promoted grain growth but also results in a void-free surface with no visible grain boundaries across the film cross section [46]. The $CsPb_{3-x}Cl_x$ sample underwent a dry etching process using a combination of HBr and Ar plasma, with which it was possible to obtain the trenches in the perovskite films, as shown in Fig. 4f.

The $CsPbBr_3$ structure was also confirmed by Raman spectroscopy analysis (Fig. 5a). The Raman spectrum corresponds to an orthorhombic phase with bands at 52 cm^{-1} and 74 cm^{-1} assigned to vibrational modes of the $[PbBr_6]^{4-}$ octahedron and the bands at 127 cm^{-1} and 151 cm^{-1} to Cs^+ ion vibrations [47, 48]. The Pb-Br rocking modes in the $[PbBr_6]^{4-}$ octahedron for Cs_4PbBr_6 have two intense bands at ~86 cm^{-1} and ~ 127 cm^{-1} [9, 49]; however, the absence of the 86 cm^{-1} band and the weak nature of the band at 127 cm^{-1} confirm that no Cs_4PbBr_6 is present. The weak nature of the 127 cm^{-1} bands is characteristic of $CsPbBr_3$ [9, 48, 49]. From the Raman spectra in Fig. 5a**,** it is evident that with the introduction of Cl, the degeneracies of Raman modes are lifted, leading to the appearance of additional phonon modes [47].

The photoluminescence (PL) spectra of the as-deposited and ion-exchanged $CsPbBr_3$ films are shown in Fig. 5b. As-deposited $CsPbBr_3$ films show a strong emission centered at 534 nm and a weak shoulder at 550 nm. Films annealed

in $PbCl_2$ show a strong emission centered at 460 nm. The weak band in the PL spectra of the thin films has been associated with several phenomena, including photon recycling [50, 51], structural differences between surface and bulk leading to slightly different band gaps [52], bound excitons [4], and defects due to grain size inhomogeneity or traces of precursor [53, 54]. Based on the SEM and XRD analysis (0.5- and 2.0-degree grazing angles), grain size inhomogeneity and precursor traces can be ruled out. Photon recycling can happen in translucent materials. The red-shifted PL band can be observed along with the original PL emission when the signal is captured from a wide area [51]. Additionally, the band gap of the $CsPbBr_3$ film was estimated at 2.32 eV and incremented to 2.62 eV with the ion-exchange treatment that further confirms the incorporation of Cl into the lattice [46] (Fig. 5c).

6 $Ga_2O_3/CsPbBr_{3-x}Cl_x$ Diodes Performance and Neutron Sensing

The performance of $CsPbBr_3$ in a diode configuration ITO/Ga_2O_3/$CsPbBr_3$/Au (Fig. 2b) has been discussed in previous sections. The fully depleted diode had a capacitance as low as 15 pF, a low leakage current of 5×10^{-8} A/mm^2 at −5 V, and rectification of ~10^4 [24]. Resistivity, mobility, and carrier concentration values of n-Ga_2O_3, determined from Hall measurements, are ~5 x10^6 Ω cm, 1 cm^2 (V s)$^{-1}$, and ~ 10^{15} cm^{-3}, respectively [24, 55]. Figure 6a shows the current-voltage plots for the Ga_2O_3/$CsPbBr_3$ devices, both for as-deposited and ion-exchanged in $PbCl_2$ vapor. Lower leakage current density (~1×10^{-8} A/mm^2) at -5 V was obtained from $PbCl_2$ ion-exchanged devices, with a rectification factor of 10^5. This value is 10× higher than the fabricated device with as-deposited $CsPbBr_3$. This performance can be attributed not only to the favorable band alignments and the high band gap of Ga_2O_3 but also to the recrystallization leading to grain growth, reduction in grain boundaries, and dopant compensation [38] that the $PbCl_2$ ion exchange provides to the $CsPbBr_3$ films. The changes observed between diodes without and with

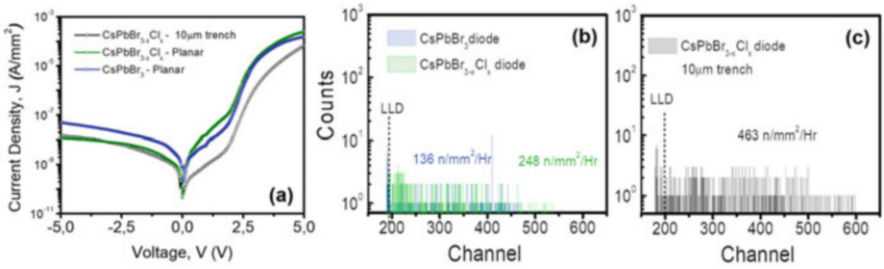


Fig. 6 (**a**) Effect of $PbCl_2$ vapor and the microstructure in $CsPbBr_3$ thin films on I-V properties of detectors; (**b**) normalized neutron response of $CsPbBr_3$- and $CsPbBr_{3-x}Cl_x$-fabricated devices; (**c**) normalized neutron response of $CsPbBr_{3-x}Cl_x$ with trenches

dry etching are mainly due to the generation of surface states on the sidewalls of the microstructures during etching. These surface states can negatively impact the electrical performance of devices.

Figure 6b shows normalized comparison of neutron response between the $CsPbBr_3$ and $CsPbBr_{3-x}Cl_x$ diodes when exposed to ^{252}Cf source. Theoretical efficiency using a ^{10}B conversion layer is ~4.5% (ref). Calculated efficiency shows approx. 2.5% for $CsPbBr_{3-x}Cl_x$ which represents a substantial increase compared to 1% for $CsPbBr_3$. The 2.5% efficiency represents 69.9% of the obtained silicon efficiency (Fig. 3c) [24, 46].

7 Radiation Detection Efficiency of Microstructured $CsPbBr_{3-x}Cl_x/Ga_2O_3$ Detectors

Calculated efficiency in $CsPbBr_{3-x}Cl_x$ with trenches (10 μm deep) represents a substantial increase compared to planar devices. The device response to the ^{252}Cf source can be seen in Fig. 6c, showing an efficiency of approx. 4.3%. This result represents 130.4% of the alpha efficiency obtained with silicon-based diodes (Fig. 3c).

Figure 7a shows the comparison of experimental thermal neutron detection efficiencies of $CsPbBr_{3-x}Cl_x$-based detectors with the theoretical efficiency calculated by MCNP. The discrepancy in experimental neutron detection efficiency compared with theoretical efficiency is ~45%. The discrepancy increases with increasing

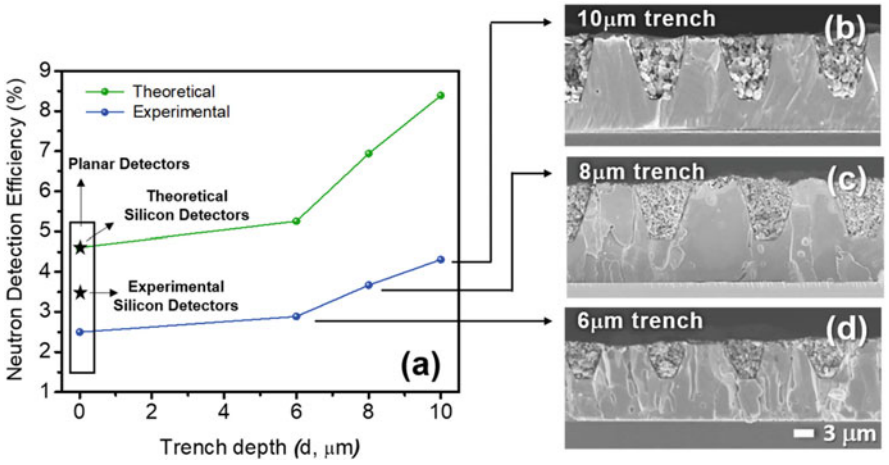


Fig. 7 (**a**) Comparison of neutron detection efficiencies between theoretical simulations and experimental results (the efficiency of planar silicon is represented using star symbol); (**b–d**) cross-sectional image of etched microstructures in $CsPbBr_{3-x}Cl_x$ thin films filled with ^{10}B conversion film

trench depth and can be attributed to two major reasons: the packing density of ^{10}B in the microstructures and poor charge collection efficiency in the detectors. It is known that the discrepancy in the efficiency of up to 25% in microstructured detectors arises from differences in experimental and theoretical packing density of ^{10}B in the microstructures [28]. In theoretical calculations, the microstructures were assumed to contain ^{10}B with 100% density, whereas in these experiments, such packing density of ^{10}B powders was not achieved. Figure 7b–d shows the SEM cross-sectional image of microstructures in $CsPbBr_3$ that are backfilled with ^{10}B powders using a sedimentation process designed to preserve the perovskite integrity.

The microstructures were successfully filled without large voids. It is mainly due to the wide opening of trenches that enabled ^{10}B particles to backfill these structures easily. The irregular shape and different sizes of ^{10}B powder particles enable the close-packed filling in the microstructures. However, tiny voids between the powder particles prevent microstructures from attaining 100% fill density. Finally, the discrepancy due to low load collection efficiency in the etched samples may be related to permanent damage to the sidewalls during trench formation. Surface recombination of charges generated by incident alpha particles on these defective surfaces is more pronounced and could negatively impact the charge collection efficiency of the detector [56].

The etched sidewalls area increases as the etch depth increases resulting in the formation of more surface defects. This can be seen in the broadening discrepancy of experimental efficiency as a trench depth function where more surface states are present.

8 X-Ray Sensing with $CsPbBr_3$ Diodes

The diodes can also be used as X-ray detectors, specifically for detecting X-rays of energies around 60 keV. X-ray detectors need a high-density material that helps to absorb high-energy photons highly. $CsPbBr_3$ has excellent high-energy photonic absorption and unique optical and electronic properties. This is due to its low number of defects and trap state density [57]. The strong stopping power for X-ray attenuation is due to high-Z elements (Cs, Pb, and Br). Other advantages of $CsPbBr_3$ include large mobility-lifetime ($\mu\tau$) products and low-temperature crystallization using low-cost solution-based methods. This makes $CsPbBr_3$ and perovskites very promising for X-ray radiation detectors [58].

Figure 8a shows the X-ray response for $CsPbBr_3$ p-n diode at -2 V. Increasing X-ray doses for an irradiation time of 15 s are used. A clear trend in the photogenerated current with increasing dose is observed. A clear signal is observed even as low as 2.8 μGy/s for a reverse bias of -2 V. As the bias increases in magnitude, the generated photocurrent also increases. Increasing the applied electric field enables better charge extraction and therefore higher sensitivity. The long transient decay time for the $CsPbBr_3$ device may be due to trapped charge either at the interface or slow relaxation of ion migration after X-ray illumination [59].

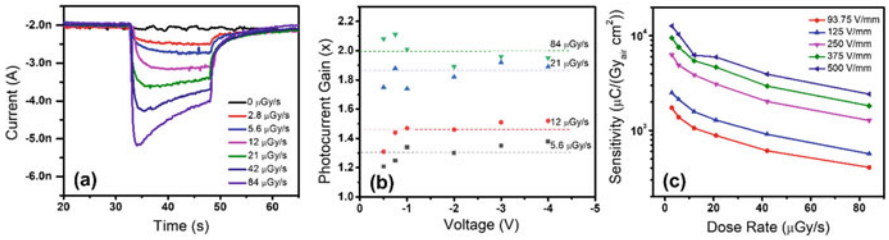


Fig. 8 (**a**) Current vs. time plots during X-ray irradiation of ITO/Ga_2O_3/$CsPbBr_3$/Au diode at −2 V. Source contained a tungsten (W) target at a maximum energy of 60 keV and highest dose of 84 μGy/s for 15 s; (**b**) photocurrent gain vs. voltage of the diode; (**c**) sensitivity vs. dose rate plots of the diode

Figure 8b shows the X-ray photoresponse of the $CsPbBr_3$ p-n diode as increasing bias voltages. Note that the average photocurrent gain – in relation to the dark current at a given irradiation dose – has no correlated trend with the applied reverse bias to the device. This is excellent information to confirm that the response signal generated from the device during irradiation is predictable for a given dosage at any applied voltage above the signal-to-noise threshold.

Figure 8c shows X-ray sensitivities as a function of dose rate. The rectification $CsPbBr_3$-based p-n device helps with the charge collection efficiency and overall X-ray sensitivity. The calculated sensitivity is approximately 10,000 $\mu C/Gy_{air}cm^2$, which is a value comparable to the reported values. It is important to note that in this case the thickness of the films is only 8 μm, while most of the reports use hundreds of microns of thickness [60]. The cost however is the slower transient time to discharge the device after irradiation. If a fast-switching mechanism is required for an application, device engineering may be required to modify this slow transient time.

9 Conclusions

A solution-free CSS process for depositing high-quality films of $CsPbBr_3$ is demonstrated and implemented in the fabrication of solid-state alpha particles, thermal neutron, and X-ray detectors. The CSS process used small crystals as precursors to deposit films with large columnar grain growth across the entire film thickness of 8–15 μm. Congruent sublimation of $CsPbBr_3$ resulted in films with a pure orthorhombic phase with no secondary phases. An ion-exchange treatment was developed to control composition and promote crystal growth, positively impacting the overall semiconducting properties of the perovskite film. Good band edge alignment, high resistivity of $CsPbBr_3$ and $CsPbBr_{3-x}Cl_x$, and the large band gap of the n-layer Ga_2O_3 result in diodes with low leakage currents (10^{-8} A/mm^2) with rectification between 10^4 and 10^5. Preliminary studies on the exposure to thermal

neutrons resulted in counts ~60 higher than the background noise. The efficiencies of the $CsPbBr_3$, $CsPbBr_{3-x}Cl_x$, and $CsPbBr_{3-x}Cl_x$ with trenches (10 μm) samples are 1.0%, 2.5%, and 4.3%, respectively, that represent 38.3%, 69.9%, and 130.4% of the alpha-capture efficiency seen in planar silicon diodes. These results are highly encouraging and highlight the promise of the CSS process in depositing perovskite films and the dry etching method to obtain microstructured perovskite films, wallowing large-area fabrication perovskite-based neutron detectors. X-ray sensitivity measurements were performed and were concluded that the $CsPbBr_3$ device produced high X-ray sensitivity, peaking near 10,000 $\mu C/Gy_{air}cm^2$ at an applied electric field of 375 V/mm. Transient trapped charge was observed in the device during the off states of irradiation with a decay time of 4.5 s.

References

1. Zhang Y, Sun R, Ou X, et al. (2019) Metal Halide Perovskite Nanosheet for X-ray High-Resolution Scintillation Imaging Screens. ACS Nano 13:2520–2525. https://doi.org/10.1021/acsnano.8b09484
2. Heo JH, Shin DH, Park JK, et al. (2018) High-Performance Next-Generation Perovskite Nanocrystal Scintillator for Nondestructive X-Ray Imaging. Advanced Materials 30:1801743. https://doi.org/10.1002/adma.201801743
3. Chen Q, Wu J, Ou X, et al. (2018) All-inorganic perovskite nanocrystal scintillators. Nature 561:88–93. https://doi.org/10.1038/s41586-018-0451-1
4. Stoumpos CC, Malliakas CD, Peters JA, et al. (2013) Crystal Growth of the Perovskite Semiconductor $CsPbBr_3$: A New Material for High-Energy Radiation Detection. Crystal Growth & Design 13:2722–2727. https://doi.org/10.1021/cg400645t
5. Li X, Wu Y, Zhang S, et al. (2016) CsPbX3 Quantum Dots for Lighting and Displays: Room-Temperature Synthesis, Photoluminescence Superiorities, Underlying Origins and White Light-Emitting Diodes. Advanced Functional Materials 26:2435–2445. https://doi.org/10.1002/adfm.201600109
6. Yettapu GR, Talukdar D, Sarkar S, et al. (2016) Terahertz Conductivity within Colloidal $CsPbBr_3$ Perovskite Nanocrystals: Remarkably High Carrier Mobilities and Large Diffusion Lengths. Nano Lett 16:4838–4848. https://doi.org/10.1021/acs.nanolett.6b01168
7. Shi Z, Lei L, Li Y, et al. (2018) Hole-Injection Layer-Free Perovskite Light-Emitting Diodes. ACS Appl Mater Interfaces 10:32289–32297. https://doi.org/10.1021/acsami.8b07048
8. Ding J, Du S, Zuo Z, et al. (2017) High Detectivity and Rapid Response in Perovskite $CsPbBr_3$ Single-Crystal Photodetector. J Phys Chem C 121:4917–4923. https://doi.org/10.1021/acs.jpcc.7b01171
9. Cha J-H, Han JH, Yin W, et al. (2017) Photoresponse of $CsPbBr_3$ and Cs_4PbBr_6 Perovskite Single Crystals. J Phys Chem Lett 8:565–570. https://doi.org/10.1021/acs.jpclett.6b02763
10. Saidaminov MI, Haque MA, Almutlaq J, et al. (2017) Inorganic Lead Halide Perovskite Single Crystals: Phase-Selective Low-Temperature Growth, Carrier Transport Properties, and Self-Powered Photodetection. Advanced Optical Materials 5:1600704. https://doi.org/10.1002/adom.201600704
11. Zhang H, Liu X, Dong J, et al. (2017) Centimeter-Sized Inorganic Lead Halide Perovskite $CsPbBr_3$ Crystals Grown by an Improved Solution Method. Crystal Growth & Design 17:6426–6431. https://doi.org/10.1021/acs.cgd.7b01086
12. Liu Z, Peters JA, Stoumpos CC, et al. (2013) Heavy metal ternary halides for room-temperature x-ray and gamma-ray detection. In: Hard X-Ray, Gamma-Ray, and Neutron Detector Physics XV. International Society for Optics and Photonics, p 88520A

13. Dirin DN, Cherniukh I, Yakunin S, et al. (2016) Solution-Grown CsPbBr $_3$ Perovskite Single Crystals for Photon Detection. Chem Mater 28:8470–8474. https://doi.org/10.1021/acs.chemmater.6b04298
14. Clark DJ, Stoumpos CC, Saouma FO, et al. (2016) Polarization-selective three-photon absorption and subsequent photoluminescence in ${\mathrm{CsPbBr}}_{3}$ single crystal at room temperature. Phys Rev B 93:195202. https://doi.org/10.1103/PhysRevB.93.195202
15. He Y, Liu Z, McCall KM, et al. (2019) Perovskite CsPbBr3 single crystal detector for alpha-particle spectroscopy. Nuclear Instruments and Methods in Physics Research Section A: Accelerators, Spectrometers, Detectors and Associated Equipment 922:217–221. https://doi.org/10.1016/j.nima.2019.01.008
16. He Y, Matei L, Jung HJ, et al. (2018) High spectral resolution of gamma-rays at room temperature by perovskite CsPbBr3 single crystals. Nat Commun 9:1609. https://doi.org/10.1038/s41467-018-04073-3
17. Glodo J, Wang Y, Shawgo R, et al. (2017) New Developments in Scintillators for Security Applications. Physics Procedia 90:285–290. https://doi.org/10.1016/j.phpro.2017.09.012
18. Cho H, Wolf C, Kim JS, et al. (2017) High-Efficiency Solution-Processed Inorganic Metal Halide Perovskite Light-Emitting Diodes. Advanced Materials 29:1700579. https://doi.org/10.1002/adma.201700579
19. Duan J, Zhao Y, Yang X, et al. (2018) Lanthanide Ions Doped CsPbBr3 Halides for HTM-Free 10.14%-Efficiency Inorganic Perovskite Solar Cell with an Ultrahigh Open-Circuit Voltage of 1.594 V. Advanced Energy Materials 8:1802346. https://doi.org/10.1002/aenm.201802346
20. Luo P, Zhou Y, Zhou S, et al. (2018) Fast anion-exchange from CsPbI3 to CsPbBr3 via Br2-vapor-assisted deposition for air-stable all-inorganic perovskite solar cells. Chemical Engineering Journal 343:146–154. https://doi.org/10.1016/j.cej.2018.03.009
21. Burwig T, Fränzel W, Pistor P (2018) Crystal Phases and Thermal Stability of Co-evaporated CsPbX3 (X = I, Br) Thin Films. J Phys Chem Lett 9:4808–4813. https://doi.org/10.1021/acs.jpclett.8b02059
22. Zhuang S, Ma X, Hu D, et al. (2018) Air-stable all inorganic green perovskite light emitting diodes based on ZnO/CsPbBr3/NiO heterojunction structure. Ceramics International 44:4685–4688. https://doi.org/10.1016/j.ceramint.2017.12.048
23. Murphy JW, Kunnen GR, Mejia I, et al. (2012) Optimizing diode thickness for thin-film solid state thermal neutron detectors. Appl Phys Lett 101:143506. https://doi.org/10.1063/1.4757292
24. Fernandez-Izquierdo L, Reyes-Banda MG, Mathew X, et al. Cesium Lead Bromide (CsPbBr3) Thin-Film-Based Solid-State Neutron Detector Developed by a Solution-Free Sublimation Process. Advanced Materials Technologies n/a:2000534. https://doi.org/10.1002/admt.202000534
25. McGregor DS, Klann RT, Gersch HK, et al. (2002) New surface morphology for low stress thin-film-coated thermal neutron detectors. IEEE Transactions on Nuclear Science 49:1999–2004. https://doi.org/10.1109/TNS.2002.801697
26. Bellinger SL, Fronk RG, McNeil WJ, et al. (2011) Enhanced variant designs and characteristics of the microstructured solid-state neutron detector. Nuclear Instruments and Methods in Physics Research Section A: Accelerators, Spectrometers, Detectors and Associated Equipment 652:387–391. https://doi.org/10.1016/j.nima.2010.08.049
27. Fronk RG, Bellinger SL, Henson LC, et al. (2015) Advancements in microstructured semiconductor neutron detector (MSND)-based instruments. In: 2015 IEEE Nuclear Science Symposium and Medical Imaging Conference (NSS/MIC). pp 1–5
28. Nandagopala Krishnan SS, Avila-Avendano C, Shamsi Z, et al. (2020) 10B Conformal Doping for Highly Efficient Thermal Neutron Detectors. ACS Sens 5:2852–2857. https://doi.org/10.1021/acssensors.0c01013
29. Fu Y, Zhu H, Stoumpos CC, et al. (2016) Broad Wavelength Tunable Robust Lasing from Single-Crystal Nanowires of Cesium Lead Halide Perovskites (CsPbX3, X = Cl, Br, I). ACS Nano 10:7963–7972. https://doi.org/10.1021/acsnano.6b03916
30. Li J, Zhang H, Wang S, et al. (2018) Inter-Conversion between Different Compounds of Ternary Cs-Pb-Br System. Materials (Basel) 11. https://doi.org/10.3390/ma11050717

31. Chen H, Zhang M, Bo R, et al. (2018) Superior Self-Powered Room-Temperature Chemical Sensing with Light-Activated Inorganic Halides Perovskites. Small 14:1702571. https://doi.org/10.1002/smll.201702571
32. Endres J, Kulbak M, Zhao L, et al. (2017) Electronic structure of the CsPbBr3/polytriarylamine (PTAA) system. Journal of Applied Physics 121:035304. https://doi.org/10.1063/1.4974471
33. Shen Y, Wei C, Ma L, et al. (2018) In situ formation of CsPbBr3/ZnO bulk heterojunctions towards photodetectors with ultrahigh responsivity. J Mater Chem C 6:12164–12169. https://doi.org/10.1039/C8TC04374D
34. Xue M, Zhou H, Ma G, et al. (2018) Investigation of the stability for self-powered CsPbBr3 perovskite photodetector with an all-inorganic structure. Solar Energy Materials and Solar Cells 187:69–75. https://doi.org/10.1016/j.solmat.2018.07.023
35. Li Y, Shi Z-F, Li S, et al. (2017) High-performance perovskite photodetectors based on solution-processed all-inorganic CsPbBr3 thin films. J Mater Chem C 5:8355–8360. https://doi.org/10.1039/C7TC02137B
36. McGregor DS, Hammig MD, Yang Y-H, et al. (2003) Design considerations for thin film coated semiconductor thermal neutron detectors—I: basics regarding alpha particle emitting neutron reactive films. Nuclear Instruments and Methods in Physics Research Section A: Accelerators, Spectrometers, Detectors and Associated Equipment 500:272–308. https://doi.org/10.1016/S0168-9002(02)02078-8
37. Murphy JW, Smith L, Calkins J, et al. (2014) Thin film cadmium telluride charged particle sensors for large area neutron detectors. Appl Phys Lett 105:112107. https://doi.org/10.1063/1.4895925
38. Wei H, DeSantis D, Wei W, et al. (2017) Dopant compensation in alloyed CH 3 NH 3 PbBr 3−x Cl x perovskite single crystals for gamma-ray spectroscopy. Nature Mater 16:826–833. https://doi.org/10.1038/nmat4927
39. He X, Qiu Y, Yang S (2017) Fully-Inorganic Trihalide Perovskite Nanocrystals: A New Research Frontier of Optoelectronic Materials. Advanced Materials 29:1700775. https://doi.org/10.1002/adma.201700775
40. Hu Y, Wang Q, Shi Y-L, et al. (2017) Vacuum-evaporated all-inorganic cesium lead bromine perovskites for high-performance light-emitting diodes. J Mater Chem C 5:8144–8149. https://doi.org/10.1039/C7TC02477K
41. Wu Y, Li X, Fu S, et al. (2019) Efficient methylammonium lead trihalide perovskite solar cells with chloroformamidinium chloride (Cl-FACl) as an additive. J Mater Chem A 7:8078–8084. https://doi.org/10.1039/C9TA01319A
42. Liashenko TG, Cherotchenko ED, Pushkarev AP, et al. (2019) Electronic structure of CsPbBr3−xClx perovskites: synthesis, experimental characterization, and DFT simulations. Phys Chem Chem Phys 21:18930–18938. https://doi.org/10.1039/C9CP03656C
43. Li B, Zhang Y, Zhang L, Yin L (2017) PbCl2-tuned inorganic cubic CsPbBr3(Cl) perovskite solar cells with enhanced electron lifetime, diffusion length and photovoltaic performance. Journal of Power Sources 360:11–20. https://doi.org/10.1016/j.jpowsour.2017.05.050
44. Zheng L, Zhang D, Ma Y, et al. (2015) Morphology control of the perovskite films for efficient solar cells. Dalton Trans 44:10582–10593. https://doi.org/10.1039/C4DT03869J
45. Zhang Y, Luo L, Hua J, et al. (2019) Moisture assisted CsPbBr3 film growth for high-efficiency, all-inorganic solar cells prepared by a multiple sequential vacuum deposition method. Materials Science in Semiconductor Processing 98:39–43. https://doi.org/10.1016/j.mssp.2019.03.021
46. Reyes-Banda MG, Fernandez-Izquierdo L, Nandagopala Krishnan SS, et al. (2021) Material Properties Modulation in Inorganic Perovskite Films via Solution-Free Solid-State Reactions. ACS Appl Electron Mater. https://doi.org/10.1021/acsaelm.1c00072
47. Calistru DM, Mihut L, Lefrant S, Baltog I (1997) Identification of the symmetry of phonon modes in CsPbCl3 in phase IV by Raman and resonance-Raman scattering. Journal of Applied Physics 82:5391–5395. https://doi.org/10.1063/1.366307
48. Zhang L, Zeng Q, Wang K (2017) Pressure-Induced Structural and Optical Properties of Inorganic Halide Perovskite CsPbBr3. J Phys Chem Lett 8:3752–3758. https://doi.org/10.1021/acs.jpclett.7b01577

49. Yin J, Zhang Y, Bruno A, et al. (2017) Intrinsic Lead Ion Emissions in Zero-Dimensional Cs4PbBr6 Nanocrystals. ACS Energy Lett 2:2805–2811. https://doi.org/10.1021/acsenergylett.7b01026
50. Dursun I, Zheng Y, Guo T, et al. (2018) Efficient Photon Recycling and Radiation Trapping in Cesium Lead Halide Perovskite Waveguides. ACS Energy Lett 3:1492–1498. https://doi.org/10.1021/acsenergylett.8b00758
51. Fang Y, Wei H, Dong Q, Huang J (2017) Quantification of re-absorption and re-emission processes to determine photon recycling efficiency in perovskite single crystals. Nat Commun 8:1–9. https://doi.org/10.1038/ncomms14417
52. Wu B, Nguyen HT, Ku Z, et al. (2016) Discerning the Surface and Bulk Recombination Kinetics of Organic–Inorganic Halide Perovskite Single Crystals. Advanced Energy Materials 6:1600551. https://doi.org/10.1002/aenm.201600551
53. Priante D, Dursun I, Alias MS, et al. (2015) The recombination mechanisms leading to amplified spontaneous emission at the true-green wavelength in CH3NH3PbBr3 perovskites. Appl Phys Lett 106:081902. https://doi.org/10.1063/1.4913463
54. Sebastian M, Peters JA, Stoumpos CC, et al. (2015) Excitonic emissions and above-band-gap luminescence in the single-crystal perovskite semiconductors CsPbBr3 and CsPbC l3. Giant-magnetoresistance anomaly associated with a magnetization process in UFe4Al8 92:235210. https://doi.org/10.1103/PhysRevB.92.235210
55. Pintor-Monroy MI, Barrera D, Murillo-Borjas BL, et al. (2018) Tunable Electrical and Optical Properties of Nickel Oxide (NiOx) Thin Films for Fully Transparent NiOx–Ga2O3 p–n Junction Diodes. ACS Appl Mater Interfaces 10:38159–38165. https://doi.org/10.1021/acsami.8b08095
56. Wright G, Cui Y, Roy UN, et al. (2002) The effects of chemical etching on the charge collection efficiency of 111 oriented Cd/sub 0.9/Zn/sub 0.1/Te nuclear radiation detectors. IEEE Transactions on Nuclear Science 49:2521–2525. https://doi.org/10.1109/TNS.2002.803852
57. Advanced Materials for Radiation Detection; Iniewski, K., Ed.; Springer International Publishing: Cham, 2022. https://doi.org/10.1007/978-3-030-76461-6.
58. Xie, A.; Nguyen, T. H.; Hettiarachchi, C.; Witkowski, M. E.; Drozdowski, W.; Birowosuto, M. D.; Wang, H.; Dang, C. (2018) Thermal Quenching and Dose Studies of X-Ray Luminescence in Single Crystals of Halide Perovskites. J. Phys. Chem. C, 122 (28), 16265–16273. https://doi.org/10.1021/acs.jpcc.8b03622.
59. Zhang, B.-B.; Wang, F.; Zhang, H.; Xiao, B.; Sun, Q.; Guo, J.; Hafsia, A. B.; Shao, A.; Xu, Y.; Zhou, J. (2020) Defect Proliferation in CsPbBr3 Crystal Induced by Ion Migration. Appl. Phys. Lett., 116 (6), 063505. https://doi.org/10.1063/1.5134108.
60. Shuigen L., Xiangyu X., Jian X., Fahui W., Jian L. and Minhua J. (2022) Review: Perovskite X-ray Detectors (1997–Present). Crystals, 12, 1563, https://doi.org/10.3390/cryst12111563.

Metal Halide Perovskite Solar Modules: Manufacturing and Performance



Angelique Montgomery and Joshua Stein

1 Introduction

Metal halide perovskites (MHPs) are favored electronic and optoelectronic semiconductor devices due to their high conversion efficiency and low cost. In 2009, MHPs were used in the development of perovskite solar cells (PSCs) with a power conversion efficiency (PCE) of 3.8% [1]. PCE has risen rapidly to 25.7% [2] in 2022 for single-junction solar cell architectures with area < 0.1 cm^2. With the current focus on low-cost, clean, and renewable energy sources, there is great interest in upscaling this technology to large-area photovoltaic (PV) modules. The Department of Energy (DOE) has defined aggressive goals to reduce the levelized cost of electricity (LCOE) for utility-scale PV to $0.02/kWh by 2030 [3–5]. Two scenarios are defined to reach this goal: (1) high performance and (2) low cost. The low-cost scenario assumes module efficiency of 20% and a cost of $0.17/W [4]. To achieve this goal, a module technology must be manufactured at a fraction of the cost of conventional crystalline silicon-based (c-Si) modules. Locally produced, solution- or vapor-processed perovskite PV modules offer a promising pathway to meet this goal. However, challenges exist in upscaling from the cell level (<10 cm^2) to the

Reprint notice: This chapter is a condensed version and reprint of a previously published chapter. For an expanded discussion more on the reliability and toxicity risks associated with MHP modules, please refer to the original print Montgomery, A.M., Doumon, N.Y., Torrence, C., Schelhas, L.T., Stein, J.S. (2023). "Metal Halide Perovskite Solar Modules: The Challenge of Upscaling and Commercializing This Technology". In: Nie, W., Iniewski, K. (eds) *Metal-Halide Perovskite Semiconductors*. Springer, Cham. https://doi.org/10.1007/978-3-031-26892-2_14.

A. Montgomery (✉) · J. Stein
Sandia National Laboratories, Albuquerque, NM, USA
e-mail: ammontg@sandia.gov

© The Author(s), under exclusive license to Springer Nature Switzerland AG 2024

S. Krishnamoorthy, K. (Kris) Iniewski (eds.), *Advances in Fabrication and Investigation of Nanomaterials for Industrial Applications*,
https://doi.org/10.1007/978-3-031-42700-8_16

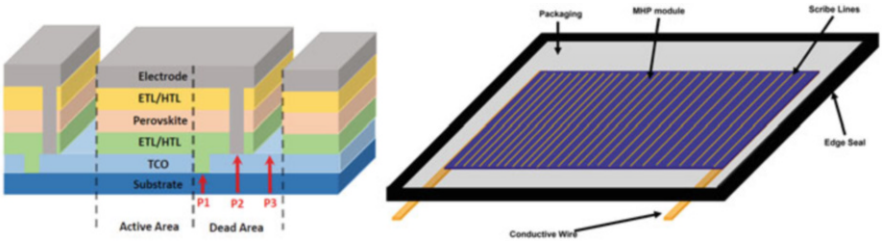


Fig. 1 (**a**) Schematic for MHP thin film including all deposited layers. ETL/HTL is alternated to either an inverted n-*i*-p or planar p-*i*-n structure. This schematic includes the separation of interconnected subcells using scribing of P1, P2, and P3. (**b**) Schematic of packaged MHP module with a glass-glass configuration

minimodule (>100–1000 cm^2) or full module level (>1000 cm^2); however, current PV technologies have overcome similar challenges. While upscaling represents a significant engineering and research effort, it is a common stage in the path to commercializing new PV technologies. In this chapter we outline two critical research areas to be addressed in this path to commercialization: manufacturing and performance characterization. Here, we provide a short introduction to each topic.

Manufacturing There are many challenges to upscaling to full-sized MHP modules and developing commercial manufacturing process. Applying uniform thin films to large areas requires fundamentally different methods than are used for small single cells. Spin coating, which has been used for most PSC research and development, is not scalable for large areas and mass production. Instead, slot-die, blading, spray coating, or vapor-based application methods are preferred [6–17]. However, changing the film application method requires changes to the precursor ink rheology and careful attention to the processing steps and the manufacturing environment to ensure a high-quality, uniform film deposition. In addition, module fabrication involves additional processing steps compared to cells. Scribing is used between film deposition steps to divide the film into separate interconnected cells (Fig. 1a). Along with careful deposition, scribe quality and scribing precision are important aspects to module fabrication to minimize electrical losses. Another approach to using perovskites in PV modules is in a tandem structure where the PSC is placed above a second solar cell. The bottom cell could be a variety of materials, for example, c-Si, CdTe, CIGS, or even other PSCs. Monolithically integrated two-terminal (2 T) and mechanically stacked four-terminal (4 T) tandem solar cells provide a solution to the critical thermalization loss and high transmission phenomenon seen in single-junction architectures. However, each approach faces different engineering challenges.

A commercial thin-film module must be protected from environmental stresses such as mechanical loading, moisture, UV radiation, etc. Typically, thin-film modules are laminated between two sheets of glass to protect the active layers from the environment as shown in Fig. 1b. Perovskites are especially sensitive to

moisture exposure; adding an additional packaging requirement to reduce water ingress as much as possible is preferred. We note that module packaging is an aspect of manufacturing that must be addressed in the path to commercialization but will not be covered in detail in this chapter.

Performance Characterization Another challenge for commercializing perovskite modules is the difficulty in characterizing module performance due to their relatively slow response and metastability. Conventional c-Si and other thin-film PV modules (e.g., CdTe and CIGS) can be characterized on the production line using a flash test, where the module is exposed to a rapid flash of light (~100 ms or less) during which an I-V curve is measured. Like other current PV technologies such as CdTe and CIGS, many PSCs are metastable when initially exposed to light. Meaning their electrical output changes rapidly until it eventually stabilizes, a process that can take several seconds to hours. Preconditioning (or stabilization) is a general technique used to bring a module into a stable state so that a characterization is repeatable. Preconditioning usually involves illuminating the module until performance is stable. However, preconditioning takes time which is non-conducive for a high-speed production line that cannot wait for each module to stabilize during production. Therefore, to satisfy the unmet challenge for rapid production rates and comparable devices in MHP modules, fast measurement techniques need to be developed and validated to support high-speed manufacturing.

This chapter will explore the challenges associated with the manufacturing and performance characterization of large-scale MHP modules.

2 Manufacturing of Perovskite PV Modules

There are two primary methods used to deposit the active perovskite layer and charge transporting layers (CTLs) for large-area modules: (i) solution- or chemical-based deposition (one-step or two -step) [6, 7, 18–30] and (ii) vapor-based deposition [20, 31–34]. Scalable solution methods include blade, slot-die, gravure, and spray coating. Vapor-based methods have been widely adopted in the PV industry for manufacturing CdTe PV modules [35, 36] but can require more challenging setups (e.g., vacuum processing) compared to solution processing methods.

To achieve high-performance modules, high-quality homogeneous films are required. High-quality films are often characterized by uniform coverage and pinhole-free films [30, 37]. However, achieving high-quality films for a seamless production requires a controlled manufacturing environment and atmosphere that includes posttreatments such as substrate heating [38], air-knife assistance [39], cosolvent incorporation [40, 41], antisolvent engineering [42], Lewis acid-base adduct method [43], additive engineering [44–46], and efficient precursor solution chemistries that enable low-defect solvent removal [47, 9]. There are a number of detailed review papers on these topics and therefore will not be covered extensively here [9, 39, 43, 46, 48–69]. Precursor rheology must also be optimized for each

application method and deposition technique. Multi-solvent blends are typically developed for large-area depositions to optimize film formation. Common solvents include dimethyl sulfoxide (DMSO), dimethylformamide (DMF), N-methyl-2-pyrrolidone (NMP), γ-butyrolactone GBL (used as cosolvent), THF, 2ME, and others. However, DMF introduces significant health risks, and GBL is subject to legal restrictions in many countries which limits their commercial viability [70]. The need for an environmentally safe nonvolatile solvent to synthesize the active and transport layers is an essential step toward commercial viability [70–74].

Green solvents exist such as ethyl acetate (EA) which is typically used as an antisolvent for perovskite precursor to optimize the perovskite/transporting material interface [75]. However, EA evaporation is slow and could impact the active layer crystallization process [75, 76]. Therefore, developing new green solvent chemistries with more volatile systems are needed for low-energy, low-cost scalable fabrication methods with limited waste and efficient precursor chemistries for large-area manufacturing [58, 71, 72, 74–79].

The need for a reliable low-cost manufacturing process depends on a reproducible method with high-throughput homogeneous deposition. Roll-to-roll and sheet-to-sheet processing are attractive options for MHP manufacturing. Roll-to-roll is a low-cost operation that allows for flexible substrates, continuous production, and high speeds [80–82]. Sheet-to-sheet processing is less susceptible to damage than roll-to-roll; however, switching to multiple substrates is easier in this method because there is only one roll holder [81, 83]. In either system, reproducibility is critical with large-area substrates to ensure the manufacturing process yields similar performance properties every time.

To make modules, it is necessary to add scribing steps between the depositions of the various layers of the MHP device (Fig. 1a). The division of the film into separate smaller series-connected subcells increases the voltage; however, the current in the module is limited by the lowest current produced by any of the subcells. Therefore, reducing resistive losses and increasing efficiency is dependent on developing homogeneous deposition processes for all functional layers. The purpose of this serial interconnection is to limit the total current loss from the transparent conductive oxide (TCO) layer and minimize resistive losses that result in a decrease in device PCE as the area is increased. However, in the case of 2 T tandems, modules are mechanically stacked and do not necessarily have scribe lines.

Scribing techniques used within the literature rely on three scribing steps P1, P2, and P3. The scribing is repeated depending on the number of subcells on a single large-area substrate. P1 patterning defines the width of a subcell and isolates the substrate from the front transparent conductive oxide (TCO) layer. After the deposition of the electron/hole transporting layers as well as the absorber layer, P2 scribing is performed. An interconnection of the neighboring subcells is produced by selectively removing the top layers of the oxide to expose the TCO layer with mechanical or laser scribing. The precision of the P2 scribe is very important because it is used to establish a series contact between the back and front conductive layers of neighboring cells in the module to ensure optimum charge conductivity [84–86]. If P2 is not precise, the current transport that is formed from the electrical

interconnection of subcells is limited [29, 85, 87]. The final P3 scribe is performed after the application of the bottom electrode which completes the monolithic series interconnection by producing electrical isolation for the top electrode and the adjacent subcells. The bottom electrode is laser scribed to electrically disconnect the back contact from subcells to form P3. The region between P1 and P3 is considered the "dead area" because it does not contribute to PV conversion under operational conditions [87, 88]. Scribing methods must be precise, and the purpose of scribing is to achieve good electrical series interconnection with low active area loss. Efficient scribe passivation and a good electrical series interconnection with very low area loss is key for high-performing modules. As more research pivots to the module scale, scribing and passivation will likely become a critical focus of the research community.

The series interconnection of subcells produces dead zones between the active solar cell strips that result in a loss of active area efficiency which is related to high resistivity of the transparent conductive oxide (TCO) layer. As the substrate area increases, the PCE suffers due to the high impact of internal resistivity of the TCO.

Inactive area losses are defined by the geometrical fill factor (GFF): the ratio between active area and total area [89]. By enlarging the module area, the GFF can be enhanced because the ratio of dead area associated with edges for encapsulation and frames is reduced [89, 90]. However, as active area width is lost, the photo-generated carriers are reduced and the efficiency suffers. Therefore, there exists a trade-off between wider cells (lower inactive area with higher resistive losses) and narrower cells (higher inactive area and lower resistive losses) [91, 92]. It is for these reasons that there is still a significant gap between cell and module efficiencies. Panasonic Corporation achieved a PCE of 16.09% for a perovskite module with an aperture area of 802 cm^2 which is 30 cm long, 30 cm wide, and 2 mm thick [93]. Careful engineering methods are needed to promote long lifetime operation stability and reliability with GFFs beyond 99% to finally close the gap in cell-to-module performance loss.

Loss in the active area is sometimes unavoidable due to processing techniques and necessary deposition parameters. In addition, possible shunts or additional series resistivity issues could arise in either scribing step. This is of utmost concern due to degradation of the electrical properties that can become an issue in nonideal removal processes. Excellent electrical properties in combination with precise scribing widths and patterning methods enable interconnections with minimal active area loss and optimum device performance. Studies show that the interconnection of subcells is the most relevant loss in perovskite solar modules [85, 94]. Once the interconnections of subcells are optimized, the next objective necessary to further increase perovskite module performance shifts from the patterning of layers and scribing to optimizing the electrode materials and upscaling high-quality large-area deposition methods.

Careful characterization and rapid production rates for large-area MHP modules are contingent upon the quality and efficiency in module performance characterization and in-process characterization methods that reflect the unique behavior of MHP. Multiple steps within perovskite module production will rely on fast

and efficient in-line characterization methods to validate module performance and identify key parameters that impact production quality for a highly controlled manufacturing process.

3 Performance Characterization

In order to produce high-quality MHP modules, process control and in-line detection methods that quickly monitor the film quality and performance of modules are needed. Performance loss under illumination is identified depending on its effects in the current-voltage (I-V) characteristics of the device [95–97]. Electronic shunts, ohmic loss (voltage drop), recombination loss, and reduced current generation all impact device performance [95]; however, most are manufacturing defects that can be improved with careful large-scale fabrication. MHP undergoes voltage changes when exposed to light and voltage bias with rates affected by temperature. Therefore, fast measurements to monitor the film quality and its electrical characteristics during multiple stages of production are critical to ensure long-term performance for project owners and investors.

Small electronic shunts originate from high resistance between the cell's two contacts that cause local heating (hot spots) and faults that influence hysteresis behavior and reduce the maximum power [98]. Uneven coverage of the absorber and contacts, inhomogeneities between the deposited layers, and rough surfaces can cause shunts that impede the current generation and performance parameters like V_{oc} and FF. As a result, power is reduced, and an undesirable I-V hysteresis may result which is mainly related to ion migration in the bulk and at the interface of the device [99–101]. I-V curves and electroluminescence (EL) imaging are typically used to monitor shunt behavior at various stages of production.

The PV community reports device performance at a fixed condition, known as standard testing conditions (STC). This is defined as a module temperature of 25 °C, solar irradiance of 1000 W/m^2, and a reference spectrum defined at air mass of AM1.5 [102]. STC creates uniformity in testing conditions for accurate comparisons of module performance from different manufacturers. In an I-V measurement, a voltage is swept across a device, and the current is recorded at each stabilized voltage step which typically takes seconds [102]. Ideally, the measured current will be dependent on the measuring conditions (voltage, temperature, irradiance, environmental conditions) and not the prior history of the device [102]. However, perovskites response times (seconds to minutes) require longer sweep times and scan rates to allow for sufficient current stabilization at each voltage step [80]. The IEC 60904-1 measurement standard describes procedures for I-V characteristics of PV devices to ensure basic requirements for I-V measurements, define procedures for different measuring techniques, and include practices to minimize measurement uncertainty [103]. However, the IEC 60904-1 standard does not describe the special treatments needed to stabilize the current before performance characterization. Characterization methods typically use simple equipment; however, due to MHP

metastability and slow responding device behavior, precise measurements require specialized equipment and expertise.

The primary measurement used to rate modules during production is the maximum output power (P_{max}) ratings at STC. This is an essential parameter for accurate output power rating nameplates and specification data sheets that distinguish between cost-dependent high-performing and low-performing perovskite modules. The higher the power rating, the more watts the module produces and the more expensive the module. Power ratings are critical because they aim to match real-life conditions for a fair understanding about how modules perform outdoors. However, accurate P_{max} is a challenge because it is difficult for a simulator to exhibit real environmental conditions by only varying the temperature and irradiance without the consideration of environmental stressors. Maximum power point (MPP) tracking is a continuous steady-state measurement to find the maximum power by using a perturb-and-observe algorithm to keep the device at its maximum power for some time, and then an average power is reported to represent P_{max}.

The repeatability and accuracy of P_{max} is significantly influenced by the spectral uniformity of the module simulator which introduces new reference calibration challenges [104]. The choice of reference devices for an I-V measurement needs accurate spectral irradiance over the widest possible wavelength in which perovskite cells respond. Selecting a reference cell that shows the same spectral response (minimal variations) as perovskites is a challenge due to the unavailability of a perfectly matched reference device [105]. A perfectly matched reference cell/module is used to bypass the spectral mismatch correction for spectral responsivity measurements and provide a more uniform spectrum for optimum measurement results [106]. Aside from this, the spectral uniformity suffers as the dimensions of the modules grow which is a huge concern for large-area MHP commercialization.

Flash tests are a quick method that can be automated on a production line and performed approximately at a rate of once per second by exposing the module to a fast (20–100+ ms) flash of light during which an I-V curve is produced and P_{max} is measured. Flash tests are a conventional method used to yield power ratings for current commercial PV technologies. Spectral uniformity match, spatial uniformity, and temporal stability are used to assess the reliability and quality of the measurement. It is performed several times during production, especially after lamination to test the functionality and performance of the completed module. Though flash testing has shown its effectiveness for current commercial PV technologies, it remains a challenge for MHP modules. Song et al. showed that fast I-V curves may overestimate I_{sc} and underestimate FF for PSCs compared to a slow asymptotic continuous scan [81, 105–107]. Increasing the scan speed is possible for a flash test; however, it could overestimate performance parameters like V_{oc}. Decreasing the scan speed could easily give time for carrier generation and extraction to come to completion; however, slow scans require different light source and increase the overall testing time. It is difficult to assume that all identical modules will respond identically to a flash test, though this test could give a close enough approximation to a consistent performance measurement to distinguish between best- and worst-performing modules. This is an area of current research.

Typical performance information can be obtained from a continuous or pulsed simulator including I-V measurements, maximum power point tracking (MPPT), stabilized current at a fixed voltage (SCFV), dynamic I-V methods, and temperature coefficient calculations. Dynamic I-V or asymptotic I-V measurements are like conventional I-V in which a stepwise I-V is produced; however, at each voltage step, a stabilization period allows the device under test sufficient time to complete current collection. Essentially it is a series of stabilized current at fixed voltage (SCFV) measurements over a specific voltage range. Dunbar et al. showed that dynamic I-V technique to produce an asymptotic P_{max} followed by light-soaking near-maximum power point voltage (V_{mpp}) and a conventional I-V curve is the most reliable performance characterization method for perovskites [108]. However, I-V curves can differ between forward and reverse scan directions, and its severity is dependent on scanning rate and prior treatments to the device.

Some MHP cells and modules exhibit different I-V behavior depending on the direction of the I-V curve (Isc to Voc vs. Voc to Isc) [49]. This I-V hysteresis behavior is dependent on parameters such as scan rate, scan direction, bias applied, preconditioning, and device architecture [99, 109–111]. Different electrical characteristics of an I-V curve limit reproducibility and lower carrier mobility and collection rates while presenting challenges for a fast-responding stable measurement. The origin of an I-V hysteresis is mainly ion migration; however, ferroelectric polarization, ion trapping, and capacitive effects are also potential causes [100, 105, 107, 112–116]. Ion migration in MHP gained much attention when Snaith et al. suggested that it was one of three possible origins for the I-V hysteresis phenomenon and showed how device architecture and process control influence the severity of the I-V hysteresis behavior [117–119]. They showed that a stabilized power output is possible under operational conditions; however, the I-V hysteresis is likely to affect MPP tracking effectiveness. More work in this area should focus on ion migration kinetics and how light illumination and dark storage impact the movement of ionic and electronic species and device stability.

The effect of operating temperature on module performance is an important parameter for yield assessment. Not many studies have been performed to measure these effects on PSCs or MHP modules. Moot et al. studied PSC performance with temperature and found the relationship to be nonlinear [120]. They showed that efficiency vs. temperature for MHPs was influenced by a change in V_{oc} and I_{sc} which is distinct from c-Si which is predominantly affected by V_{oc} [120, 121]. Accurate temperature coefficient calculations are necessary for the commercialization of this technology. More work is needed in this area.

3.1 Future Work and Challenges

The commercialization of MHP solar modules is a promising technology for achieving the US government's decarbonization goals of 100% carbon-free electricity generation by 2035 [3]. MHP modules are on the cusp of commercialization with

several research and manufacturing gaps as final barriers. Reproducible deposition of efficient thin-film MHP solar modules needs to be demonstrated at large areas and rapid processing rates. Characterization methods are needed to monitor the quality and performance of the products coming off these high-speed production lines.

Acknowledgments This material is based upon work supported by the US Department of Energy's Office of Energy Efficiency and Renewable Energy (EERE) under the Solar Energy Technologies Office Award Number 38050.

Sandia National Laboratories is a multimission laboratory managed and operated by National Technology & Engineering Solutions of Sandia, LLC, a wholly owned subsidiary of Honeywell International Inc., for the US Department of Energy's National Nuclear Security Administration under contract DE-NA0003525.

The views expressed in the article do not necessarily represent the views of the DOE or the US government. The US government retains and the publisher, by accepting the article for publication, acknowledges that the US government retains a nonexclusive, paid-up, irrevocable, worldwide license to publish or reproduce the published form of this work, or allows others to do so, for US government purposes.

References

1. A. Kojima, K. T., Y. Shirai, T. Miyasaka. Organometal Halide Perovskites as Visible-Light Sensitizers for Photovoltaic Cells. *American Chemical Society* **131**, 6050–6051 (2009).
2. Bellini, E. *UNIST, EPFL claim 25.6% efficiency world record for perovskite solar cell*, 2021).
3. Siegler, T. D. *et al.* The Path to Perovskite Commercialization: A Perspective from the United States Solar Energy Technologies Office. *ACS Energy Letters*, 1728–1734, https://doi.org/10.1021/acsenergylett.2c00698 (2022).
4. B.L. Smith, M. W., K.A.W Horowitz, T.J. Silverman, J. Zuboy, R.M. Margolis. Photovoltaic (PV) Module Technologies_ 2020 Benchmark costs and technology evolution framework results. (NREL, 2021).
5. Wilson, G. M. *et al.* The 2020 photovoltaic technologies roadmap. *Journal of Physics D: Applied Physics* **53**, https://doi.org/10.1088/1361-6463/ab9c6a (2020).
6. Pérez-Gutiérrez, E. *et al.* Organic solar cells all made by blade and slot–die coating techniques. *Solar Energy* **146**, 79–84, https://doi.org/10.1016/j.solener.2017.02.004 (2017).
7. Z. Yang, W. Z., S. Wu, H. Zhu, Z. Liu, Z. Lui, Z. Jiang, R. Chen., J. Zhou. Slot-die coating large-area formamidinium-cesium perovskite film for efficient and stable parallel solar module. (2021).
8. Rong, Y. *et al.* Toward Industrial-Scale Production of Perovskite Solar Cells: Screen Printing, Slot-Die Coating, and Emerging Techniques. *J Phys Chem Lett* **9**, 2707–2713, https://doi.org/10.1021/acs.jpclett.8b00912 (2018).
9. Liu, C., Cheng, Y. B. & Ge, Z. Understanding of perovskite crystal growth and film formation in scalable deposition processes. *Chem Soc Rev* **49**, 1653–1687, https://doi.org/10.1039/c9cs00711c (2020).
10. Bishop, J. E., Smith, J. A. & Lidzey, D. G. Development of Spray-Coated Perovskite Solar Cells. *ACS Appl Mater Interfaces* **12**, 48237–48245, https://doi.org/10.1021/acsami.0c14540 (2020).
11. Lee, D. S. *et al.* Fully Scalable and Stable CsPbI2Br Solar Cells Realized by an All-Spray-Coating Process. *ACS Appl Mater Interfaces* **14**, 7926–7935, https://doi.org/10.1021/acsami.1c21644 (2022).
12. Parida, B. *et al.* Recent Developments in Upscalable Printing Techniques for Perovskite Solar Cells. *Adv Sci (Weinh)*, e2200308, https://doi.org/10.1002/advs.202200308 (2022).

13. Howard, I. A. *et al.* Coated and Printed Perovskites for Photovoltaic Applications. *Adv Mater* **31**, e1806702, https://doi.org/10.1002/adma.201806702 (2019).
14. Castro-Hermosa, S. *et al.* Efficient fully blade-coated perovskite solar cells in air with nanometer-thick bathocuproine buffer layer. *Nano Research* **14**, 1034–1042, https://doi.org/10.1007/s12274-020-3147-4 (2020).
15. Liang, Q. *et al.* Manipulating Crystallization Kinetics in High-Performance Blade-Coated Perovskite Solar Cells via Cosolvent-Assisted Phase Transition. *Adv Mater*, e2200276, https://doi.org/10.1002/adma.202200276 (2022).
16. Razza, S. *et al.* Perovskite solar cells and large area modules (100cm2) based on an air flow-assisted PbI2 blade coating deposition process. *Journal of Power Sources* **277**, 286–291, https://doi.org/10.1016/j.jpowsour.2014.12.008 (2015).
17. Ouyang, Z., Yang, M., Whitaker, J. B., Li, D. & van Hest, M. F. A. M. Toward Scalable Perovskite Solar Modules Using Blade Coating and Rapid Thermal Processing. *ACS Applied Energy Materials* **3**, 3714–3720, https://doi.org/10.1021/acsaem.0c00180 (2020).
18. Liu, Z. *et al.* A holistic approach to interface stabilization for efficient perovskite solar modules with over 2,000-hour operational stability. *Nature Energy* **5**, 596–604, https://doi.org/10.1038/s41560-020-0653-2 (2020).
19. Tong, G. *et al.* Scalable Fabrication of >90 cm2 Perovskite Solar Modules with >1000 h Operational Stability Based on the Intermediate Phase Strategy. *Advanced Energy Materials* **11**, https://doi.org/10.1002/aenm.202003712 (2021).
20. Sha, Y. *et al.* A Scalable Integrated Dopant-Free Heterostructure to Stabilize Perovskite Solar Cell Modules. *Advanced Energy Materials* **11**, https://doi.org/10.1002/aenm.202003301 (2020).
21. Jiang, Y. *et al.* Combination of Hybrid CVD and Cation Exchange for Upscaling Cs-Substituted Mixed Cation Perovskite Solar Cells with High Efficiency and Stability. *Advanced Functional Materials* **28**, https://doi.org/10.1002/adfm.201703835 (2018).
22. Jiang, Y. *et al.* Negligible-Pb-Waste and Upscalable Perovskite Deposition Technology for High-Operational-Stability Perovskite Solar Modules. *Advanced Energy Materials* **9**, https://doi.org/10.1002/aenm.201803047 (2019).
23. Bu, T. *et al.* Dynamic Antisolvent Engineering for Spin Coating of 10×10 cm2 Perovskite Solar Module Approaching 18%. *Solar RRL* **4**, https://doi.org/10.1002/solr.201900263 (2019).
24. Dai, X. *et al.* Scalable Fabrication of Efficient Perovskite Solar Modules on Flexible Glass Substrates. *Advanced Energy Materials* **10**, https://doi.org/10.1002/aenm.201903108 (2019).
25. Chiang, C.-H., Nazeeruddin, M. K., Grätzel, M. & Wu, C.-G. The synergistic effect of H2O and DMF towards stable and 20% efficiency inverted perovskite solar cells. *Energy & Environmental Science* **10**, 808–817, https://doi.org/10.1039/c6ee03586h (2017).
26. Hu, C. *et al.* Discovery of a New Intermediate Enables One-Step Deposition of High-Quality Perovskite Films via Solvent Engineering. *Solar RRL* **5**, https://doi.org/10.1002/solr.202000712 (2021).
27. Im, J.-H., Kim, H.-S. & Park, N.-G. Morphology-photovoltaic property correlation in perovskite solar cells: One-step versus two-step deposition of CH3NH3PbI3. *APL Materials* **2**, https://doi.org/10.1063/1.4891275 (2014).
28. Liu, Z. *et al.* Scalable one-step heating up synthesis of Cu2ZnSnS4 nanocrystals hole conducting materials for carbon electrode based perovskite solar cells. *Solar Energy* **224**, 51–57, https://doi.org/10.1016/j.solener.2021.05.089 (2021).
29. Christians, J. A. *et al.* Stability at Scale: Challenges of Module Interconnects for Perovskite Photovoltaics. *ACS Energy Letters* **3**, 2502-2503, https://doi.org/10.1021/acsenergylett.8b01498 (2018).
30. Yang, M. *et al.* Perovskite ink with wide processing window for scalable high-efficiency solar cells. *Nature Energy* **2**, https://doi.org/10.1038/nenergy.2017.38 (2017).
31. Nair, S., Patel, S. B. & Gohel, J. V. Recent trends in efficiency-stability improvement in perovskite solar cells. *Materials Today Energy* **17**, https://doi.org/10.1016/j.mtener.2020.100449 (2020).

32. Qiu, L. *et al.* Hybrid chemical vapor deposition enables scalable and stable Cs-FA mixed cation perovskite solar modules with a designated area of 91.8 cm2 approaching 10% efficiency. *Journal of Materials Chemistry A* **7**, 6920–6929, https://doi.org/10.1039/c9ta00239a (2019).
33. Leyden, M. R., Jiang, Y. & Qi, Y. Chemical vapor deposition grown formamidinium perovskite solar modules with high steady state power and thermal stability. *Journal of Materials Chemistry A* **4**, 13125–13132, https://doi.org/10.1039/c6ta04267h (2016).
34. Li, J. *et al.* Highly Efficient Thermally Co-evaporated Perovskite Solar Cells and Mini-modules. *Joule* **4**, 1035–1053, https://doi.org/10.1016/j.joule.2020.03.005 (2020).
35. Compaan, A. D., Gupta, A., Lee, S., Wang, S. & Drayton, J. High efficiency, magnetron sputtered CdS/CdTe solar cells. *Solar Energy* **77**, 815–822, https://doi.org/10.1016/j.solener.2004.06.013 (2004).
36. Ramanujam, J. *et al.* Flexible CIGS, CdTe and a-Si:H based thin film solar cells: A review. *Progress in Materials Science* **110**, https://doi.org/10.1016/j.pmatsci.2019.100619 (2020).
37. Han, G. S. *et al.* Spin-Coating Process for 10 cm × 10 cm Perovskite Solar Modules Enabled by Self-Assembly of SnO2 Nanocolloids. *ACS Energy Letters* **4**, 1845–1851, https://doi.org/10.1021/acsenergylett.9b00953 (2019).
38. Park, N.-G. & Zhu, K. Scalable fabrication and coating methods for perovskite solar cells and solar modules. *Nature Reviews Materials* **5**, 333–350, https://doi.org/10.1038/s41578-019-0176-2 (2020).
39. Cheng, R. *et al.* An Air Knife-Assisted Recrystallization Method for Ambient-Process Planar Perovskite Solar Cells and Its Dim-Light Harvesting. *Small* **15**, e1804465, https://doi.org/10.1002/smll.201804465 (2019).
40. Zhang, X., Yang, W., Qi, J. & Hu, Y. Preparing Ambient-Processed Perovskite Solar Cells with Better Electronic Properties via Preheating Assisted One-Step Deposition Method. *Nanoscale Res Lett* **15**, 178, https://doi.org/10.1186/s11671-020-03407-9 (2020).
41. Li, P., Omer Mohamed, M. I., Xu, C., Wang, X. & Tang, X. Electrical property modified hole transport layer (PEDOT:PSS) enhance the efficiency of perovskite solar cells: Hybrid co-solvent post-treatment. *Organic Electronics* **78**, https://doi.org/10.1016/j.orgel.2019.105582 (2020).
42. Li, C.-Y. *et al.* Anti-solvent mixture-mediated reduction of photocurrent hysteresis in high-impurity perovskite precursor based MAPbI3 solar cells. *Solar Energy* **214**, 86–92, https://doi.org/10.1016/j.solener.2020.11.062 (2021).
43. Lee, D.-K., Lim, K.-S., Lee, J.-W. & Park, N.-G. Scalable perovskite coating via anti-solvent-free Lewis acid–base adduct engineering for efficient perovskite solar modules. *Journal of Materials Chemistry A* **9**, 3018–3028, https://doi.org/10.1039/d0ta10366g (2021).
44. Zhang, F. & Zhu, K. Additive Engineering for Efficient and Stable Perovskite Solar Cells. *Advanced Energy Materials* **10**, https://doi.org/10.1002/aenm.201902579 (2019).
45. Liu, Y. *et al.* Ionic additive engineering for stable planar perovskite solar cells with efficiency >22%. *Chemical Engineering Journal* **426**, https://doi.org/10.1016/j.cej.2021.130841 (2021).
46. Li, Y., Dailey, M., Lohr, P. J. & Printz, A. D. Performance and stability improvements in metal halide perovskite with intralayer incorporation of organic additives. *Journal of Materials Chemistry A* **9**, 16281–16338, https://doi.org/10.1039/d1ta05252g (2021).
47. Conings, B. *et al.* The impact of precursor water content on solution-processed organometal halide perovskite films and solar cells. *Journal of Materials Chemistry A* **3**, 19123–19128, https://doi.org/10.1039/c5ta06199g (2015).
48. Sakai, N. *et al.* Controlling Nucleation and Growth of Metal Halide Perovskite Thin Films for High-Efficiency Perovskite Solar Cells. *Small* **13**, https://doi.org/10.1002/smll.201602808 (2017).
49. Cheng, Y., Peng, Y., Jen, A. K. Y. & Yip, H.-L. Development and Challenges of Metal Halide Perovskite Solar Modules. *Solar RRL*, https://doi.org/10.1002/solr.202100545 (2021).
50. Zhong, J. X., Wu, W. Q., Ding, L. & Kuang, D. B. Blade-coating Perovskite Films with Diverse Compositions for Efficient Photovoltaics. *Energy & Environmental Materials* **4**, 277–283, https://doi.org/10.1002/eem2.12118 (2020).

51. Gao, L.-L., Li, C.-X., Li, C.-J. & Yang, G.-J. Large-area high-efficiency perovskite solar cells based on perovskite films dried by the multi-flow air knife method in air. *Journal of Materials Chemistry A* **5**, 1548–1557, https://doi.org/10.1039/c6ta09565h (2017).
52. Abdelsamie, M. *et al.* Impact of Processing on Structural and Compositional Evolution in Mixed Metal Halide Perovskites during Film Formation. *Advanced Functional Materials* **30**, https://doi.org/10.1002/adfm.202001752 (2020).
53. Zhang, H. *et al.* A universal co-solvent dilution strategy enables facile and cost-effective fabrication of perovskite photovoltaics. *Nat Commun* **13**, 89, https://doi.org/10.1038/s41467-021-27740-4 (2022).
54. Liu, R. *et al.* The synergistic effect of co-solvent engineering and thermal engineering towards phase control two-dimensional perovskite solar cells. *Solar Energy* **209**, 446–453, https://doi.org/10.1016/j.solener.2020.09.006 (2020).
55. Ha, S. T., Su, R., Xing, J., Zhang, Q. & Xiong, Q. Metal halide perovskite nanomaterials: synthesis and applications. *Chem Sci* **8**, 2522–2536, https://doi.org/10.1039/c6sc04474c (2017).
56. Sun, J., Li, F., Yuan, J. & Ma, W. Advances in Metal Halide Perovskite Film Preparation: The Role of Anti-Solvent Treatment. *Small Methods* **5**, e2100046, https://doi.org/10.1002/smtd.202100046 (2021).
57. Li, M. *et al.* Enhanced Efficiency and Stability of Perovskite Solar Cells via Anti-Solvent Treatment in Two-Step Deposition Method. *ACS Appl Mater Interfaces* **9**, 7224–7231, https://doi.org/10.1021/acsami.7b01136 (2017).
58. Lee, D. S. *et al.* Grain Quality Engineering for Organic Metal Halide Perovskites Using Mixed Antisolvent Spraying Treatment. *Solar RRL* **4**, https://doi.org/10.1002/solr.201900397 (2019).
59. Moot, T. *et al.* CsI-Antisolvent Adduct Formation in All-Inorganic Metal Halide Perovskites. *Advanced Energy Materials* **10**, https://doi.org/10.1002/aenm.201903365 (2020).
60. Lee, J. W., Kim, H. S. & Park, N. G. Lewis Acid-Base Adduct Approach for High Efficiency Perovskite Solar Cells. *Acc Chem Res* **49**, 311–319, https://doi.org/10.1021/acs.accounts.5b00440 (2016).
61. Wang, S. *et al.* Lewis acid/base approach for efficacious defect passivation in perovskite solar cells. *Journal of Materials Chemistry A* **8**, 12201–12225, https://doi.org/10.1039/d0ta03957h (2020).
62. Jia, Q. *et al.* Large-Grained All-Inorganic Bismuth-Based Perovskites with Narrow Band Gap via Lewis Acid-Base Adduct Approach. *ACS Appl Mater Interfaces* **12**, 43876–43884, https://doi.org/10.1021/acsami.0c14512 (2020).
63. Abbas, M. *et al.* A Critical Review on Crystal Growth Techniques for Scalable Deposition of Photovoltaic Perovskite Thin Films. *Materials (Basel)* **13**, https://doi.org/10.3390/ma13214851 (2020).
64. Reddy, S. S. *et al.* Lewis acid-base adduct-type organic hole transport material for high performance and air-stable perovskite solar cells. *Nano Energy* **58**, 284–292, https://doi.org/10.1016/j.nanoen.2019.01.041 (2019).
65. Heo, Y. J. *et al.* Enhancing Performance and Stability of Tin Halide Perovskite Light Emitting Diodes via Coordination Engineering of Lewis Acid–Base Adducts. *Advanced Functional Materials* **31**, https://doi.org/10.1002/adfm.202106974 (2021).
66. Sun, H. *et al.* Strategies and methods for fabricating high quality metal halide perovskite thin films for solar cells. *Journal of Energy Chemistry* **60**, 300–333, https://doi.org/10.1016/j.jechem.2021.01.001 (2021).
67. Liu, C. *et al.* Tailoring C60 for Efficient Inorganic CsPbI2 Br Perovskite Solar Cells and Modules. *Adv Mater* **32**, e1907361, https://doi.org/10.1002/adma.201907361 (2020).
68. Abdelsamie, M. *et al.* Mechanism of Additive-Assisted Room-Temperature Processing of Metal Halide Perovskite Thin Films. *ACS Appl Mater Interfaces* **13**, 13212–13225, https://doi.org/10.1021/acsami.0c22630 (2021).
69. Liu, Z., Ono, L. K. & Qi, Y. Additives in metal halide perovskite films and their applications in solar cells. *Journal of Energy Chemistry* **46**, 215–228, https://doi.org/10.1016/j.jechem.2019.11.008 (2020).

70. Ling, J. *et al.* A Perspective on the Commercial Viability of Perovskite Solar Cells. *Solar RRL* **5**, https://doi.org/10.1002/solr.202100401 (2021).
71. Vesce, L. *et al.* Ambient Air Blade-Coating Fabrication of Stable Triple-Cation Perovskite Solar Modules by Green Solvent Quenching. *Solar RRL* **5**, https://doi.org/10.1002/solr.202100073 (2021).
72. Tian, S. *et al.* A facile green solvent engineering for up-scaling perovskite solar cell modules. *Solar Energy* **183**, 386–391, https://doi.org/10.1016/j.solener.2019.03.038 (2019).
73. Zhang, M., Xin, D., Zheng, X., Chen, Q. & Zhang, W.-H. Toward Greener Solution Processing of Perovskite Solar Cells. *ACS Sustainable Chemistry & Engineering* **8**, 13126–13138, https://doi.org/10.1021/acssuschemeng.0c04289 (2020).
74. Hoang, M. T. *et al.* Towards the environmentally friendly solution processing of metal halide perovskite technology. *Green Chemistry* **23**, 5302–5336, https://doi.org/10.1039/d1gc01756j (2021).
75. Cui, Y., Wang, S., Ding, L. & Hao, F. Green–Solvent–Processable Perovskite Solar Cells. *Advanced Energy and Sustainability Research* **2**, https://doi.org/10.1002/aesr.202000047 (2020).
76. Ahmed, D. S., Mohammed, B. K. & Mohammed, M. K. A. Long-term stable and hysteresis-free planar perovskite solar cells using green antisolvent strategy. *Journal of Materials Science* **56**, 15205–15214, https://doi.org/10.1007/s10853-021-06200-w (2021).
77. Bu, T. *et al.* Synergic Interface Optimization with Green Solvent Engineering in Mixed Perovskite Solar Cells. *Advanced Energy Materials* **7**, https://doi.org/10.1002/aenm.201700576 (2017).
78. Worsley, C. *et al.* γ-Valerolactone: A Nontoxic Green Solvent for Highly Stable Printed Mesoporous Perovskite Solar Cells. *Energy Technology* **9**, https://doi.org/10.1002/ente.202100312 (2021).
79. Worsley, C. *et al.* Green solvent engineering for enhanced performance and reproducibility in printed carbon-based mesoscopic perovskite solar cells and modules. *Materials Advances* **3**, 1125–1138, https://doi.org/10.1039/d1ma00975c (2022).
80. Li, H. *et al.* Recent progress towards roll-to-roll manufacturing of perovskite solar cells using slot-die processing. *Flexible and Printed Electronics* **5**, https://doi.org/10.1088/2058-8585/ab639e (2020).
81. Angmo, D. *et al.* A Lab-to-Fab Study toward Roll-to-Roll Fabrication of Reproducible Perovskite Solar Cells under Ambient Room Conditions. *Cell Reports Physical Science* **2**, https://doi.org/10.1016/j.xcrp.2020.100293 (2021).
82. Martin, B., Amos, D., Brehob, E., van Hest, M. F. A. M. & Druffel, T. Techno-economic analysis of roll-to-roll production of perovskite modules using radiation thermal processes. *Applied Energy*, https://doi.org/10.1016/j.apenergy.2021.118200 (2021).
83. Zhong, Z. W., Shan, X. C. & Wong, S. J. Roll-to-roll large-format slot die coating of photosensitive resin for UV embossing. *Microsystem Technologies* **17**, 1703–1711, https://doi.org/10.1007/s00542-011-1344-5 (2011).
84. Rakocevic, L. *et al.* Interconnection Optimization for Highly Efficient Perovskite Modules. *IEEE Journal of Photovoltaics* **7**, 404–408, https://doi.org/10.1109/jphotov.2016.2626144 (2017).
85. Yang, M. *et al.* Highly Efficient Perovskite Solar Modules by Scalable Fabrication and Interconnection Optimization. *ACS Energy Letters* **3**, 322–328, https://doi.org/10.1021/acsenergylett.7b01221 (2018).
86. C. Bailie, C. E., E. Gehan, R. Bramante, M. Hest. in *IEEE 46th Photovoltaic Specialists Conference* 1–5 (2019).
87. Kim, D. H., Whitaker, J. B., Li, Z., van Hest, M. F. A. M. & Zhu, K. Outlook and Challenges of Perovskite Solar Cells toward Terawatt-Scale Photovoltaic Module Technology. *Joule* **2**, 1437–1451, https://doi.org/10.1016/j.joule.2018.05.011 (2018).
88. Razza, S., Pescetelli, S., Agresti, A. & Di Carlo, A. Laser Processing Optimization for Large-Area Perovskite Solar Modules. *Energies* **14**, https://doi.org/10.3390/en14041069 (2021).

89. Rong, Y. *et al.* Challenges for commercializing perovskite solar cells. *Science* **361**, https://doi.org/10.1126/science.aat8235 (2018).
90. Di Giacomo, F. *et al.* Upscaling Inverted Perovskite Solar Cells: Optimization of Laser Scribing for Highly Efficient Mini-Modules. *Micromachines (Basel)* **11**, https://doi.org/10.3390/mi11121127 (2020).
91. Klaus Ellmer, A. K. B. R. *Transparent Conductive Zinc Oxide*. 104 (Springer, 2007).
92. Walter, A. *et al.* Closing the Cell-to-Module Efficiency Gap: A Fully Laser Scribed Perovskite Minimodule With 16% Steady-State Aperture Area Efficiency. *IEEE Journal of Photovoltaics* **8**, 151–155, https://doi.org/10.1109/jphotov.2017.2765082 (2018).
93. Panasonic, Japan's NEDO and Panasonic Achieve the World's Highest Conversion Efficiency of 16.09% for Largest-area Perovskite Solar Cell Module. https://news.panasonic.com/global/press/data/2020/02/en200207-2/en200207-2.html. Accessed February 2020.
94. Gehlhaar, R. *et al.* Perovskite solar modules with minimal area loss interconnections. *SPIE Newsroom*, https://doi.org/10.1117/2.1201509.006116 (2015).
95. Moon, S.-J. *et al.* Laser-Scribing Patterning for the Production of Organometallic Halide Perovskite Solar Modules. *IEEE Journal of Photovoltaics* **5**, 1087–1092, https://doi.org/10.1109/jphotov.2015.2416913 (2015).
96. Meroni, S. M. P. *et al.* Scribing Method for Carbon Perovskite Solar Modules. *Energies* **13**, https://doi.org/10.3390/en13071589 (2020).
97. Markauskas, E., Gečys, P., Repins, I., Beall, C. & Račiukaitis, G. Laser lift-off scribing of the CZTSe thin-film solar cells at different pulse durations. *Solar Energy* **150**, 246–254, https://doi.org/10.1016/j.solener.2017.01.074 (2017).
98. Castriotta, L. A. *et al.* Reducing Losses in Perovskite Large Area Solar Technology: Laser Design Optimization for Highly Efficient Modules and Minipanels. *Advanced Energy Materials*, https://doi.org/10.1002/aenm.202103420 (2022).
99. Taheri, B. *et al.* Laser-Scribing Optimization for Sprayed SnO2-Based Perovskite Solar Modules on Flexible Plastic Substrates. *ACS Appl Energy Mater* **4**, 4507–4518, https://doi.org/10.1021/acsaem.1c00140 (2021).
100. Lee, D.-K. & Park, N.-G. Materials and Methods for High-Efficiency Perovskite Solar Modules. *Solar RRL*, https://doi.org/10.1002/solr.202100455 (2021).
101. Jung, E. H. *et al.* Efficient, stable and scalable perovskite solar cells using poly(3-hexylthiophene). *Nature* **567**, 511–515, https://doi.org/10.1038/s41586-019-1036-3 (2019).
102. Deng, Y. *et al.* Surfactant-controlled ink drying enables high-speed deposition of perovskite films for efficient photovoltaic modules. *Nature Energy* **3**, 560–566, https://doi.org/10.1038/s41560-018-0153-9 (2018).
103. Commission, I. E. in *Measurement of Photovoltaic Current-Voltage Characteristics* (CEI/IEC, Switzerland, 2006–09).
104. M. Bliss, R. G. in *24th European PV Solar Energy Conference* (Hamburg, Germany, 2009).
105. T. Silverman, U. J., M. Apolloni, A. Louwen, M. Schweiger, G. Bellurado, J. Wagner, A. Tetzlaff, P. Ingenhoven, D. Moser. Characterisation of Performance of Thin Film PV Technologies. (INTERNATIONAL ENERGY AGENCY Project: IEA PVPS Task 13, 2014).
106. T. Silverman, U. J., G. Friesen, M. Pravettoni, M. Apolloni, A. Louwen, M. Schweiger, G. Bellurado, J. Wagner, A. Tetzlaff, I.D. Moser. IEA-PVPS_T13-02_2014_Characterization_ThinFilm_Modules. (2014).
107. T.J. Silverman, U. J., G. Friesen, M. Pravettoni, M. Apolloni, A. Louwen, WGJHM van Sark, M. Schweiger, G. Belluardo, J. Wagner, A. Tetzlaff, P. Ingenhoven, D. Moser. in *IEA International Energy Agency* (SFOE NREL, 2020).
108. Dunbar, R. B. *et al.* How reliable are efficiency measurements of perovskite solar cells? The first inter-comparison, between two accredited and eight non-accredited laboratories. *Journal of Materials Chemistry A* **5**, 22542–22558, https://doi.org/10.1039/c7ta05609e (2017).
109. Bardizza, G., Müllejans, H., Pavanello, D. & Dunlop, E. D. Metastability in performance measurements of perovskite PV devices: a systematic approach. *Journal of Physics: Energy* **3**, https://doi.org/10.1088/2515-7655/abd678 (2021).

110. Fu, Y. Stabilization of Metastable Halide Perovskite Lattices in the 2D Limit. *Adv Mater* **34**, e2108556, https://doi.org/10.1002/adma.202108556 (2022).
111. Fell, C. J. Standardising current–voltage measurements for metastable solar cells. *Journal of Physics: Energy* **2**, https://doi.org/10.1088/2515-7655/ab55cc (2019).
112. T.J. Silverman, M. G. D., B. Marion, S.R. Krutz. in *2014 IEEE 40th Photovoltaic Specialist Conference (PVSC)* (2014).
113. Yan, X. *et al.* Ion migration in hybrid perovskites: Classification, identification, and manipulation. *Nano Today* **44**, https://doi.org/10.1016/j.nantod.2022.101503 (2022).
114. Deceglie, M. G. *et al.* Validated Method for Repeatable Power Measurement of CIGS Modules Exhibiting Light-Induced Metastabilities. *IEEE Journal of Photovoltaics* **5**, 607–612, https://doi.org/10.1109/jphotov.2014.2376056 (2015).
115. Zhang, S. *et al.* Improved performance and stability of perovskite solar modules by interface modulating with graphene oxide crosslinked CsPbBr3 quantum dots. *Energy & Environmental Science* **15**, 244–253, https://doi.org/10.1039/d1ee01778k (2022).
116. Kim, H. S. *et al.* Control of I-V hysteresis in CH3NH3PbI3 perovskite solar cell. *J Phys Chem Lett* **6**, 4633–4639, https://doi.org/10.1021/acs.jpclett.5b02273 (2015).
117. Yan, W. F., F. Cheng, H. Sun, C. Xu, L. Wang, Z. Kang, Y. Zhang. Ion migration in perovskite solar cells. *Science Direct* (2022).
118. Xiaoxue Ren, L. Z., Yongbo Yuan, Liming Ding. Ion migration in perovskite solar cells. *Journal of Semiconductors*, https://doi.org/10.1088/1674-4926/42/1/010201 (2021).
119. Zhu, W. *et al.* Ion Migration in Organic-Inorganic Hybrid Perovskite Solar Cells: Current Understanding and Perspectives. *Small* **18**, e2105783, https://doi.org/10.1002/smll.202105783 (2022).
120. Elumalai, N. K. & Uddin, A. Hysteresis in organic-inorganic hybrid perovskite solar cells. *Solar Energy Materials and Solar Cells* **157**, 476–509, https://doi.org/10.1016/j.solmat.2016.06.025 (2016).
121. Martiradonna, L. Riddles in perovskite research. *Nat Mater* **17**, 377, https://doi.org/10.1038/s41563-018-0072-y (2018).

Naturally Inspired Heme-Like Chemistries for the Oxygen Reduction Reaction: Going Beyond Platinum Group Metals in Proton Exchange Membrane Fuel Cell Catalysis



Robin J. White

1 Introduction

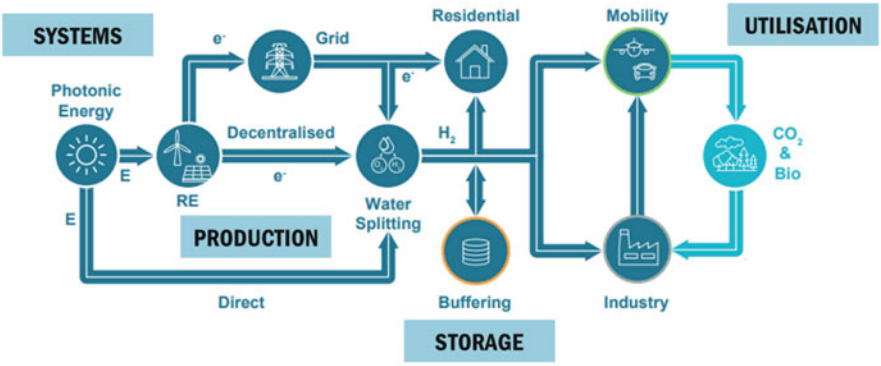
With an eye on achieving national renewable energy and emission reduction targets, there is an increasingly strong impetus (e.g. from the European Commission [1]) to implement 10 s if not 100 s of gigawatts (GW) of green hydrogen (H_2) production capacity (e.g. from renewable energy (RE)) over the coming decades [2]. Accompanying the expected mass roll-out of green hydrogen production (e.g. via water electrolysers), a range of other technologies will need to be developed, scaled up (e.g. in manufacturing capacity) and deployed across an ever more closely integrated energy/chemistry value chain if a low-emission hydrogen economy is to be established (Scheme 1). In this context, a fuel cell (FC) is an electrochemical device that converts chemically stored energy in fuel (H_2) and oxygen (O_2) into electricity (Fig. 1) [3, 4]. As part of a RE-powered economy, FCs will complement other technologies (e.g. electrolysers, lithium-ion batteries, etc.), offering specific advantages in terms of high efficiency, high power/energy density and low-temperature operation [5].

Amongst different FC types, proton exchange membrane FCs (denoted hereon as PEMFC) are perhaps the most common variant and are foreseen as an enabling technology across a number of sectors (e.g. residential, personal mobility, etc.) as a consequence of potential high-power density, durability and relative compactness. In a mobility context, FCs deployed in transport offer scope for zero emissions at the exhaust (reducing urban emissions), fast refuelling times (e.g. 3 min at a H_2 tank station) and mileage range ($\gg$ 500 km) comparable to existing modes (e.g.

R. J. White (✉)
Luxembourg Institute of Science & Technology, Material Research & Technology Department, Belvaux, Luxembourg
e-mail: robin.white@list.lu

© The Author(s), under exclusive license to Springer Nature Switzerland AG 2024

S. Krishnamoorthy, K. (Kris) Iniewski (eds.), *Advances in Fabrication and Investigation of Nanomaterials for Industrial Applications*,
https://doi.org/10.1007/978-3-031-42700-8_17



Scheme 1 An example of a renewable (e.g. solar) energy-driven hydrogen economy

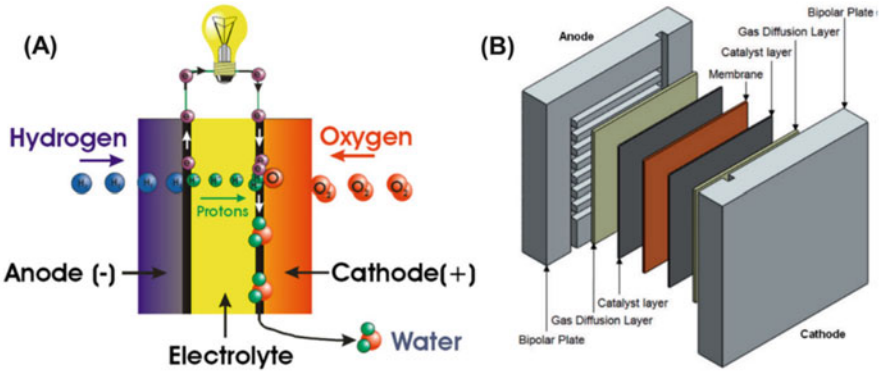


Fig. 1 (**a**) Simplified depiction of PEMFC operation (Reproduced with permission from Ref. [7]) and (**b**) a single-cell PEMFC depicting the respective components (Reproduced with permission from Ref. [8]); multiple single cells are repeated to form the FC stack

vs. a petrol-fuelled car) [6]. PEMFCs are also under strong consideration as the mode of choice to deliver zero-emission power generation in the electrification of transportation (e.g. heavy-duty logistic trucking). It is to be noted that the mass production and commercialisation of FC in general has been relatively slow, partially limited by the availability of affordable green H_2, fuelling infrastructure, device cost competitiveness (e.g. at current stack production costs) and non-ideal performance characteristics (e.g. power densities, durability and/or device lifetimes, etc.).

The key reaction determining performance in an FC is the oxygen reduction reaction (ORR; at the cathode under acidic conditions). The ORR is desirable if it proceeds along a $4e^-$ transfer pathway to produce H_2O (i.e. under acidic conditions) at the FC cathode. Under basic conditions the ORR proceeds to yield HO^-. The ORR can proceed via different routes, namely, the direct $4e^-$ pathway [1] or an indirect "$2 + 2e^-$" pathway [2], represented as follows (in acidic medium):

$$[1]\ O_2 + 4H^+ + 4e^- \rightarrow 2H_2O \quad E^o = 1.229\ V$$
$$[2]\ O_2 + 2H^+ + 2e^- \rightarrow H_2O_2 \quad E^o = 0.670\ V$$
$$H_2O_2 + 4H^+ + 4e^- \rightarrow 2H_2O \quad E^o = 1.770\ V$$

In alkaline medium, the respective direct [3] and indirect reactions [4] proceed as follows:

$$[3]\ O_2 + 2H_2O + 4e^- \rightarrow 4HO^- \quad E^o = 0.401\ V$$
$$[4]\ O_2 + H_2O + 2e^- \rightarrow HO_2{}^- + HO \quad E^o = 0.065V$$
$$HO_2{}^- + H_2O + 2e^- \rightarrow 3HO^- \quad E^o = 0.867\ V$$

The ORR is FC performance determining given it is kinetically sluggish, and thus consequentially high overpotentials are observed. This arises due to the limiting activation/cleavage of O=O double bond, particularly in a low-pH environment. With regard to electrocatalyst choice, the ORR relies on relatively high loading of platinum (Pt) in current commercial PEMFCs, equating to ca. 8 times more Pt used at the cathode than at the anode (where it also promotes the hydrogen oxidation reaction (HOR)) [9, 10]. Thus catalyst loading at the cathode contributes to ca. 80% of the whole catalyst used in a PEMFC and in turn ca. 55% of the total capital expenditure in commercial-scale production [11, 12]. Considering complete PEMFC systems, Pt use at current loadings is reported to account for ca. 41% of total stack capital expenditure [13]. Pt is currently used at 30 g per commercial PEMFC stack (e.g. in a Toyota Mirai FC car), whilst certain R&D roadmaps indicate this should be reduced to 5 g per vehicle if FC-powered mobility is to become affordable and receive mass market adoption [14]. Furthermore, Pt utilisation at ca. 0.25 g(Pt)/kW is considered uneconomical for transport applications. Additionally, and applicable independently of catalyst type used, durability, degradation and electrode instability are other potential bottlenecks to widespread device deployment [15].

Reliance on Pt as both anode and cathode electrocatalyst, and specifically the comparatively high loading at the cathode (to catalyse the ORR), generates the aforementioned high stack costs and in the long term (e.g. at high unit volume production) will generate supply chain security issues given that Pt is classified as a critical raw material (CRM) [16]. Reducing and/or substituting Pt use without compromising ORR performance is a top R&D focus in the field. The ORR proceeds at the electrode-electrolyte interface, being defined by mass transport and electron transfer processes, alongside reactant/intermediate/product adsorption and desorption processes, etc., which all can limit reaction rate. As a consequence, it is paramount that (with respect to PGM replacement) efficient and stable catalysts are implemented to accelerate the reaction (e.g. at high current densities, optimised triple-phase boundary/[O_2] transport, etc.) and achieve the key performance indicators (e.g. >10 k hours of operation, targeted power densities, appropriate pore structure, mass transport properties and stability/durability). This will be achieved through deepening models of both catalyst design principles and reaction

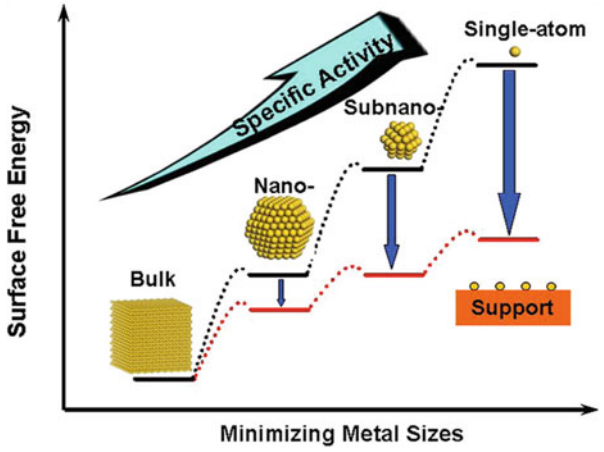
mechanism over new sites, whilst also integrating identified catalytic systems in functional FCs (e.g. improving the connection between material innovation and device integration) [17, 18]. This latter point is relevant with respect to translating more fundamental performance evaluation (e.g. of catalyst inks on a rotating disc electrode (RDE)) to functional membrane electrode assemblies (MEA; the core of the FC stack).

In the following, development of alternative catalysts and specifically platinum group metal (PGM)-free ORR catalysts will be discussed with respect to the challenges faced (e.g. delivering appropriate power densities) and their translation to functional MEAs and FCs. In specific focus, as a consequence of promising reported activity levels, is the class of electrocatalysts commonly referred to as M-N-C, where M is a metal, often a transition metal such as iron (Fe), and N-C refers to a specifically structured nitrogen containing carbon/organic-based motif (e.g. as integrated into a suitable structured catalyst support). A number of recent reviews are also recommended to the reader [10, 19–24].

1.1 Transitioning Catalysis: From Classical Nanoparticles to Single-Atom Catalysts

Catalysts provide alternative pathways for a reaction via lower activation energy barriers, thus aiding to promote and accelerate chemical reactions, and it is in this respect that single-atom catalysts (SACs) offer significant advantages (e.g. relationship of specific activity and surface free energy vs. nanoparticle systems) (Scheme 2) [25]. Enzymes (nature's catalysts) are well known as being capable of catalysing often complex chemical reaction at ambient conditions, with certain examples (e.g. cytochrome-C-oxidase) known to perform also the ORR. Such natural systems do not use PGMs to achieve high performance (e.g. cytochrome-C-oxidase presents turnover frequencies (TOF) $\sim 500\ s^{-1}$ – 20x higher compared to Pt nanoparticles (NP)) [26, 27]. Such natural systems have provided inspiration for the development of synthetic equivalents [28]. Relating specifically to FCs, it was shown as far back as 1964 that macrocyclic cobalt-phthalocyanine (an analogue of the oxygen-binding heme molecule) was able to catalyse the ORR [29]. However, it is to be noted that such organo-metallic macrocycles are typically unstable in the acidic conditions encountered in a PEMFC. Current commercial PEMFCs rely on high loadings of Pt at the cathode typically found as NPs as supported on a conductive support, typically a nanoparticulate or nanoporous carbon material. As seen in the literature and in the FC market, there is a drive to reduce Pt use, currently not necessarily driven as a consequence of material criticality and potential supply chain issues, but rather through cost competitivity and a desire to increase activity normalised to catalyst mass.

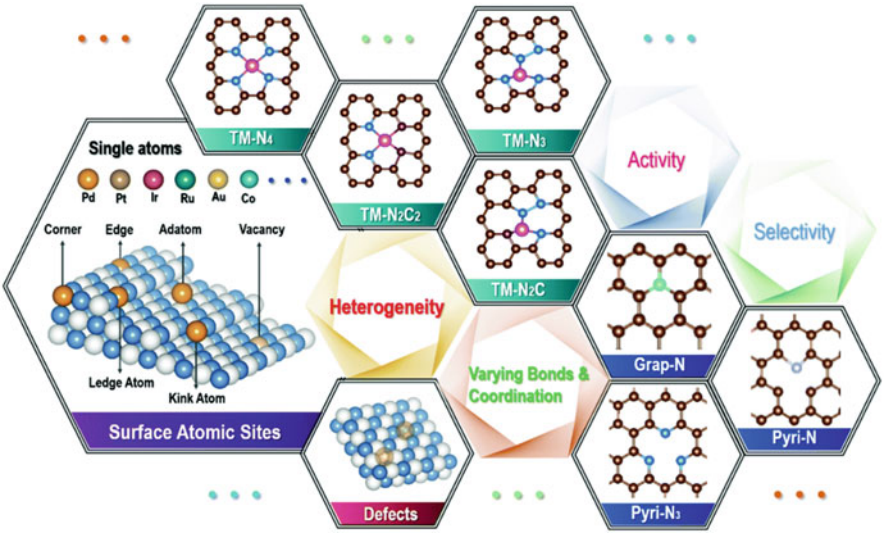
The ORR proceeds over Pt surfaces at a rate sensitive to electrode material, its surface structure and electrolyte chemistry [30–32]. There is also a subtle relation-



Scheme 2 Illustration demonstrating the changes of surface free energy and specific activity per metal atom with metal particle size and the support effects on stabilizing single atoms. (Reproduced with permission from Ref. [19])

ship between the reaction intermediate binding energies at the electrode surface and observed catalytic activity (e.g. leading to specific ORR structure/activity relationships over Pt) [33–35]. Thus controlling active site number and type (e.g. with optimal coordination number per unit mass) can enable improved mass activity of Pt NPs for the ORR. Synthesis of Pt NP with a precisely defined size however represents a challenge, particularly if the target is uniform, spherical NPs with diameters <2 nm (NB: commercial Pt/C catalysts feature NPs with diameters of ca. 2 nm) [36, 37]. Learning from this and indeed with an eye on the future drive of material criticality and sustainability, there has been a growing body of R&D performed not only on improving Pt NP mass activity but also with respect to its replacement with alternative materials [38–40]. Non-precious metals have been extensively explored (e.g. as NPs or clusters) but conventionally still present low catalytic activity/stability (under ORR conditions) [41]. A variety of options have been explored including metal-free carbon materials, transition-metal oxides, nitrides, carbides and chalcogenides, although these all face their respective challenges [42, 43].

With a desire to optimise intrinsic activity and reduce dependence on critical materials, whilst also taking inspiration from aforementioned natural systems (e.g. enzymes), a strong focus has been placed on SACs and in particular M-N-C structures (Scheme 3) [44–46]. In comparison to more classical NP-based catalysts, SACs are distinct with respect to the separation of active site in the form of single atoms (e.g. as coordinated in a specific chemical structure) without forming NPs or clusters [47]. From a theoretical point of view, SACs are of specific interest as they can potentially deliver 100% atomic utilisation efficiency – extremely valuable aspect regarding resource use optimisation, especially for CRMs. SACs feature



Scheme 3 Different types of single-atom catalysts (SACs) as reflected by differing surface hetero-compound construction; a number of defects and coordination chemistry give rise to different single-atom environment, thus creating different bond and coordination environments for isolated atoms, with transition metal (e.g. Fe) "anchored" or coordinated within an N-doped graphitic plane being a classic example in the case of FC electrocatalyst development. (Reproduced with permission from Ref. [40])

anchoring of single atoms on or within supports with appropriate functionality to facilitate chemical coordination [48]. This coordination can facilitate advantageous metal-support interaction(s) and generate strong chemical bonding (beneficial with respect to stability) and charge transfer properties [49–51]. As a consequence of defining active centre/chemical environment regularity, the electronic orbital distribution at a SAC site can be viewed as quantised, and thus product selectivity is often improved (vs. a benchmark) [52]. Successfully applying SAC in electrochemical cells has the potential benefit of effectively reducing metal consumption and thus cost, whilst simultaneously loading very small catalyst amounts at electrodes and maintaining desirable active mass loadings for high energy output [53, 54]. At the PEMFC system level for mobility applications, replacing PGM use with lighter, less dense materials also has potential benefits.

For PEMFCs, transition metal-nitrogen-carbon (M-N-C) catalysts are considered some of the most promising SAC alternatives to PGM-based ORR catalysts. M-N-C catalysts often feature first-row transition-metal ions (e.g. Fe, Co, etc.) and increasingly show performance which makes them promising electrocatalysts. As far back as 1989, it was found that pyrolysis of a mixture of metals, nitrogen-containing organic precursors and carbon supports gave yield to M-N-C catalysts which had exciting ORR performance [55]. If M-N-C catalysts are to be competitive with Pt, the corresponding cathodes must deliver comparable activity and stability

under PEMFC operating conditions. Thus the global challenge relates to the deposition of suitably stable M-N-C catalyst layer(s) (with a suitable densification of active sites) to facilitate efficient ORR at the triple-phase boundary (TPB; where solid catalyst layer, electrolyte and gas meet). Recent reports highlight the potential scope offered by M-N-C catalysts with respect to delivering practically relevant activity and stability, even for the demanding performance expected in certain applications (e.g. automotive sector).

2 M-N-C Catalysts and Their Synthesis

M-N-Cs are a class of SACs that are increasingly in focus for a range of applications including FCs [43, 44, 56, 57]. Aside from the ORR, recent reports also demonstrate their use in other electrochemical applications including CO_2 electroreduction [58, 59] and N_2 electroreduction [60]. M-N-Cs have been prepared by various routes of which the most common are pyrolysis-based syntheses. High-temperature pyrolysis has been applied since the 1970s and has delivered significant improvements regarding both activity and stability (e.g. in acid electrolytes) [61, 62]. Subsequent R&D has focussed on substituting expensive metal-macrocycles as precursors with more common nitrogen-containing organic precursors, inorganic metal sources and high-surface-area carbon supports [63, 64]. Selection of nitrogen, carbon and metal precursors has also been shown to dictate ORR performance. A classic example of this was the seminal report by Lefèvre et al. on the ball milling and pyrolysis (under Ar (g) and then NH_3 (g)) of a carbon support, phenanthroline and ferrous acetate to yield a Fe-N-C material which gave an ORR activity equal to a Pt-based cathode (loading of 0.4 mg(Pt)/cm^2) at a cell voltage of $\geq$0.9 volt (Fig. 2) [31]. Subsequent reports have shown Fe-based systems to be most active M, followed by Co and Mn [65, 66].

To increase active site density and mass transport features, R&D is proceeding on the optimisation of morphology through nano-structuration (e.g. beneficial porosity, accessible surface area, etc.). This is approached in tandem with delivering homogeneous, structurally well-defined and ideally isolated single-atom active sites. Here the use of model systems has been explored as this enables a far deeper fundamental understanding of active site chemistry/environment and towards establishing the basis for certain structure/activity relationships.

Regarding active site characterisation, advances in high-resolution characterisation techniques (e.g. electron microscopy and X-ray absorption spectroscopy (XAS)) have enabled a deeper and more accurate identification of atomically dispersed and N-coordinated metal sites (e.g. Fe-N_4, Co-N_4, Mn-N_4) in M-N-C catalysts. For Fe-based M-N-C, the logical use of Mössbauer spectroscopy in tandem with computational tools has been very successful with respect to active site characterisation. The recent report of Krewald, Kramm et al. discusses the construction of Fe-N-C active site model based on a combination of in situ and operando [56]Fe Mössbauer spectroscopy in tandem with quantum chemistry calcu-

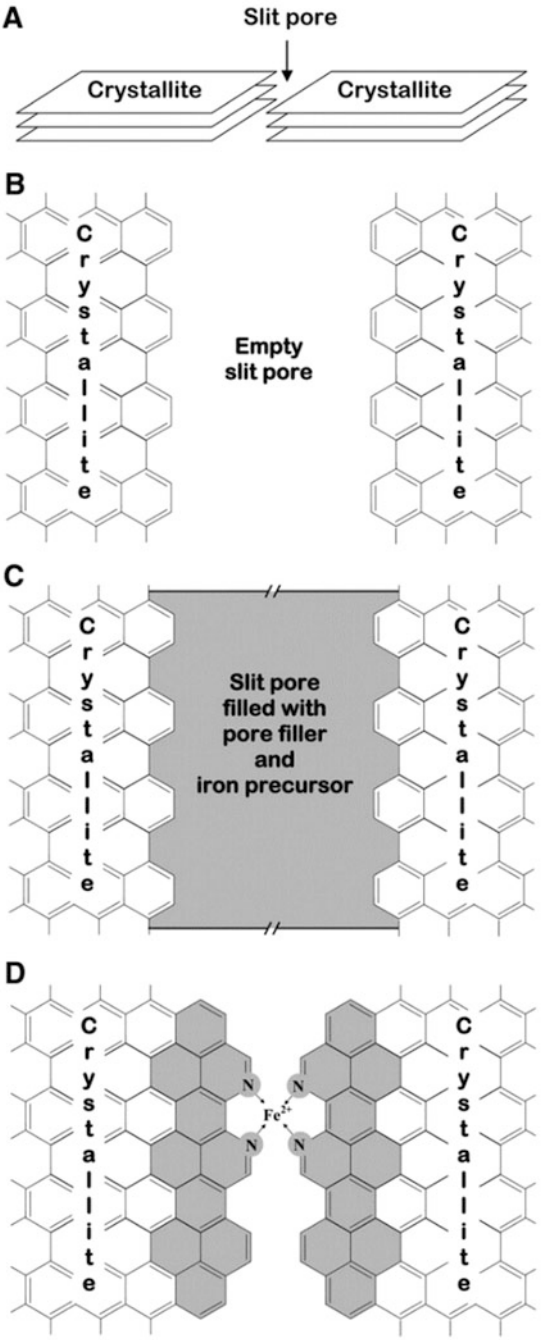


Fig. 2 Synthesis of Fe-N-C electrocatalysts as reported by Lefèvre et al., based on the impregnation of a porous carbon with appropriate precursors and pyrolysis under controlled conditions; (Reproduced with permission from Ref. [31])

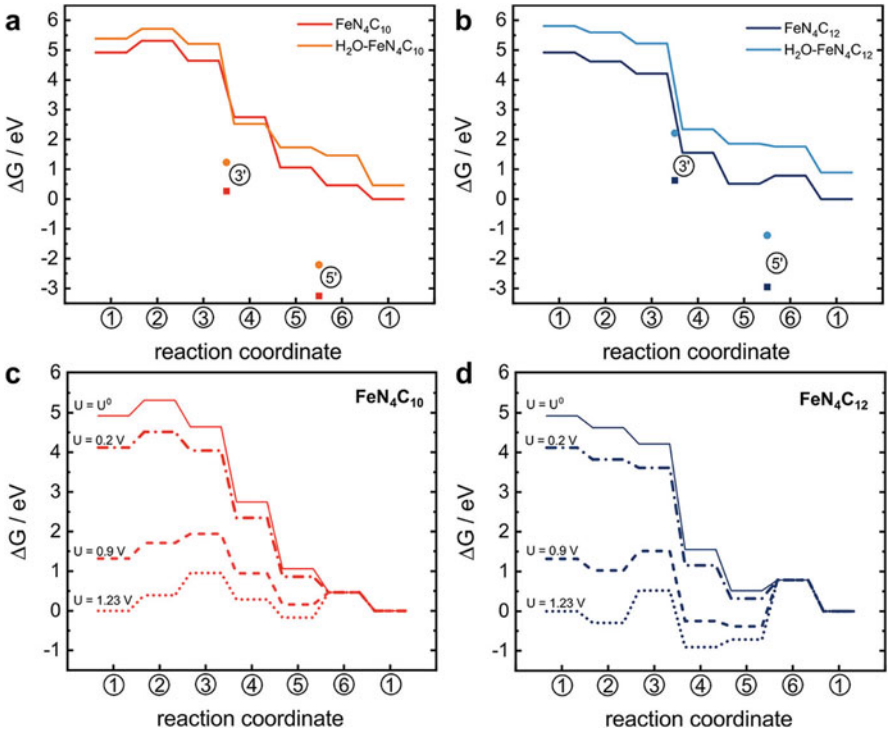


Fig. 3 Thermodynamic profiles of the Fe-C-N catalyst models as reported by Krewald, Kramm et al.; (**a**, **b**) relative Gibbs free enthalpies (eV) for models Fe-N_4C_{10} (red) and H_2O–Fe-N_4C_{10} (orange) or Fe-N_4C_{12} (dark blue) and H_2O–Fe-N_4C_{12} (light blue); the energetic positions of ③′ and ⑤′ are based on their estimated redox potentials relative to ③ and ⑤. (Reproduced with permission from Ref. [68])

lations [67]. It was reported that pyrrolic N-coordination (i.e. FeN_4C_{12}) represented a spectroscopically and thermodynamically consistent model for the entire ORR cycle (vs. to pyridinic N-coordination) and thus overcomes previously conflicting structural assignments for the active site (Fig. 3). This has been complimented by the application of computational approaches (e.g. DFT) to active site and reaction mechanism determination; combining such approaches will enable further finer refinement of catalyst material chemistry [68]. However, if M-N-C catalysts are to receive adoption in commercial PEMFC, further advances are still required, specifically relating to the enhancement of intrinsic activity and an increase in active site density. This obviously will have a strong dependency on precursors and synthetic method choice with respect to engineering the coordination environments of the active site(s).

2.1 Promoting the 4e- ORR Pathway and d-Block M-N-Cs

Based on theoretical predictions, Xiao et al. reported on an iridium M-N-C catalyst derived from the thermal decomposition of a zeolite imidazolate framework-8 precursor [69]. The ORR activity of this electrocatalyst presented an ultrahigh $E_{onset} = 0.97\,V$, $E_{1/2} = 0.864\,V$ (vs. RHE), a high TOF = 24.3 e per site per second (at 0.85 V vs. RHE) and a mass activity of 12.2 A/mg(Ir), performance better than the benchmark Pt catalyst under acidic conditions. Combining atomic structural analysis and DFT calculations, it was proposed that Ir-N_4 sites were most attractive to regulate the adsorption energy of ORR intermediates and enhancing observed activity. Based on the conversion of graphene oxide in the presence of ruthenium salts, Zhang et al. reported on the synthesis and application of Ru–N-doped graphene (Ru-NG) catalysts [70]. Atomically dispersed Ru was characterised as anchored on a NG matrix as synthesised via thermal annealing of graphene oxide in the presence of Ru salts under an NH_3 (g). The catalyst provided excellent $4e^-$ ORR activity, achieving an onset potential of 0.89 V (vs. RHE) and a half-wave potential of 0.75 V (vs. RHE) in acidic conditions (0.1 M $HClO_4$ (aq)). Combining XANES, EXAFS and DFT simulations, Ru-oxo-N_4 moieties found in the Ru–NG prepared at T = 750 °C were proposed to lead to improved ORR performance. However replacing Pt with other PGM-based catalysts is considered not entirely advantageous, although such works bring additional learnings which will be applied to other systems.

As alternatives to PGM-based catalysts, d-block element-based M-N-C material class and especially Fe-N-Cs have received the widest attention, arising primarily from attractive ORR catalytic activity [15, 71, 72]. Meng et al. reported on a method to obtain a variety of SACs of the motif M-N-graphene (where M = Fe, Co, Ni, etc.) as anchored on hollow N-doped graphene supports (N-graphene). Using high-resolution spectroscopy (spherical aberration correction HAADF-STEM and XAFS), atomically dispersed and local coordination configuration of M-N-graphene was observed (Fig. 4) [73]. The prepared M-N-graphene had excellent ORR activity, whilst varying the d-block element resulted in differing performance in the order of catalytic performance: Fe > Co > Ni. $E_{1/2}$ values and kinetic current densities (J_k) for M-N-graphene where M = Fe were 0.87 V and 10.8 mA/cm^2 at 0.85 V, respectively, and were shown to significantly outperform the commercial Pt/C benchmark. Catalysts were reported as having >1.2 atom% (5.85 wt.%) metal loadings and a very high diffusion-limiting current (6.82 mA/cm^2). The superior performance of the Fe-N-graphene example was attributed to a unique electron structure, (more) exposed active sites and the robust hollow framework (arising from a ZnO templating approach), whilst high current retention (95.6% over 40,000s) was also reported.

To obtain quantitative insights into (e.g. mass-based) active site density under real operational conditions, a number of model systems based on the M-N-C motif have been examined (e.g. Ref. [68]). It is to be noted that there is a subtle interactivity between the M-N and M-C moieties as well as bulk contributions that determine

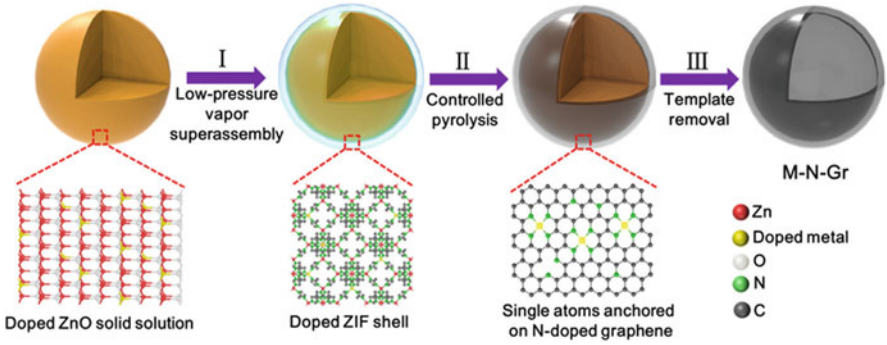


Fig. 4 Illustration of the synthetic approach adopted by Meng et al. for the preparation of M-N-graphene materials based on doped ZnO solid solutions. (Reproduced with permission from Ref. [67])

collectively ORR catalyst performance [74, 75]. This latter is important with respect to the carbon chemistry into which the M-N-C motif is supported/evolved. Based on literature reports, an understanding at atomic level regarding active site construction suggests that carbon-embedded N-coordinated Fe (Fe-N_4) are particularly attractive ORR active sites; however carbons with inhomogeneous N-functionalities (e.g. varying amounts of pyrrolic, pyridinic, etc. groups), whilst capable of binding Fe species and generating useful activities [76], could be further optimised (e.g. via increasing control of N-containing functionality), although this is somewhat challenging given the complexity and thermodynamics of commonly employed synthesis approaches (e.g. organic precursor pyrolysis). The environment in which the M-N-C functionality is "embedded" also plays an important role in influencing ORR activity. Locating M-N-C in carbon material micropores has been found to not only lead to improved performance, but also N-doped carbon micropores play a critical role in defining active site accessibility and ionomer distribution (e.g. to further improve ORR performance; 5% ORR performance decay following 30 k cycles) [77].

Whilst Fe-N-Cs are considered the most promising ORR catalysts, dissolved Fe species can act as a Fenton reagent – this is potentially problematic for long-term FC operation, as dissolution of Fe species can lead to degradation of ionomer and/or membrane (e.g. via radical degradation mechanisms) [78]. Using Co instead of Fe is potentially beneficial in this context, but its material criticality at large-scale device production is a concern. Alternative transitional metals (e.g. Mn) are potentially also interesting but can ultimately form inactive (oxide, carbide) phases (e.g. during material annealing), thus reducing active site density per unit area. Therefore, through intelligent materials design, the challenges faced by M-N-C material can potentially be addressed to deliver particularly attractive Pt substitutes for FC device deployment.

2.2 Improving M-N-C Catalyst Activity and Durability

M-N-C ORR catalysts are commonly synthesised via the carbonisation/pyrolysis of an N-containing carbon precursor in the presence of a suitable M-precursor. To improve ORR performance, increasing intrinsic active site density is important (e.g. Fe-N_4) as this leads to faster reaction kinetics [79]. In addition modulation of local chemistry/chemical coordination is performance dictating and can be influenced via a number of approaches including via ligand additionality and/or introducing additional catalyst functionality (e.g. dual-metal active sites) [80, 81]. The anchoring and tailoring thereof in M-N-C catalysts (e.g. via carbon support chemistry) represents an interesting route to improving ORR performance. Amongst others, approaches further densifying active sites, maximising element utilisation and promoting beneficial metal-support interaction(s) are being exploited [82]. Analogous to other catalysis disciplines, heteroatom doping of carbon is an interesting route to achieving enhanced ORR performance (e.g. via modulation of conductivity, metal-support interactions, etc.) [83, 84]. Examples have been demonstrated employing heteroatom doping with metal (e.g. Co, Mn and Cu) [78] and non-metal atoms (e.g. B, S and P) [85].

Optimising M-N-C properties to direct the electronic structure in favour of a lower energy ORR pathway has also been discussed in the literature. In this respect, bridged Fe-O-Fe across two adjacent Fe-N_4 sites has been discussed with respect to improving ORR activity in acid electrolyte [38]. DFT calculations described the ORR energy pathways over such electrocatalysts, indicating the thermodynamic barrier is considerably reduced thanks to this oxy-bridging, the result of the subtle modification of the Fe d-orbital electronic structure. Other reports highlight metal coordination with other atoms apart from N. Single-atom Mo catalysts as coordinated with O and S were reported to generate highly active and selective ORR catalysts (i.e. via the two-electron pathway), highlighting the importance of M-dopant electronic interaction(s) [86].

Analytical techniques have also been employed to characterise and determine active site chemistry and coordination environment. With respect to different axial ligands on Fe-N-C, catalyst sites have been described via techniques including in situ Mössbauer spectroscopy, XAS, nuclear inelastic scattering or electron paramagnetic resonance [87, 88]. Again similarities to natural occurring systems (e.g. heme moieties) have been described. Discerning and describing active site chemistry is a challenging endeavour for these typically heterogeneous M-N-C catalysts [89]. Thus, generating structure-activity relations with significant translation potentiality is hard. To this end, computational tools are providing avenues to overcome experimental limitations. In this context, the impact of O axial ligands on model Fe-N-C systems has been calculated based on DFT modelling (Fig. 5) [90, 91], although further work is required to describe the impact of other possible axial ligands on different M and specifically Fe sites as anchored in differing chemical environments (e.g. mixed pyridinic and pyrrolic coordination) [92].

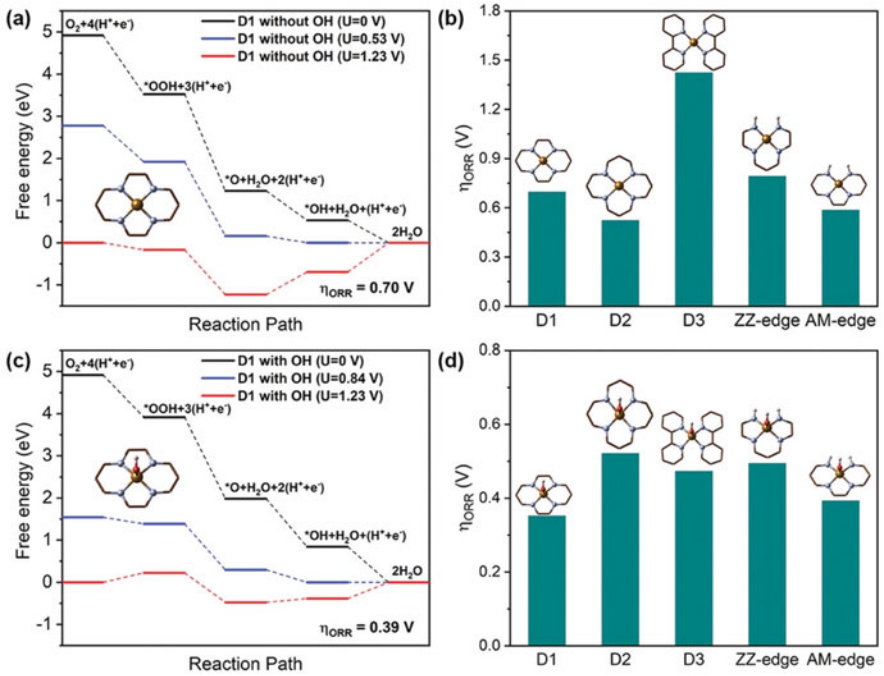


Fig. 5 Example of computational tools used to elucidate beneficial coordination chemistries with respect to ORR performance (e.g. with respect to overpotentials); (**a**) free energy diagram for ORR on bulk-hosted Fe-N_4 structure (D1); (**b**) computational ORR overpotentials for different Fe-N_4-C structures; (**c**) free energy diagram for ORR on bulk-hosted Fe-N_4 structure with an axial OH ligand; and (**d**) computational ORR overpotentials for different Fe-N_4-C structures with an axial OH ligand. (Reproduced with permission from Ref. [38])

To further enhance performance, the appropriate catalyst site needs to be "densified" within a 3D interconnected hierarchically porous structure to facilitate accessibility to the intrinsic active sites, thus maximising utilisation [93]. In this respect, synthetic routes should selectively form a high density of atomic M-sites and avoid undesired functionality formation (e.g. Fe-induced carbothermal reduction). Here the work of Fellinger and co-workers is noted as important as it highlighted the necessity to decouple the high-temperature pyrolysis synthesis step from M (e.g. Fe) loading, which can potentially be achieved using a suitable N_x site template(s) [94–97].

Fellinger et al. have recently reported bulk Fe-N_x site density of up to 7.4×10^{20} sites/g(Fe-N-C) based on Mössbauer spectroscopy. In situ nitrite stripping indicated a site density of 4.7×10^{19} sites/g(Fe-N-C), although electrochemical utilisations of total Fe and Fe-N_x sites were both reported at ca. 6% [88]. The amount of surface (accessible) Fe-N_x site density was also calculated as 1021 sites/g(Fe-N-C) indicating bulk (i.e. inaccessible) Fe-N_x site density approached this limit and promisingly the possibility to increase Fe-N_x site density. Reflecting on this high

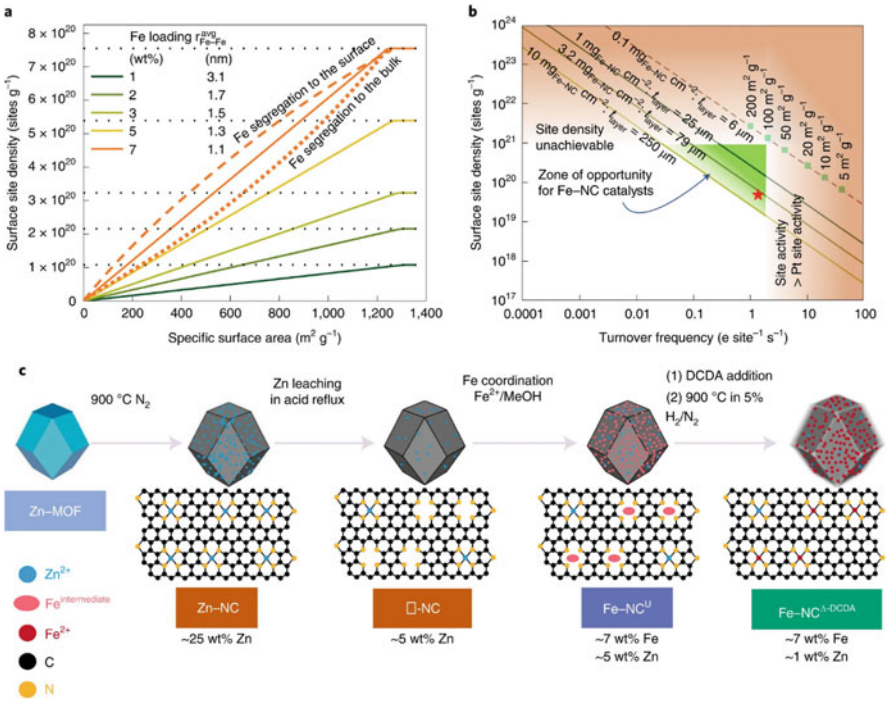


Fig. 6 ORR catalyst reported by Kucernak et al.; (**a**) calculated surface site density as a function of different Fe loadings and catalyst-specific surface area; (**b**) surface site density versus TOF plot indicating Fe-N-C catalyst requirements to achieve an area-specific current density of 0.044 A/cm^2 at 0.90 V (as a function of catalyst loading (solid lines)); * = site density and TOF values achieved (vs. a commercial Pt/C catalyst); (**c**) synthetic approach of Kucernak et al. to achieve high Fe loading. (Reproduced with permission from Ref. [90])

Fe-N_x density, it should be noted the important role of high N-doping content in the carbon material which may constrain the TOF (e.g. reflecting electrical conductivity). Kucernak et al. reported on an approach to increasing the active site loading for Fe-N-C ORR catalysts based on the use of a sacrificial metal (Zn) in the initial synthesis step (Zn-MOF pyrolysis at 900 °C) followed by its exchange for Fe [90]. Through this metal exchange approach, 7 wt.%(Fe) could be achieved as solely coordinated single atom at N_4 sites. The character of these sites was identified based on [56]Fe cryogenic Mössbauer spectroscopy and XAS, whilst active site density was calculated based on in situ nitrite stripping and ex situ CO chemisorption methods (respectively, as 4.7 × 10^{19} and 7.8 × 10^{19} sites/g) (Fig. 6). Regarding electrocatalytic performance a TOF of 5.4 electrons per site per second at 0.80 V (0.5 M H_2SO_4 electrolyte) was recorded.

It is also important to note that the carbon support (e.g. chemistry, porosity, etc.) has a significant role to play in delivering an attractive electrocatalyst durability profile. Whilst anchoring can be achieved of M-N-C on a conductive support, the

carbon material itself must also be resistive to the highly anticorrosive conditions found at the cathode in a PEMFC [98]. As examples, certain heavily coordinated metal-organic systems such as metal-organic frameworks (MOFs) are considered as a potential precursor for M-N-C synthesis, often presenting promising porous structure(s), high levels of graphitisation, abundant metal ions and tuneable composition and morphology. Within the MOF class of materials, zeolitic imidazolate frameworks (denoted as ZIFs) can be viewed as excellent precursors (e.g. metal-, carbon- and nitrogen-containing materials) for M-N-C provided catalyst synthesis results in heteroatom-doped carbon electrocatalysts featuring abundant M-N-C motifs [99–101]. In a simplistic description, during the carbonisation/pyrolysis step, nitrogen species are proposed to form chemical bonds with metal species and serve as the heteroatoms in the forming N-doped carbon materials [102]. The challenge in this respect is to synthesise materials featuring suitable porosity and graphitic character degree.

Wang et al. reported on the pyrolytic M-N-C synthesis of a high-performance N-coordinated single Co atom catalyst, as derived from Co-doped ZIF through a one-step thermal activation [103]. The use of aberration-corrected electron microscopy combined with XAS provided evidence of Co-N_4 coordination in the catalysts (e.g. before and after ORR testing) (Fig. 7). The authors investigated the impact of variation of Co content alongside the temperature of the synthesis. This gave scope to further refine the optimal catalyst structure, morphology and activity. The authors describe the basis for a synthesis-structure-property relationship which provides valuable knowledge for further M-N-C catalyst design and structure refinement. In this study both RDE in aqueous electrolyte and fuel cell tests with solid-state proton exchange membrane (i.e. Nafion) were performed and confirmed the high ORR performance of the investigated Co-N-C.

The performance of the reported Co-N-C ORR catalysts was reported as comparable to Fe-based analogues and 60 mV lower than Pt/C (60 $\mu g(Pt)/cm^2$). Single-cell FC tests confirmed that catalyst activity and stability can translate to high-performance cathodes for use in PEMFCs. It is to be noted that although performance degradation still occurred at a relatively high potential/voltage of 0.7 V, the Co-N-C catalyst exhibited improved durability in both 0.5 M H_2SO_4 electrolyte and as deployed in an MEA cathode architecture. The authors attributed the high performance to result from highly dispersed atomic Co-N_4 sites as embedded in a porous and partially graphitised carbon (derived from the MOF precursor), as opposed to formation of inactive metallic aggregates (e.g. as enclosed in graphitised carbon shells/layers). The authors highlight the benefit of structurally and chemically defined MOF nanocrystal precursors when it comes to the synthesis of aromatic N-containing ligand motifs suitable for active Co coordination. The use of Co is interesting as it potentially removes the challenge often encountered for Fe-M-C ORR catalysts and the potentiality for Fenton reagents to form (e.g. during long-term PEMFC operation). Some recent reviews provide more details and insight on the use of MOFs as precursors for the preparation of ORR catalysts [104–106].

Regarding durability and metal leaching, there are still challenges to be addressed with specific reference to Fe-N-C ORR catalysts. If Fe leaches during cell operation,

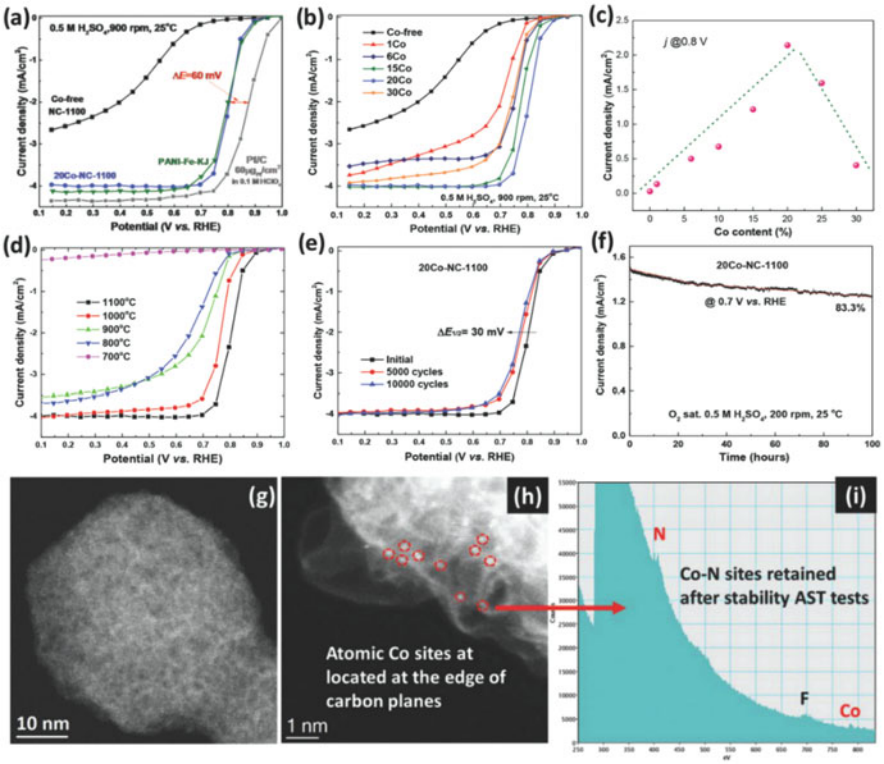


Fig. 7 Electrochemical performance of Co-ZIF-derived catalysts as reported by Wang et al.; (**a**) steady-state ORR polarisation plots for 20Co-NC-1100, state-of-the-art Fe-N-C (0.5 M H_2SO_4) and Pt/C (0.1 M $HClO_4$). (**b**) ORR polarisation plots for various Co contents; (**c**) volcano plot correlation between Co loading and activity (as a function of current density at 0.8 V); (**d**) ORR polarisation of Co-N-C material as synthesised at various temperatures; (**e**) potential cycling (0.6–1.0 V) stability in O_2-saturated 0.5 M H_2SO_4; (**f**) potential stability at 0.7 V. [Catalyst loading for Co-NC was 0.8 mg/cm^2. Pt loading was 60 μg_{Pt}/cm^2]; (**g–i**) characterisation of Co-N-C catalyst particles and atomic Co sites after potential cycling by high-resolution aberration-corrected electron microscopy and X-ray absorption spectroscopy. (Reproduced with permission from Ref. [97])

the Fenton reaction is essentially unavoidable (e.g. leading to proton-conducting membrane degradation). Thus design of more stable or indeed Fe-free M-N-C electrocatalyst would be of interest. Regarding Fe-free systems, a Co-N-C ORR catalyst has been reported with a high activity in acidic electrolyte in an H_2/O_2 PEMFC, providing a current density of 0.022 A/cm^2 (working voltage of 0.9 V; iR-free) and a peak power density of 640 mW/cm^2 [107]. Experimental evidence for high ORR activity in acidic media was complimented by DFT modelling, revealing Co-N_4 moieties have low activity towards radical-generating Fenton reactions (vs. Fe-based catalyst) that yields promising stability. Chemical oxidation of the M-N-C catalyst by radicals and active site demetallation are known to be

strongly influencing catalytic degradation. Significantly radical and demetallation degradation pathways were reported to be more challenging for Co-N-C relative to similarly synthesised Fe-N-C catalyst. Going beyond Fe and Co M-N-C catalysts, a Sn-based M-N-C-type ORR has been reported for use in cathodes of PEMFCs [108]. This catalyst exhibited a 40–50% enhancement in current density at cell voltages <0.7 V and is significant as the use of p-block metals in M-N-C ORR catalyst optimisation could break the traditional transition-metal catalyst-oxygen adsorptions dynamics, whereby partially filled d-orbitals in transition metals control oxygenated species absorption behaviour. Complete d-orbitals in p-block elements would have conversely clear interaction(s) with oxygenated species, and further work in this direction could lead to a deeper understanding and design of such M-N-C-type ORR catalysts.

3 Transitioning M-N-Cs to Real Fuel Cell Operation

A number of challenges still need to be addressed if M-N-C-type catalysts are to find large-scale commercial adoption (e.g. metal leaching, carbon corrosion, micropore flooding and active site poisoning). Significant progress on improving Beginning-of-Life performance has been achieved (as highlighted in earlier examples); however the developing library of literature needs to be further strengthened with respect to developing a deeper understanding of active M-N-C site chemistries (e.g. local and bulk electrochemistry) and associated degradation mechanism(s) particularly when deployed in real MEAs as part of single cell and ultimately PEMFC stacks. Deepening insights here will deliver desirable End-of-Life performance and thus make M-N-C more attractive towards commercial FC manufacturers. Positively, significant progress has been made with M-N-Cs towards competent ORR catalysts in a relatively short time; for example, N-coordinated single Fe in porous carbon architectures have been reported that deliver a current density of 1.55 A/cm^2 and a power density of 655 mW/cm^2 (working V = 0.43); [109] however the degradation rate and expected lifetime of the employed catalysts were not reported. The previously mentioned ORR catalyst of Kucernak et al. delivered excellent PEMFC performance, generating current densities of 41.3 mA/cm^2 (at 0.90 ViR-free) using pure H_2-O_2 feeds and 145 mA /cm^2 at 0.80 V (199 mA/cm^2 at 0.80 ViR-free) using a H_2-air feed [90].

As introduced earlier, PEMFC operation is determined from an electrochemical point of view by two key reactions, namely, the ORR and the hydrogen oxidation reaction (HOR). Through the combination of these reactions in the electrochemical cell, the high energy content of H_2 is converted to electricity (e.g. which then drives a motor in a mobility context). As conventionally catalysed by Pt-based electrocatalysts, the transition to PGM-free catalysts particularly for the cathodic ORR increases is complex in nature, particularly when transitioning from the classical lab experiment (e.g. based on an RDE) to the preparation and implementation of the MEA in a functional “real” PEMFC (Fig. 8) [110].

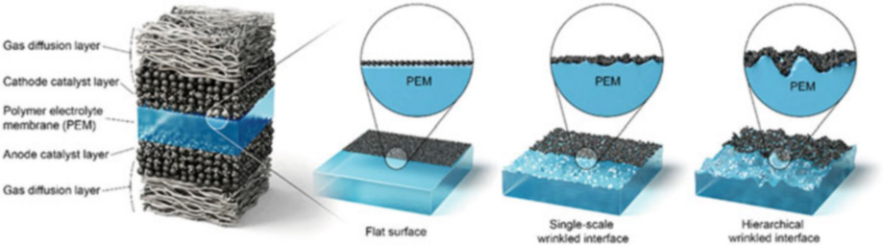


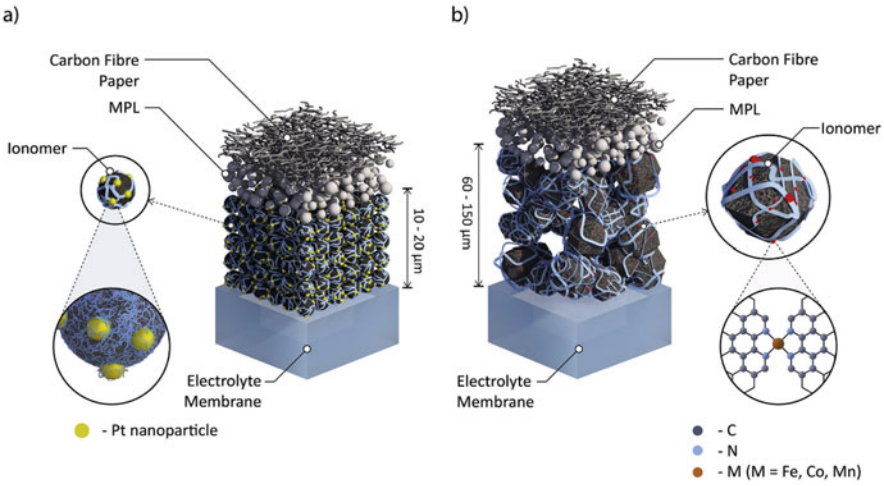
Fig. 8 Illustration of the membrane electrode assembly (MEA) of a PEMFC, depicting examples of nano-structuring at the catalyst/membrane interface. (Reproduced with permission from Ref. [101])

The MEA consists of the PEM as sandwiched between the anode and cathode forming the basis for the single cell, the electrodes themselves being a composition of a catalytic layer often based on the active catalyst as supported on a porous, conductive material (e.g. nanoparticles of conductive carbon), which itself is supported on a gas diffusion layer (GDL) which regulates gas fluxes in and out of the active area (e.g. the triple-phase boundary). Thus when discussing the deployment of M-N-C catalysts towards real PEMFCs, consideration of these respective layers and their interplay must be addressed (e.g. to consider the physicochemical properties of the often-thicker PGM-free catalytic layer).

It is also known that typical Fe-N-C cathode catalyst layers reported for PEMFC are ca. 100 μm thick [111, 112]; as a result there will be inherently some (e.g. mass) transport limitations. Therefore M-N-C layer thickness should be minimised with some report highlighting these should not exceed 10 μm (e.g. equating roughly to conventional Pt/C FC electrode catalyst layer thickness) [40]. A 100 μm thickness for an Fe-N-C catalyst layer would equate to loading of 4 mg(cat)/cm^2 per MEA. This is important with respect to cell performance with high thickness limiting total Fe-N_x sites in PEMFC cathodes in terms of sites/g(Fe-N-C) and sites/cm(Fe-N-C) (Scheme 4) [113].

Therefore approaches to cathode structures that maximise electrochemical accessibility to M-N-C active sites are fundamental to delivering commercially relevant PEMFCs. In doing so, this would go some way to fully exploiting atomically dispersed active sites in a manner with 100% metal utilisation.

Positively, previous reports highlight significant progress. On feed gas accessibility of Fe-N_x sites, this has been reported to reach 100% (as determined by ex situ cryo CO sorption) [86]. Conversely, there has been a limited advance with respect to maximising the ratio of electrochemically accessible active sites. Focusing on Fe-N-C materials, to achieve this the active site should preferentially be located at an optimal triple-phase boundary position. Following on from the important report on the development of a utilisation metric for Fe-N_x sites [114], Wan et al. reported on the critical nature of mesoporosity in determining site utilisation (Fig. 9) [115]. In this report an active site $\text{Utilisation}_{\text{Nitrite/ICP}}$ and $\text{Utilisation}_{\text{Nitrite/Mössbauer}}$ of 43% with a Fe-N-C ORR catalyst was reported; it is important to note the reported



Scheme 4 Representation of (**a**) Pt/C catalyst layer and (**b**) M-N-C catalyst layer – substantial differences in size, morphology and interaction with ionomer between the two cases are evidenced, as discussed by Osmieri and Meyer. (Reproduced with permission from Ref. [40])

catalyst featured a low nitrite determined site density (1.32×10^{19} sites/g(Fe-N-C)), with active site utilisation found to be inversely proportional to the calculated nitrite site density value. Low electrochemical active site utilisation values could be anticipated for real PEMFCs where active sites (as a consequence of a higher complexity system) are typically embedded in a thick catalyst layer (4 mg(Fe-C-N)/cm^2; thickness ca. 100 μm). Thus, to maximise metal utilisation, catalytic layers that feature defined Fe-N_x sites in tandem with a hierarchical pore structure are considered beneficial as such properties should facilitate efficient O_2 transport along with uniform ionomer dispersion.

Given that M-N-C ORR performance is generally dictated by uniformly dispersed metal active sites, local binding environment, crystallinity and porosity (which in turn determine active site utilisation, accessibility and transport properties under real FC operation), finer control and optimisation of fabrication strategies (e.g. at scale) are required to optimise further M-N-C properties for commercial deployment. For example, high-temperature annealing of metalloorganic precursors does not guarantee that the resulting catalyst has a homogenous size and uniform active site dispersion. Therefore, adopting approaches that are amenable to synthesis at low(er) temperatures would be more attractive in terms of delivering homogenous dispersions of catalyst particles featuring uniformly distributed single-atom sites throughout the doped carbon matrix. In this context, an approach employing cadmium as a sacrificial metal has been reported to yield Fe-based ORR M-N-C-type catalysts at a low annealing temperature [116]. The resulting Fe-N-C ORR catalyst (prepared at T = 950 °C) delivered a current density of 44 mA/cm^2

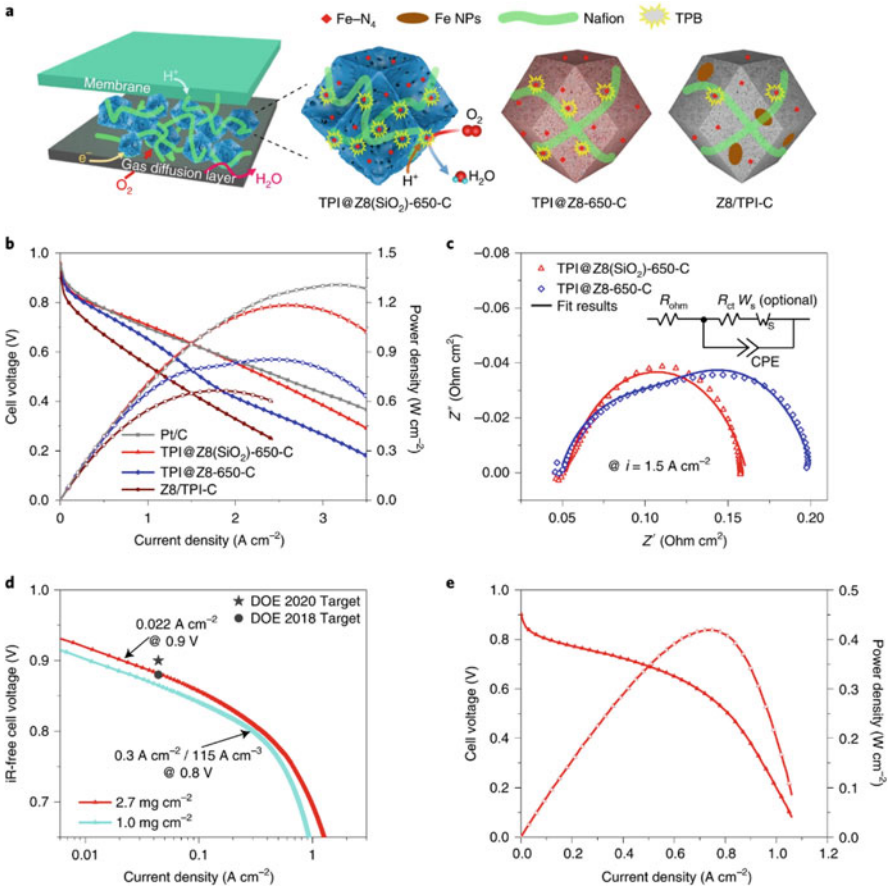


Fig. 9 (**a**) Illustration of TPB active sites in three representative Fe-N-C-based electrodes; (**b**) associated polarisation and power density curves; conditions: cathode loading 2.7 mg/cm^2 for Fe-N-C and 0.2 mg_{Pt}/cm^2 for Pt/C benchmark, anode loading 0.2 mg_{Pt}/cm^2, Nafion®-211 membrane, 5 cm^2 electrode, 80 °C, 100% relative humidity (RH) and 2.5 bar H_2-O_2 at flow rates of 300 or 400 ml/min; (**c**) Nyquist plots for PEMFCs of indicated cathode catalysts at a current density of 1.5 A/cm^2; inset: equivalent circuit model, Z′ and Z″ are real and imaginary impedance components; (**d**) Tafel plot, TPI@Z8(SiO_2)-650-C activity at 0.9 $V_{iR\text{-}free}$ and volumetric activity at 0.8 $V_{iR\text{-}free}$ at 1 bar H_2-O_2; (**e**) polarisation and power density curves for TPI@Z8(SiO_2)-650-C (loading: 2.0 mg/cm^2 at 1 bar(H_2-air) at flow rates of 300 or 500 ml/min). (Reproduced with permission from Ref. [109])

(working voltage of 0.87 V; iR-free) with a power density of 680 mW/cm^2 when investigated in a MEA test (in single-cell setup).

Another element of this complexity relates to performance comparisons. When discussing PGM alternatives as electrocatalysts to PGMs for real PEMFCs, quan-

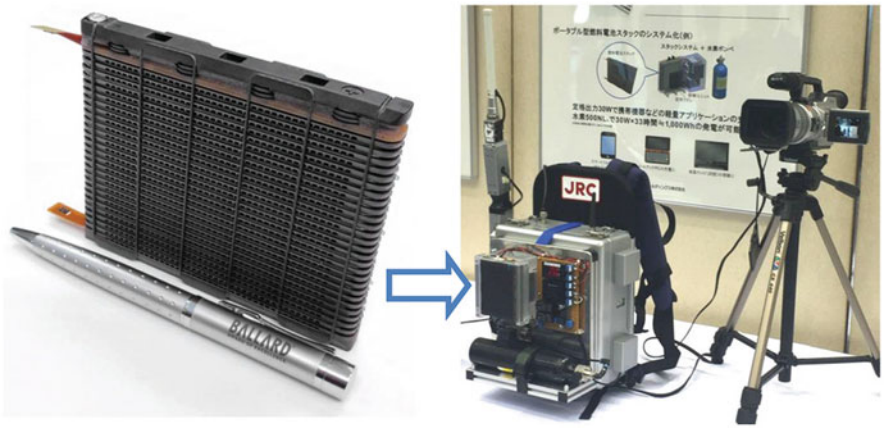


Fig. 10 FCgen-micro (NPMC) PEMFC system commercialised through the collaboration of Ballard with Nisshinbo; the device utilises a PGM-free, M-N-C catalyst at the cathode. It is designed to provide emergency power in the form of Wi-Fi backpack to be used by Japan Radio Co. (Reproduced with permission from Ref. [40])

titative measures are required that provided a fair comparison. The first entry for comparison is logically PGM loading. Previous discussions have targeted the ultimate PGM loading in a PEMFC should be <0.125 g(PGM)/kW [117]. As a consequence, intrinsic PGM-based catalytic activity is represented quantitatively in terms of PGM mass activity at the kinetic-controlled voltage (i.e. 0.90 V). PEMFC electrocatalysts normally feature 3 nm diameter Pt NPs supported on a commercial carbon material and typically geometrically constrained to 35% of Pt atoms exposed at the NP surface [118]. Additionally, PEMFC cathodes conventionally feature a ratio of specific Pt surface area (m^2/g(Pt)) to Pt catalyst (m^2/g(Pt)) in range of ≈70–90%, reflecting typically the preparation route employed. The electrochemical utilisation of total Pt content at the PEMFC cathode is ca. 25–32% for commercial Pt/C ORR catalyst(s) [119]. This equates to a Pt surface site density of ca. 1.3×10^{21} sites /g(Pt) and thus demonstrates that improvement in the amount of accessible surface M-N-C sites is critical if competitive PGM-free catalysts are to be delivered.

The use of M-N-C-type catalysts has been reported in real PEMFC systems, with the commercialisation (through a close collaboration with Nisshinbo) of Ballard's FCgen-micro (NPMC) in 2017 (Fig. 10) [120]. Whilst the Ballard system is potentially useful in a stationary context, for other demanding applications (e.g. automotive drive trains), further R&D on both catalyst and catalyst layer design are needed if the targets for activity, stability and durability for such applications are to be achieved.

4 Outlook and Summary

PGM-free and in particular M-N-C ORR electrocatalysts are considered interesting based initially on the anticipated cost savings (>40% of stack cost at high volumes); at current PEMFC device production volumes, the use of PGMs amounts to ca. 15% of total stack, with ca. 80% of which arising at the cathode [117]. Thus, replacing PGM use with a M-N-C catalyst at the cathode has the potential to deliver <15% stack cost savings (based on the expectation that the used PGM-free catalyst is also "free" from a cost perspective). It is important to note that whilst raw material costs are low in comparison to PGMs, at low device production volumes, manufacturing costs are more than likely comparable (e.g. cost reductions through economies of scale are not realised), although depending on the actual synthesis of the M-N-C and the manner of deposition in the MEA, it may potentially lead to higher costs. Thus, savings in capital expenditure from substituting PGMs with M-N-C will only be realised when manufacturing lines are optimised, and devices are mass manufactured. Regarding RDI on M-N-C catalysts, researchers also need to critique the validity of comparison means; for example, a comparison of the overall current density of the electrodes, which determines that intrinsic catalytic activity, should be evaluated quantitatively based on current density at a cell voltage >0.8 V. It is important to note that M-N-C-type ORR catalysts are often discussed in the context of operation in basic electrolyte and there is significant work to be done in combination with stability assessment in strongly acid environments if commercially relevant performance is to be achieved, although this is an exciting area of investigation [121]. This has to be achieved in tandem with increasing active site loading/density which is particularly challenging if the single site nature is continued to be resolved and isolated in the final catalyst layer [122]. Further important parameters of performance evaluation include the reported power density at a working voltage and peak power density (PPD), which facilitate overall polarisation performance evaluation. These performance indicators will be highly dependent upon catalyst features, namely, electronic conductivity and mass transfer properties. Therefore delivering coherent R&D programmes that accelerated candidate M-N-C materials from lab experiments to real PEMFCs is critical particularly if they enable rapid screening and evaluation in line with standardised degradation analysis. For specific applications, certain technical issues regarding M-N-C catalysts must be addressed. This is particularly relevant in the context of mobility and specific personal automobility applications if PEMFCs based on M-N-C are to be considered suitable power sources.

In terms of performance, one significant benefit of M-N-C ORR catalysts is their tolerance towards airborne contaminants (i.e. vs. Pt-based catalysts) [123], although further R&D is required to assess the sensitivity of these catalysts to other poisoning (e.g. from nitrous oxides). This can be potentially used to an advantage with some research groups investigating active site(s) "memory" arising from contaminant exposure [124]. M-N-C catalysts are close to achieving targets for non-automotive applications (e.g. for backup power), but for automobiles and indeed trucking,

a number of challenges still remain to be addressed. These relate to delivering high activity and achieving high catalyst loadings and active site density (i.e. a compact and lightweight FC stack as possible as well as high power delivery). Synthetic routes to these M-N-Cs, particularly those supported and/or integrated into a carbon material, often suffer from the development of SAC consuming side-phases, which increase the complexity of many applied synthetic approaches (e.g. thermal annealing, carbonisation, acid washing, etc.), particularly when high(er) catalyst loadings are targeted. This represents a significant challenge for the M-N-Cs and in particular Fe-N-Cs, which are by far the most popular cathode/ORR catalysts investigated for PEMFCs. For certain applications, high current densities $\geq$1.5 A/cm^2 and cell voltages $\geq$0.65 V (to handle heat rejection requirements) are required (e.g. automotive drive trains). As discussed earlier, M-N-C catalyst layers are typically much thicker $\gg$50 μm) compared to Pt/C commercial ORR electrodes. As a consequence, there will be inherent transport losses at higher current densities. To overcome this, M-N-C layers will have to be reduced by 5–10 times. Another challenge relates to lifetimes (e.g. for automotive applications, stacks are expected to operate for >20 k hours [125]), although progress is being made.

From a material R&D perspective, the synthesis and description of novel nanocarbons (e.g. as M-N-C supports or carrier) with diverse properties reflecting higher graphitisation, (additional) heteroatom doping and rich (optimised) porosity would be advantageous to improve M-N-C-catalysed PEMFC performance. As for the current state-of-the-art PEMFCs, various materials have been proposed (e.g. as Pt/C alternatives) including catalyst compositions, support materials and interface chemistry (e.g. as moderation via surface modification). The next step forward is the successful and optimal integration of these different aspects to enable optimal utilisation of the M-N-C dynamic, considering both the current positive and negative aspects. Any new M-N-C electrocatalyst has to be supported on an appropriate material (e.g. a solid or porous carbon, doped or otherwise), which is also amenable to surface modification if needed. This latter point could take the form of the deeper integration of support and catalyst (e.g. M-N-C is formed in a porous carbon structure), but any porosity and surface chemistry must be suitable for the establishment of an efficient triple-phase boundary, catalyst/ionomer interactions and transport properties. These could be potentially taken to higher levels of layer integration including the membrane side of the gas diffusion layer.

Therefore in summary, the outlook is positive, but significant steps forward to the commercialisation of M-N-C catalysts for a broad range of PEMFC applications are required. It is expected that over the coming decade, the true potential of the heme-inspired catalytic M-N-C site in combination with a synthetically optimised conductive support (e.g. carbon) matrix will be characterised to be sufficiently performing to justify firstly deployment as PGM replacements (e.g. in mobility applications) and secondly reduce the overall PEMFC stack costs, ultimately resulting in a commercially viable fuel cell product, with improved sustainability credentials.

References

1. European Commission – A European Green Deal – https://commission.europa.eu/strategy-and-policy/priorities-2019-2024/european-green-deal_en
2. European Commission – Electrolyser Summit Joint Declaration 04/05/2022 – https://ec.europa.eu/docsroom/documents/50014/attachments/1/translations/en/renditions/native
3. M. K. Debe, Nature, 2012, 486, 43
4. Y. Shao, J. P. Dodelet, G. Wu, P. Zelenay, Adv. Mater., 2019, 31, 1807615
5. I. E. L. Stephens, J. Rossmeisl, I. Chorkendorff, Science, 2016, 354, 1378
6. G. Shen, J. Liu, H. B. Wu, P. Xu, F. Liu, C. Tongsh, K. Jiao, J. Li, M. Liu, M. Cai, J. P. Lemmon, G. Soloveichik, H. Li, J. Zhu, Y. Lu, Nat. Commun., 2020, 11, 1191
7. S. J. Peighambardoust, S. Rowshanzamir, M. Amjadi, Int. J. Hydrogen Energy, 2010, 35, 9349.
8. J. P. Kone, X. Zhang, Y. Yan, G. Hu, G. Ahmadi, J. Comp. Multiphase Flows, 2017, 9, 1, 3
9. M. Shao, Q. Chang, J. P. Dodelet, R. Chenitz, Chem. Rev., 2016, 116, 3594
10. Y. He, S. Liu, C. Priest, Q. Shi, G. Wu, Chem. Soc. Rev., 2020, 49, 3484
11. S. T. Thompson, D. Papageorgopoulos, Nat. Catal., 2019, 2, 558
12. D. D. Papageorgopoulos, U.S Department of Energy, 2019
13. A. Wilson, G. Kleen, D. Papageorgopoulos, Fuel Cell System Cost–2017 (DOE Hydrogen and Fuel Cells Program, 2017)
14. A. Holewinski, J.-C. Idrobo, S. Linic, Nat. Chem., 2014, 6, 828
15. L. Osmieri, J. Park, D. A. Cullen, P. Zelenay, D. J. Meyers, K. C. Neyerlin, Curr. Opin. Electrochem., 2021, 25, 100627
16. G. Andrea Blengini, P. Nuss, J. Dewulf, V.Nita, L. Talens Peirò, B. Vidal-Legaz, C. Latunussa, L. Mancini, D. Blagoeva, D. Pennington, M. Pellegrini, A. Van Maercke, S. Solar, M. Grohol, C. Ciupagea, Resource Policy, 2017, 53, 12–19.
17. K. Ehelebe, D. Seeberger, M. T. Y. Paul, S. Thiele, K. J. J. Mayrhofer, S. Cherevko, J. Electrochem. Soc., 2019, 166, F1259
18. Y. Nie, L. Li, Z. Wei, Chem. Soc. Rev., 2015, 44, 2168
19. Y. Wang, F. Chu, J. Zeng, Q. Wang, T. Naren, Y. Li, Y. Cheng, Y. Lei, F. Wu, ACS Nano, 2021, 15, 1, 21
20. H. Zhang, G. Liu, L. Shi, J. Ye, Adv. Energy Mater., 2018, 8, 1701343
21. J. Liu, Curr. Opin. Green Sustain. Chem., 2020, 22, 54
22. A. Wang, J. Li, T. Zhang, Nature Reviews Chemistry, 2018, 2, 65
23. J. S. Bates, M. R. Johnson, F. Khamespanah, T. W. Root, S. S. Stahl, Chem. Rev., 2022, https://doi.org/10.1021/acs.chemrev.2c00424
24. U. Martinez, S. Komini, E. F. Holby, H. T. Chung, X. Yin, P. Zelenay, Adv. Mater. 2019, 31, 1806545
25. X. F. Yang, A. Wang, B. Qiao, J. Li, J. Liu, T. Zhang, Acc. Chem. Res., 46, 8, 1740
26. H. A. Gasteiger, N. M. Markovic, Science, 2009, 324, 48
27. S. Mukherjee, A. Mukherjee, A. Bhagi-Damodaran, M. Mukherjee, Y. Lu, A. Dey, Nat. Commun., 2015, 6, 8467
28. L. Que Jr., W. B. Tolman, Nature, 2008, 455, 333
29. R. Jasinski, Nature, 1964, 201, 1212
30. V. Čolić, A. S. Bandarenka, ACS Catal., 2016, 6, 5378
31. J. Fichtner, B. Garlyyev, S. Watzele, H. A. El-sayed, J. Schwaemmlein, W. J. Li, F. Maillard, L. Dubau, J. Michalicka, J. Macak, A. W. Holleitner, A. S. Bandarenka, ACS Appl. Mater. Interfaces, 2019, 11, 5129
32. B. Garlyyev, S. Xue, M. D. Pohl, D. Reinisch, A. S. Bandarenka, ACS Omega, 2018, 3, 15325
33. J. Greeley, I. E. L. Stephens, A. S. Bondarenko, T. P. Johansson, H. A. Hansen, T. F. Jaramillo, J. Rossmeisl, I. Chorkendorff, J. K. Nørskov, Nat. Chem., 2009, 1, 552
34. J. K. Nørskov, J. Rossmeisl, A. Logadottir, L. Lindqvist, J. R. Kitchin, T. Bligaard, H. Jónsson, J. Phys. Chem. B, 2004, 108, 17886

35. M. Rück, A. S. Bandarenka, F. Calle-Vallejo, A. Gagliardi, J. Phys. Chem. Lett., 2018, 9, 4463
36. M. Nesselberger, M. Roefzaad, F. R. Hamou, P. U. Biedermann, F. F. Schweinberger, S. Kunz, K. Schloegl, G. K. H. Wiberg, S. Ashton, U. Heiz, K. J. J. Mayrhofer, M. Arenz, Nat. Mater., 2013, 12, 919
37. K. Yamamoto, T. Imaoka, W.-J. Chun, O. Enoki, H. Katoh, M. Takenaga, A. Sonoi, Nat. Chem., 2009, 1, 397
38. H. T. Chung, D. A. Cullen, D. Higgins, B. T. Sneed, E. F. Holby, K. L. More, P. Zelenay, Science, 2017, 357, 479
39. M. Lefèvre, E. Proietti, F. Jaouen, J. P. Dodelet, Science, 2009, 324, 71
40. H. A. Gasteiger, S. S. Kocha, B. Sompalli, F. T. Wagner, Appl. Catal. B, 2005, 56, 9
41. Z. H. Tang, W. Wu, K. Wang, Catalysts, 2018, 8, 65
42. Z. Chen, D. Higgins, A. Yu, L. Zhang, J. Zhang, Energy Environ. Sci., 2011, 4, 3167
43. A. A. Gewirth, J. A. Varnell, A. M. DiAscro, Chem. Rev., 2018, 118, 2313
44. S. K. Kaiser, Z. Chen, D. Faust Akl, S. Mitchell, J. Pérez-Ramírez, Chem. Rev., 2020, 120, 21, 11703
45. A. Wang, J. Li, T. Zhang, Nat. Rev. Chem., 2018, 2, 65
46. S. Tajik, Z. Dourandish, F. G. Nejad, H. Beitollahi, A. A. Afshar, P. M. Jahani, A. Di Bartolomeo, J. Electrochem. Soc., 2022, 169, 4, 046504
47. Z. Kou, W. Zang, P. Wang, X. Li, J. Wang, Nanoscale Horiz., 2020, 5, 757
48. Y. J. Chen, S. F. Ji, W. M. Sun, Y. P. Lei, Q. C. Wang, A. Li, W. X. Chen, G. Zhou, Z. D. Zhang, Y. Wang, L. R. Zheng, Q. H. Zhang, L. Gu, X. D. Han, D. S. Wang, Y. D. Li, Angew. Chem., Int. Ed., 2020, 59, 1295
49. Y. Xiong, W. M. Sun, P. Y. Xin, W. X. Chen, X. S. Zheng, W. S. Yan, L. R. Zheng, J. C. Dong, J. Zhang, D. S. Wang, Y. D. Li, Adv. Mater., 2020, 32, 2000896
50. Y. P. Lei, Y. C. Wang, Y. Liu, C. Y. Song, Q. Li, D. S. Wang, Y. D. Li, Angew. Chem., Int. Ed., 2020, 59, 20794
51. N. Q. Zhang, C. L. Ye, H. Yan, L. C. Li, H. He, D. S. Wang, Y. D. Li, Nano Res., 2020, 13, 3165
52. Y. C. Wang, Y. Liu, W. Liu, J. Wu, Q. Li, Q. G. Feng, Z. Y. Chen, X. Xiong, D. S. Wang, Y. P. Lei, Energy Environ. Sci., 2020, 13, 4609
53. H. L. Fei, J. C. Dong, M. J. Arellano-Jiménez, G. L. Ye, N. D. Kim, E. L. G. Samuel, Z. W. Peng, Z. Zhu, F. Qin, J. M. Bao, M. J. Yacaman, P. M. Ajayan, D. L. Chen, J. M. Tour, Nat. Commun., 2015, 6, 8668
54. B. T. Qiao, A. Q. Wang, X. F. Yang, L. F. Allard, Z. Jiang, Y. T. Cui, J. Y. Liu, J. Li, T. Zhang, Nat. Chem., 2011, 3, 634
55. S. Gupta, D. Tryk, I. Bae, W. Aldred, E. Yeager, J. Appl. Electrochem., 1989, 19, 19
56. X. Cui, W. Li, P. Ryabchuk, K. Junge, M. Beller, Nat. Catal., 2018, 1, 385
57. W. Wang, Q. Jia, S. Mukerjee, S. Chen, ACS Catal., 2019, 9, 10126
58. A. S. Varela, N. Ranjbar Sahraie, J. Steinberg, W. Ju, H. S. Oh, P. Strasser, Angew. Chem. Int. Ed., 2015, 54, 10758
59. J. Li, P. Pršlja, T. Shinagawa, A. J. Martín Fernández, F. Krumeich, K. Artyushkova, P. Atanassov, A. Zitolo, Y. Zhou, R. García-Muelas, N. López, J. Pérez-Ramírez, F. Jaouen, ACS Catal., 2019, 9, 11, 10426
60. Z. Geng, Y. Liu, X. Kong, P. Li, K. Li, Z. Liu, J. Du, M. Shu, R. Si, J. Zeng, Adv. Mater,. 2018, 30, 1803498
61. H. Jahnke, M. Schönborn, G. Zimmermann, Top. Curr. Chem., 1976, 61, 133
62. J. A. R. Van Veen, J. F. van Baar, K. J. Kroese, J. Chem. Soc., Faraday Trans., 1981, 1, 77, 2827
63. T. Sun, B. Tian, J. Lu, C. Su, J. Mater. Chem. A, 2017, 5, 18933
64. Z. Qiao, H. G. Zhang, S. Karakalos, S. Hwang, J. Xue, M. J. Chen, D. Su, G. Wu, Appl. Catal., B, 2017, 219, 629
65. J. Liu, X. Sun, P. Song, Y. Zhang, W. Xing, W. Xu, Adv. Mater., 2013, 25, 6879
66. Q. Cheng, L. Yang, L. Zou, Z. Zou, C. Chen, Z. Hu, H. Yang, ACS Catal., 2017, 7, 6864

67. L. Ni, C. Gallenkamp, S. Wagner, E. Bill, V. Krewald, U. I. Kramm, J. Am. Chem. Soc., 2022, 144, 37
68. S. Zhang, Y. Qin, S. Ding, Y. Su, ChemPhysChem, 2022, 23, 15, e202200165
69. M. Xiao, J. Zhu, G. Li, N. Li, S. Li, Z. P. Cano, L. Ma, P. Cui, P. Xu, G. Jiang, H. Jin, S. Wang, T. Wu, J. Lu, A. Yu, D. Su, Z. Chen, Angew. Chem. Int. Ed., 2019, 58, 9640
70. C. Zhang, J. Sha, H. Fei, M. Liu, S. Yazdi, J. Zhang, Q. Zhong, X. Zou, N. Zhao, H. Yu, Z. Jiang, E. Ringe, B. I. Yakobson, J. Dong, D. Chen, J. M. Tour, ACS Nano, 2017, 11, 7, 6930
71. K. Yuan, D. Lützenkirchen-Hecht, L. Li, L. Shuai, Y. Li, R. Cao, M. Qui, X. Zhuang, M. K. H. Leung, Y. Chen, U. Scherf, J. Am. Chem. Soc., 2020, 142, 2404
72. R. Jiang, L. Li, T. Sheng, G. Hu, Y. Chen, L. Wang, J. Am. Chem. Soc., 2018, 140, 11594
73. J. Meng, J. Li, J. Liu, X. Zhang, G. Jiang, L. Ma, Z. Y. Hu, S. Xi, Y. Zhao, M. Yan, P. Wang, X. Liu, Q. Li, J. Z. Liu, T. Wu, L. Mai, ACS Cent. Sci., 2020, 6, 8, 1431
74. S. Wang, L. Shang, L. Li, Y. Yu, C. Chi, K. Wang, J. Zhang, R. Shi, H. Shen, G. I. Waterhouse, S. Liu, J. Tian, T. Zhang, H. Liu, Adv. Mater., 2016, 28, 8379
75. G. Chen, P. Liu, Z. Liao, F. Sun, Y. He, H. Zhong, T. Zhang, E. Zschech, M. Chen, G. Wu, J. Zhang, X. Feng, Adv. Mater., 2020, 32, 1907399.
76. X. Wang, Y. Jia, X. Mao, D. Liu, W. He, J. Li, J. Liu, X. Yan, J. Chen, L. Song, A. Du, X. Yao, Adv. Mater., 2020, 32, 2000966
77. G. Wu, K. L. More, C. M. Johnston, P. Zelenay, Science, 2011, 332, 443
78. J. Li, M. Chen, D. A. Cullen, S. Hwang, M. Wang, B. Li, K. Liu, S. Karakalos, M. Lucero, H. Zhang, C. Lei, H. Xu, G. E. Sterbinsky, Z. Feng, D. Su, K. L. More, G. Wang, Z. Wang, G. Wu, Nat. Catal., 2018, 1, 935
79. S. H. Ahn, X. W. Yu, A. Manthiram, Adv. Mater., 2017, 29, 1606534
80. A. Pedersen, J. Barrio, A. Li, R. Jervis, D. J. L. Brett, M. M. Titirici, I. E. L. Stephens, Adv. Energy Mater., 2022, 12, 2102715
81. J. Wang, Z. Huang, W. Liu, C. Chang, H. Tang, Z. Li, W. Chen, C. Jia, T. Yao, S. Wei, Y. Wu, Y. Li, J. Am. Chem. Soc., 2017, 139, 17281
82. W. Zang, Z. Kou, S. J. Pennycook, J. Wang, Adv. Energy Mater., 2020, 10, 1903181
83. H. Xu, D. Cheng, D. Cao, X. C. Zeng, Nat. Catal., 2018, 1, 339
84. B. Lu, Q. Liu, S. Chen, ACS Catal., 2020, 10, 7584
85. H. J. Shen, E. Gracia-Espino, J. Y. Ma, K. T. Zang, J. Luo, L. Wang, S. S. Gao, X. Mamat, G. Z. Hu, T. Wagberg, S. J. Guo, Angew. Chem., Int. Ed., 2017, 56, 13800
86. C. Tang, Y. Jiao, B. Shi, J.-N. Liu, Z. Xie, X. Chen, Q. Zhang, S.-Z. Qiao, Angew. Chem. Int. Ed., 2020, 59, 9171
87. L. Ni, C. Gallenkamp, S. Paul, M. Kübler, P. Theis, S. Chabbra, K. Hofmann, E. Bill, A. Schnegg, B. Albert, V. Krewald, U. I. Kramm, Adv. Energy Sustainability Res., 2021, 2, 2000064
88. J. Li, M. T. Sougrati, A. Zitolo, J. M. Ablett, I. C. Oğuz, T. Mineva, I. Matanovic, P. Atanassov, Y. Huang, I. Zenyuk, A. Di Cicco, K. Kumar, L. Dubau, F. Maillard, G. Dražić, F. Jaouen, Nat. Catal., 2021, 4, 10
89. C. Gallenkamp, U. I. Kramm, V. Krewald, Chem. Commun., 2021, 57, 859
90. P. Hutchison, P. S. Rice, R. E. Warburton, S. Raugei, S. Hammes-Schiffer, J. Am. Chem. Soc., 2022, 144, 16524
91. X. Yang, D. Xia, Y. Kang, H. Du, F. Kang, L. Gan, J. Li, Adv. Sci., 2020, 7, 2000176
92. X. She, J. Gao, Y. Gao, H. Tang, K. Li, Y. Wang, Z. Wu, New J. Chem., 2022, 46, 16138
93. W. Li, W. Ding, J. X. Jiang, Q. He, S. C. Tao, W. L. Wang, J. Li, Z. D. Wei, J. Mater. Chem., A 2018, 6, 878
94. A. Mehmood, J. Pampel, G. Ali, H. Y. Ha, F. Ruiz-Zepeda, T.-P. Fellinger, Adv. Energy Mater., 2018, 8, 1701771
95. L. Jiao, J. Li, L. L. Richard, Q. Sun, T. Stracensky, E. Liu, M. T. Sougrati, Z. Zhao, F. Yang, S. Zhong, H. Xu, S. Mukerjee, Y. Huang, D. A. Cullen, J. H. Park, M. Ferrandon, D. J. Myers, F. Jaouen, Q. Jia, Nat. Mater., 2021, 20, 1385
96. A. Mehmood, M. Gong, F. Jaouen, A. Roy, A. Zitolo, A. Khan, M. Sougrati, M. Primbs, A. M. Bonastre, D. Fongalland, G. Drazic, P. Strasser, A. Kucernak, Nat. Catal., 2022, 5, 311

97. D. Menga, F. Ruiz-Zepeda, L. Moriau, M. Šala, F. Wagner, B. Koyutürk, M. Bele, U. Petek, N. Hodnik, M. Gaberšček, T. Fellinger, Adv. Energy Mater., 2019, 9, 1902412
98. H. Peng, Z. Mo, S. Liao, H. Liang, L. Yang, F. Luo, H. Song, Y. Zhong, B. Zhang, Sci. Rep., 2013, 3, 1765
99. T. Palaniselvam, B. P. Biswal, R. Banerjee, S. Kurungot, Chem. Eur. J., 2013, 19, 9335
100. P. Zhang, F. Sun, Z. Xiang, Z. Shen, J. Yun, D. Cao, Energy Environ. Sci., 2014, 7, 442
101. Q. Lin, X. Bu, A. Kong, C. Mao, X. Zhao, F. Bu, P. Feng, J. Am. Chem. Soc., 2015, 137, 2235
102. H. Furukawa, K. E. Cordova, M. O'Keeffe, O. M. Yaghi, Science, 2013, 341, 1230444
103. X. X. Wang, D. A. Cullen, Y. T. Pan, S. Hwang, M. Wang, Z. Feng, J. Wang, M. H. Engelhard, H. Zhang, Y. He, Y. Shao, D. Su, K. L. More, J. S. Spendelow, G. Wu, Adv. Mater., 2018, 30, 1706758
104. H. Zhang, H. Osgood, X. Xie, Y. Shao, G. Wu, Nano Energy, 2017, 31, 331
105. H. F. Wang, L. Chen, H. Pang, S. Kaskel, Q. Xu, Chem. Soc. Rev., 2020, 49, 141
106. H. Chang, L. N. Shi, Y. H. Chao, P. F. Wang, T. F. Yi, Coordination Chem. Rev., 2022, 473, 214839
107. S. Y. Lim, S. Martin, G. Gao, Y. Dou, S. B. Simonsen, J. O. Jensen, Q. Li, K. Norrman, S. Jing, W. Zhang, Adv. Funct. Mater., 2020, 30, 2006771
108. F. Luo, A. Roy, L. Silvioli, D. A. Cullen, A. Zitolo, M. T. Sougrati, I. C. Oguz, T. Mineva, D. Teschner, S. Wagner, J. Wen, F. Dionigi, U. I. Kramm, J. Rossmeisl, F. Jaouen, P. Strasser, Nat. Mater., 2020, 19, 1215
109. H. Yang, X. Chen, W. T. Chen, Q. Wang, N. C. Cuello, A. Nafady, A. M. Al-Enizi, G. I. N. Waterhouse, G. A. Goenaga, T. A. Zawodzinski, P. E. Kruger, J. E. Clements, J. Zhang, H. Tian, S. G. Telfer, S. Ma, ACS Nano, 2019, 13, 8087
110. D.-H Lee, G.-T. Yun, G. Doo, S. Yuk, H. Guim, Y. Kim, W.-B. Jung, H.-T. Jung, H.-T. Kim, Nano Lett., 2022, 22, 3, 1174
111. A. M. Damjanović, B. Koyutürk, Y.-S. Li, D. Menga, C. Eickes, H. A. El-Sayed, H. A. Gasteiger, T.-P. Fellinger, M. Piana, J. Electrochem. Soc., 2021, 168, 114518
112. T. A. M. Suter, K. Smith, J. Hack, L. Rasha, Z. Rana, G. M. A. Angel, P. R. Shearing, T. S. Miller, D. J. L. Brett, Adv. Energy Mater., 2021, 11, 2101025
113. L. Osmieri, Q. Meyer, Curr. Opin. Electrochem., 2022, 31, 100847
114. N. R. Sahraie, U. I. Kramm, J. Steinberg, Y. Zhang, A. Thomas, T. Reier, J.-P. Paraknowitsch, P. Strasser, Nat. Commun., 2015, 6, 8618
115. X. Wan, X. Liu, Y. Li, R. Yu, L. Zheng, W. Yan, H. Wang, M. Xu, J. Shui, Nat. Catal., 2019, 2, 259
116. T. Al-Zoubi, Y. Zhou, X. Yin, B. Janicek, C. Sun, C. E. Schulz, X. Zhang, A. A. Gewirth, P. Huang, P. Zelenay, H. Yang, J. Am. Chem. Soc. 2020, 142, 5477
117. D. Banham, S. Ye, ACS Energy Lett., 2017, 2, 629.
118. R. Van Hardeveld, F. Hartog, Surf. Sci., 1969, 15, 189
119. F. Jaouen, D. Jones, N. Coutard, V. Artero, P. Strasser, A. Kucernak, Johnson Matthey Technol. Rev., 2018, 62, 231
120. Ballard Power Systems, News Releases, http://ballard.com/about-ballard/newsroom/news-releases/2017/09/13/ballard-to-offer-world-s-first-pem-fuel-cell-product-using-non-precious-metal-catalyst (accessed: January 2023).
121. H. Adabi, P. G. Santori, A. Shakouri, X. Peng, K. Yassin, I. G. Rasin, S. Brandon, D. R. Dekel, N. U. Hassan, M. T. Sougrati, A. Zitolo, J. R. Varcoe, J. R. Regalbuto, F. Jaouen, W. E. Mustain, Materials Today Adv., 2021, 12, 100179
122. D. F. Yan, Y. X. Li, J. Huo, R. Chen, L. M. Dai, S. Y. Wang, Adv. Mater., 2017, 29, 1606459
123. D. Malko, T. Lopes, E. Symianakis, A. R. Kucernak, J. Mater. Chem. A, 2016, 4, 142
124. J. L. Kneebone, S. L. Daifuku, J. A. Kehl, G. Wu, H. T. Chung, M. Y. Hu, E. E. Alp, K. L. More, P. Zelenay, E. F. Holby, M. L. Neidig, J. Phys. Chem. C, 2017, 121, 16283
125. Clean Hydrogen JU – SRIA Key Performance Indicators (KPIs) – https://www.clean-hydrogen.europa.eu/document/download/8a35a59b-a689-4887-a25a-6607757bbd43_en?filename=Clean%20Hydrogen%20JU%20SRIA%20-%20approved%20by%20GB%20-%20clean%20for%20publication%20%28ID% 2013246486%29.pdf

Integration of Electrical Energy Storage Devices with Photovoltaic Solar Cells in One Hybrid System



Shikhamir Eminov, Arif Hashimov, Alovsat Rajabli, Jafar Guliev, Gultekin Mammadova, Samira Abdulayeva, and Aysel Karimova

1 Introduction

As the most valued renewable and pure energy source, solar energy has gained great practical interest [1–29, 45–58]. Two main types of solar energy technologies are used nowadays to convert solar light into electricity: concentrated solar power (CSP) and photovoltaic (PV). The first one is an indirect method that generates electricity by converting the sun's energy into thermal energy using various mirror configurations [5, 6]. This energy can be used to spin a turbine or power an engine to generate electricity. In contrast, a photovoltaic solar cell (PVSC) is a p-n junction device with a large surface area that uses the photovoltaic (PV) effect to transform the adsorbed solar energy into electricity [1–4, 7–18] without using any machines or moving parts.

However, for a given geographical location, solar energy intensity varies greatly depending on the season and the time of day because of the relative motion of the sun. When the solar cell's illumination stops, its voltage will immediately fall to zero. Their efficiency highly depends on the level of cloudiness and drops several times in the evening and night times when solar energy is absent and no energy conversion is possible. For that reason, solar systems can convert energy only during the daytime. Due to the intermittent nature of solar irradiation, it becomes vital to hybridize the PVSCs with electrical energy storage (EES) devices such as Li-ion batteries, capacitors, and supercapacitors in one single power unit component. Should PVSCs get connected to an EES device, no instant voltage fall to zero will occur. Thus, the absence of light will not affect the power supply.

S. Eminov (✉) · A. Hashimov · A. Rajabli · J. Guliev · G. Mammadova · S. Abdulayeva · A. Karimova
Institute of Physics of the Ministry of Sciences and Education of Azerbaijan, Baku, Azerbaijan

© The Author(s), under exclusive license to Springer Nature Switzerland AG 2024

S. Krishnamoorthy, K. (Kris) Iniewski (eds.), *Advances in Fabrication and Investigation of Nanomaterials for Industrial Applications*,
https://doi.org/10.1007/978-3-031-42700-8_18

A recently developed method to enable both the EES devices and PVSC to function as two mutually independent units connected by external wires [7] makes it possible to produce and store energy simultaneously. Nonetheless, this method has some drawbacks, such as being complicated, not handy, inflexible, space-consuming, and energy-inefficient due to loss of energy at external wires to connect the EES and PVSC. So such devices are not considered entirely integrated solutions. The physical integration of these two devices into one allows it to escape the abovementioned disadvantages by achieving compactness as well as saving on energy loss due to a decrease in the required amount of wires to connect the two units [4–11]. The manufacturing process of a complete integrated device is foreseen as one of the main motivations of physical integration because it might mean a reduction of the amount of materials and energy in comparison with separately fabricating all components. Such a system can decrease fluctuations from the generation side and mismatches between local power generation and consumption. Such devices can be used as power sources for hybrid electric vehicles and small residential premises located in hard-to-reach mountainous areas. Numerous review papers on various PVSC [12–29], EES devices [29–48], and integrated systems [1–12] have been published recently.

A typical thin-film PVSC structure comprises a highly doped coating on a semiconductor substrate where a similar but moderately doped absorber layer is deposited on top of it. High optical absorption coefficient, high mobility, good carrier lifetime, and improved crystallographic characteristics are required of absorber layers. Above the absorber layer, a heavily but opposite conductive semiconductor material is doped that functions as an emitter or window layer. The window layer in a heterojunction thin-film solar cell is primarily used to form a p-n junction with the absorber layer. This layer is desired to achieve a high bandgap, small thickness, and low series resistance for high optical throughput.

As much as 90% of the worldwide PV market is currently dominated by the first-generation Si-based PVSCs to have a high power conversion efficiency (PCE) of as high as 27% [12, 21], as well as good stability and fixed industrial production standards. Nevertheless, certain limitations attributed to their high cost, environmental pollution issues, as well as rigidness of PV cells serve as an obstacle in their wider market scattering. Inorganic thin-film solar cells based on amorphous α-Si [12], GaAs and other III-V compounds [13], CdTe and CIGS [14–19], organic SCs [20], hybrid organic-inorganic lead or tin halide-based perovskite SCs [21, 22], quantum dot solar cells [23], and dye-sensitized solar cells (DSSCs) [24–27] have gradually replaced these cells. There are consolidated tables in [28] that display the maximum PCE values measured under the Airmass 1.5 (AM 1.5) Standard Spectrum for both single solar cells and the modules fabricated from various semiconductor materials used in solar cells.

It is CdTe/CdS or CIGS/CdS thin-film heterojunction solar cells with a predicted PCE limit of 17.5% that are attributed to the category of the most acclaimed PVSCs [13–19, 28]. In these cells, CdS – the direct-bandgap (E_g ~ 2.5 eV) semiconductor with n-conductivity – is grown on CdTe for lattice matching and also performs as a window layer for light to come in and be absorbed near the junction. Here,

p-doped CdTe with a bandgap energy of 1.5 eV is used as an absorbing layer. Several studies demonstrate the favorable intermixing between CdS and CdTe, which removes native defects and brings the CdTe/CdS interface extremely close to a homojunction [17, 18]. In this regard, CdS is the most suitable material to combine with CdTe to obtain a high-efficiency PVSC structure. CdTe/CdS-based PVSC was first introduced in 1972 with a PCE of 6% [16]. During the past 50 years, PVSCs have been extensively developed, and their efficiency has gradually improved. The world record PCE of 16.5% on laboratory samples of CdS/CdTe PVSCs was achieved at the NREL as early as 2001 and is still widely used today. Over the past 20 years, these solar cells have been improved even more, and to this day, their PCE reaches 22.1% [17].

Electrical energy storage devices such as batteries, supercapacitors, and fuel cells form an integral part of cell phones, remote communication, walkie-talkies, etc. telecommunication devices, standby power systems, and electric hybrid vehicles. In the field of energy storage, two main parameters are fundamental for these devices: energy density and power density. The first parameter defines the amount of energy that can be stored in a given volume or weight, while the second parameter describes the speed at which energy is stored in or discharged from the device. The ideal storage device should simultaneously have both high energy density and high power density. Hence, the integration of conventional primary energy storage units (e.g., batteries and fuel cells) and electric energy storage devices in high-power or pulse-power forms (e.g., capacitors) become the prime concern in the development of new power systems. On the other hand, the energy densities of conventional capacitors are usually too low to be acceptable for several future applications; the development of capacitors with high energy densities (i.e., SCs) for these applications has become an exciting subject of much research for electrochemical energy storage and conversion systems.

Electrochemical Li-ion batteries (LIBs) [29, 74, 77, 78], capacitors, and electrochemical supercapacitors (SCs) [30–45, 72–76] are the primary EES components at the moment. The primary distinction between SCs and LIBs is how they operate their charge storage systems. In contrast to SCs, where this process occurs in the space between the electrodes and the electrolytes and this causes an electrochemical double-layer (EDL) formation, ECBs store charges in the bulk electrodes [30, 31].

LIBs consist of three major components: anode, cathode, and electrolyte. The device functions by converting a chemical potential into electrical energy via faradaic reactions, which include heterogeneous charge transfer processes occurring at the surface of an electrode. The Li-ion secondary battery charging process involves an energy conversion from electrical energy to chemical potential. These Faradic reactions are accompanied by mass and charge transfer within the electrodes and dimensional variation; therefore, the surface area and migration distance are critical parameters that determine battery performance. The composition, crystal structure, and morphology can dictate the reaction rate and transfer processes for the electrode materials and can be manipulated to alter the overall electrochemical performance. For the past few decades, the use of LIBs has been extensive in the

automotive and consumer electronics industries, and it will continue to dominate in the future too.

In addition to the accelerated development of standard and novel types of rechargeable batteries for electricity storage purposes, more and more attention has recently been paid to SCs as a qualitatively new type of capacitor. SC can store a million times more energy per unit mass or volume compared to electrolytic capacitors. It comprises two electrodes of high surface area separated by an insulating material that is ionically conducting and stores electrical energy in an electrochemical double layer formed at the electrode-electrolyte interface. While charging, the positive and negative charges from the electrolyte get accumulated at the surface of the electrodes and compensate for the electronic charges at the electrode surface. Electrodes made with porous materials can provide a massive electrolyte-accessible surface area for charge accumulation [33, 41, 45, 46, 79].

SCs can be categorized into two types: electrical double-layer capacitors (EDLCs), known as non-faradaic and faradaic (or redox) pseudocapacitors, depending on how they store energy [30, 33, 34]. The EDLC often used negative electrodes based on conductive porous carbon materials such as activated carbon, graphite, nanostructured graphene, carbon nanotubes (CNTs), and other carbonaceous materials to store charges [34–37]. These electrodes accumulate electrical power at the electrode due to the physical adsorption of electrolytic ions on the electrode surface-electrolyte interface, which, in turn, causes a double layer of charges (DLC) to develop. Electrostatic attraction causes the charges to physically deposit themselves, resulting in fast charging and discharging kinetics and a high power density [34]. Additionally, since no chemical reaction takes place at the electrode-electrolyte interface, EDLC has a long life cycle. When carbonaceous materials, especially CNTs, are composited with conducting polymers with high electrical conductivities and redox activities, such as poly(3,4-ethylene dioxythiophene) or PEDOT, poly(pyrrole) or PP, sulfonated poly(amic acid), and others, the resulting composites typically have high specific capacitances. Compared with other materials, PEDOT has numerous favorable qualities. For instance, the polymer possesses good stability, a moderate bandgap, high conductivity, and a low redox potential while being optically transparent in its conducting form [38, 71]. In this regard, in [38], by homogenously composing PEDOT onto the CNT electrode using in situ polymerization, the energy density of a CNT-based PC was enhanced by four times, up to 11.3 Wh/kg.

In contrast to EDLC, pseudocapacitors use a quick and reversible faradaic redox process to store electrical energy by transferring charges from electrode to electrolyte. They have a greater ED value than EDLC, but chemical processes reduce their power density and shorten their lifespan [39–43]. An important family of pseudocapacitive electrode materials for supercapacitors in which transition metals (group IV to VII B elements) are linked to oxygen atoms includes transition metal oxides (TMOs) like RuO_2, MnO_2, V_2O_5, ZnO, Fe_2O_3, Co_3O_4, and NiO [42–44]. In terms of energy density, specific capacitance (1000–2000 F/g), and chemical stability, TMOs perform better than carbon-based materials. They also perform better in terms of energy density than conductive polymers. A hybrid supercapacitor that

combines pseudocapacitive materials and electrochemical double-layer capacitors [45, 72–75] can offer greater energy and power density than each material used alone.

Over time, the development of nanostructured materials has opened up possibilities for cost reduction and improving power conversion efficiency for both nanostructured PVSCs and EES devices [45–52]. Due to their radically reduced dimensions and single-crystalline structures with changeable atomic composition, semiconductor nanowires, nanorods, and nanopillars have distinctive electrical, optical, and mechanical capabilities. Ordered arrays of nanostructures transfer solar energy more effectively than disordered ones [46–51] due to structural advantages. Nanomaterials have also received a lot of attention for electrochemical energy storage due to their attractive physicochemical, electrical, and mechanical properties [32, 33, 42, 43].

As noted earlier, active SC electrodes are made of a nanoporous carbonaceous material with both high porosity and specific surface area. Anodic porous aluminum oxide (also known as nanoporous alumina arrays or AAO membranes) template-directed fabrication by anodization of aluminum [43, 46, 70, 80] is one of the fabrication techniques for self-organized highly ordered nanoporous thin-film arrays [60–65] with hexagonal honeycomb-like pores with controlled dimensions and very high density (10^{10} cm^{-2}). AAO is produced via the electrochemical oxidation of an aluminum substrate, which is usually performed in a two-electrode electrochemical cell, where the working electrode is aluminum. Anodic alumina membranes can be used as the mold for a number of deposition methods, such as atomic layer deposition (ALD), chemical vapor deposition (CVD), electrochemical deposition, etc., to create nanowires, nanopillars, nanotubes, and other nanostructured materials made of various semiconductor and conductor materials. Arrays of such nanostructures created in transparent AAO templates offer substantial advantages over thin films in the fields of optical and electrical properties due to their three-dimensional structure and unidirectional electric channel for electron transport. As a result, charge carrier recombination can be significantly reduced, and energy conversion efficiency can be increased. Recently, CdS nanopillars with a vertical orientation embedded in an AAO membrane have replaced planar CdS thin film as the window layer in PVSCs based on nanowire CdS/CdTe PVSCs [46–49]. The CdS nanowires have also been coated with CdTe. For instance, Javey's group [49] has developed PVSCs based on interpenetrated CdS and CdTe nanopillar arrays utilizing AAO templates and demonstrates a technique by which these structures can be mass-produced large-scale flexible modules.

Several review studies have examined the numerous ways that PVSCs and energy storage devices can be combined into a single component during the past several years [2–11] for a variety of applications. These publications classify and identify earlier attempts to create integrated devices, including PVSC/SC [2–6], PVSC/thermal [7, 8], hierarchical PVSC/battery/SC [9], and PVSC/fuel cell/SC systems [10, 11]. Devices that combine solar cells and SC are referred to as photo-supercapacitors (PSCs) or solar capacitors [3]. The majority of these integrated devices exhibit a monolithic (planar) structure or a fiber-shaped con-

figuration. In these devices, multiple solar cells technologies mentioned above (e.g., dye-sensitized, organic, perovskite, and silicon) and SC types (double layer, pseudocapacitors, and hybrid) have been combined following different approaches. The efficiency of the integrated device and the technical difficulties that were faced when refining these devices are described, in addition to their functioning processes.

Hereinafter we have described the construction of the hybrid PVSC device integrated with a supercapacitor and the main steps to its fabrication. This device combines SC based on NiO_2 nanotubes grown in an AAO template with PVSC based on an array of CdS/CdTe nanostructured heterojunctions which are also grown inside an AAO template. It is a fully integrated device, with a monolithic structure, where the solar cell and energy storage segments share a common substrate in the form of a transparent glass wafer, both sides of which are covered with a conductive ITO layer and AAO template, and may be referred to as a photo-supercapacitor or solar capacitor. A detailed presentation of the experimental study findings on the fabrication of the photovoltaic component of this device is also made.

2 Experimental

2.1 Device Design and Fabrication

Figure 1a, b schematically illustrates the cross section and 3D view of a proposed power unit. Here, a PVSC is positioned on the light-receiving side of a transparent glass slide (1) that has been covered on both sides with conductive ITO thin film (2) and an AAO template.

The SC part of the device is located on the rear side of the glass slide. The PVSC part itself consists of a freestanding CdS NRs (3) array that is electrochemically grown inside AAO nanopores, a thermally deposited CdTe thin layer (4), a transparent ZnO front layer (5), and current leads (6 and 7) to ohmic contacts (Te, Sb) to CdTe. Further, the supercapacitor part consists of freestanding NiO_2 nanotubes (8) embedded into the electrolyte (9) and electrically in contact with the positive electrode (10) through the ITO layer, activated carbon serving as a negative

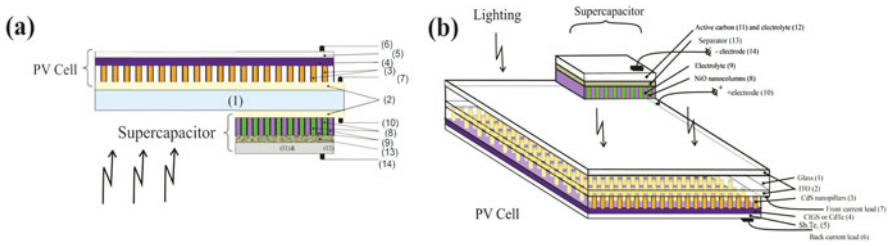


Fig. 1 Cross section (**a**) and 3D view (**b**) of the integrated power unit

electrode (11), electrolyte (12), a porous separator (13) between the positive and negative electrodes, as well as lead (14) to the negative electrode.

The main operations for the manufacture of the proposed device are listed below:

(a) Deposition of ITO and Al layers on both sides of a glass plate, followed by their anodic oxidation on both sides to synthesize a nanoporous AAO structure
(b) Electrochemical deposition of CdS and CdTe in AAO pores to create a nanostructured array of CdS/CdTe heterojunctions on the PVSC side
(c) Electrochemical deposition of Ni into AAO pores on the capacitor side to create Ni nanotubes
(d) Sintering of the entire structure in the air at 400–500 °C for the simultaneous carrying out of three processes: crystallization of freshly deposited amorphous CdS, formation of a CdTe/CdS heterojunction, and the formation of NiO nanotubes through oxidation of Ni.
(e) Installation of a porous separating layer and a porous carbon-negative electrode in a supercapacitor and then filling an array of NiO nanotubes with an appropriate alkaline electrolyte and sealing

The manufacturing steps are described below:

1. Deposition of ITO and aluminum layers by magnetron deposition simultaneously on both sides of the glass substrate: first ITO and then Al [70]
2. Simultaneous anodic oxidation of Al on both sides of the glass substrate to the creation of AAO templates on both sides of the glass plate [61–66]
3. Electrochemical deposition of both CdS nanowires and Ni nanotubes in AAO templates on the front and rear sides [54, 55, 70]
4. Creation of matrices of freestanding CdS nanopillars and Ni nanotubes simultaneously on the front and back sides of the structure by removing alumina in NaOH solution
5. Deposition of a thin absorbing p-CdTe film over an array of CdS nanowires by magnetron sputtering or close spacing sublimation methods [59]
6. The sintering of the whole structure in the air at 400–500 °C with simultaneous crystallization of electrochemically deposited amorphous CdS, formation of CdTe/CdS heterojunction nanowires, and formation of NiO_2 nanotubes by oxidation of Ni in air medium
7. Preparing of supercapacitor side

A flowchart of the initial one to four stages of the manufacturing process is shown in Fig. 2.

As can be seen from Fig. 2, the manufacturing stages nos. 1, 2, 4, 5, and 6, used for the manufacture of PVSC and SC, are similar and are carried out simultaneously. Therefore, the design features of the device allow the combining and simultaneous execution of some similar fabrication operations which would have to be carried out in the case of separate fabrication manufacture of the constituent elements of the device and thereby significantly reducing the number of production operations. As opposed to constructing each component independently, we believe that using the

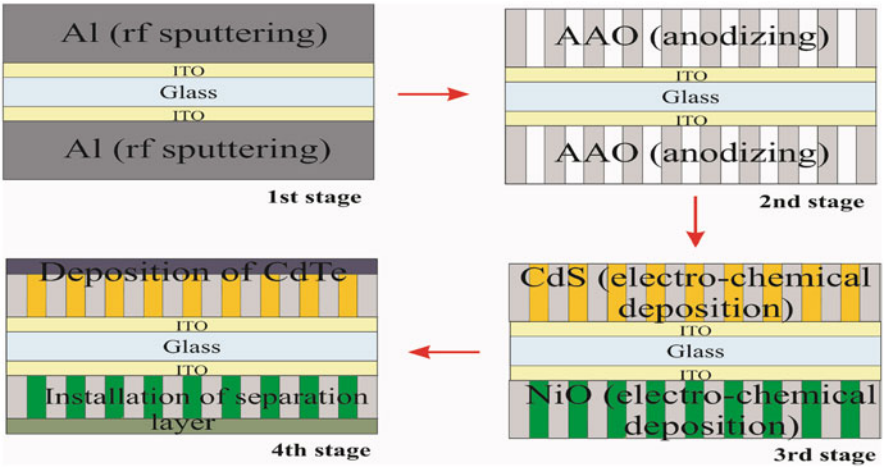


Fig. 2 Flowchart of one to four stages of the fabrication process

same production procedures will reduce the number of materials and energy needed and lower the cost of solar energy collecting. Additionally, putting the capacitors on the same substrate as the PV cell will make the system more compact.

To date, we have carried out experimental studies on the practical implementation of the photovoltaic part of the device [70]. At present, our efforts are directed toward the practical implementation of the capacitor part of the device.

2.2 Preparation of the Glass/ITO/AAO/CdS Structure

To implement the PVSC section of the subject device, as the first preparation stage, all 1.5 × 2 × 0.05 cm glass substrates were ultrasonically degreased in acetone and isopropyl alcohol, rinsed in deionized water, and subsequently then dried in poor nitrogen flow for 15 min before loading into the deposition chamber. Afterward, substrates were loaded into the vacuum deposition chamber of the Leybold Heraeus-Z550 RF magnetron sputtering system equipped with a turbomolecular vacuum pump system. As radio-frequency (RF) magnetron sputtering is a plasma- or ion-assisted deposition process, the slightest variation in deposition parameters may cause changes in the structure and bonding of the deposited material [27, 28]. Such changes may lead to both advantageous and detrimental effects for photovoltaic applications. For this reason, deposition parameters play a wide role in the preferential growth process in sputtering. Thus, optimization of growth parameters in RF magnetron sputtering is crucial. Initially, ITO films with different film thicknesses from 200 to 300 nm were prepared on an unheated glass substrate by radio-frequency (RF) magnetron sputtering using a 75 mm diameter ITO target

(90% In_2O_3 and 10% SnO_2). The target-to-substrate distance was fixed at 10 cm. The sputtering chamber was vacuumed to a base pressure of 5×10^{-3} Pa, and a pure argon gas flow of 5 sccm was introduced as a reactive sputtering gas through a mass flow controller. Before deposition, the target was RF pre-sputtered in argon plasma for 20 min at a power level of 50 watts to remove contaminants from the surface of the target. The ITO deposition process was conducted at a working pressure of 3.3 Pa and with the power level fixed at 200 W for different deposition times (20–40 min) depending on the thickness of the film. Thereafter, an Al film with a thickness in the range of 200–300 nm was deposited onto a glass/ITO substrate using a 75 mm diameter aluminum target (99.99% pure) under similar conditions. Following that, the electrochemical anodization of the Al film was performed in a two-electrode cell using 0.3 M oxalic acid solution at constant potentials from 10 to 40 V at a temperature of 3–5 °C for 10–20 min. The CdS nanowires were electrodeposited in AAO nanopores at 110 °C from the electrolyte solution consisting of 0.055 M $CdCl_2$ and 0.19 M elemental sulfur dissolved in ethylene glycol. In preliminary experiments to evaluate the efficiency of a solution of this composition before CdS deposition into aluminum oxide pores, a technique was developed for deposition of CdS thin film on ITO surface, and the characteristics of the resulting film were studied. The entire glass/ITO/CdS structure was sintered in the air at 400 °C. A method for depositing CdS thin films on ITO surfaces was devised, and the properties of the resulting films were examined, as part of early studies to assess the effectiveness of a solution of this composition prior to CdS deposition into aluminum oxide pores.

2.3 Characterization Techniques

Investigation of the surface morphology of the samples and determination of the elemental composition of CdS and ITO films were carried out by using Supra TM35vp scanning electron microscopy with the attached energy-dispersive X-ray (EDX) system. X-ray diffraction patterns were obtained using an X-Ray D2Phaser (Bruker) diffractometer (Cu-Kα ($\lambda = 1.5402$ Å)). The UV-Vis optical transmittance spectrum was recorded by using a Specord-210 spectrophotometer in the range of 300–1100 nm. A Nanofinder 30-NM01 Confocal Raman microscope with an excitation 633 nm laser was used to study the vibrational properties of the samples.

3 Results and Discussion

Figure 3a displays a cross-sectional SEM image of the broad view of a glass/ITO/CdS structure (x100K), whereas Fig. 3b shows its more detailed image (x200K), which indicates the CdS layer's thickness. Figure 3c depicts a visual representation of CdS (yellow-color) deposition in nanopores of AAO layers of the

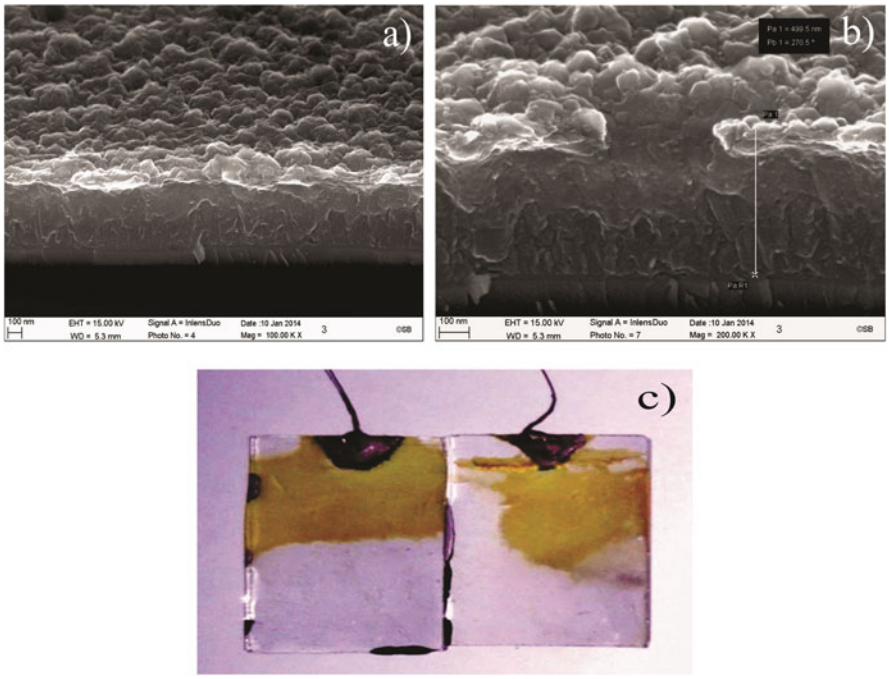


Fig. 3 SEM images of glass/ITO/CdS structure (**a**) and (**b**), the visual image of CdS (yellow-colored) deposited in AAO pores (**c**)

structures. In Fig. 3a, the ITO layer is shown as a gray band that lies between the lower (black-colored) glass substrate and the exterior, a relatively light CdS layer. Figure 3a shows that the CdS layer is approximately 500 nm thick and that the ITO layer beneath it is approximately 100 nm thick.

The XRD pattern of the annealed glass/ITO/CdS structure with indications of lattice spaces (d(Å)) is presented in Fig. 4. The pattern demonstrates the polycrystalline nature of the film, which has diffraction peaks at 25.03° (d(Å) = 3.5718 Å), 26.62°(3.3463 Å), and 28.36°(3.1550 Å), respectively, corresponding to the (100), (002), and (101) planes for the CdS phase with the hexagonal wurtzite crystal structure (PDF No. 41–1049). Other relatively weak peaks located at 44.05° and 52.33°are corresponding to the (220) and (311) planes, respectively, for the CdS phase with cubic structure according to the card number PDF10-0454 [49]. The structural properties of the grown films are consistent with previous research on the structural properties of CdS thin films prepared on conducting glass/ITO utilizing thermal deposition [50], chemical bath deposition [51, 52], electrodeposition [53–55], and RF magnetron sputtering methods [57, 58].

The average value of the crystallite size (D) can be defined by Scherer's equation [52, 54] for line broadening of the stronger diffraction peak: $D = 0.9\lambda/\beta \cos \theta$, where $\lambda = 1.5406$ Å is the X-ray wavelength of Cu-Kα radiation, β is the full width

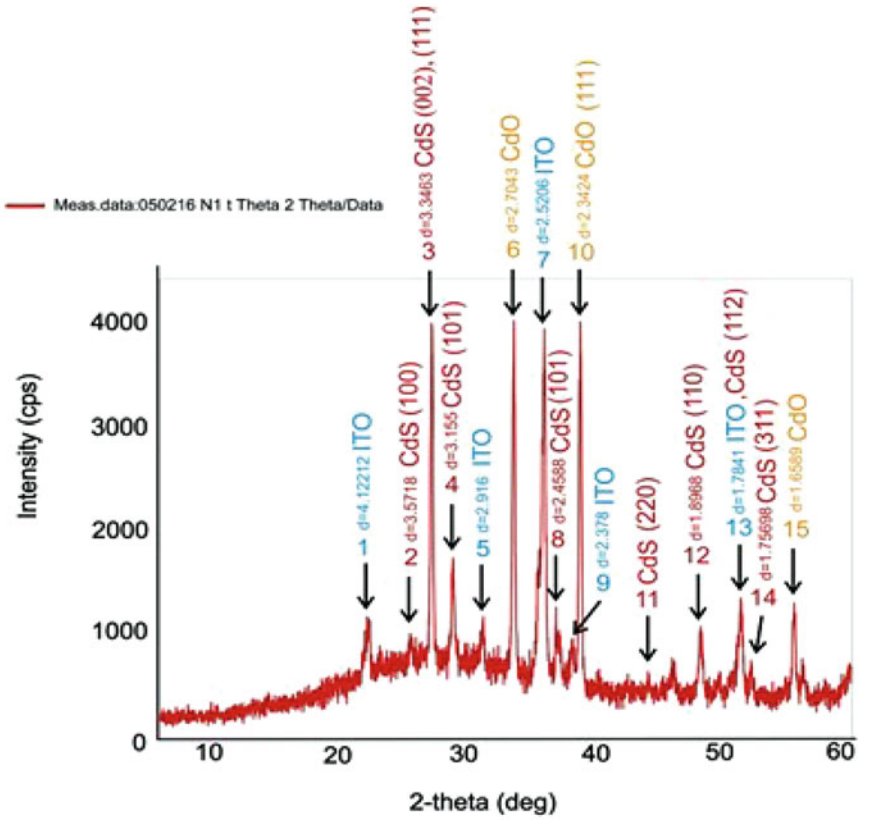


Fig. 4 XRD pattern of the glass/ITO/CdS structure (ICDD card no. PDF 10-0454)

at half-maximum intensity (FWHM), and θ is the diffraction angle. According to this equation and Fig. 4 (the stronger peak no. 3), the calculated value of the average CdS crystallite size, D, was determined to be 23 nm. The obtained results are well in agreement with earlier research on CdS thin-film chemical bath deposition [52] and electrodeposition [54, 55].

EDX measurements have been used to estimate the chemical composition of the glass/ITO/CdS thin-film structure. Figure 5 displays a typical EDX spectrum (with a 5% accuracy of the entire structure). The values of the measured atom composition of Cd, S, and certain impurities including Cl, O, Na, K, Si, and In are shown in the inset table in the figure.

As can be seen from both the EDX spectrum and the inset table, the atomic ratio of cadmium to sulfur in the film is typically 1:0.97 (Cd = 36.73%, S = 36.60 at %). The sulfur deficiency in the film indicates the presence of sulfur vacancies, which act as donors in CdS and determine its n-type electrical conductivity [48, 51]. Therefore, it can be assumed that film's composition is very close to the

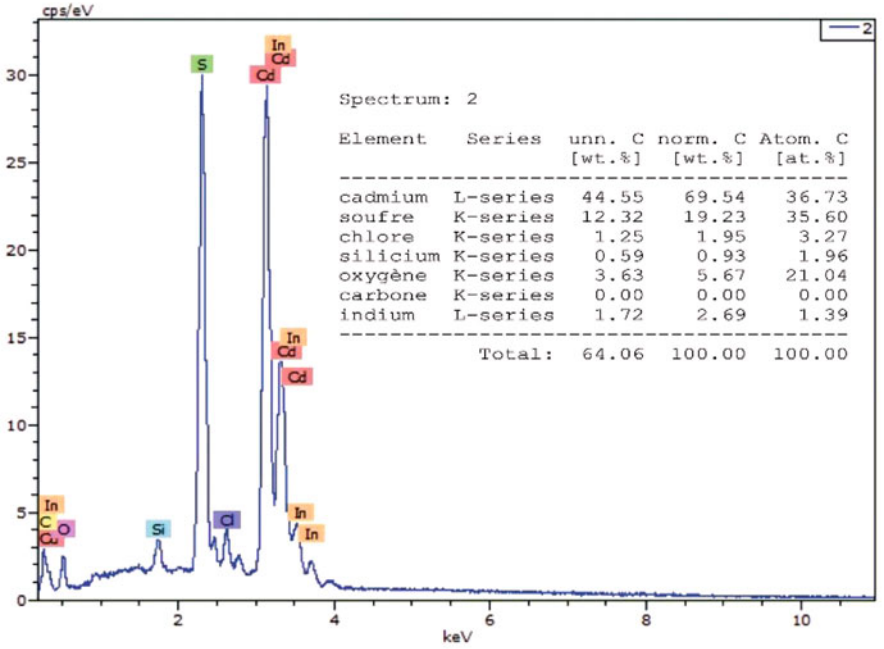


Fig. 5 EDX spectrum data of the glass/ITO/CdS structure

stoichiometric. Additionally, we assume that the conductive ITO layer and the glass substrate on top of which these CdS layers were grown are likely the sources of impurities like Si, Ca, Na, In, and O, whereas Cl originates from the $CdCl_2$ used in the electrolyte. The obtained results are in good agreement with the earlier reports on electrodeposited CdS thin films [53, 54].

The UV-visible transmittance spectrum of 500 nm-thick CdS thin film grown on a glass/ITO substrate is shown in Fig. 6. The films are transparent with an average transmittance of 40% over the wavelength range of 400 nm to 1000 nm. We used the Tauc relation [66] to get the optical bandgap energy (E_g) value of 2.25 eV for the film samples. This result is consistent with other studies describing the development of CdS thin films on conducting glass/ITO substrates employing CBD [51, 52], electrodeposition [53–55], and RF magnetron deposition [57, 58].

Raman spectroscopy offers a rapid and simple way to determine a material's various phases, degree of crystallinity, and whether it is amorphous, crystalline, or nanocrystalline, making it a particularly useful nondestructive tool for researching material structure. The comparison of Raman studies of CdS thin films carried out by various research groups has attracted significant attention in the literature [67–69]. The room-temperature Raman spectra of a CdS thin sheet are shown in Fig. 7.

The spectra show small modes in the 200–250 cm^{-1} range that can be correlated with modes that are typical for bulk CdS and which have been extensively discussed

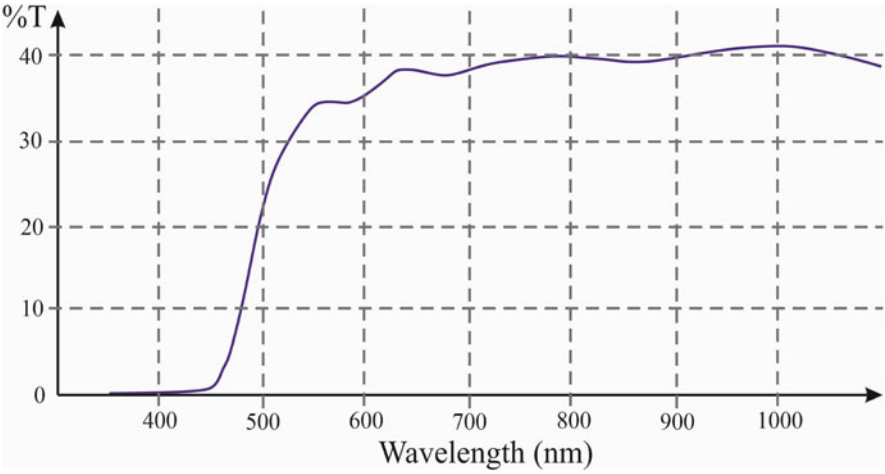


Fig. 6 Transmittance spectra of the CdS thin film

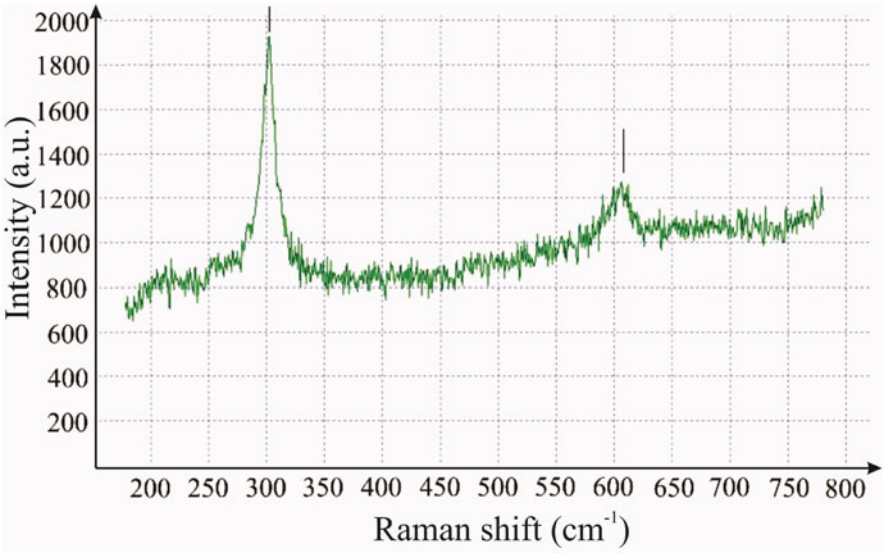


Fig. 7 Raman spectrum of CdS thin film

in numerous articles [67–69]. Along with them, the spectrum displays a relatively sharp, crystal-like first-order peak in the longitudinal mode (1LO) with an FWHM of 20 cm^{-1} at 305 cm^{-1} and its first overtone (2LO phonon mode) at 610 cm^{-1}. The modes we observe are typical of wurtzite-structured CdS. Only two of the characteristic longitudinal optical phonon peaks of CdS are evident here because an excitation laser at a wavelength of 633 nm (with energy less than the bandgap of CdS) was utilized. The surface optical phonon mode effect is responsible for the

CdS crystal's LO phonon shift. SOP modes are usually observed for particles whose diameters are less than the wavelength of the laser light that is stimulated inside the particles. These tiny particle modes are typically found in polar crystals [67, 69].

4 Conclusion

In conclusion, we have proposed the integration of energy conversion (PVSC based on an array of nanostructured CdS/CdTe heterojunctions) and storage (SC based on NiO nanotubes) into one system. The SC and PVSC were built in AAO nanoporous templates that were synthesized on mutually opposite sides of a common glass wafer that was covered with a conductive ITO layer and AAO template. It is a fully integrated device with a monolithic structure, where the solar cell and energy storage segments share a common substrate in the form of a transparent and conductive glass wafer and may be referred to as a photo-supercapacitor or solar capacitor. The suggested device may have better volumetric and gravimetric energy densities than a solar power system made up of discrete components due to its more compact structure, fewer wiring in the system, and sharing of substrate and electrodes. Further, in the fabrication of this device, multiple solar cells and SC fabrication technologies have been integrated. It was shown that the design features of the device allow combining and simultaneous execution of some similar fabrication operations, which would have to be carried out in the case of separate manufacture of the constituent elements of the device. This alignment of the same fabrication operations will reduce the number of them. Integration of solar cells and supercapacitors into a single hybrid device in which energy-harvesting and storing units are combined into one system will lead to rising demand for green energy, miniaturization, and mini-electronic wearable devices.

Experimental research on the practical implementation of the device's photovoltaic component has been done thus far. AAO nanostructures based on the glass-ITO-Al thin-film structure were created by using magnetron deposition of both ITO and Al thin films on the front and rear sides of the glass substrate, followed by the anodic oxidation of aluminum in oxalic acid, to implement the PV-cell part of the proposed device. Additionally, a technique has been created for the electrochemical deposition of thin CdS films in the AAO nanopores as well as on the ITO layer. SEM, X-ray diffraction, UV-visible spectroscopy, and Raman spectroscopy were used to characterize the morphological, structural, and optical characteristics of the produced structures. An analysis of the results of the study showed that the obtained materials are quite suitable as a starting material for the manufacture of solar cells. Our current efforts are concentrated on the actual implementation of the device's supercapacitor component.

References

1. Lee TD, Ebong AU. A review of thin-film solar cell technologies and challenges. *Renewable and Sustainable Energy Reviews*. 2017; 70:1286–1297. https://doi.org/10.1016/j.rser.2016.12.028
2. Nordin NA, Ansari M, Nomanbhay SM, et al. Integrating photovoltaic (PV) solar cells and supercapacitors for sustainable energy devices: A review. *Energies.* 2021;14:7211. https://doi.org/10.3390/en14217211
3. Vega-Garita V, Ramirez-Elizondo L, Narayan N, et al. Integrating a photovoltaic storage system in one device: A critical review. *Progress in Photovoltaics: Research and Applications*. 2018; https://doi.org/10.1002/pip.3093
4. Xu, J, Ku Z, Zhang Y, Chao D, et al. Integrated photo-supercapacitor based on PEDOT modified printable perovskite solar cell. *Advanced Materials Technologies*. 2016; 1(5): 1600074. https://doi.org/10.1002/admt.201600074
5. Dong P, Rodrigues MF, Zhang J, etal. Flexible solar cell/supercapacitor integrated energy device. *Nano Energy*. 2017;42:181–186. https://doi.org/10.1016/j.nanoen.2017.10.035
6. Liu R, Wang J, Sun Tet al. Silicon nanowire/polymer hybrid solar cell-supercapacitor: A self-charging power unit with a total efficiency of 10.5%. *Nano Letters*. 2017:17(7):4240–4247. https://doi.org/10.1021/acs.nanolett.7b01154
7. Gomaa MR, Mustafa RJ, Rezk H. An experimental implementation and testing of a concentrated hybrid photovoltaic/thermal system with monocrystalline solar cells using linear Fresnel reflected mirrors. *Int J Energy Res.* 2019; 1–14. https://doi.org/10.1002/er.4862
8. Yongtai He, Lixian Xiao, Lei Li. Research on the influence of PV cell to thermal characteristics of photovoltaic/thermal solar systems. *Int J Energy Res. 2017*; 41: 1287–1294. https://doi.org/10.1002/er.3711
9. Yuan Y, Lu Y, Jia BE, *et al.* Integrated system of solar cells with hierarchical $NiCo_2O_4$ battery-supercapacitor hybrid devices for self-driving light-emitting diodes. *Nano-Micro Lett.* 2019; 11: 42. https://doi.org/10.1007/s40820-019-0274-0
10. Salameh T, Abdelkareem MA, Olabi AG, et al. Integrated standalone hybrid solar PV, fuel cell and diesel generator power system for battery or supercapacitor storage systems in Khorfakkan, United Arab Emirates. *International Journal of Hydrogen Energy*. 2021;46:6014–6027. https://doi.org/10.1016/j.ijhydene.2020.08.153
11. Jayalakshmi NS, Gaonkar DN, Pramod BN. Power control of PV/fuel cell/supercapacitor hybrid system for stand-alone applications *Int. J. Renewable Energy Research*. 2016; 6:2. https://doi.org/10.20508/ijrer.v6i2.3489.g6833
12. Qu X, He Y, Qu M, et al. Identification of embedded nanotwins at c- Si/a-Si:H interface limiting the performance of high-efficiency silicon heterojunction solar cells. Nature Energy. 2021; 6(2), 194–202. https://doi.org/10.1038/s41560-020-00768-4
13. Papež, N, Dallaev R, Ţălu Ş, Kaštyl J. Overview of the Current State of Gallium Arsenide-Based Solar Cells. *Materials,* (2021 *14(11), 3075.*https://doi.org/10.3390/ma14113075
14. Barbato M, Artegiani E, Bertoncello M, et al. CdTe solar cells: technology, operation and reliability *J. Phys. D: Appl. Phys.* 2021;54: 333002 https://doi.org/10.1088/1361-6463/ac04e3
15. Sharma DK, Ilango MS, Ramasesha SK. Efficiency enhancement of the CdS/CdTe solar nanostructured cell using electron-reflecting layer. *IEEE Transactions on Electron Devices.* 2021;68:1129–1134.
16. Kapadia R, Fan Z, Javey A. Design constraints and guidelines for CdS/CdTe nanopillar-based photovoltaics. *Appl. Phys. Lett*. 2010; 96:103116. https://doi.org/10.1063/1.3340938
17. Wu X, Keane JC, Dhere RG et al., 16.5%-efficient CdS/CdTe polycrystalline thin-film solar cells," in *Proceedings of the 17th European Photovoltaic Solar Energy Conference and Exhibition (PVSEC '01)*, 2001; 995–1000.
18. Romeo A, Artegiani E. CdTe-based thin-film solar cells: Past, present and future. *Energies*, 2021; 14(6): 1684. https://doi.org/10.3390/en14061684

19. Wang J, Liu S, Mu Y, Liu L, et al. Embedded vertically aligned cadmium telluride nanorod arrays grown by one-step electrodeposition for enhanced energy conversion efficiency in three-dimensional nanostructured solar cells. *Colloid Interface Sci.* 2017; 505:1047–1054. https://doi.org/10.1016/j.jcis.2017.07.00
20. Jia Z, Qin S, Meng L. High-performance tandem organic solar cells via a strongly infrared-absorbing narrow bandgap acceptor. *Nat Commun*. 2021;12: 178. https://doi.org/10.1038/s41467-020-20431-6
21. Liu Y, Chen Y. Integrated perovskite/bulk-heterojunction organic solar cells. *Advanced Materials,* 2019; 32(3): 1805843. https://doi.org/10.1002/adma.201805843
22. Snaith HJ. Perovskites: The emergence of a new era for low-cost, high-efficiency solar cells. *J. Phys. Chem. Lett*. 2013, 4 (21), 3623–3630, https://doi.org/10.1021/jz4020162
23. Kamat PV. Quantum Dot Solar Cells. The next big thing in photovoltaics. *The Journal of Physical Chemistry Letters*. 2013; 4: 908–918. https://doi.org/10.1021/jz400052e
24. Yahya M, Bouziani A, Ocak C, et al. Organic/metal-organic photosensitizers for dye-sensitized solar cells (DSSC): Recent developments, new trends, and future perceptions. *Dyes and Pigments*. 2021; 2021192, 109227. https://doi.org/10.1016/j.dyepig.109227
25. Rahman NA, Hanifah SA, Mobarak NN, et al. Chitosan as a paradigm for biopolymer electrolytes in solid-state dye-sensitized solar cells. *Polymer*. 2021; 230:124092. https://doi.org/10.1016/j.polymer.2021.124092
26. Fagiolari L, Varaia E, Mariotti N, et al. Poly(3,4-ethylene dioxythiophene) in dye-sensitized solar cells: toward solid-state and platinum-free photovoltaics. *Advanced Sustainable Systems*, 2021;2100025. https://doi.org/10.1002/adsu.202100025
27. De Haro JC, Tatsi E, Fagiolari L, et al. Lignin-based polymer electrolyte membranes for sustainable aqueous dye-sensitized solar cells. ACS Sustainable Chemistry & Engineering, 2021; 9 (25): 8550–8560. https://doi.org/10.1002/aenm.202102913
28. Green MA, Hishikawa Y, Warta W, et al. Solar cell efficiency tables (version 50). Progress in Photovoltaics: Research and Applications. 2017; 25(7): 668–676. https://doi.org/10.1002/pip.2909
29. Riaz A, Sarker MR, Saad MHM, Mohamed R. Review on comparison of different energy storage technologies used in micro-energy harvesting, WSNs, low-cost microelectronic devices: challenges and recommendations. *Sensors.* 2021; 21: 5041. https://doi.org/10.3390/s21155041
30. Balasubramaniam S, Mohanty A, Kannan S, etal. Comprehensive insight into the mechanism, material selection, and performance evaluation of supercapatteries. *Nano-Micro Letters*. 2020;12:85. https://doi.org/10.1007/s40820-020-0413-7
31. Akin M, Zhou X. Recent advances in solid-state supercapacitors: From emerging materials to advanced applications. *Int J Energy Res*. 2022; 1–64. https://doi.org/10.1002/er.7918
32. Galek P, Mackowiak A, Bujewska P. Three-dimensional architectures in electrochemical capacitor applications- insights, opinions, and perspectives. *Front. Energy Res.* 2020;8:139. https://doi.org/10.3389/fenrg.2020.00139
33. Thirumurugan, A. et al. Nanostructured materials for supercapacitors. In: Thomas, S., Gueye, A.B., Gupta, R.K. (eds) Nanostructured Materials for Supercapacitors. *Advances in Material Research and Technology*. 2022. Springer, Cham. https://doi.org/10.1007/978-3-030-99302-3
34. Reina M, Scalia A, Auxilia G, Fontana M, et al. Boosting electric double layer capacitance in laser-induced graphene-based supercapacitors. *Adv. Sustainable Syst*. 2022; 6:2100228. https://doi.org/10.1002/adsu.202100228
35. Chen X, Paul R, Dai L. Carbon-based supercapacitors for efficient energy storage. *National Science Review*. 2017;4(3): 453–489. https://doi.org/10.1093/nsr/nwx009
36. Shrestha LK, Shrestha RG, Maji S, et al. High surface area nanoporous graphitic carbon materials derived from lapse seed with enhanced super capacitance. *Nanomaterials.* 2020; 10(4): 728. https://doi.org/10.3390/nano10040728
37. Sridhar D, Yu H, Meunier J-L et al. Carbon nano-fiber forest foundation for ruthenium oxide pseudo-electrochemical capacitors. *Materials Advances.* 2020; 1: 215–227. https://doi.org/10.1039/d0ma00023j

38. Bai X, Hu X, Zhou S et al. In situ polymerization and characterization of grafted poly (3,4-ethylenedioxythiophene)/multiwalled carbon nanotubes composite with high electrochemical performances. *Electrochim Acta.* 2013; 87: 394–400. https://doi.org/10.1016/j.electacta.2012.09.079
39. Yang Y, Zhu T, Shen L, et al. Recent progress in the all-solid-state flexible supercapacitors. *Smart Mat*. 2022; 1–35. https://doi.org/10.1002/smm2.1103YANGETAL.35
40. Chakrabarti BK, Gençten M, Bree G, et al. Modern practices in electrophoretic deposition to manufacture energy storage electrodes. *Int. J. Energy Res*. 2022;1–46 https://doi.org/10.1002/er.8103
41. Moossa B, James J, Ramazan A, et al. Utilization of symmetric electrode materials in energy storage application: A review. *Int. J. Energy Res*. 2022; 46: 8590–8624 https://doi.org/10.1002/er.7771
42. Kumar A, Rathore HK, Sarkar D, et al. Nanoarchitectured transition metal oxides and their composites for supercapacitors. *Electrochem Sci Adv*. 2021; e2100187. https://doi.org/10.1002/elsa.202100187
43. Dar FI, Moonoosawmy KR, Es-Souni M. Morphology and property control of NiO nanostructures for supercapacitor applications. *Nanoscale Res Lett.* 2013; 8:363. https://doi.org/10.1186/1556-276X-8-363
44. Yang Y, Li S, Liu F, Wen J, et al. Enhanced performance of multi-dimensional CoS nanoflake/NiO nanosheet architecture with synergetic effect for asymmetric supercapacitor. *Nanotechnology.* 2018; 29(45):455401. https://doi.org/10.1088/1361-6528/aadd63
45. Rajagopal S, Pulapparambil VR, Mohamed Ibrahim M, Velev DG. Electrode materials for supercapacitors in hybrid electric vehicles: challenges and current progress. *Condens. Matter*, 2022; 7: 6. https://doi.org/10.3390/condmat7010006
46. Wu C, Wang K, Batmunkh M et al. Multifunctional nanostructured materials for next-generation photovoltaics. *Nano Ener*gy, 2020; 70:104480. https://doi.org/10.1016/j.nanoen.2020.104480
47. Dang H, Singh VP, Guduru S *et al.* Nanotube photovoltaic configuration for enhancement of carrier generation and collection. *Nano Res.* 2015;8: 3186–3196 https://doi.org/10.1007/s12274-015-0818-7
48. Liu P, Singh VP, Jarro CA, Rajaputra S. Cadmium sulfide nanowires for the window semiconductor layer in thin-film CdS–CdTe solar cells. *Nanotechnology.* 2011; 22: 145304. https://doi.org/10.1088/0957-4484/22/14/145304
49. Fan ZY, Ruebusch DJ, Rathore AA, Javey A. Challenges and prospects of nanopillar-based solar cells. *Nano Res.* 2009; 2: 829–843. https://doi.org/10.1007/s12274-009-9091-y
50. Bakr NA, Mustafa FI, Mohammed RJ. Structural, optical and electrical properties of thermally deposited CdS thin films. *Journal of Chemical, Biological and Physical Sciences*. 2017;7(4) 881–889. https://doi.org/10.24214/jcbps.C.7.488189
51. Demir R, Gode F. Structural, optical and electrical properties of nanocrystalline CdS thin films grown by chemical bath deposition. *Chalcogenide Letters*. 2015;12:43–50.
52. Ouachtari F, Rmili A, Elidrissi B, et al. Influence of bath temperature, deposition time and [S]/[Cd] ratio on the structure, surface morphology, chemical composition and optical properties of CdS thin films elaborated by chemical bath deposition. *Journal of Modern Physics,* 2011; 02(09): 1073–1082. https://doi.org/10.4236/jmp.2011.29131
53. Kadirgan F, Mao D, Song W, et al. Properties of electrodeposited cadmium sulfide films for photovoltaic devices with comparison to CdS films prepared by other methods. *Turk J. Chem*., Tubitak. 2000; 24:21–23. https://doi.org/10.3906/che-3-98073
54. Alam AE, Cranton WE, Dharmadasa IM. Electrodeposition of CdS thin-films from cadmium acetate and ammonium thiosulphate precursors. *J Mater Sci: Mater Electron.* 2019;30:4580–4589. https://doi.org/10.1007/s10854-019-00750-1
55. Abdul-Manaf NA, Weerasinghe AR, Echendu OK, et al. Electro-plating and characterization of cadmium sulfide thin films using ammonium thiosulfate as the sulfur source. *J Mater Sci: Mater Electron.* 2015;26:2418–2429. https://doi.org/10.1007/s10854-015-2700-5

56. Dang, H, Singh VP. Nanowire CdS-CdTe solar cells with Molybdenum Oxide as a contact. *Scientific Reports,* 2015; *5:*1–7.https://doi.org/10.1038/srep14859
57. Doroody C, Rahman KS, Rosly HN et al. A comparative study of CdS thin films grown on ultra-thin glass substrates by RF magnetron sputtering and chemical bath deposition. *Materials Science in Semiconductor Processing. 2021; 133: 105935.*https://doi.org/10.1016/j.mssp.2021.105935
58. Kulkarni R, Pawbake A, Waykar R. Single crystal, high bandgap CdS thin films grown by RF magnetron sputtering in Argon atmosphere for solar cell applications. *Journal of Nano- and Electronic Physics*. 2018;10:0305–18. https://doi.org/10.21272/jnep.10(3).03005
59. Rahman S, Al Ahmed S. Photovoltaic performance enhancement in CdTe thin-film heterojunction solar cell with Sb_2S_3 as the hole transport layer, *Solar Energy*, 2021;230:605–617. https://doi.org/10.1016/j.solener.2021.10.036
60. Santos JS, Araújo PS, Pissolitto YB, et al. The use of anodic oxides in practical and sustainable devices for energy conversion and storage. *Materials*. 2021; 14; 383. https://doi.org/10.3390/ma14020383
61. Zhang H, Zhou M, Zhao H, Lei Y. Ordered nanostructures arrays fabricated by anodic aluminum oxide (AAO) template-directed methods for energy conversion. *Nanotechnology.* 2021;32:50. https://doi.org/10.1088/1361-6528/ac268b
62. Lee W. Structural engineering of porous anodic aluminum oxide (AAO) and applications. In: Losic, D., Santos, A. (eds) Nanoporous alumina. *Springer Series in Materials Science*. 2015: 219: Springer, Cham. https://doi.org/10.1007/978-3-319-20334-8_4
63. Xifre-Perez E., Marsal LF, Recent advances in nanoporous anodic alumina: principles, engineering, and applications. *Nanomaterials*. 2021; 11:430. https://doi.org/10.3390/nano1102430
64. Ruiz-Clavijo A, Caballero-Calero O, Martín-González M. Revisiting anodic alumina templates: from fabrication to applications. *Nanoscal*e. 2021;13(4): 2227–2265. https://doi.org/10.1039/d0nr07582e
65. Choudhari KS, Choi CH, Chidangil S, et al. Recent progress in the fabrication and optical properties of nanoporous anodic alumina. *Nanomaterials*. 2022;12(3): 444 https://doi.org/10.3390/nano12030444
66. Tauc J. Amorphous and liquid semiconductor. New York, NY: Plenum Press; 1974.
67. Trajić J, Gilić M, Romčević N. Raman spectroscopy of optical properties in CdS thin films. *Science of Sintering*. 2015; 47:145–152. https://doi.org/10.2298/SOS1502145T
68. Keshav R, Rao A, Mahesha MG. Raman spectroscopy and low temperature electrical conductivity study of thermally evaporated CdS thin films. *Optical and Quantum Electronics.* 2018; 50(4*)*.https://doi.org/10.1007/s11082-018-1451
69. Saleem MF, Zhang H, Deng Y, Wang D. Resonant Raman scattering in nanocrystalline thin CdS film. *Journal of Raman Spectroscopy.* 2016; *48(2), 224–229.*https://doi.org/10.1002/jrs.5002
70. Eminov SO, Tagiyev DB, Aliyev AS, Guliyev JA, et al. Photo and electrical peculiarities of the nanostructured glass/ITO/AAO and glass/ITO/CdS systems. *Journal of Materials Science: Materials in Electronics*. 2016; 27:9853–9860. https://doi.org/10.1007/s10854-016-5053-9
71. Bhujel R, Rai S, Deka U et al. Bandgap engineering of PEDOT:PSS/rGO a hole transport layer for SiNWs hybrid solar cells. *Bull Mater Sci*. 2021;44: 72 https://doi.org/10.1007/s12034-021-02376-8
72. Patil S et al. Hybrid solid state supercapacitors (HSSC's) for high energy & power density: an overview. *Engineered Science,* 2020, 12, 38–51. https://doi.org/10.30919/es8d1140
73. Supercapacitors as next generation energy storage devices: Properties and applications Energy, 2022*,* 248(12):123617
74. Sayed ET, Olabi AG, Alami AH et al. Renewable Energy and Energy Storage Systems. *Energies,* 2023, 16: 1415. https://doi.org/10.3390/en16031415
75. Stevic Z, Radovanovic I. Supercapacitors: The Innovation of Energy Storage, 2023 https://doi.org/10.5772/intechopen.106705
76. Subasinghage K, Gunawardane K, Padmawansa N, et al. Modern supercapacitors technologies and their applicability in mature electrical engineering applications. *Energies,* 2022, 15: 7752. https://doi.org/10.3390/en15207752

77. Naskar A, Ghosh A, Roy A, et al. Polymer-Ceramic Composite Electrolyte for Li-Ion Batteries, Editor(s): M.S.J. Hashmi, Encyclopedia of Materials: Plastics and Polymers, Elsevier, 2022, 1031–1039, ISBN 9780128232910. https://doi.org/10.1016/B978-0-12-820352-1.00123-1.
78. Kushwaha 1 Lt. Col Pankaj, Dr. Asha Gaikwad2Review: Li-ion Batteries: Basics, Advancement, Challenges & Applications in Military. *IJRASET*, 2021: 9 (VIII): 3009–3020. https://doi.org/10.22214/ijraset.2021.37905
79. Aval LF, Ghoranneviss M, Pour GB. High-performance supercapacitors based on the carbon nanotubes, graphene and graphite nanoparticles electrodes. Heliyon, 2018, 4(11): e00862. https://doi.org/10.1016/j.heliyon.2018.e0086
80. Ruiz-Clavijo A., Caballero-Calero O., Martín-González M. Revisiting anodic alumina templates: from fabrication to applications. *Nanoscale*, 2021: 13, 2227–2265

Design and Optimization of CdTe QDs Luminescent Solar Concentrators Based on Analytic and Simulation Models



Alvaro Flores-Pacheco, Rosendo López-Delgado, Arturo A. Ayón, and Mario Enrique Álvarez-Ramos

1 Introduction

The development of highly luminescent nanomaterials such as quantum dots (QDs) has reignited the research of luminescent solar concentrators (LSCs) [1]. LSCs are photonic devices fabricated with a semitransparent material that hosts highly efficient luminophores; these devices have an exposed large-area surface that absorbs the incident solar light, which act as the excitation source for the luminophores; the resulting emission is waveguided by total internal reflection to the concentration walls (with smaller areas) where solar cells are optically coupled.

The relationship between the area of the LSC exposed to the solar radiation and the area of its edges is called geometric gain factor and, if properly designed, could increase the flux density incident on the solar cell. In practice, the effective change in flux will depend on the geometric gain factor and the optical loss mechanisms of the device, characterized by the concentration factor *C*, which describes the enlargement (or contraction) of the photon flux density incident to the photovoltaic (PV) device when it is coupled to an LSC (LSC-PV system).

A. Flores-Pacheco (✉) · M. E. Álvarez-Ramos
Departamento de Física, Posgrado en Nanotecnología, Universidad de Sonora, Hermosillo, Sonora, Mexico
e-mail: a215290120@correoa.uson.mx

R. López-Delgado
Departamento de Física, Cátedras CONACYT, Universidad de Sonora, Hermosillo, Sonora, Mexico

A. A. Ayón
Department of Physics and Astronomy, MEMS Research Lab, University of Texas at San Antonio, San Antonio, TX, USA

© The Author(s), under exclusive license to Springer Nature Switzerland AG 2024

S. Krishnamoorthy, K. (Kris) Iniewski (eds.), *Advances in Fabrication and Investigation of Nanomaterials for Industrial Applications*,
https://doi.org/10.1007/978-3-031-42700-8_19

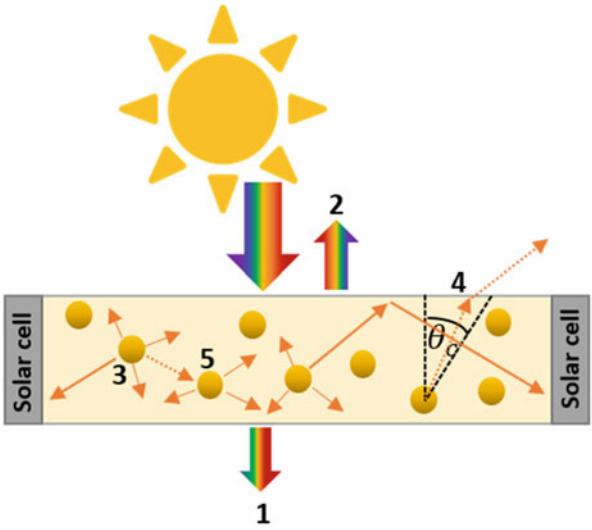


Fig. 1 Schematic description of the LSC operation and optical loss mechanisms

The operation of a LSC (Fig. 1) is prone to multiple optical loss mechanisms, including (1) the transparency to a portion of the solar spectrum, (2) reflectance of the concentrator material, (3) quantum yield of the LSC luminophore, (4) light leakage by the escape cone, and (5) reabsorptions. Even with these practical drawbacks, LSCs can enable novel energy conversion devices like photovoltaic windows with certain shading or coloring for architectonical applications and are still under active investigation [2–4].

Even though the methodology for calculation of the overall performance of a LSC is not standardized yet [5–9], in this chapter, the approach by Bomm et al. [10] for the power conversion efficiency (PCE) calculation is used, since it gives a more absolute description of the LSC efficiency. In Bomm's work, the efficiency is given by the absolute ratio between the maximum power generated by the solar cells ($P_{out} = I_{sc}V_{oc}FF$) and the total incident power reaching the LSC ($P_{in} = P_S A_{LSC}$) using the expression $PCE = I_{sc}V_{oc}FF/P_S A_{LSC}$, where I_{sc} is the short-circuit current, V_{oc} is the open-circuit voltage, FF is the fill factor, $P_S = 100$ mW/cm^2 is the AM 1.5G spectrum power density (illumination source), and A_{LSC} is the exposed area of the LSC.

Cadmium telluride quantum dots (CdTe QDs) exhibit attractive optical features as LSC's luminophores, since they absorb electromagnetic radiation in the UV-visible range and have intense emission peaks that are size-dependent [11]. Thin films based on CdTe QDs, applied on the surface of silicon solar cells, have proven to be efficient spectral converters, to enhance the performance of photovoltaic systems [12, 13]. The down-shifting properties (Stokes shift) of the CdTe QDs are attractive for applications in LSC-PV systems, given the better spectral match of the QDs photoluminescent emission with the spectral response of Si solar cells.

This chapter details a concentration factor optimization methodology, previously reported by our workgroup [14], for LSCs based on green-, yellow-, and red-emitting CdTe QDs. This was achieved using an analytical model [15] and the optical features (absorption and emission spectra) of each luminophore. To predict the power conversion efficiency (*PCE*) of each prospective luminescent solar concentrator, the product of the concentration factor and the photoluminescence spectrum of each LSC act as illumination source for a COMSOL silicon solar cell simulation model.

The prediction of the power generation and power conversion efficiency as a function of the luminophore concentration and LSC dimensions, described in the following pages, provides a design tool to accomplish the transparency and size requirements of the desired application.

2 Analytical Model for Optical Efficiency and Concentration Factor Determination

A LSC absorbs a portion of an incident photon flux Φ_1 (usually the solar spectrum) from an exposed large area A_1, and the subsequent emission is waveguided to the smaller-area edges A_2 (photon flux Φ_2) where photovoltaic devices are optically coupled to generate solar energy (Fig. 2). A key parameter in the performance of a LSC is the optical efficiency η_{opt}, which is defined as the ratio of photons Φ_2 that effectively reach the coupled solar cell to the total incident photon flux Φ_1 ($\eta_{opt} = \Phi_2/\Phi_1$). Taking into account the photon flux density ϕ_2 ($\phi_2 = \Phi_2/A_2$) reaching the solar cell and the solar flux density incident on the concentrator's surface ϕ_1 ($\phi_1 = \Phi_1/A_1$), the concentration factor $C = \phi_2/\phi_1$ is defined. Since the geometric gain factor G is defined as the ratio between the collection and emission areas ($G = A_1/A_2$), the concentration factor can be expressed as $C = \phi_2/\phi_1 = G\eta_{opt}$, which represents a more descriptive expression and will be employed in the present exercise.

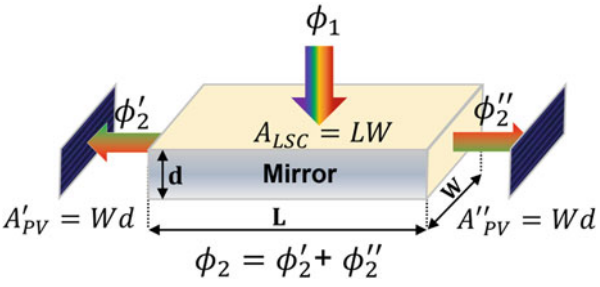


Fig. 2 Proposed LSC geometry

Klimov et al. [15] proposed analytical expressions, with comparable results to the computationally expensive Monte Carlo ray-tracing simulations, for the optical efficiency and concentration factor of planar luminescent solar concentrators.

In their study, the optical efficiency η_{opt} was expressed in terms of the device's optical characteristics, namely, absorptance η_{abs}, photoluminescence quantum yield of the luminophore η_{PL}, light-trapping efficiency η_{trap}, and the waveguide efficiency of the LSC η_{wg}:

$$\eta_{opt} = \frac{\Phi_2}{\Phi_1} = \eta_{abs}\eta_{trap}\eta_{PL}\eta_{wg}. \tag{1}$$

The LSC's absorptance η_{abs} is defined as the fraction of photons absorbed by the luminophore and is expressed as the number of photons that are not reflected $(1 - R)$ nor transmitted $\left(1 - e^{-\alpha_1 d}\right)$ through an absorbing slab of thickness d and absorption coefficient α_1 at the incident wavelength:

$$\eta_{abs} = \left(1 - R\right)\left(1 - e^{-\alpha_1 d}\right). \tag{2}$$

For normal incident light and with the imaginary part of the refractive index $k \ll 1$, the Fresnel reflection coefficient R [16] is defined as $R = \frac{(n-1)^2}{(n+1)^2}$. The most popular candidates as transparent matrix for luminophores in LSCs are PMMA and window glass; hence, a semitransparent slab with refractive index value $n = 1.5$ [17] was considered, which gives a reflection coefficient $R = 0.04$.

For isotropic emitters such as quantum dots, the light-trapping efficiency is defined as $\eta_{trap} = \cos\theta_r$, where $\theta_r = \arcsin(1/n)$ is the critical angle for total internal reflection. A refractive index $n = 1.5$ produces a light-trapping efficiency $\eta_{trap} = 0.75$.

A photoluminescence quantum yield value of 80% ($\eta_{PL} = 0.8$) was proposed, since it fits within the average reported values of CdTe QDs [18–20], which will be used as the LSC's luminophores in this exercise.

Based on the LSC waveguiding analysis of Weber and Lambe [21], Klimov et al. [15] developed an analytical expression to calculate η_{wg}. Considering the repeating reabsorption-reemission events of the luminescent nanoparticles inside the LSC, the waveguide efficiency could be expressed as $\eta_{wg} = [1 + \beta\alpha_2 L(1 - \eta_{PL}\eta_{trap})]^{-1}$, where the factor β accounts for the scattering losses of the waveguide and α_2 is the absorption coefficient of the luminophore at the maximum emission wavelength. After thorough comparisons against Monte Carlo ray-tracing simulations, Klimov et al. proposed the expression $\beta = 1.4 + 0.5(L/150)^{1/2}$ applicable for LSC with lengths up to 2000 cm. Additionally, the partial light recovery in the waveguide due to isotropic emission after reabsorption within the escape cone can be included introducing a constant factor of ~1.05 in the overall optical efficiency. Employing all these considerations, the optical efficiency could be modeled as:

$$\eta_{opt} = \frac{\Phi_2}{\Phi_1} = \frac{(1-R)\left(1-e^{-\alpha_1 d}\right)\eta_{PL}\eta_{trap}}{1+\beta\alpha_2 L\left(1-\eta_{PL}\eta_{trap}\right)}. \tag{3}$$

As shown in Fig. 2, the planar LSC geometry will be described by the dimensions L (length), W (width), and d (height); the LSC slab will have two perfectly reflective mirrors on the sidewalls. The output flux density will be divided between the left and right sides ($\phi_2 = \phi_2' + \phi_2''$) in this configuration. The geometric gain factor G of the device will be given by the relation between the concentrator surface ($A_1 = LW$) and the area of the solar cells ($A_2 = 2Wd$) with the expression $= \frac{L}{2d}$.

Considering the optical efficiency and the proposed geometry, the concentration factor of the LSC can be determined as:

$$C = \frac{\phi_2}{\phi_1} = \frac{(1-R)\left(1-e^{-\alpha_1 d}\right)\eta_{PL}\eta_{trap}}{1+\beta\alpha_2 L\left(1-\eta_{PL}\eta_{trap}\right)}\left(\frac{L}{2d}\right). \tag{4}$$

Also, as may be noticed, the developed expressions for optical efficiency and concentration factor only take into account a monochromatic light source. However, under normal operation, a LSC would be illuminated with a non-monochromatic illumination source characterized by a spectral profile $S_{in}(\lambda)$ (AM 1.5G solar spectrum). Therefore, to consider this incident spectrum, a spectrally corrected absorption coefficient $\langle\alpha_1\rangle$ is required for the LSC efficiency calculations:

$$\langle\alpha_1\rangle = -\frac{1}{d}\ln\left(\frac{\int_0^{\lambda_g} S_{in}(\lambda)\, e^{-\alpha(\lambda)d}\, d\lambda}{\int_0^{\lambda_g} S_{in}(\lambda)\, d\lambda}\right) \tag{5}$$

where λ_g is the bandgap wavelength of the luminophore and $\alpha(\lambda)$ its absorption spectrum. Since the most attractive luminophores used in LSCs, such as semiconductor quantum dots, have relatively wide luminescent emissions characterized by $S_{QD}(\lambda)$, it is necessary to determine the corrected value $\langle\alpha_2\rangle$ for the emission range:

$$\langle\alpha_2\rangle = \frac{\int S_{QD}(\lambda)\,\alpha(\lambda)\, d\lambda}{\int S_{QD}(\lambda)\, d\lambda}. \tag{6}$$

Replacing the single-wavelength values of α_1 and α_2 in Eqs. (3) and (4) with the averaged $\langle\alpha_1\rangle$ and $\langle\alpha_2\rangle$ values obtained from Eqs. (5) and (6), the final expressions for optical efficiency and concentration factor can be obtained:

$$\eta_{opt} = \frac{(1-R)\left(1-e^{-\langle\alpha_1\rangle d}\right)\eta_{PL}\eta_{trap}}{1+\beta\,\langle\alpha_2\rangle\, L\left(1-\eta_{PL}\eta_{trap}\right)} \tag{7}$$

$$C = \frac{(1-R)\left(1-e^{-\langle\alpha_1\rangle d}\right)\eta_{PL}\eta_{trap}}{1+\beta\,\langle\alpha_2\rangle\, L\left(1-\eta_{PL}\eta_{trap}\right)}\left(\frac{L}{2d}\right). \tag{8}$$

A good LSC luminophore should have a high absorption coefficient at the incident wavelength region $\langle \alpha_1 \rangle$ and the smallest possible absorption coefficient in the emission wavelength region $\langle \alpha_2 \rangle$ to minimize the reabsorption losses. The parameters $\langle \alpha_1 \rangle$ and $\langle \alpha_2 \rangle$ and consequently η_{opt} and C play a fundamental role in the performance of the LSC-PV systems.

3 Synthesis of the LSC Luminophores (CdTe QDs)

Quantum dot synthesis has evolved from the high-temperature growth of semiconductor nanocrystals inside host glasses [22–24], high-temperature aerosol reactions [25–27], and RF sputtering [28, 29] to the now widely adopted techniques based on the controlled growth of colloidal quantum dots passivated with organic surfactants at lower temperatures [30–33].

Due to the high reactivity of the precursors with oxygen, most colloidal CdTe QDs synthesis methods require inert atmosphere conditions [34–36], which increases complexity and costs. In this exercise, the Wu et al. [18] methodology is used to obtain water-soluble CdTe quantum dots under standard laboratory conditions and without the generation of highly dangerous middle products such as H_2Te [37].

The synthesis process is started with 0.2 mmol (53 mg) of cadmium acetate dihydrate ($Cd(CH_3COO)_2{\cdot}2H_2O$) dissolved in 50 mL of deionized (DI) water, then 0.2 mmol (14 μl) of thioglycolic acid (TGA) was added, and the pH was adjusted to 10.5 with a 1 M NaOH solution. After stirring for 5 min, a 50 ml solution containing 0.04 mmol (10 mg) of potassium tellurite (K_2TeO_3) was added to the Cd-TGA mixture and stirred for 5 min. Once the solutions were fully incorporated, 80 mg of sodium borohydride was added to the final precursor solution as reducing agent (to obtain a 10:1 molar of $NaBH_4$:Cd^{2+}) and was allowed to react for 5 minutes. Afterward, the solution was transferred to a single-neck, round-bottom flask attached to a condenser and refluxed at 100 °C in a PolyScience circulating bath. CdTe QDs with different sizes could be obtained by the variation of the final reaction time. Here, QDs with three different sizes were produced in 0.5, 2, and 12 h of reaction (further referred to as green, yellow, and red CdTe, respectively).

The proposed chemical reaction route begins with the dissociation of cadmium acetate in water:

$$Cd(CH_3COO)_2 \rightarrow Cd^{2+} + 2CH_3COO^{-}. \tag{9}$$

After the thioglycolic acid (TGA) is added to the cadmium acetate solution, the measured pH value was around 6; this is above the first acid dissociation constant of TGA ($pKa_{COOH} = 3.67$) [38] and promotes the following reaction:

$$HSCH_2CO_2H \rightleftarrows HSCH_2CO_2^{-} + H^{+}. \tag{10}$$

After raising the pH value to 10.5 with NaOH, the second dissociation constant of TGA is exceeded ($pKa_{SH} = 10.31$) [38], which gives a doubly deprotonated thioglycolic acid molecule:

$$HSCH_2CO_2^- \rightleftarrows {}^-SCH_2CO_2^- + H^+. \tag{11}$$

In the second solution, potassium tellurite dissociates in water:

$$K_2TeO_3 \rightarrow 2K^+ + TeO_3^{2-} \tag{12}$$

$$TeO_3{}^{2-} \rightarrow Te^{4+} + 3O^{2-}. \tag{13}$$

After mixing the first and second solutions, which contain the Cd^{2+} and Te^{4+} ions, respectively, there won't be CdTe formation. The CdTe nucleation process will start after the addition of the $NaBH_4$ reducing agent, which, after dissociation, reduces Te^{4+} to Te^{2-}.

When the final solution is transferred to the recirculating bath at 100 °C, the CdTe cluster growth rate increases due to the additional energy given by the temperature rise. It is important to consider the molar ratio of the precursors, in this case 1:1:0.2 for Cd^{2+}:TGA:$TeO_3{}^{2-}$; thus the CdTe reaction quickly stops, given the fact that the telluride ion is the limiting reagent. Under the high-temperature condition, TGA continues decomposing and releases S^{2-} ions, which are available to react with the excess Cd^{2+} ions and create a CdS shell around the CdTe core. Finally the remaining TGA molecules will form CdS-TGA complexes in the CdS surface due the strong binding of the cadmium atoms in the CdS lattice with the thiol component of TGA [39], creating a TGA-functionalized core-shell structure shown in Fig. 3.

4 Optical Features of the CdTe QDs

The optimization methodology will be based on the experimental optical features of the proposed luminophores, namely, photoluminescence and absorption spectra. Figure 4a shows the absorption coefficient and the photoluminescent spectra of the green-, yellow-, and red-emitting CdTe QDs. Figure 4a also includes the AM 1.5G spectral profile, given the fact that the solar radiation will be the real-world illumination source for the QD-based LSCs.

As shown in Eq. (5), the determination of $\langle \alpha_1 \rangle$ must be performed in shorter wavelengths than the luminophore's bandgap wavelength λ_g; this is required to only take into account photons with enough energy to promote optical transitions in the luminophore. The bandgap of the CdTe QDs was obtained from the absorption coefficient of each color (Fig. 4a) using the graphical method proposed by Tauc et al. [40]:

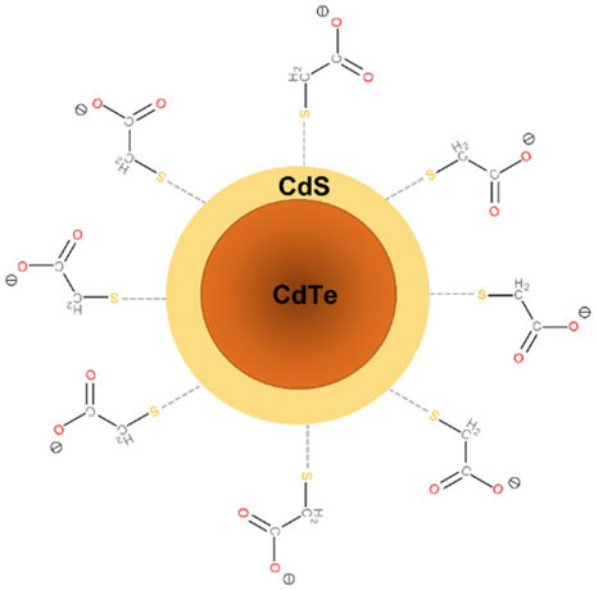


Fig. 3 Proposed CdTe QDs core-shell structure

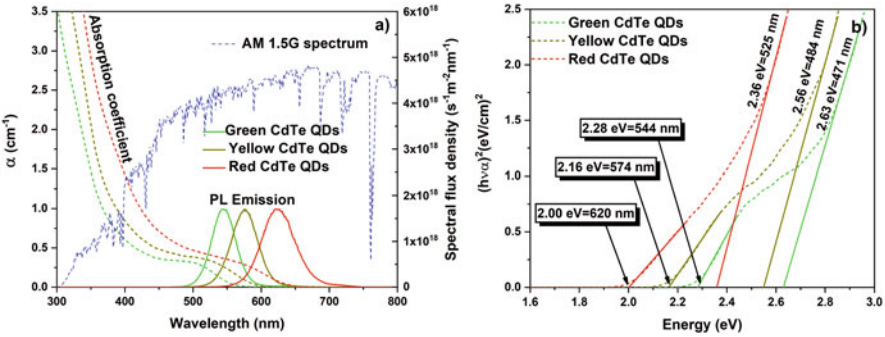


Fig. 4 (**a**) Absorption coefficient (dashed lines) and PL emission (solid lines) spectra of the different CdTe QDs (the AM 1.5G spectral profile is shown as reference). (**b**) Bandgap calculation of green, yellow, and red CdTe QDs using Tauc's graphical method

$$(\alpha h\upsilon)^{1/t} = B\left(h\upsilon - E_g\right) \tag{14}$$

where h is Planck's constant, υ is the photon's frequency, α is the absorption coefficient, B is a proportionality constant, and t denotes the nature of the electronic transition, whether allowed or forbidden and direct or indirect. For semiconductors with direct allowed transitions, such as CdTe, t= 1/2.

The plots of Eq. (14) for the green, yellow, and red CdTe QDs are shown in Fig. 4b. Near the bandgap value, the absorption quickly increases, exhibiting a

region of linearity in $(\alpha hv)^2$, and the data is then extrapolated to the energy axis ($(\alpha hv)^2 = 0$) to obtain the bandgap value. For the CdTe QDs, there are two main regions where this criterion is fulfilled. The lower energy region (2.28, 2.16, and 2.00 eV for the green, yellow, and red CdTe QDs, respectively) can be associated with the excitonic absorption [41], while the higher energy region (2.63, 2.56, and 2.36 eV for the green, yellow, and red CdTe QDs, respectively) can be associated with the semiconductor bandgap. Given the fact that the light absorption starts at the excitonic regime, the $\langle\alpha_1\rangle$ values were calculated employing the wavelengths of the excitonic absorptions (λ_g= 544, 574, and 620 nm for green, yellow, and red CdTe QDs, respectively) as the integral limit in Eq. (5).

Figure 4a also shows the expected progressive red shift in the absorption spectra from the green- to the red-emitting CdTe QDs provided by the increment of the QDs size due to the reaction time. The higher product of the absorption coefficient and the incident photon flux (AM 1.5G) was achieved for the red CdTe QDs, allowing the absorption of a higher photon count, leading to incremental $\langle\alpha_1\rangle$ values from 0.44 and 0.46 to 0.52 cm^{-1} for the green, yellow, and red CdTe QDs, respectively. Also, considering the product between the absorption coefficient and the luminescent spectrum, Eq. (6) renders $\langle\alpha_2\rangle$ values of 0.12, 0.11, and 0.09 cm^{-1} for the green, yellow, and red CdTe QDs, respectively. As found in the calculated values, the red-emitting CdTe QDs provide the lowest $\langle\alpha_2\rangle$ value, which reduces reabsorption losses. Both the $\langle\alpha_1\rangle$ and $\langle\alpha_2\rangle$ parameters of the red CdTe QDs are expected to be beneficial for the concentration factor of the LSC.

The influence of the LSC's dimensions in the optical efficiency and concentration factor was analyzed for different LSC lengths, considering a fixed height of d= 0.3 cm. This height was chosen since it is the standard building window thickness and could be used in potential architectonical applications [42]. Fig. 5 shows the optical efficiency and concentration factor C of prospective LSCs using the parameters $\eta_{PL} = 0.8$ and $\eta_{trap} = 0.75$. As the L value increases, there is a higher probability of reabsorption, causing optical efficiency losses with length. However, in terms of concentration factor, this behavior is compensated by the geometric gain factor (also L dependent), achieving the maximum values of 1.31, 1.44, and 1.88 for the green, yellow, and red CdTe QDs LSCs. The concentration factor maximum values were found in devices with lengths within 100–120 cm. It is worth to mention that all the CdTe QD-based LSCs achieved C values above 1, meaning that the proposed devices can effectively operate as concentrators by increasing the photon flux density at the output edges.

5 Optimization of the Concentration Factor of CdTe QDs LSCs

The optical efficiencies and concentration factors shown on Fig. 5 were calculated using the corrected absorption coefficients $\langle\alpha_1\rangle$ and $\langle\alpha_2\rangle$ obtained from the absorp-

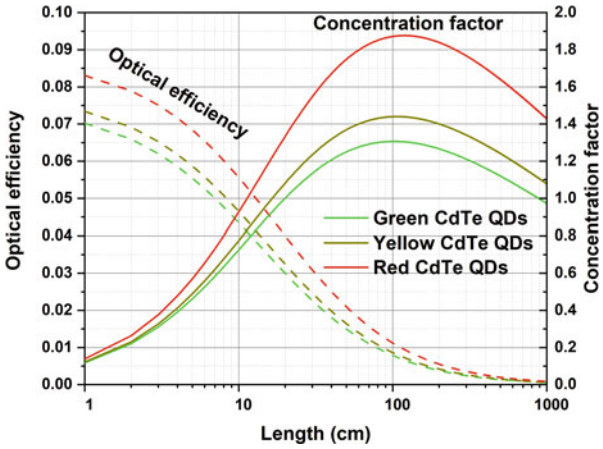


Fig. 5 Optical efficiency (dashed lines) and concentration factor (solid lines) of LSCs with green, yellow, and red CdTe QD as a function of L. The LSCs have $\eta_{PL} = 0.8$, $\eta_{trap} = 0.75$, and $d = 0.3\ cm$

tion spectrum of each as-synthesized CdTe QDs luminophore. Eqs. (5) and (6) show that the $\langle\alpha_1\rangle$ and $\langle\alpha_2\rangle$ values depend on $\alpha(\lambda)$ and are correlated, under this principle, the absorption coefficient $\alpha(\lambda)$ of the devices, and thus, the $\langle\alpha_1\rangle$ and $\langle\alpha_2\rangle$ values can be modified adjusting the concentration of the CdTe nanoparticles embedded in the semitransparent material.

Figure 6 shows the concentration factor of green, yellow, and red CdTe QDs LSCs as a function of $\langle\alpha_1\rangle$ and $\langle\alpha_2\rangle$, for different lengths.

Figure 6 shows that the concentration factor can be maximized for each length with the modification of the QDs concentration (described by $\langle\alpha_1\rangle$ and $\langle\alpha_2\rangle$). Analyzing Fig. 6c it seems that a concentration factor above 2.1 can be achieved using red CdTe QDs with $\langle\alpha_1\rangle < 0.1\ \text{cm}^{-1}$ in the LSC with L = 120 cm. However, to fulfill this requirement, the QDs concentration and therefore the absorption coefficient must be drastically reduced as shown in Fig. 6d. Even the fact that this concentration factor could double the photon flux density reaching the coupled solar cell, the drastic decrease on the absorption of photons within the range of 400–500 nm will produce a very low luminescent flux density reaching the solar cell, making this limit practically unfeasible.

Figure 5 shows that smaller devices lead to higher optical efficiencies but lower concentration factors and the opposite for longer devices. Under this consideration, there is a length range where both parameters are attractive (5–80 cm). Table 1 shows the optimized $\langle\alpha_1\rangle$ and $\langle\alpha_2\rangle$ values (named $\langle\alpha_{1opt}\rangle$ and $\langle\alpha_{2opt}\rangle$) and the maximum concentration factor C_{opt} achieved in a sweep of lengths from 5 to 80 cm, for the green, yellow, and red CdTe QD-based LSC.

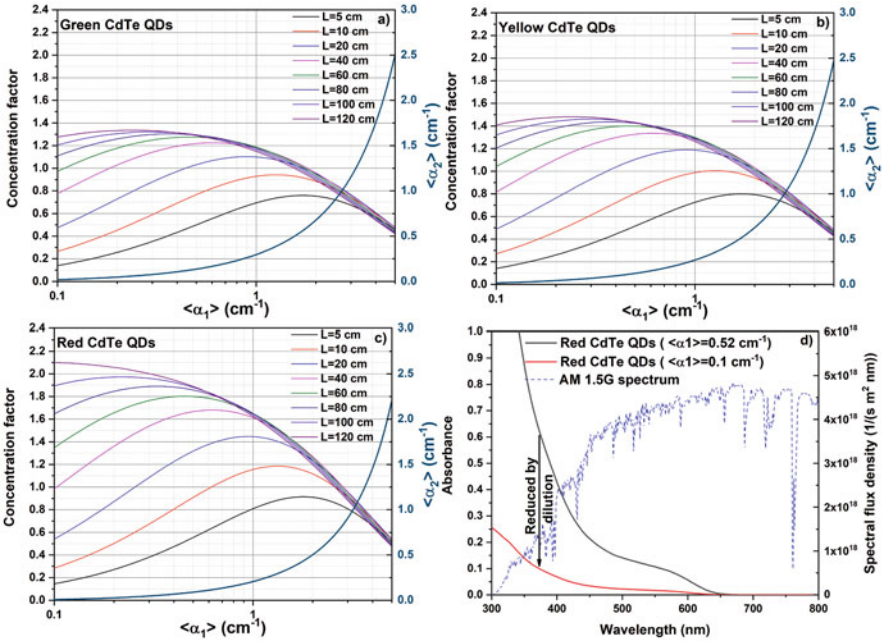


Fig. 6 Concentration factor of LSCs of different lengths with (**a**) green, (**b**) yellow, and (**c**) red CdTe QD as a function of $\langle\alpha_1\rangle$ and $\langle\alpha_2\rangle$. (**d**) Modification of the absorbance and $\langle\alpha_1\rangle$ value by dilution of the red CdTe QDs

Table 1 Optimized concentration factor (C_{opt}) for different length values of green, yellow, and red CdTe QDs LSCs

	Green CdTe QDs		Yellow CdTe QDs		Red CdTe QDs	
Length (cm)	$\langle\alpha_{1opt}\rangle$, $\langle\alpha_{2opt}\rangle$ (cm^{-1})	C_{opt}	$\langle\alpha_{opt}\rangle$, $\langle\alpha_{2opt}\rangle$ (cm^{-1})	C_{opt}	$\langle\alpha_{opt}\rangle$, $\langle\alpha_{2opt}\rangle$ (cm^{-1})	C_{opt}
5	1.72, 0.56	0.76	1.72, 0.52	0.80	1.80, 0.44	0.91
10	1.26, 0.39	0.94	1.27, 0.36	1.00	1.33, 0.26	1.18
20	0.90, 0.26	1.10	0.91, 0.24	1.19	0.95, 0.19	1.45
40	0.61, 0.17	1.22	0.62, 0.16	1.34	0.62, 0.12	1.68
60	0.46, 0.12	1.28	0.47, 0.11	1.40	0.45, 0.08	1.80
80	0.37, 0.10	1.30	0.38, 0.09	1.44	0.33, 0.05	1.89

6 Photovoltaic Simulation for the Optimized QDs LSCs

The ultimate goal of the optimization methodology requires a way to predict the expected photovoltaic performance of LSCs coupled to solar cells. For this purpose, a modified version of the 1D silicon solar cell model from the COMSOL semiconductor module was implemented. This module solves Poisson's equation,

using the continuity and drift-diffusion equations considering the finite element method.

Poisson's equation, derived from Gauss's law, reads as $\nabla \bullet \mathrm{E} = \frac{\rho}{\varepsilon}$, where E is the electric field, ρ is the charge density, and ε is the permittivity, which describes the polarizability of the material. Under an electrostatic potential ψ, the electric field will be $\mathrm{E} = -\nabla \psi$, leading to the expression:

$$\nabla \bullet (\varepsilon \nabla \psi) = -\rho. \tag{15}$$

The semiconductor charge density can be written as $\rho = q\Big(p - n + N_D^+ - N_A^-\Big)$, as is composed of ionized donors N_D^- and acceptors N_A^+, free holes p, and electrons n; q is the elementary charge. Poisson's equation can be written as:

$$\nabla^2 \psi = \frac{q}{\varepsilon}\left(n - p + N_{\mathrm{A}}^- - N_D^+\right). \tag{16}$$

The continuity equation (derived from Gauss's and Ampere's laws) reads:

$$\nabla \bullet \mathrm{J} + \frac{\partial \rho}{\partial t} = 0. \tag{17}$$

The current density J is split into $\mathrm{J_n}$ and $\mathrm{J_p}$ for the contribution of electrons and holes, respectively. Taking into account the electron and hole recombination (R_n, R_p) and generation (G_n, G_p) rates of the charge carriers in the semiconductor, continuity equations for electrons and holes can be written as:

$$\nabla \bullet \mathrm{J_n} - q\frac{\partial n}{\partial t} = +q\,(R_n - G_n) \tag{18}$$

$$\nabla \bullet \mathrm{J_p} + q\frac{\partial p}{\partial t} = -q\left(R_p - G_p\right). \tag{19}$$

The generation and recombination rates of electrons and holes are expressed using physically or empirically based models. In most circumstances the generation and recombination rates for electrons and holes are equal. For this work, the electron and hole generation rates ($G_n = G_p$) will be given by the solar cell's photogeneration model, and the loss mechanisms (including the recombination rate) will be modeled using the solar cell's external quantum efficiency (EQE) which will be detailed in the simulation section of this chapter.

The drift-diffusion model, derived under thermal equilibrium [43], describes the electron and hole current relations containing the carrier drift and diffusion:

$$\mathrm{J_n} = qn\mu_n \mathrm{E} + q\,D_n \nabla n \tag{20}$$

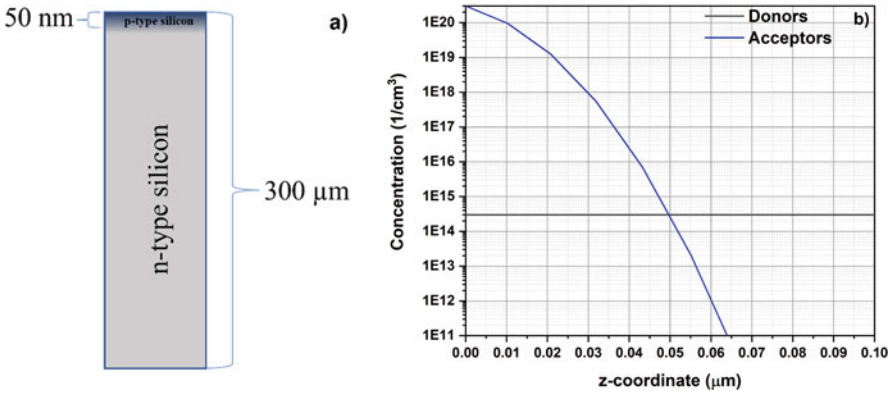


Fig. 7 (**a**) 1D doping model of the simulated solar cell (not in scale). (**b**) Donor and acceptor concentration distribution as a function of the device thickness

$$\mathrm{J_p} = qn\mu_p \mathrm{E} - qD_p \nabla p \tag{21}$$

where μ_n and μ_p are the electron and hole carrier mobilities and D_n and D_p the electron and hole diffusion coefficients that are described by Einstein's relation:

$$D_n = \mu_n \frac{k_B T_L}{q},\ D_p = \mu_p \frac{k_B T_L}{q} \tag{22}$$

where k_B is Boltzmann's constant and T_L the lattice temperature. The implementation of these equations in the software uses extended versions of the continuity and drift-diffusion equations that include non-isothermal modeling and degenerate materials with nonuniform band structures [44, 45].

The simulation setup uses the COMSOL built-in silicon material database. The solar cell architecture consists of an n-type silicon substrate with thickness of 300 μm and donor concentration of $N_D = 3 \times 10^{14}$ cm^{-3}; then, an acceptor concentration of $N_A = 3 \times 10^{20}$ cm^{-3} was introduced on the front surface using an error-function decay as the p-type doping profile. This p-n junction is formed 50 nm below the surface (Fig. 7a). When a solar cell is under normal operation, the photogenerated carriers are swept to each side of the depletion region of the p-n junction; a forward-biased voltage is applied to simulate a load and extract the electrical power; therefore the simulation will run with a voltage sweep from 0 to 0.65 V. The proposed semiconductor parameters are experimentally achievable [46] and will be used to approximate the performance of commercial-grade solar cells previously reported [47] to get a realistic photogeneration prediction of the LSC-PV devices.

The photogeneration rate for electrons and holes across the device $G(z) = G_n = G_p$ was modeled as a function of the solar cell depth z using an integral expression [48], which is calculated in terms of the incident solar photon flux density $S_{in}(\lambda)$

and the silicon absorption coefficient $\alpha_{Si}(\lambda)$:

$$G(z) = \int_0^{\infty} \alpha_{Si}\,(\lambda)\, S_{in}\,(\lambda)\, e^{-\alpha_{Si}(\lambda)z} d\lambda. \tag{23}$$

The overall losses of the simulated devices can be modeled using the external quantum efficiency (*EQE*), defined as the ratio of the photogenerated carriers to the number of photons of given energy reaching the solar cell surface:

$$EQE\,(\lambda) = \frac{I_{pc}\,(\lambda)}{q\phi_{ph}\,(\lambda)} \tag{24}$$

where I_{pc} represent the number of photogenerated carriers, ϕ_{ph} is the incident photon flux, and q is the electron charge. Instead of using modeled loss mechanisms like recombination (R_n, R_p), all the performance detrimental factors were incorporated to the photogeneration rate expression by the inclusion of the EQE spectrum in the photogeneration expression:

$$G(z) = \int_0^{\infty} EQE\,(\lambda)\,\alpha_{Si}\,(\lambda)\, S_{in}\,(\lambda)\, e^{-\alpha_{Si}(\lambda)z} d\lambda. \tag{25}$$

The carrier generation rate under AM 1.5G illumination, given by Eq. (25), will provide the electron and hole generation rates required for solving the continuity and drift-diffusion equations for each step in the z-coordinate (inset of Fig. 8b). The voltage swept within 0–0.65 V is done in a stationary study using the solution from a semiconductor equilibrium step as the initial condition to obtain the solar cell current-voltage characteristics.

Figure 8b shows the simulated I-V characteristics and power generation curves for a 3 cm^2 reference silicon solar cell (d=0.3 cm, W= 10 cm), illuminated with

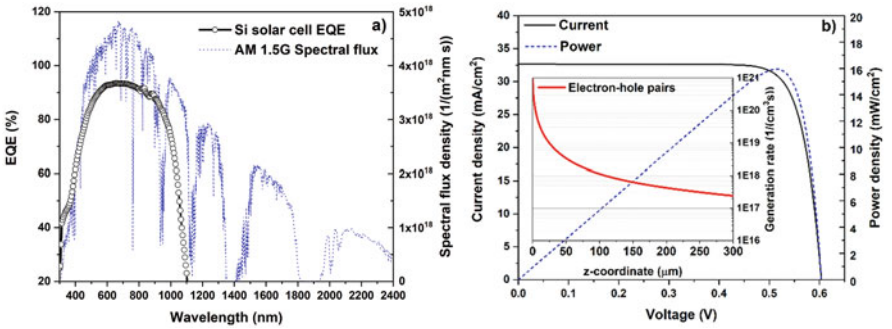


Fig. 8 (**a**) Spectral response (EQE) and illumination source for the reference Si solar cell simulation. (**b**) Current-voltage (I-V) characteristic of a simulated silicon solar cell (3 cm^2 reference); the inset shows the photogeneration rate $G(z)$ of the solar cell model

the AM 1.5G solar spectrum (100 mW/cm^2). The simulated reference presented the following performance parameters: short-circuit current density J_{sc}= 32.66 mA/cm^2, open-circuit voltage V_{oc}= 0.60 V, and fill factor FF= 81.01%, generating a power output of 47.83 mW and a power conversion efficiency (*PCE*) of 15.94%.

When the complete LSC-PV device is simulated, the solar cells coupled to the edges of the proposed LSCs are illuminated by the emission spectrum of each luminophore under the influence of all the loss mechanisms and the geometric gain factor (considered in the concentration factor). For the LSC-PV systems, the AM1.5G incident spectral flux density $S_{in}(\lambda)$ in Eq. (25) is replaced by the photon flux density given by the concentration factor and the experimental emission spectra of the green, yellow, and red CdTe QDs ($C \bullet S_{QD}(\lambda)$). Also, considering the LSC geometry (Fig. 2), the photon flux has two possible escape routes, so the flux density reaching each edge is ($C \bullet S_{QD}(\lambda)/2$). After these considerations, the photogeneration rate for a solar cell attached to one side the luminescent solar concentrator ($G_{LSC}(z)$) is expressed as:

$$G_{LSC}(z) = \frac{C}{2}\int_0^{\infty} EQE\,(\lambda)\,\alpha_{Si}\,(\lambda)\,S_{QD}\,(\lambda)\,e^{-\alpha_{Si}(\lambda)z}d\lambda \tag{26}$$

which now accounts the overall photovoltaic losses by the *EQE* and the concentrated photon flux density given by the quantum dots experimental emission spectra ($C \bullet S_{QD}(\lambda)/2$) reaching the simulated photovoltaic device.

The power conversion efficiency of the LSC-PV system (*PCE*), composed by the simulated solar cell coupled to one edge of the CdTe-based LSC is calculated as follows:

$$PCE = \frac{P_{out}}{P_{in}} = \frac{I_{sc}V_{oc}FF}{P_S A_{LSC}} \tag{27}$$

where P_{out} is the total power extracted from the device and the total incident power P_{in} is given by the AM 1.5G spectrum power density P_S (100 mW/cm^2) multiplied by the LSC surface area A_{LSC}.

The optimized concentration factors C_{opt} from the proposed LSCs from Table 1 and the experimental emission spectrum of each CdTe QDs luminophore (green, yellow, and red) were employed as the illumination source to analyze the photovoltaic response of the COMSOL-simulated solar cells. The *PCE* values of the solar cells connected to one edge of the LSCs were calculated from the obtained I-V characteristics of each configuration employing Eq. (27). The photovoltaic performance of each of the CdTe QDs LSC-PV systems was simulated considering LSCs with lengths in the previously mentioned interest range (5, 10, 40, 60, and 80 cm).

Since the photovoltaic simulation model takes into account the performance of only one solar cell attached to one edge of the LSC, the total power output of the LSC-PV system (P_{tot}) can be obtained by "connecting" two solar cells in series. This means doubling the voltage and consequently the power output and *PCE*:

Table 2 Total power conversion efficiency (PCE_{tot}) using the optimized concentration factor (C_{opt}) for different length values of green, yellow, and red CdTe QDs LSCs

	Green CdTe QDs		Yellow CdTe QDs		Red CdTe QDs	
Length (cm)	P_{tot} (mW)	PCE_{tot} (%)	P_{tot} (mW)	PCE_{tot} (%)	P_{tot} (mW)	PCE_{tot} (%)
5	67.74	1.35	72.94	1.46	84.51	1.69
10	84.53	0.85	92.02	0.92	110.75	1.11
20	99.57	0.50	110.25	0.55	137.18	0.69
40	110.85	0.28	124.73	0.31	159.81	0.40
60	116.53	0.19	130.53	0.22	171.65	0.29
80	118.42	0.15	134.40	0.17	180.53	0.23

$$PCE_{tot} = 2PCE. \tag{28}$$

The total power conversion efficiency (PCE_{tot}), given by Eq. (28) for green, yellow, and red QDs LSC-PV systems, obtained by using the optimized concentration factor (C_{opt}) value of each length is summarized in Table 2.

Table 2 shows that the maximum PCE_{tot} values of the LSCs are 1.35, 1.46, and 1.69% for green, yellow, and red CdTe QDs LSCs, respectively, which are comparable with previously reported QD-based LSCs coupled to silicon solar cells [6]. Despite that the PCE_{tot} decreases as the length of the LSC increases, the amount of solar power generated by the LSC keeps increasing. As may be seen in Table 2, starting from 20 cm LSCs (for green and yellow CdTe QDs) and 10 cm LSCs for red, it is possible to deliver higher power output than the 95.66 mW generated by two stand-alone reference solar cells (47.83 mW each) directly illuminated by the AM 1.5G spectrum.

In all cases, the use of red CdTe QDs as LSC luminophore gives the highest PCE performance due to the combined effect of the $\langle\alpha_1\rangle$ and $\langle\alpha_2\rangle$ values and the better match of the solar cell spectral response and the red CdTe QDs photoluminescent emission.

7 Conclusions

The design and optimization process of luminescent solar concentrators (LSCs) involves multiple parameters: the analysis of the optical properties of the proposed luminophores, geometry optimization of the optical device embedded with luminescent nanoparticles (LSC), and the evaluation of the photovoltaic response of the solar cells attached to the LSC.

This chapter presents a design and optimization methodology that includes the analysis of the optical features of the proposed luminophores (CdTe QDs) given by the parameters $\langle\alpha_1\rangle$, $\langle\alpha_2\rangle$, η_{opt}, and C, in addition with a realistic COMSOL model to describe the photovoltaic performance of silicon solar cells, which was employed to evaluate the total power generated by the proposed LSC-PV systems.

It was found that smaller luminescent solar concentrators based on green, yellow, and red CdTe QDs were able to generate 67.74, 72.94, and 84.51 mW, respectively, which represent PCE_{tot} values of 1.35, 1.46, and 1.69%, considering devices of A_{LSC}= 5 × 10 cm^2 attached to 0.3 × 10 cm^2 silicon solar cells. Bigger LSC devices (A_{LSC}= 80 × 10 cm^2) were able to generate 118.42, 134.40, and 180.53 mW, equivalent to PCE_{tot} of 0.15, 0.17, and 0.23% with the same luminophores. As expected, larger LSCs presented lower PCE_{tot}; however, they were able to generate more power employing the same solar cell active area. These results provide a tool that could help to choose the LSCs size and concentration parameters according to the design needs (window size or shading). In this sense, the LSC large and clear or small but darker photovoltaic windows could be proposed to fit each potential application. It is important to mention that this design and optimization methodology could be applied to any system based on a transparent matrix and luminophores with isotropic emission embedded whose experimental emission and absorption characteristics are known.

References

1. R. Mazzaro and A. Vomiero, "The Renaissance of Luminescent Solar Concentrators: The Role of Inorganic Nanomaterials," *Adv. Energy Mater.*, vol. 8, no. 33, pp. 1–19, 2018, https://doi.org/10.1002/aenm.201801903.
2. P. Moraitis, G. van Leeuwen, and W. van Sark, "Visual appearance of nanocrystal-based luminescent solar concentrators," *Materials (Basel).*, vol. 16, no. 6, 2019, https://doi.org/10.3390/ma12060885.
3. A. R. Abou Elhamd, K. A. Al-Sallal, and A. Hassan, "Review of core/shell quantum dots technology integrated into building's glazing," *Energies*, vol. 12, no. 6, 2019, https://doi.org/10.3390/en12061058.
4. G. Liu *et al.*, "Role of refractive index in highly efficient laminated luminescent solar concentrators," *Nano Energy*, vol. 70, no. 308, p. 104470, Apr. 2020, https://doi.org/10.1016/j.nanoen.2020.104470.
5. P. Moraitis, R. E. I. Schropp, and W. G. J. H. M. van Sark, "Nanoparticles for Luminescent Solar Concentrators - A review," *Opt. Mater. (Amst).*, vol. 84, no. July, pp. 636–645, 2018, https://doi.org/10.1016/j.optmat.2018.07.034.
6. M. Rafiee, S. Chandra, H. Ahmed, and S. J. McCormack, "An overview of various configurations of Luminescent Solar Concentrators for photovoltaic applications," *Opt. Mater. (Amst).*, vol. 91, no. January, pp. 212–227, 2019, https://doi.org/10.1016/j.optmat.2019.01.007.
7. C. Li *et al.*, "Large Stokes Shift and High Efficiency Luminescent Solar Concentrator Incorporated with CuInS 2/ZnS Quantum Dots," *Sci. Rep.*, vol. 5, no. August, pp. 1–9, 2015, https://doi.org/10.1038/srep17777.
8. S. J. Ha, J. H. Kang, D. H. Choi, S. K. Nam, E. Reichmanis, and J. H. Moon, "Upconversion-Assisted Dual-Band Luminescent Solar Concentrator Coupled for High Power Conversion Efficiency Photovoltaic Systems," *ACS Photonics*, vol. 5, no. 9, pp. 3621–3627, 2018, https://doi.org/10.1021/acsphotonics.8b00498.
9. A. R. Frias *et al.*, "Sustainable luminescent solar concentrators based on organic-inorganic hybrids modified with chlorophyll," *J. Mater. Chem. A*, vol. 6, no. 18, pp. 8712–8723, 2018, https://doi.org/10.1039/c8ta01712c.
10. J. Bomm *et al.*, "Fabrication and full characterization of state-of-the-art quantum dot luminescent solar concentrators," *Sol. Energy Mater. Sol. Cells*, vol. 95, no. 8, pp. 2087–2094, 2011, https://doi.org/10.1016/j.solmat.2011.02.027.

11. J. Wang, Y. Long, Y. Zhang, X. Zhong, and L. Zhu, "Preparation of highly luminescent CdTe/CdS core/shell quantum dots," *ChemPhysChem*, vol. 10, no. 4, pp. 680–685, 2009, https://doi.org/10.1002/cphc.200800672.
12. U. Tronco-Jurado, E. Saucedo-Flores, R. Ruelas, R. López, M. E. Alvarez-Ramos, and A. A. Ayón, "Synergistic effects of nanotexturization and down shifting CdTe quantum dots in solar cell performance," *Microsyst. Technol.*, vol. 23, no. 9, pp. 1–9, 2015, https://doi.org/10.1007/s00542-015-2748-4.
13. A. Flores-Pacheco, M. E. Álvarez-Ramos, and A. Ayón, "Down-shifting by quantum dots for silicon solar cell applications," in *Solar Cells and Light Management*, Elsevier, 2020, pp. 443–477.
14. A. Flores-Pacheco, R. López-Delgado, and M. E. Álvarez-Ramos, "Determination of power conversion efficiency of CdTe QDs luminescent solar concentrators by analytic model and COMSOL photogeneration model," *Optik (Stuttg).*, vol. 248, no. June, p. 168024, 2021, https://doi.org/10.1016/j.ijleo.2021.168024.
15. V. I. Klimov, T. A. Baker, J. Lim, K. A. Velizhanin, and H. McDaniel, "Quality Factor of Luminescent Solar Concentrators and Practical Concentration Limits Attainable with Semiconductor Quantum Dots," *ACS Photonics*, vol. 3, no. 6, pp. 1138–1148, 2016, https://doi.org/10.1021/acsphotonics.6b00307.
16. S. Perkowitz, *Optical Characterization of Semiconductors*. Academic Press, 1993.
17. M. N. Polyanskiy, "Refractive index database." https://refractiveindex.info
18. S. Wu, J. Dou, J. Zhang, and S. Zhang, "A simple and economical one-pot method to synthesize high-quality water soluble CdTe QDs," *J. Mater. Chem.*, vol. 22, no. 29, p. 14573, 2012, https://doi.org/10.1039/c2jm31409f.
19. Z. Li, Q. Sun, Y. Zhu, B. Tan, Z. P. Xu, and S. X. Dou, "Ultra-small fluorescent inorganic nanoparticles for bioimaging," *J. Mater. Chem. B*, vol. 2, no. 19, pp. 2793–2818, 2014, https://doi.org/10.1039/C3TB21760D.
20. H. Bao, Y. Gong, Z. Li, and M. Gao, "Enhancement effect of illumination on the photoluminescence of water-soluble CdTe nanocrystals: Toward highly fluorescent CdTe/CdS core-shell structure," *Chem. Mater.*, vol. 16, no. 20, pp. 3853–3859, 2004, https://doi.org/10.1021/cm049172b.
21. W. H. Weber and J. Lambe, "Luminescent greenhouse collector for solar radiation," *Appl. Opt.*, vol. 15, no. 10, p. 2299, Oct. 1976, https://doi.org/10.1364/ao.15.002299.
22. A. I. Ekimov, A. L. Efros, and A. A. Onushchenko, "Quantum size effect in semiconductor microcrystals," *Solid State Commun.*, vol. 56, no. 11, pp. 921–924, 1985, https://doi.org/10.1016/S0038-1098(85)80025-9.
23. A. Tanaka, S. Onari, and T. Arai, "Raman scattering from CdSe microcrystals embedded in a germanate glass matrix," *Phys. Rev. B*, vol. 45, no. 12, pp. 6587–6592, 1992, https://doi.org/10.1103/PhysRevB.45.6587.
24. N. Peyghambarian *et al.*, "Femtosecond optical nonlinearities of CdSe quantum dots," *IEEE J. Quantum Electron.*, vol. 25, no. 12, pp. 2516–2522, 1989, https://doi.org/10.1109/3.40636.
25. K. A. Littau, P. J. Szajowski, A. J. Muller, A. R. Kortan, and L. E. Brus, "A luminescent silicon nanocrystal colloid via a high-temperature aerosol reaction," *J. Phys. Chem.*, vol. 97, no. 6, pp. 1224–1230, Feb. 1993, https://doi.org/10.1021/j100108a019.
26. A. Gurav, T. Kodas, T. Pluym, and Y. Xiong, "Aerosol Processing of Materials," *Aerosol Sci. Technol.*, vol. 19, no. 4, pp. 411–452, Jan. 1993, https://doi.org/10.1080/02786829308959650.
27. I. Maximov, A. Gustafsson, H.-C. Hansson, L. Samuelson, W. Seifert, and A. Wiedensohler, "Fabrication of quantum dot structures using aerosol deposition and plasma etching techniques," *J. Vac. Sci. Technol. A Vacuum, Surfaces, Film.*, vol. 11, no. 4, pp. 748–753, 1993, https://doi.org/10.1116/1.578341.
28. H. Nasu, K. Tsunetomo, Y. Tokumitsu, and Y. Osaka, "Semiconducting CdTe Microcrystalline-Doped SiO2 Glass Thin Films Prepared by Rf-Sputtering," *Jpn. J. Appl. Phys.*, vol. 28, no. Part 2, No. 5, pp. L862–L864, May 1989, https://doi.org/10.1143/JJAP.28.L862.

29. J. Matsuoka, Y. Kawasaki, H. N. Hiroyuki Nasu, and K. K. Kanichi Kamiya, "Observation of Electroluminescence from CdSe-Microcrystal-Embedded Indium Tin Oxide Film," *Jpn. J. Appl. Phys.*, vol. 35, no. 7R, p. 3928, Jul. 1996, https://doi.org/10.1143/JJAP.35.3928.
30. X. Peng *et al.*, "Shape control of CdSe nanocrystals," *Nature*, vol. 404, no. 6773, pp. 59–61, Mar. 2000, https://doi.org/10.1038/35003535.
31. D. Vasudevan, R. R. Gaddam, A. Trinchi, and I. Cole, "Core-shell quantum dots: Properties and applications," *J. Alloys Compd.*, vol. 636, pp. 395–404, 2015, https://doi.org/10.1016/j.jallcom.2015.02.102.
32. M. M. Emara, S. J. Burya, and P. G. Van Patten, "Enhancement of biexciton generation via resonance energy transfer in nanoclusters of colloidal CdTe quantum dots for optical gain applications," *Mater. Chem. Phys.*, vol. 277, no. August 2020, p. 125540, Feb. 2022, https://doi.org/10.1016/j.matchemphys.2021.125540.
33. S. B. Brichkin, M. G. Spirin, E. G. Mart'yanova, D. A. Kozhukhina, V. V. Trepalin, and V. F. Razumov, "Specifics of the spectral and luminescent properties of ensembles of colloidal quantum dots," *High Energy Chem.*, vol. 50, no. 3, pp. 192–195, 2016, https://doi.org/10.1134/S0018143916030061.
34. X. Y. Qi *et al.*, "Cadmium telluride nanocrystals: Synthesis, growth mode and effect of reaction temperature on crystal structures," *Nano*, vol. 3, no. 2, pp. 109–115, 2008, https://doi.org/10.1142/S1793292008000873.
35. J. Sun, L. W. Wang, and W. E. Buhro, "Synthesis of cadmium telluride quantum wires and the similarity of their effective band gaps to those of equidiameter cadmium telluride quantum dots," *J. Am. Chem. Soc.*, vol. 130, no. 25, pp. 7997–8005, 2008, https://doi.org/10.1021/ja800837v.
36. H. Shen, J. Niu, H. Wang, and L. S. Li, "One-pot synthesis of high quality CdE (E = Te, Te xSe 1-x, Se) nanocrystals without using pyrophoric reagents," *Mater. Chem. Phys.*, vol. 135, no. 2–3, pp. 1122–1127, 2012, https://doi.org/10.1016/j.matchemphys.2012.06.032.
37. M. Shen *et al.*, "Luminescent properties of CdTe quantum dots synthesized using 3-mercaptopropionic acid reduction of tellurium dioxide directly," *Nanoscale Res. Lett.*, vol. 8, no. 1, p. 1, 2013, https://doi.org/10.1186/1556-276x-8-253.
38. A. R. Attar, D. E. Blumling, and K. L. Knappenberger, "Photodissociation of thioglycolic acid studied by femtosecond time-resolved transient absorption spectroscopy," *J. Chem. Phys.*, vol. 134, no. 2, 2011, https://doi.org/10.1063/1.3526746.
39. V. Swayambunathan, D. Hayes, K. H. Schmidt, Y. X. Liao, and D. Meisel, "Thiol surface complexation on growing cadmium sulfide clusters," *J. Am. Chem. Soc.*, vol. 112, no. 10, pp. 3831–3837, May 1990, https://doi.org/10.1021/ja00166a017.
40. J. Tauc, R. Grigorovici, and A. Vancu, "Optical Properties and Electronic Structure of Amorphous Germanium," *Phys. status solidi*, vol. 15, no. 2, pp. 627–637, 1966, https://doi.org/10.1002/pssb.19660150224.
41. W. W. Yu, L. Qu, W. Guo, and X. Peng, "Experimental determination of the extinction coefficient of CdTe, CdSe, and CdS nanocrystals," *Chem. Mater.*, vol. 15, no. 14, pp. 2854–2860, 2003, https://doi.org/10.1021/cm034081k.
42. Pilkington North America, "Architectural Glass Product Guide," 2017. https://www.pilkington.com/-/media/pilkington/site-content/usa/products/0907_catalog_pna2017_us_0710web.pdf
43. G. K. Wachutka, "Rigorous thermodynamic treatment of heat generation and conduction in semiconductor device modeling," *IEEE Trans. Comput. Des. Integr. Circuits Syst.*, vol. 9, no. 11, pp. 1141–1149, 1990, https://doi.org/10.1109/43.62751.
44. U. Lindefelt, "Current-density relations for nonisothermal modeling of degenerate heterostructure devices," *J. Appl. Phys.*, vol. 75, no. 2, pp. 958–966, 1994, https://doi.org/10.1063/1.356451.
45. A. H. Marshak and C. M. Van Vliet, "Electrical Current and Carrier Density in Degenerate Materials with Nonuniform Band Structure," *Proc. IEEE*, vol. 72, no. 2, pp. 148–164, 1984, https://doi.org/10.1109/PROC.1984.12836.

46. Y. Gao, S. Zhou, Y. Zhang, C. Dong, X. Pi, and D. Yang, "Doping silicon wafers with boron by use of silicon paste," *J. Mater. Sci. Technol.*, vol. 29, no. 7, pp. 652–654, 2013, https://doi.org/10.1016/j.jmst.2013.04.009.
47. A. Zazueta-Raynaud, R. Lopez-Delgado, J. E. Pelayo-Ceja, M. E. Alvarez-Ramos, and A. Ayon, "Utilization of down-shifting photoluminescent ZnO quantum dots on solar cells," *Mater. Res. Express*, vol. 4, no. 7, 2017, https://doi.org/10.1088/2053-1591/aa7824.
48. A. Luque and S. Hegedus, *Handbook of Photovoltaic Science and Engineering*. Chichester, UK: John Wiley & Sons, Ltd, 2003.

Index

A
Absorption coefficient, 121, 129, 176, 177, 196, 197, 205, 224–226, 300, 354, 376–382, 386
Aerogel, 150–162, 164
Anodized aluminium oxide (AAO), 357–362, 366
APbX3 photovoltaics, 232
Artificial photosynthesis, 133–145

B
Bandgap, 92, 99–101, 111, 112, 114, 122, 126–128, 135, 136, 138, 141, 155, 163, 169, 170, 191, 194, 195, 205, 206, 208, 209, 217, 239, 241, 249, 258, 260, 261, 279, 354–356, 364, 365, 377, 379–381
Berreman effect, 184, 185, 188–190, 200

C
Cadmium selenium (CdSe), 31–34, 77, 78, 137, 141, 151, 153, 155–164, 249
Cadmium telluride (CdTe), 33, 53, 77, 91, 115, 137, 151, 169, 205, 293, 310, 354, 374
Cadmium zinc telluride (CdZnTe), 111–131, 205, 206, 209–214, 216, 218, 219, 243, 244, 251, 261, 293
Cancer screening, 91–108
Carcinoembryonic antigen detection, 91–108
Cathodoluminescence (CL), 212, 217–219
CdS/CdTe nanowires, 357, 359
Cesium lead bromide ($CsPbBr_3$), 239, 240, 243, 246, 247, 249, 250, 284, 285, 287, 288, 293–305
Charge carrier dynamics, 138, 239–252
Charged particle and photon sensing, 296
Close space sublimation (CSS), 294–296, 304, 305
Cluster beam, 1–25
Colloids, 29–46, 54, 155–157, 378
Concentration factor, 373, 375–377, 381–383, 387, 388
Core-shell structures, 379, 380

D
Defect engineering, 205–219
Density functional theory (DFT), 163–165, 333
Dislocation filtering layers (DFL), 209–212
Doctor-blade coating, 280–281, 287

E
Electrocatalysts, 328, 330, 332, 336, 339, 344–346
Electroluminescence, 314
Electron transfer kinetics, 144
Electro-optic device, 71–85, 170
Electrospinning, 52, 56–57, 61–63
Elpasolites, 263–265
Emission quantum yield, 232–234
Epilayers and superlattices, 177–178

© The Editor(s) (if applicable) and The Author(s), under exclusive license to Springer Nature Switzerland AG 2024

S. Krishnamoorthy, K. (Kris) Iniewski (eds.), *Advances in Fabrication and Investigation of Nanomaterials for Industrial Applications*,
https://doi.org/10.1007/978-3-031-42700-8

Etch pit density (EPD) measurements, 212, 215
Explosives, 52, 54, 55, 61–65

F
Far-infrared reflectivity/transmission, 171–175, 177–178, 182, 183, 187, 188
Fingerprint detection, 65
Forensics, 51–66

G
Gallium arsenide (GaAs), 170, 171, 176–186, 191–196, 206–212, 215–219, 225, 245, 354
Gamma-ray, 170, 241, 261
Gamma-ray radiation detection, 239–252
Gamma-ray spectra, 261
Gamma-ray spectroscopy, 206
Graphene, 53, 55, 81, 334, 335, 356
Gas sensing, 6, 11, 12, 14

H
Halide perovskites, 135, 223, 224, 226, 227, 239–252, 277, 279, 283–288, 293–305, 309–317
Heteroepitaxial II-VI semiconductors, 219
High-energy radiation detectors, 257–269
High-resolution synchrotron extended x-ray absorption, 173
High-resolution x-ray diffraction, 213

I
II-VI semiconductors, 205–206, 219
Immunosensor, 91–108
Inter-particle charge transfer, 149–151, 159, 160, 162, 164

L
Large area perovskite solar modules, 311–314
Liquid crystal alignment, 71–85
Liquid crystals, 71–85, 94, 95, 107
Low-cost manufacturing of radiation detectors, 289
Luminescence, 149, 174, 217, 240, 250, 252, 262, 294
Luminescent solar concentrator, 373–389

M
Metal halide perovskite nanocrystal, 239, 241, 244, 246, 247, 250, 251, 276, 277, 279, 282–288
Metal halide perovskite solar cells, 309–317
Metal-nitrogen-carbon (M-N-C) catalysts, 330–341, 343, 345–347
Metal-organic frameworks (MOFs), 99, 339
Metal oxide nanostructures, 14
Molecular beam epitaxy (MBE), 169, 171, 172, 205, 206, 208–212, 217
Multilayer optics, 171, 183, 199

N
Nanofibers, 52, 53, 55–64
Nanoparticles, 18, 21, 25, 34, 35, 52–55, 63, 71–85, 135, 328–331, 342, 376, 382
Nanoporous AAO, 357, 359, 366
Nanostructured films, 1–25
Nematic liquid crystals (NLC), 71–85
NiO_2, 358, 359

O
Optical efficiency, 375–378, 381, 382
Oxygen reduction reaction, 325–347

P
Perovskite materials, 246, 260, 276–279, 281, 282, 285, 289
Perovskite photodetector, 282, 288
Photocatalysis, 99
Photoelectric, 91, 92, 102–104, 112–124, 277, 278
Photoelectrochemical sensor, 91–108
Photogenerated carrier recombination dynamics, 228, 386
Photoluminescence, 63, 75, 136, 143, 152, 155, 212, 228–231, 250, 269, 300, 375, 376, 379
Photovoltaic simulation, 383–388
Photovoltaic solar cells, 205, 353–366
Platinum-group metals (PGM), 25, 327, 330, 334, 341, 342, 344–347
Power conversion efficiency (PCEs), 223, 354, 357, 374, 375, 387, 388
Printable metal-halide perovskites, 283–288
Proton exchange membrane fuel cells, 325–347

Q
Quantum dots (QDs), 29–46, 53–55, 59, 61, 73, 77, 78, 133–145, 149–164, 170, 209, 219, 240, 249, 287, 288, 354, 373–389

R
Radiation detection, 239–252, 257–270, 275–280, 283–288, 294, 302–303
Raman scattering, 170, 173–174, 184, 188–190, 199
Roll-to-roll printing, 279–282, 287
Roll-to-roll production, 325
Room-temperature semiconductor radiation detectors, 257, 258

S
Scanning photodielectric spectroscopy (SPDS), 111–131
Scintillation radiation detector, 242
Semiconductor nanomaterials, 357
Semiconductor nanostructures, 135, 357
Single atom catalysts (SACs), 328–331, 334
Solar energy, 133, 326, 353, 360, 375
Sol-gel, 63, 153, 155
Solution processable perovskites, 279, 283, 285–287, 289
Spectroscopic ellipsometry, 174–176, 182
Strained CdZnTe/CdTe superlattice, 209, 213, 219
Successive Ionic Layer Adsorption and Reaction (SILAR), 30–33, 46
Supercapacitors, 353, 355–359, 366
Supersonic Cluster Beam Deposition (SCBD), 1–25

T
Thallium (Tl)-based materials, 257, 262
Thallium bromide (TlBr), 243, 248, 258–260
Thick $CsPbBr_3$ films, 294, 297
3D printing, 95
$TlPbI_3$ perovskite, 260, 261, 263, 269

U
Ultrasensitive detection, 55
Upscaling production of perovskite solar cells, 309, 310

W
Wettability, 15, 21–22
Wide-area coverage radiation detectors, 301
Wide-gap semiconductor, 137

X
X-ray and gamma-ray detector, 239–252, 258, 269